



**Universita' degli Studi di Brescia**

**DOTTORATO DI RICERCA IN PRECISION MEDICINE**

**settore scientifico disciplinare: MED/31 OTORINOLARINGOIATRIA**

**CICLO XXXV**

**Immune contexture monitoring in solid tumors  
focusing on Head and Neck Cancer**

**Francesco Missale (69793)**

Supervisor: Prof. William Vermi



## Contents

	<b>Page</b>
Abstract . . . . .	5
Riassunto . . . . .	7
<b>1 General introduction and outline of this thesis</b>	<b>9</b>
1.1 Cancer Immunosurveillance and Immunoediting . . . . .	9
1.2 The tumor immune contexture, friend or foe . . . . .	10
1.3 Head and neck cancer and tumor microenvironment . . . . .	11
1.4 The modern concept of precision oncology in Head and Neck Cancer . . . . .	12
1.5 Aims and outline of this thesis . . . . .	13
1.6 References . . . . .	14
<b>I Part One</b>	<b>21</b>
<b>2 Tumor-associated neutrophils in human carcinoma-draining lymph nodes</b>	<b>23</b>
<b>3 Pro-tumoral B cells in laryngeal cancer</b>	<b>45</b>
<b>4 Infiltrating CD8+CD28- T Lymphocytes in Head and Neck Cancer</b>	<b>83</b>
<b>5 Host Immune Features and Nodal Involvement Are Associated with Oncological Outcomes in OSCC</b>	<b>103</b>
<b>6 Immune-Contexture in Ovarian Cancer Subtypes</b>	<b>121</b>
<b>7 TIM4+FOLR2+ Macrophages Localized in TLS Correlate to an Active Immune Infiltrate Across Several Cancer Types</b>	<b>141</b>

---

<b>II Part Two</b>	<b>157</b>
<b>8 Predictive nomograms for oral tongue SCC</b>	<b>159</b>
<b>9 Compartmental surgery vs WLE in oral tongue and FOM cancer</b>	<b>173</b>
<b>10 Laryngeal Compartmentalization Does Not Affect the Prognosis of LSCC Treated by Total Laryngectomy</b>	<b>185</b>
<b>11 Validation of the ELS classification of glottic vascular changes as seen by NBI</b>	<b>205</b>
<b>12 Immunonutrition in head and neck surgery: analysis of peri-operative outcomes</b>	<b>219</b>
<b>13 Conclusion and future perspectives</b>	<b>235</b>
<b>14 List of publications 11/2019 - 11/2022</b>	<b>237</b>



## Abstract

Strong evidences demonstrate a close interplay between the immune system and the biological development and clinical progression of solid tumors. The functional orientation, density and location of immune cells in solid tumors is defined as *immune contexture*, whose composition is proved to be related with also the clinical behavior of the disease. Nevertheless, the current clinical management of patients affected by cancer does not take into account any immunological features either for the staging or for the treatment choices. Head and Neck Squamous Cell Carcinoma (HNSCC) represents the 7th most common cancer worldwide and it is characterized by a relatively poor prognosis and detrimental effect of treatments on the quality of life of patients. Beyond surgery and radiotherapy, few systemic treatments are available, mainly represented by platinum-based chemotherapy or cetuximab. Immunotherapy is a new therapeutical strategy, which is currently still limited to the palliative setting (recurrent not resectable or metastatic disease). The search for new biomarkers or possible new targetable mechanisms is meaningful. This thesis focuses on studying the role of three possible pro-tumoral immune populations in HNSCC: the tumor associated neutrophils (TAN), intratumoral B-cells with a immunosuppressive phenotype and the CD8+ T-regs. Biostatistical and bioinformatical techniques are applied to analyze complex information derived from multiparametric clinical and immunological variables and to validate in-situ derived findings through gene expression data from public available datasets. The second part of the thesis presents some relevant clinical research projects, aimed at improving precision oncology in HNSCC by developing survival prediction models, comparing alternative oncological procedures, validating new classifiers or testing the use of novel clinical protocols as the use of immunonutrition.



Forti evidenze dimostrano una stretta interazione tra il sistema immunitario e lo sviluppo biologico e la progressione clinica dei tumori solidi. Il fenotipo funzionale, la densità e localizzazione delle cellule immunitarie nei tumori solidi è definito come *immune contexture*, la cui composizione è stata dimostrata essere associata al comportamento clinico della malattia. Nonostante ciò, l'attuale gestione clinica dei pazienti affetti da cancro non tiene conto di alcuna caratteristica immunologica né per la stadiazione né per le scelte terapeutiche. Il tumore della testa e del collo (HNSCC) rappresenta il settimo tumore più comune al mondo ed è caratterizzato da una prognosi relativamente sfavorevole e dall'effetto negativo dei trattamenti sulla qualità della vita dei pazienti. Oltre alla chirurgia e alla radioterapia, sono disponibili pochi trattamenti sistemici, rappresentati principalmente dalla chemioterapia a base di platino-derivati o dal cetuximab. L'immunoterapia è una nuova strategia terapeutica ancora limitata al setting palliativo (malattia ricorrente non resecabile o metastatica). La ricerca di nuovi biomarcatori o possibili nuovi meccanismi target è molto rilevante quindi nel contesto clinico dell'HNSCC. In questa tesi ci si concentrerà sullo studio di tre possibili popolazioni immunitarie pro-tumorali studiate nell'HNSCC: i neutrofili tumore-associati (TAN), le cellule B intratumorali con fenotipo immunosoppressivo e i T-reg CD8+. Particolare attenzione è data all'applicazione di moderne tecniche biostatistiche e bioinformatiche per riassumere informazioni complesse derivate da variabili cliniche e immunologiche multiparametriche e per validare risultati derivati *in situ*, attraverso dati di espressione genica derivati da dataset pubblici. Infine, la seconda parte della tesi prenderà in considerazione progetti di ricerca clinica rilevanti, volti a migliorare l'oncologia di precisione nell'HNSCC, sviluppando modelli predittivi di sopravvivenza, confrontando procedure oncologiche alternative, validando nuovi classificatori o testando l'uso di nuovi protocolli clinici come l'uso dell'immunonutrizione.



## General introduction and outline of this thesis

### 1.1 Cancer Immunosurveillance and Immunoediting

The identification of a close interplay between the immune system and cancer cells dates back to 1970, when Burnet and Thomas theorized the immunosurveillance hypothesis, attributing to the immune system the role of recognizing and eliminating newly transformed cells [1]. Such theory was later supported by in-vivo experiments with the use of mice knockout for the recombina-1 or recombina-2 genes (RAG-1<sup>-/-</sup> or RAG-2<sup>-/-</sup>), a murine model lacking T, NKT and B lymphocytes, but with an intact myeloid compartment. Specifically, immunodeficient mice were more susceptible to spontaneous or carcinogen induced tumor compared to the immunocompetent counterpart [2]. This finding was confirmed also after depletion of single crucial components of the immune system, as NK lymphocytes, NKT lymphocytes, T lymphocytes [3,4], T $\alpha\beta$  lymphocytes and T $\gamma\delta$  lymphocytes [5], perforin [6-8] and IL-12 [3,9]. The immunosurveillance theory was thus proved in the murine models, giving to the immune system the role of recognizing and eliminating newly formed tumor cells. Evidence of this theory was also observed in human cancers, from epidemiological studies showing an increased rate of solid tumors in immunodeficient or immunosuppressed individuals, as observed in cohorts of transplanted patients [10], pharmacologically immunocompromised or of patients with primary [11], or acquired immunodeficiencies [12]. The crucial experiments, by Shankaran et al. in 2001, showed that the interplay between the immune system and tumor cells was far way more complex. Tumors generated in immunodeficient mice were eliminated when implanted in immunocompetent mice; on the contrary, those grown in immunocompetent mice display a progressive growth [2]. This observation established the concept of "Cancer Immunoediting", a process in which the immune system has both the ability to prevent and limit the development of neoplasms, but at the same time it sculpts the tumor mass with a selective pressure mechanism analogous to a Darwinian process. The elimination of highly immunogenic tumor cells, more easily recognizable and eliminable by the immune system, selects for less immunogenic neoplastic cells capable to elude the appropriate recognition and elimination by the immune system. Such process is envisioned in three phases, not necessarily temporally distinct, referred as "Elimination", "Equilibrium" and "Escape" [13]. During

the Escape phase, the tumor cells acquire sufficient genetic mutations to develop resistance to the immune-mediated recognition and elimination, and they can grow out of control in an immunocompetent individual being clinically evident as a solid tumor. In this phase multiple factors can play a crucial role, determining the immune evasion. Among the others, the alteration of tumor cells themselves, which does not allow recognition leads to resistance to elimination with the establishment of an immunosuppressive microenvironment at the tumor site through either the secretion of immunosuppressive cytokines, such as TGF- $\beta$ , IL-10 or VEGF, or cell-mediated mechanisms, by recruitment of Treg lymphocytes (CD4<sup>+</sup>CD25<sup>+</sup>) or by immunoregulatory molecules as PD-1 / PD-L1. The main strategies by which poorly immunogenic tumor cells overcome the control of the immune system are the loss of the expression of tumor antigens, the loss of the MHC class I complex, the insensitivity to IFN- $\gamma$  and the resistance to immune-mediated cytotoxic effects, with the activation of anti-apoptotic mechanisms (increased expression of STAT-3 or anti-apoptotic molecules as Bcl2) [14,15]. Therefore, the "escape" phase represents the failure of the immune system in controlling the tumor growth and is expressed clinically with the manifestation of the disease [16].

## 1.2 The tumor immune contexture, friend or foe

As soon as the interaction between the immune system and solid tumor was proven, the interest in studying the immune infiltrates in cancer exploded. The studies by J. Galon and co-authors on colorectal carcinoma are one of the milestones that opened the road to an extensive evaluation on the immune infiltrates in all tumor types. With an unbiased approach, based on objective quantification of immune infiltrates on tumor sections, they showed that the higher density and the location of lymphocyte subpopulations (CD3<sup>+</sup>, CD8<sup>+</sup> and CD45RO<sup>+</sup> T-cells) were correlated with a better prognosis, independently of the disease stage [17,18]. In the reviews by Friedman et al. in 2012 [19] and in 2017 [20], analyzing 200 articles involving more than 25000 patients, the presence of different immune cell subtypes resulted to be associated with different outcomes in a tumor-specific way. As leading findings, CD8<sup>+</sup> T cells infiltration or enrichment of tertiary lymphoid structures (TLS) are associated with a better oncological outcome, whereas M2 subtype macrophages with a worse outcome [20].

Among solid tumors, 90% of cancer-related deaths depends on the development of metastases [21]. For this reason the understanding of the molecular and immunological phenomena that could contribute to the metastatic process is crucial. The long-term aims are the identification of biomarkers that better stratify patients to the current available treatments or new compounds. The metastatic dissemination is a multi-phase process. Tumor cells located in the primary tumor should acquire the capability to invade lymphatic or hematic vessels (1), survive in the circulation (2), extravasate in distant sites (3), and here to adapt and proliferate (4) generating a distant metastasis [22-25].

As a consequence of the immunoediting theory, and the outstanding results obtained by Jerome Galon and co-authors studying the tumor microenvironment in colon cancer and its prognostic significance [18,26], the view on cancer has changed consistently and a tumor is no longer considered as a bulk

of malignant cancer cells, but rather as a complex environment, enriched by pro-tumoral immune cells corrupted by cancer itself or recruited into it, to form a self-sufficient biological structure [27]. The stromal component of the tumor microenvironment is composed of multiple different cell types, such as cancer-associated fibroblasts, neutrophils, macrophages, regulatory T cells, B-cells, myeloid-derived suppressor cells, natural killer cells, platelets, and mast cells. These subpopulations of cells can interact with each other as well as with cancer cells through complex communication networks based on various secreted cytokines, chemokines, growth factors, and proteins [28]. Several pre-clinical models suggest that immune cells populations of the tumor microenvironment could exert also pro-tumoral or immunosuppressive actions, such as the pro-tumoral tumor-associated macrophages (TAM2) [29,30], the pro-tumoral tumor-associated neutrophils (TAN2)[31], regulatory CD4<sup>+</sup> T-cells [32-34], regulatory CD8<sup>+</sup> T-cells [35-37] and regulatory B-cells [38]. The sum of pro-tumor and anti-tumor immune populations at the tumor site is defined as "immune contexture".

### **1.3 Head and neck cancer and tumor microenvironment**

Head and neck (H&N) cancers are one of the malignant tumors associated with the most severe impact on the quality of life of the patients, mainly related to the functional and aesthetic effect of the treatments, the relatively low responsiveness to treatment and severe drug-resistance with a small armamentarium of effective drugs [39]. Over 90% of these tumors are head and neck squamous cell carcinoma (HNSCC) [40], which represent the seventh most prevalent cancer worldwide [41,42]. Furthermore, the survival of patients affected by such tumors is poor; moreover, up to 25% of patients develop secondary cancer within five years after the diagnosis [43], related to the long-term pathogenetic effect of risk factors like tobacco, alcohol consumption, HPV and EBV infection [41,44,45]. The most relevant prognostic determinant of HNSCC tumors is still considered the presence of lymph node metastases, since metastatic lymphatic spread correlates with a significant decrease in the survival rate of patients [46]. Up to now, also in the recently revised version of the UICC TNM staging system in 2017, the overall stage, that should represent a predictor of overall survival, is derived from morphologic and morphometric features of the primary tumor and the clinical features of lymph node or distant site metastasis. The oropharyngeal site was the only one in which the evidence of an HPV etiology of the tumor, by overexpression of the p16 protein in tumor cells, can modify the staging system (with a more favorable outcome), despite the fact that changing of the treatment plan, for such tumors, is still not allowed outside from clinical trials [47-49]. As many other solid tumors, HNSCC develops in an immune suppressive contexture, [50]. Among HNSCC, the analysis of tumor-infiltrating immune cells, being T lymphocytes, B lymphocytes and tumor-associated macrophages as most studied populations, provided information on the prognosis, helping a better-tailored treatment for new patients [51]. In particular, about HNSCC, it is known that T CD3<sup>+</sup> and T CD8<sup>+</sup> lymphocytes are the predominant immune component being a favorable prognostic factors of overall survival [52], in agreement with what is already observed among solid tumors of different sites [53].

## **1.4 The modern concept of precision oncology in Head and Neck Cancer**

From a clinical point of view, the treatment of patients affected by Head and Neck Cancer is challenging. The anatomical structures of the head and neck region are crucial for several vital functions. On top of that, the attention to the aesthetic of the face is of most relevance when dealing with tumors located on or near the nose, the ear, the mouth, the eyes. Most of the tumors arising in this region are squamous cell carcinomas (HNSCC), for which the possible available treatment modalities are limited to surgery, radiotherapy, platinum-based chemotherapy (Cisplatin, Carboplatin), anti-EGFR monoclonal antibody (Cetuximab) and, lastly, still limited to the palliative setting, anti-PD-1 immunotherapy (Nivolumab and Pembrolizumab) [41]. The development of new technologies in the last 30 years permitted the improvement of the diagnostic evaluations, as shown for instance by the advent of high defined ultrasonography (US), computerized tomography (CT) and magnetic resonance imaging (MRI) scans [54], PET-CT [55], PET-MRI [56], high resolution and definition endoscopic imaging and bioendoscopy tools (NBI, SPIES, iSCAN) [57-59]. The routine use of such technologies in the clinical practice allows nowadays for an accurate macroscopic evaluation of the primary tumor, its anatomical location, the involvement of critical structures such as muscles, nerves, bone and other soft tissues, the involvement of the cervical nodes (in most of the cases the first metastatic station), and the screening for distant metastasis. Alongside, technical improvements were also achieved in surgical approaches with the advent of mini-invasive surgery such as transoral laser microsurgery, endoscopic endonasal surgery or robotic surgery [60], sentinel node procedure, microsurgical reconstructions, or with the advent of intensity-modulated radiotherapy (IMRT) or proton-therapy [41]. The aim of the application of such technical improvements is the achievement of an equally-radical treatment with less side effects, with the quality of life being one of the crucial parameters to take into account also during the decision-making process. Besides technical advancements, the availability of medical treatments for patient affected by HNSCC, in the curative setting, is still limited to the platinum-based regimen or to the use of Cetuximab [41]. As observed also for other solid tumors, an encouraging role for immunotherapy could be seen in head and neck cancer. The results of phase I-II trials in HNSCC suggest the best efficacy of immunotherapy in the neoadjuvant setting, before the standard of care, where the pathological response to immunotherapy represents a good biomarker for long-term good prognosis [61,62]. A better understanding of the mechanisms that take place inside the tumor, and specifically its interaction with the host's immune system, is a mandatory trajectory for the identification of new possible therapeutical targets or for the identification of subgroups of patients that could benefit of a de-intensified treatment regimen reducing the tremendous toxicity of the current treatments modalities for HNSCC.



## 1.5 Aims and outline of this thesis

This thesis is a collection of the most relevant works of the last three years of my career as researcher. This PhD project is the result of the conjunction of already acquired knowledges in the field of Head and Neck Cancer, as ENT specialist, the interest for the understanding of the complex relationship between the tumor microenvironment and the progression of solid tumors and the passion for the analytical processes (biostatistics and bioinformatics) involved in clinical and translational research. The presented studies are already published or submitted for publication in peer-review international journals. In the first part of the thesis, from **Chapter 2** to **Chapter 7**, I have reported the results of translational studies for which I had a primary or prominent role and focusing on the immunotexture in solid tumors including Head and Neck Cancer. Emphasis is given to the study of protumoral immune cell populations in HNSCC. In **Chapter 2** the prognostic role of tumor infiltrating neutrophils is investigated in oral cavity squamous cell carcinoma (OCSCC). An association between tumor-associated neutrophils (TAN) and a good prognosis was detected in early stages tumors and with a worse outcome in advanced ones, especially if TANs are present also in metastatic deposits in neck lymph nodes. This supports the hypothesis of a phenotypic change of TANs during the progression of the disease, from a predominant anti-tumor phenotype (TAN1) to a pro-tumoral one (TAN2). Through the analysis of a wide set of pan-cancer metastatic nodes, a recurrent occurrence of neutrophils in metastatic deposits was observed; TANs were also observed in lymphatic tumor emboli in primary tumors. These descriptive findings further support the hypothesis of the contribution of TAN in the lymphatic metastatic process. In **Chapter 3** an exploratory analysis is performed on a cohort of surgically treated laryngeal squamous cell carcinomas (LSCC) to understand whether the tumor microenvironment contribute to different oncological outcomes. Interestingly, the enrichment of the B-cell population resulted to be associated with a poorer distant recurrence along the follow-up time. This observation guided an in-depth research on tumor-infiltrating B-cells in patients that experienced distant metastases in order to understand the phenotype of these cells. Tumor infiltrating B-cells resulted naïve and expressing TGF $\beta$ , supporting the hypothesis of the presence of regulatory B-cells with a possible pro-tumoral effect in the tumor microenvironment of LSCC. The widely unexplored population of regulatory CD8<sup>+</sup> T-cells is investigated in the field of HNSCC in **Chapter 4**. This is a prospective observational study, for which I directly enrolled a cohort of patients affected by oropharyngeal squamous cell carcinomas and treated by non-surgical protocols. This project was aimed at studying the intratumoral and peripheral T-cells subpopulations by flow-cytometry. Patients that were refractory to radiotherapy had a higher fraction of intratumoral CD8<sup>+</sup> T-reg, whose enrichment was also associated with a poorer overall survival. In **Chapter 5**, by the use of a biostatistical technique aimed at summarizing multiple variables of a OCSCC dataset into metavariables (classifiers) including information from clinical parameters, peripheral immunological features and intratumoral ones were compared to the current TNM staging system, obtaining from most of the outcomes a better predictive performance. This project is meaningful as suggests a method easily applicable to summarize

and translate into clinical practice (for example in terms of survival prediction), the complex information obtainable by multiparametric immunological features. **Chapter 6** and **7** include research projects for which my contribution was deeply focused on bioinformatical analysis of public data repository, as gene expression data of the tissue cancer genome atlas (TCGA) projects. This allowed to validate preliminary findings obtained in the lab, thus strengthening and increasing the relevance of the in-situ obtained results. In the second part, from **Chapter 8** to **Chapter 12**, I have reported studies, for which I had a primary or prominent role, dealing with diagnostic, treatment stratification, personalized prognosis, innovative treatments for the management of patients affected by HNSCC.

## 1.6 References

- 1 Burnet FM. The concept of immunological surveillance. *Prog Exp Tumor Res* 1970;13:1-27.
- 2 Shankaran V, Ikeda H, Bruce AT, White JM, Swanson PE, Old LJ, et al. IFN $\gamma$  and lymphocytes prevent primary tumour development and shape tumour immunogenicity. *Nature* 2001;410:1107-11. doi:10.1038/35074122.
- 3 Smyth MJ, Thia KY, Street SE, Cretney E, Trapani JA, Taniguchi M, et al. Differential tumor surveillance by natural killer (NK) and NKT cells. *J Exp Med* 2000;191:661-8.
- 4 Smyth MJ, Godfrey DI, Trapani JA. A fresh look at tumor immunosurveillance and immunotherapy. *Nat Immunol* 2001;2:293-9. doi:10.1038/86297.
- 5 Girardi M, Oppenheim DE, Steele CR, Lewis JM, Glusac E, Filler R, et al. Regulation of cutaneous malignancy by gammadelta T cells. *Science* (80- ) 2001;294:605-9. doi:10.1126/science.1063916.
- 6 Street SE, Cretney E, Smyth MJ. Perforin and interferon-gamma activities independently control tumor initiation, growth, and metastasis. *Blood* 2001;97:192-7.
- 7 Smyth MJ, Thia KY, Street SE, MacGregor D, Godfrey DI, Trapani JA. Perforin-mediated cytotoxicity is critical for surveillance of spontaneous lymphoma. *J Exp Med* 2000;192:755-60.
- 8 van den Broek ME, Kagi D, Ossendorp F, Toes R, Vamvakas S, Lutz WK, et al. Decreased tumor surveillance in perforin-deficient mice. *J Exp Med* 1996;184:1781-90.
- 9 Noguchi Y, Jungbluth A, Richards EC, Old LJ. Effect of interleukin 12 on tumor induction by 3-methylcholanthrene. *Proc Natl Acad Sci U S A* 1996;93:11798-801.
- 10 Malignant Tumors in Organ Transplant Recipients. 1st ed. Springer-Verlag Berlin Heidelberg; 1970.

- 11 Gatti RA, Good RA. Occurrence of malignancy in immunodeficiency diseases. A literature review. *Cancer* 1971;28:89-98.
- 12 Boshoff C, Weiss R. AIDS-related malignancies. *Nat Rev Cancer* 2002;2:373-82. doi:10.1038/nrc797.
- 13 Dunn GP, Old LJ, Schreiber RD. The three Es of cancer immunoediting. *Annu Rev Immunol* 2004;22:329-60. doi:10.1146/annurev.immunol.22.012703.104803.
- 14 Schreiber RD, Old LJ, Smyth MJ. Cancer immunoediting: integrating immunity's roles in cancer suppression and promotion. *Science (80- )* 2011;331:1565-70. doi:10.1126/science.1203486.
- 15 Mittal D, Gubin MM, Schreiber RD, Smyth MJ. New insights into cancer immunoediting and its three component phases—elimination, equilibrium and escape. *Curr Opin Immunol* 2014;27:16-25. doi:10.1016/j.coi.2014.01.004.
- 16 Vesely MD, Kershaw MH, Schreiber RD, Smyth MJ. Natural innate and adaptive immunity to cancer. *Annu Rev Immunol* 2011;29:235-71. doi:10.1146/annurev-immunol-031210-101324.
- 17 Pages F, Berger A, Camus M, Sanchez-Cabo F, Costes A, Molidor R, et al. Effector memory T cells, early metastasis, and survival in colorectal cancer. *N Engl J Med* 2005;353:2654-66. doi:10.1056/NEJMoa051424.
- 18 Galon J, Costes A, Sanchez-Cabo F, Kirilovsky A, Mlecnik B, Lagorce-Pages C, et al. Type, density, and location of immune cells within human colorectal tumors predict clinical outcome. *Science (80- )* 2006;313:1960-4. doi:10.1126/science.1129139.
- 19 Fridman WH, Pages F, Sautes-Fridman C, Galon J. The immune contexture in human tumours: impact on clinical outcome. *Nat Rev Cancer* 2012;12:298-306. doi:10.1038/nrc3245.
- 20 Fridman WH, Zitvogel L, Sautés-Fridman C, Kroemer G. The immune contexture in cancer prognosis and treatment. *Nat Rev Clin Oncol* 2017;14:717-34. doi:10.1038/nrclinonc.2017.101.
- 21 Chaffer CL, Weinberg RA. A perspective on cancer cell metastasis. *Science* 2011;331:1559-64. doi:10.1126/science.1203543.
- 22 Fridlender ZG, Albelda SM. Tumor-associated neutrophils: friend or foe? *Carcinogenesis* 2012;33:949-55. doi:10.1093/carcin/bgs123.
- 23 Hanahan D, Weinberg RA. Hallmarks of cancer: the next generation. *Cell* 2011;144:646-74. doi:10.1016/j.cell.2011.02.013.
- 24 Pantel K, Brakenhoff RH. Dissecting the metastatic cascade. *Nat Rev Cancer* 2004;4:448-56. doi:10.1038/nrc1370.

- 25 van Zijl F, Krupitza G, Mikulits W. Initial steps of metastasis: cell invasion and endothelial transmigration. *Mutat Res* 2011;728:23-34. doi:10.1016/j.mrrev.2011.05.002.
- 26 Galon J, Mlecnik B, Bindea G, Angell HK, Berger A, Lagorce C, et al. Towards the introduction of the 'Immunoscore' in the classification of malignant tumours. *J Pathol* 2014;232:199-209. doi:10.1002/path.4287.
- 27 Peltanova B, Raudenska M, Masarik M. Effect of tumor microenvironment on pathogenesis of the head and neck squamous cell carcinoma: A systematic review. *Mol Cancer* 2019. doi:10.1186/s12943-019-0983-5.
- 28 Cavalieri S, Rivoltini L, Bergamini C, Locati LD, Licitra L, Bossi P. Immuno-oncology in head and neck squamous cell cancers: News from clinical trials, emerging predictive factors and unmet needs. *Cancer Treat Rev* 2018. doi:10.1016/j.ctrv.2018.03.003.
- 29 Mantovani A, Marchesi F, Malesci A, Laghi L, Allavena P. Tumour-associated macrophages as treatment targets in oncology. *Nat Rev Clin Oncol* 2017;14:399-416. doi:10.1038/nrclinonc.2016.217.
- 30 Cook J, Hagemann T. Tumour-associated macrophages and cancer. *Curr Opin Pharmacol* 2013;13:595-601. doi:10.1016/j.coph.2013.05.017.
- 31 Fridlender ZG, Sun J, Kim S, Kapoor V, Cheng G, Ling L, et al. Polarization of tumor-associated neutrophil phenotype by TGF-beta: 'N1' versus 'N2' TAN. *Cancer Cell* 2009;16:183-94. doi:10.1016/j.ccr.2009.06.017.
- 32 Plitas G, Rudensky AY. Regulatory T Cells in Cancer. *Annu Rev Cancer Biol* 2020;4:459-77. doi:10.1146/annurev-cancerbio-030419-033428.
- 33 McNally A, Hill GR, Sparwasser T, Thomas R, Steptoe RJ. CD4+CD25+ regulatory T cells control CD8+ T-cell effector differentiation by modulating IL-2 homeostasis. *Proc Natl Acad Sci U S A* 2011;108:7529-34. doi:10.1073/pnas.1103782108.
- 34 Yang P, Li Q-J, Feng Y, Zhang Y, Markowitz GJ, Ning S, et al. TGF- $\beta$ -miR-34a-CCL22 signaling-induced Treg cell recruitment promotes venous metastases of HBV-positive hepatocellular carcinoma. *Cancer Cell* 2012;22:291-303. doi:10.1016/j.ccr.2012.07.023.
- 35 Rifa'i M, Kawamoto Y, Nakashima I, Suzuki H. Essential roles of CD8+CD122+ regulatory T cells in the maintenance of T cell homeostasis. *J Exp Med* 2004;200:1123-34. doi:10.1084/jem.20040395.
- 36 Kim H-J, Verbinnen B, Tang X, Lu L, Cantor H. Inhibition of follicular T-helper cells by CD8(+) regulatory T cells is essential for self tolerance. *Nature* 2010;467:328-32. doi:10.1038/nature09370.

- 37 Mishra S, Liao W, Liu Y, Yang M, Ma C, Wu H, et al. TGF- $\beta$  and Eomes control the homeostasis of CD8<sup>+</sup> regulatory T cells. *J Exp Med* 2021;218. doi:10.1084/jem.20200030.
- 38 Wang L, Fu Y, Chu Y. Regulatory B Cells. *Adv Exp Med Biol* 2020;1254:87-103.
- 39 Melo Filho MR de, Rocha BA, Pires MB de O, Fonseca ES, Freitas EM de, Martelli H, et al. Quality of life of patients with head and neck cancer. *Braz J Otorhinolaryngol* 2013. doi:10.5935/1808-8694.20130014.
- 40 Stewart BW, Wild CP. World cancer report 2014. World Heal Organ 2014. doi:9283204298.
- 41 Chow LQM. Head and Neck Cancer. *N Engl J Med* 2020;382:60-72. doi:10.1056/NEJMra1715715.
- 42 Parkin DM, Bray F, Ferlay J, Pisani P. Global Cancer Statistics, 2002. *CA Cancer J Clin* 2005. doi:10.3322/canjclin.55.2.74.
- 43 Chuang SC, Scelo G, Tonita JM, Tamaro S, Jonasson JG, Kliewer E V., et al. Risk of second primary cancer among patients with head and neck cancers: A pooled analysis of 13 cancer registries. *Int J Cancer* 2008. doi:10.1002/ijc.23798.
- 44 Castellsagué X, Quintana MJ, Martínez MC, Nieto A, Sánchez MJ, Juan A, et al. The role of type of tobacco and type of alcoholic beverage in oral carcinogenesis. *Int J Cancer* 2004. doi:10.1002/ijc.11627.
- 45 Mork J, Lie AK, Glatte E, Clark S, Hallmans G, Jellum E, et al. Human Papillomavirus Infection as a Risk Factor for Squamous-Cell Carcinoma of the Head and Neck. *N Engl J Med* 2002. doi:10.1056/nejm200104123441503.
- 46 Brockstein B, Haraf DJ, Rademaker AW, Kies MS, Stenson KM, Rosen F, et al. Patterns of failure, prognostic factors and survival in locoregionally advanced head and neck cancer treated with concomitant chemoradiotherapy: A 9-year, 337-patient, multi-institutional experience. *Ann Oncol* 2004. doi:10.1093/annonc/mdh308.
- 47 Brierley JD, Gospodarowicz MK, Wittekind C. TNM classification of malignant tumours - 8th edition. Union Int Cancer Control 2017. doi:10.1002/ejoc.201200111.
- 48 Adelstein DJ, Ismaila N, Ku JA, Burtness B, Swiecicki PL, Mell L, et al. Role of Treatment Deintensification in the Management of p16<sup>+</sup> Oropharyngeal Cancer: ASCO Provisional Clinical Opinion. *J Clin Oncol Off J Am Soc Clin Oncol* 2019;37:1578-89. doi:10.1200/JCO.19.00441.
- 49 Sung S-Y, Kim Y-S, Kim SH, Lee SJ, Lee S-W, Kwak Y-K. Current Evidence of a Deintensification Strategy for Patients with HPV-Related Oropharyngeal Cancer. *Cancers (Basel)* 2022;14. doi:10.3390/cancers14163969.

- 50 Duray A, Demoulin S, Hubert P, Delvenne P, Saussez S. Immune Suppression in Head and Neck Cancers: A Review. *Clin Dev Immunol* 2010. doi:10.1155/2010/701657.
- 51 Lechner A, Schlösser H, Rothschild SI, Thelen M, Reuter S, Zentis P, et al. Characterization of tumor-associated T-lymphocyte subsets and immune checkpoint molecules in head and neck squamous cell carcinoma. *Oncotarget* 2017. doi:10.18632/oncotarget.17901.
- 52 Balermipas P, Rödel F, Rödel C, Krause M, Linge A, Lohaus F, et al. CD8+ tumour-infiltrating lymphocytes in relation to HPV status and clinical outcome in patients with head and neck cancer after postoperative chemoradiotherapy: A multicentre study of the German cancer consortium radiation oncology group (DKTK-ROG). *Int J Cancer* 2016. doi:10.1002/ijc.29683.
- 53 Fridman WH, Pagés F, Sauts-Fridman C, Galon J. The immune contexture in human tumours: Impact on clinical outcome. *Nat Rev Cancer* 2012. doi:10.1038/nrc3245.
- 54 Junn JC, Soderlund KA, Glastonbury CM. Imaging of Head and Neck Cancer With CT, MRI, and US. *Semin Nucl Med* 2021;51:3-12. doi:10.1053/j.semnuclmed.2020.07.005.
- 55 Wong WL. PET-CT for Staging and Detection of Recurrence of Head and Neck Cancer. *Semin Nucl Med* 2021;51:13-25. doi:10.1053/j.semnuclmed.2020.09.004.
- 56 Szyszko TA, Cook GJR. PET/CT and PET/MRI in head and neck malignancy. *Clin Radiol* 2018;73:60-9. doi:10.1016/j.crad.2017.09.001.
- 57 Hamada K, Ishihara R, Yamasaki Y, Akasaka T, Arao M, Iwatsubo T, et al. Transoral endoscopic examination of head and neck region. *Dig Endosc Off J Japan Gastroenterol Endosc Soc* 2018;30:516-21. doi:10.1111/den.13071.
- 58 Valls-Mateus M, Nogués-Sabaté A, Blanch JL, Bernal-Sprekelsen M, Avilés-Jurado FX, Vilaseca I. Narrow band imaging for head and neck malignancies: Lessons learned from mistakes. *Head Neck* 2018;40:1164-73. doi:10.1002/hed.25088.
- 59 Hawkshaw MJ, Sataloff JB, Sataloff RT. New concepts in vocal fold imaging: a review. *J Voice* 2013;27:738-43. doi:10.1016/j.jvoice.2013.05.011.
- 60 Finegersh A, Holsinger FC, Gross ND, Orosco RK. Robotic Head and Neck Surgery. *Surg Oncol Clin N Am* 2019;28:115-28. doi:10.1016/j.soc.2018.07.008.
- 61 Saito S, Shibata H, Adkins D, Uppaluri R. Neoadjuvant Immunotherapy Strategies in HPV-Related Head-and-Neck Cancer. *Curr Otorhinolaryngol Rep* 2022;10:108-15. doi:10.1007/s40136-021-00389-9.

- 62 Vos JL, Elbers JBW, Krijgsman O, Traets JJH, Qiao X, van der Leun AM, et al. Neoadjuvant immunotherapy with nivolumab and ipilimumab induces major pathological responses in patients with head and neck squamous cell carcinoma. *Nat Commun* 2021;12:7348. doi:10.1038/s41467-021-26472-9.





# **Part I**

## **Part One**



## Tumor-associated neutrophils in human carcinoma-draining lymph nodes

Lonardi, S.#  
**Missale F#**  
Calza, S.  
Bugatti, M.  
Vescovi, R.  
Debora, B.  
Uppaluri, R.  
Egloff, A. M.  
Mattavelli, D.  
Lombardi, D.  
Benerini Gatta, L.  
Marini, O.  
Tamassia, N.  
Gardiman, E.  
Cassatella, M. A.  
Scapini, P.  
Nicolai, P., &  
Vermi, W.

Clinical & translational immunology  
2021;10(2), e1252. <https://doi.org/10.1002/cti2.1252>.


#equally contributed as first authors



Supplementary material:

## ORIGINAL ARTICLE

**Tumor-associated neutrophils (TANs) in human carcinoma-draining lymph nodes: a novel TAN compartment**

Silvia Lonardi<sup>1,2,†</sup> , Francesco Missale<sup>3,4,†</sup>, Stefano Calza<sup>5,6,7</sup>, Mattia Bugatti<sup>1,2</sup>, Raffaella Vescovi<sup>1</sup>, Bresciani Debora<sup>1,2</sup>, Ravindra Uppaluri<sup>8</sup>, Ann Marie Egloff<sup>8</sup>, Davide Mattavelli<sup>3</sup>, Davide Lombardi<sup>2,3</sup>, Luisa Benerini Gatta<sup>1,2</sup>, Olivia Marini<sup>9</sup>, Nicola Tamassia<sup>9</sup>, Elisa Gardiman<sup>9</sup>, Marco A Cassatella<sup>9</sup>, Patrizia Scapini<sup>9</sup>, Piero Nicolai<sup>2,3</sup> & William Vermi<sup>1,2,10</sup>

<sup>1</sup>Section of Pathology, Department of Molecular and Translational Medicine, University of Brescia, Brescia, Italy

<sup>2</sup>ASST- Spedali Civili di Brescia, Brescia, Italy

<sup>3</sup>Unit of Otorhinolaryngology - Head and Neck Surgery, Department of Surgical Specialties, Radiological Sciences, and Public Health, University of Brescia, Brescia, Italy

<sup>4</sup>IRCCS Ospedale Policlinico San Martino, Unit of Otorhinolaryngology, Head and Neck Surgery, Department of Surgical and Diagnostic Integrated Sciences, University of Genoa, Genoa, Italy

<sup>5</sup>Unit of Biostatistics, Department of Molecular and Translational Medicine, University of Brescia, Brescia, Italy

<sup>6</sup>Department of Medical Epidemiology and Biostatistics, Karolinska Institutet, Stockholm, Sweden

<sup>7</sup>Big&Open Data Innovation Laboratory, University of Brescia, Brescia, Italy

<sup>8</sup>Department of Surgery/Otolaryngology, Brigham and Women's Hospital and Dana-Farber Cancer Institute and Harvard Medical School, Boston, MA, USA

<sup>9</sup>Section of General Pathology, Department of Medicine, University of Verona, Verona, Italy

<sup>10</sup>Department of Pathology and Immunology, Washington University, Saint Louis, MO, USA

**Correspondence**

W Vermi, Department of Molecular and Translational Medicine, Section of Pathology, P.le Spedali Civili 1, 25123 Brescia, Italy.  
E-mail: william.vermi@unibs.it

<sup>†</sup>Equal contributors.

Received 28 August 2020;  
Revised 4 December 2020  
and 19 January 2021;  
Accepted 19 January 2021

doi: 10.1002/cti2.1252

*Clinical & Translational Immunology*  
2021; 10: e1252

**Abstract**

**Objectives.** The role of tumor-associated neutrophils (TANs) in the nodal spread of cancer cells remains unexplored. The present study evaluates the occurrence and clinical significance of human nodal TANs. **Methods.** The relevance, derivation, phenotype and interactions of nodal TANs were explored *via* a large immunohistochemical analysis of carcinoma-draining lymph nodes, and their clinical significance was evaluated on a retrospective cohort of oral squamous cell carcinomas (OSCC). The tumor-promoting function of nodal TAN was probed in the OSCC TCGA dataset combining TAN and epithelial-to-mesenchymal transition (EMT) signatures. **Results.** The pan-carcinoma screening identified a consistent infiltration (59%) of CD66b<sup>+</sup> TANs in tumor-draining lymph nodes (TDLNs). Microscopic findings, including the occurrence of intra-lymphatic conjugates of TANs and cancer cells, indicate that TANs migrate through lymphatic vessels. *In vitro* experiments revealed that OSCC cell lines sustain neutrophil viability and activation via release of GM-CSF. Moreover, by retrospective analysis, a high CD66b<sup>+</sup> TAN density in M-TDLNs of OSCC ( $n = 182$  patients) predicted a worse prognosis. The analysis of the OSCC-TCGA dataset unveiled that the expression of a set of neutrophil-specific genes in the primary tumor (PT) is highly associated with an EMT signature, which predicts nodal spread. Accordingly, in the PT of OSCC cases, CD66b<sup>+</sup>TANs co-localised with PDPN<sup>+</sup>S100A9<sup>-</sup> EMT-switched tumor cells in areas of

lymphangiogenesis. The pro-EMT signature is lacking in peripheral blood neutrophils from OSCC patients, suggesting tissue skewing of TANs. **Conclusion.** Our findings are consistent with a novel pro-tumoral TAN compartment that may promote nodal spread *via* EMT, through the lymphatics.

**Keywords:** carcinoma, epithelial-to-mesenchymal transition, lymph nodes, metastasis, tumor-associated neutrophils

### INTRODUCTION

Tumor-associated myeloid cells encompass a large variety of circulating and tissue cellular components at various stages of differentiation. Among them, tumor-associated macrophages, dendritic cells and neutrophils represent the most well-characterised cell populations.<sup>1-3</sup> As a group, tumor-associated myeloid cells exert pro-tumor functions, but recent data have challenged this view, suggesting an extreme plasticity of these cells modulated by the tumor microenvironment at various disease stages.<sup>4</sup>

Emergency granulopoiesis<sup>5</sup> is prominent in late-stage cancer and mostly accounts for the high neutrophil count and the altered neutrophil-to-lymphocyte ratio (NLR) in advanced stages. Within the expanded granulocyte compartment, various subpopulations have been identified based on their ontogeny, fraction in the density gradient separation, phenotype and function.<sup>5-7</sup> Among the circulating neutrophils, immunosuppressive low-density neutrophils (LDNs), known as polymorphonuclear myeloid-derived suppressor cells (PMN-MDSCs), have recently gained great attention.<sup>7</sup> An additional granulocyte population is represented by neutrophils found within the tumor tissues, the so-called tumor-associated neutrophils (TANs).<sup>8</sup> Their connection with LDNs/PMN-MDSCs and normal circulating neutrophils still remains unclear due to the lack of specific markers. Similarly to tumor-associated macrophages,<sup>2</sup> TANs can be polarised *in vitro*.<sup>9,10</sup> N1-type TANs, induced by type I IFN, mainly exert anti-tumoral functions<sup>10</sup> and promote cancer cell elimination. On the contrary, N2-type TANs are TGF- $\beta$ -driven and sustain tumor cell proliferation, angiogenesis, invasion, metastasis and immune escape.<sup>8,9,11</sup> Data on TAN polarisation are limited to murine models, and it is still unknown whether human TANs display similar polarisation. Most of the studies performed in retrospective cancer cohorts<sup>12</sup> have supported a pro-tumor function of

TANs, with a high TAN tumor density significantly associated with a worse outcome.<sup>13</sup> Although this finding supports a dominant N2 polarisation of TANs in human cancer, emerging data have revealed extreme plasticity of these cells. Specifically, when purified from early-stage cancers, TANs exert anti-tumor activities and display a hybrid phenotype together with antigen-presenting cell features.<sup>14,15</sup>

Data on the biological and clinical significance of TANs have been obtained with the leading assumption that they execute their programs at the primary tumor (PT) site or in distant metastasis and largely ignoring their role in the tumor-draining lymph nodes (TDLNs). Nodal colonisation by cancer cells is a harbinger of systemic tumor spread and this is clinically relevant in a significant fraction of cancer types.<sup>16</sup> In addition, TDLNs are crucial sites for the organisation of the immune response to tumor antigens. A significant component of the tumor-promoting activity of LDNs/PMN-MDSCs and TANs derives from their negative modulation of the anti-tumor T-cell response.<sup>5,7,8</sup> Recent studies in mouse models have shown that neutrophil entry into the node results in a potent negative regulation of the specific T-cell response to pathogens.<sup>17-19</sup> However, very limited data are available on the identification of nodal TANs and their characterisation during cancer evolution in humans.

Herein, by performing a screening of human cancer tissues including PTs and TDLNs, we identified that high CD66b<sup>+</sup> TAN density is common in TDLNs from various primary sites. CD66b<sup>+</sup> TANs in TDLNs co-express classical neutrophil markers, as well as the recently identified markers of PMN-MDSCs such as S100A9,<sup>20</sup> arginase-1, pSTAT3 and cEBP $\beta$ .<sup>21</sup> Our data support the notion that TANs could enter the TDLN via lymphatic vessels, forming intraluminal conjugates with cancer cells. The preferential TAN interplay with cancer cells has

recently been reported including in squamous cell carcinomas (SCC).<sup>22–25</sup> By the analysis of a retrospective cohort, colonisation of carcinoma-draining lymph nodes by TANs predicts poor outcome in advanced oral squamous cell cancer (OSCC). Accordingly, increased CD66b<sup>+</sup> TAN density correlated with recurrent head and neck SCC. By *in silico* evaluation of the OSCC TCGA dataset, we found that expression of a set of neutrophil-specific genes at the PT is associated with an epithelial-to-mesenchymal transition (EMT) signature, the latter known to predict nodal spread in OSCC.<sup>26</sup> These findings highlight a hitherto unrecognised contribution of TANs in nodal colonisation by modulating EMT-dependent lymphatic spread.

## RESULTS

### CD66b<sup>+</sup> TANs recurrently accumulate in carcinoma-draining lymph nodes

A large number of studies have documented the clinical relevance of TANs infiltrating the primary tumor (PT) site and distant metastasis.<sup>9,13</sup> We recently observed that CD66b<sup>+</sup> TANs are also found in metastatic tumor-draining lymph nodes (M-TDLNs) from patients with colon carcinomas.<sup>27</sup> To further follow up this finding, we extended our characterisation to a larger cohort of cancer patients. Compared to other myeloid markers, CD66b is selectively expressed by granulocytes. Clone G10F5 is suitable for staining on FFPE sections and, among immune cells, it is selectively restricted to mature neutrophils, as demonstrated by the analysis of primary ( $n = 6$ ) and secondary ( $n = 30$ ) lymphoid organs (Supplementary figure 1a–h). In inflamed lymph nodes from non-tumor-bearing hosts ( $n = 21$ ), CD66b<sup>+</sup> neutrophils are generally scant and limited to the HEV dilated lumen (Supplementary figure 1e) with the exception of suppurative necrotising lymphadenitis of infectious origin ( $n = 3$ ; Supplementary figure 1f). By using archival material, we analysed a total of 278 M-TDLNs of carcinomas from various primary sites (Supplementary table 1). Nodal localisation of CD66b<sup>+</sup> TANs was observed in 59% of M-TDLNs ( $n = 165/278$ ). Based on a three-tiered scoring system (score 0, 1 and 2; illustrated in Supplementary figure 2 and detailed in the Methods), CD66b<sup>+</sup> TAN infiltration was highly dense (score 2) in 31.5% of the M-TDLNs ( $n = 52/$

165) from various primary sites and with different histologies (Figure 1a, Supplementary figure 2 and Supplementary table 1). Dense CD66b<sup>+</sup> TAN infiltration was common in head and neck squamous cell carcinomas, adenocarcinomas of the gastrointestinal tract, of the pancreas, of the thyroid and ovary, as well as in urothelial bladder cancer. On the contrary, CD66b<sup>+</sup> TANs were rarely observed in breast carcinoma (Supplementary table 1 and Figure 1a). We extended the latter finding on breast carcinoma to an additional cohort ( $n = 38$ ) and compared concurrently removed M-TDLNs and PT ( $n = 22$ ). A low CD66b<sup>+</sup> TAN density was confirmed in the majority of the cases including in the PTs (Supplementary figure 2i, j).

In term of nodal localisation (Figure 1b–f and Supplementary figure 3), CD66b<sup>+</sup> TANs in M-TDLNs were localised within and immediately around the metastatic deposits (M-TDLN<sup>M</sup>) ( $n = 100/165$ ; 60.6% CI<sub>95%</sub> 52.7–68.1%) (Figure 1b and d green asterisks). They were also present in the remaining spared nodal parenchyma (M-TDLN<sup>P</sup>), where they were located mainly within the lumen of marginal, intermediate and medullary lymphatic sinuses ( $n = 90/165$ ; 54.5% CI<sub>95%</sub> 46.6–62.3%; Figure 1b, c and e red asterisks). The identity of the expanded lymphatic sinuses was confirmed by using a set of endothelial cell markers including podoplanin, CD31, Lyve-1, CD34, ERG, Factor VIII, and CLA/HECA 452 (Figure 1f, Supplementary figure 4a–e) in M-TDLNs cases ( $n = 10$ ). CD66b<sup>+</sup> TANs frequently engulfed some dilated HEVs (Supplementary figure 4f). However, as evaluated by double immunohistochemistry, CD66b<sup>+</sup> TANs were only rarely observed as transmigrating cells (Supplementary figure 4g) or closely surrounding HEV ( $n = 10$ ).

The expression of a panel of neutrophil-specific molecules suitable for archival tissue was analysed in a set of M-TDLNs and matched PTs ( $n = 9$ ). CD66b<sup>+</sup> TANs showed a segmented nucleus and co-expressed CD11b, CD10, CD16, myeloperoxidase, neutrophil elastase and cytoplasmic granule-associated molecules confirming their neutrophil identity and mature phenotype (Supplementary figure 5a–j).

### CD66b<sup>+</sup> TANs engulf lymphatic vessels of the PTs and predict the TDLN colonisation of cancer cells

Recently, by using murine models, a number of studies have shown that neutrophils can also

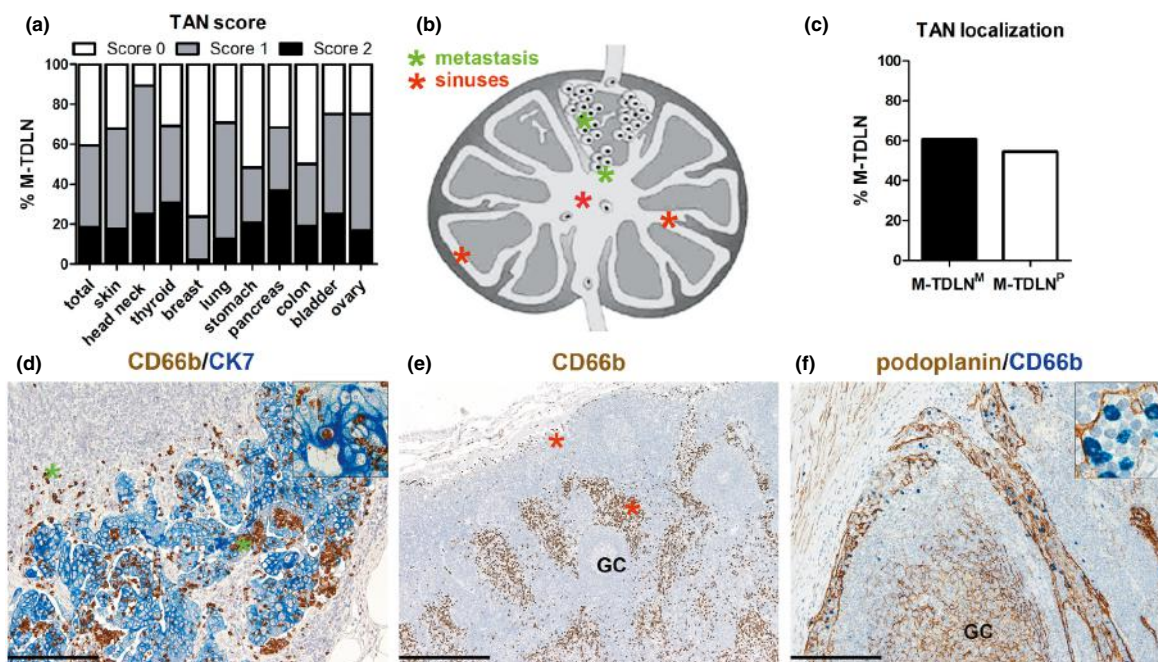


**Figure 1.** CD66b<sup>+</sup> TAN density and localisation in M-TDLN. **(a)** The density of CD66b<sup>+</sup> TANs expressed as TAN score (S0 = white, S1 = grey, S2 = black; three-tiered score is reported in the Methods section) in 278 M-TDLNs obtained from various primary carcinomas. **(b)** The distribution of CD66b<sup>+</sup> TANs in different LN compartments (red asterisks indicate marginal, intermediate sinuses and medullary sinuses whereas green asterisks indicate CD66b<sup>+</sup> cells within and around the metastatic nest). **(c)** The density of CD66b<sup>+</sup> TANs localised in the metastatic nest (M-TDLN<sup>M</sup>, black column) and in the surrounding nodal parenchyma (M-TDLN<sup>P</sup>, white column). Sections are from cases of M-TDLN of colon carcinoma **(d)** and head and neck squamous cell carcinoma **(e, f)**, stained as labelled (CK = cytokeratin 7) and illustrating CD66b<sup>+</sup> TANs within and around **(d, green asterisks)** the metastatic nests, within marginal and intermediate sinuses **(e, red asterisk and f)**. In **f**, lymphatic sinuses are identified by positivity for podoplanin. Sections are counterstained with haematoxylin. Original magnification: 40× **(e, scale bar 500 μm)**, 100× **(d, f, scale bar 200 μm)**, 400× (inset in **d**), 600× (inset in **f**). GC, germinal centre.

traffic through the lymph in response to pathogens,<sup>17,18,28</sup> raising the possibility that neutrophils modulate adaptive immunity directly within the lymph node.<sup>29</sup> Our data on the localisation of CD66b<sup>+</sup> TANs in nodal sinuses of TDLNs strongly support their migration from the primary tumor site through the lymphatic system. This hypothesis is further strengthened by a set of indirect findings. First, CD66b<sup>+</sup> TANs from M-TDLNs are negative for active caspase-3 ( $n = 10$ ) and ki-67 (Figure 2a–d) ( $n = 13$ ), indicating that the CD66b<sup>+</sup>TAN pool is less susceptible to spontaneous apoptosis and independent from local self-renewal, as other tumor-associated innate components.<sup>30</sup> Moreover, by comparative analysis of PTs and matched M-TDLNs ( $n = 45$ ), we found a high correlation (Spearman  $r = 0.77$ ;  $P < 0.0001$ ) between CD66b<sup>+</sup> TAN density scores (Supplementary figure 2g–l). Finally, as observed by double immunohistochemistry on serial

sections of M-TDLNs ( $n = 4$ ), CD66b<sup>+</sup> TANs in the PTs were often detected within enlarged lymphatic vessels in the form of multicellular tumor emboli admixed with carcinoma cells (Figure 2e and f), T cells (Figure 2g) and macrophages (Figure 2h). Remarkably, this multicellular interaction was not limited to the PT lymphatic vessels, but was also detectable within the marginal sinuses of M-TDLNs (Figure 2i;  $n = 5$ ). TAN migration *via* lymphatics requires endothelial activation for adhesion, integrin-mediated binding through ICAM-1 and VCAM-1 and CXCL8-dependent chemotaxis.<sup>31–33</sup> We found that CXCL8 is expressed in PT cases ( $n = 5$ ) with massive CD66b<sup>+</sup> TAN embolisation (Figure 2j and k), with the main cellular source represented by the CD66b<sup>+</sup> TANs themselves (Figure 2j and inset); CXCL8<sup>+</sup>CD66b<sup>+</sup> TANs were also detected in lymphatic sinuses of M-TDLNs (Figure 2l). Since TANs and tumor cells share their path to TDLNs, it

is conceivable that TANs contribute to organising the pre-metastatic niche, as previously proposed for distant metastasis.<sup>3,34</sup> We thus extended our analysis to 175 non-metastatic TDLNs (NM-TDLNs, Supplementary table 1). Notably, we also observed nodal localisation of CD66b<sup>+</sup> TANs in a significant fraction of the NM-TDLNs (77/175, 44.0% CI<sub>95%</sub> 36.5–51.7%). In terms of nodal localisation in NM-TDLNs, high CD66b<sup>+</sup> TAN density was found within the lymphatic sinuses (67/77, 87.0% CI<sub>95%</sub> 77.4–93.6%; Supplementary figures 3 and 4). Also, within the nodal sinuses, CD66b<sup>+</sup> TANs co-existed with numerous CD163<sup>+</sup> macrophages and CD3<sup>+</sup> lymphocytes ( $n = 5$ ; Supplementary figure 4h, i). These findings suggest that multiple interactions of TANs within the lymphatic sinuses might occur and may establish a pre-metastatic niche in TDLNs similar to distant sites.<sup>35,36</sup>

#### **CD66b<sup>+</sup> TAN immune-contexture in squamous cell carcinoma of the oral cavity (OSCC)**

In our screening cohort, CD66b<sup>+</sup> TAN infiltration in TDLNs was striking in head and neck squamous cell carcinoma (Figure 1a, Supplementary table 1). By co-culture experiments combining circulating neutrophils with three human OSCC lines, we found that OSCC cells provide a significant survival signal to neutrophils as measured by Vibrant dye assay (Figure 3a and Supplementary figure 6). A similar response, albeit attenuated, was seen with exposure of neutrophils to OSCC-derived supernatants (Figure 3b), which also induced neutrophil activation as revealed by membrane up-regulation of CD11b (Figure 3c) and down-regulation of CD62L (Figure 3d). By ELISA and blockade experiments, we found these effects were mostly dependent on GM-CSF, but not IL-6, released by OSCC cells (Figure 3b–e). To establish the clinical significance of CD66b<sup>+</sup> TAN infiltration, we measured CD66b<sup>+</sup> TAN density in a large retrospective cohort of OSCC ( $n = 182$ ). We identified OSCC patients who underwent radical surgery of the PT with node dissection. Clinical details of the cohort are reported in Supplementary tables 2 and 4. A representative tissue block of the PT and at least one block containing multiple TDLNs were available for the analysis. For N<sup>+</sup> patients ( $\geq$  Stage III AJCC), M-TDLNs were included (Supplementary figure 7). Data and representative images are shown in

Figure 3, Supplementary figure 8 and Supplementary tables 2 and 3. In the PT, we analysed a mean tumor area of  $105 \pm 71 \text{ mm}^2$ . The median density of CD66b<sup>+</sup> TANs was 175 cells  $\text{mm}^{-2}$ , and it was significantly higher in the invasive margin (IM) compared to the centre of the tumor (CT) (194 cells  $\text{mm}^{-2}$  vs 155 cells  $\text{mm}^{-2}$ ;  $P < 0.0001$ ; Supplementary table 4, Figure 3f).

We subsequently tested CD66b<sup>+</sup> TAN density in TDLNs by analysing M-TDLNs ( $n = 219$ ), and NM-TDLNs ( $n = 626$ ). For M-TDLNs, counts were also performed in the two distinct compartments, the metastatic nest (M-TDLN<sup>M</sup>) and the surrounding nodal parenchyma (M-TDLN<sup>P</sup>), the latter mainly accounting for CD66b<sup>+</sup> TANs within the lymphatic sinuses. TAN density in the PT showed a strong direct correlation with TAN density in TDLNs, particularly in the M-TDLNs ( $r = 0.5$ ;  $P < 0.001$ ; Figure 3g, Supplementary table 4). Remarkably, the strongest correlation between sub-regions was observed between the CT of the PT and the M-TDLN<sup>M</sup> (Spearman  $r = 0.49$ ,  $P < 0.001$ ; Figure 3g), consistent with CT CD66b<sup>+</sup> TANs receiving an appropriate imprinting signal(s) to establish a nodal pre-metastatic niche.

#### **Clinical significance of TAN immune-contexture in OSCC compartments**

Data on the prognostic significance of TAN density in human cancer are still inconclusive. We tested the clinical relevance of CD66b<sup>+</sup> TAN density in PTs and TDLNs. Univariate analysis of clinical-pathologic prognosticators for overall survival (OS) confirms that T stage, AJCC stage, nodal status and lympho-vascular invasion represented the strongest prognostic factors (Supplementary table 2). In particular and as previously recognised,<sup>37</sup> the occurrence of extracapsular spread (ECS) resulted in a striking decrease of survival estimates in patients with nodal metastasis. Moreover, the multivariable analysis confirmed nodal status as the most powerful independent prognosticator (Supplementary table 2). We then tested the prognostic significance of CD66b<sup>+</sup> TAN, as continuous variable, by performing a multivariable analysis including interaction terms in the model. Of note, when measured in the entire tumor area, the CD66b<sup>+</sup> TAN density was not significantly associated with prognosis. However, CD66b<sup>+</sup> TAN densities measured at the CT or at the IM were predictive of survival ( $P = 0.019$  and  $P = 0.033$ ,



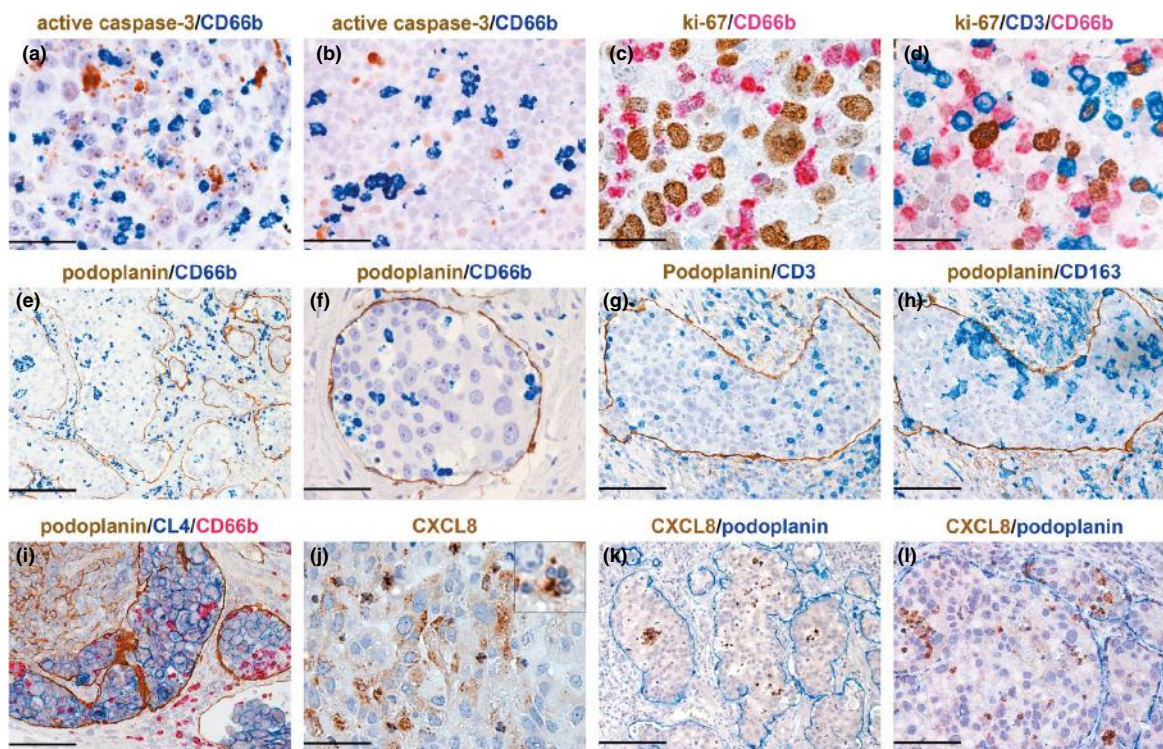


**Figure 2.** Lymphatic derivation of nodal CD66b<sup>+</sup> TANs. Sections of M-TDLNs (**a-d, i, l**) [from lung carcinoma (**a-d**) and gastric carcinoma (**i, l**)] and of PT (**e-h, j, k**) [from gastric (**e, f, k**) and lung (**g, h, j**) carcinomas] stained as labelled. As illustrated by double stain, most of CD66b<sup>+</sup> TANs from M-TDLNs are negative for active caspase-3 (**a, b**) and ki-67 (**c, d**) in both M-TDLN compartments (M-TDLN<sup>M</sup> [**a, c**]; M-TDLN<sup>P</sup> [**b, d**]). In primary carcinomas, CD66b<sup>+</sup> TANs are found within podoplanin<sup>+</sup> lymphatic vessels (**e, f**) similarly to CD3<sup>+</sup> T cells (**g**) and CD163<sup>+</sup> macrophages (**h**), frequently admixed to carcinoma cells (**e-h**); this finding is confirmed in M-TDLN by a triple stain for podoplanin, CD66b and the carcinoma cell marker claudin 4 (CL4) (**i**). Neoplastic cells (**j**) and TANs (inset in **j, k** and **l**) express CXCL8, also within lymphatic vessels (**k, l**). The latter finding is observed in a primary gastric carcinoma (**k**) and in the corresponding M-TDLN (**l**). Sections are counterstained with haematoxylin. Original magnification: 100× (**e, k**, scale bar 200 μm), 200× (**g-i, l**, scale bar 100 μm), 400× (**a, b, f, j**, scale bar 50 μm), 600× (**c, d** and inset in **j**, scale bar 33 μm).

respectively; Table 1). Moreover, a significant interaction of the variables was identified with the AJCC stage ( $P = 0.013$  and  $P = 0.013$ , respectively; Table 1). Specifically, a higher CD66b<sup>+</sup> TAN density in the IM associated with worse prognosis in early stages I and II (H.R. 1.53, 0.87–2.71), whereas it predicted a better outcome in advanced stages III and IV (H.R. 0.42, 0.16–1.11; Figure 3h). By contrast, a higher CD66b<sup>+</sup> TAN density in the CT associated with worse prognosis in advanced stages III-IV (H.R. 1.59, 1.06–2.39) and with a better outcome in earlier stages I-II (H.R. 0.42, 0.16–1.11; Figure 3i and j).

Including M-TDLNs TAN densities, thus limiting the analysis to N<sup>+</sup> patients, a higher TAN density in the M-TDLN<sup>M</sup> was associated with worse prognosis ( $P = 0.004$ ; Figure 3k and l), suggesting

a pro-tumor function of nodal TANs. The significant interaction detected between M-TDLNs TAN density and ECS status ( $P = 0.036$ ) led to a stronger effect of the M-TDLNs TAN density on the outcome prediction in ECS positive patients (H.R. 2.19, 1.28–3.73) compared to ECS negative ones (1.22, 1.00–1.48; Table 1, Figure 3l).

We further extended these analyses on the clinical significance of CD66b<sup>+</sup> TAN<sup>Hi</sup> in the TDLN<sup>M</sup> by identifying the appropriate cut-off of TAN density at 163 cells mm<sup>-2</sup> ( $P = 0.07$ ). Of note, CD66b<sup>+</sup> TAN<sup>Hi</sup> density in the M-TDLN<sup>M</sup> confirms its detrimental effect in terms of 5 year-OS (14% CI<sub>95%</sub> 4–52%, vs 49% CI<sub>95%</sub> 37–63% Figure 3m). Moreover, when the ECS was considered, the M-TDLN<sup>M</sup> CD66b<sup>+</sup> TAN<sup>Hi</sup> / ECS<sup>+</sup> group showed the worst OS (2y-OS 17% CI<sub>95%</sub> 3–99%, 5y-OS:

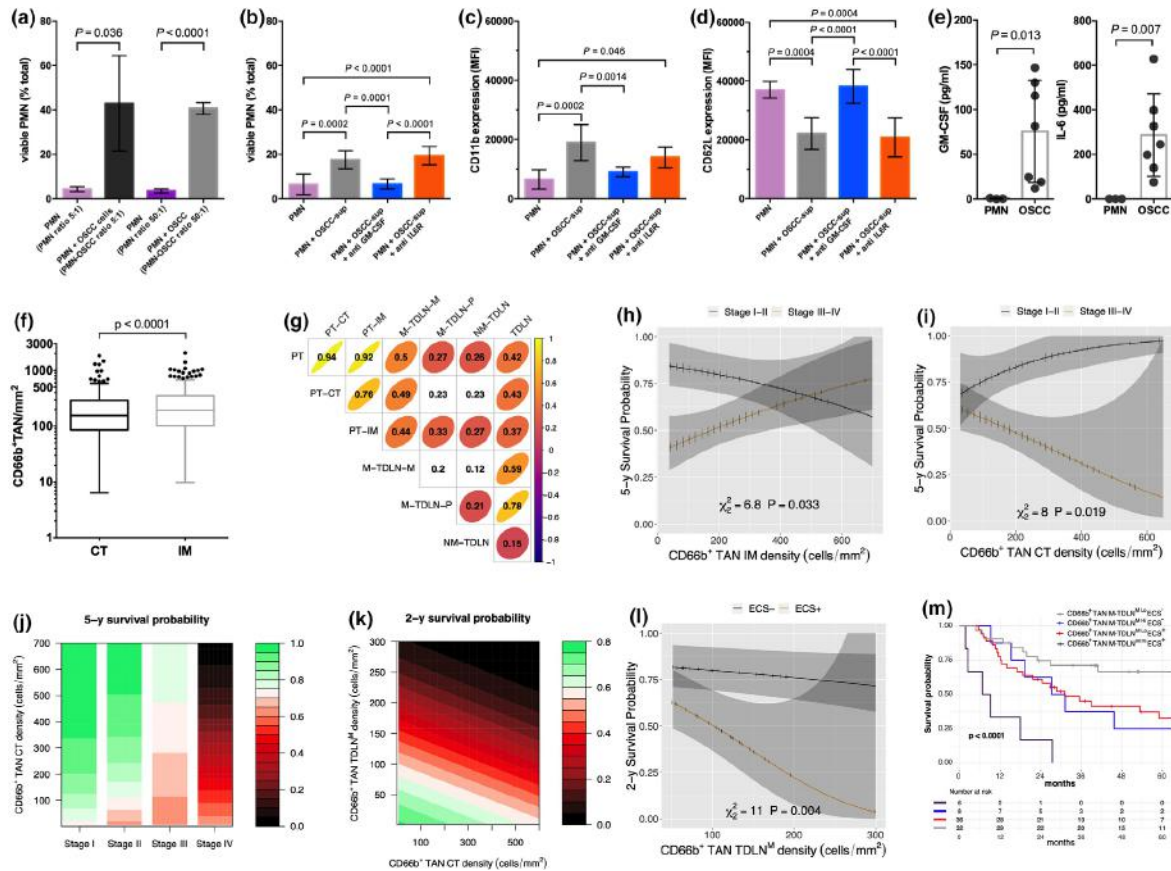


**Figure 3.** Clinical significance of CD66b<sup>+</sup> TANs in OSCC primary tumors (PTs) and TDLNs. Bar plots indicate the mean  $\pm$  SD percentage of alive PMN after co-culture for 40 h with or without OSCC cell lines (SCC-4,  $n = 3$ ; SCC-25,  $n = 2$  or CAL-27,  $n = 2$ ) (a). PMN negative for vibrant staining were considered to be viable (see the Methods section); for conditioned media experiments, PMN were cultured for up to 40 h with or without OSCC-derived conditioned media (SCC-4  $n = 3$ , SCC-25  $n = 3$  or CAL-27  $n = 3$ ) in the presence or absence of  $10 \mu\text{g mL}^{-1}$  neutralising human anti-GM-CSF Ab or anti-IL-6R Ab (b–d). In b, bar plots display the mean  $\pm$  SD percentage of alive PMN at 40 h; in c and d, bar plots show the PMN mean  $\pm$  SD fluorescence intensity (MFI) membrane expression of CD11b and CD62L, respectively, analysed at 20 h by flow cytometry; GM-CSF and IL-6 levels, as measured by ELISA, in cell-free supernatants collected from  $2.5 \times 10^5 \text{ mL}^{-1}$  neutrophils and  $5 \times 10^4 \text{ mL}^{-1}$  OSCC cell lines cultured for up to 40 h (e);  $P$ -values were estimated by the one-way ANOVA followed by the Tukey’s correction for pairwise comparisons (a–d) or by the unpaired  $t$ -test (e). Boxplots of CD66b<sup>+</sup> TAN density in the OSCC PT compartments (f);  $P$ -values were estimated by the Mann–Whitney  $U$ -test. Correlogram of CD66b<sup>+</sup> TAN density correlations among different tumor areas,  $r$  values are shown and ellipses show significant results ( $P < 0.05$ , Spearman test) (g). Multivariable survival analysis (Overall Survival) graphs showing survival probability at 5 years according to Stage I and II or III and IV and CD66b<sup>+</sup> TAN density in the invasive margin (IM) (h) or in the centre of the tumor (CT) (i). Heatmap showing the 5 years overall survival probability according to AJCC stage and CD66b<sup>+</sup> TAN density in the CT, adjusted for CD66b<sup>+</sup> TAN density in the IM (j). Heatmap showing the 2 years overall survival probability according to CD66b<sup>+</sup> TAN density in the CT and CD66b<sup>+</sup> TAN density in M-TDLN<sup>M</sup>, adjusted for ECS status (k). Multivariable survival analysis (Overall Survival) graph showing survival probability at 2 years according to ECS status and CD66b<sup>+</sup> TAN density in M-TDLN<sup>M</sup> (l). Kaplan Meier curves of the univariate survival analysis according to the M-TDLN<sup>M</sup> CD66b<sup>+</sup> TAN score (cut-off  $163 \text{ cells mm}^{-2}$ ) showing subgroups of patients according to M-TDLN<sup>M</sup> CD66b<sup>+</sup> TAN score and ECS status (m), all pairwise comparisons (Holm adjusted) showed significant differences except between CD66b<sup>+</sup> TAN M-TDLN<sup>M</sup> <sup>HI</sup> ECS<sup>-</sup> and CD66b<sup>+</sup> TAN M-TDLN<sup>M</sup> <sup>Lo</sup> ECS<sup>+</sup> ( $P = 0.93$ ).

insufficient patients at risk) followed by the M-TDLN<sup>M</sup> CD66b<sup>+</sup> TAN<sup>Hi</sup>/ECS<sup>-</sup> (5y-OS 25% CI<sub>95%</sub> 8–83%) and M-TDLN<sup>M</sup> CD66b<sup>+</sup> TAN<sup>Lo</sup>/ECS<sup>+</sup> (33% CI<sub>95%</sub> 19–55%) groups. The 5y-OS in the M-TDLN<sup>M</sup>

CD66b<sup>+</sup> TAN<sup>Lo</sup>/ECS<sup>-</sup> reached 67% (CI<sub>95%</sub> 52–86%;  $P < 0.0001$ ) confirming the detrimental value of the high CD66b<sup>+</sup> TAN density in M-TDLNs (Figure 3k).

**Table 1.** Multivariable overall survival analysis of CD66b<sup>+</sup> TANs in OSCC primary tumors and TDLNs

Wald statistics				Effects	
Factor	Chi-square	d.f.	P	Factor	H.R. (95% C.I.)
Multivariable model 1					
AJCC stage	15.96	3	0.0012	AJCC stage (Stage III-IV : Stage I-II)	2.98 (1.6–5.55)
TAN density CT	7.98	2	0.0185	TAN density CT <sup>a</sup>	0.42 (0.16–1.11)
TAN density IM	6.84	2	0.0327	TAN density IM <sup>a</sup>	1.53 (0.87–2.71)
AJCC stage * TAN density CT	6.16	1	0.0130	TAN density CT <sup>b</sup>	1.59 (1.06–2.39)
AJCC stage * TAN density IM	6.06	1	0.0138	TAN density IM <sup>b</sup>	0.63 (0.42–0.96)
Multivariable model 2					
TAN density CT	0.72	1	0.3967	TAN density CT	1.27 (0.73–2.22)
TAN density IM	1.42	1	0.2327	TAN density IM	0.68 (0.36–1.29)
TAN density NM-TDLN	1.95	1	0.1624	TAN density NM-TDLN	1.3 (0.9–1.88)
TAN density M-TDLN <sup>p</sup>	2.01	1	0.1561	TAN density M-TDLN <sup>p</sup>	0.77 (0.53–1.11)
ECS	16.77	2	0.0002	ECS+ : ECS- <sup>c</sup>	2.48 (1.18–5.2)
TAN density M-TDLN <sup>M</sup>	11.03	2	0.0040	TAN density M-TDLN <sup>Mc</sup>	1.22 (1–1.48)
TAN density M-TDLN <sup>M</sup> * ECS	4.41	1	0.0358	TAN density M-TDLN <sup>Md</sup>	2.19 (1.28–3.73)

CT, centre of the tumor; C.I., confidence interval; d.f., degrees of freedom; ECS, extracapsular spread; H.R., hazard ratio; IM, invasive margin.

\* Interaction.

<sup>a</sup>Adjusted to Stage I-II, TAN density CT = 155; TAN density IM = 194.

<sup>b</sup>Adjusted to Stage III-IV, TAN density CT = 155, TAN density IM = 194.

<sup>c</sup>Adjusted to ECS-, TAN density M-TDLN<sup>M</sup> = 64.

<sup>d</sup>Adjusted to ECS+, TAN density M-TDLN<sup>M</sup> = 64.

### Stable TAN phenotype in OSCC compartments

The current understanding of markers uniquely associated with pro-tumor functions of human TANs is very limited. Our clinical data on OSCC highlight variability of TAN density in terms of prognostic significance, likely indicating the existence of stage or regional functional TAN subsets. We compared the expression of putative PMN-MDSC markers in various PT and TDLN compartments by using immunohistochemistry. In addition, a new specialised CD66b<sup>+</sup> TAN subset (referred as ‘hybrid TANs’) with anti-tumor capabilities and a mixed phenotype (additional expression of HLA-DR, CD14, CD206, CD86 and CCR7) was recently reported in the early-stage non-small-cell lung carcinoma.<sup>14,38</sup> We therefore tested also for the presence of this subset. These analyses were performed on TANs from PT early-stage OSCC cases with very good prognosis (for markers of hybrid TANs), PT late-stage OSCC with poor prognosis and their matched M-TDLNs (for putative PMN-MDSC markers). CD66b<sup>+</sup> TANs from PT early-stage OSCC cases with very good prognosis ( $n = 10$ ) lacked nuclear morphology of hybrid TANs (round to oval), maintaining nuclear segmentation of canonical mature neutrophils as

shown by DAPI stain (Figure 4a). In addition, by double staining, co-expression of HLADR, CD14 and CD66b was only limited to HLADR<sup>+</sup>/CD14<sup>+</sup> macrophages phagocytosing CD66b<sup>+</sup> TANs (Figure 4b and c). Neutrophil phagocytosis was also confirmed by double staining of CD66b and CD163 and CD68 (Figure 4d and inset). In addition, TANs from late-stage OSCC PTs with poor prognosis and their matched M-TDLNs (Figure 4e–t) showed the same expression levels of putative PMN-MDSC markers<sup>20,21</sup> S100A9, arginase-1, *c/EBPβ* and pSTAT3 ( $n = 4$ ). These markers were also observed in CD66b<sup>+</sup> neutrophils found in early-stage PTs and suppurative lymphadenitis (Figure 4h, l, p, t;  $n = 3$ ).

Together, these findings indicate that novel biomarkers of clinical relevance are needed to identify TAN subsets with distinct biological properties.

### CD66b<sup>+</sup> TANs in M-TDLNs interact with T cells

By using markers for lymphoid and dendritic cells, we next analysed cell interactions between CD66b<sup>+</sup> TANs and immune cells in a set of M-TDLNs ( $n = 9$ ) positive for CD66b<sup>+</sup> TANs. CD66b<sup>+</sup> TANs frequently co-localise with CD3<sup>+</sup>, CD8<sup>+</sup> T cells



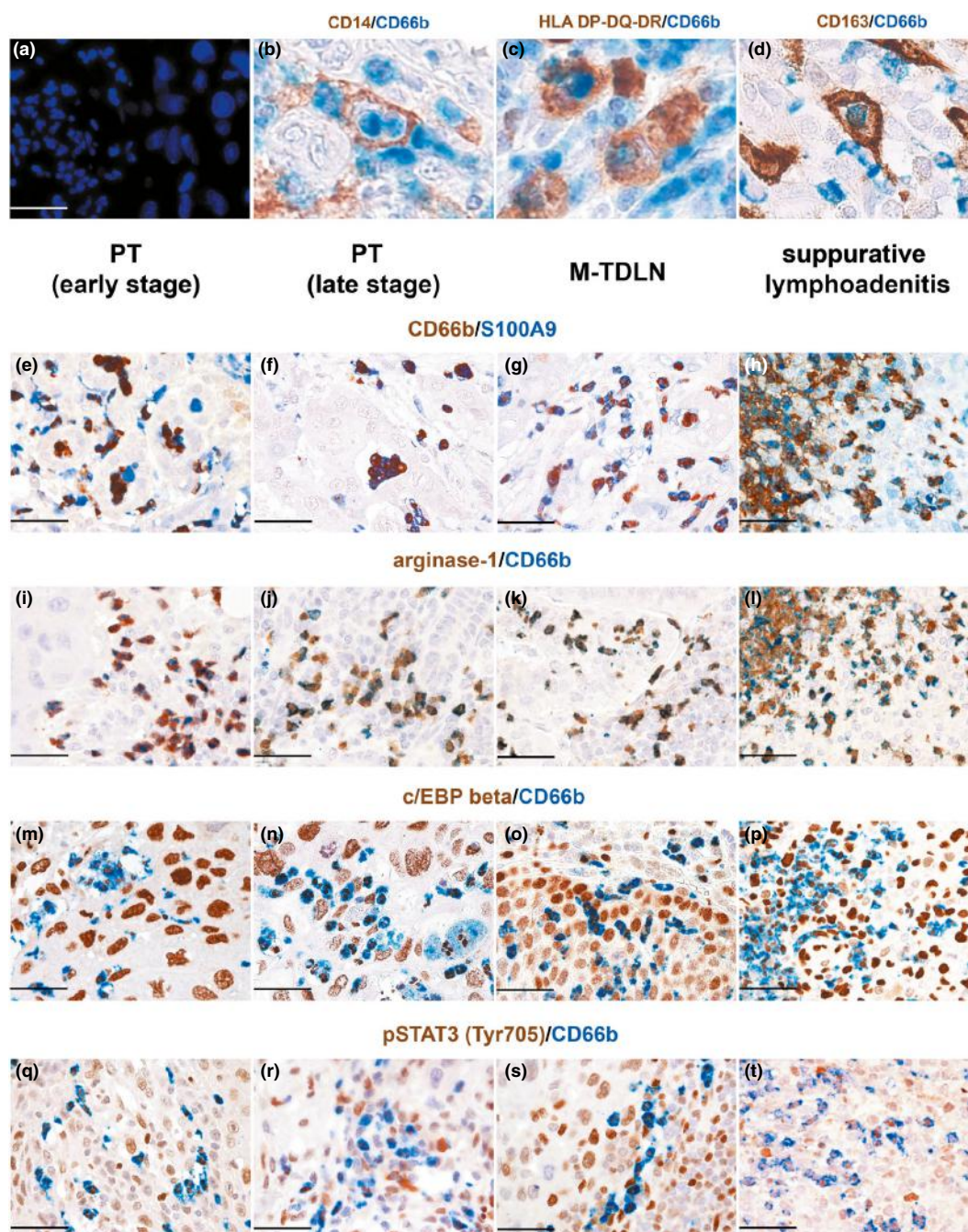


**Figure 4.** Analysis of the MDSC and hybrid TAN markers. Sections are from representative cases of primary tumors (PTs) and M-TDLNs at different disease stage, as labelled. DAPI highlighting TANs morphology and markers of hybrid TANs (**a-d**) and of MDSCs (**e-t**) are shown. The phenotype of neutrophils from suppurative lymphadenitis is shown as the control (**h, l, p, t**). CD66b<sup>+</sup> TANs are negative of CD14 and HLA-DR; occasionally, they are found within the cytoplasm of CD14<sup>+</sup> (**b**) and HLA-DR<sup>+</sup> (**c**) cells, co-expressing the macrophage marker CD163 (**d**). Sections are from early-stage OSCC PT ( $n = 2$ ) (**a-e, i, m, q**) and late-stage PT from the stomach (**f**), pancreas (**j**), lung (**n**) and OSCC (**r**) coupled with their matched M-TDLNs (**g, k, o, s**); a suppurative lymphadenitis case from non-tumor-bearing patients is included as control (**h, l, p, t**). S100A9, c/EBPβ and pSTAT3 are also expressed on neoplastic cells and/or stromal cells. Sections are counterstained with haematoxylin. Original magnification: 400× (**e-t**, scale bar 50 μm); 600× (**a**, scale bar 33 μm). **b-d** are digitally resized to show phagocytosis.

and BDCA2<sup>+</sup> plasmacytoid dendritic cells (PDCs). While T cells are regularly found within the metastatic nest (M-TDLN<sup>M</sup>) and in the surrounding nodal parenchyma (M-TDLN<sup>P</sup>), PDCs are mainly restricted to the M-TDLN<sup>P</sup> (Figure 5a). We expanded this observation by enumerating cell contacts between TANs and nodal CD3<sup>+</sup> T cells, using a recently designed image analysis algorithm<sup>39</sup> on double stained slides (see the Methods for details;  $n = 9$ ). These data confirm that a significant fraction of CD66b<sup>+</sup> TANs contact T cells, particularly in the M-TDLN<sup>P</sup> (Figure 5b and Supplementary figure 9a–d). Among T cells, a fraction of CD3<sup>+</sup> T cells interacting with CD66b<sup>+</sup> TANs express CD8 (Figure 5b and Supplementary figure 9e, f). We further explored TAN/T cell interaction and, by triple staining performed in M-TDLNs ( $n = 3$ ), we detected conjugates of CD66b<sup>+</sup> TANs with CD3<sup>+</sup> T cells and S100<sup>+</sup> interdigitating dendritic cells (Figure 5c and d) in all cases. These findings indicate that functional interactions of TANs with T cells might occur also in M-TDLNs.

The occurrence of numerous cell contacts between CD66b<sup>+</sup> TANs and CD3<sup>+</sup> T cells in M-TDLNs (Figure 5b and Supplementary figure 9a, b) prompted us to investigate the T-cell status in M-TDLNs from the OSCC cohort. Most of T cells interacting with CD66b<sup>+</sup> TANs are negative for activated caspase-3 in both M-TDLN compartments (Supplementary figure 9c, d). We then tested the proliferation index (by ki-67 expression) of nodal T cells in M-TDLNs (Figure 5e–h). This analysis was performed in CD66b<sup>+</sup> TAN<sup>Lo</sup> ( $n = 10$ ) good prognosis and CD66b<sup>+</sup> TAN<sup>Hi</sup> ( $n = 10$ ) worse prognosis tumor cases. Dermatopathic lymphadenitis (D-LD) ( $n = 10$ ) samples served as a control group. We found that the proliferation index of CD3<sup>+</sup> T cells in the M-TDLN<sup>M</sup> was significantly increased compare to M-TDLN<sup>P</sup> and D-LD; of note, no differences were noted by sub-grouping for TAN density (Figure 5e). We then tested the T-regulatory phenotype using a triple staining for CD66b, Foxp3 and CD3 ( $n = 10$ ) (Figure 5i–l). Again, the frequency of Foxp3<sup>+</sup>CD3<sup>+</sup> regulatory T cells was increased in the M-TDLN<sup>M</sup> compared to M-TDLN<sup>P</sup> and D-LD; no significant differences were noted with respect to TAN density (Figure 5i). Sequential double staining for ki-67, CD3 and Foxp3 confirmed that the large majority (72.2%) of proliferating T cells in the M-TDLN<sup>M</sup> corresponded to Foxp3 regulatory T cells (Figure 5m). In summary, these data suggest that

the T-cell proliferation and polarisation towards a regulatory T-cell phenotype that dominates the M-TDLN<sup>M</sup> compartment requires a complex modulation that is likely independent of TANs.

### **TAN signature in OSCC correlates with an EMT switch at the invasive margin of the PT**

Our microscopic findings suggest that TANs directly interact with cancer cells within lymphatic vessels. Epithelial-to-mesenchymal transition (EMT) promotes epithelial tumor spread and recent observations suggest that neutrophils can efficiently escort tumor cells from blood vessels to metastatic tissues<sup>40</sup> and promote EMT.<sup>41–43</sup> Remarkably, the EMT signature is enriched in the basal and mesenchymal subtypes of OSCC, representing an independent predictor of nodal metastasis.<sup>26,44</sup> By analysing the TCGA-HNSC (The Cancer Genome Atlas-Head and Neck Squamous Cell Carcinoma) dataset containing 308 OSCC cases, we found that a partial EMT signature (Supplementary figure 10) correlates with a signature of genes highly expressed by neutrophils (Supplementary table 5). The neutrophil signature was obtained from previous studies<sup>12,45,46</sup> and validated using RNAseq analysis of highly pure peripheral blood neutrophils (not shown). Among top neutrophil-specific targets more associated with an EMT signature, we found TNFAIP6, MMP9, OLR1, MME, CXCR1, KCNJ15, TNFRSF10C, FCGRB3, CEACAM8 and FPR2 to be specific to PMNs,<sup>10</sup> Supplementary figure 11a and Supplementary table 6). Remarkably, this association was consistent for many of these targets also in early-stage OSCC (Supplementary figure 11b, c and Supplementary table 6). Of note, PMNs<sup>10</sup> were significantly enriched in basal and mesenchymal subtypes of OSCC (Figure 6a and b). Previous studies indicate a localisation of the p-EMT program to tumor cells found at the invasive margin (IM), indicating a contribution from the tumor microenvironment, likely driven by local availability of TGF- $\beta$  from cancer associated fibroblasts.<sup>26,47</sup> Remarkably, TANs at the IM in OSCC also surround tumor areas showing an EMT switch and lymphangiogenesis. By triple staining, this observation was documented in a set of N<sup>+</sup> OSCC cases ( $n = 10$ ) showing highly recurrent co-localisation of TANs with PDPN<sup>+</sup>ki-67<sup>+</sup> proliferative lymphatics<sup>48,49</sup> around S100A9<sup>+</sup>/PDPN<sup>+</sup> cancer cells (Figure 6c–f), a phenotype highly correlated with EMT.<sup>26</sup>



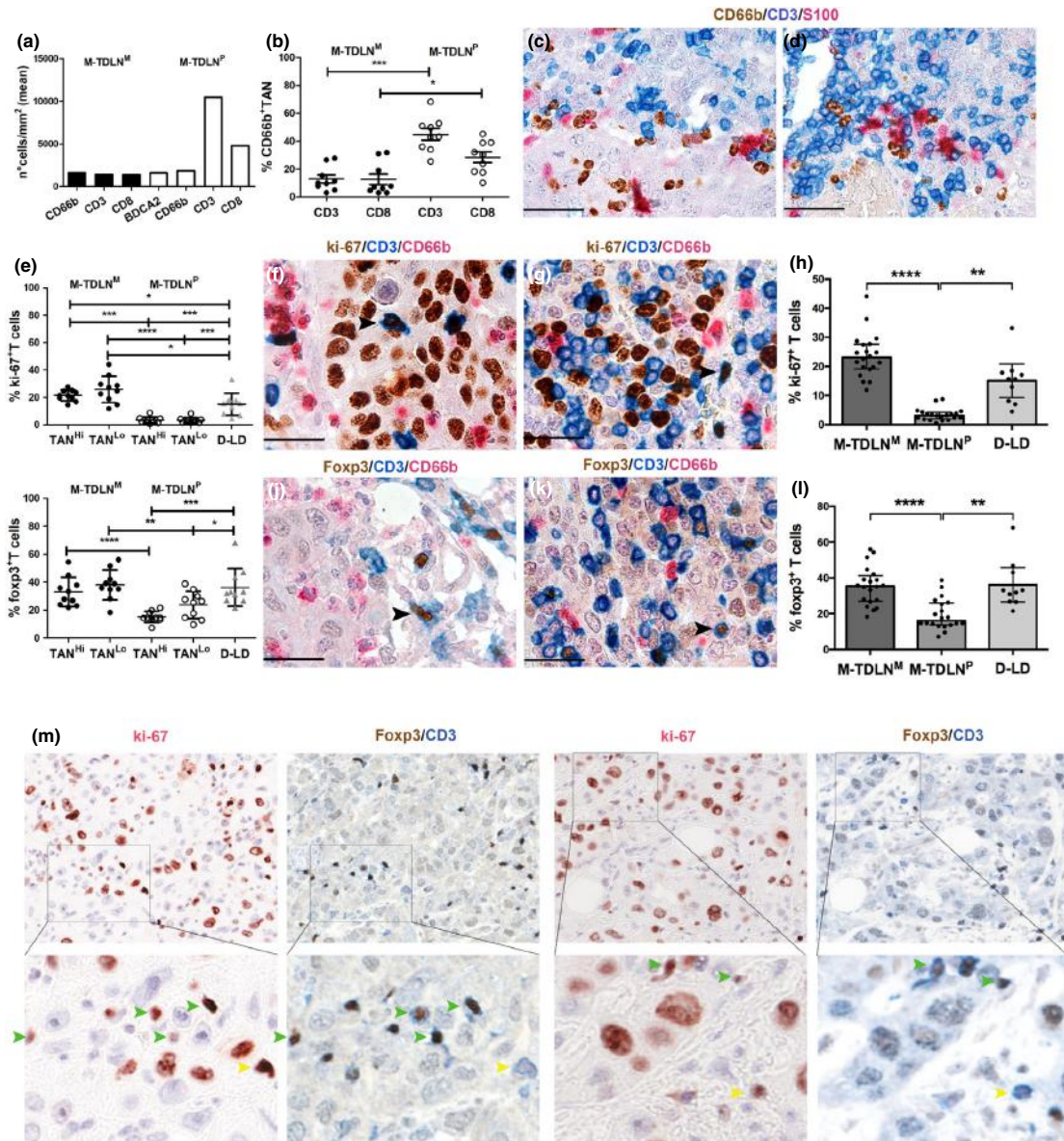


**Figure 5.** TAN/T-cell interactions and TANS polarisation in TDLNs. Graphs illustrate the frequency of different immune cell types **(a)** and the percentage of TANS interacting with T cells **(b)** in the metastatic nest (M-TDLN<sup>M</sup>, black bars/circles) and nodal parenchyma (M-TDLN<sup>P</sup>, white bars/circles) M-TDLN compartments quantified by using a digital microscopy algorithm by ImageJ software. Section of M-TDLN from gastric carcinoma illustrating a triple interaction between T cells, CD66b<sup>+</sup> TANS and S100<sup>+</sup> interdigitating dendritic cells **(c, d)** in M-TDLN<sup>M</sup> **(c)** and M-TDLN<sup>P</sup> **(d)** nodal compartments. The graphs illustrate the percentage of ki-67<sup>+</sup>CD3<sup>+</sup> proliferating T cells **(e)** and of foxp3<sup>+</sup>CD3<sup>+</sup> regulatory T cells **(h)** based on counts performed on triple stains **(f, g, j, k)**. The analysis has been performed in the metastatic nest (M-TDLN<sup>M</sup>, black circles, **f, j**) and nodal parenchyma (M-TDLN<sup>P</sup>, white circles, **g, k**) compartments of M-TDLNs CD66b<sup>+</sup> TAN<sup>HI</sup> with worse prognosis ( $n = 10$ ) compared with CD66b<sup>+</sup>TAN<sup>LO</sup> with good prognosis ( $n = 10$ ). As control group, dermatopathic lymphadenitis has been included (grey triangles, **d-l**). Boxplots reporting median and interquartile ranges of proliferating ki-67<sup>+</sup> T cells (%), **(h)** and of foxp3<sup>+</sup> regulatory T cells (%) **(l)** in M-TDLN<sup>M</sup>, M-TDLN<sup>P</sup> or D-LD;  $P$ -values were estimated by the Kruskal–Wallis test and pairwise comparisons using the Dunn’s procedure with a Bonferroni correction for multiple comparisons ( $*P < 0.05$ ,  $**P < 0.01$ ,  $***P < 0.001$ ,  $****P < 0.0001$ ). M-TDLNs shown are from OSCC cases ( $n = 4$ ) **(f, g, j, k, m)** and stained as labelled. In **m**, images are taken as snapshot (from Aperio Scanscope) of digitalised slides and resized (bottom panels). Green arrow heads indicate ki-67<sup>+</sup>CD3<sup>+</sup>foxp3<sup>+</sup> T cells, and yellow arrow heads indicate ki-67<sup>+</sup>CD3<sup>+</sup>foxp3<sup>-</sup> T cells. Sections are counterstained with haematoxylin. Original magnification: 400 $\times$  **(c, d)**, scale bar 50  $\mu$ m), 600 $\times$  **(f, g, j, k)**, scale bar 33  $\mu$ m).

### TAN modulate EMT signature in OSCC

We tested the hypotheses that this EMT-imprinting is acquired by circulating neutrophils from cancer patients. To this end, we prospectively collected peripheral blood from OSCC cases ( $n = 15$ ) and matched controls ( $n = 13$ ) and tested for the PMN<sup>10</sup> signature. The clinical and laboratory findings of this cohort are reported in Supplementary table 7 and Supplementary figure 12. Of relevance, the frequency of CD66b<sup>+</sup> neutrophils, most of which displayed a CD10<sup>+</sup> mature phenotype, as well as the neutrophil-to-lymphocyte ratio (NLR) were significantly increased in the OSCC group (Supplementary figure 12). The latter observations were consistent with our data collected from a larger patient cohort.<sup>50</sup> By phenotypic analysis of the circulating compartment of neutrophils, we could not detect significant differences for activation markers (CD62L, CD16, CD11b, CD54 or CD274), adhesion molecules (CD11c or CD11a) and chemotactic receptors, (CCR7, CXCR1, CXCR2 or C5aR), with the exception of a significantly increased expression of CXCR4 observed in the OSCC group (Supplementary figure 13). By reverse transcription quantitative PCR (RT-qPCR) analysis of the PMN<sup>10</sup> signature performed on total RNA extracted from circulating neutrophils, we could not detect significant differences between the OSCC and the control group. One exception was MME (alias CD10), that was significantly increased in the OSCC group (Figure 6g). These findings suggest that a full pro-EMT phenotype is likely acquired by local interaction of cancer cells with TANs.

### DISCUSSION

By completing a large-scale analysis of human carcinoma samples, this study identified that CD66b<sup>+</sup> TANs recurrently colonise TDLNs, and that their high nodal density is associated with a detrimental prognosis in advanced stages squamous cell carcinomas (SCC). Based on direct and indirect evidence, we surmise that TANs in PTs and in TDLNs are major contributors in the organisation and evolution of the nodal metastatic niche, likely by modulating EMT. This hypothesis requires additional analysis using appropriate animal models for *in vivo* tracing and modulation of TAN functions. Importantly, lymph node metastasis can fuel distant metastasis in a

significant fraction of cancers,<sup>16,32</sup> as also recently demonstrated by molecular analysis,<sup>16</sup> thus supporting an additional role of TANs in promoting systemic spread.

Similar to TANs in the PT, the TDLN cellular counterpart shows a segmented nuclear morphology and expresses a panel of neutrophil-specific molecules, including cytoplasmic granule-associated molecules and CD10, confirming their neutrophil identity and a mature phenotype.<sup>51</sup> In addition, at similar levels to the PT, the TANs in TDLNs express recently identified putative PMN-MDSC markers, including S100A9, arginase-1, pSTAT3 and  $\alpha$ EBP $\beta$ . It should be noted that this phenotype is observed also in neutrophils from suppurative lymphadenitis, indicating that co-expression of these markers by CD66b<sup>+</sup> cells is insufficient to define a TAN phenotype. In particular, a dense CD66b<sup>+</sup> TAN infiltration was identified in head and neck SCC, gastric and pancreatic adenocarcinoma and transitional bladder cancer. By contrast, breast carcinoma TDLNs are largely devoid of CD66b<sup>+</sup> TANs. In breast carcinoma, a lower CD66b<sup>+</sup> TAN density was also evident in the corresponding PT, suggesting site- and tumor-specific differences likely due to limited homing of the circulating TAN precursors from the blood.

An important and novel finding of this study is that CD66b<sup>+</sup> TANs in the PT form conjugates with cancer cells within lymphatic emboli. Accordingly, they reproduce similar conjugates in the marginal and intermediate sinuses of the corresponding TDLNs, within micro-metastatic foci. TAN entry into the TDLNs might occur via lymphatic vessels from the PT or, alternatively, through the blood circulation *via* high endothelial venules.<sup>52</sup> Our microscopic analysis supports the hypothesis that TANs could enter the TDLN via the lymphatic route with a potential role played by CXCL8, a chemokine known to regulate TAN recruitment and angiogenesis and supporting tumor progression.<sup>33,53,54</sup> CD66b<sup>+</sup> TANs are also found within sinuses of non-metastatic TDLNs (this study), suggesting that a steady lymphatic circulation of TANs might establish the pre-metastatic niche as observed in distant sites.<sup>34,36,55</sup> We hypothesise that TANs provide a survival signal to tumor cells or other cells (i.e. macrophages) co-existing in the nodal sinuses. Bidirectional signals between cancer cells and TANs might also result in the activation of TANs in proximity of tumor emboli.<sup>56,57</sup> TANs facilitate

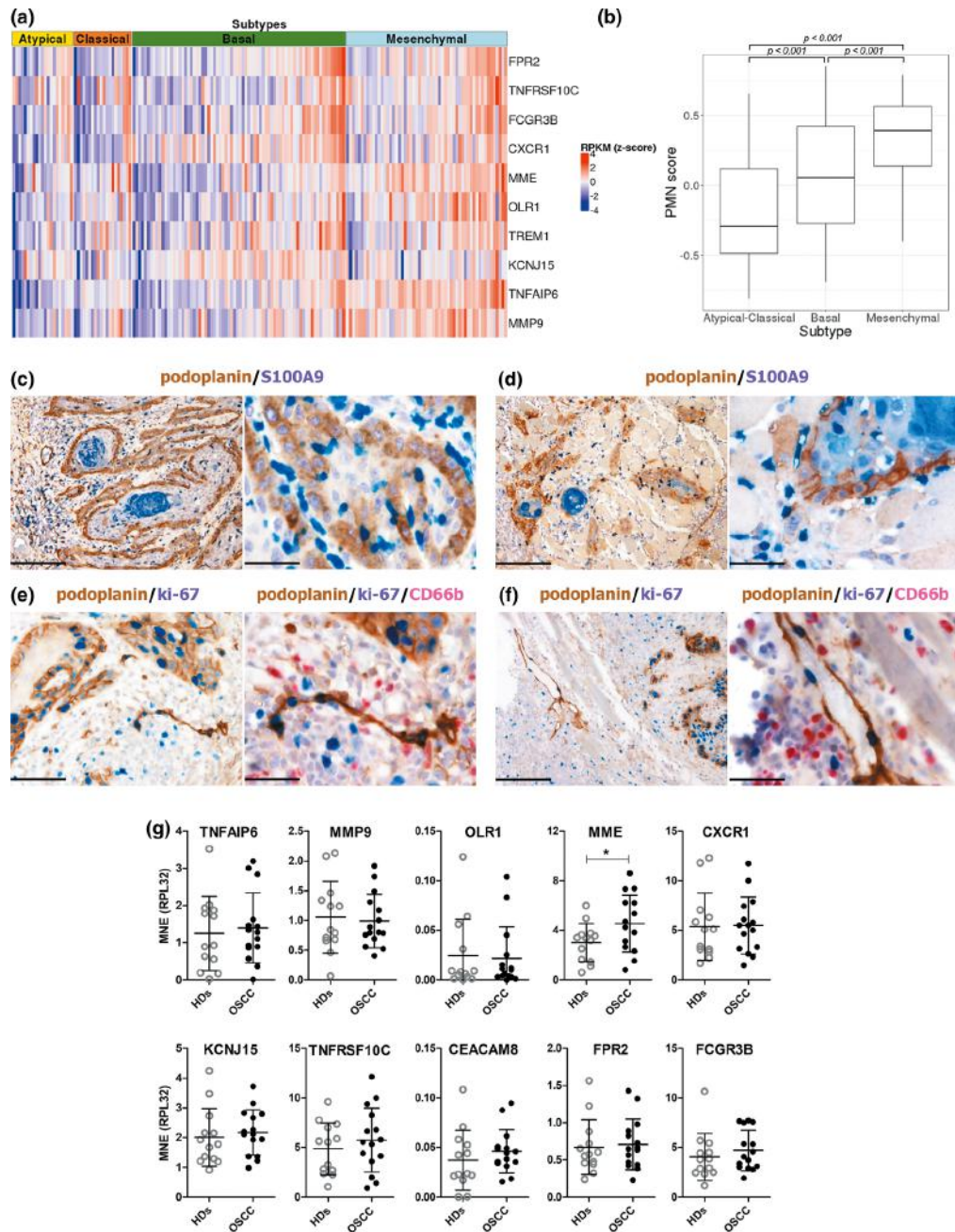


**Figure 6.** PMN signature in OSCC. **(a)** The heatmap shows the log<sub>2</sub> RPKM values for the PMN signature genes grouped by Subtype annotation ( $n = 171$  OSCC samples from the TCGA with available annotation). Samples are ordered in increasing overall expression values within Subtypes. **(b)** The boxplot of PMN score (computed using GSVA algorithm) separately for Subtype annotation.  $P$  values are estimated by a linear model and pairwise multiple comparisons adjusted for multiple tests with the Tukey–Kramer method. **(c–f)** Sections are from three OSCC PT (**d** and **f** single case) and stained as labelled. Sections are counterstained with haematoxylin. Original magnification: 100× (scale bar 200  $\mu$ m; **c**, **d**, **f** images on the left), 200× (scale bar 100  $\mu$ m; **e** image on the left) and 400× (scale bar 50  $\mu$ m; **c–f** images on the right). **(g)** Dot plots show the mRNA expression of the PMN<sup>10</sup> in circulating neutrophils freshly isolated from HDs or OSCC patients, as evaluated by RT-qPCR. Gene expression is shown as mean normalised expression (MNE) units after RPL32 mRNA normalisation (mean  $\pm$  SD). Each symbol stands for a single HD (open circle;  $n = 13$ ) or OSCC patient (black circle;  $n = 15$ ). \* $P \leq 0.05$  by the unpaired  $t$ -test.



tumor cell migration, extravasation and subsequent invasion, thus fostering cancer cell arrest and growth at the metastatic site.<sup>33</sup> Notably, a set of proteases released by activated TANs has been implicated in the formation and dissemination of tumor aggregates in form of emboli.<sup>58</sup> These findings support the hypothesis that nodal TANs can promote cancer cell extravasation from the lymphatic sinuses, as well as their subsequent growth and invasion of the nodal parenchyma.<sup>55</sup> Since TAN density in the PT and in the M-TDLN<sup>M</sup> is highly correlated, we surmise that only TANs receiving the appropriate imprinting signals in the PT can execute a pro-metastatic program in TDLNs.

Neutrophils are abundant in carcinomas showing squamous histology (SCC) mainly due to cancer cell intrinsic molecular traits such as SOX2 over-expression.<sup>22–25</sup> The latter occurs in SCC from various primary sites<sup>59</sup> including OSCC.<sup>59–61</sup> Moreover, TANs are known to foster squamous cell fate in murine models.<sup>23</sup> We found that OSCCs provide a significant survival and activation signal to TANs *via* GM-CSF expression. Mechanistically, the expression of a set of neutrophil genes is significantly associated with a partial EMT signature in OSCC. As recently proposed, EMT in cancer cells enhances their capacity to disseminate also *via* lymphatics,<sup>62</sup> which is highly relevant in terms of OSCC prognosis. Of note, EMT in OSCC represents an independent predictor of nodal metastasis and EMT-switched tumor cells localise to the IM, an area also enriched with lymphatic vessels.<sup>26,44,48</sup> We found that the top ten neutrophil-specific genes associated with the pro-EMT signature (referred as PMN<sup>10</sup>), are detected also in a subset of early-stage OSCC and are enriched in the basal and mesenchymal OSCC subtypes, typically associated with an EMT switch.<sup>26,44</sup> By the analysis of peripheral blood of OSCC patients, we also demonstrate that the expression of PMN<sup>10</sup> is very limited in circulating neutrophils, with only MME (alias CD10) being over-expressed. By contrast, over-expression of CXCR4, a chemokine receptor relevant in the neutrophil homeostasis,<sup>63</sup> in EMT of OSCC<sup>64</sup> and in neutrophil-mediated pro-metastatic function,<sup>65</sup> occurs early in circulating neutrophils from OSCC patients. Recent data on carcinomas from different sites have proposed TANs as a relevant player in promoting EMT.<sup>41–43</sup> Multiple findings from this study further strengthen this observation supporting that a full pro-EMT signature in OSCC is likely acquired at the TAN stage within the tumor tissue.

To establish the clinical relevance of nodal TAN infiltration, we performed a large-scale analysis of CD66b<sup>+</sup> TAN density on a cohort of OSCC samples. In this cohort, high neutrophil count and NLR<sup>50</sup> were associated with poor prognosis. Data on the clinical relevance of CD66b<sup>+</sup> TANs by IHC are partially conflicting, mainly due to differences in the analysis methods. However, recent computational approaches on a pan-cancer study revealed that TAN abundance represents a predictor of poor outcome.<sup>12</sup> To minimise the analytical biases in tissue monitoring, we strictly adhered to recently introduced guidelines.<sup>66</sup> We used a highly specific marker and measured a highly representative PT tissue area on whole digitalised slide ( $105 \pm 71 \text{ mm}^2$ ). A significant interaction was observed between TAN density in the CT and in the IM and tumor Stage. A higher density in the CT was associated with worse prognosis only in advanced stage III and IV, whereas it predicted better prognosis in the earlier stages I and II; an opposite effect is observed for TAN density in the IM. Stage-dependent and spatially oriented molecular analysis of TAN are required to further expand our knowledge on this finding. However, this level of stage- and site-dependent functional heterogeneity requires further investigation. Among potential explanations, the existence of different TAN subsets, as recently described<sup>67</sup> supports the hypothesis of a dynamic change of pro-tumor TAN localisation along with disease progression. Among anti-tumor TANs, Eruslanov's groups have recently reported a specialised TAN subset with a hybrid phenotype found in early-stage non-small-cell lung cancer and associated with good prognosis.<sup>14,38</sup> As in other studies on human lymph nodes, these cells are found to express MHC-II molecules.<sup>68</sup> We could not identify a similar population in OSCC, likely indicating that hybrid anti-tumor TANs are primary site specific.

Our study identifies a contribution of nodal TANs in OSCC prognosis with a high TAN density in the metastatic nests (M-TDLN<sup>M</sup>) predicting worse overall survival. This might indicate that nodal TANs can promote systemic spread, likely by immune escape. We found that TANs in TDLNs recurrently interact with T cells and interdigitating dendritic cells. Consistently, by image analysis we found that in M-TDLN, T-cell proliferation and polarisation towards a regulatory phenotype was significantly increased,

but not affected by a higher TAN density. Notably, we also found that TANs interact with nodal PDCs, a major source of type I IFN in human lymph nodes.<sup>69</sup> This finding might suggest that polarisation to N1 TANs via type I IFN<sup>10</sup> could occur<sup>67</sup> and likely be obtained by TLR8 or TLR9 agonists (Clinicaltrials.gov study identifiers: NCT02644967, NCT03445533, NCT03052205, NCT02521870, NCT03084640 and NCT0266877).

Overall, this study identifies and characterises the clinical relevance of a novel TAN compartment in carcinomas, particularly in SCC. Microscopic analysis and the clinical findings from the OSCC cohort highlight the relevance and the plasticity of TAN compartments in various disease stages and their role in promoting EMT. Tailored site and stage-dependent modulation of TANs from various compartments should be considered to be therapeutic option for carcinoma patients and in particular SCC.

## METHODS

### Tissues

This part of the study was approved by the local IRB to WV (VW-IMMUNOCANCER<sup>hum</sup>, NP-906). Formalin-fixed paraffin embedded (FFPE) tissue blocks used for this study were retrieved from the tissue bank of the Department of Pathology (ASST Spedali Civili di Brescia, Brescia, Italy). Human tissues included human bone marrow, thymus, spleen, tonsil, lymph node, small bowel and appendix. In all, 278 metastatic (M-TDLNs) and 175 non-metastatic tumor-draining lymph nodes (NM-TDLNs), obtained from a total of 216 patients with primary carcinomas from different primary sites (skin, head and neck, thyroid, breast, lung, stomach, pancreas, colon, bladder and ovary) or cutaneous melanoma (17 cases). Details of M-TDLNs analysed are reported in Supplementary table 1. A total of 45 cases of primary melanoma (9 cases) and carcinoma from various sites were selected for a comparative analysis with M-TDLNs.

### OSCC cohort

This part of the study was approved by the local IRB to WV (H&N Cancer, NP-2066). The retrospective study population included 182 histologically confirmed cases of oral cavity squamous cell cancer (OSCC) who underwent radical surgical resection and neck dissection between 2000 and 2014 (Otorhinolaryngology Department, ASST Spedali Civili di Brescia, Brescia, Italy). Patients with at least 12 months of follow-up or earlier death or recurrence were included. Salvage surgery, metastatic disease, immunological disorders or prior systemic treatment for malignancy represented exclusion criteria. Patients were regularly followed with clinical examinations and neck MRI or CT

every 3-6 months. Details of the cohort are reported in Supplementary table 2. A prospective cohort, enrolled between June 2014 and December 2014, included patients affected by head and neck SCC, that underwent pre-treatment full blood collection for flow cytometry analysis and reverse transcription quantitative real-time PCR analysis; immunological disorders or prior systemic treatment for malignancy represented exclusion criteria.

### Immunohistochemistry

Four-micron thick FFPE sections were used for immunohistochemical staining. The primary antibodies for this study are listed in the Supplementary table 8. The antibody used to detect granulocytes/TANs is CD66b diluted 1:200, clone G10F5, from BioLegend (San Diego, CA). The reaction was revealed by Novolink Polymer (Leica Microsystems, Wetzlar, Germany) followed by DAB. For double immunohistochemistry, after completing the first immune reaction, the second was visualised using Mach 4 MR-AP (Biocare Medical, Concord, CA), followed by Ferangi Blue (Biocare Medical) or New Fuchsin (Agilent Technologies, Santa Clara, CA) as chromogen. For triple immunohistochemistry, after completing the second immune reaction, the third was visualised using a biotinylated system (Agilent) followed by AP-streptavidin and New Fuchsin as chromogen. Sections were then counterstained with haematoxylin.

For the screening cohort, a training set of 15 cases on digitalised slides (IHC nuclear algorithm, Aperio Scanscope, Leica Microsystems) was used to define a three-tiered score for CD66b<sup>+</sup> TANs as it follows: S0 = ≤ 20 cell mm<sup>-2</sup> (mean 12); S1 = ≤ 100 cells mm<sup>-2</sup> (mean 59); S2 = > 100 cells mm<sup>-2</sup> (mean 235). Neutrophils interactions with PDCs and T cells were analysed using a specifically designed algorithm in Image J by processing 10 captured high power field on CD66b/BDCA2, CD66b/CD3 and CD66b/CD8 double stained sections. Enumeration of proliferating (CD66b, CD3 and ki-67) and of regulatory (CD66b, CD3 and foxp3) T cells was performed by using ImageScope (Aperio Counter Tool) on triple stained sections of 20 M-TDLN cases from the OSCC cohort. Control cases were represented by six dermatopathic lymphadenitis.

For double sequential immunostains, the first reaction is deleted after first chromogen de-stain and stripping. Anti-ki-67 was used for the first immune reaction, revealed using Novolink Polymer and developed in 3-amino-9-ethylcarbazole chromogen (AEC), counterstained with haematoxylin and cover-slipped using gelatin. Subsequently, the slides were digitally scanned, using Aperio Scanscope CS (Leica Microsystems). After cover slip removal AEC was washed out and the slides were eluted using a 2-Mercaptoethanol/SDS solution (20 mL 10% w/v SDS with 12.5 mL 0.5 M Tris-HCl, pH6.8, 67.5 mL distilled water and 0.8 mL 2-ME). Slides were subsequently incubated in this solution in a water-bath pre-heated at 56°C for 30 min. Sections were washed for 1 h in distilled water. After unmasking in microwave, anti-foxp3 was revealed using Raton-Mouse HRP polymer (Biocare Medical) and 3,3'-Diaminobenzidine. CD3 was revealed using Mach 4 MR-AP and Ferangi blue as chromogen and slides were counterstained with haematoxylin, cover-slipped and

digitally scanned. The two digital slides were processed using ImageScope. Slides were synchronised and corresponding tissue regions were analysed using the counter tool.

### Immunoscore definition by image analysis

Stained slides were acquired using a ScanScope digital scanner. Images were viewed and organised using ImageScope software. Each scanned image was annotated manually and IHC Nuclear Image Analysis algorithm was chosen for the analysis. Areas of suppurative necrosis were excluded from the count. Data are expressed as number of CD66b<sup>+</sup> cells per mm<sup>2</sup>. In the primary tumor (PT), immune cell density was measured either in the centre of the tumor (CT) and in the invasive margin (IM). The invasive margin was defined as the tissue area of 1 mm wide from the front of invasion of the tumor<sup>700</sup>. For the analysis of tumor-draining lymph nodes (TDLNs) at least one non-metastatic TDLN (NM-TDLN) was analysed; in N<sup>+</sup> patients, slides containing metastatic TDLN (M-TDLN) have been included. The density of CD66b<sup>+</sup>TAN in M-TDLNs was counted in the metastatic nests (M-TDLN<sup>M</sup>) and surrounding lymph node tissue (M-TDLN<sup>P</sup>).

### Isolation of neutrophils

Circulating neutrophils were isolated by density gradient centrifugation (Ficoll-Paque; GE Healthcare Life Sciences, Marlborough, MA) of whole blood collected in BD Vacutainer tubes with K<sub>2</sub>EDTA (BD Biosciences, Franklin Lakes, NJ) from patients with OSCC or HDs or from buffy coats of healthy donors and further purified (approximately 99.7% purity) by negative selection using the EasySep neutrophil enrichment kit (StemCell Technologies, Vancouver, Canada) as previously described.<sup>711</sup> Human samples were obtained following informed, written, consent by healthy donors, in accordance with the Declaration of Helsinki. This study was carried out in accordance with the recommendations of Ethic Committee of the Azienda Ospedaliera Universitaria Integrata di Verona (Italy).

### Cell cultures

Human oral squamous cell carcinoma (OSCC) cell lines, CAL-27 (DSMZ n° ACC 446), SCC-4 (DSMZ n° ACC 618), SCC-25 (DSMZ n° ACC 617), were purchased from Leibniz Institute DSMZ-German Collection of Microorganisms and Cell Cultures GmbH (DMSZ, Braunschweig, Germany). CAL-27 cell line was expanded in Dulbecco's modified Eagle medium (DMEM)(Corning, NY) at 37°C/5% CO<sub>2</sub>, while SCC-25 and SCC-4 cell lines were expanded in DMEM:Ham's F12 (Euroclone, Pero, Milan, Italy) at a 1:1 ratio. All tissue culture media were supplemented with 10% FBS (< 0.5 EU per mL endotoxin, BioWhittaker-Lonza, Basel, Switzerland) and 1% of penicillin/streptomycin (pen/strep) (Corning).

### Neutrophils co-culture with OSCC cell lines

Co-culture experiments were performed in 24-well culture plates (Corning) at 37°C/5% CO<sub>2</sub>. Cell lines were plated at

$5 \times 10^4$  mL<sup>-1</sup> in RPMI (10% FBS, 1% P/S) 24 h prior the addition of neutrophils, to permit their adhesion to the plates. After the isolation, neutrophils were then suspended at 0.25 and  $2.5 \times 10^6$  mL<sup>-1</sup> in RPMI 1640 medium (Corning), containing 10% FBS and 1% of pen/strep and they were either plated alone, or directly added to the cell lines (at neutrophil:cell line ratios of 5:1 and 50:1), to be cultured for up to 40 h.

At the end of the incubation time, neutrophils were detached from the co-cultures by gently pipetting, then centrifuged at  $300 \times g$  for 5 min and finally suspended in 50  $\mu$ L phosphate-buffered saline (PBS) at  $1 \times 10^6$  mL<sup>-1</sup> containing 2% FBS and 15 mM EDTA for flow cytometry assays.

### Conditioned media experiments

Neutrophil were suspended in RPMI (10% FBS, 1% P/S) or conditioned media harvested from OSCC cell lines (CAL-27, SCC-4, SCC-25) plated at  $5 \times 10^6$  mL<sup>-1</sup> in 96-well culture plates (Corning) and then cultured for up to 40 h. Cytokine blocking experiments were conducted by culturing neutrophils in OSCC-derived conditioned media, previously pre-incubated for 30 min at 37°C in the presence of specific neutralising monoclonal antibodies (mAb) towards GM-CSF (10  $\mu$ g mL<sup>-1</sup>, R&D Systems, Minneapolis, MN). Alternatively, neutrophils were pre-incubated with IL-6R (10  $\mu$ g mL<sup>-1</sup> for 30 min, R&D Systems). After the incubation, neutrophils were then centrifuged at  $300 \times g$  for 5 min and finally suspended in 50  $\mu$ L phosphatase-buffered saline (PBS) at  $1 \times 10^6$  mL<sup>-1</sup> containing 2% FBS and 2 mM EDTA for flow cytometry assays.

### Flow cytometry

Neutrophils were incubated with 5% human serum (BioWhittaker-Lonza) for 5 min on ice and then stained for 30 min at 4°C using the following anti-human fluorochrome-conjugated mAbs or specific isotype controls listed in Supplementary table 8. For immunophenotypic characterisation of neutrophils from HD or OSCC patients, events were acquired on an eight-colour three-laser-MACSQuant Analyzer (Miltenyi Biotec, Bergish Gladbach, Germany) while for co-culture and conditioned media experiments, flow cytometry was performed by the use of a FACS MACSQuant Analyzer 16 Flow Cytometer (Miltenyi Biotec). Neutrophils were identified on the basis of their morphological parameters (forward scatter/side scatter) and the CD66b expression. Phenotypic analysis was performed on live cells, identified as Vybrant-negative (Vybrant® DyeCycle™ Violet; Life Technologies, Waltham, MA) or propidium iodide (Life Technologies) negative cells. Cell viability was defined as the percentage of cells that were negative for vibrant staining.

Data analysis was performed by using FlowJo software (Tree Star). The median fluorescence intensity (MFI) relative to each molecule was obtained by subtracting either the MFI of the correspondent isotype control or cell autofluorescence. Unpaired *t*-tests or one-way ANOVA analysis were performed, as appropriate.

### Reverse transcription quantitative real-time PCR (RT-qPCR)

Immediately after purification, total RNA (0.1 µg) was extracted from  $1 \times 10^6$  neutrophils by the RNeasy mini kit (Qiagen, Venlo, Limburg, The Netherlands) and reverse transcribed for RT-qPCR, performed as previously described,<sup>722</sup> utilising the gene-specific primer pairs (listed in Supplementary table 9), all purchased from Thermo Fisher Scientific). Data were calculated by Q-Gene software (<http://www.gene-quantification.de/download.html>) and expressed as mean normalised expression (MNE) units, after RPL32 normalisation.

### Cytokines production

Cytokine concentrations in cell-free supernatants were measured by commercially available ELISA kits, specific for human IL-6 (Mabtech, Nacka Strand, Sweden) and GM-CSF (BioLegend). Detection limits of these ELISA were as follows: 10 pg mL<sup>-1</sup> for IL-6 and 7.8 pg mL<sup>-1</sup> for GM-CSF.

### Data preprocessing and statistical analysis of the TCGA dataset

Raw counts for primary solid tumor samples were downloaded from GDC portal harmonised repository using TCGAbiolinks R/Bioconductor package ( $n = 528$ ). FFPE samples were removed, and only samples corresponding to Oral Cavity anatomical area were kept ( $n = 308$ ). Gene differential expression was tested, after library size normalisation based on TMM (the trimmed mean of M-values), using LIMMA linear modelling<sup>733</sup> function were used to model mean-variance relationship<sup>744</sup>. Single gene expression used as biomarker was computed as log<sub>2</sub>-RPKM. A global score for signature expression (either neutrophil or pEMT) was computed using single sample enrichment based on GSVA<sup>755</sup> algorithm: single sample enrichment score represents the degree to which the genes in a particular gene set are coordinately up- or down-regulated within a sample and were used as a global score for signature expression. Hierarchical clustering was performed using correlation based (Spearman) distance matrices and complete agglomeration method.

A filtering procedure to determine the PMN signature genes most associated with pEMT signature was performed based on two phases: first we performed a regularised Canonical Correlation Analysis (rCCA). This multivariate statistical procedure serves to identify linear combinations among variables between two datasets in order to maximise their correlation. The (two) new sets of canonical variates, constructed based on the original datasets, determine a pair of canonical variates with a maximised simple correlation. Each set of constructed canonical variates are uncorrelated with each other. Genes of both signatures are represented on a correlation circle plot where coordinates represent the correlation between each gene and the corresponding dimension. The correlation between genes in the two signatures can be visualised through the angles between two vectors (from the origin to the gene): if the angle is sharp, the

correlation is positive, if the angle is obtuse the correlation is negative and if the angle is right the correlation is null. Therefore, PMN genes close to the bulk of pEMT genes and far from the origin are likely to be associated with the pEMT signature. In a second step we performed simple linear regression of pEMT score versus each PMN gene separately. PMN genes with a positive coefficient and significant *P*-value (not adjusted), were retained in the filtering procedure. This was performed for all samples and separately for low (I and II) and high (III and IV) stage.

### Statistical analyses

Standard descriptive statistics were used for expressing means, standard deviations and CV. The Mann–Whitney *U*-test or the Kruskal–Wallis test was used for group comparisons, as appropriate. Differences in CD66b<sup>+</sup>TAN density among different areas were analysed using nonparametric Spearman's rank correlation. For survival analysis, the overall survival (OS) was chosen as the end-point. Univariate survival curves were estimated using the Kaplan–Meier method and compared by the log-rank test. Cut-off in continuous predictors was estimated using maximally selected log-rank statistic. Multivariable analyses were performed using Cox proportional hazard models and expressed as hazard ratio (HR) with 95% confidence intervals (CI). To assess the clinical relevance of infiltrating CD66b<sup>+</sup> TANs in the PTs and lymph node areas, we modelled immune cells densities as continuous variables and their functional relationship with survival outcomes were evaluated investigating interactions with relevant clinical variables. In all the analysis, a significance level of 5% was used. GraphPad Prism Version 6.0 (San Diego, CA) and R (version 3.5.1) were used for statistical analysis.

### ACKNOWLEDGMENTS

This work was supported by grants from Associazione Italiana per la Ricerca sul Cancro – Italy to WV (AIRC, IG-15378) and MAC (AIRC, IG-20339); we are grateful to Fondazione Beretta (Brescia, Italy) for support to SL and DB. We thank the pathologists (Drs Lucini, Battocchio and Ardighieri), technicians, clinicians, nurses and administrative employers who have provided support to the study and to the follow-up of OSCC patients. We are grateful to the Graphic Designer Matteo Vermi for help and supervision of the graphical abstract.

### CONFLICTS OF INTEREST

The authors declare no competing financial interests.

### AUTHOR CONTRIBUTION

**William Vermi:** Conceptualization; Formal analysis; Investigation; Supervision; Writing-original draft; Writing-review & editing. **Silvia Lonardi:** Conceptualization; Formal analysis; Methodology; Writing-original draft. **Francesco**

**Missale:** Conceptualization; Data curation; Formal analysis; Methodology; Software; Writing-original draft; Writing-review & editing. **Stefano Calza:** Data curation; Methodology; Software; Writing-original draft. **Mattia Bugatti:** Data curation; Formal analysis; Investigation; Methodology. **Raffaella Vescovi:** Data curation; Formal analysis; Methodology. **Debora Bresciani:** Data curation; Investigation. **Ravindra Uppaluri:** Conceptualization; Investigation; Writing-original draft. **Anne Egloff:** Data curation; Formal analysis. **Davide Mattavelli:** Data curation; Investigation. **Davide Lombardi:** Conceptualization; Data curation; Formal analysis; Investigation. **Luisa Benerini Gatta:** Methodology. **Olivia Marini:** Data curation; Investigation; Methodology. **Nicola Tamassia:** Data curation; Formal analysis; Investigation. **Elisa Gardiman:** Data curation; Formal analysis. **Marco Cassatella:** Conceptualization; Writing-original draft. **Patrizia Scapini:** Conceptualization; Data curation; Formal analysis; Investigation; Writing-original draft. **Piero Nicolai:** Resources.

## REFERENCES

- Mantovani A, Cassatella MA, Costantini C, Jaillon S. Neutrophils in the activation and regulation of innate and adaptive immunity. *Nat Rev Immunol* 2011; **11**: 519–531.
- Mantovani A, Sozzani S, Locati M, Allavena P, Sica A. Macrophage polarization: tumor-associated macrophages as a paradigm for polarized M2 mononuclear phagocytes. *Trends Immunol* 2002; **23**: 549–555.
- Talmadge JE, Gabrilovich DI. History of myeloid-derived suppressor cells. *Nature Rev Cancer* 2013; **13**: 739–752.
- Jaillon S, Ponzetta A, Di Mitri D, Santoni A, Bonecchi R, Mantovani A. Neutrophil diversity and plasticity in tumour progression and therapy. *Nature Rev Cancer* 2020; **20**: 485–503.
- Moses K, Brandau S. Human neutrophils: Their role in cancer and relation to myeloid-derived suppressor cells. *Semin Immunol* 2016; **28**: 187–196.
- Scapini P, Marini O, Tecchio C, Cassatella MA. Human neutrophils in the saga of cellular heterogeneity: insights and open questions. *Immunol Rev* 2016; **273**: 48–60.
- Bronte V, Brandau S, Chen S-H *et al.* Recommendations for myeloid-derived suppressor cell nomenclature and characterization standards. *Nat Commun* 2016; **7**: 12150.
- Galdiero MR, Bonavita E, Barajon I, Garlanda C, Mantovani A, Jaillon S. Tumor associated macrophages and neutrophils in cancer. *Immunobiology* 2013; **218**: 1402–1410.
- Fridlender ZG, Sun J, Kim S *et al.* Polarization of tumor-associated neutrophil phenotype by TGF- $\beta$ : "N1" versus "N2" TAN. *Cancer Cell* 2009; **16**: 183–194.
- Andzinski L, Kasnitz N, Stahnke S *et al.* Type I IFNs induce anti-tumor polarization of tumor associated neutrophils in mice and human. *Int J Cancer* 2016; **138**: 1982–1993.
- Rotondo R, Barisione G, Mastracci L *et al.* IL-8 induces exocytosis of arginase 1 by neutrophil polymorphonuclears in non-small cell lung cancer. *Int J Cancer* 2009; **125**: 887–893.
- Gentles AJ, Newman AM, Liu CL *et al.* The prognostic landscape of genes and infiltrating immune cells across human cancers. *Nat Med* 2015; **21**: 938–945.
- Shen M, Hu P, Donskov F, Wang G, Liu Q, Du J. Tumor-associated neutrophils as a new prognostic factor in cancer: a systematic review and meta-analysis. *PLoS One* 2014; **9**: e98259.
- Singhal S, Bhojnagarwala PS, O'Brien S *et al.* Origin and role of a subset of tumor-associated neutrophils with antigen-presenting cell features in early-stage human lung cancer. *Cancer Cell* 2016; **30**: 120–135.
- Ponzetta A, Carriero R, Carnevale S *et al.* Neutrophils driving unconventional T cells mediate resistance against murine sarcomas and selected human tumors. *Cell* 2019; **178**: 346–360 e324.
- Naxerova K, Reiter JG, Brachtel E *et al.* Origins of lymphatic and distant metastases in human colorectal cancer. *Science* 2017; **357**: 55–60.
- Yang CW, Strong BS, Miller MJ, Unanue ER. Neutrophils influence the level of antigen presentation during the immune response to protein antigens in adjuvants. *J Immunol* 2010; **185**: 2927–2934.
- Yang CW, Unanue ER. Neutrophils control the magnitude and spread of the immune response in a thromboxane A2-mediated process. *J Exp Med* 2013; **210**: 375–387.
- Glodde N, Bald T, van den Boorn-Konijnenberg D *et al.* Reactive neutrophil responses dependent on the receptor tyrosine kinase c-MET limit cancer immunotherapy. *Immunity* 2017; **47**: 789–802 e789.
- Ortiz ML, Lu L, Ramachandran I, Gabrilovich DI. Myeloid-derived suppressor cells in the development of lung cancer. *Cancer Immunol Res* 2014; **2**: 50–58.
- McClure C, McPeak MB, Youssef D, Yao ZQ, McCall CE, El Gazzar M. Stat3 and C/EBP $\beta$  synergize to induce miR-21 and miR-181b expression during sepsis. *Immunol Cell Biol* 2017; **95**: 42–55.
- Nagaraj AS, Lahtela J, Hemmes A *et al.* Cell of origin links histotype spectrum to immune microenvironment diversity in non-small-cell lung cancer driven by mutant kras and loss of Lkb1. *Cell Rep* 2017; **18**: 673–684.
- Mollaoglu G, Jones A, Wait SJ *et al.* The lineage-defining transcription factors SOX2 and NKX2-1 determine lung cancer cell fate and shape the tumor immune microenvironment. *Immunity* 2018; **49**(764–779): e769.
- Ferone G, Song JY, Sutherland KD *et al.* SOX2 is the determining oncogenic switch in promoting lung squamous cell carcinoma from different cells of origin. *Cancer Cell* 2016; **30**: 519–532.
- Kargl J, Busch SE, Yang GH *et al.* Neutrophils dominate the immune cell composition in non-small cell lung cancer. *Nat Commun* 2017; **8**: 14381.
- Puram SV, Tirosh I, Parikh AS *et al.* Single-cell transcriptomic analysis of primary and metastatic tumor ecosystems in head and neck cancer. *Cell* 2017; **171**: 1611–1624 e1624.
- Vermi W, Micheletti A, Lonardi S *et al.* slanDCs selectively accumulate in carcinoma-draining lymph nodes and marginate metastatic cells. *Nature Commun* 2014; **5**: 3029.
- Chtanova T, Schaeffer M, Han SJ *et al.* Dynamics of neutrophil migration in lymph nodes during infection. *Immunity* 2008; **29**: 487–496.

29. Hampton HR, Bailey J, Tomura M, Brink R, Chtanova T. Microbe-dependent lymphatic migration of neutrophils modulates lymphocyte proliferation in lymph nodes. *Nat Commun* 2015; **6**: 7139.
30. Giurisato E, Lonardi S, Telfer B et al. Extracellular-regulated protein kinase 5-mediated control of p21 expression promotes macrophage proliferation associated with tumor growth and metastasis. *Cancer Res* 2020; **80**: 3319–3330.
31. Rigby DA, Ferguson DJ, Johnson LA, Jackson DG. Neutrophils rapidly transit inflamed lymphatic vessel endothelium via integrin-dependent proteolysis and lipoxin-induced junctional retraction. *J Leukoc Biol* 2015; **98**: 897–912.
32. De Larco JE, Wuertz BR, Furcht LT. The potential role of neutrophils in promoting the metastatic phenotype of tumors releasing interleukin-8. *Clin Cancer Res* 2004; **10**: 4895–4900.
33. Chen MB, Hajal C, Benjamin DC et al. Inflamed neutrophils sequestered at entrapped tumor cells via chemotactic confinement promote tumor cell extravasation. *Proc Natl Acad Sci USA* 2018; **115**: 7022–7027.
34. Wculek SK, Malanchi I. Neutrophils support lung colonization of metastasis-initiating breast cancer cells. *Nature* 2015; **528**: 413–417.
35. Kaplan RN, Rafii S, Lyden D. Preparing the "soil": the premetastatic niche. *Cancer Res* 2006; **66**: 11089–11093.
36. Psaila B, Lyden D. The metastatic niche: adapting the foreign soil. *Nature Rev Cancer* 2009; **9**: 285–293.
37. Ferlito A, Rinaldo A, Devaney KO et al. Prognostic significance of microscopic and macroscopic extracapsular spread from metastatic tumor in the cervical lymph nodes. *Oral Oncol* 2002; **38**: 747–751.
38. Mishalian I, Bayuh R, Eruslanov E et al. Neutrophils recruit regulatory T-cells into tumors via secretion of CCL17—a new mechanism of impaired antitumor immunity. *Int J Cancer* 2014; **135**: 1178–1186.
39. Vescevi R, Monti M, Moratto D et al. Collapse of the plasmacytoid dendritic cell compartment in advanced cutaneous melanomas by components of the tumor cell secretome. *Cancer Immunol Res* 2019; **7**: 12–28.
40. Szczerba BM, Castro-Giner F, Vetter M et al. Neutrophils escort circulating tumour cells to enable cell cycle progression. *Nature* 2019; **566**: 553–557.
41. Kalluri R, Weinberg RA. The basics of epithelial-mesenchymal transition. *J Clinical Invest* 2009; **119**: 1420–1428.
42. Zhang W, Gu J, Chen J et al. Interaction with neutrophils promotes gastric cancer cell migration and invasion by inducing epithelial-mesenchymal transition. *Oncol Rep* 2017; **38**: 2959–2966.
43. Wang Y, Chen J, Yang L et al. Tumor-contacted neutrophils promote metastasis by a CD90-TIMP-1 juxtacrine-paracrine loop. *Clin Cancer Res* 2019; **25**: 1957–1969.
44. Puram SV, Parikh AS, Tirosh I. Single cell RNA-seq highlights a role for a partial EMT in head and neck cancer. *Mol Cell Oncol* 2018; **5**: e1448244.
45. Abbas AR, Baldwin D, Ma Y et al. Immune response in silico (IRIS): immune-specific genes identified from a compendium of microarray expression data. *Genes Immun* 2005; **6**: 319–331.
46. Veglia F, Perego M, Gabrilovich D. Myeloid-derived suppressor cells coming of age. *Nat Immunol* 2018; **19**: 108–119.
47. Natsuzaka M, Whelan KA, Kagawa S et al. Interplay between Notch1 and Notch3 promotes EMT and tumor initiation in squamous cell carcinoma. *Nature Commun* 2017; **8**: 1758.
48. Agarwal D, Pardhe N, Bajpai M et al. Characterization, localization and patterning of lymphatics and blood vessels in oral squamous cell carcinoma: a comparative study using D2–40 and CD-34 IHC marker. *J Clin Diagnostic Res* 2014; **8**: Zc86–89.
49. Balsat C, Signolle N, Goffin F et al. Improved computer-assisted analysis of the global lymphatic network in human cervical tissues. *Mod Pathol* 2014; **27**: 887–898.
50. Mattavelli D, Lombardi D, Missale F et al. Prognostic nomograms in oral squamous cell carcinoma: the negative impact of low neutrophil to lymphocyte ratio. *Front Oncol* 2019; **9**: 339.
51. Marini O, Costa S, Bevilacqua D et al. Mature CD10+ and immature CD10- neutrophils present in G-CSF-treated donors display opposite effects on T cells. *Blood* 2017; **129**: 1343–1356.
52. Leliefeld PH, Koenderman L, Pillay J. How neutrophils shape adaptive immune responses. *Front Immunol* 2015; **6**: 471.
53. Krzystek-Korpacka M, Matusiewicz M, Diakowska D et al. Elevation of circulating interleukin-8 is related to lymph node and distant metastases in esophageal squamous cell carcinomas-implication for clinical evaluation of cancer patient. *Cytokine* 2008; **41**: 232–239.
54. Chalikvendra V, Kanchi KL, Onken MD, Winkler AE, Mardis E, Uppaluri R. Genomic analysis to define molecular basis of aggressiveness in a mouse model of oral cancer. *Genom Data* 2015; **3**: 61–62.
55. Sionov RV, Fridlender ZG, Granot Z. The multifaceted roles neutrophils play in the tumor microenvironment. *Cancer Microenviron* 2015; **8**: 125–158.
56. Kamioka Y, Takakura K, Sumiyama K, Matsuda M. Intravital Forster resonance energy transfer imaging reveals osteopontin-mediated polymorphonuclear leukocyte activation by tumor cell emboli. *Cancer Sci* 2017; **108**: 226–235.
57. Fidler IJ, Gersten DM, Hart IR. The biology of cancer invasion and metastasis. *Adv Cancer Res* 1978; **28**: 149–250.
58. Yui S, Tomita K, Kudo T, Ando S, Yamazaki M. Induction of multicellular 3-D spheroids of MCF-7 breast carcinoma cells by neutrophil-derived cathepsin G and elastase. *Cancer Sci* 2005; **96**: 560–570.
59. Ren ZH, Zhang CP, Ji T. Expression of SOX2 in oral squamous cell carcinoma and the association with lymph node metastasis. *Oncol Lett* 2016; **11**: 1973–1979.
60. Chou MY, Hu FW, Yu CH, Yu CC. Sox2 expression involvement in the oncogenicity and radiochemoresistance of oral cancer stem cells. *Oral Oncol* 2015; **51**: 31–39.
61. Liang X, Deng M, Zhang C et al. Combined class I histone deacetylase and mTORC1/C2 inhibition suppresses the initiation and recurrence of oral squamous cell carcinomas by repressing SOX2. *Cancer Lett* 2019; **454**: 108–119.

62. Pang M-F, Georgoudaki A-M, Lambut L et al. TGF- $\beta$ 1-induced EMT promotes targeted migration of breast cancer cells through the lymphatic system by the activation of CCR7/CCL21-mediated chemotaxis. *Oncogene* 2016; **35**: 748–760.
63. Devi S, Wang Y, Chew WK et al. Neutrophil mobilization via plerixafor-mediated CXCR4 inhibition arises from lung demargination and blockade of neutrophil homing to the bone marrow. *J Exp Med* 2013; **210**: 2321–2336.
64. Duan Y, Zhang S, Wang L et al. Targeted silencing of CXCR4 inhibits epithelial-mesenchymal transition in oral squamous cell carcinoma. *Oncol Lett* 2016; **12**: 2055–2061.
65. Tulotta C, Stefanescu C, Chen Q, Torraca V, Meijer AH, Snaar-Jagalska BE. CXCR4 signaling regulates metastatic onset by controlling neutrophil motility and response to malignant cells. *Sci Rep* 2019; **9**: 2399.
66. Galon J, Mlecnik B, Bindea G et al. Towards the introduction of the 'Immunoscore' in the classification of malignant tumours. *J Pathol* 2014; **232**: 199–209.
67. Zilionis R, Engblom C, Pfirschke C et al. Single-cell transcriptomics of human and mouse lung cancers reveals conserved myeloid populations across individuals and species. *Immunity* 2019; **50**: 1317–1334.e10.
68. Lok LSC, Dennison TW, Mahbubani KM, Saeb-Parsy K, Chilvers ER, Clatworthy MR. Phenotypically distinct neutrophils patrol uninfected human and mouse lymph nodes. *Proc Natl Acad Sci USA* 2019; **116**: 19083–19089.
69. Cella M, Jarrossay D, Facchetti F et al. Plasmacytoid monocytes migrate to inflamed lymph nodes and produce large amounts of type I interferon. *Nat Med* 1999; **5**: 919–923.
70. Galon J, Pages F, Marincola FM et al. Cancer classification using the Immunoscore: a worldwide task force. *J Transl Med* 2012; **10**: 205.
71. Calzetti F, Tamassia N, Arruda-Silva F, Gasperini S, Cassatella MA. The importance of being "pure" neutrophils. *J Allergy Clin Immunol* 2017; **139**: 352–355.e356.
72. Arruda-Silva F, Bianchetto-Aguilera F, Gasperini S et al. Human neutrophils produce CCL23 in response to various TLR-Agonists and TNF $\alpha$ . *Front Cell Infect Microbiol* 2017; **7**: 176.
73. Ritchie ME, Phipson B, Wu D et al. limma powers differential expression analyses for RNA-sequencing and microarray studies. *Nucleic Acids Res* 2015; **43**: e47.
74. Law CW, Chen Y, Shi W, Smyth GK. voom: precision weights unlock linear model analysis tools for RNA-seq read counts. *Genome Biol* 2014; **15**: R29.
75. Hanzelmann S, Castelo R, Guinney J. GSEA: gene set variation analysis for microarray and RNA-seq data. *BMC Bioinformatics* 2013; **14**: 7.

### Supporting Information

Additional supporting information may be found online in the Supporting Information section at the end of the article.



This is an open access article under the terms of the Creative Commons Attribution-NonCommercial-NoDerivs License, which permits use and distribution in any medium, provided the original work is properly cited, the use is non-commercial and no modifications or adaptations are made.





## Pro-tumoral B cells in laryngeal cancer

**Missale, F.**  
Bugatti, M.  
Marchi, F.  
Mandelli, G.E.  
Bruni, M.  
Palmerini, G.  
Monti, M.  
Bozzola, A.M.  
Arena, G.  
Guastini, L.  
Boggio, M.  
Parrinello, G.  
Peretti, G.  
Vermi, W.

Clinical & translational immunology  
2022 - Under Review - Minor review received

### **Abstract**

#### **Objectives**

Laryngeal squamous cell carcinomas (LSCC) are characterized by an excellent prognosis for stage I tumors but a significant risk of locoregional and distant recurrence for intermediate to advanced disease. This study will investigate the clinical relevance of the tumor microenvironment in a large cohort of treatment-naïve patients affected by stage II-IV LSCC.

#### **Methods**

Whole slide-based digital pathology analysis was applied to measure six immune cell populations identified by immunohistochemistry (IHC) staining for CD3, CD8, CD20, CD66b, CD163 and CD38. Survival analysis was performed by Cox proportional-hazards models and unsupervised hierarchical clustering by k-means method. Double IHC staining and *in-situ* hybridization by RNAscope allowed further analysis of a pro-tumoral B-cells population.

#### **Results**

A cohort of 98 patients was enrolled and analyzed. The cluster of immune-infiltrated LSCC experienced a significantly worse disease-specific survival. As novel finding, we uncover an association between high CD20<sup>+</sup> B-cells and a worse distant recurrence. The phenotypic analysis of infiltrating CD20<sup>+</sup> B-cells showed a naïve (BCL6<sup>-</sup>CD27<sup>-</sup>Mum1<sup>-</sup>) regulatory phenotype, producing TGFβ but not IL10, according to an active TGFβ pathway, as proved by positivity of pSMAD2 staining.

#### **Conclusion**

The identification of regulatory B-cells in the context of LSCC, along with the activation of the TGFβ pathway, could be a further hint for new trial designs investigating the efficacy of already available molecules targeting the TGFβ pathway in the context of LSCC.

**Keywords:** laryngeal neoplasms, tumor microenvironment, B-cells, B-reg, prognosis

### Introduction

One of the main goals of modern precision oncology is the ability to predict outcomes and modulate treatment at individual patient level by profiling the immune and molecular tumor landscape. During the last decades, several preclinical and clinical observations established the crucial role of cancer immunosurveillance in controlling cancer growth.<sup>1-4</sup> However, most clinically apparent and progressing human neoplasms have escaped cancer immunosurveillance emerging as variants with reduced immunogenicity through an immunoediting process. As a result, a fraction of human cancers are immune-desert whereas others are infiltrated by myeloid and lymphoid immune-suppressive cells.<sup>5</sup> The extensive works in colorectal carcinoma<sup>6,7</sup> and other solid tumors<sup>8,9</sup> confirmed that the analysis of the tumor microenvironment (TME) allows the identification of patients subgroups with different prognoses and predicts response to immune checkpoint inhibitors (ICI) as immunotherapy.<sup>10</sup> Among head and neck cancer the indication for ICIs outside clinical trials is still limited to non-resectable platinum-resistant tumors<sup>11,12</sup> with an improvement of survival, compared to standard of care; however, long-term stable complete response is still unpredictable.<sup>13</sup> Promising results of ICIs in the neoadjuvant setting suggest a new clinical scenario for the treatment of these tumors.<sup>14-19</sup> The identification of biomarkers of response is urgently needed to guide current and future therapeutic options. Recent analysis revealed that head and neck squamous cell carcinomas (HNSCC) are highly mutated and distinct in molecular subtypes, including the HPV-driven subgroup showing improved prognosis.<sup>20</sup> As a result of a high tumor mutational burden of HNSCC, neoantigens load could represent an indicator of response to immunotherapies.<sup>21</sup>

Laryngeal squamous cell carcinoma (LSCC) represents one of the most frequent HNSCC with an overall estimate of 184'615 new cases and 99'840 new deaths in 2020. The clinical behavior of stage I glottic tumors is favorable, with an excellent long-term prognosis;<sup>22</sup> by contrast, the survival of patients with intermediate-advanced stage LCSS is still very poor.<sup>23</sup> Specifically, in addition to locoregional recurrence, up to 15-20% of patients develop hematogenous distant spread with limited treatment options and a median overall survival of 10 months.<sup>24,25</sup> Few studies analyzed the TME of LSCCs and revealed that infiltration of CD8<sup>+</sup> T cells predicts better prognosis, whereas enrichment of tumor-infiltrating macrophages identifies LSCCs with worse outcomes.<sup>26-31</sup> No definitive data are available on the clinical relevance of tumor-infiltrating B-cells, an immune population largely unexplored<sup>26-31</sup>.

The present study proposes the analysis of the TME in a large retrospective cohort of LSSC. Eighty-eight treatment-naïve patients with intermediate to advanced stage tumors were included. Whole-slide digital pathology analysis was performed by counting six immune cell populations: CD3<sup>+</sup> T-cells, CD8<sup>+</sup> T-cells, CD20<sup>+</sup> B-cells, CD38<sup>+</sup> plasma cells, CD66b<sup>+</sup> neutrophils and CD163<sup>+</sup> macrophages. Immune enriched tumors experienced a poorer disease-specific survival, supported by the multivariable analysis. Furthermore, our results identify an association between the density of tumor-infiltrating CD20<sup>+</sup> B-cells and higher risk of distant recurrence. The in-depth analysis of this subgroup showed a naïve phenotype of B-cells (BCL6<sup>-</sup>, CD27<sup>-</sup> and Mum1<sup>-</sup>) and their localization in a TGFβ rich microenvironment, supporting the hypothesis of the presence of a regulatory B-cells (B-reg) population in the immune-contexture of LSCC.

## Results

### *1) Coordinate infiltration of immune cells in LSCC*

Ninety-eight patients (PT) were enrolled for this study including 83 males (84.7%) and 15 females (15.3%). The mean age at the time of the treatment was 67 years (range 43-89). As surgical treatment 62 PT (63.3%) received transoral laser microsurgery (TLM), 14 (14.3%) open partial horizontal laryngectomies (OPHL) and 22 (22.4%) a total laryngectomy (TL). According to the TNM staging system, 45 PT (45.9%) were defined as pT2, 34 PT (34.7%) as pT3 and 19 PT (19.4%) as pT4a. Based on the regional lymph nodes involvement, 75 PT (76.5%) were defined as N0, 8 PT (8.2%) as pN1, 6 PT (6.1%) as pN2 and 9 PT (9.2%) as pN3. Risk factors such as perineural invasion (PNI) or lymphovascular invasion (LVI) were present in 44 (44.9%) and 38 (38.8%) PT, respectively (**Table 1**). The median follow-up time was 49 months (CI95% 45-58 months). During the follow-up period, 25 (25.5%) PTs developed locoregional recurrence whereas 15 (15.3%) PT distant hematogenous metastases; 18 (18.4%) PTs died due to disease progression (**Table 1**).

Digital microscopy analysis was performed on immune-stained sections to quantify tumor-associated CD3<sup>+</sup> T-cells, CD8<sup>+</sup> T-cells, CD20<sup>+</sup> B-cells, CD38<sup>+</sup> plasma cells, CD66b<sup>+</sup> neutrophils<sup>32</sup> and CD163<sup>+</sup> macrophages (**Figure 1a**, **Supplementary Table S1**). The median area of analyzed tissue was 37.4 mm<sup>2</sup> (range 3.0 – 320.4 mm<sup>2</sup>; IQR 15.6-90.3 mm<sup>2</sup>). Using a cell recognition algorithm, the median densities of immune cells resulted respectively of 443 cells mm<sup>-2</sup> (range 68-2210 cells mm<sup>-2</sup>) for CD3<sup>+</sup> T-cells, of 457 cells mm<sup>-2</sup> (range 30-3200 cells mm<sup>-2</sup>) for CD8<sup>+</sup> T-cells, of 178 cells mm<sup>-2</sup> (range 11-1230 cells mm<sup>-2</sup>) for CD20<sup>+</sup> B-cells, of 310 cells mm<sup>-2</sup> (range 5-2580 cells mm<sup>-2</sup>) for CD38<sup>+</sup> plasma cells, and of 140 cells mm<sup>-2</sup> (range 1-819 cells mm<sup>-2</sup>) for CD66b<sup>+</sup> neutrophils. The CD163<sup>+</sup> macrophages infiltrate, analyzed with a pixel count algorithm, occupied a median area of 2.94% (range 0.005-18.29%) (**Supplementary Table S2**).

Correlation analysis of the quantitative measurements of tumor immune infiltrates, as performed by Spearman's correlation test, showed a strong direct correlation between all the immune cell populations analyzed, with the exception of the CD66b<sup>+</sup> cells (**Figure 1b**). Among the individual cells counted CD3<sup>+</sup> cells represent a median 46.4% of the immune infiltrate (range 9.5-85.4%), CD8<sup>+</sup> a median 33.2% (range 3.4-85.4%), CD38<sup>+</sup> a median 26.6% (range 0.3-65.9%), CD20<sup>+</sup> a median 12.3% (range 1.9-51.3%), CD66b<sup>+</sup> a median 9.6% (range 0.1-63.4%) (**Figure 1c** and **Supplementary Table S3**); for this analysis CD163<sup>+</sup> were not includible as measured as % of the tumor surface. At the single tumor level, computing a tSNE dimensionality reduction of immune infiltrates identified the co-existence of most of them and confirmed the independent enrichment of CD66b<sup>+</sup> neutrophils (**Figure 1d-i**). Association analysis between clinical variables and immune cell infiltration did not any reveal meaningful relationship (**Supplementary Table S4-S8**).

### *2) Immune infiltrated LSCC display a worse prognostic phenotype*

Considering the Z-score for immune cells infiltration, by the *average silhouette* method, the cohort can be best subdivided into two clusters (**Figure 2a**). Unsupervised *k-means* partitioning, as shown in **Figure 2b**, identified a dominant cluster (Cluster 1) characterized by Immune<sup>Cold</sup> tumors and a minor cluster (Cluster 2) displaying enrichment of all immune cells analyzed (Immune<sup>Hot</sup>). Cluster 2 was confirmed to be highly

infiltrated of all immune-cells tested ( $P < 0.05$ ; **Figure 2c**), whereas no association with most relevant clinical features (pT category, pN involvement, PNI, LVI) was observed ( $p > 0.05$ , **Supplementary Table S9**). Considering the survival end-points in multivariable models including Age, pT category and pN category as covariates, the Cluster 2 was independently associated with a worsen disease-specific survival (DSS) (H.R. 6.03; CI95% 1.66-21.87;  $P = 0.006$ ), as also shown in adjusted survival curves in **Figure 2d**. pT4a category represented a significant and independent risk factor (H.R. 25.81; CI95% 5.35-124.45;  $P < 0.0001$ ), as shown in **Figure 2e** and in **Figure 2f** combining its marginal effect with those of the clusters.

### *3) Dense CD3<sup>+</sup> T-cells and CD20<sup>+</sup> B-cells infiltration predict unfavorable prognosis in LSCC*

The prognostic significance of each immune cell population was investigated separately building a multivariable model for each outcome and evaluating the AIC. Expectedly, Age, pT4a category and LVI were covariates significantly associated with the OS (**Figure 3a**).<sup>33</sup> A non-linear effect was observed for the Age variable, being a risk factor at the lowest and highest value (**Figure 3b**). The CD3 density was kept in the model but none association with the OS was observed. The DSS analysis confirmed Age and pT4a category of being independent clinical covariates related to this outcome (**Figure 3c**); the effect of the Age followed a non-linear shape, as for OS (**Figure 3d**). The CD3 density represented a risk factor (**Figure 3e-3f**) with an H.R. of 2.12 for each doubling of the CD3 density value (CI95% 1.23-3.68;  $P = 0.007$ ), coherently with the result showing a detrimental prognostic role of Cluster 2. Notably, when considering locoregional recurrence free survival (LRFS), CD3 density was the only covariate independently associated with the outcome (**Figure 4a**) in form of risk factor with an H.R. of 1.73 for each doubling value (CI95% 1.17-2.7;  $P = 0.014$ ; **Figure 4b-c**). Interestingly, a significant interaction between the density of CD3<sup>+</sup> and pT category was observed ( $P = 0.0274$ ), as shown in **Figure 4d**, with a remarkable effect on prognosis in pT4a group, as seen for the DSS. Analyzing the distant recurrence free survival (DRFS) as oncological outcome both pT4a category and N3 category were associated with a worse prognosis ( $P < 0.001$ ), compared to the reference categories (pT2 and N0). Among tumor infiltrating immune cells, a higher density of CD20<sup>+</sup> B-cells was associated with a worse outcome (H.R. 5.79; CI95%, 2.23-14.98;  $P < 0.001$ ), whereas enrichment of CD8<sup>+</sup> T-cells resulted protective (H.R. 0.54; CI95% 0.30-0.97;  $P = 0.04$ ) (**Figure 4e-i**). Contour plots in **Figure 4j-l** illustrate the combined effect of each immune cell density measure in the model, to predict the 5-y DRFS.

### *4) Occurrence and localization of CD20<sup>+</sup> B-cells in LSCC*

The evidence of the worse prognostic significance of CD20<sup>+</sup> B-cells infiltration guided to an in-depth analysis of their localization within the TME. B-cells were organized in form of aggregates (median, 36.0%; min-max, 0%-83.7%) also identifiable as tertiary lymphoid structures, based on the occurrence of BCL6<sup>+</sup> germinal center B-cells (CD20<sup>TLS</sup>); alternatively, CD20<sup>+</sup> B-cells were in form of diffuse stromal/intratumoral infiltrate (CD20<sup>T</sup>), (median, 64.0%; min-max, 16.3%-100%). The TLS frequency in terms of number of TLS per squared millimeter was also taken into account, having in the whole cohort a median value of 0.131 TLS mm<sup>-2</sup> (min-max, 0.010-2.32 TLS mm<sup>-2</sup>). The density of CD20<sup>+</sup> B-cells measured in the different areas of interest

(CD20<sup>TLS</sup> and CD20<sup>IT</sup>) were highly directly correlated ( $P < 0.0001$ , **Figure 5a-c**), suggesting a coordinated recruitment of B-cells organized as TLS or diffuse into the tumor/stroma. A significant decrease of TLS was observed in advanced T and N categories, along with the progression of the disease, and for tumors harboring risk factors, such as PNI and/or LVI, a significant decrease of TLS density was also observed (**Figure 5d-e**). A further multivariable model was fitted to dissect the clinical relevance of CD20<sup>TLS</sup> and CD20<sup>IT</sup> in terms of distant recurrence. Adding the TLS density as covariate, this did not result in an improvement of the regression model (AIC<sub>pre</sub> 102.68, AIC<sub>post</sub> 104.35) and this variable was not even associated with a different DRFS (H.R. 1.26; CI95% 0.574-2.763;  $P = 0.5647$ , **Figure 5f-I**), still being the whole CD20<sup>+</sup> density a significant risk factor (H.R. 5.053; CI95% 1.771-14.419;  $P = 0.002$ , **Figure 5f-I**). Thus, the enrichment of CD20<sup>+</sup> B-cells and not their differential localization is relevant for the risk of distant recurrence in LSCC.

#### 5) In situ characterization of pro-metastatic B-cells

Tumor-infiltrating B-cells are in general poorly characterized and data on head and neck squamous cell carcinoma are limited to the oral cavity, oropharynx and hypopharynx sites,<sup>34</sup> being their study in the laryngeal site included in mixed cohorts.<sup>28</sup> Literature data indicate that B-cells can localize both in the tumoral or stromal compartment, and they often contribute to the composition of TLS, although their exact function and clinical relevance are not yet completely understood.<sup>35</sup> To investigate the phenotype of CD20<sup>IT</sup> B-cells, we tested a set of B-cell antigens including CD20, Pax5, Bcl6, Mum1 and CD27 on serial and double-stained sections of a set of cases that experienced distant recurrence along the follow-up time (n=15).<sup>36,37</sup> The TLS structures, defined as aggregates of B and T cells showing a BCL6<sup>+</sup> germinal center phenotype, were excluded from this analysis (**Figure 6a-b**). Based on double stains we found that most CD20<sup>IT</sup> lacked CD27, (median fraction of CD27<sup>+</sup>/CD20<sup>+</sup> < 1%) and Mum1 reactivity (median fraction of MUM1<sup>+</sup>/CD20<sup>+</sup> < 1%) thus corresponding to mature B-cells with naïve phenotype lacking a plasma cell differentiation (**Figure 6c**).<sup>36,37</sup>

#### 6) Functional analysis of pro-metastatic B-cells

To extend our analysis at the functional level, we tested the expression of IL-10 and TGFβ by using RNAscope (n=13). IL-10 and TGFβ probes were validated in cell-blocks of monocyte-derived macrophages showing, as expected, a selective expression of IL-10 on M2 macrophages and a diffuse expression of TGFβ both on M1 and M2 type macrophages; this observation was also validated by RT-qPCR data (**Supplementary Figure S2**).

Based on RNAscope findings, TGFβ mRNA resulted strongly and diffusely expressed by tumor cells and cells of the TME (mean ± SD scores  $1.6 \pm 1.0$  and  $2.2 \pm 0.8$  on 0-3 scale; **Figure 7a**), whereas IL-10 signal was limited to the TME compartment (**Figure 7a**). Specifically, by using a set of immunohistochemical markers, we found that among TME cells, TGFβ transcript were detected in CD20<sup>IT</sup>, CD163<sup>+</sup> macrophages and SMA<sup>+</sup> fibroblasts (**Figure 7b**), whereas IL-10 expression was limited to CD163<sup>+</sup> macrophages (**Figure 7b**). Furthermore, by triple immunohistochemical staining for FOXP3, CD20 and CD3 or CD8 we could demonstrate recurrent cell interaction between CD20<sup>IT</sup> and CD3<sup>+</sup>FOXP3<sup>+</sup> T-cells, the latter displaying a CD8<sup>+</sup>

CD3<sup>+</sup> Treg phenotype (**Figure 7c** and **Supplementary Figure S3**). Thus, our data support the identification in LSCC of a subset of naïve CD20<sup>+</sup> TGFβ<sup>+</sup> coherents with the so called tumor-evoked regulatory B-cells (tBreg), previously identified as promoters of breast cancer metastasis through conversion of resting CD4<sup>+</sup> T cells to regulatory T-cells.<sup>38</sup> Furthermore, testing for pSMAD2 reactivity, its nuclear positivity was observed in most of tumor infiltrating CD20<sup>+</sup> B-cells (TIB) of such cases and on tumor cells, further supporting the activation of the TGFβ pathway (**Figure 7d**), by contrast they were negative for PD-L1 staining (**Figure 7e**).

### Discussion

In the present study we have characterized the TME of a homogeneous retrospective cohort of patients affected by LSCC and surgically treated in a referral center. Among relevant findings, a cluster of immune infiltrated cases (Immune<sup>Hot</sup>), representing one-third of the cohort, experienced a significantly worse DSS as confirmed at multivariable analysis. Furthermore, the investigation of different survival outcomes identified the association between a high CD20<sup>+</sup> B-cells density with a worse distant recurrence. The immuno-phenotype of the intratumoral CD20<sup>+</sup> B-cells was coherent with a naïve B-cell phenotype with production of TGFβ, likely corresponding to regulatory B phenotype.

Studies on colorectal carcinoma,<sup>6,39</sup> subsequently extended to other cancer types<sup>8</sup>, have shown that the type and density of immune cells in the TME is one of the key prognosticators of the clinical outcomes of patients, beyond the classical staging criteria.<sup>40</sup> The available literature on LSCC TME is limited to few studies based on tissue microarray samples and computing only OS and DFS as outcomes.<sup>26-31,41,42</sup> Most authors confirmed the positive prognostic role of high CD8<sup>+</sup> T-cells density,<sup>26,28,30,31</sup> as was also observed in our analysis concerning the distant recurrence, as outcome. The favorable effect of a high CD8<sup>+</sup> T-cells density was also already proved by a meta-analysis by Rodrigo et al. both considering the overall and disease-free survivals as outcomes.<sup>43</sup> However, as one of the main findings of this study, we identified an association between an immune-rich TME and a worse DSS. Although surprising, this observation is not limited to our cohort. Hoing et al. observed a worse OS in LSCC patients with a high CD45<sup>+</sup> cells infiltration;<sup>27</sup> similar observations were obtained in cohorts of renal clear cell carcinoma.<sup>9,44,45</sup> A possible explanation of such phenomenon is the switch towards an exhausted tumor microenvironment,<sup>45,46</sup> and this is coherent with the observed significant interaction between CD3<sup>+</sup> T-cells and T stage in the survival analysis, meaning a worse prognostic effect in advance T categories. Limited data, furthermore, suggests also to be relevant the ratio between CD3<sup>+</sup> T-cells and CD4<sup>+</sup> T-cells whose higher value are related to a better overall and disease-free survivals, meaning a microenvironment skewed toward an enrichment of CD8<sup>+</sup> T-cells and paucity of CD4<sup>+</sup> T-cells.<sup>43</sup> This finding was also confirmed by the analysis conducted by Zhang et al. on the HNSCC cohort of the “The Cancer Genome Atlas” (TCGA) dataset.<sup>47</sup>

The investigation in our cohort of different survival outcomes allowed the identification in the tumoral area of a population of CD20<sup>+</sup> B-cells associated with a worse distant recurrence. Previous hints from the HNSCC literature also support this observation. Whole genome expression analysis in a matched cohort of 49 primary HNSCC showed an enrichment of plasma cells and T-reg, estimated with a deconvolution algorithm, in the

group that experienced distant recurrence.<sup>48</sup> Data on clinical and biological relevance of TIB in the immune contexture of solid tumors are limited.<sup>49</sup> The emerging literature, mostly derived from the analysis of cohorts of patients treated with immunotherapy, suggests the contribution of B-cells in the anti-tumor response, selectively in the context of mature TLS, whereas the extra-TLS component likely promotes immunosuppression.<sup>50,51</sup>

The existence of immunosuppressive and tumor-promoting B-cells (Breg) was described since the 1990s<sup>52,53</sup> in the mouse system. The most studied population is characterized by the B10 phenotype, identified by Yanaba et al.<sup>54</sup> and subsequently confirmed in human solid tumors.<sup>55,56</sup> B10 cells (CD1d<sup>hi</sup>CD5<sup>+</sup>CD19<sup>+</sup>) are located in lymphoid organs, express switched (IgM<sup>-</sup>) or unswitched (IgM<sup>+</sup>) B-memory (CD27<sup>+</sup>) phenotype<sup>57</sup> and produce IL-10.<sup>56,58</sup>

Several studies reported the crucial role of IL-10 in the B-cells regulation.<sup>49</sup> However IL-10-independent regulatory functions were identified as mediated by TGFβ.<sup>59</sup> Preclinical studies indicate that a population of TGFβ<sup>+</sup> Breg can be generated starting from a pool of naïve B-cells exposed to tumor-derived factors, as exosomes,<sup>60</sup> in agreement with the observed mature naïve phenotype of TIB in the context of LSCC (BCL6<sup>-</sup>, CD27<sup>-</sup> and Mum1<sup>-</sup>).

The subset of Breg, also referred as tumor evoked Breg (tBreg),<sup>38</sup> was identified both in the murine and solid tumors models by Olkhanud et al.,<sup>38</sup> and its properties and phenotype are coherent with the above identified TIB described in LSCC patients of our study (CD20<sup>+</sup>, PAX1<sup>+</sup>, CD27<sup>-</sup>, Mum1<sup>-</sup>, IL10<sup>-</sup>, TGFβ<sup>+</sup>, FOXP3<sup>-</sup>, PD-L1<sup>-</sup>). tBreg regulatory functions are IL-10-independent; by secreting TGFβ they promote FOXP3<sup>+</sup> Treg<sup>38,61</sup> conversion. Furthermore, by flow cytometry, the tBreg phenotype was described as mature B2 CD19<sup>+</sup>pSTAT3<sup>+</sup>CD81<sup>hi</sup>CD25<sup>+</sup>CD27<sup>-</sup>IgD<sup>+</sup> and the results from a breast cancer mouse model support their key-role in promoting cancer metastasis.<sup>38,61</sup>

Given the occurrence of B-reg populations in the immune contexture of solid tumors, the therapeutical benefit of the depletion of the B-cells has been tested with rituximab. However, the results were disappointing and the treatment greatly enhanced cancer progression and metastasis.<sup>62</sup> In contrast, the positive results obtained in the murine models targeting the TGFβ pathway, paved the way for the design of clinical trials in human solid tumors.<sup>63,64</sup> Despite several molecules targeting the TGFβ pathway were designed and multiple trials conducted in the last 15 years, a clinical approval of these compounds outside clinical trials is still lacking.<sup>64,65</sup> As these drugs do not exploit a direct cytotoxic effect on cancer cells, ongoing studies are testing the best clinical scenarios (i.e., drugs combination, biomarkers of response). Of note, in the HNSCC field the Bintrafusp alfa (M7824) molecule, combining a target effect on TGFβ and PD-L1, has shown promising preliminary results with an objective response rate ranging from 13% to 30.5%, with the highest observed in HPV related tumors.<sup>64,66,67</sup> Currently, M7824 is under investigation in the NCT04220775 trial (NCT number), combined with stereotaxic radiotherapy in recurrent or second primary HNSCCs, and definitive results in the neoadjuvant setting, from the NCT04247282 and NCT04428047 trials, whose enrollments is already completed, are expected within 1 year.



In terms of biomarker of response, a rationale exists for pSMAD2 expression.<sup>64</sup> In our series, the evidence of diffuse positivity of pSMAD2 both on TIB and tumor cells supports the rationale of considering this pathway active and targetable in the clinical context of LSCC.<sup>64</sup>

In conclusion, this work identifies a subset of TIB likely promoting failure in the distant control of LSCC. These preliminary findings require additional validation on LSCC and extension to other cancer types whose producing TGF $\beta$ .

### Methods

#### *Study design and cohort of patients.*

The study is an retrospective and translational study, retrieving clinical data and pathologic specimens of a homogeneous cohort of patients affected by LSCC and treated at Otorhinolaryngology Unit of IRCCS Ospedale Policlinico San Martino, University of Genoa, Italy (IRB approval: CER Liguria 230/2019).

As inclusion criteria we enrolled patients affected by intermediate to advance T category LSCC that underwent surgery as primary treatment between 2012 and 2016, with at least 12 months of follow-up or earlier death or recurrence. Early T stage tumors (T1 category), salvage surgery, metastatic disease, or prior systemic treatment for malignancy represented exclusion criteria. Patients were regularly followed with clinical examinations and neck MRI or CT every 3-6 months. For pTNM staging the 8<sup>th</sup> ed. of TNM was applied.<sup>40</sup> Surgical procedures encompassed transoral laser microsurgery, open partial horizontal laryngectomy or total laryngectomy. Patients with clinically positive nodes, with high-risk features, or submitted to open neck surgery underwent lateral and central compartment neck dissection. Patients affected by advanced staged tumors, with high risk features such as perineural invasion, vascular invasion, multiple positive lymph nodes or positive margin were submitted to adjuvant radiotherapy or chemo-radiotherapy, following the NCCN guidelines<sup>68</sup>. Clinical and pathological data taken into account included: age, gender, smoke and alcohol consumption habits, site of the neoplasm, treatment modality, pT category, pN category, overall Stage, Grading, Cartilage invasion (cricoid or thyroid), laryngeal motility, extranodal extension (ENE) for positive lymph-nodes, surgical margins (negative or positive) and follow-up data. As survival endpoints were considered the locoregional recurrence free survival (LRFS), the distant recurrence free survival (DRFS), the overall survival (OS) and the disease specific survival (DSS), defined as the time between surgery and the date of the corresponding event (locoregional recurrence, distant metastasis, death for any cause, cancer related death) or censoring at the last follow-up visit. Details of the cohort are reported in **Table 1**.

#### *Immunohistochemical staining*

Immunohistochemistry (IHC) was performed on a set of tissues samples obtained from the archive of the Department of Pathology (Policlinico San Martino, Genova). For each patient, tissues included a representative whole tissue formalin-fixed, paraffin-embedded (FFPE) block of primary carcinoma. Immunostaining was performed using four micron-thick tissue sections and a set of primary antibodies (**Supplementary Table S1**).

The reaction was revealed using Novolink Polymer (Leica Microsystems) followed by diaminobenzidine (DAB, Dako, Glostrup, Denmark). Finally, the slides were counterstained with Meyer's Haematoxylin.

For double staining, after completing the first immune reaction, the second was visualized using Mach 4 MR-AP (Biocare Medical), followed by Ferangi Blue (Biocare Medical). For triple IHC the third immune reaction was revealed using Novolink Polymer (Leica Microsystems), and developed in 3-amino-9-ethylcarbazole chromogen (AEC), counterstained with hematoxylin and cover-slipped using gelatin. Single staining for CD3, CD8, CD20, CD66b, CD163 and CD38 were applied to identify T-cells, B-cells, Neutrophils, Macrophages, and Plasma cells, respectively. To characterize the phenotype and the localization of tumor-associated B-cells, we performed double and triple immunostaining for a set of B-cells markers including CD20, BCL6, CD27, PAX5, MUM1, CD38, FOXP3, PD-L1 and pSMAD2.

### *Digital microscopy analysis*

The CD3, CD8, CD20, CD66b, CD163 and CD38 stained slides were digitalized using the Aperio CS2 digital scanner and ScanScope software (Aperio Technologies, Leica Biosystem, New Castle Ltd, U.K.) at 20x magnification and analyzed using ImageScope (Leica Microsystems). Each scanned image is annotated manually, and IHC Nuclear Image Analysis algorithm or V9-pixel count algorithm (Leica biosystems, New Castle Ltd, U.K.) is chosen for the computerized whole slide analysis. From each case we obtained the quantitative measure of immune cells density (number of cells/mm<sup>2</sup> or the relative frequency of the area positive to the biomarker) of the entire tumor area, including the invasive margin of the tumor, the latter considered as an area 500  $\mu$ m wide beneath the tumor nests. Examples of counted fields are provided in **Supplementary Figure S1**. For each section stained for CD20, these cells were organized in form of aggregates also identifiable as tertiary lymphoid structures, based on the occurrence of BCL6<sup>+</sup> germinal center B-cells and localization in the same region of T cells, seen on the section stained for CD3 (CD20<sup>TLS</sup>) or in form of diffuse stromal/intratumoral infiltrate (CD20<sup>IT</sup>). The density of CD20<sup>IT</sup> (number of CD20<sup>+</sup> cells mm<sup>-2</sup>-1), excluding the aggregates of B-cells and the TLS density (number of TLS/mm<sup>2</sup>) were measured.

### *RNAscope*

To localize IL10 and TGF $\beta$  positive cells, tissues were analyzed with RNAscope assay (Advanced Cell Diagnostics, Newark, CA, USA) using RNAscope 2.5 HD Assay-RED kit, Hs-IL10 probe (Cat No. 602051) recognizing the nt 122 - 1163 of the IL10 reference sequence NM\_000572.2 and Hs-TGF $\beta$  probe (Cat No. 400881) recognizing the nt 170 to 1649 of the TGF $\beta$  reference sequence NM\_000660.4. The sections from fixed human tissue blocks were treated following the manufacturer's instructions. Briefly, freshly cut 3  $\mu$ m sections were deparaffinized in xylene and treated with the peroxidase block solution for 10 minutes at room temperature followed by the retrieval solution for 15 minutes at 98  $^{\circ}$ C and by protease plus at 40  $^{\circ}$ C for 30 minutes. Control probes included Hs-PPIB (Cat No. 313901) and DapB (Cat No. 310043). The hybridization was performed for 2 h at 40  $^{\circ}$ C. The signal was revealed using RNAscope 2.5 HD Detection Reagent-RED. Combined RNAscope and immunohistochemistry (for CD20, CD163, CD66b, SMA) were used to identify the cellular source of IL10 and TGF $\beta$  positive cells. To this end, IL10 and TGF $\beta$  detection by RNAscope was

followed by immunoreaction was visualized using Mach 4 MR-AP (Biocare Medical) followed by Ferangi Blue (Biocare Medical).

### *Cell-block preparation*

Cell suspensions of monocyte-derived macrophages (MDM) were centrifuged for 10 minutes at 3000 rpm. A solution of plasma (100  $\mu$ L, kindly provided by Centro TrASFusionale, ASST Spedali Civili, Brescia) and HemosIL8 RecombiPlasTin 2G (200  $\mu$ L, Instrumentation Laboratory, Bedford Ma, USA, cat. no.0020003050) (1:2) were added to cell pellets, mixed until the formation of a clot, then placed into a labeled cassette. The specimen was fixed in 10% formalin for 1 hour followed by paraffin inclusion.

### *Real-Time PCR*

IL-10 and TGF $\beta$  mRNA targets were quantified by reverse transcription-polymerase chain reaction (qRT-PCR) assay using the Vii-A 7 Real-Time PCR System (Applied Biosystems, Thermo Fisher Scientific, Waltham, MA, USA). Total RNA was purified from M0, M1 and M2 macrophages ( $n = 1$ ), as previously reported<sup>69</sup>. The cDNA was synthesized by iScript gDNA cDNA Synthesis kit (cat. n. 1725035; Biorad, Hercules, CA, USA) from 500 ng of total RNA, in a total volume of 20  $\mu$ L. One  $\mu$ L of the cDNA synthesis reaction was used for the specific amplification of the target transcripts. The HPRT1 transcript was used as normalization control. The qPCR was performed in a total volume of 10  $\mu$ L with TaqMan® Universal Master Mix II (cat. no. 4369016, Applied Biosystems, Thermo Fisher Scientific) and the Gene Expression Assay for IL10 (Hs00961622-m1), TGFB1 (Hs00998133-m1) and HPRT1 (Cat. n. 4333768T) (Applied Biosystems, Thermo Fisher Scientific). The threshold cycle (Ct) was determined for each sample and quantification was performed using the comparative  $\Delta\Delta$ Ct method.  $\Delta$ Ct was derived as  $Ct_{\text{Target}} - Ct_{\text{Housekeeping}}$ , then  $\Delta\Delta$ Ct was derived as  $\Delta Ct_{\text{Target sample (M1}\phi \text{ or M2}\phi)} - \Delta Ct_{\text{Control sample (M0}\phi)}$ .

### *Statistical analysis*

Standard descriptive statistic was used for data summarizing, expressing means, medians, interquartile range, and ranges. Shapiro-Wilk test was applied to verify the normality of continuous variables distribution. Missing values of clinical variables were imputed with Multivariate Imputation by Chained Equations (MICE)<sup>70</sup>.

Correlation analysis between immune cells densities was done using nonparametric Spearman's rank correlation. Wilcoxon-Mann-Whitney test or Kruskal-Wallis test (followed by Bonferroni p-values adjustment) were used for group comparisons in quantitative variables, and Fisher's exact test for qualitative ones, as appropriate. For achieving a qualitative description of cohabiting immune cells, an Exact Barnes-Hut t-Distributed Stochastic Neighbor Embedding (tSNE) was computed considering Z-scored immune cells infiltration, with Euclidean distance as similarity measure<sup>71</sup>.

The median follow-up time was estimated with the reverse Kaplan-Meier method. Multivariable semi-parametric Cox proportional-hazards models presented, for each outcome, were built estimating the linear predictors of the full models (including all candidate predictors) and developing simplified models that can

predict the predicted values of the full model with high accuracy ( $R^2 \geq 0.85$ ). The simplification is done using an Akaike's Information Criterion (AIC) guided fast backward stepdown against the full model predicted values. Each model was internally validated using bootstrap with 300 resamples. Discrimination was measured by the concordance index (c-index), reported as naive model estimates, its bootstrap estimate (average of individual bootstrap estimates) as well as optimism-corrected one.

For clustering analysis, the optimum number of clusters for subdividing the cohort into groups according to the Z-scored immune cells infiltration, was chosen applying the average silhouette method<sup>72</sup>. Cluster partitioning was performed applying the k-means algorithm with 1000 repetitions. A heatmap was built for graphical evaluation of the results. Comparisons of clusters have been performed by Fisher's exact test or Wilcoxon-Mann-Whitney test.

In all the analyses, a significance level of 5% was used. R (version 4.0.2) and R studio were used for statistical analysis.

### Availability of data and materials

Full dataset is available at: "Larynx\_GE\_TILS\_Dataset", Mendeley Data, V1, <https://doi.org/10.17632/zgp6yt5s2m.1> (Embargo date: 5<sup>th</sup> May 2023).

### Acknowledgments

WV is funded by "Associazione Italiana per la Ricerca sul Cancro" (AIRC-IG-23179).

### References

- 1 Dunn GP, Old LJ, Schreiber RD. The three Es of cancer immunoediting. *Annu Rev Immunol* 2004; **22**: 329–360.
- 2 Mittal D, Gubin MM, Schreiber RD, Smyth MJ. New insights into cancer immunoediting and its three component phases--elimination, equilibrium and escape. *Curr Opin Immunol* 2014; **27**: 16–25.
- 3 Koebel CM, Vermi W, Swann JB *et al.* Adaptive immunity maintains occult cancer in an equilibrium state. *Nature* 2007; **450**: 903–907.
- 4 Dunn GP, Bruce AT, Ikeda H, Old LJ, Schreiber RD. Cancer immunoediting: from immunosurveillance to tumor escape. *Nat Immunol* 2002; **3**: 991–998.
- 5 Teng MWL, Ngjow SF, Ribas A, Smyth MJ. Classifying Cancers Based on T-cell Infiltration and PD-L1. *Cancer Res* 2015; **75**: 2139–2145.
- 6 Galon J, Costes A, Sanchez-Cabo F *et al.* Type, density, and location of immune cells within human colorectal tumors predict clinical outcome. *Science (80- )* 2006; **313**: 1960–1964.
- 7 Bindea G, Mlecnik B, Tosolini M *et al.* Spatiotemporal dynamics of intratumoral immune cells reveal the immune landscape in human cancer. *Immunity* 2013; **39**: 782–795.
- 8 Fridman WH, Pages F, Sautes-Fridman C, Galon J. The immune contexture in human tumours:

- impact on clinical outcome. *Nat Rev Cancer* 2012; **12**: 298–306.
- 9 Fridman WH, Zitvogel L, Sautès-Fridman C, Kroemer G. The immune contexture in cancer prognosis and treatment. *Nat Rev Clin Oncol* 2017; **14**: 717–734.
  - 10 Grivas P, Monk BJ, Petrylak D *et al.* Immune Checkpoint Inhibitors as Switch or Continuation Maintenance Therapy in Solid Tumors: Rationale and Current State. *Target Oncol* 2019; **14**: 505–525.
  - 11 Ferris RL, Blumenschein GJ, Fayette J *et al.* Nivolumab for Recurrent Squamous-Cell Carcinoma of the Head and Neck. *N Engl J Med* 2016; **375**: 1856–1867.
  - 12 Cohen EEW, Soulières D, Le Tourneau C *et al.* Pembrolizumab versus methotrexate, docetaxel, or cetuximab for recurrent or metastatic head-and-neck squamous cell carcinoma (KEYNOTE-040): a randomised, open-label, phase 3 study. *Lancet (London, England)* 2019; **393**: 156–167.
  - 13 Mehra R, Seiwert TY, Gupta S *et al.* Efficacy and safety of pembrolizumab in recurrent/metastatic head and neck squamous cell carcinoma: pooled analyses after long-term follow-up in KEYNOTE-012. *Br J Cancer* 2018; **119**: 153–159.
  - 14 Uppaluri R, Campbell KM, Egloff AM *et al.* Neoadjuvant and Adjuvant Pembrolizumab in Resectable Locally Advanced, Human Papillomavirus-Unrelated Head and Neck Cancer: A Multicenter, Phase II Trial. *Clin cancer Res an Off J Am Assoc Cancer Res* 2020; **26**: 5140–5152.
  - 15 Schoenfeld JD, Hanna GJ, Jo VY *et al.* Neoadjuvant Nivolumab or Nivolumab Plus Ipilimumab in Untreated Oral Cavity Squamous Cell Carcinoma: A Phase 2 Open-Label Randomized Clinical Trial. *JAMA Oncol* 2020; **6**: 1563–1570.
  - 16 Uppaluri R, Zolkind P, Lin T *et al.* Neoadjuvant pembrolizumab in surgically resectable, locally advanced HPV negative head and neck squamous cell carcinoma (HNSCC). *J Clin Oncol* 2017; **35**: 6012.
  - 17 Zuur L, Vos JL, Elbers JB *et al.* LBA40 Neoadjuvant nivolumab and nivolumab plus ipilimumab induce (near-) complete responses in patients with head and neck squamous cell carcinoma: The IMCISION trial. *Ann Oncol* 2020; **31**: S1169.
  - 18 Zuur CL, Elbers JBW, Vos JL *et al.* Feasibility and toxicity of neoadjuvant nivolumab with or without ipilimumab prior to extensive (salvage) surgery in patients with advanced head and neck cancer (the IMCISION trial, NCT03003637). *J Clin Oncol* 2019; **37**: 2575.
  - 19 Horton JD, Knochelmann H, Armeson K, Kaczmar JM, Paulos C, Neskey D. Neoadjuvant presurgical PD-1 inhibition in oral cavity squamous cell carcinoma. *J Clin Oncol* 2019; **37**: 2574.
  - 20 Lawrence MS, Sougnez C, Lichtenstein L *et al.* Comprehensive genomic characterization of head and neck squamous cell carcinomas. *Nature* 2015; **517**: 576–582.
  - 21 Mandal R, Şenbabaoğlu Y, Desrichard A *et al.* The head and neck cancer immune landscape and its immunotherapeutic implications. *JCI insight* 2016; **1**: e89829.
  - 22 Vaculik MF, MacKay CA, Taylor SM, Trites JRB, Hart RD, Rigby MH. Systematic review and meta-analysis of T1 glottic cancer outcomes comparing CO(2) transoral laser microsurgery and

- radiotherapy. *J Otolaryngol - head neck Surg = Le J d'oto-rhino-laryngologie Chir cervico-faciale* 2019; **48**: 44.
- 23 Hoffman HT, Porter K, Karnell LH *et al.* Laryngeal Cancer in the United States : Changes in Demographics , Patterns of Care , and Survival. *Laryngoscope* 2006; **116**: 1–13.
- 24 Vermorken JB, Mesia R, Rivera F *et al.* Platinum-based chemotherapy plus cetuximab in head and neck cancer. *N Engl J Med* 2008; **359**: 1116–1127.
- 25 Duprez F, Berwouts D, De Neve W *et al.* Distant metastases in head and neck cancer. *Head Neck* 2017; **39**: 1733–1743.
- 26 Zhou L, Li Y, Gao W *et al.* Assessment of tumor-associated immune cells in laryngeal squamous cell carcinoma. *J Cancer Res Clin Oncol* 2019; **145**: 1761–1772.
- 27 Höing B, Kanaan O, Altenhoff P *et al.* Stromal versus tumoral inflammation differentially contribute to metastasis and poor survival in laryngeal squamous cell carcinoma. *Oncotarget* 2018; **9**: 8415–8426.
- 28 Karpathiou G, Casteillo F, Giroult JB *et al.* Prognostic impact of immune microenvironment in laryngeal and pharyngeal squamous cell carcinoma: Immune cell subtypes, immuno-suppressive pathways and clinicopathologic characteristics. *Oncotarget* 2017; **8**: 19310–19322.
- 29 Hoesli R, Birkeland AC, Rosko AJ *et al.* Proportion of CD4 and CD8 tumor infiltrating lymphocytes predicts survival in persistent/recurrent laryngeal squamous cell carcinoma. *Oral Oncol* 2018; **77**: 83–89.
- 30 Zhang D, Tang D, Heng Y *et al.* Prognostic Impact of Tumor-Infiltrating Lymphocytes in Laryngeal Squamous Cell Carcinoma Patients. *Laryngoscope* 2021; **131**: E1249–E1255.
- 31 Chatzopoulos K, Kotoula V, Manoussou K *et al.* Tumor Infiltrating Lymphocytes and CD8+ T Cell Subsets as Prognostic Markers in Patients with Surgically Treated Laryngeal Squamous Cell Carcinoma. *Head Neck Pathol* 2020; **14**: 689–700.
- 32 Lonardi S, Missale F, Calza S *et al.* Tumor-associated neutrophils (TANs) in human carcinoma-draining lymph nodes: a novel TAN compartment. *Clin Transl Immunol* 2021; **10**: e1252.
- 33 El-Naggar AK, Chan JKC, Grandis JR, Takata T, Slootweg PJ. *WHO classification of head and neck tumours*. International Agency for Research on Cancer (IARC): Lyon, 2017.
- 34 Wondergem NE, Nauta IH, Muijlwijk T, Leemans CR, van de Ven R. The Immune Microenvironment in Head and Neck Squamous Cell Carcinoma: on Subsets and Subsites. *Curr Oncol Rep* 2020; **22**: 81.
- 35 Wieland A, Patel MR, Cardenas MA *et al.* Defining HPV-specific B cell responses in patients with head and neck cancer. *Nature* 2021; **597**: 274–278.
- 36 Wang S-S, Liu W, Ly D, Xu H, Qu L, Zhang L. Tumor-infiltrating B cells: their role and application in anti-tumor immunity in lung cancer. *Cell Mol Immunol* 2019; **16**: 6–18.
- 37 Rekhman N, Bishop JA. *Quick reference handbook for surgical pathologists*. Springer, 2011.
- 38 Olkhanud PB, Damdinsuren B, Bodogai M *et al.* Tumor-evoked regulatory B cells promote breast

- cancer metastasis by converting resting CD4<sup>+</sup> T cells to T-regulatory cells. *Cancer Res* 2011; **71**: 3505–3515.
- 39 Pages F, Berger A, Camus M *et al.* Effector memory T cells, early metastasis, and survival in colorectal cancer. *N Engl J Med* 2005; **353**: 2654–2666.
- 40 Amin MB, Edge SB. *AJCC cancer staging manual*. Springer International Publishing, 2017.
- 41 Lin J-Y, Li X-Y, Tadashi N, Dong P. Clinical significance of tumor-associated macrophage infiltration in supraglottic laryngeal carcinoma. *Chin J Cancer* 2011; **30**: 280–286.
- 42 Mann JE, Smith JD, Birkeland AC *et al.* Analysis of tumor-infiltrating CD103 resident memory T-cell content in recurrent laryngeal squamous cell carcinoma. *Cancer Immunol Immunother* 2019; **68**: 213–220.
- 43 Rodrigo JP, Sánchez-Canteli M, López F *et al.* Tumor-Infiltrating Lymphocytes in the Tumor Microenvironment of Laryngeal Squamous Cell Carcinoma: Systematic Review and Meta-Analysis. *Biomedicines* 2021; **9**. doi:10.3390/biomedicines9050486.
- 44 Becht E, Giraldo NA, Beuselinck B *et al.* Prognostic and theranostic impact of molecular subtypes and immune classifications in renal cell cancer (RCC) and colorectal cancer (CRC). *Oncoimmunology* 2015; **4**: e1049804.
- 45 Giraldo NA, Becht E, Vano Y *et al.* Tumor-Infiltrating and Peripheral Blood T-cell Immunophenotypes Predict Early Relapse in Localized Clear Cell Renal Cell Carcinoma. *Clin cancer Res an Off J Am Assoc Cancer Res* 2017; **23**: 4416–4428.
- 46 Sorrentino C, D’Antonio L, Fieni C, Ciummo SL, Di Carlo E. Colorectal Cancer-Associated Immune Exhaustion Involves T and B Lymphocytes and Conventional NK Cells and Correlates With a Shorter Overall Survival. *Front Immunol* 2021; **12**: 778329.
- 47 Zhang Y, Li L, Zheng W, Zhang L, Yao N. CD8(+) T-cell exhaustion in the tumor microenvironment of head and neck squamous cell carcinoma determines poor prognosis. *Ann Transl Med* 2022; **10**: 273.
- 48 Alfieri S, Carenzo A, Platini F *et al.* Tumor Biomarkers for the Prediction of Distant Metastasis in Head and Neck Squamous Cell Carcinoma. *Cancers (Basel)* 2020; **12**. doi:10.3390/cancers12040922.
- 49 Wang L, Fu Y, Chu Y. Regulatory B Cells. *Adv Exp Med Biol* 2020; **1254**: 87–103.
- 50 Cabrita R, Lauss M, Sanna A *et al.* Tertiary lymphoid structures improve immunotherapy and survival in melanoma. *Nature* 2020; **577**: 561–565.
- 51 Kinker GS, Vitiello GAF, Ferreira WAS, Chaves AS, Cordeiro de Lima VC, Medina T da S. B Cell Orchestration of Anti-tumor Immune Responses: A Matter of Cell Localization and Communication. *Front cell Dev Biol* 2021; **9**: 678127.
- 52 Wolf SD, Dittel BN, Hardardottir F, Janeway CA. Experimental autoimmune encephalomyelitis induction in genetically B cell-deficient mice. *J Exp Med* 1996; **184**: 2271–2278.
- 53 Mizoguchi A, Mizoguchi E, Smith RN, Preffer FI, Bhan AK. Suppressive role of B cells in chronic

- colitis of T cell receptor alpha mutant mice. *J Exp Med* 1997; **186**: 1749–1756.
- 54 Yanaba K, Bouaziz J-D, Matsushita T, Tsubata T, Tedder TF. The development and function of regulatory B cells expressing IL-10 (B10 cells) requires antigen receptor diversity and TLR signals. *J Immunol* 2009; **182**: 7459–7472.
- 55 Mao Y, Wang Y, Dong L *et al*. Circulating exosomes from esophageal squamous cell carcinoma mediate the generation of B10 and PD-1(high) Breg cells. *Cancer Sci* 2019; **110**: 2700–2710.
- 56 DiLillo DJ, Matsushita T, Tedder TF. B10 cells and regulatory B cells balance immune responses during inflammation, autoimmunity, and cancer. *Ann N Y Acad Sci* 2010; **1183**: 38–57.
- 57 Mehdipour F, Razmkhah M, Faghieh Z, Bagheri M, Talei A-R, Ghaderi A. The significance of cytokine-producing B cells in breast tumor-draining lymph nodes. *Cell Oncol (Dordr)* 2019; **42**: 381–395.
- 58 Mauri C, Bosma A. Immune regulatory function of B cells. *Annu Rev Immunol* 2012; **30**: 221–241.
- 59 Teichmann LL, Kashgarian M, Weaver CT, Roers A, Müller W, Shlomchik MJ. B cell-derived IL-10 does not regulate spontaneous systemic autoimmunity in MRL.Fas(lpr) mice. *J Immunol* 2012; **188**: 678–685.
- 60 Han S, Feng S, Ren M *et al*. Glioma cell-derived placental growth factor induces regulatory B cells. *Int J Biochem Cell Biol* 2014; **57**: 63–68.
- 61 Biragyn A, Lee-Chang C, Bodogai M. Generation and identification of tumor-evoked regulatory B cells. *Methods Mol Biol* 2014; **1190**: 271–289.
- 62 Bodogai M, Lee Chang C, Wejksza K *et al*. Anti-CD20 antibody promotes cancer escape via enrichment of tumor-evoked regulatory B cells expressing low levels of CD20 and CD137L. *Cancer Res* 2013; **73**: 2127–2138.
- 63 Morris JC, Tan AR, Olencki TE *et al*. Phase I study of GC1008 (fresolimumab): a human anti-transforming growth factor-beta (TGFβ) monoclonal antibody in patients with advanced malignant melanoma or renal cell carcinoma. *PLoS One* 2014; **9**: e90353.
- 64 Ciardiello D, Elez E, Tabernero J, Seoane J. Clinical development of therapies targeting TGFβ: current knowledge and future perspectives. *Ann Oncol* 2020; **31**: 1336–1349.
- 65 Liu S, Ren J, Ten Dijke P. Targeting TGFβ signal transduction for cancer therapy. *Signal Transduct Target Ther* 2021; **6**: 8.
- 66 Cho BC, Daste A, Ravaud A *et al*. Bintrafusp alfa, a bifunctional fusion protein targeting TGF-β and PD-L1, in advanced squamous cell carcinoma of the head and neck: results from a phase I cohort. *J Immunother cancer* 2020; **8**. doi:10.1136/jitc-2020-000664.
- 67 Strauss J, Gatti-Mays ME, Cho BC *et al*. Bintrafusp alfa, a bifunctional fusion protein targeting TGF-β and PD-L1, in patients with human papillomavirus-associated malignancies. *J Immunother cancer* 2020; **8**. doi:10.1136/jitc-2020-001395.
- 68 Pfister D, Spencer S, Adelstein D. *NCCN Guidelines Version 3.2019 Head and Neck Cancers*. 2019.
- 69 Ardighieri L, Missale F, Bugatti M *et al*. Infiltration by CXCL10 Secreting Macrophages Is



- Associated With Antitumor Immunity and Response to Therapy in Ovarian Cancer Subtypes. *Front Immunol* 2021; **12**: 690201.
- 70 van Buuren S, Groothuis-Oudshoorn K. mice: Multivariate Imputation by Chained Equations in R. *J Stat Software; Vol 1, Issue 3* 2011.<https://www.jstatsoft.org/v045/i03>.
- 71 Van der Maaten L, Hinton G. Visualizing data using t-SNE. *J Mach Learn Res* 2008; **9**.
- 72 Gentle JE, Kaufman L, Rousseeuw PJ. Finding Groups in Data: An Introduction to Cluster Analysis. *Biometrics* 1991. doi:10.2307/2532178.

## Tables

**Table 1:** Summary statistics of the cohort. *Legend: OPHL, open partial horizontal laryngectomy; TL, total laryngectomy; TLM, transoral laser microsurgery; ENE, extranodal extension.*

Variable	Overall (N=98)	Variable	Overall (N=98)
<b>Age</b>		<b>Cartilage invasion</b>	
Mean (SD)	67.4 (9.82)	No	74 (75.5%)
Median [Min, Max]	67.0 [43.0, 89.0]	Yes	24 (24.5%)
<b>Gender</b>		<b>N category</b>	
Male	83 (84.7%)	N0	75 (76.5%)
Female	15 (15.3%)	N1	8 (8.2%)
<b>Habits</b>		N2	6 (6.1%)
None	7 (7.1%)	N3	9 (9.2%)
Smoke or alcohol	49 (50.0%)	<b>ENE</b>	
Both	42 (42.9%)	N0	75 (76.5%)
<b>Site</b>		N+ ENE-	13 (13.3%)
Glottis	55 (56.1%)	N+ ENE+	10 (10.2%)
Supraglottis	28 (28.6%)	<b>Stage</b>	
Transglottic	15 (15.3%)	Stage II	39 (39.8%)
<b>Surgery</b>		Stage III	33 (33.7%)
OPHL	14 (14.3%)	Stage IV	26 (26.5%)
TL	22 (22.4%)	<b>Grading</b>	
TLM	62 (63.3%)	G1	8 (8.2%)
<b>Node dissection</b>		G2	74 (75.5%)
No	50 (51.0%)	G3	16 (16.3%)
Yes	48 (49.0%)	<b>PNI</b>	
<b>Margins</b>		No	54 (55.1%)
Negative	68 (69.4%)	Yes	44 (44.9%)
Positive	30 (30.6%)	<b>LVI</b>	
<b>T category</b>		No	60 (61.2%)
pT2	45 (45.9%)	Yes	38 (38.8%)
pT3	34 (34.7%)		
pT4a	19 (19.4%)		

Figures

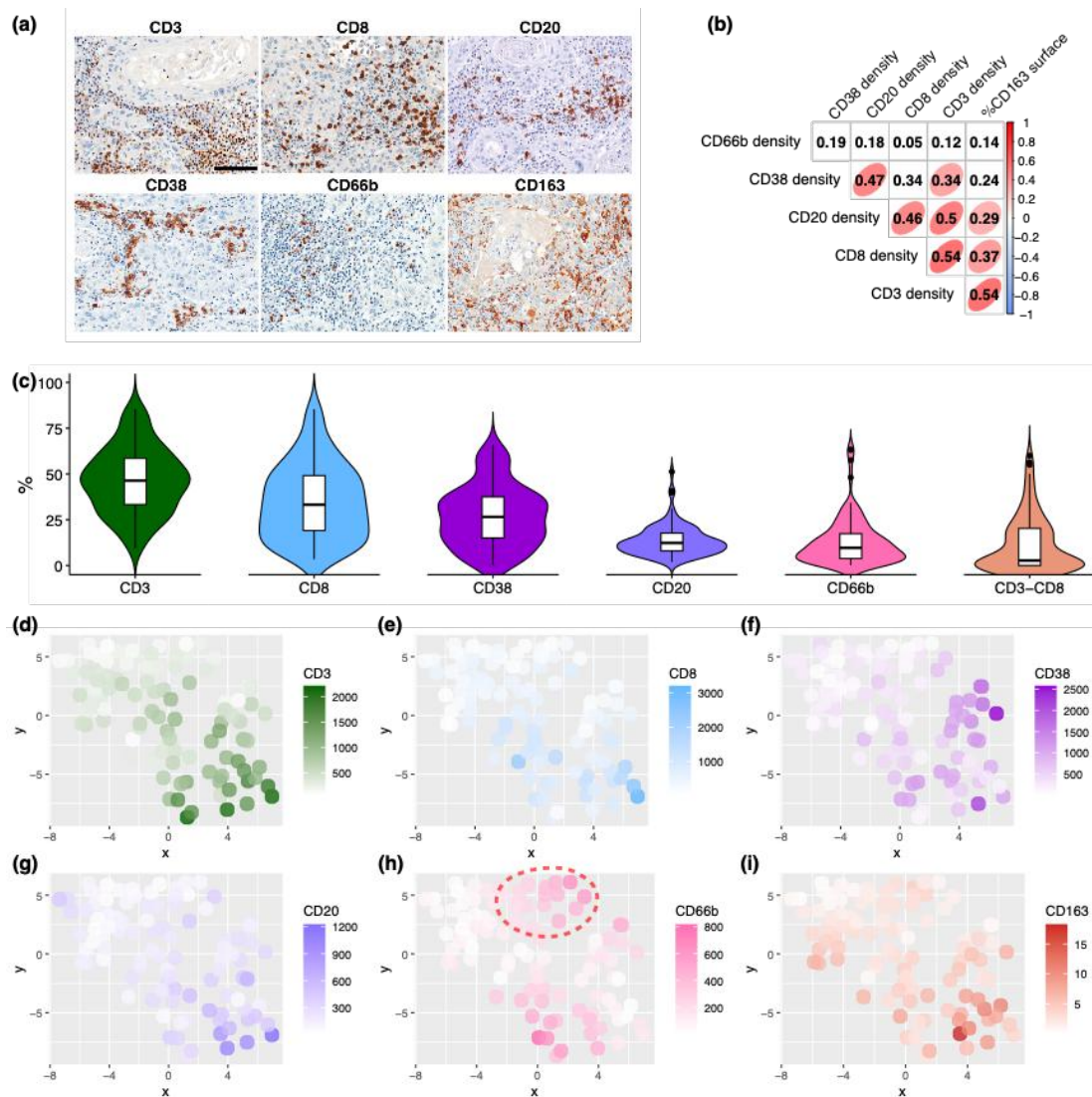


**Figure 1:** Representative immunohistochemical panel for immune cells quantification performed on LSCC sections, scale bar 100um (a). Spearman correlogram of immune cells density (b), R coefficient are shown and significant results, adjusted for multiple comparisons, are highlighted with colored ellipses. Violin plots of relative fraction of immune cells densities (c). Plots of tSNE of z-scored immune cells density (d-i); a transversal immune-rich cluster can be identified, as well as one rich of CD66b+ cells (dotted red circle).

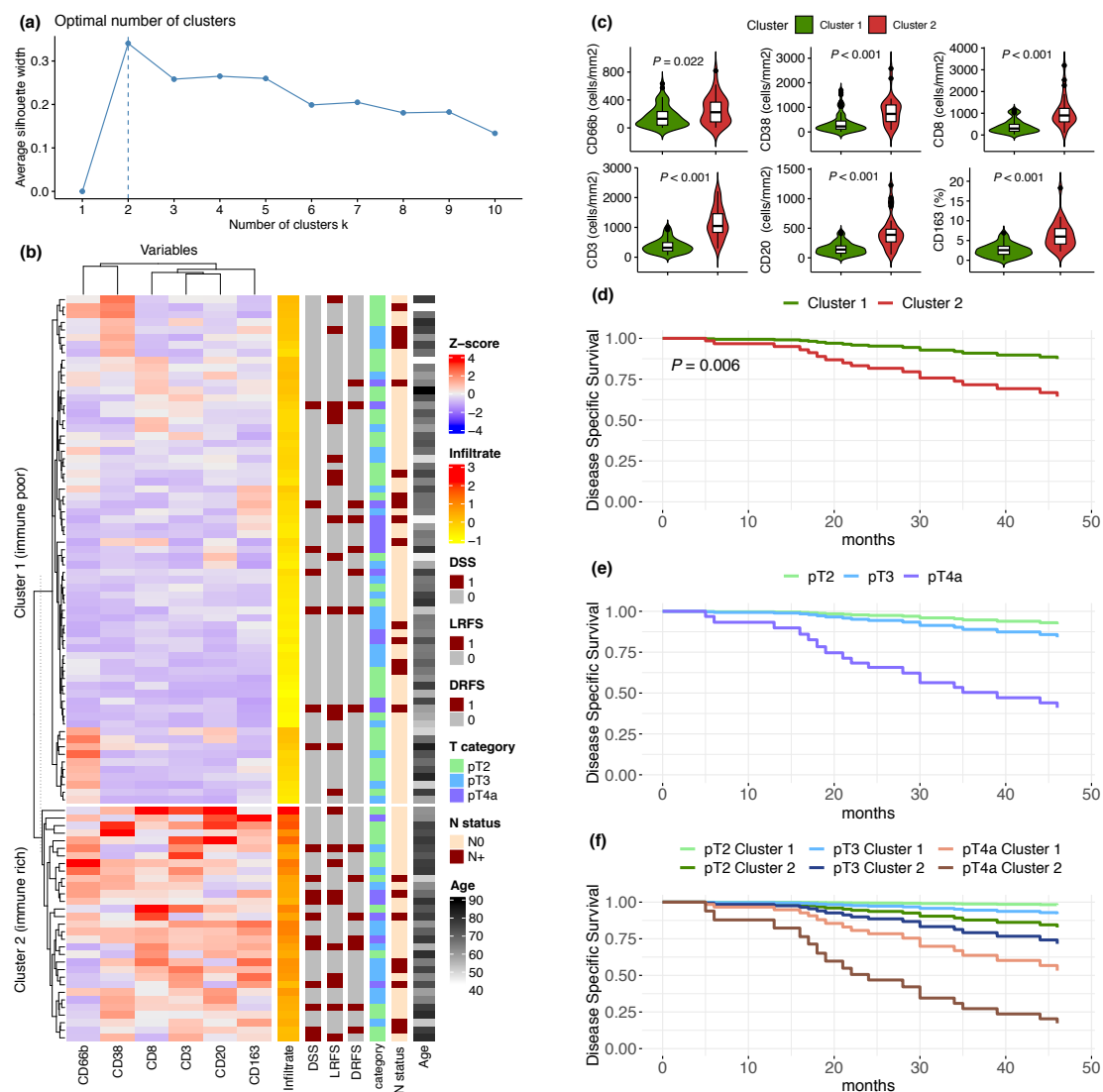


**Figure 2:** Maximizing the average silhouette, considering the immune cells density, an optimum number of 2 cluster for k-means partitioning was identified (a). Heatmap showing the k-means unsupervised clustering between samples, according to immune cells densities (b); right annotations showing the average immune cells density, occurrence of survival endpoints events along the follow-up and the main clinical features. Violin plots comparing immune cells densities among the cluster 1 and cluster 2 identified by the unsupervised k-means clustering confirming that cluster 2 is enriched of all immune cells measured (c). The multivariable model for DSS including as covariates Age, T category, N category and Clusters. Immune rich cluster ( $P = 0.006$ ), pT4 category ( $P < 0.0001$ ) and Age ( $P = 0.015$ ) were independent significant prognostic factors; the adjusted survival plots for the Cluster (d), the pT category (e) and their combinations (f) is shown. Legend: DSS, disease specific survival event; LRFS, locoregional recurrence survival event; DRFS, distant recurrence survival event.

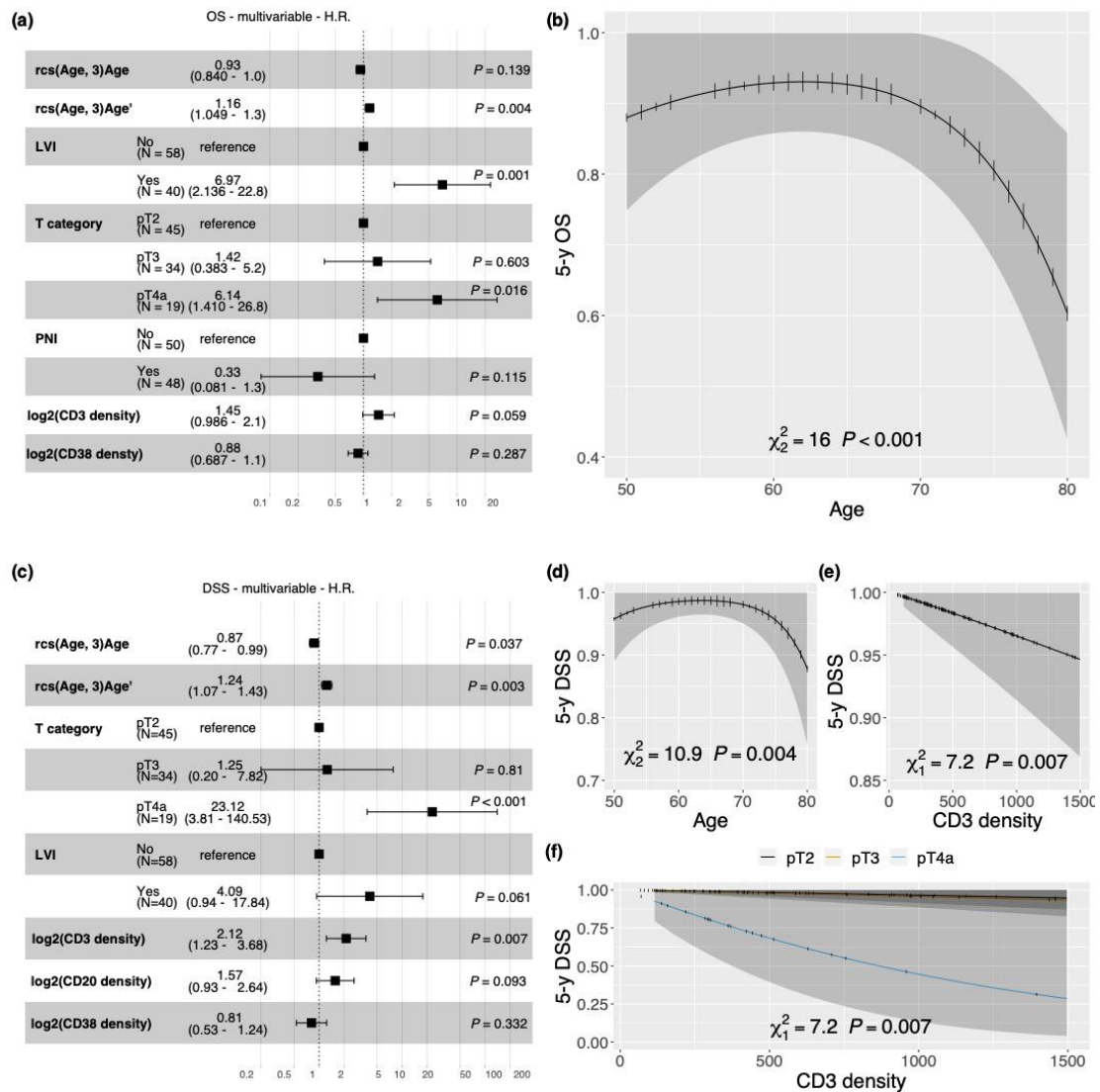


**Figure 3:** Forest plot of the multivariable overall survival (OS) model (a). Plot showing the adjusted effect of Age on the 5-year OS probability derived from the multivariable OS model (b). Forest plot of the multivariable disease specific survival (DSS) model (c). Plots showing the adjusted effect of Age (d), CD3<sup>+</sup> T-cell density (e) and the combined effect of CD3<sup>+</sup> T-cell density and pT category (f) on the 5-year DSS probability derived from the multivariable DSS model.

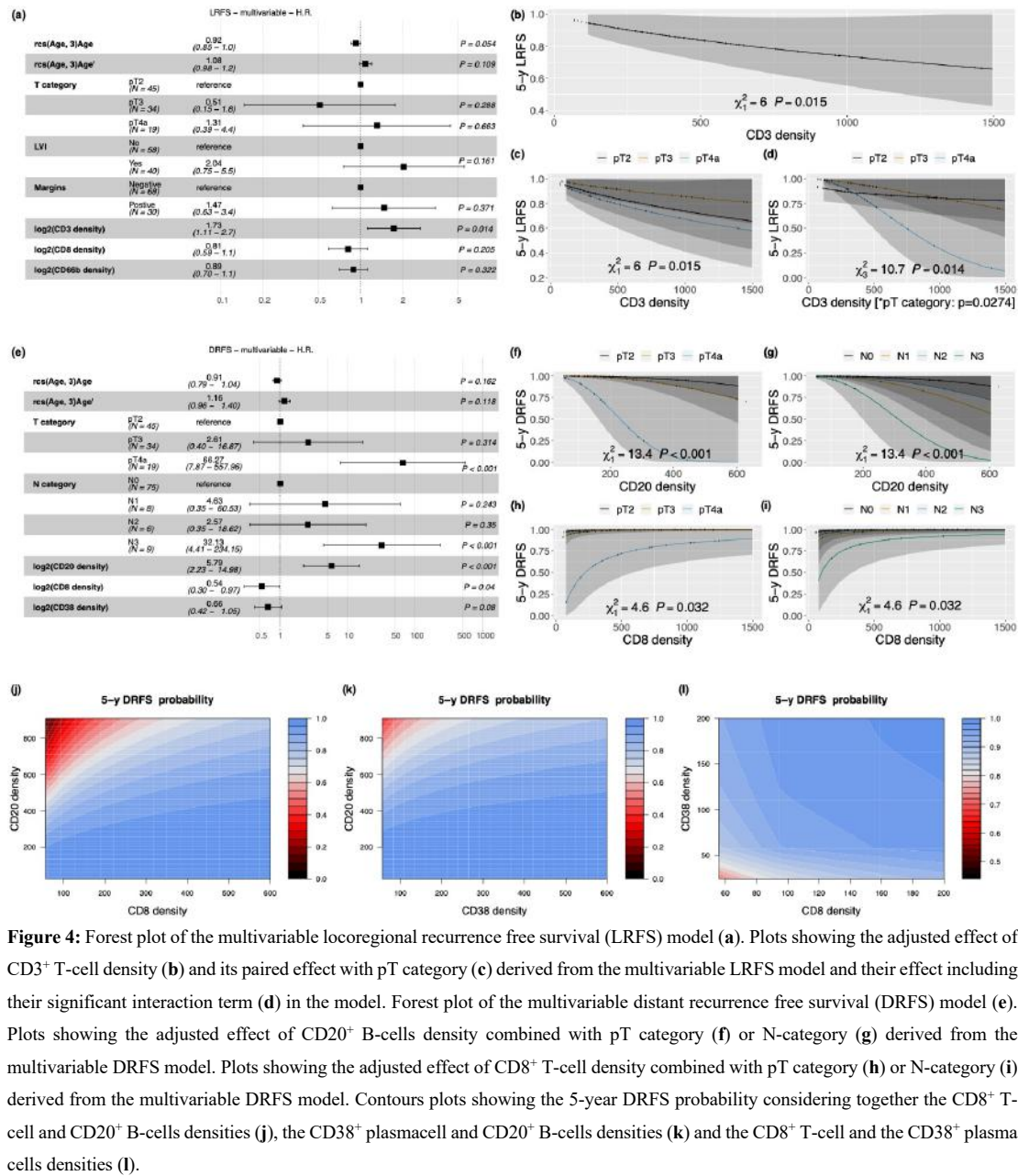


**Figure 4:** Forest plot of the multivariable locoregional recurrence free survival (LRFs) model (a). Plots showing the adjusted effect of CD3<sup>+</sup> T-cell density (b) and its paired effect with pT category (c) derived from the multivariable LRFs model and their effect including their significant interaction term (d) in the model. Forest plot of the multivariable distant recurrence free survival (DRFs) model (e). Plots showing the adjusted effect of CD20<sup>+</sup> B-cells density combined with pT category (f) or N-category (g) derived from the multivariable DRFs model. Plots showing the adjusted effect of CD8<sup>+</sup> T-cell density combined with pT category (h) or N-category (i) derived from the multivariable DRFs model. Contours plots showing the 5-year DRFs probability considering together the CD8<sup>+</sup> T-cell and CD20<sup>+</sup> B-cells densities (j), the CD38<sup>+</sup> plasmacell and CD20<sup>+</sup> B-cells densities (k) and the CD8<sup>+</sup> T-cell and the CD38<sup>+</sup> plasma cells densities (l).



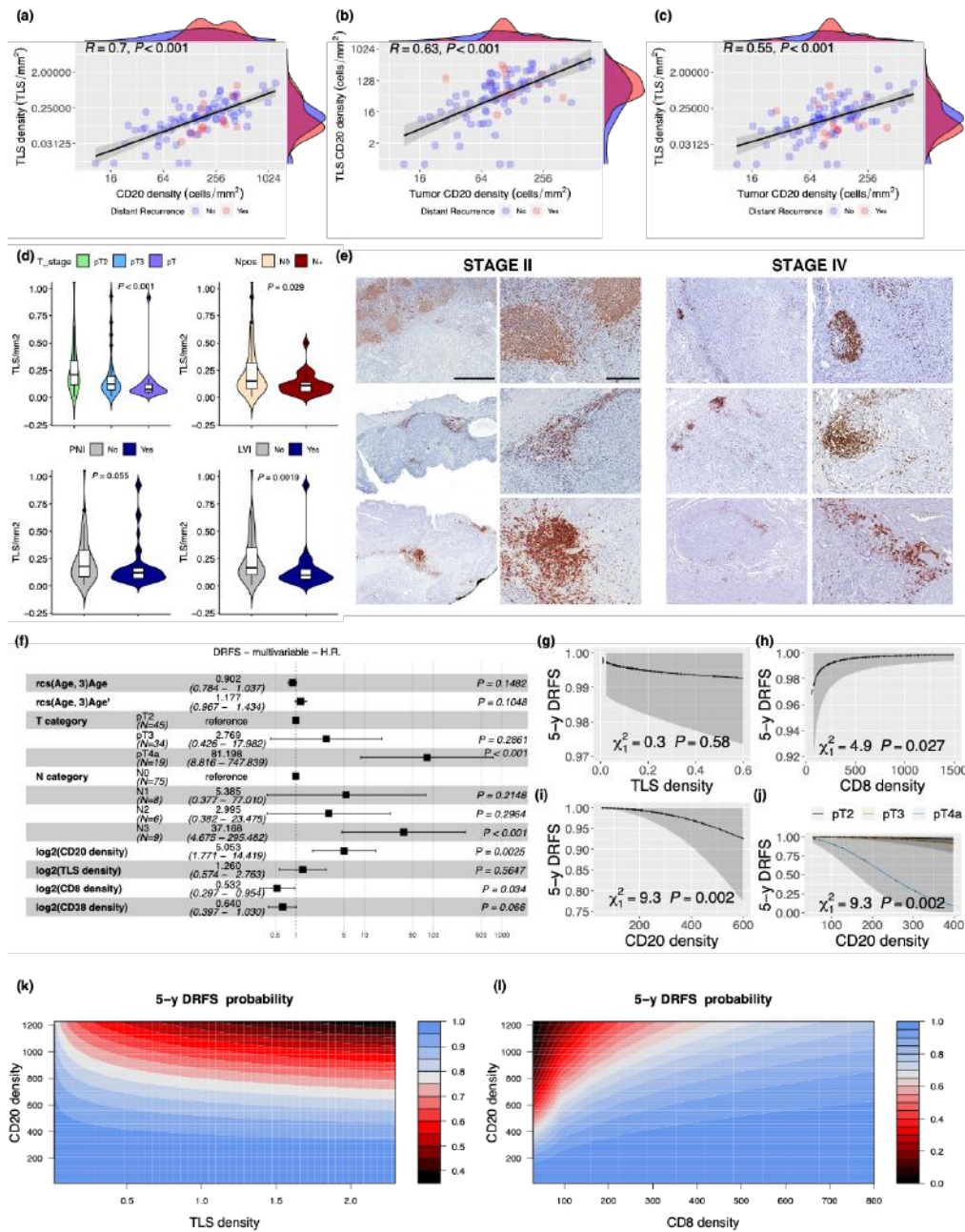


**Figure 5:** Scatter plots showing the significant direct correlation between CD20<sup>+</sup> B-cells density and TLS density (a), between CD20<sup>+</sup> B-cells density and CD20<sup>TLS</sup> B-cell density (b) and between CD20<sup>T</sup> B-cells density and TLS density (c). Violin plots showing the significant decreasing density of clusters of B-cells among the progression of the disease (d) considering both pT category, nodal involvement, and presence of risk factors as PNI and LVI. Sections from representative Stage II (n=3) or Stage IV (n=3) LSCC cases immunostained as labeled (e), first and third column scale bar 1 mm, second and fourth column scale bar 200  $\mu$ m. Forest plot of the multivariable distant recurrence free survival (DRFS) model including density of B-cells as covariate (f). Plots showing the adjusted not significant effect of the density of B-cells clusters (g) and the significant ones of CD8<sup>+</sup> T-cells (h) and CD20<sup>+</sup> B-cells (i-j). Contours plots showing the 5-year DRFS probability significantly associated with CD20<sup>+</sup> B-cells (k) and CD8<sup>+</sup> T-cells (l) densities and not with the density of clusters of B-cells.

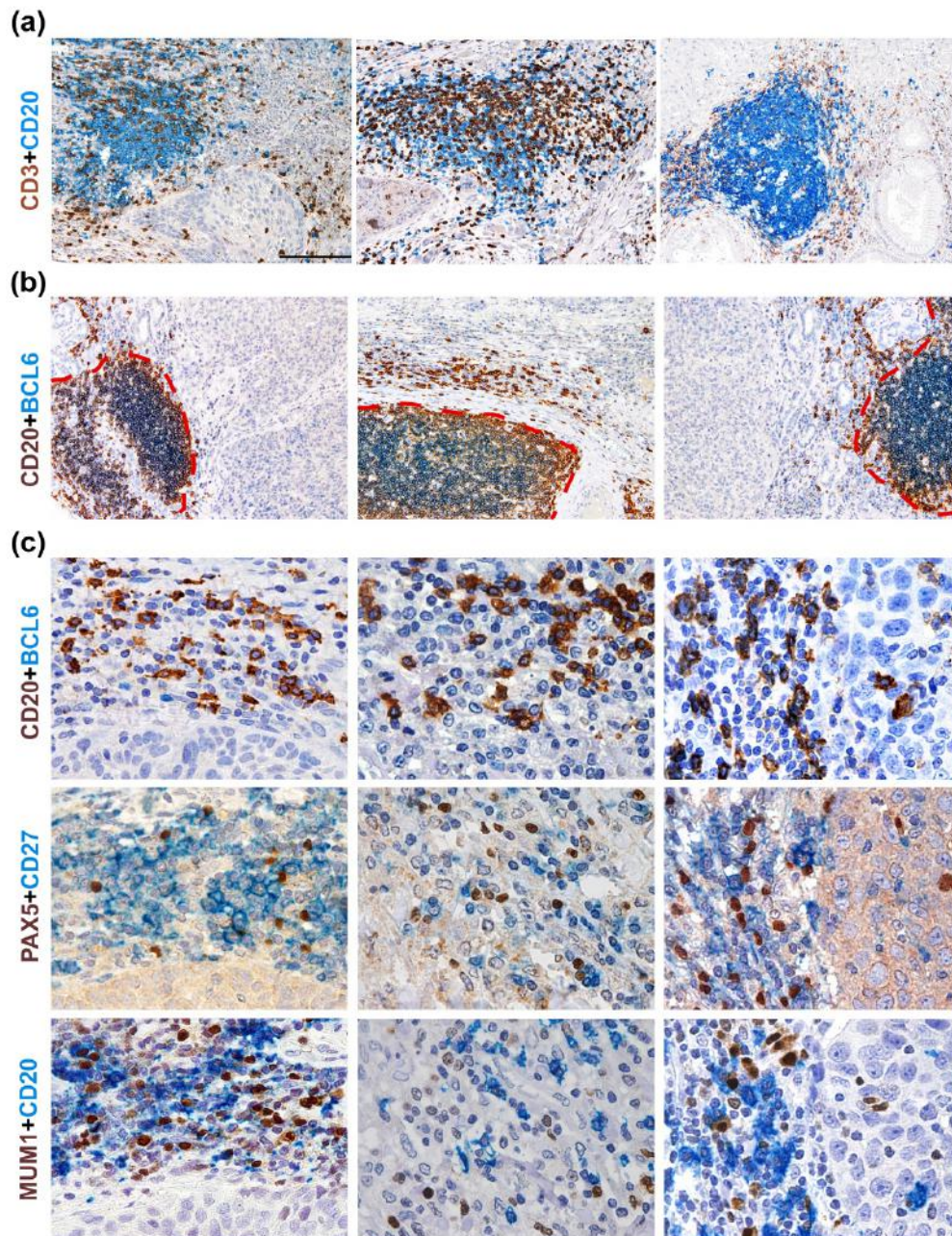


**Figure 6:** Sections from LSCC cases that experienced distant recurrence (N = 15) stained as labeled showing the *in-situ* characterization of pro-metastatic B-cells; slides in each column belong to the same LSCC case (N = 3). In (a) is shown double IHC for CD3 and CD20 showing the identification of TLS (N = 3), magnification 100X, scale bar 200um. In (b) areas of interest outside the TLS (outside the dotted red lines) are shown; TLS are identified by double IHC for CD20 and BCL6 (N = 3), magnification 100X. Scale bar 200 um. In (c) representative high-power fields of serial sections double stained for CD20/BCL6, PAX5/CD27, MUM1/CD20 are shown; B cells (CD20<sup>+</sup> or PAX5<sup>+</sup>) result largely negative for CD27 and MUM1, defining a B-cell mature naïve phenotype (N = 3); magnification 400X. Scale bar 50 um.



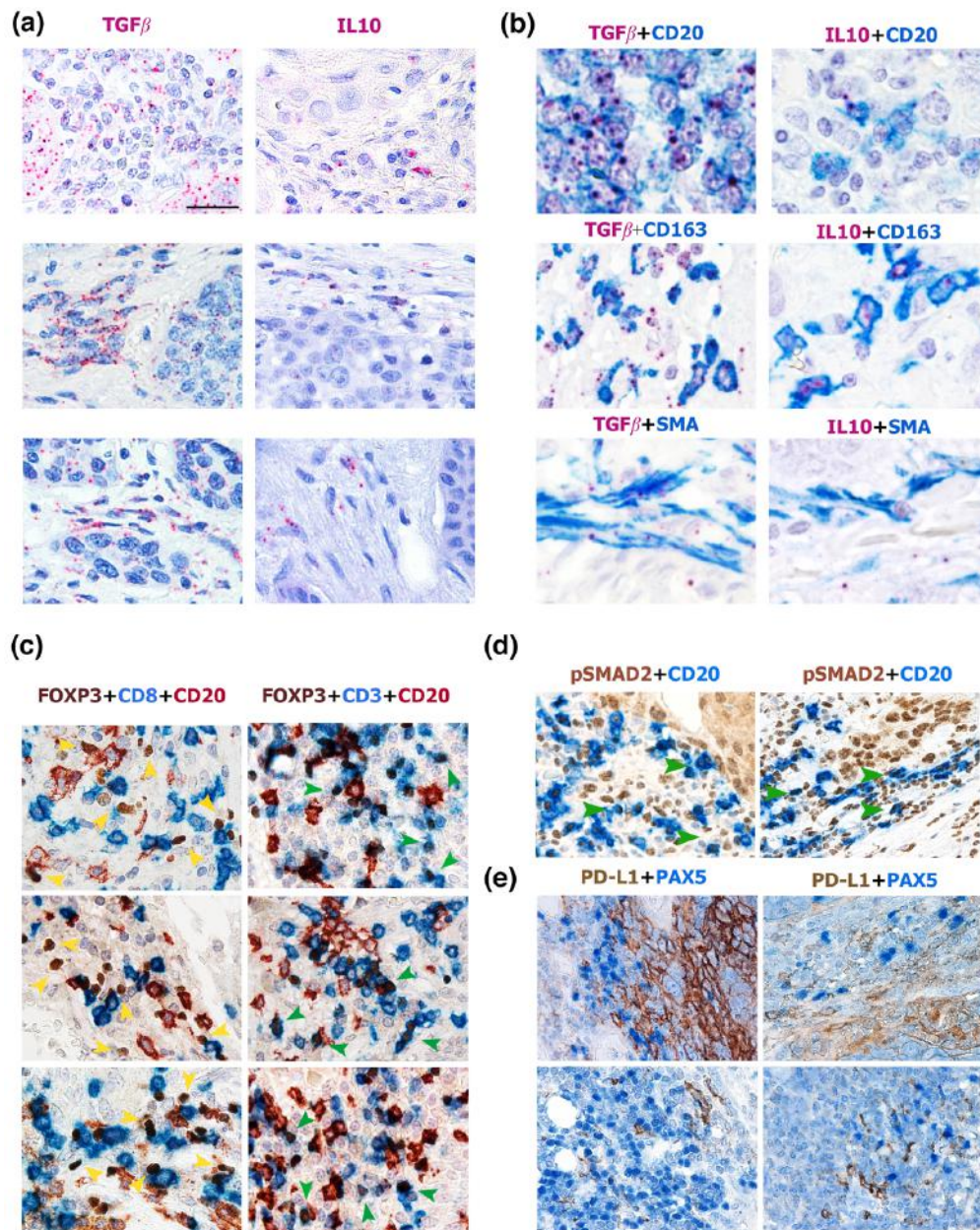


**Figure 7:** Sections from LSCC cases that experienced distant recurrence (N = 15) and stained as labeled. In (a), *in situ* hybridization for TGFβ and IL-10 using RNAscope is shown (N = 3); magnification 400x scalebar 50 μm. In (b), *in situ* hybridization for TGFβ and IL-10 is combined with immunohistochemistry for CD20, CD163 and SMA and confirm the positivity of TGFβ on CD20<sup>+</sup> B-cells, CD163<sup>+</sup> macrophages and on SMA<sup>+</sup> tumor-associated fibroblasts; conversely, IL-10 expression is limited to CD163<sup>+</sup> macrophages; magnification 600X scalebar 33 μm. In (c), co-localization of CD20<sup>+</sup> B-cells together with CD3<sup>+</sup> T-reg (CD3<sup>+</sup>FOXP3<sup>+</sup>CD8<sup>-</sup>) is shown; FOXP3 reactivity is found on CD3<sup>+</sup> (green arrowhead) CD8<sup>-</sup> (yellow arrowhead) cells (N=3); magnification 400x scalebar 50 μm. In (d), double staining for pSMAD2 and CD20 confirmed the activation of TGFβ pathway in a relevant fraction of CD20<sup>+</sup> B-cells (green arrowhead) (N = 2); magnification 400X Scale bar 50 μm. In (e) is shown that both in PD-L1<sup>+</sup> (upper row) and PD-L1<sup>-</sup> tumors (lower row) no PD-L1 reactivity was seen on PAX5<sup>+</sup> B-cells (N=4), magnification 400x scalebar 50 μm.

## Supplementary Material

### Supplementary Tables

**Supplementary Table S1:** List of the antibodies used for immunohistochemistry (IHC).

Reagent	Immune cell population	Clone	Dilution	Source
CD3	Pan-T cell	SP7	1:100	Thermo Scientific
CD8	Cytotoxic T cell	C8/144B	1:30	Dako
CD66b	Neutrophil	G10F5	1:200	BioLegend
CD163	Macrophage	10D6	1:50	Thermo Scientific
CD20	Pan-B cell	L26	1:150	Novocastra
CD38	Plasma cell	ber-MAC-DRC	1:50	Dako
PAX5	Pan-B cell	24/PAX5	4/PAX5	4/PAX5
BCL6	Germinal Center cell		1:600	By Dr. Giovanna Roncador (Monoclonal Antibodies Unit, Spanish National Cancer Research Center, CNIO, Madrid)
CD27	Activated B cell	137B4	137B4	137B4
MUM1	Activated B cell	MUM1p	MUM1p	MUM1p
Foxp3	T-regulatory cell	PCH101	1:200	eBioscience
PD-L1	Immune check point	SP263	Ready to use	Ventana
pSMAD2	TGFβ-expressing cell	Ser465, Ser467, polyclonal Rabbit	1:2000	Invitrogen

**Supplementary Table S2:** Summary statistics of digital pathology counts.

	Overall (N=98)
<b>CD3<sup>+</sup> density (cells/mm<sup>2</sup>)</b>	
Mean (SD)	618 (500)
Median [Min, Max]	443 [67.9, 2210]
<b>CD8<sup>+</sup> density (cells/mm<sup>2</sup>)</b>	
Mean (SD)	600 (550)
Median [Min, Max]	457 [29.6, 3200]
<b>CD66b<sup>+</sup> density (cells/mm<sup>2</sup>)</b>	
Mean (SD)	191 (173)
Median [Min, Max]	140 [1.42, 819]
<b>CD38<sup>+</sup> density (cells/mm<sup>2</sup>)</b>	
Mean (SD)	517 (505)
Median [Min, Max]	310 [5.20, 2580]
<b>CD163<sup>+</sup> area (%)</b>	
Mean (SD)	3.74 (2.92)
Median [Min, Max]	2.94 [0.00491, 18.3]
<b>CD20<sup>+</sup> density (cells/mm<sup>2</sup>)</b>	
Mean (SD)	240 (217)
Median [Min, Max]	178 [10.7, 1230]
<b>TLS density (TLS/mm<sup>2</sup>)</b>	
Mean (SD)	0.226 (0.297)
Median [Min, Max]	0.131 [0.0100, 2.32]
<b>CD20<sup>IT</sup> density (cells/mm<sup>2</sup>)</b>	
Mean (SD)	145 (140)
Median [Min, Max]	104 [10.7, 842]
<b>TLS area (%)</b>	
Mean (SD)	3.26 (3.51)
Median [Min, Max]	2.04 [0.0500, 16.6]
<b>TLS area (mm<sup>2</sup>)</b>	
Mean (SD)	0.184 (0.162)
Median [Min, Max]	0.157 [0.0100, 1.27]

**Supplementary Table S3:** Summary statistics of immune cells fractions and CD20<sup>+</sup> cells localization.

<b>Cells fractions</b> (% of counted immune cells)	<b>Overall (N=98)</b>
<b>CD3<sup>+</sup> percentage</b>	
Mean (SD)	46.4 (17.9)
Median [Min, Max]	46.4 [9.45, 85.4]
<b>CD8<sup>+</sup> percentage</b>	
Mean (SD)	34.7 (20.4)
Median [Min, Max]	33.2 [3.42, 85.4]
<b>CD38<sup>+</sup> percentage</b>	
Mean (SD)	27.0 (16.5)
Median [Min, Max]	26.6 [0.278, 65.9]
<b>CD20<sup>+</sup> percentage</b>	
Mean (SD)	13.6 (8.28)
Median [Min, Max]	12.3 [1.94, 51.3]
<b>CD66b<sup>+</sup> percentage</b>	
Mean (SD)	13.0 (12.8)
Median [Min, Max]	9.64 [0.113, 63.4]
<b>CD3<sup>+</sup> - CD8<sup>+</sup> percentage</b>	
Mean (SD)	11.7 (15.2)
Median [Min, Max]	2.72 [0, 60.0]
<b>Cells fractions</b> (% of counted CD20 <sup>+</sup> cells)	
<b>TLS localization</b>	
Mean (SD)	36.4 (19.9)
Median [Min, Max]	36.0 [0, 83.7]
<b>Intratumoral/stromal localization</b>	
Mean (SD)	63.6 (19.9)
Median [Min, Max]	64.0 [16.3, 100]

**Supplementary Table S4:** Association analysis between immune cells infiltration and overall pathologic Stage; p values estimated by Kruskal-Wallis test.

	Stage II (N=39)	Stage III (N=33)	Stage IV (N=26)	P-value
<b>CD3<sup>+</sup> density (cells/mm<sup>2</sup>)</b>				
Mean (SD)	688 (580)	636 (495)	491 (344)	0.583
Median [Min, Max]	511 [67.9, 2210]	444 [80.3, 1750]	396 [69.4, 1390]	
<b>CD8<sup>+</sup> density (cells/mm<sup>2</sup>)</b>				
Mean (SD)	632 (647)	546 (416)	622 (557)	0.972
Median [Min, Max]	467 [46.6, 3200]	412 [29.6, 1680]	431 [74.7, 2280]	
<b>CD66b<sup>+</sup> density (cells/mm<sup>2</sup>)</b>				
Mean (SD)	209 (175)	207 (189)	144 (143)	0.159
Median [Min, Max]	158 [13.5, 819]	150 [1.42, 635]	80.8 [2.55, 455]	
<b>CD38<sup>+</sup> density (cells/mm<sup>2</sup>)</b>				
Mean (SD)	614 (630)	437 (426)	474 (357)	0.534
Median [Min, Max]	317 [5.20, 2580]	278 [6.59, 1510]	376 [48.6, 1220]	
<b>CD163<sup>+</sup> area (%)</b>				
Mean (SD)	2.95 (1.95)	3.88 (2.94)	4.75 (3.76)	0.0565
Median [Min, Max]	2.62 [0.454, 8.89]	2.91 [0.105, 10.9]	3.91 [0.00491, 18.3]	
<b>CD20<sup>+</sup> density (cells/mm<sup>2</sup>)</b>				
Mean (SD)	277 (267)	236 (177)	188 (172)	0.308
Median [Min, Max]	208 [17.3, 1230]	185 [10.7, 629]	151 [23.3, 872]	
<b>TLS density (TLS/mm<sup>2</sup>)</b>				
Mean (SD)	0.259 (0.216)	0.263 (0.424)	0.129 (0.170)	0.00317
Median [Min, Max]	0.209 [0.0100, 1.07]	0.125 [0.0100, 2.32]	0.0892 [0.0264, 0.914]	
<b>CD20<sup>DIFF</sup> density (cells/mm<sup>2</sup>)</b>				
Mean (SD)	179 (181)	126 (93.1)	116 (110)	0.123
Median [Min, Max]	121 [16.2, 842]	90.7 [10.7, 387]	86.7 [22.1, 503]	

**Supplementary Table S5:** Association analysis between immune cells infiltration and nodal involvement; p values estimated by Mann-Whitney U test.

	<b>N0 (N=75)</b>	<b>N+ (N=23)</b>	<b>P-value</b>
<b>CD3<sup>+</sup> density (cells/mm<sup>2</sup>)</b>			
Mean (SD)	635 (512)	564 (462)	0.595
Median [Min, Max]	472 [67.9, 2210]	422 [69.4, 1750]	
<b>CD8<sup>+</sup> density (cells/mm<sup>2</sup>)</b>			
Mean (SD)	598 (549)	609 (564)	0.957
Median [Min, Max]	469 [29.6, 3200]	411 [78.7, 2280]	
<b>CD66b<sup>+</sup> density (cells/mm<sup>2</sup>)</b>			
Mean (SD)	201 (181)	158 (141)	0.395
Median [Min, Max]	143 [1.42, 819]	138 [3.54, 455]	
<b>CD38<sup>+</sup> density (cells/mm<sup>2</sup>)</b>			
Mean (SD)	500 (526)	572 (435)	0.272
Median [Min, Max]	278 [5.20, 2580]	493 [48.6, 1510]	
<b>CD163<sup>+</sup> area (%)</b>			
Mean (SD)	3.51 (2.94)	4.49 (2.77)	0.0599
Median [Min, Max]	2.78 [0.00491, 18.3]	4.14 [0.276, 11.0]	
<b>CD20<sup>+</sup> density (cells/mm<sup>2</sup>)</b>			
Mean (SD)	261 (237)	170 (109)	0.144
Median [Min, Max]	198 [10.7, 1230]	150 [39.8, 457]	
<b>TLS density (TLS/mm<sup>2</sup>)</b>			
Mean (SD)	0.257 (0.329)	0.125 (0.105)	0.029
Median [Min, Max]	0.152 [0.0100, 2.32]	0.108 [0.0154, 0.500]	
<b>CD20<sup>DIFF</sup> density (cells/mm<sup>2</sup>)</b>			
Mean (SD)	160 (155)	94.9 (49.1)	0.0896
Median [Min, Max]	116 [10.7, 842]	90.2 [29.2, 216]	

**Supplementary Table S6:** Association analysis between immune cells infiltration and evidence of lympho-vascular invasion; p values estimated by Mann-Whitney U test.

	<b>LVI No (N=60)</b>	<b>LVI Yes (N=38)</b>	<b>P-value</b>
<b>CD3<sup>+</sup> density (cells/mm<sup>2</sup>)</b>			
Mean (SD)	689 (537)	507 (416)	0.086
Median [Min, Max]	514 [80.3, 2210]	381 [67.9, 1750]	
<b>CD8<sup>+</sup> density (cells/mm<sup>2</sup>)</b>			
Mean (SD)	619 (563)	571 (534)	0.523
Median [Min, Max]	481 [46.6, 3200]	393 [29.6, 2280]	
<b>CD66b<sup>+</sup> density (cells/mm<sup>2</sup>)</b>			
Mean (SD)	201 (173)	175 (174)	0.206
Median [Min, Max]	156 [1.42, 819]	95.7 [3.54, 572]	
<b>CD38<sup>+</sup> density (cells/mm<sup>2</sup>)</b>			
Mean (SD)	576 (560)	425 (391)	0.225
Median [Min, Max]	326 [6.45, 2580]	306 [5.20, 1510]	
<b>CD163<sup>+</sup> area (%)</b>			
Mean (SD)	3.29 (2.39)	4.44 (3.52)	0.0795
Median [Min, Max]	2.64 [0.105, 10.9]	3.65 [0.00491, 18.3]	
<b>CD20<sup>+</sup> density (cells/mm<sup>2</sup>)</b>			
Mean (SD)	268 (241)	194 (164)	0.132
Median [Min, Max]	203 [10.7, 1230]	155 [17.3, 872]	
<b>TLS density (TLS/mm<sup>2</sup>)</b>			
Mean (SD)	0.272 (0.340)	0.153 (0.197)	0.00517
Median [Min, Max]	0.160 [0.0100, 2.32]	0.0964 [0.0100, 0.926]	
<b>CD20<sup>DIF</sup> density (cells/mm<sup>2</sup>)</b>			
Mean (SD)	166 (159)	111 (96.7)	0.0367
Median [Min, Max]	119 [10.7, 842]	86.7 [17.3, 503]	

**Supplementary Table S7:** Association analysis between immune cells infiltration and evidence of perineural invasion; p values estimated by Mann-Whitney U test.

	<b>PNI No (N=54)</b>	<b>PNI Yes (N=44)</b>	<b>P-value</b>
<b>CD3<sup>+</sup> density (cells/mm<sup>2</sup>)</b>			
Mean (SD)	625 (515)	610 (486)	0.935
Median [Min, Max]	498 [67.9, 2210]	434 [69.4, 2080]	
<b>CD8<sup>+</sup> density (cells/mm<sup>2</sup>)</b>			
Mean (SD)	602 (593)	598 (498)	0.708
Median [Min, Max]	457 [46.6, 3200]	439 [29.6, 2280]	
<b>CD66b<sup>+</sup> density (cells/mm<sup>2</sup>)</b>			
Mean (SD)	229 (181)	144 (151)	0.00329
Median [Min, Max]	175 [13.5, 819]	82.8 [1.42, 555]	
<b>CD38<sup>+</sup> density (cells/mm<sup>2</sup>)</b>			
Mean (SD)	590 (573)	428 (393)	0.595
Median [Min, Max]	307 [5.20, 2580]	310 [6.59, 2180]	
<b>CD163<sup>+</sup> area (%)</b>			
Mean (SD)	3.03 (2.10)	4.61 (3.52)	0.0113
Median [Min, Max]	2.59 [0.454, 10.9]	3.73 [0.00491, 18.3]	
<b>CD20<sup>+</sup> density (cells/mm<sup>2</sup>)</b>			
Mean (SD)	237 (205)	243 (233)	0.724
Median [Min, Max]	184 [10.7, 1230]	174 [23.3, 1010]	
<b>TLS density (TLS/mm<sup>2</sup>)</b>			
Mean (SD)	0.269 (0.346)	0.174 (0.217)	0.00473
Median [Min, Max]	0.183 [0.0100, 2.32]	0.0964 [0.0264, 0.926]	
<b>CD20<sup>DIF</sup> density (cells/mm<sup>2</sup>)</b>			
Mean (SD)	145 (135)	144 (148)	0.443
Median [Min, Max]	117 [10.7, 842]	91.2 [19.7, 672]	



**Supplementary Table S8:** Association analysis between immune cells infiltration and differentiation; p values estimated by Kruskal-Wallis test.

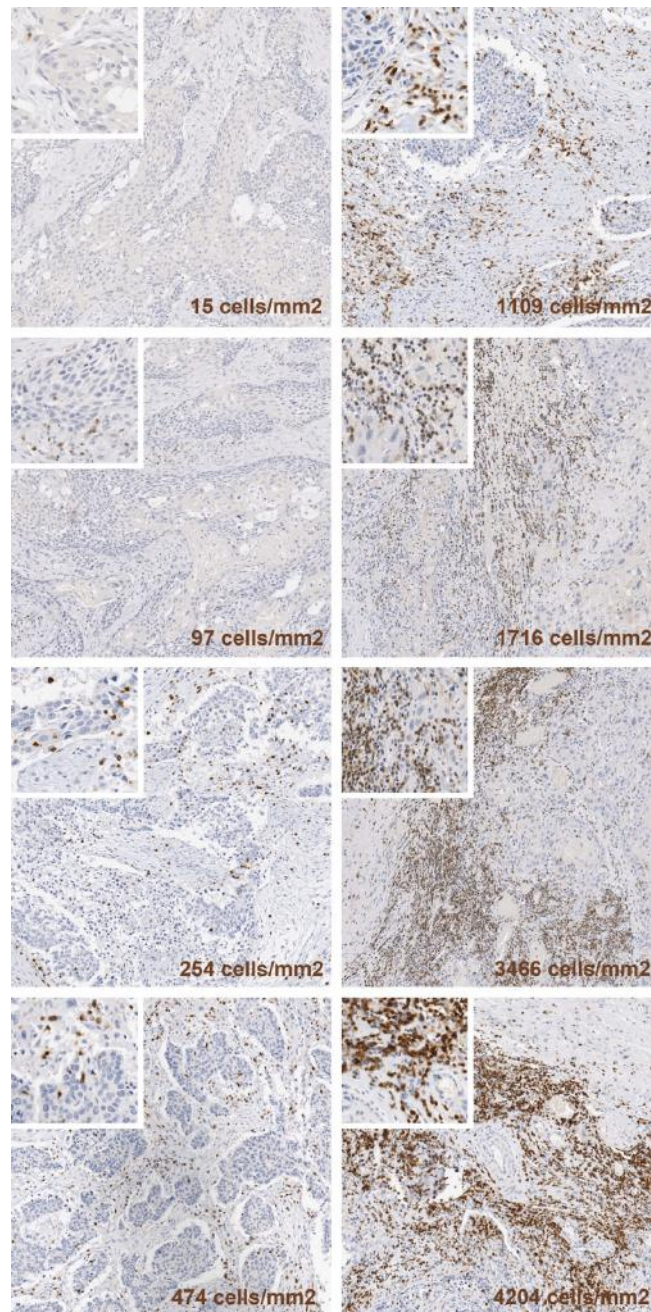
	<b>G1 (N=8)</b>	<b>G2 (N=74)</b>	<b>G3 (N=16)</b>	<b>P-value</b>
<b>CD3<sup>+</sup> density (cells/mm<sup>2</sup>)</b>				
Mean (SD)	623 (690)	656 (506)	443 (329)	0.329
Median [Min, Max]	341 [67.9, 2140]	483 [93.7, 2210]	402 [69.4, 1460]	
<b>CD8<sup>+</sup> density (cells/mm<sup>2</sup>)</b>				
Mean (SD)	739 (1040)	574 (472)	654 (586)	0.88
Median [Min, Max]	400 [46.6, 3200]	457 [59.4, 2530]	481 [29.6, 2280]	
<b>CD66b<sup>+</sup> density (cells/mm<sup>2</sup>)</b>				
Mean (SD)	163 (108)	209 (183)	119 (131)	0.137
Median [Min, Max]	146 [47.6, 403]	168 [1.42, 819]	70.2 [7.09, 436]	
<b>CD38<sup>+</sup> density (cells/mm<sup>2</sup>)</b>				
Mean (SD)	483 (409)	540 (508)	428 (550)	0.538
Median [Min, Max]	394 [14.7, 1090]	307 [5.20, 2580]	274 [6.45, 2180]	
<b>CD163<sup>+</sup> area (%)</b>				
Mean (SD)	2.72 (1.43)	3.98 (3.16)	3.14 (2.09)	0.566
Median [Min, Max]	3.10 [0.735, 4.38]	2.96 [0.00491, 18.3]	2.85 [0.488, 8.89]	
<b>CD20<sup>+</sup> density (cells/mm<sup>2</sup>)</b>				
Mean (SD)	229 (408)	248 (194)	208 (205)	0.126
Median [Min, Max]	97.1 [17.3, 1230]	206 [10.7, 1010]	165 [59.1, 939]	
<b>TLS density (TLS/mm<sup>2</sup>)</b>				
Mean (SD)	0.192 (0.356)	0.239 (0.313)	0.181 (0.175)	0.157
Median [Min, Max]	0.0762 [0.0100, 1.07]	0.153 [0.0100, 2.32]	0.112 [0.0612, 0.631]	
<b>CD20<sup>DIFF</sup> density (cells/mm<sup>2</sup>)</b>				
Mean (SD)	172 (276)	145 (119)	128 (149)	0.37
Median [Min, Max]	91.3 [16.2, 842]	111 [10.7, 624]	85.8 [36.4, 672]	

**Supplementary Table S9:** Association analysis between Cluster group identified in Figure 2 and clinical variables or immune cells infiltration; p values estimated by Mann-Whitney U test (†) or Fisher's exact test (‡).

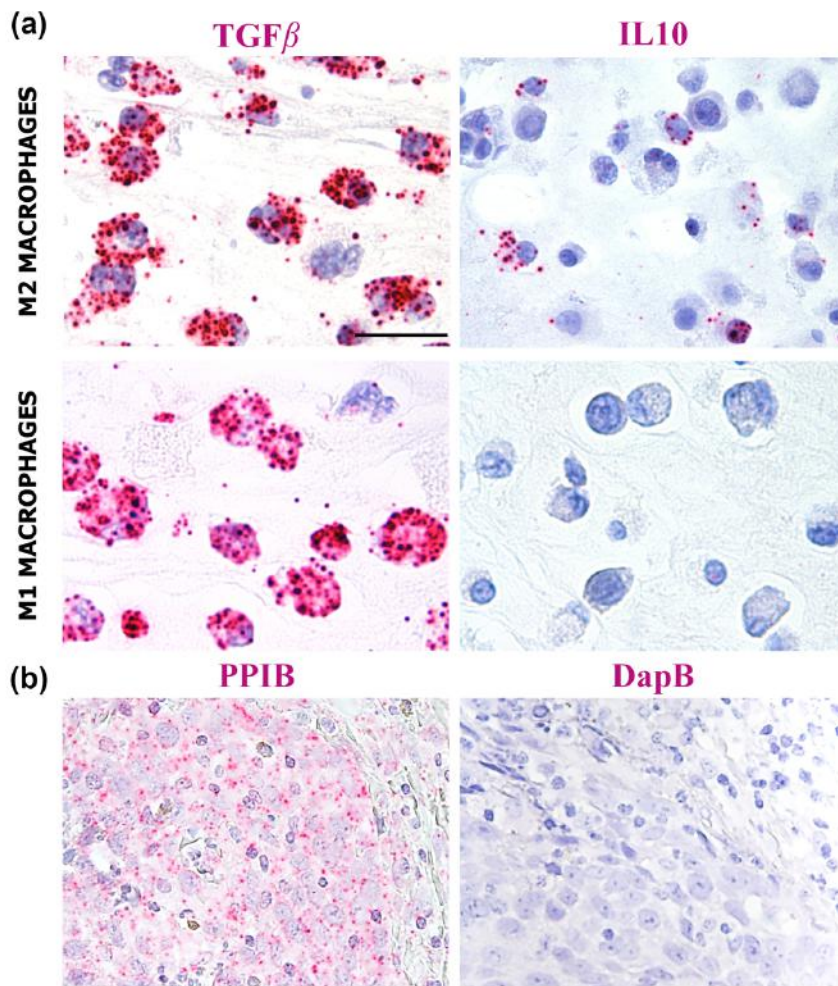
	<b>Cluster 1</b> N = 67 (68.4%)	<b>Cluster 2</b> N = 31 (31.6%)	<b>P-value</b>
<b>Age</b>			
Mean (SD)	66.1 (10.0)	70.2 (8.86)	0.049 †
Median [Min, Max]	66.0 [43.0, 89.0]	74.0 [51.0, 81.0]	
<b>T category</b>			
pT2	32 (47.8%)	13 (41.9%)	0.848 ‡
pT3	22 (32.8%)	12 (38.7%)	
pT4a	13 (19.4%)	6 (19.4%)	
<b>N involvement</b>			
N0	52 (77.6%)	23 (74.2%)	0.799 ‡
N+	15 (22.4%)	8 (25.8%)	
<b>N category (8th)</b>			
N0	52 (77.6%)	23 (74.2%)	0.702 ‡
N1	5 (7.5%)	3 (9.7%)	
N2	5 (7.5%)	1 (3.2%)	
N3	5 (7.5%)	4 (12.9%)	
<b>AJCC Stage (8th)</b>			
Stage II	28 (41.8%)	11 (35.5%)	0.793 ‡
Stage III	21 (31.3%)	12 (38.7%)	
Stage IV	18 (26.9%)	8 (25.8%)	
<b>PNI</b>			
No	34 (50.7%)	16 (51.6%)	1.0 ‡
Yes	33 (49.3%)	15 (48.4%)	
<b>LVI</b>			
No	38 (56.7%)	20 (64.5%)	0.514 ‡
Yes	29 (43.3%)	11 (35.5%)	
<b>CD3<sup>+</sup> density</b>			
Mean (SD)	372 (229)	1150 (514)	<0.001 †
Median [Min, Max]	319 [67.9, 1010]	1050 [296, 2210]	
<b>CD8<sup>+</sup> density</b>			
Mean (SD)	393 (303)	1050 (686)	<0.001 †
Median [Min, Max]	297 [29.6, 1140]	899 [92.9, 3200]	
<b>CD38<sup>+</sup> density</b>			
Mean (SD)	370 (401)	835 (564)	<0.001 †
Median [Min, Max]	225 [5.20, 1700]	734 [85.5, 2580]	
<b>CD66b<sup>+</sup> density</b>			
Mean (SD)	161 (150)	256 (201)	0.022 †
Median [Min, Max]	131 [1.42, 635]	224 [3.54, 819]	
<b>CD20<sup>+</sup> density</b>			
Mean (SD)	153 (102)	426 (277)	<0.001 †
Median [Min, Max]	139 [10.7, 440]	389 [56.5, 1230]	
<b>% area CD163<sup>+</sup></b>			
Mean (SD)	2.55 (1.63)	6.31 (3.41)	<0.001 †
Median [Min, Max]	2.56 [0.00491, 6.91]	6.00 [2.24, 18.3]	

### Supplementary Figures

**Supplementary Figure S1:** Representative panel including eight illustrative fields of sections immunostained for CD3, and ordered by increasing density measurement, using the cells recognition algorithm (Aperio Scanscope).

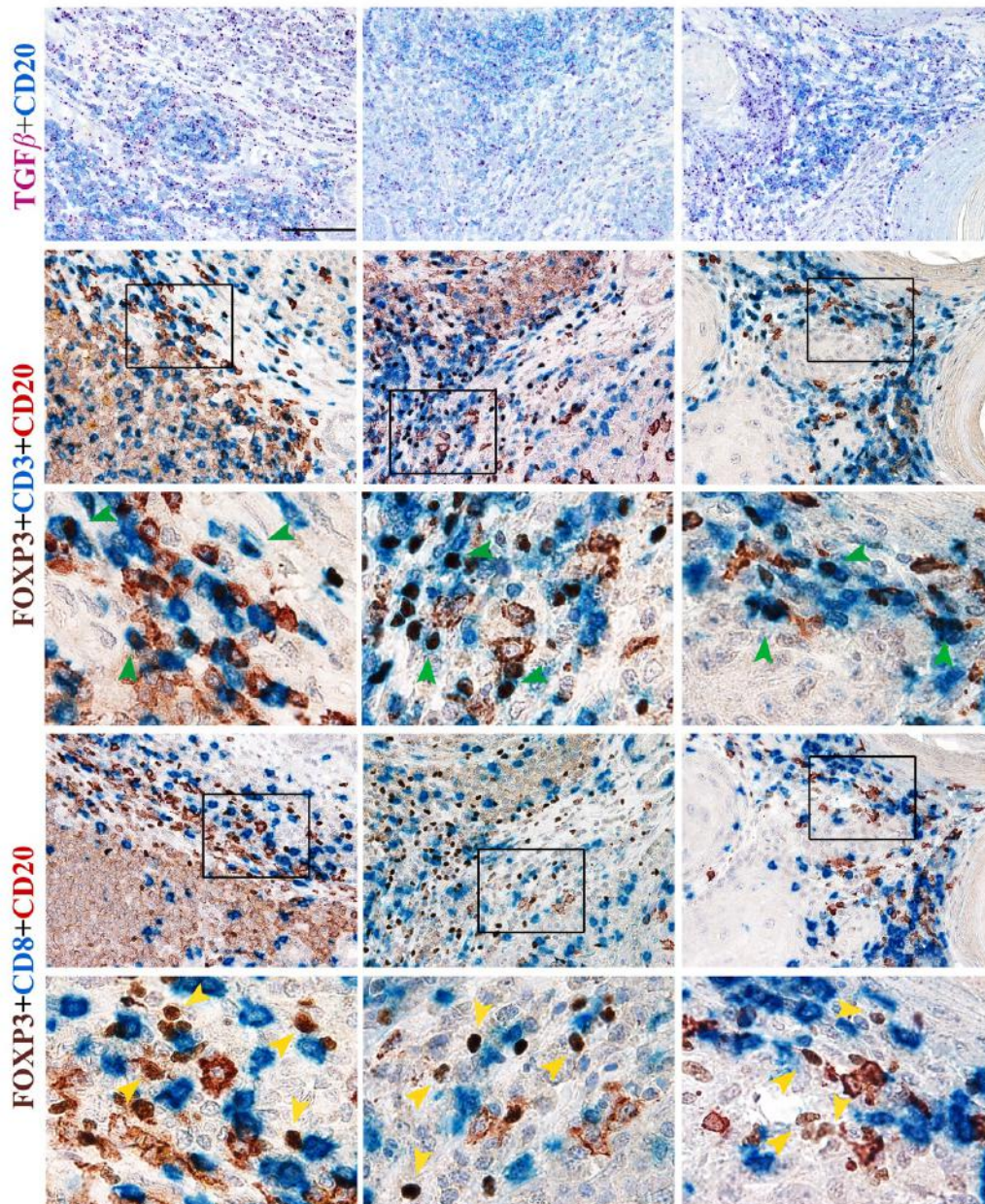


**Supplementary Figure S2:** *In-situ* hybridization for TGF $\beta$  and IL-10 by RNAscope assays, in (a) showing that M1 type and M2 type M $\phi$  generated from peripheral blood monocytes express TGF $\beta$ , whereas IL-10 is selectively expressed on M2 type M $\phi$ , magnification 600X, scalebar 33  $\mu$ m. In (b) are shown tissue controls, magnification 400X, scalebar 50  $\mu$ m.





**Supplementary Figure S3:** Further N=3 cases stained as labeled (one in each column), showing recurrent identification in  $CD20^+TGF\beta^+$  areas of  $FOXP3^+CD3^+$  T-cells (green arrowheads), identifiable also as  $FOXP3^+CD8^-$  (yellow arrowheads), no  $FOXP3^+CD8^+$  cell was identified; high magnification fields are highlighted in low magnification pictures; magnification 200X (first, second and fourth row), scale bar 100um; magnification 600X (third and fifth row), scale bar 33um.





## Infiltrating CD8+CD28- T Lymphocytes in Head and Neck Cancer

Fenoglio, D.  
Belgioia, L.  
Parodi, A.  
**Missale, F.**  
Bacigalupo, A.  
Tarke, A.  
Incandela, F.  
Negrini, S.  
Vecchio, S.  
Altosole, T.  
Vlah, S.  
Astone, G.  
Costabile, F.  
Ascoli, A.  
Ferrera, F.  
Schenone, G.  
De Palma, R.  
Signori, A.  
Peretti, G.  
Corvó, R.  
Filaci, G.











Cancers. 2021; 13(9):2234. <https://doi.org/10.3390/cancers13092234>



Supplementary material:

## Article

# Development of Exhaustion and Acquisition of Regulatory Function by Infiltrating CD8+CD28- T Lymphocytes Dictate Clinical Outcome in Head and Neck Cancer

Daniela Fenoglio <sup>1,2</sup> , Liliana Belgioia <sup>3,4</sup> , Alessia Parodi <sup>2</sup>, Francesco Missale <sup>5,6</sup> , Almalina Bacigalupo <sup>3,4</sup>, Alison Tarke <sup>1</sup> , Fabiola Incandela <sup>7</sup>, Simone Negrini <sup>1,8</sup>, Stefania Vecchio <sup>9</sup> , Tiziana Altosole <sup>1</sup>, Sara Vlah <sup>1</sup>, Giuseppina Astone <sup>1</sup>, Francesca Costabile <sup>1</sup> , Alessandro Ascoli <sup>6,10</sup>, Francesca Ferrera <sup>1</sup> , Guido Schenone <sup>6</sup>, Raffaele De Palma <sup>8,11</sup> , Alessio Signori <sup>12</sup>, Giorgio Peretti <sup>6,10</sup>, Renzo Corvò <sup>3,4</sup>  and Gilberto Filaci <sup>1,2,\*</sup> 

<sup>1</sup> Centre of Excellence for Biomedical Research and Department of Internal Medicine, University of Genoa, 16132 Genoa, Italy; daniela.fenoglio@unige.it (D.F.); alisontarke@gmail.com (A.T.); negrini@unige.it (S.N.); 2910019@studenti.unige.it (T.A.); sara.vlah@hotmail.it (S.V.); giusyastone@outlook.it (G.A.); francescacostabile@libero.it (F.C.); fferrera@unige.it (F.F.)

<sup>2</sup> Bioterapy Unit, IRCCS Ospedale Policlinico San Martino, 16132 Genoa, Italy; Alessia.Parodi@hsanmartino.it

<sup>3</sup> Department of Health Science, University of Genoa, 16132 Genoa, Italy; liliana.belgioia@unige.it (L.B.); almalina.bacigalupo@hsanmartino.it (A.B.); renzo.corvo@unige.it (R.C.)

<sup>4</sup> Radiation Oncology Unit, IRCCS Ospedale Policlinico San Martino, 16132 Genoa, Italy

<sup>5</sup> Department of Molecular and Translational Medicine, University of Brescia, 25123 Brescia, Italy; f.missale@unibs.it

<sup>6</sup> Unit of Otorhinolaryngology—Head and Neck Surgery, IRCCS Ospedale Policlinico San Martino, 16132 Genoa, Italy; 3380411@studenti.unige.it (A.A.); guido.schenone@hsanmartino.it (G.S.); giorgio.peretti@unige.it (G.P.)

<sup>7</sup> Department of Otorhinolaryngology, Maxillofacial and Thyroid Surgery, Fondazione IRCCS, National Cancer Institute of Milan, University of Milan, 20133 Milan, Italy; fabiola.incandela@istitutotumori.mi.it

<sup>8</sup> Unit of Internal Medicine, Clinical Immunology and Translational Medicine, IRCCS Ospedale Policlinico San Martino, 16132 Genoa, Italy; raffaele.depalma@unige.it

<sup>9</sup> Medical Oncology Unit, IRCCS Ospedale Policlinico San Martino, 16132 Genoa, Italy; stefania.vecchio@hsanmartino.it

<sup>10</sup> Department of Surgical Sciences and Integrated Diagnostics (DISC), University of Genoa, 16132 Genoa, Italy

<sup>11</sup> Department of Internal Medicine, University of Genoa, 16132 Genoa, Italy

<sup>12</sup> Biostatistics Unit, Department of Health Science, University of Genoa, 16132 Genoa, Italy; alessio.signori@medicina.unige.it

\* Correspondence: gfilaci@unige.it; Tel.: +39-010-353-8984



check for updates

**Citation:** Fenoglio, D.; Belgioia, L.; Parodi, A.; Missale, F.; Bacigalupo, A.; Tarke, A.; Incandela, F.; Negrini, S.; Vecchio, S.; Altosole, T.; et al. Development of Exhaustion and Acquisition of Regulatory Function by Infiltrating CD8+CD28- T Lymphocytes Dictate Clinical Outcome in Head and Neck Cancer. *Cancers* **2021**, *13*, 2234. <https://doi.org/10.3390/cancers13092234>

Academic Editor: David Wong

Received: 23 February 2021

Accepted: 27 April 2021

Published: 6 May 2021

**Publisher's Note:** MDPI stays neutral with regard to jurisdictional claims in published maps and institutional affiliations.



**Copyright:** © 2021 by the authors. Licensee MDPI, Basel, Switzerland. This article is an open access article distributed under the terms and conditions of the Creative Commons Attribution (CC BY) license (<https://creativecommons.org/licenses/by/4.0/>).

**Simple Summary:** CD8+ T lymphocytes are among the immune cells reputed to kill tumor cells. Head and neck squamous cell carcinoma (HNSCC) has a poor clinical outcome despite the presence of a rich CD8+ T cell tumor infiltrate. This may be due to alterations of tumor infiltrating CD8+ T cells. Here, we performed a characterization of infiltrating CD8+ T cells in a cohort of 30 HNSCC patients. The results showed that differential intratumoral frequency of CD8+CD28+ T cells, CD8+CD28- T cells, and CD8+CD28-CD127-CD39+ Treg distinguished between HNSCC patients who did or did not respond to treatment. Moreover, we identified an intratumoral CD8+CD28- T cell subpopulation, which expressed markers of both exhausted (i.e., with impaired effector functions) and regulatory (i.e., exerting suppressive activities) cells. This suggests that in HNSCC effector T cells progressively undergo exhaustion and acquisition of regulatory properties, hampering their anti-tumor functions.

**Abstract:** Head and neck squamous cell carcinoma (HNSCC) has a poor clinical outcome despite the presence of a rich CD8+ T cell tumor infiltrate in the majority of patients. This may be due to alterations of tumor infiltrating CD8+ T cells. Here, we performed a characterization of HNSCC infiltrating CD8+ T cells in a cohort of 30 patients. The results showed that differential intratumoral frequency of CD8+CD28+ T cells, CD8+CD28- T cells, and CD8+CD28-CD127-CD39+ Treg distinguished between HNSCC patients who did or did not respond to treatment. Moreover, high PD1 expression identified a CD8+CD28- T cell subpopulation, phenotypically/functionally corresponding to CD8+CD28-CD127-CD39+ Treg, which showed a high expression of markers of exhaustion.



This observation suggests that development of exhaustion and acquisition of regulatory properties may configure the late differentiation stage for intratumoral effector T cells, a phenomenon we define as effector-to-regulatory T cell transition.

**Keywords:** head-neck cancer; CD8+ T lymphocytes; regulatory T cells; exhaustion

## 1. Introduction

Head and neck squamous cell carcinoma (HNSCC) is a relevant medical issue since it is the sixth most common cancer globally and its incidence is increasing (mainly in HPV+ patients). Despite several options being available for treatment [1–8], the mortality rates for patients with HNSCC are still very high (mainly in advanced/metastatic or recurrent disease) [7,9,10]. It is possible that the poor clinical outcome of HNSCC patients depends on the characteristics of their tumor immune infiltrate. Specifically, highly infiltrated tumors (“hot tumors”) have a better prognosis than poorly infiltrated ones (“cold tumors”) [11], and a robust CD8+ T cell infiltration showed a positive prognostic impact on several types of tumors [12–18]. However, HNSCCs are tumors with a rich immune infiltrate, particularly characterized by high frequencies of CD8+ T cells, yet they have a poor clinical outcome, independent from the adopted therapy [9]. Moreover, the prognostic role of CD8+ T cells in individual patients is ambiguous, as there are reports assessing either a positive or a negative association between the degree of CD8+ T cell HNSCC infiltration and the clinical outcome [15,19–21]. It is possible that the basis for this conundrum relies on functional alterations of tumor infiltrating CD8+ T cells. Indeed, several dysfunctions may affect intratumoral CD8+ T cells [22,23]. Moreover, they may acquire regulatory functions, as we showed that tumor infiltrates contain a variable frequency of immune suppressive CD8+ T cells characterized by the CD8+CD28–CD127–CD39+ phenotype [24,25]. These CD8+CD28–CD127–CD39+ regulatory T cells (Treg) localize in the primary and metastatic sites of tumors, and are able to inhibit both T cell proliferation and cytotoxicity [24,25]. Hence, we hypothesized that an in-depth characterization of the dynamics of effector T lymphocytes toward exhaustion and acquisition of regulatory function at the tumor site could provide clues helping to explain the unsolved pathogenic aspects of HNSCC.

## 2. Materials and Methods

### 2.1. Patients

This was a descriptive observational clinical study. Peripheral blood and tumor samples were collected from 30 patients affected by HNSCC who were enrolled at the Radiation Oncology Department and Otorhinolaryngology Unit of the IRCCS Policlinico San Martino Hospital.

The enrollment was divided into two phases: (a) the former cohort included 20 patients with oropharyngeal squamous cell cancer (OPSCC) treated with non-surgical radical treatment (Table 1 shows their clinical characteristics). To evaluate if some investigated parameters could be used to predict a clinical outcome, this first cohort was divided into two subgroups (Group 1: non-responders and Group 2: responders) according to their response to therapy. Responders were defined as patients that obtain a complete response at radiological re-evaluation after treatment.

(b) The second cohort included 10 patients affected by HNSCC submitted to radical surgery ± adjuvant treatment according to international guidelines. This latter group was considered to better characterize specific T cell populations from fresh tissue samples originating not from exiguous bioptic samples but from wider surgical specimens. This second cohort included recently diagnosed patients with a too-short follow-up for allowing any judgment on treatment efficacy.

**Table 1.** Patient characteristics.

Demographic and Clinical Variables	Overall ( <i>n</i> <sup>a</sup> = 20)
<b>Age</b>	
Mean (SD)	65.1 (11.6)
Median (Min, Max)	65.0 (35.0, 83.0)
<b>Gender <i>n</i> (%)</b>	
F	4 (20.0%)
M	16 (80.0%)
<b>Smoke <i>n</i> (%)</b>	
No	5 (25.0%)
Yes	15 (75.0%)
<b>Alcohol drinker <i>n</i> (%)</b>	
No	13 (65.0%)
Yes	7 (35.0%)
<b>HPV (p16) <i>n</i> (%)</b>	
Negative	10 (50.0%)
Positive	10 (50.0%)
<b>Site</b>	
Oropharynx	20 (100.0%)
<b>cT category (7th ed.) <i>n</i> (%)</b>	
T1	2 (10.0%)
T2	6 (30.0%)
T4	12 (60.0%)
<b>cN category (7th ed.) <i>n</i> (%)</b>	
N0	2 (10.0%)
N1	3 (15.0%)
N2	14 (70.0%)
N3	1 (5.0%)
<b>cStage (7th ed.) <i>n</i> (%)</b>	
II	2 (10.0%)
III	2 (10.0%)
IV	16 (80.0%)
<b>Therapy</b>	
RT <sup>b</sup> alone	3 (15.0%)
RT + CHT <sup>c</sup>	16 (80.0%)
Surgery	1 (5.0%)
<b>Response <i>n</i> (%)</b>	
Not responder (Group 1)	7 (35.0%)
Responder (Group 2)	13 (65.0%)

<sup>a</sup> *n*: Number; <sup>b</sup> RT: radiotherapy; <sup>c</sup> CHT: chemotherapy.

The study was carried out in compliance with the Helsinki Declaration and approved by the Ethical Committee of the San Martino Hospital in Genoa (P.R.133REG2017). All enrolled patients provided written informed consent.

## 2.2. Monoclonal Antibodies (mAbs) and Immunofluorescence Analyses

Lymphocytes from surgical specimens were purified filtering minced tissues using a sterile cell strainer (Falcon, BD Biosciences, San Jose, CA, USA) and running the collected cells on Ficoll-Hypaque gradient (Biochrom AG, Berlin, Germany) for 30 min at 1800 rpm. Due to the low number of infiltrating CD3+ T lymphocytes in many biopsies

and the subsequent impossibility to perform Fluorescence Minus One (FMO) control for exhaustion and activation markers, we preliminarily applied the same multiparametric panels to PBMC purified from heparinized blood samples derived from the same patients by centrifugation on Ficoll-Hypaque gradient. This strategy allowed us to identify a population not expressing the marker of interest (i.e., circulating naive CD8+ T cells) to set the positivity threshold of each marker for each patient. Immunofluorescence analyses were performed on  $1 \times 10^6$  cells in 100  $\mu$ L of PBS incubating with specific fluorochrome-conjugated mAbs. The following mAbs specific for surface markers were used: Brilliant Violet(BV)605-conjugated anti-CD45RA clone HI100 (BD Biosciences), phycoerythrin (PE) or cyanin (Cy) 7-conjugated anti-CCR7 clone 3D12 ((BD Biosciences), phycoerythrin (PE)-conjugated or BV421-conjugated anti-CD127 clone HIL-7R-M21 (BD Biosciences), Peridinin Chlorophyll Protein Complex-cyanin 5.5 (PerCP-Cy5.5)-conjugated or PE-Cy5.5-conjugated anti-CD28 clone CD28.2 (BD Biosciences), fluorescein isothiocyanate (FITC)-conjugated anti-CD25 clone M-A251 (BD Biosciences), BV711-conjugated anti-CD39 clone TU66 (BD Biosciences), BV650-conjugated anti-TIM-3 clone 7D3 (BD Biosciences), BV786-conjugated anti-PD-1 clone MIH4 (BD Biosciences), allophycocyanin (APC)-conjugated anti-CD152 (CTLA-4) clone BNI3 (BD Biosciences), APC-H7-conjugated anti-CD4 clone RPA-T4 (BD Biosciences), BV 421-conjugated or or Alexa Fluor 647-conjugated or PerCP-Cy5.5-conjugated anti-CD8 clone RPA-T8 (BD Biosciences), BV450-conjugated or Alexa Fluor 700-conjugated anti-CD3 clone UCHT1 (BD Biosciences), PE-conjugated anti-CD103 clone Ber-ACT8 (BD Biosciences), PE-conjugated anti CD137 (4IBB) clone 4B4-1 (BD Biosciences). To exclude dead cells, the samples were incubated with Aqua dead (Molecular Probes, Thermo Fisher) for 15 min at room temperature, before proceeding with surface staining. Cells were washed with PBS-BSA 0.01% and incubated with the surface mAbs. After surface staining, the cells were fixed and permeabilized by Transcription Buffer Set (BD Pharmingen) prior to performing intracellular staining for 30 min in the dark with the following mAbs: FITC mouse anti-Ki-67 (BD Biosciences), PE-CF594-conjugated anti-FoxP3 clone 259D/C7 (BD Biosciences), PE-conjugated anti-EOMES clone X4-83 (BD Biosciences). The cells were washed with 1 mL of PBS-BSA 0.01% and resuspended in 300  $\mu$ L of PBS. The samples were analyzed by a BD Fortessa X20 flow cytometer (BD Biosciences) using the BD FACS Diva™ software version 8.0 (BD Biosciences).

### 2.3. Evaluation of HLA-A2 Positive Patients

Fifty  $\mu$ L samples of fresh blood were incubated with 10  $\mu$ L of un-conjugated anti-HLA-A2 BB7.2 mAb (Biolegend, San Diego, CA, USA) for 20 min at room temperature. The cells were then washed and incubated with the FITC-conjugated Goat anti mouse IgG1 secondary antibody (Millipore) for 30 min at room temperature. Red cells were lysed with 2 mL of FACS Lysing solution (BD Biosciences) and resuspended in 200  $\mu$ L of the same solution. Tubes were analyzed by a BD Fortessa X20 flow cytometer (BD Biosciences) using the BD FACS Diva™ software version 8.0 (BD Biosciences).

### 2.4. Multidimensional Data Reduction Analysis

Flow cytometric data were exported with compensated parameters in FCS express software v6.03.0011 (DeNovo Software, Pasadena, CA, USA). *t*-dependent Stochastic Neighbor Embedding (*t*-SNE) analysis was performed on live CD8+ T cells on the transformed data for CD28, CD127, CD39, PD-1, TIM-3, EOMES, CD137, CD103, CD45 RA, CCR7, EOMES, and Ki-67 antigens using Barnes-Hut SNE approximations. This generated 2-D plots that clustered cells on the basis of marker expression profiles.

### 2.5. Analysis of G250/CAIX Specific CD8+ T Lymphocytes

Cells ( $1 \times 10^6$ ) derived from biopsy were incubated with PE conjugated HLA-A\*02:01 G250 HLSTAFARV<sub>217-225</sub> pentamers (Proimmune, Oxford, UK), or with PE conjugated HLA-A\*02:01 hTert ILAKFLHWL<sub>540-548</sub> pentamers (Proimmune) as negative control, for 15 min at 4 °C. Cells were washed with PBS-BSA 0.01% and incubated with Aqua dead

(Molecular Probes, Thermo Fisher Scientific, Waltham, MA, USA) for 15 min at room temperature. Cells were washed with PBS-BSA 0.01% and incubated with the following mAbs: Alexa Fluor-700-conjugated anti-CD3 clone UCHT1 (BD Biosciences) PerCP-Cy5.5-conjugated anti-CD8 clone RPA-T8 (BD Biosciences), PE-Cy5-conjugated anti-CD28 clone CD28.2 (BD Biosciences), APC-H7-conjugated anti-CD4 clone RPA-T4 (BD Biosciences), BV605-conjugated anti-CD45RA clone HI100 (BD Biosciences), PE-Cy7-conjugated anti-CCR7 clone 3D12 ((BD Biosciences), BV421-conjugated anti-CD127 clone HIL-7R-M21 (BD Biosciences), BV711-conjugated anti-CD39 clone TU66 (BD Biosciences), BV650-conjugated anti-TIM-3 clone 7D3 (BD Biosciences), BV786-conjugated anti-PD-1 clone MIH4 (BD Biosciences). After the staining the tubes were washed with 1 mL of PBS-BSA 0.01% and resuspended in 300  $\mu$ L of BD FACS Lysing solution (BD Biosciences). The samples were acquired by a BD Fortessa X20 flow cytometer (BD Biosciences) using the BD FACS Diva™ software version 8.0 (BD Biosciences). The analysis of T cell populations was performed by FlowJo version 10.4 (FlowJo, L.L.C., Ashland, OR, USA)

### 2.6. Proliferation Suppression Assay

CD8+ T lymphocytes were purified from the tumor immune infiltrate by immunomagnetic beads using microbeads conjugated with mAb-specific for the CD8 antigen (Miltenji Biotec, Bergisch Gladbach, Germany). Due to the paucity of purified cells, no further selection procedures were possible. In the case of patients #5 CD8+CD28- T cell percentage on total purified CD8+ T cells was >80%, so their suppressive activity was tested. Hence, PBMC ( $1 \times 10^5$  cells/well) from a healthy donor, stained with carboxyfluorescein succinimidyl ester (CFDA-SE) (5  $\mu$ M) (Thermo Fisher), were pulsed with the anti-CD3 UCTH-1 mAb (5  $\mu$ g/mL, BD Bioscience) and incubated for 5 days in a 96-well U bottomed plate in the presence or not of purified CD8+CD28- T cells ( $1 \times 10^5$  cells/well). Then, the samples were washed in PBS and analyzed by a BD Fortessa X20 flow cytometer (BD Biosciences) using the BD FACS Diva™ software version 8.0 (BD Biosciences) in order to monitor the inhibition of dye dilution. Dead cells were excluded from analysis by adding 7-aminoactinomycin D (BD Biosciences) before the analysis. Suppression activity was expressed as a percentage reduction of proliferation in the presence of tumor infiltrating CD8+CD28- T lymphocytes compared to the levels of proliferation observed in control cultures of PBMCs alone.

### 2.7. Statistical Analyses

Results were reported as mean and standard deviation (SD). To compare the frequency of the different T cell subsets between the tumor infiltrates of the two groups, we used the independent samples Student's *t*-test for not skewed populations or non-parametric Mann-Whitney test for all other populations; two-sided tests were always applied. The overall survival at 2 years was calculated using the Kaplan-Meier method. The association between overall survival and T cell subsets was assessed using the log-rank test. Multivariable survival analysis was performed by Cox proportional hazard models including as covariates each tested T cell subset and the HPV status. Each T cell subset was binarized according to the median value and the overall survival of patients with lower and higher values was compared. Pearson's correlation between percentages of CD8+CD28-CD127<sup>lo</sup>CD39+PD-1<sup>hi</sup> Treg and CD8+CD28--PD1<sup>hi</sup> T cells was calculated. Analyses were performed by GraphPad Prism 5 for Mac OS X (San Diego, CA, USA), Stata Statistical Software, Release 16 (StataCorp. LLC, College Station, TX, USA) and R software (version 3.6.2) (Free Software Foundation).

## 3. Results

### 3.1. Comparative Phenotypic and Functional Characterization of Intratumoral T cells between HNSCC Patients with Poor (Group 1) or Good (Group 2) Response to Therapy

In order to achieve a detailed picture of tumor infiltrating T cell subsets in HNSCC patients and to define their eventual prognostic value, we examined the intratumoral

frequency of the T cell subpopulations listed in Table S1. T cell subsets were selected for (a) maturation stage, in terms of naïve, central memory (CM), effector memory (EM), and terminal effector memory cells (TEM); (b) regulatory commitment, in terms of both CD4+CD25<sup>hi</sup>FoxP3+ and CD8+CD28-CD127-CD39+ Treg, respectively; (c) expression of T cell inhibitory receptors (CTLA-4, PD-1, CD39, TIM-3).

Next, we investigated whether any of these defined T cell subsets could be used to predict a clinical outcome. To determine this, the first 20 HNSCC patients enrolled, quite homogeneous for tumor site and treatment (Table 1), were monitored for at least 18 months and up to 32 months, and divided into two subgroups according to their response to therapy. Group 1 included 7 patients showing early disease progression or death (non-responders), while Group 2 included 13 patients with stable complete responses to treatments (responders). Then, we compared the frequency of the different T cell subsets between the tumor infiltrates of the two groups.

No significant differences between responder and non-responder patients were observed concerning any tumor infiltrating CD4+ T cell subsets (Table 2).

**Table 2.** Percent frequencies of HNSCC infiltrating CD3+ and CD4+ T cell subsets in Group 1 and Group 2.

T Cell Subsets	Group 1 (n = 7)		Group 2 (n = 13)		p-Value
	Median	IQR	Median	IQR	
CD3+ /total cells	8	7–48	27	9–36.1	0.38
CD4+ /CD3+	61	56–71	70	54–80	0.94
Naïve CD4+	3.3	0.5–5.2	0.8	0.3–1.1	0.19
CM CD4+	8.5	1.9–17	4.4	2–7.6	0.69
EM CD4+	82	72–83	83	78–89	0.50
TEM CD4+	7	1.3–13	8	4–13	0.63
Naïve CD4+PD1+	4.5	1.8–10	1.9	0.8–4	0.25
CM CD4+PD1+	9	5.2–20	5	3.8–12	0.41
EM CD4+PD1+	64	58–75	74	56–81	0.75
TEM CD4+PD1+	8.5	3.6–24	14	6–18	0.69
CD4+CD25 <sup>hi</sup> FoxP3+ (CD4+ Treg)	22	11.5–25	16.4	11.7–20.4	0.69
CD4+CD25 <sup>hi</sup> FoxP3+ /CD3+	14.5	9.9–15.6	8.8	7.9–15.4	0.46
CD4+PD1+ Treg	47	23–53	43	21–48	0.59
CD4+CD152+ Treg	59	34–72	62	45–72	0.84
CD4+CD39+ Treg	48	46–94	74	54–87	0.96
CD4+PD-1+ /	50	37–67	50	44–63	0.81
CD4+CD152+	27	7.2–40	29	13.2–50	0.63
CD4+CD39+	48	12–61	33	19–55	0.99
CD4+ CD39+PD1+	35	6–59	20	7–32	0.50
CD4+CD152+PD1+	15	4.8–20	13	8–32	0.94

Concerning intratumoral CD8+ T cell subsets, we found decreased frequencies of CD8+CD28+ T cells and increased frequencies of both CD8+CD28- T lymphocytes and CD8+CD28-CD127-CD39+ Treg in Group 1 with respect to Group 2 (Table 3, Figure 1A–C, Figure S1). We found predictive value for prognosis in these T cell subsets when we divided the HNSCC patients based on cutoffs for the median frequency of either CD8+CD28+ (> or <47.50%), CD8+CD28- T lymphocytes (> or <52.5%) or CD8+CD28-CD127-CD39+ Treg (> or <13.5%); specifically, patients with CD8+CD28+ T cell values lower than the

cutoff, or CD8+CD28- T cells and CD8+CD28-CD127-CD39+ Treg values greater than the cut-off, had remarkably reduced survival (Figure 1D–F). Moreover, in bivariate Cox models including T cells fractions and HPV status such prognostic effects were confirmed to be significant ( $p < 0.05$ ).

**Table 3.** Percent frequencies of HNSCC infiltrating CD8+ T cell subsets in Group 1 and Group 2.

T Cell Subsets	Group 1 ( <i>n</i> = 7)		Group 2 ( <i>n</i> = 13)		<i>p</i> -Value
	Median	IQR	Median	IQR	
CD3+CD8+/CD3+	40.7	29–44.1	20	17–45	0.63
CD8+CD28+/CD8+	23	15–34	74	67–82	0.0006
CD8+CD28- /CD8+	77	66–85	26	18–33	0.0006
Naïve CD8+/CD8+	1	0.2–4.1	0.6	0.3–1.7	0.66
CM CD8+/CD8+	1.8	0.1–3.3	1.2	0.4–2.5	0.72
EM CD8+/CD8+	62	49–74	79	63–84	0.07
TEM CD8+/CD8+	31	24–50	17	14–32	0.14
CD8+CD28-CD127-CD39+ (CD8+ Treg)	28.9	16–51	6.2	4.4–15.9	0.03
CD8+CD28-CD127-CD39+PD-1+	10.6	2.1–27.9	2.1	0.4–2.8	0.18
CD8+PD-1+	60	36.4–81	61	52–67	0.99
CD8+PD-1-	37	18–51	34	23–38	0.84
CD8+CD152+	5	2–8.7	2.3	1.5–8	0.69
CD8+CD39+	50	25–54	20.6	12–47.5	0.25
CD8+PD1+CD152+	4	0.7–7	1.7	0.5–4.5	0.51
CD8+PD1+CD39+	38	4.3–48	18	10–39	0.61

### 3.2. Phenotypic Characterization of CD8+CD28- HNSCC Infiltrating T Cells

CD8+CD28+ T cells belong to the naïve and memory T cell compartments. Antigen priming of CD8+CD28+ T cells induces progressive downregulation of CD28 expression [22,26]. The finding that Group 1 patients showed reduced CD8+CD28+ T cell frequency with respect to Group 2 patients suggests (a) an increased rate of conversion of CD8+CD28+ T cells to CD8+CD28- effector T cells and/or (b) a reduced process of replenishing the intratumoral CD8+CD28- pool in Group 1 patients. Whatever the mechanism, it appears paradoxical that Group 1 patients, who have an increased frequency of CD8+CD28- T cells, which belong to the subset of effector CD8+ T cells [22], could manifest a poorer response to therapy than Group 2 patients. Hence, we focused on this cell subset in order to achieve any insight to shed light on this apparent paradox.

We noted that tumor infiltrating CD8+CD28- T cells of HNSCC patients could be divided in three subgroups (CD8+CD28-PD-1<sup>hi</sup>, CD8+CD28-PD-1<sup>int</sup> and CD8+CD28-PD-1<sup>lo/absent</sup> T cells) based on their PD-1 mean fluorescence intensity (MFI), reminiscent of what was recently observed in CD8+ T cells from the infiltrate of lung cancer (Figure 2A,C, Figure 2B left panels) [27]. Interestingly, a gradient of expression paralleling that of PD-1 (from low to intermediate to high) was also observed for CD39 and TIM-3 on CD8+CD28- T cells (Figure 2A,C, Figure 2B, right panels).

To achieve a better characterization, we applied the t-SNE algorithm to the multiparametric analyses performed on these T cells. Thus, we observed that the clusters relative to CD8+CD28-PD-1<sup>hi</sup> T cells lacked expression of both CD45RA and CCR7 (Figure 3A), indicating a maturation stage corresponding to that of effector-memory T lymphocytes.

A portion of these cells also expressed CD39, TIM-3 and EOMES, demonstrating their exhausted status [28–31].

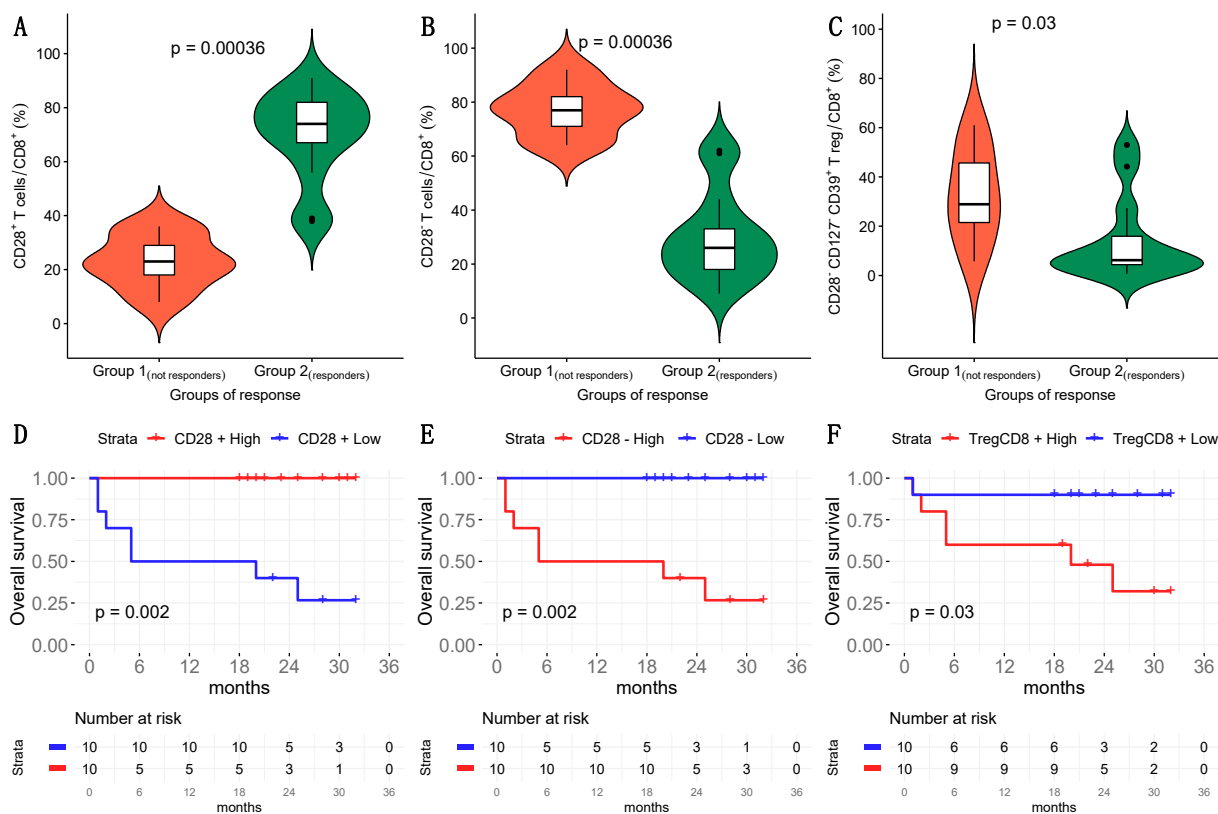


**Figure 1.** Frequency of tumor infiltrating CD8+CD28+ T cells, CD8+CD28- T cells and CD8+CD28-CD127-CD39+ Treg from HNSCC patients. (A–C): Comparative analysis of the frequencies of CD8+CD28+ T cells (Panel A), CD8+CD28- T cells (Panel B) and CD8+CD28-CD127-CD39+ Treg (Panel C) between Group 1 and Group 2 patients. (D–F): Survival of HNSCC patients divided into two groups based on the median (calculated in the overall population) of frequency of either CD8+CD28+ T lymphocytes (> or <47.5%) (Panel D), CD8+CD28- T lymphocytes (> or <52.5%) (Panel E) or CD8+CD28-CD127-CD39+ Treg (> or <13.5%) (Panel F).

Knowing that the exhaustion mechanism heavily hampers the activity of effector T cells, we further analyzed the CD8+CD28- T cells taking into consideration only the subpopulations that did not express T cell inhibitory receptor markers of exhaustion such as CD39 and PD-1. Figure 3C shows that CD8+CD28-CD39-PD-1- T cells were a minority of the total CD8+CD28- T cells and their frequencies were comparable between Group 1 and Group 2.

These findings suggest that exhaustion targets the majority of effector CD8+ T cells in HNSCC, thus likely representing a remarkable mechanism determining the poor prognosis of these patients. However, it also suggests that the difference in rates of T cell exhaustion is not a discriminating element for distinguishing between responder and non-responder patients to therapy.

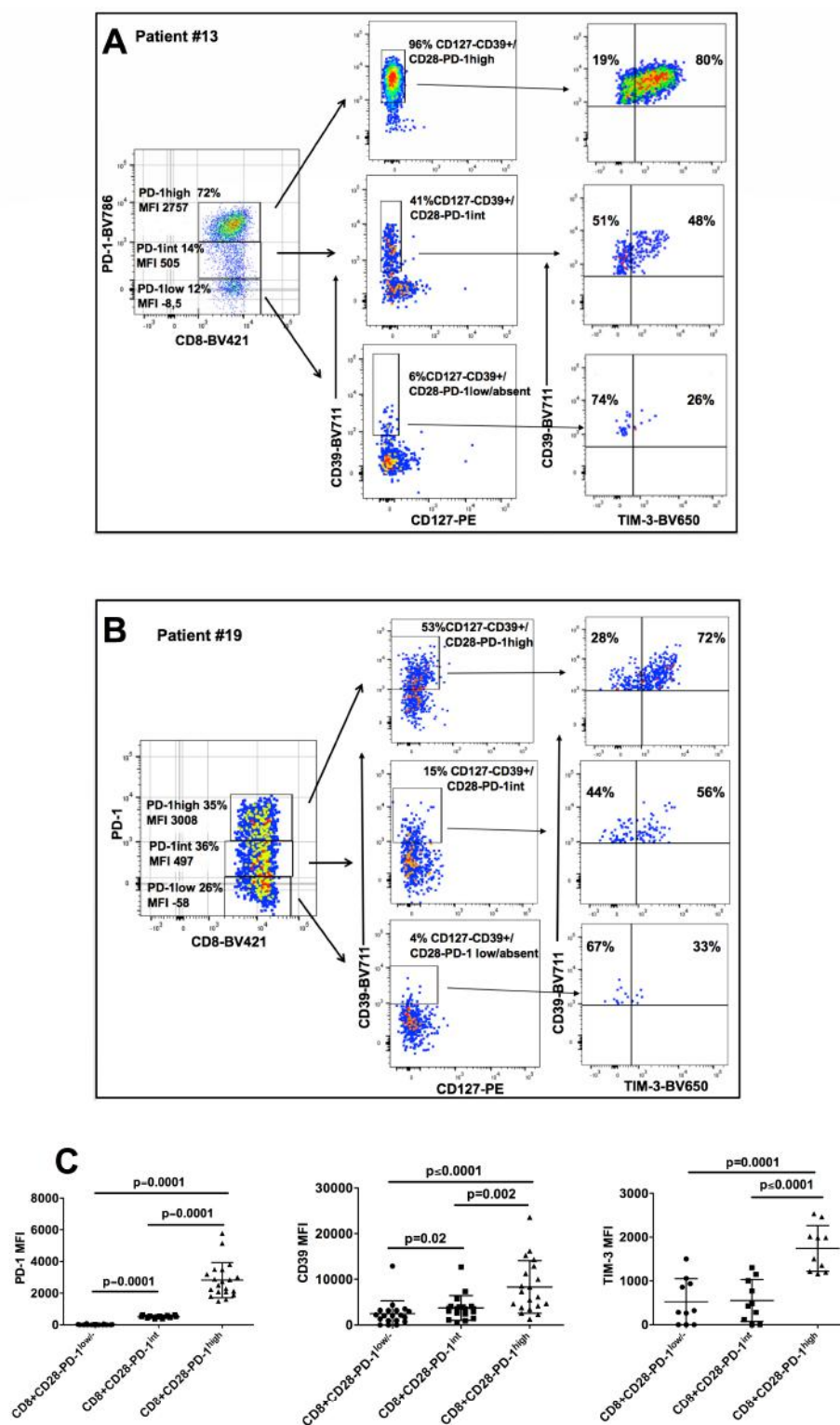
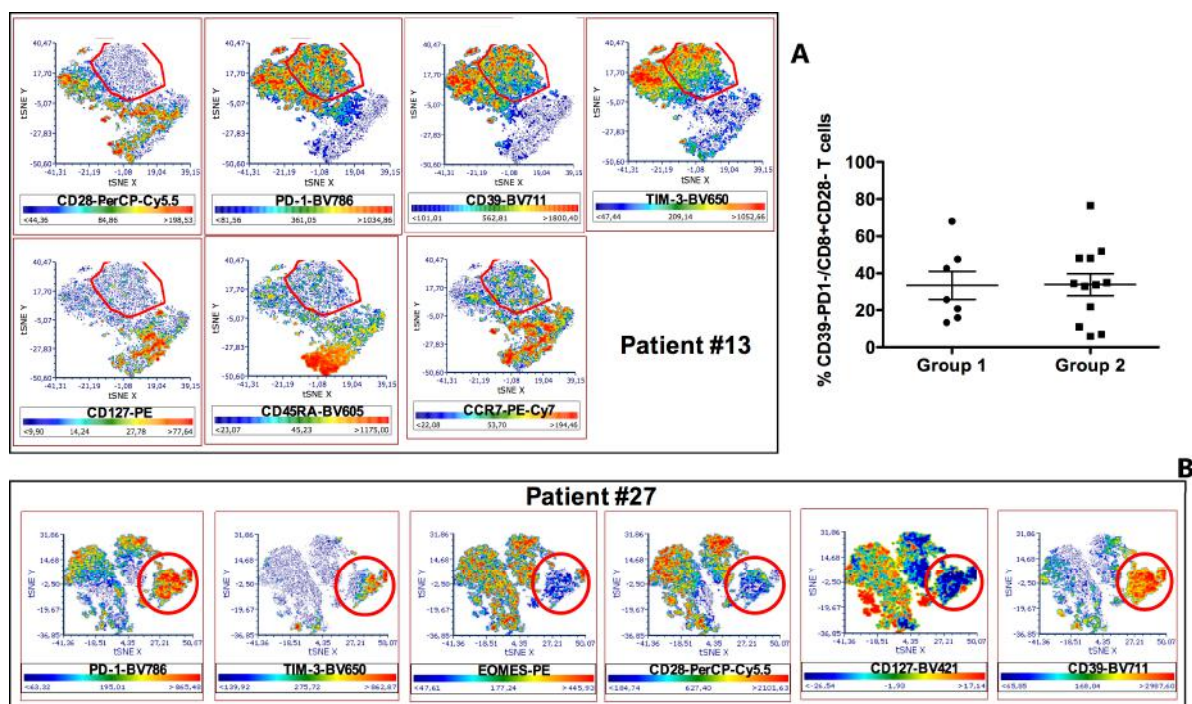


**Figure 2.** Phenotypic characterization of tumor infiltrating CD8+CD28- T cells based on the levels of PD-1 expression. A and B. CD28- T cells were gated and tumor infiltrating CD8+CD28- T cells from representative patients #13 (A) and #19 (B) were divided in three subpopulations (CD8+CD28-PD-1<sup>hi</sup>, CD8+CD28-PD-1<sup>int</sup> and CD8+CD28-PD-1<sup>lo/-</sup>, respectively)



based on the mean fluorescent intensity (MFI) of PD-1 expression (left panels). CD8+CD28–PD-1<sup>hi</sup>, CD8+CD28–PD-1<sup>int</sup> and CD8+CD28–PD-1<sup>lo</sup> were considered cells with PD-1 MFI > 10<sup>3</sup>, >10<sup>2</sup> and <10<sup>3</sup>, or <10<sup>2</sup>, respectively. The frequencies of CD127–CD39+ T cells (middle panels) and of CD39+TIM-3+ T cells (right panels) are separately shown for CD8+CD28–PD-1<sup>hi</sup>, CD8+CD28–PD-1<sup>int</sup> and CD8+CD28–PD-1<sup>lo</sup>. (C) MFI mean values of PD-1 (left panel), CD39 (middle panel) and TIM-3 (right panel) in CD8+CD28–PD-1<sup>hi</sup>, CD8+CD28–PD-1<sup>int</sup> and CD8+CD28–PD-1<sup>lo</sup>/– tumor infiltrating T cells from our series of HNSCC patients.



### 3.3. Characterization of CD8+CD28–PD1<sup>hi</sup> T cells as CD8+CD28–CD127–CD39+ Treg

Notably, our previous studies demonstrated that tumor infiltrating CD8+CD28– T cells may be highly immunosuppressive, since these cells contain and are also precursors of CD8+CD28–CD127–CD39+ Treg [24,25,32,33]. Importantly, in the present study we observed that not only the CD8+CD28– T cell subset but also the subpopulation constituted of CD8+CD28–CD127–CD39<sup>hi</sup> Treg was significantly increased in Group 1 with respect to Group 2. These data raised the question about the possible existence of relationships between intratumoral CD8+CD28– T cells and CD8+CD28–CD127–CD39+ Treg in HNSCC. Interestingly, t-SNE maps unveiled that the cellular clusters corresponding to CD8+CD28–PD1<sup>hi</sup> T lymphocytes overlapped those of CD8+CD28–CD127–CD39+ Treg (Figure 3A,B). Accordingly, the frequency of CD8+CD28–CD127–CD39+ Treg was significantly higher among CD8+CD28–PD1<sup>hi</sup> T lymphocytes than among CD8+CD28–PD-1<sup>int</sup>

or CD8+CD28–PD-1<sup>+</sup> T lymphocytes (Figure 2A,B, middle panels, Figure 4A), and a very high level of statistical correlation was observed between the intratumoral frequencies of the two T cell subpopulations (Figure 4B). These observations indicate that the tumor microenvironment of HNSCC patients is highly enriched in CD8+CD28–PD-1<sup>hi</sup> T cells that are phenotypically indistinguishable from the CD8+CD28–CD127–CD39+ Treg subpopulation. Interestingly, CD8+ T cells sorted from the infiltrate of patient #5 contained similar frequencies of CD8+CD28–PD-1<sup>hi</sup> T cells (66%) and CD8+CD28–CD127–CD39+ Treg (60%), and these cells exerted a remarkable suppressive function, demonstrating the intratumoral acquisition of regulatory activity by this originally effector-memory T cell subset (Figure 4C). This finding is of interest since it suggests that intratumoral T cell exhaustion may be associated with acquisition of regulatory activities.

Enrollment of 10 new patients affected by HNSCC and surgically treated allowed an in-depth phenotypic characterization showing that both CD8+CD28–PD-1<sup>hi</sup> T cells and CD8+CD28–CD127–CD39+PD-1<sup>hi</sup> Treg may express the CD103 integrin, characterizing stably resident cells within the tumor (Figure 5A), as well as the CD137 antigen, a marker of recently TCR-stimulated T lymphocytes with potential anti-tumor reactivity (Figure 5B) [34–37]. The fact that CD8+CD28–PD-1<sup>hi</sup>CD137+ T cells were shown to be positive for ki67 staining suggests that these T cells were proliferating in response to a recent TCR stimulation (Figure 5B). Altogether, these data suggest that both CD8+CD28–PD-1<sup>hi</sup> T cells and CD8+CD28–CD127–CD39+PD-1<sup>hi</sup> Treg might be cells that were longtime residents within the tumor microenvironment where a portion of them were responding to specific antigens. Hypothesizing that part of these cells could be tumor-reactive, we analyzed tumor infiltrating T cells from an HLA-A2+ HNSCC patient for their capacity to bind an HLA-A2 pentamer loaded with G250/CAIX, a tumor antigen frequently expressed by HNSCC cells [38]. Figure 5C shows that 0.8% of total tumor infiltrating CD8+ T cells, 0.28% of CD8+CD28–PD-1<sup>hi</sup> T cells and 0.5% of CD8+CD28–CD127–CD39+PD-1<sup>hi</sup> Treg bound specifically to the HLA-A2 G250/CAIX loaded pentamer, demonstrating that they contained tumor-reactive CD8+ T cells. Collectively, these data indicate that effector CD8+ T cells, at least partly tumor-specific, become exhausted and acquire regulatory activity within the tumor microenvironment, a phenomenon we define here as “effector-to-regulatory CD8+ T cell transition”.

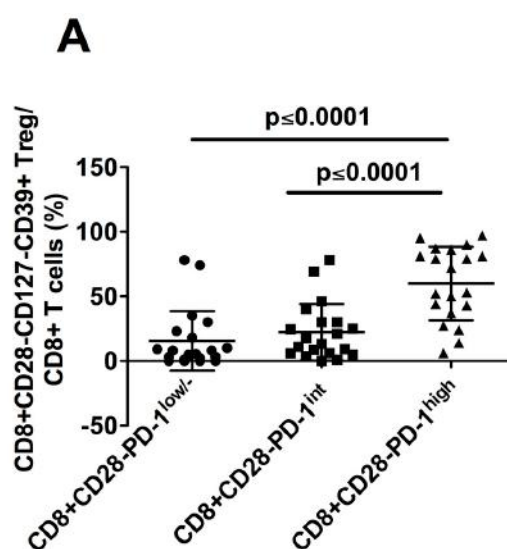
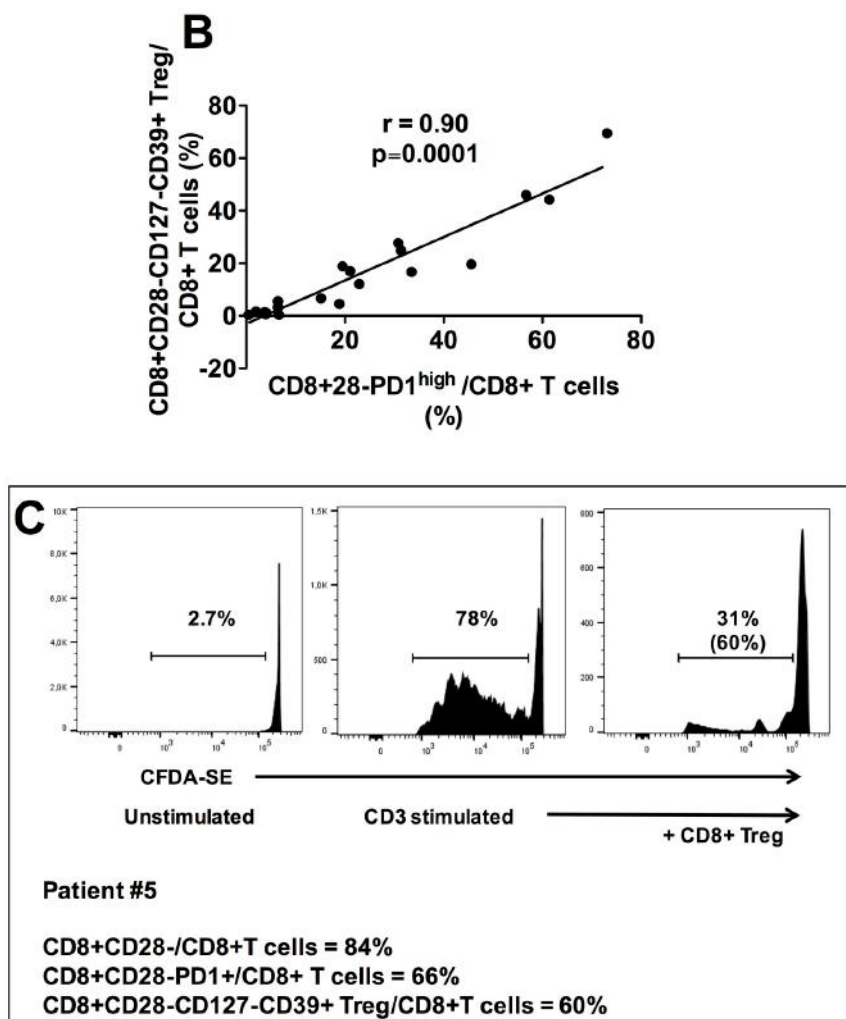
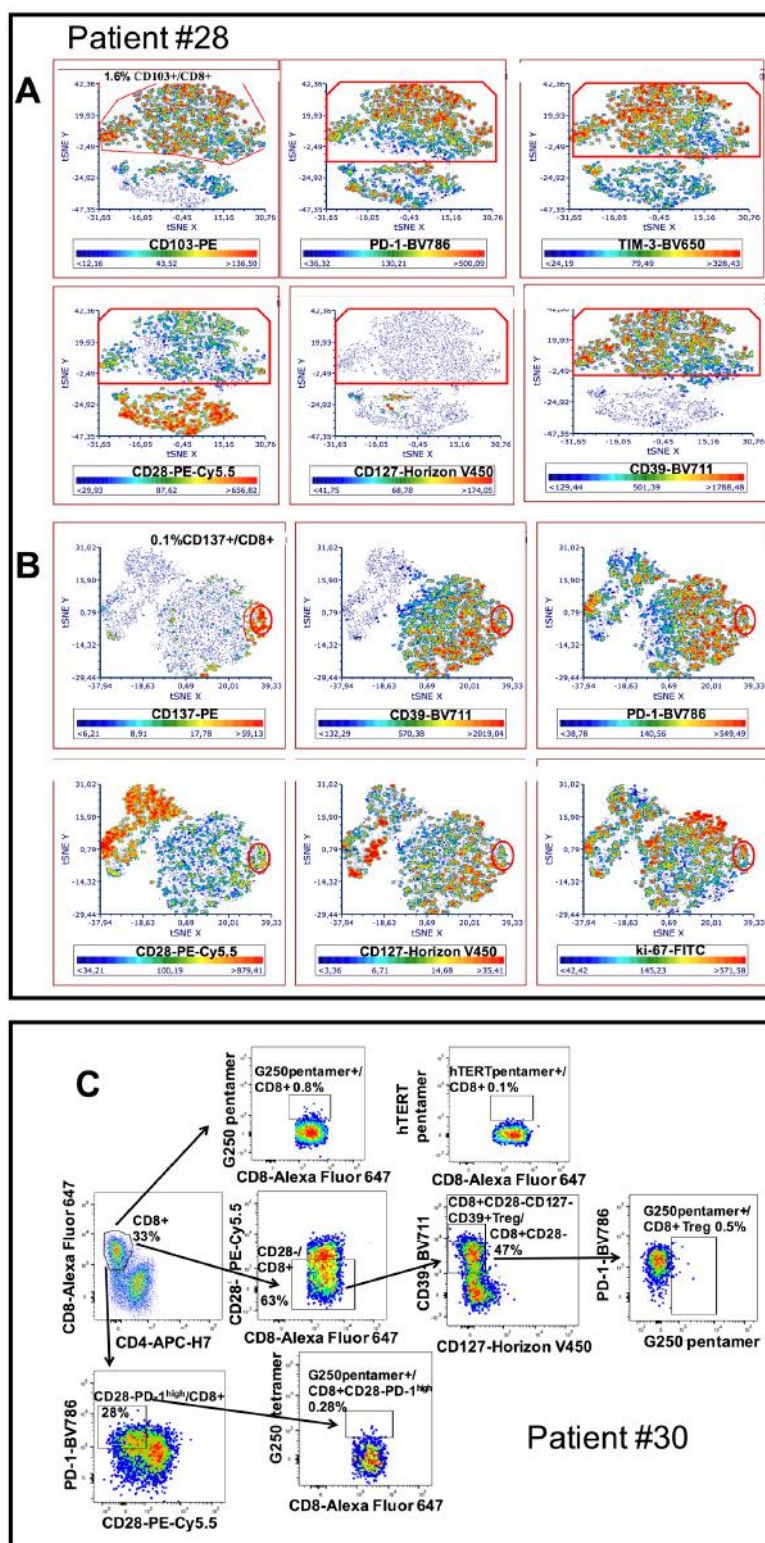


Figure 4. *Cont.*



**Figure 4.** Relationship between tumor infiltrating CD8+CD28–PD1<sup>hi</sup> T cells and CD8+CD28–CD127–CD39+ Treg in HNSCC patients. (A): Mean frequencies of CD8+CD28–CD127–CD39+ Treg among CD8+CD28–PD-1<sup>lo</sup>, CD8+CD28–PD-1<sup>int</sup> and CD8+CD28–PD-1<sup>hi</sup> T cell subpopulations. Statistical significant differences are evidenced. (B): Statistical correlation between the frequency of tumor infiltrating CD8+CD28–PD-1<sup>hi</sup> T cells and that of tumor infiltrating CD8+CD28–CD127–CD39+ Treg in our cohort of HNSCC patients. (C): Proliferation suppression assay performed with the CD8+ T cell infiltrate from the representative patient #5 containing comparable frequencies of CD8+CD28–PD-1<sup>hi</sup> (66%) and CD8+CD28–CD127–CD39+ Treg (60%). The percentages of T cell proliferation under unstimulated conditions (left panel) or anti-CD3 UCHT1 mAb–stimulated conditions in absence (middle panel) or presence (right panel) of tumor infiltrating CD8+CD28–CD127–CD39+ Treg (CD8+ Treg in the Figure) are shown; the percentage of proliferation inhibition by CD8+CD28–CD127–CD39+Treg is shown in parentheses in the right panel. One out of two concordant experiments performed with cells of different patients.



**Figure 5.** Further phenotypic characterization of tumor infiltrating CD8+CD28–PD-1<sup>hi</sup>/CD8+CD28–CD127–CD39+ T cells. (A): t-SNE algorithm was applied to the analysis of tumor infiltrating CD8+ T cells from patient #28. A red frame identifies a map area where cell clusters, negative for CD28 and CD127 expression and highly positive for CD39, PD-1,



TIM-3 and CD103 expression, segregate. The colorimetric scale of expression is shown below each graph (blue clusters indicate absent expression, red clusters represent high expression). (B): t-SNE algorithm was applied to the analysis of tumor infiltrating CD8+ T cells from patient #28. A red circle identifies a map area where cell clusters, negative for CD28 and CD127 expression and highly positive for CD39, PD-1, CD137 and ki-67 expression, segregate. The colorimetric scale of expression is shown below each graph (blue clusters indicate absent expression, red clusters represent high expression). (C): Staining of tumor infiltrating CD8+ T cells (upper row), CD8+CD28-CD127-CD39+ Treg (middle row) and CD8+CD28-PD-1<sup>hi</sup> T cells (lower row) from patient #30 with a G250 HLSTAFARV<sub>217-225</sub> loaded HLA-A2 pentamer. An unrelated, hTert ILAKFLHWL<sub>540-548</sub> loaded HLA-A2 pentamer was used as negative control (upper, right panel).

#### 4. Discussion

CD8+ T lymphocytes are deputed to recognition and lysis of endogenous cells altered by the presence of an infecting agent (i.e., a virus) or by cancer transformation. However, in cancer patients, oncogenic cells progressively escape immune control, until ultimately the cancer develops and progresses [39]. What differentiates the effective CD8+ T cells of healthy subjects from the dysfunctional ones in infiltrating tumors is still poorly understood.

A rich CD8+ T cell infiltrate correlates generally with a better prognosis, although this is not a unique finding [12–17,40–45]. There is evidence that the level of CD8+ T cell infiltrate has a prognostic value even in HNSCC. In fact, HPV+ HNSCC, which is generally more infiltrated by T cells than HPV- HNSCC, has a better prognosis than the corresponding HPV- tumor [16,46,47], unless HPV+ HNSCC has a low T cell infiltrate [48]. Moreover, the application of Immunoscore to HNSCC showed a prognostic advantage for T cell rich tumors [49,50]. Similarly, tumors, including HNSCC, highly infiltrated by CD8+ T cells have a better outcome after immunotherapy than poorly infiltrated ones [51,52]. Overall, these findings suggest that CD8+ T cells play a role in the control of HNSCC growth, a role that is likely hampered by their progressive alteration, leading to tumor escape and cancer progression. Indeed, an array of alterations has been described in tumor infiltrating lymphocytes targeting both effector and memory CD8+ T cell subsets [22,26,34]. Dysfunctional CD8+ T cells are characterized phenotypically by a high expression of molecules related to functional exhaustion (including PD-1, TIM-3, EOMES, CD39), and functionally by progressive loss of effector functions [22,26].

Based on this knowledge, our demonstration that what differentiates between HNSCC patients responding or not responding to therapies is their relative frequencies of CD8+CD28+ and CD8+CD28- T cells, is of relevance. In fact, CD28, essential during T cell priming to prevent anergy and tolerance, is expressed mainly by naïve and central memory T cells; antigen stimulation of these T cell subsets leads to differentiation into effector memory T cells and downregulation of CD28 [22,26]. Hence, CD8+CD28+ T cells represent the reservoir for effector memory T cells and, subsequently, their depletion may halt chronic, long-lasting immune responses. Our finding that reduced frequency of CD8+CD28+ T cells as well as increased frequency of CD8+CD28- T cells are associated with poor prognosis, suggest that a progressive deterioration of intratumoral immune response, characterized by loss of memory T cells and functional exhaustion of effector T cell subsets, is a relevant pathogenic mechanism of tumor immune escape in HNSCC.

Intriguingly, we also found that exhausted CD8+CD28- T cells from HNSCC exert suppressive function and that the CD8+CD28- T cell subset highly expressing PD-1 phenotypically overlap with CD8+CD28-CD127-CD39 Treg. This indicates that T cell exhaustion at the tumor site may be associated with the acquisition of regulatory properties, since CD8+CD28-CD127-CD39 Treg, highly concentrated within the tumor microenvironment, exerts remarkable immunosuppressive activity targeting both T cell proliferation and cytotoxicity [24,25,32,33]. This finding sheds new light on CD8+ T cell exhaustion, interpreting this phenomenon not only as the loss of effector activities but also as a progressive functional switch from effector to regulatory functions. The recent finding that enrichment of peripheral CD8+PD1+ T cell associates with poor overall survival in a cohort of patients affected by metastatic cancer (≈50% HNSCC) and submitted to immune-checkpoint

inhibitors [53] may be interpreted as a clinical consequence of the biologic phenomena highlighted by our data.

Interestingly, we show that CD8+CD28-CD127-CD39+ Treg may belong to the pool of tumor resident T cells (since they express CD103) and that they may be specific for a tumor-associated antigens. These findings suggest that these cells originate from effector cells that convert their activity to regulatory functions within the tumor microenvironment: a phenomenon we define as “effector-to-regulatory CD8+ T cell transition”. A schematic representation of this phenomenon is illustrated in Figure 6.

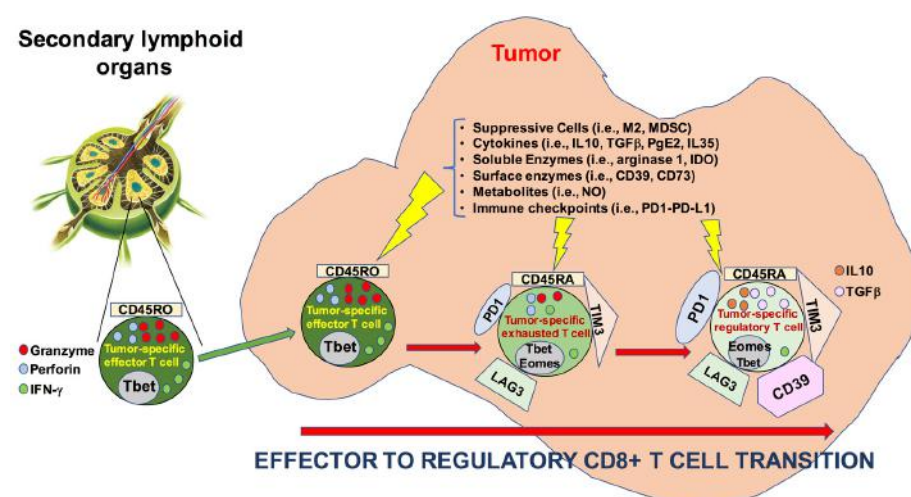


**Figure 6.** Schematic representation of the “effector-to-regulatory CD8+ T cell transition” at the tumor site.

Future work will be necessary to verify whether such effector-to-regulatory CD8+ T cell transition could be reversed by exposure to different and/or combined immune checkpoint blockers.

## 5. Conclusions

The results of our study show that: (a) differential intratumoral frequency of three T cell subsets, CD8+CD28+ T cells, CD8+CD28- T cells, and CD8+CD28-CD127-CD39+ Treg, distinguished between HNSCC patients who did or did not respond to treatment; (b) high PD-1 expression identified a CD8+CD28- T cell subpopulation phenotypically/functionally corresponding to CD8+CD28-CD127-CD39+ Treg; (c) CD8+CD28- T cell and CD8+CD28-CD127-CD39+ Treg subpopulations showed high expression of markers of exhaustion associated with regulatory function.

Although with the limit relative to the small number of patients included in our series, collectively our data may have a pathogenic relevance. In fact, they describe the process we define “effector-to-regulatory CD8+ T cell transition”, which determines both the loss of effector activities and the acquisition of regulatory properties by effector CD8+ T cells infiltrating HNSCC. This process may be a clue to explaining the failure of intratumoral CD8+ T cells in destroying tumors. Future molecular analyses at the single-cell level will be useful to unveil the pathways involved in this process, perhaps allowing us to identify new molecules to be addressed by a specific targeted therapy.

Lastly, our findings may also impact on therapeutic choices since they show that TIM-3 expression closely parallels that of PD-1 on HNSCC infiltrating CD8+CD28-CD127-CD39+ Treg. This makes it possible to speculate that combinatorial therapeutic strategies associating blockers of both PD-1 and TIM-3 could be effective in this tumor in order to antagonize CD8+ T cell exhaustion and suppressive activity.

**Supplementary Materials:** The following are available online at <https://www.mdpi.com/article/10.3390/cancers13092234/s1>, Figure S1: Phenotypic characterization of intratumoral CD8+CD28–CD127–CD39+ Treg, Table S1: T cell subpopulations analyzed in the study.

**Author Contributions:** Conceptualization, D.F., L.B., R.D.P., G.P., R.C. and G.F.; methodology, D.F.; validation, R.C. and G.F.; formal analysis, A.S.; investigation, D.F., L.B., A.P., A.T., T.A., G.A., F.C., S.V. (Sara Vlah), F.F., F.M., A.B., F.I., S.N., S.V. (Stefania Vecchio), A.A. and G.S.; data curation, D.F. and L.B.; writing—original draft preparation, D.F., L.B., G.F.; writing—review and editing, R.D.P., G.P., R.C. and G.F.; supervision, G.F.; project administration, G.P., R.C. and G.F.; funding acquisition, G.F. All authors have read and agreed to the published version of the manuscript.

**Funding:** This research was funded by a grant from Ministero della Salute-Fondi 5x1000 2016.

**Institutional Review Board Statement:** The study was conducted according to the guidelines of the Declaration of Helsinki, and approved by the Ethical Committee of the San Martino Hospital in Genoa (P.R.133REG2017, 2017).

**Informed Consent Statement:** Informed consent was obtained from all subjects involved in the study.

**Data Availability Statement:** The data presented in this study are available in this article (and Supplementary Materials).

**Conflicts of Interest:** The authors declare no conflict of interest.

## References

1. Grégoire, V.; Lefebvre, J.L.; Licitra, L.; Felip, E.; EHNS-ESMO-ESTRO Guidelines Working Group. Squamous cell carcinoma of the head and neck: EHNS-ESMO-ESTRO Clinical Practice Guidelines for diagnosis, treatment and follow-up. *Ann. Oncol.* **2010**, *21* (Suppl. 5), v184–v186. [[CrossRef](#)] [[PubMed](#)]
2. Belgioia, L.; Bacigalupo, A.; Missale, F.; Vecchio, S.; Chiola, I.; Callegari, S.; Verzanini, E.; Peretti, G.; Corvò, R. Individualized treatment of head neck squamous cell carcinoma patients aged 70 or older with radiotherapy alone or associated to cisplatin or cetuximab: Impact of weekly radiation dose on loco-regional control. *Med. Oncol.* **2019**, *36*, 42. [[CrossRef](#)]
3. Bonner, J.A.; Harari, P.M.; Giralt, J.; Azarnia, N.; Shin, D.M.; Cohen, R.; Jones, C.U.; Sur, R.; Raben, D.; Jassem, J.; et al. Radiotherapy plus cetuximab for squamous-cell carcinoma of the head and neck. *N. Engl. J. Med.* **2006**, *354*, 567–578. [[CrossRef](#)]
4. Vermorken, J.B.; Mesia, R.; Rivera, F.; Remenar, E.; Kawecki, A.; Rottey, S.; Erfan, J.; Zabolotnyy, D.; Kienzer, H.R.; Cupissol, D.; et al. Platinum-based chemotherapy plus cetuximab in head and neck cancer. *N. Engl. J. Med.* **2008**, *359*, 1116–1127. [[CrossRef](#)]
5. Maddalo, M.; Borghetti, P.; Tomasini, D.; Corvò, R.; Bonomo, P.; Petrucci, A.; Paiar, F.; Lastrucci, L.; Bonù, M.L.; Greco, D.; et al. Cetuximab and radiotherapy versus cisplatin and radiotherapy for locally advanced head and neck cancer: Long term survival and toxicity outcomes of a randomized phase ii trial. *Int. J. Radiat. Oncol. Biol. Phys.* **2020**, *107*, 469–477. [[CrossRef](#)]
6. Ling, D.C.; Bakkenist, C.J.; Ferris, R.L.; Clump, D.A. Role of Immunotherapy in Head and Neck Cancer. *Semin. Radiat. Oncol.* **2018**, *28*, 12–16. [[CrossRef](#)]
7. von der Grün, J.; Rödel, F.; Brandts, C.; Fokas, E.; Guckenberger, M.; Rödel, C.; Balcermpas, P. Targeted Therapies and Immune-Checkpoint Inhibition in Head and Neck Squamous Cell Carcinoma: Where Do We Stand Today and Where to Go? *Cancers* **2019**, *11*, 472. [[CrossRef](#)]
8. Le, Q.T.; Colevas, A.D.; O'Sullivan, B.; Lee, A.W.M.; Lee, N.; Ma, B.; Siu, L.L.; Waldron, J.; Lim, C.M.; Riaz, N.; et al. Current Treatment Landscape of Nasopharyngeal Carcinoma and Potential Trials Evaluating the Value of Immunotherapy. *J. Natl. Cancer Inst.* **2019**, *111*, 655–663. [[CrossRef](#)]
9. Mandal, R.; Şenbabaoglu, Y.; Desrichard, A.; Havel, J.J.; Dalin, M.G.; Riaz, N.; Lee, K.-W.; Ganly, I.; Hakimi, A.A.; Chan, T.A.; et al. The head and neck cancer immune landscape and its immunotherapeutic implications. *JCI Insight* **2016**, *1*, e89829. [[CrossRef](#)]
10. McDermott, J.D.; Bowles, D.W. Epidemiology of Head and Neck Squamous Cell Carcinomas: Impact on Staging and Prevention Strategies. *Curr. Treat. Options Oncol.* **2019**, *20*, 43. [[CrossRef](#)]
11. Lee, N.; Zakka, L.R.; Mihm, M.C., Jr.; Schatton, T. Tumour-infiltrating lymphocytes in melanoma prognosis and cancer immunotherapy. *Pathology* **2016**, *48*, 177–187. [[CrossRef](#)] [[PubMed](#)]
12. Erdag, G.; Schaefer, J.T.; Smolkin, M.E.; Deacon, D.H.; Shea, S.M.; Dengel, L.T.; Patterson, J.W.; Slingluff, C.L., Jr. Immunotype and immunohistologic characteristics of tumor infiltrating immune cells are associated with clinical outcome in metastatic melanoma. *Cancer Res.* **2012**, *72*, 1070–1080. [[CrossRef](#)]
13. Sharma, P.; Shen, Y.; Wen, S.; Yamada, S.; Jungbluth, A.A.; Gnjatich, S.; Bajorin, G.F.; Reuter, V.E.; Herr, H.; Old, L.J.; et al. CD8 tumor-infiltrating lymphocytes are predictive of survival in muscle-invasive urothelial carcinoma. *Proc. Natl. Acad. Sci. USA* **2007**, *104*, 3967–3972. [[CrossRef](#)] [[PubMed](#)]
14. Sideras, K.; Biermann, K.; Verheij, J.; Takkenberg, B.R.; Mancham, S.; Hansen, B.E.; Schutz, H.M.; de Man, R.A.; Sprengers, D.; Buschow, S.I.; et al. PD-L1, Galectin-9 and CD8+ tumor-infiltrating lymphocytes are associated with survival in hepatocellular carcinoma. *Oncoimmunology* **2017**, *6*, e1273309. [[CrossRef](#)] [[PubMed](#)]

15. Balermipas, P.; Rödel, F.; Rödel, C.; Krause, M.; Linge, A.; Lohaus, F.; Baumann, M.; Tinhofer, I.; Budach, V.; Gkika, E.; et al. CD8+ tumour-infiltrating lymphocytes in relation to HPV status and clinical outcome in patients with head and neck cancer after postoperative chemoradiotherapy: A multicentre study of the German cancer consortium radiation oncology group (DKTK-ROG). *Int. J. Cancer* **2016**, *138*, 171–181. [[CrossRef](#)] [[PubMed](#)]
16. Partlova, S.; Boucek, J.; Kloudova, K.; Lukesova, E.; Zabrodsky, M.; Grega, M.; Fučíková, J.; Truxová, I.; Tachezy, R.; Špišek, R.; et al. Distinct patterns of intratumoral immune cell infiltrates in patients with HPV-associated compared to non-virally induced head and neck squamous cell carcinoma. *Oncimmunology* **2015**, *4*, e965570. [[CrossRef](#)]
17. Balermipas, P.; Michel, Y.; Wagenblast, J.; Seitz, O.; Weiss, C.; Rödel, F.; Rödel, C.; Fokas, E. Tumour-infiltrating lymphocytes predict response to definitive chemoradiotherapy in head and neck cancer. *Br. J. Cancer* **2014**, *110*, 501–509. [[CrossRef](#)]
18. Fridman, W.H.; Zitvogel, L.; Sautès-Fridman, C.; Kroemer, G. The immune contexture in cancer prognosis and treatment. *Nat. Rev. Clin. Oncol.* **2017**, *14*, 717–734. [[CrossRef](#)]
19. Ono, T.; Azuma, K.; Kawahara, A.; Akiba, J.; Kakuma, T.; Chitose, S.; Umeno, H. Pre-treatment CD8+ tumour-infiltrating lymphocyte density predicts distant metastasis after definitive treatment in patients with stage III/IV hypopharyngeal squamous cell carcinoma. *Clin. Otolaryngol.* **2018**, *43*, 1312–1320. [[CrossRef](#)]
20. De Meulenaere, A.; Vermassen, T.; Aspeslagh, S.; Zwaenepoel, K.; Deron, P.; Duprez, F.; Rottey, S.; Ferdinande, L. Prognostic markers in oropharyngeal squamous cell carcinoma: Focus on CD70 and tumour infiltrating lymphocytes. *Pathology* **2017**, *49*, 397–404. [[CrossRef](#)]
21. van der Heijden, M.; Essers, P.B.M.; de Jong, M.C.; de Roestm, R.H.; Sanduleanu, S.; Verhagen, C.V.M.; Hamming-Vrieze, O.; Hoebers, F.; Lambin, P.; Bartelink, H.; et al. Biological Determinants of Chemo-Radiotherapy Response in HPV-Negative Head and Neck Cancer: A Multicentric External Validation. *Front. Oncol.* **2020**, *9*, 1470. [[CrossRef](#)]
22. Reading, J.L.; Gálvez-Cancino, F.; Swanton, C.; Lladser, A.; Peggs, K.S.; Quezada, S.A. The function and dysfunction of memory CD8+ T cells in tumor immunity. *Immunol. Rev.* **2018**, *283*, 194–212. [[CrossRef](#)]
23. Crespo, J.; Haoyu, S.; Welling, T.H.; Tian, Z.; Zou, W. T cell anergy, exhaustion, senescence and stemness in the tumour microenvironment. *Curr. Opin. Immunol.* **2013**, *25*, 214–221. [[CrossRef](#)]
24. Filaci, G.; Fenoglio, D.; Fravega, M.; Ansaldo, G.; Borgonovo, G.; Traverso, P.; Villaggio, B.; Ferrera, A.; Kunkl, A.; Rizzi, M.; et al. CD8+ CD28- T regulatory lymphocytes inhibiting T cell proliferative and cytotoxic functions infiltrate human cancers. *J. Immunol.* **2007**, *179*, 4323–4334. [[CrossRef](#)]
25. Parodi, A.; Battaglia, F.; Kalli, F.; Ferrera, F.; Conteduca, G.; Tardito, S.; Stringara, S.; Ivaldi, F.; Negrini, S.; Borgonovo, G.; et al. CD39 is highly involved in mediating the suppression activity of tumor-infiltrating CD8+ T regulatory lymphocytes. *Cancer Immunol. Immunother.* **2013**, *62*, 851–862. [[CrossRef](#)] [[PubMed](#)]
26. Huff, W.X.; Kwon, J.H.; Henriquez, M.; Fetcko, K.; Dey, M. The Evolving Role of CD8+CD28- Immunosenescent T Cells in Cancer Immunology. *Int. J. Mol. Sci.* **2019**, *20*, 2810. [[CrossRef](#)] [[PubMed](#)]
27. Thommen, D.S.; Koelzer, V.H.; Herzig, P.; Roller, A.; Trefny, M.; Dimeloe, S.; Kiialainen, A.; Hanhart, J.; Schill, C.; Hess, C.; et al. A transcriptionally and functionally distinct PD-1+ CD8+ T cell pool with predictive potential in non-small-cell lung cancer treated with PD-1 blockade. *Nat. Med.* **2018**, *24*, 994–1004. [[CrossRef](#)] [[PubMed](#)]
28. Paley, M.A.; Kroy, D.C.; Odorizzi, P.M.; Johnnidis, J.B.; Dolfi, D.V.; Barnett, B.E.; Bikoff, E.K.; Robertson, E.J.; Lauer, G.M.; Reiner, S.L.; et al. Progenitor and terminal subsets of CD8+ T cells cooperate to contain chronic viral infection. *Science* **2012**, *338*, 1220–1225. [[CrossRef](#)]
29. Reiser, J.; Banerjee, A. Effector, Memory, and Dysfunctional CD8(+) T Cell Fates in the Antitumor Immune Response. *J. Immunol. Res.* **2016**, *2016*, 8941260. [[CrossRef](#)]
30. Canale, F.P.; Ramello, M.C.; Núñez, N.; Araujo Furlan, C.L.; Bossio, S.N.; Gorosito Serrán, M.; Tosello Boari, J.; Del Castillo, A.; Ledesma, M.; Sedlik, C.; et al. CD39 Expression Defines Cell Exhaustion in Tumor-Infiltrating CD8+ T Cells. *Cancer Res.* **2018**, *78*, 115–128. [[CrossRef](#)]
31. Wherry, E.J.; Ha, S.J.; Kaech, S.M.; Haining, W.N.; Sarkar, S.; Kalia, V.; Subramaniam, S.; Blattman, J.N.; Barber, D.L.; Ahmed, R. Molecular signature of CD8+ T cell exhaustion during chronic viral infection. *Immunity* **2007**, *27*, 670–684. [[CrossRef](#)]
32. Fenoglio, D.; Ferrera, F.; Fravega, M.; Balestra, P.; Battaglia, F.; Proietti, M.; Andrei, C.; Olive, D.; La Cava, A.; Indiveri, F.; et al. Advancements on phenotypic and functional characterization of non-antigen-specific CD8+CD28- regulatory T cells. *Hum. Immunol.* **2008**, *69*, 745–750. [[CrossRef](#)]
33. Filaci, G.; Fravega, M.; Negrini, S.; Procopio, F.; Fenoglio, D.; Rizzi, M.; Brenci, S.; Contini, P.; Olive, D.; Ghio, M.; et al. Nonantigen specific CD8+ T suppressor lymphocytes originate from CD8+CD28- T cells and inhibit both T-cell proliferation and CTL function. *Hum. Immunol.* **2004**, *65*, 142–156. [[CrossRef](#)]
34. Corgnac, S.; Boutet, M.; Kfoury, M.; Naltet, C.; Mami-Chouaib, F. The Emerging Role of CD8+ Tissue Resident Memory T (TRM) Cells in Antitumor Immunity: A Unique Functional Contribution of the CD103 Integrin. *Front. Immunol.* **2018**, *9*, 904. [[CrossRef](#)]
35. Mami-Chouaib, F.; Blanc, C.; Corgnac, S.; Hans, S.; Malenica, I.; Granier, C.; Tihy, I.; Tartour, E. Resident memory T cells, critical components in tumor immunology. *J. Immunother. Cancer* **2018**, *6*, 87. [[CrossRef](#)] [[PubMed](#)]
36. Li, Q.; Carr, A.; Ito, F.; Teitz-Tennenbaum, S.; Chang, A.E. Polarization effects of 4-1BB during CD28 costimulation in generating tumor-reactive T cells for cancer immunotherapy. *Cancer Res.* **2003**, *63*, 2546–2552. [[PubMed](#)]



37. Wolf, M.; Kuball, J.; Ho, W.Y.; Nguyen, H.; Manley, T.J.; Bleakley, M.; Greenberg, P.D. Activation-induced expression of CD137 permits detection, isolation, and expansion of the full repertoire of CD8+ T cells responding to antigen without requiring knowledge of epitope specificities. *Blood* **2007**, *110*, 201–210. [[CrossRef](#)]
38. Schmitt, A.; Barth, T.F.; Beyer, E.; Borchert, F.; Rojewski, M.; Chen, J.; Guillaume, P.; Gronau, S.; Greiner, J.; Möller, P.; et al. The tumor antigens RHAMM and G250/CAIX are expressed in head and neck squamous cell carcinomas and elicit specific CD8+ T cell responses. *Int. J. Oncol.* **2009**, *34*, 629–639. [[CrossRef](#)] [[PubMed](#)]
39. Schreiber, R.D.; Old, L.J.; Smyth, M.J. Cancer immunoediting: Integrating immunity's roles in cancer suppression and promotion. *Science* **2011**, *331*, 1565–1570. [[CrossRef](#)] [[PubMed](#)]
40. Yeung, J.T.; Hamilton, R.L.; Ohnishi, K.; Ikeura, M.; Potter, D.M.; Nikiforova, M.N.; Ferrone, S.; Jakacki, R.I.; Pollack, I.F.; Okada, H. LOH in the HLA class I region at 6p21 is associated with shorter survival in newly diagnosed adult glioblastoma. *Clin. Cancer Res.* **2013**, *19*, 1816–1826. [[CrossRef](#)]
41. Mittelbronn, M.; Simon, P.; Löffler, C.; Capper, D.; Bunz, B.; Harter, P.; Schlaszus, H.; Schleich, A.; Tabatabai, G.; Goepfert, B.; et al. Elevated HLA-E levels in human glioblastomas but not in grade I to III astrocytomas correlate with infiltrating CD8+ cells. *J. Neuroimmunol.* **2007**, *189*, 50–58. [[CrossRef](#)] [[PubMed](#)]
42. Leclerc, B.G.; Charlebois, R.; Chouinard, G.; Allard, B.; Pommey, S.; Saad, F.; Stagg, J. CD73 Expression Is an Independent Prognostic Factor in Prostate Cancer. *Clin. Cancer Res.* **2016**, *22*, 158–166. [[CrossRef](#)]
43. Ness, N.; Andersen, S.; Valkov, A.; Nordby, Y.; Donnem, T.; Al-Saad, S.; Busund, L.T.; Bremnes, R.M.; Richardsen, E. Infiltration of CD8+ lymphocytes is an independent prognostic factor of biochemical failure-free survival in prostate cancer. *Prostate* **2014**, *74*, 1452–1461. [[CrossRef](#)]
44. Kärjä, V.; Aaltomaa, S.; Lipponen, P.; Isotalo, T.; Talja, M.; Mokka, R. Tumour-infiltrating lymphocytes: A prognostic factor of PSA-free survival in patients with local prostate carcinoma treated by radical prostatectomy. *Anticancer Res.* **2005**, *25*, 4435–4438. [[PubMed](#)]
45. Gu, F.M.; Gao, Q.; Shi, G.M.; Zhang, X.; Wang, J.; Jiang, J.H.; Wang, X.-Y.; Shi, Y.-H.; Ding, Z.-B.; Fan, J.; et al. Intratumoral IL-17<sup>+</sup> cells and neutrophils show strong prognostic significance in intrahepatic cholangiocarcinoma. *Ann. Surg. Oncol.* **2012**, *19*, 2506–2514. [[CrossRef](#)]
46. Näsman, A.; Romanitan, M.; Nordfors, C.; Grün, N.; Johansson, H.; Hammarstedt, L.; Marklund, L.; Munck-Wikland, E.; Dalianis, T.; Ramqvist, T. Tumor infiltrating CD8+ and Foxp3+ lymphocytes correlate to clinical outcome and human papillomavirus (HPV) status in tonsillar cancer. *PLoS ONE* **2012**, *7*, e38711. [[CrossRef](#)]
47. Krupar, R.; Robold, K.; Gaag, D.; Spanier, G.; Kreutz, M.; Renner, K.; Hellerbrand, C.; Hofstaedter, F.; Bosserhoff, A.K. Immunologic and metabolic characteristics of HPV-negative and HPV-positive head and neck squamous cell carcinomas are strikingly different. *Virchows Arch.* **2014**, *465*, 212–299. [[CrossRef](#)]
48. Ward, M.J.; Thirdborough, S.M.; Mellows, T.; Riley, C.; Harris, S.; Suchak, K.; Webb, A.; Hampton, C.; Patel, N.N.; Randall, C.J.; et al. Tumour-infiltrating lymphocytes predict for outcome in HPV-positive oropharyngeal cancer. *Br. J. Cancer* **2014**, *110*, 489–500. [[CrossRef](#)]
49. Zhang, X.M.; Song, L.J.; Shen, J.; Yue, H.; Han, Y.Q.; Yang, C.L.; Liu, S.-Y.; Deng, J.-W.; Jiang, Y.; Fu, G.-H.; et al. Prognostic and predictive values of immune infiltrate in patients with head and neck squamous cell carcinoma. *Hum. Pathol.* **2018**, *82*, 104–112. [[CrossRef](#)]
50. Economopoulou, P.; de Bree, R.; Kotsantis, I.; Psyrris, A. Diagnostic Tumor Markers in Head and Neck Squamous Cell Carcinoma (HNSCC) in the Clinical Setting. *Front. Oncol.* **2019**, *9*, 827. [[CrossRef](#)]
51. Linette, G.P.; Carreno, B.M. Tumor-Infiltrating Lymphocytes in the Checkpoint Inhibitor Era. *Curr. Hematol. Malign. Rep.* **2019**, *14*, 286–291. [[CrossRef](#)] [[PubMed](#)]
52. Hecht, M.; Gostian, A.O.; Eckstein, M.; Rutzner, S.; Von der Grün, J.; Illmer, T.; Hautmann, M.G.; Klautke, G.; Laban, S.; Brunner, T.; et al. Safety and efficacy of single cycle induction treatment with cisplatin/docetaxel/durvalumab/tremelimumab in locally advanced HNSCC: First results of CheckRad-CD8. *J. Immunother. Cancer* **2020**, *8*, e001378. [[CrossRef](#)] [[PubMed](#)]
53. Zhou, J.-G.; Donaubaue, A.-J.; Frey, B.; Becker, I.; Rutzner, S.; Eckstein, M.; Sun, R.; Ma, H.; Schubert, P.; Schweizer, C.; et al. Prospective development and validation of a liquid immune profile-based signature (LIPS) to predict response of patients with recurrent/metastatic cancer to immune checkpoint inhibitors. *J. Immunother. Cancer* **2021**, *9*, e001845. [[CrossRef](#)] [[PubMed](#)]



## Host Immune Features and Nodal Involvement Are Associated with Oncological Outcomes in OSCC

**Missale, F.**  
Bugatti, M.  
Mattavelli, D.  
Lonardi, S.  
Lombardi, D.  
Nicolai, P.  
Piazza, C.  
Battocchio, S.  
Bozzola, A.M.  
Calza, S.  
Vermi, W.

Cells

2021;10(9),2203. <https://doi.org/10.3390/cells10092203>



Supplementary material:



Article

# Metavariables Resuming Host Immune Features and Nodal Involvement Are Associated with Oncological Outcomes in Oral Cavity Squamous Cell Carcinoma

Francesco Missale <sup>1,2,\*</sup> , Mattia Bugatti <sup>3</sup>, Davide Mattavelli <sup>4</sup> , Silvia Lonardi <sup>3</sup>, Davide Lombardi <sup>4</sup> , Piero Nicolai <sup>5</sup>, Cesare Piazza <sup>4</sup>, Simonetta Battocchio <sup>3</sup>, Anna Maria Bozzola <sup>3</sup>, Stefano Calza <sup>6,7</sup> and William Vermi <sup>1,3,8,\*</sup>

- <sup>1</sup> Department of Molecular and Translational Medicine, University of Brescia, 25125 Brescia, Italy
  - <sup>2</sup> Department of Head & Neck Oncology & Surgery Otorhinolaryngology, Antoni Van Leeuwenhoek, Nederlands Kanker Instituut, 1066 Amsterdam, The Netherlands
  - <sup>3</sup> Unit of Pathology, ASST Spedali Civili di Brescia, 25100 Brescia, Italy; mattia.bugatti@unibs.it (M.B.); silvia.lona@gmail.com (S.L.); simonetta.battocchio@gmail.com (S.B.); anna.bozzola@gmail.com (A.M.B.)
  - <sup>4</sup> Unit of Otorhinolaryngology—Head and Neck Surgery, Department of Medical and Surgical Specialties, Radiological Sciences, and Public Health, University of Brescia, 25123 Brescia, Italy; davide.mattavelli@unibs.it (D.M.); davinter@libero.it (D.L.); ceceplaza@libero.it (C.P.)
  - <sup>5</sup> Section of Otorhinolaryngology—Head and Neck Surgery, Department of Neurosciences, University of Padua, Via Giustiniani, 2-35128 Padua, Italy; pieronicolai@icloud.com
  - <sup>6</sup> Unit of Biostatistics, Department of Molecular and Translational Medicine, University of Brescia, 25125 Brescia, Italy; stefano.calza@unibs.it
  - <sup>7</sup> BDbiomed, Big and Open Data Innovation Laboratory, University of Brescia, 25125 Brescia, Italy
  - <sup>8</sup> Department of Pathology and Immunology, Washington University School of Medicine, St. Louis, MO 63130, USA
- \* Correspondence: missale.francesco@gmail.com (F.M.); william.vermi@unibs.it (W.V.)



**Citation:** Missale, F.; Bugatti, M.; Mattavelli, D.; Lonardi, S.; Lombardi, D.; Nicolai, P.; Piazza, C.; Battocchio, S.; Bozzola, A.M.; Calza, S.; et al. Metavariables Resuming Host Immune Features and Nodal Involvement Are Associated with Oncological Outcomes in Oral Cavity Squamous Cell Carcinoma. *Cells* **2021**, *10*, 2203. <https://doi.org/10.3390/cells10092203>

Academic Editors: Iwona Wertel, Michal Zarobkiewicz, Wioleta Kowalska and Agnieszka Bojarska-Junak

Received: 18 July 2021  
Accepted: 19 August 2021  
Published: 26 August 2021

**Publisher's Note:** MDPI stays neutral with regard to jurisdictional claims in published maps and institutional affiliations.



**Copyright:** © 2021 by the authors. Licensee MDPI, Basel, Switzerland. This article is an open access article distributed under the terms and conditions of the Creative Commons Attribution (CC BY) license (<https://creativecommons.org/licenses/by/4.0/>).

**Abstract:** Oral cavity squamous cell carcinoma (OSCC) is a common head and neck cancer characterized by a poor prognosis associated with locoregional or distant failure. Among the predictors of prognosis, a dense infiltration of adaptive immune cells is protective and associated with improved clinical outcomes. However, few tools are available to integrate immune contexture variables into clinical settings. By using digital microscopy analysis of a large retrospective OSCC cohort ( $n = 182$ ), we explored the clinical significance of tumor-infiltrating CD8<sup>+</sup> T-cells. To this end, CD8<sup>+</sup> T-cells counts were combined with well-established clinical variables and peripheral blood immune cell parameters. Through variable clustering, five metavariables (MV) were obtained and included descriptors of nodal (NODAL<sup>MV</sup>) and primary tumor (TUMOR<sup>MV</sup>) involvement, the frequency of myeloid (MYELOID<sup>MV</sup>) or lymphoid (LYMPHOID<sup>MV</sup>) peripheral blood immune cell populations, and the density of tumor-infiltrating CD8<sup>+</sup> T-cells (TI-CD8<sup>MV</sup>). The clinical relevance of the MV was evaluated in the multivariable survival models. The NODAL<sup>MV</sup> was significantly associated with all tested outcomes ( $p < 0.001$ ), the LYMPHOID<sup>MV</sup> showed a significant association with the overall, disease-specific and distant recurrence-free survival ( $p < 0.05$ ) and the MYELOID<sup>MV</sup> with the locoregional control only ( $p < 0.001$ ). Finally, TI-CD8<sup>MV</sup> was associated with distant recurrence-free survival ( $p = 0.029$ ). Notably, the performance in terms of survival prediction of the combined effect of NODAL<sup>MV</sup> and immune metavariables (LYMPHOID<sup>MV</sup>, MYELOID<sup>MV</sup> and TI-CD8<sup>MV</sup>) was superior to the TNM stage for most of the outcomes analyzed. These findings indicate that the analysis of the baseline host immune features are promising tools to complement clinical features, in stratifying the risk of recurrences.

**Keywords:** oral neoplasms; lymphocyte; CD8; biomarker; survival modeling; data reduction; PCA; TIL; peripheral; head and neck

### 1. Introduction

Oral cavity squamous cell carcinoma (OSCC) is one of the most frequent head and neck tumors [1] with a rising incidence in the Western countries [2,3]. The clinical behavior of OSCC is characterized by the occurrence of early lymphatic spreading to regional lymph nodes. Among clinical and pathological features, nodal involvement is per se one of the most relevant prognostic factors [4,5], with an upstage to Stage III–IV and 42–43% 5-year estimated overall survival [5,6]. Furthermore, despite achieving early diagnosis, OSCC is characterized by a poor prognosis when locoregional or distant failure occurs [7], thus including the mandatory management of the neck with elective node dissection [8] or sentinel node biopsy [9] also for low-stage tumors. The main treatment modality for naïve tumors is still represented by radical surgery retaining radiotherapy (RT) or cisplatin-based chemo-radiotherapy (CT-RT) as adjuvant treatments.

The spectrum of available treatment options in the metastatic/recurrent not resectable setting, for which the median survival ranges between 6 and 15 months, is limited to conventional cytotoxic therapy (platinum-based chemotherapy, fluorouracil and taxanes), molecular target agents as anti-EGFR monoclonal antibodies and immunotherapy with PD-L1/PD-1 checkpoint inhibitors. The results obtained with the CheckMate 141, the KEYNOTE-012, and the KEYNOTE-048 trials established the role and use of pembrolizumab or nivolumab (PD-1 checkpoint inhibitors) with or without chemotherapy as first-line therapy in this clinical scenario [10–12]. The evaluation of the PD-L1 expression on tumor cells and tumor infiltrating cells, in the so-called CPS score [13], nowadays represent the key biomarker for the choice of systemic therapy modality [14]. However, its efficacy in patients' selection is still debated. Several prognostic and predictive biomarkers have been recently proposed and tested in a wide retrospective cohort of OSCC patients, including a measure of the immune contexture on tissue slides. In addition to novel histological features [15,16] and morphology-based immune contexture parameters [17], recent meta-analysis showed that, in OSCC, a favorable overall outcome is associated with a high density of tumor infiltrating lymphocytes (TIL) as NK-cells, CD45RO<sup>+</sup> T-cells and CD8<sup>+</sup> T-cells, mainly if measured in the tumoral site [18,19], whereas tumor-associated CD68<sup>+</sup> or CD163<sup>+</sup> macrophages predict a worse prognosis [19]. The routine availability of pre-treatment blood samples raised the interest of studying circulating biomarkers. Among these, the neutrophil, lymphocyte, monocyte or platelet counts and the derived ratios have shown prognostic relevance among solid tumors with myeloid predominance, mainly associated with the worse outcomes [20–22]. One of the main limitations of the available literature is the paucity of analysis considering specific oncologic outcomes, including the locoregional or distant failures separately. For biomarkers analysis, the identification of cut-offs is still a matter of debate [23], likely overcome by avoiding dichotomization and keeping the whole information of a continuous variable [24]. Moreover, few attempts have been made to combine peripheral and tumoral immune-features in a unique classifier [25].

Within a homogeneous cohort of surgically treated OSCCs, we combined peripheral and tissue immune features with demographic, clinical and pathological characteristics to generate meta-variables (MVs). The MV describing the nodal involvement was confirmed to be detrimental for any survival end-points, whereas the peripheral blood myeloid-related MV and the CD8<sup>+</sup> T-cells infiltration MV were significant predictors of locoregional or distant failure, respectively.

### 2. Materials and Methods

#### 2.1. Clinical Cohort

A retrospective observational study was carried out, enrolling one hundred eighty-two histologically confirmed cases of oral cavity squamous cell carcinoma (OSCC) who underwent radical surgical resection and neck dissection between 2000 and 2014 (Otorhinolaryngology Department, ASST Spedali Civili di Brescia, Brescia, Italy). This study was approved by the local IRB to WV (H&N Cancer, NP-2066). Patients with at least 12 months of follow-up or earlier death or recurrence were included. Salvage surgery, metastatic

disease, immunological disorders or prior systemic treatment for malignancy represented the exclusion criteria. Patients were regularly followed up with clinical examinations and neck MRI or CT every 3–6 months. Preliminary clinical and oncological findings are reported in our previous works [26,27]. Last follow-up was updated until September 2020.

### 2.2. Blood Samples

Preoperative blood cell counts were retrieved. The absolute counts of full white blood cells (WBC), neutrophils, lymphocytes, monocytes and platelets were considered as the biomarkers of interest. Further derived parameters of clinical interest according to the recent literature, the neutrophil-to-lymphocyte ratio (NLR) [22,28], i.e., the ratio between neutrophils and lymphocytes counts and the platelet-to-lymphocyte ratio (PLR) [29], i.e., the ratio between platelets and lymphocytes counts were obtained.

### 2.3. Tissues

Formalin-fixed paraffin embedded (FFPE) tissue blocks of a representative section of the primary tumor (PT) were retrieved from the tissue bank of the Department of Pathology (ASST Spedali Civili di Brescia, Brescia, Italy). Four-micron thick FFPE sections were used for immunohistochemical staining and as a primary antibody, the anti-CD8 (clone C8/144B, dilution 1:30, Dako) was used. The reaction was revealed by EnVision (Dako) followed by DAB. Sections were then counterstained with hematoxylin.

### 2.4. Digital Pathology Analysis

Stained slides were acquired using a ScanScope CS (Leica Microsystems, Wetzlar, Germany) digital scanner. Images were viewed and organized using ImageScope software (version 12.03.5048, Leica biosystems, Wetzlar, Germany). Each scanned image was manually annotated and the IHC nuclear image analysis algorithm was chosen for the analysis. Data are expressed as the number of CD8<sup>+</sup> cells per mm<sup>2</sup>. Primary tumor (PT) was analyzed measuring the immune cell density either in the center of the tumor (CT) and in the invasive margin (IM) (Figure 1). The invasive margin was defined as the tissue area of 1 mm wide from the front of invasion of the tumor [30].

### 2.5. Statistical Analysis

The main goal was to summarize all the available clinical and biomarkers data in a minimal number of synthetic components, each representing a set of highly correlated variables, therefore identifying a few homogeneous latent variables. Applying a data reduction method allows the multivariable survival modelling of cohorts with a limited sample size and event rates [31].

Firstly, clinical, pathological and biomarkers variables were clustered using hierarchical clustering with a bottom-up agglomerative algorithm. This algorithm aimed to maximize the clusters' homogeneity, defined as the proximity of each variable in the cluster to a synthetic centroid, using as proximity metrics either the Pearson correlation coefficient for quantitative variables or the correlation ratio for qualitative ones [32]. The optimal number of partitions was determined evaluating clusters' stability measured by the Rand index between the observed hierarchy and a random sample of dendrograms generated by bootstrap ( $B = 200$ ). Finally, a synthetic variable representing each cluster was computed as the first principal component derived by a mixed principal component analysis (PCAmix) performed on the variable within the cluster [32,33].

Quantitative variables were summarized using the mean, standard deviation, median and range, while qualitative variables were described as counts and proportions. For group comparisons in qualitative variables, Fisher's exact test was applied, and for quantitative ones, the Wilcoxon test or Kruskal-Wallis test was applied. Missing data, representing 2.6% of the measured data, were imputed with multivariate imputation by chained equations (MICEs) [34].



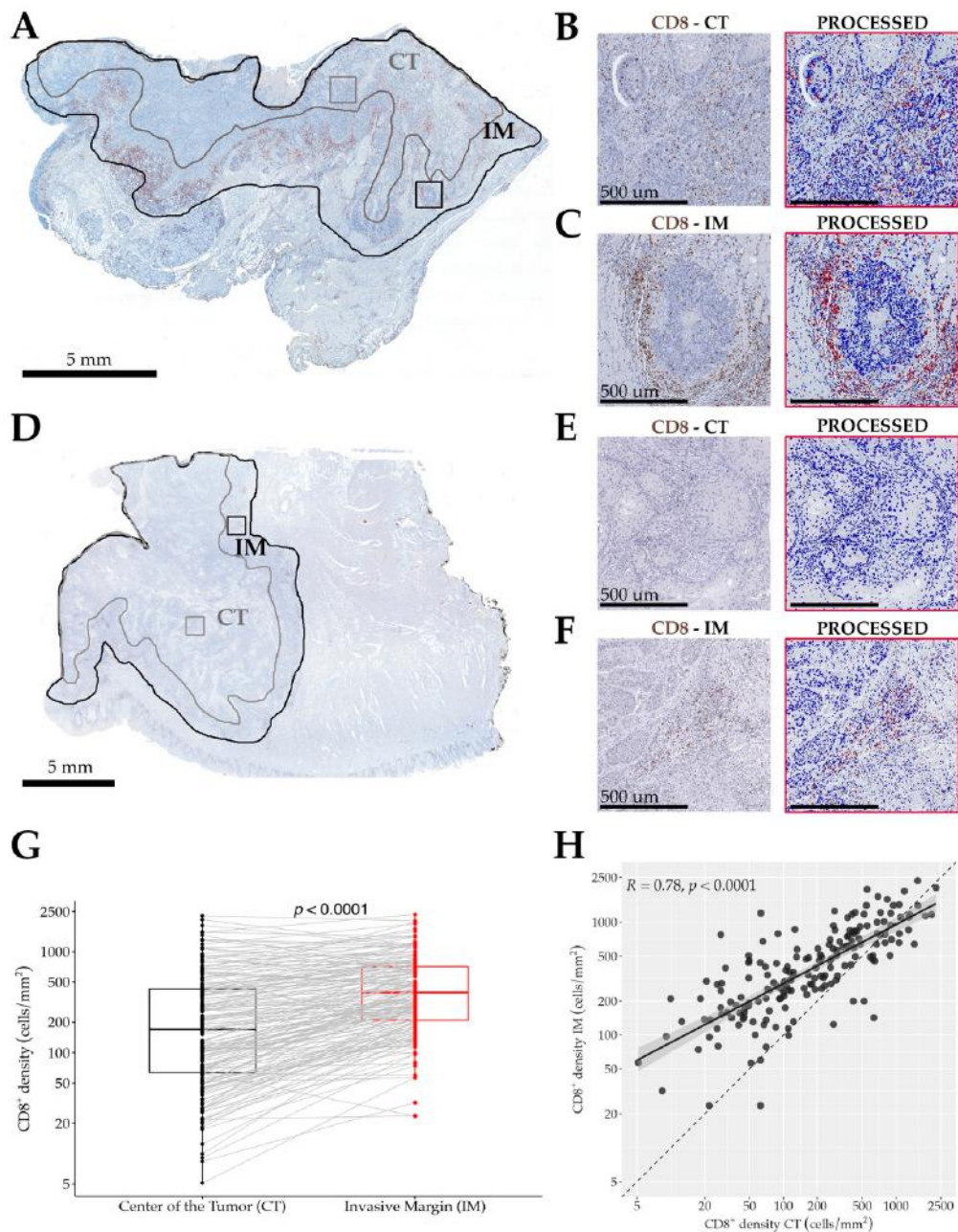


**Figure 1.** Panel showing whole tumor sections stained for CD8 in two representative cases (A–C and D–F). In (A) and (D), the selection of areas of interest is shown: the center of the tumor (CT) and the invasive margin (IM)—whilst the black line defines the whole tumoral bed. Representative high magnification immunostained (left) and processed (right) sections showing the immune cells recognition and counting algorithm (B,C,E,F). In (B) and (C), the example fields of 1 mm<sup>2</sup> of the case presented in (A) taken from the CT (554 CD8<sup>+</sup> T-cells) or IM (1159 CD8<sup>+</sup> T-cells), respectively. In (E) and (F), the example fields of 1 mm<sup>2</sup> of the case presented in (D) are taken from the CT (26 CD8<sup>+</sup> T-cells) or IM (294 CD8<sup>+</sup> T-cells), respectively. The box plots (G) show a higher density of CD8<sup>+</sup> T-cells in the IM compared to the CT (grey lines connecting the measures of CD8<sup>+</sup> T-cell density in each single patient) and the scatter plot (H) illustrates a significant direct correlation of CD8<sup>+</sup> T-cells’ density between those regions (H); p values estimated by the Wilcoxon matched-pairs signed rank test (G) or Spearman rank correlation test (H). Scale bars: (A,D), 5 mm; (B,C,E,F), 500  $\mu$ m.

The survival endpoints considered are the overall (OS), the disease-specific (DSS), the locoregional recurrence-free survival (LRFS), and the distant recurrence-free (DRFS) survival. The OS was defined as the time between the date of surgery and the date of death for any causes; the DSS as the time between the date of surgery and the date of cancer-related death; the LRFS as the time between the date of surgery and the date of local or nodal recurrence; and the DRFS as the time between the date of surgery and the date of distant recurrence. For each outcome, patients now having the event were censored at the last follow-up.

Survival analysis was performed fitting multivariable Cox proportional-hazards models, estimating  $p$  values by the Wald statistic. The relationship between continuous predictor and the outcomes was modelled with restricted cubic splines with 4 knots [35]; not linear terms were retained in the presented models for variables mostly explaining the  $X^2$  statistic [36]. The likelihood ratio test was applied for comparing nested models. Decision curve analysis (DCA) [37–39] was used to evaluate the net benefit of each proposed model compared to the one fitted considering the UICC overall pathological stage alone. Survival estimates were reported as hazard ratios (HR) with 95% confidence interval (95% CI) and estimating the 2- and 5-year survival probability with 95% CI for the variables of main clinical interest. Proportional hazards assumption was tested examining Schoenfeld residuals [40]. Data reduction analysis was performed with the ‘ClustOfVar’ package [32]. Contour plots were drawn with the ‘visreg’ package [41] and DCA was performed with the ‘dcurves’ one. In all analyses, two-tail tests with a significance level of 5% were applied; adjusted  $p$  values for multiple tests were corrected with Bonferroni’s method. R version 4.1.0 (R Foundation for Statistical Computing, Vienna, Austria) was used for statistical analysis.

### 3. Results

#### 3.1. Clinical Findings of the OSCC Cohort

One hundred and eighty-two patients were enrolled for data analysis; the cohort was composed of 115 males (63.2%) with a mean  $\pm$  SD age of  $63.6 \pm 13.1$  years. Among the clinical, pathological and biomarker variables of interest, missing data accounted for 2.6% of the dataset, with no variable with “missingness”  $\geq 10\%$  (Supplementary Figure S1 and Supplementary Table S1). Considering already imputed data (Table 1), the cohort was well balanced among all pT categories, and metastatic lymph-node involvement was recorded in 85 cases (46.7%), and in 42 cases (23.1%), evidence of pathologic extranodal extension was observed. The mean  $\pm$  SD number of involved positive nodes was  $1.54 \pm 2.84$ , ranging from 0 to 18. Adverse pathological features as perineural invasion (PNI) or lymphovascular invasion (LVI) were present in 90 (49.5%) and 52 (28.6%) cases, respectively. The rate of positive margin was 17.6%. The treatments included surgery alone in 78 patients (42.9%), surgery and adjuvant radiotherapy (RT) in 61 (33.5%), and surgery followed by adjuvant chemo-radiotherapy (CRT) in 43 (23.6%).

The mean follow-up time was 71.5 months (IQR 24.3–105.8, range 1–214 months). During the follow-up course, 71 patients (39.0%) experienced at least one recurrence event, 42 (23.1%) experienced locoregional recurrence alone, 14 (7.7%) distant recurrence alone and 15 (8.2%) both locoregional and distant recurrences. At the last follow-up available, 78 patients (42.9%) were dead and for 53 of these (67.9%), the cause of death was related to disease progression.



**Table 1.** Summary statistics of the cohort.

Variable	Overall (N = 182)	Variable	Overall (N = 182)
<b>Age</b>		<b>Margins</b>	
Mean (SD)	63.6 (13.1)	Positive	32 (17.6%)
Median (Min, Max)	64.0 (26.0, 93.0)	Close	54 (29.7%)
<b>Sex</b>		Negative	96 (52.7%)
Male	115 (63.2%)	<b>Treatment</b>	
Female	67 (36.8%)	Surgery	78 (42.9%)
<b>pT category (8th Ed.)</b>		Surgery+RT	61 (33.5%)
pT1	23 (12.6%)	Surgery+CRT	43 (23.6%)
pT2	41 (22.5%)	<b>WBC (10<sup>9</sup>/L)</b>	
pT3	85 (46.7%)	Mean (SD)	7.41 (1.94)
pT4	33 (18.1%)	Median (Min, Max)	7.39 (2.77, 13.7)
<b>pN category (8th Ed.)</b>		<b>Lymphocytes (10<sup>9</sup>/L)</b>	
pN0	96 (52.7%)	Mean (SD)	1.82 (0.535)
pN1	24 (13.2%)	Median (Min, Max)	1.78 (0.690, 3.69)
pN2a	6 (3.3%)	<b>Neutrophils (10<sup>9</sup>/L)</b>	
pN2b	16 (8.8%)	Mean (SD)	4.79 (1.64)
pN2c	2 (1.1%)	Median (Min, Max)	4.76 (1.04, 10.1)
pN3b	38 (20.9%)	<b>Monocytes (10<sup>9</sup>/L)</b>	
<b>Npos</b>		Mean (SD)	0.585 (0.231)
pN0	97 (53.3%)	Median (Min, Max)	0.550 (0.160, 1.53)
pN+	85 (46.7%)	<b>PLT (10<sup>9</sup>/L)</b>	
<b>ENE</b>		Mean (SD)	228 (68.6)
No	140 (76.9%)	Median (Min, Max)	220 (51.0, 431)
Yes	42 (23.1%)	<b>NLR</b>	
<b>Nodal ratio</b>		Mean (SD)	2.83 (1.31)
Mean (SD)	0.0326 (0.0558)	Median (Min, Max)	2.53 (0.799, 7.55)
Median (Min, Max)	0 (0, 0.320)	<b>PLR</b>	
<b>Total Number</b>		Mean (SD)	134 (52.7)
<b>Positive Nodes</b>		Median (Min, Max)	129 (31.1, 315)
Mean (SD)	1.54 (2.84)	<b>CD8 density Total (cells/mm<sup>2</sup>)</b>	
Median (Min, Max)	0 (0, 18.0)	Mean (SD)	418 (403)
<b>LVI</b>		Median (Min, Max)	279 (16, 2180)
No	130 (71.4%)	<b>CD8 density CT (cells/mm<sup>2</sup>)</b>	
Yes	52 (28.6%)	Mean (SD)	333 (406)
<b>PNI</b>		Median (Min, Max)	170 (5, 2270)
No	92 (50.5%)	<b>CD8 density IM (cells/mm<sup>2</sup>)</b>	
Yes	90 (49.5%)	Mean (SD)	520 (429)
<b>Differentiation</b>		Median (Min, Max)	394 (24, 2340)
G1	18 (9.9%)		
G2	87 (47.8%)		
G3	77 (42.3%)		
<b>Bone invasion</b>			
No	148 (81.3%)		
Cortical	16 (8.8%)		
Medullary	18 (9.9%)		

### 3.2. Clinical Relevance of CD8 Immune Contexture and Peripheral Blood Biomarkers in OSCC

By digital image analysis, the CD8<sup>+</sup> T-cell infiltration of tumor tissue was evaluated by measuring a mean ± SD area of 108.7 ± 73 mm<sup>2</sup> (range 4.2–319.9 mm<sup>2</sup>). Analyzing both the center of the tumor (CT) and the invasive margin (IM), the latter was significantly enriched ( $p < 0.0001$ ) of CD8<sup>+</sup> T-cells (median 394 cells/mm<sup>2</sup>, IQR 210–712) compared to the CT (median 170 cells/mm<sup>2</sup>, IQR 64–430), as shown in Figure 1G; furthermore, a strong direct correlation between the density of CD8 T-cells in CT and IM was evident ( $R = 0.78$  (CI<sub>95%</sub> 0.71–0.83,  $p < 0.0001$ , Figure 1H)); representative fields of the analysis are shown in

Figure 1. Whilst testing for associations and correlations, a lower  $^{IM}CD8^+$  T-cells density was observed in patients with evidence of LVI ( $p = 0.032$ ); no other meaningful association with further clinical or pathological features was observed (Supplementary Tables S1–S9). Finally, no correlation was observed between intratumoral  $CD8^+$  T-cells density and any of the available peripheral blood biomarkers (Supplementary Table S1).

Analyzing the available pre-operative peripheral blood biomarkers, a significant association was observed, as expected, between the sex and all the absolute biomarkers and lymphocyte counts (Supplementary Table S2). Furthermore, no relevant associations or correlations were observed between such measures and the other clinical and pathological features (Supplementary Tables S1–S9).

### 3.3. Identification of the Meta-Variables in OSCC

With the aim of summarizing all available clinical and biomarkers variables in a minimal number of synthetic components, a data reduction algorithm was applied [32,33]. The available 24 variables were resumed into metavariables (MV). The aggregation of highly correlated variable was obtained by ascending hierarchical clustering, (Figure 2A). By inspecting the scree plot (Figure 2B), five clusters were identified, from here on referred to as metavariables (MVs). Specifically, the identified MV are the  $IT-CD8^{MV}$ ,  $MYELOID^{MV}$ ,  $LYMPHOID^{MV}$ ,  $TUMORAL^{MV}$  and  $NODAL^{MV}$ , whose composition is highlighted by dashed rectangles in Figure 2A. The relationship between the MV scores and the variables is shown in Figure 2C and summarized in Supplementary Figure S2–S6; full details of the squared loadings (as a measure of the weight of each variable within the MV) are reported in Supplementary Table S10. MVs did not show significant correlations, except for a slight direct correlation ( $R = 0.27$ ,  $p = 0.002$ ) between the  $TUMORAL^{MV}$  and  $NODAL^{MV}$  (Figure 2D), confirming the appropriate segregation of the associated variables.

### 3.4. $NODAL^{MV}$ Is Highly Related to OS and DSS

The  $NODAL^{MV}$ , whose lower values (Supplementary Figure S2) are correlated with a high nodal category, high nodal burden (both lymph node ratio and number of positive nodes), presence of pathologic risk factors as ENE, PNI, LVI or high grade and positive margins was highly associated with all survival endpoints.  $NODAL^{MV}$  and the  $LYMPHOID^{MV}$  were significantly associated ( $p < 0.0001$  and  $p = 0.0165$ , respectively) with OS (Figure 3A). Specifically,  $NODAL^{MV}$  showed a linear relationship (Figure 3B), whereas  $LYMPHOID^{MV}$  displayed a non-linear effect (Figure 3C) with the best outcome at its mid-values (Supplementary Table S11). The contour plot in Figure 3D represents isoprognostic areas according to the combined value of  $NODAL^{MV}$  and  $LYMPHOID^{MV}$ . Applying the likelihood ratio test, we found that the removal of the  $LYMPHOID^{MV}$  from the model significantly reduced its accuracy ( $p = 0.028$ ), further supporting the relevance of this variable in the OS outcome. By decision curve analysis (DCA), the model including MVs was comparable to the UICC-TNM pathological Stage in terms of 5 years OS prediction (Figure 3E).

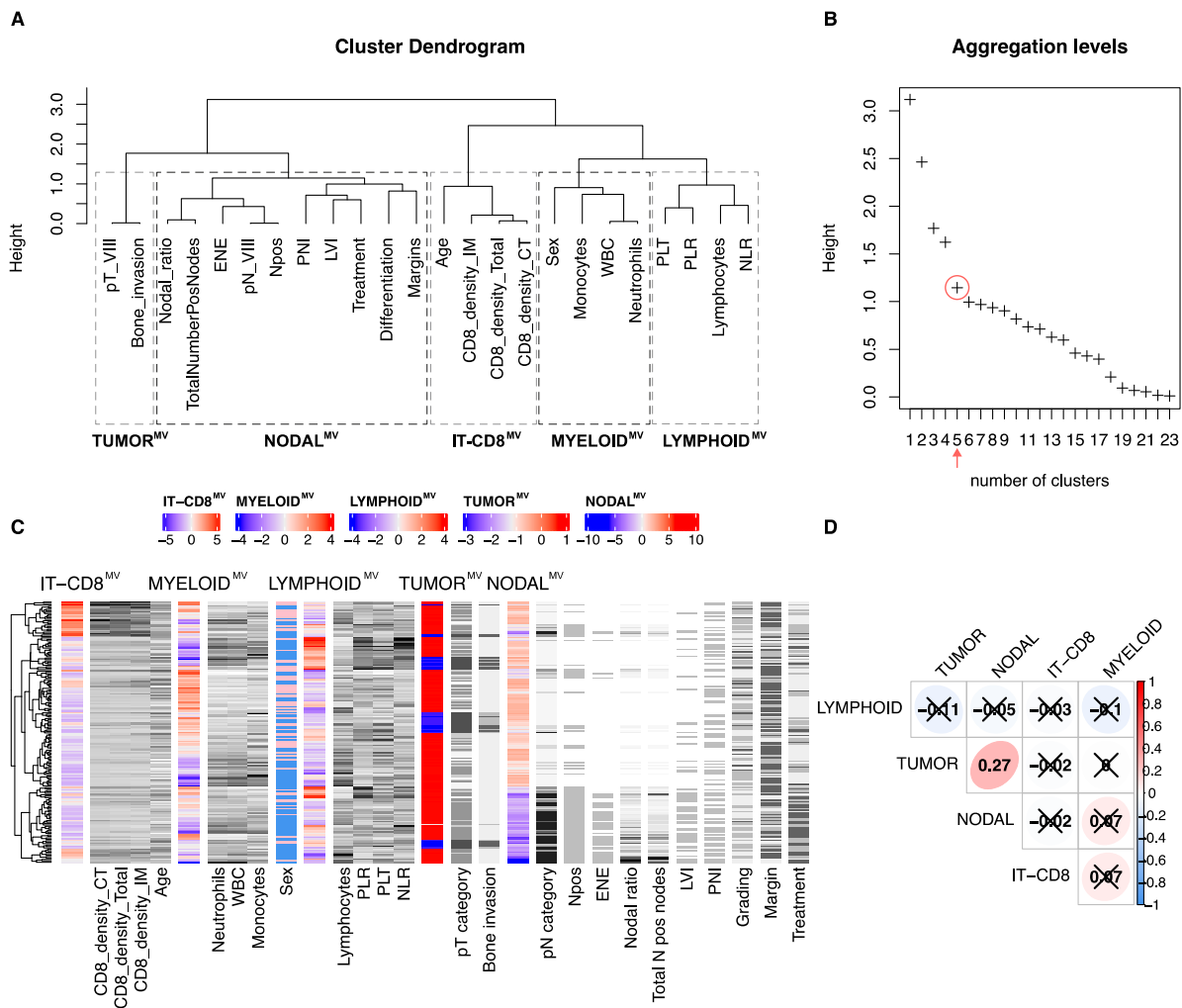


**Figure 2.** Dendrogram of the hierarchical ascending clustering of the 24 demographic, clinical, pathological and peripheral and tissue biomarkers according to their correlation ratio (A); aggregation level plot related to the number of clusters of variables, red circle showing the chosen 5 clusters as optimum choice (B); heatmap showing the relationship between each meta-variable (MV) and the original variables from which is derived (columns on the right of each meta-variable) (C); and correlogram showing the Spearman correlation between each meta-variable, R coefficient is shown, adjusted not significant comparisons are covered with a cross (D). Dashed rectangles in A highlight which original variable is included in each MV.

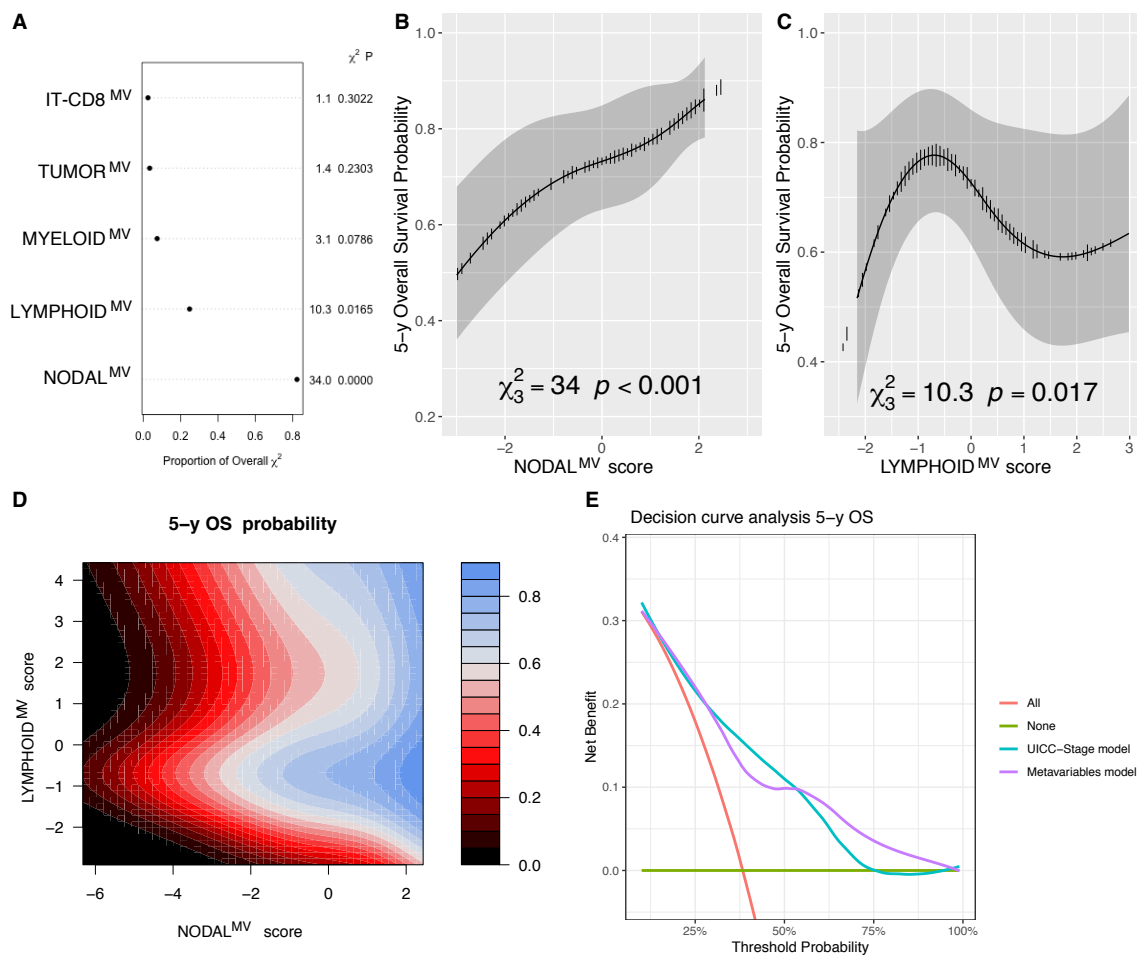


**Figure 3.** Chunk test results on the OS multivariable model reporting the proportion of the overall  $\chi^2$  of the model explained by each variable, the partial  $\chi^2$  and P value of the Wald test, testing the association between each variable and the outcome (A); adjusted marginal effect plot of the NODAL<sup>MV</sup> score for the 5-year OS estimate with the CI<sub>95%</sub> gray band (B); adjusted marginal effect plot of the LYMPHOID<sup>MV</sup> score for the 5-year OS estimate with CI<sub>95%</sub> gray band (C); contour plot showing isoprognostic OS bands according to the combined effect of the NODAL<sup>MV</sup> and LYMPHOID<sup>MV</sup> scores for the 5-year OS estimate, the color scale represents the 5 y OS probability (D); and decision curve analysis (DCA) analysis showing comparable results of the model including metavariabes and to the one fitted with UICC overall stage alone in predicting the 5-year OS (E).

Analyzing the DSS, the NODAL<sup>MV</sup> and MYELOID<sup>MV</sup> were significantly associated with the outcome ( $p < 0.0001$  and  $p = 0.0123$ , respectively; Figure 4A–C, Supplementary Table S11). Specifically, for MYELOID<sup>MV</sup>, higher scores (associated with leukopenia, neutropenia, monocytopenia and female sex) were associated with a poorer DSS, as shown in Figure 4C. The combined partial effect of NODAL<sup>MV</sup> and MYELOID<sup>MV</sup> on the 5-year DSS estimate is shown with the contour plot in Figure 4D that illustrates the detrimental contribution of different MYELOID<sup>MV</sup> scores along the different values of NODAL<sup>MV</sup> scores. By using the likelihood ratio test, the removal of the MYELOID<sup>MV</sup> from the model significantly reduced its accuracy ( $p = 0.011$ ), further supporting the relevance of such a variable for the DSS outcome. By DCA, the model including MVs showed a benefit in terms of the prediction of the 5-year DSS compared to the UICC-TNM pathological stage, (Figure 4E).

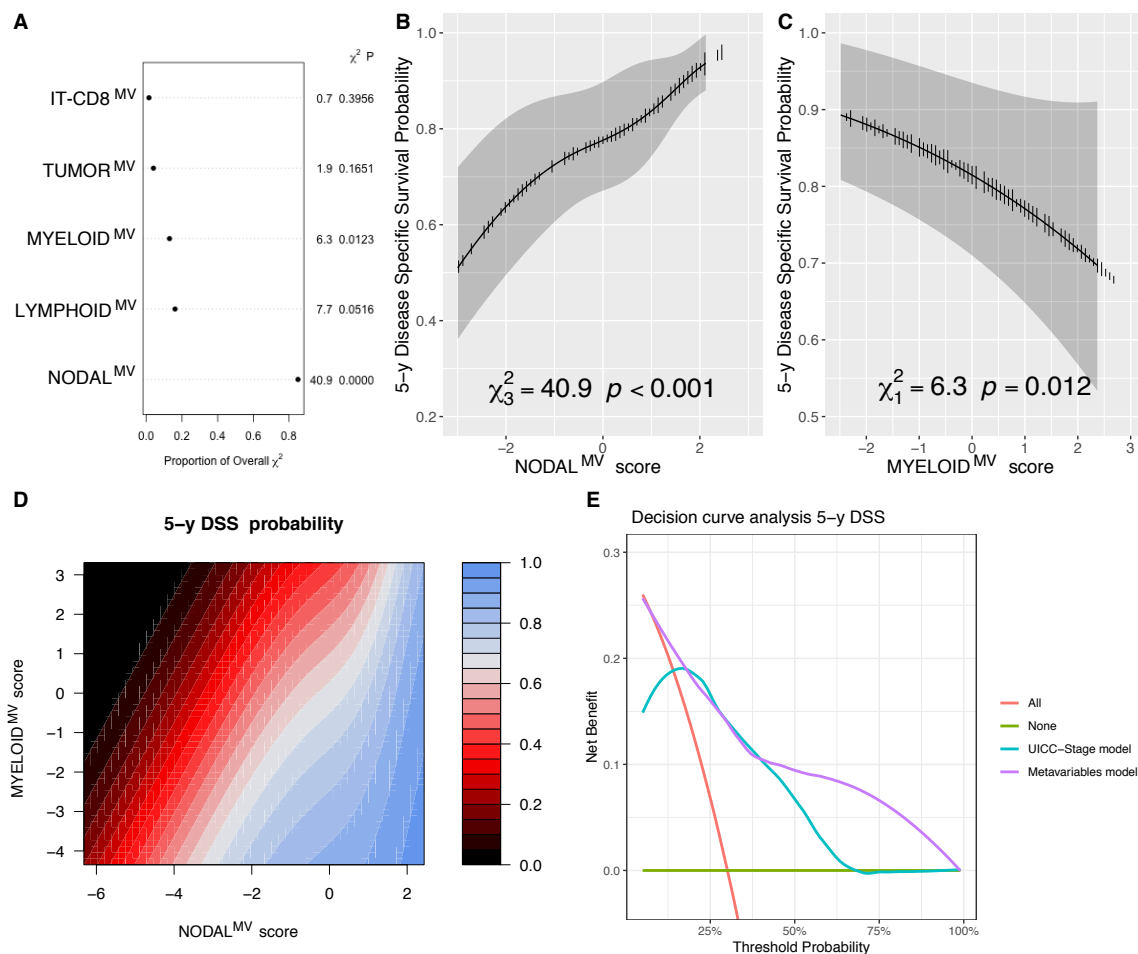


**Figure 4.** Chunk test results on the DSS multivariable model reporting the proportion of the overall  $\chi^2$  of the model explained by each variable, the partial  $\chi^2$  and  $p$  value of the Wald test, testing the association between each variable and the outcome (A); adjusted marginal effect plots for the 5-year DSS with  $CI_{95\%}$  (gray bands) of the NODAL<sup>MV</sup> (B) and MYELOID<sup>MV</sup> (C) scores; contour plot showing isoprognostic DSS bands according to the combined effect of the NODAL<sup>MV</sup> and MYELOID<sup>MV</sup> scores for the 5-year DSS estimate, the color scale represents the 5 y DSS probability (D); and decision curve analysis (DCA) showing the advantages of the model including MV compared to the one fitted with UICC overall stage alone in predicting the 5-year DSS (E).

### 3.5. Immune MV as Predictor of Loco-Regional and Distant Failure

During the follow-up course, 57 patients (31.3%) developed locoregional recurrence with a 5-year LRFS estimate of 78% ( $CI_{95\%}$  72–84%) and 29 distant metastases (15.9%), with an estimate of DRFS at 5 years of 85% ( $CI_{95\%}$  79–90%). Modelling the LRFS outcome, we could confirm the detrimental prognostic significance of the NODAL<sup>MV</sup> ( $p < 0.001$ ), MYELOID<sup>MV</sup> ( $p = 0.009$ ) and TUMOR<sup>MV</sup> ( $p = 0.032$ ) (Figure 5A–D, Supplementary Table S11). The contour plot shown in Figure 5E illustrates the combined effect of NODAL<sup>MV</sup> and MYELOID<sup>MV</sup> scores for the 5-year LRFS prediction with iso-prognostic levels (color gradient) strictly dependent on both variables. By the likelihood ratio test, the removal of the MYELOID<sup>MV</sup> from the model significantly reduced its accuracy ( $p = 0.004$ ), further supporting the relevance of this variable for the LRFS outcome. By DCA and compared to the UICC-TNM pathological stage, the model including MVs showed a benefit in terms of predicting the 5-year LRFS, specifically in the lowest and highest ranges of the estimated risks (Figure 5F).

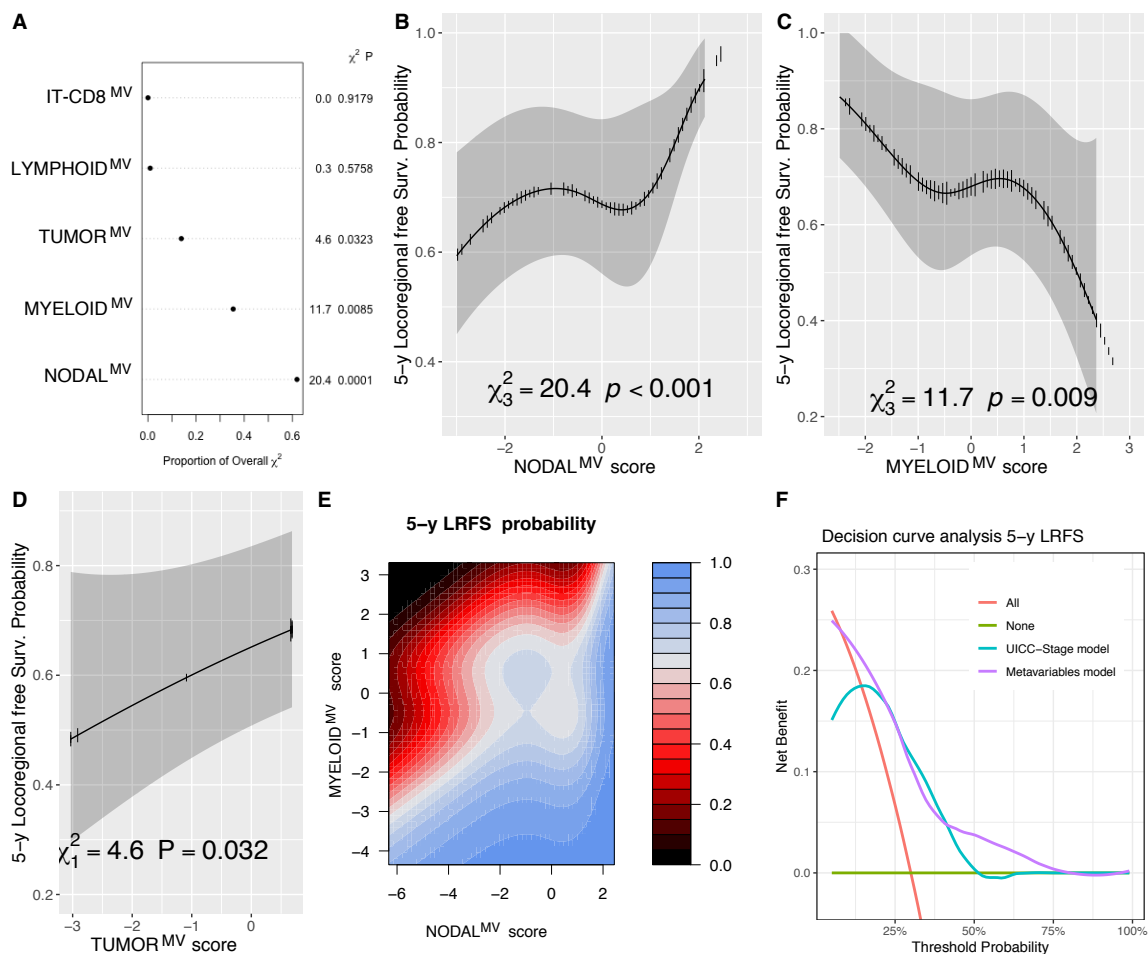


**Figure 5.** Chunk test results on the LRFS multivariable model reporting the proportion of the overall  $\chi^2$  of the model explained by each variable, the partial  $\chi^2$  and P value of the Wald test, testing the association between each variable and the outcome (A); adjusted marginal effect plots for the 5-year LRFS with CI<sub>95%</sub> (gray bands) of the NODAL<sup>MV</sup> (B); MYELOID<sup>MV</sup> (C), and TUMOR<sup>MV</sup> (D) scores; contour plot showing isoprognostic LRFS bands according to the combined effect of the NODAL<sup>MV</sup> and MYELOID<sup>MV</sup> scores for the 5-year LRFS estimate—the color scale representing the 5 y LRFS probability (E); and decision curve analysis (DCA) showing a better performance of the model including MVs compared to the one fitted with the UICC overall stage alone in predicting the 5-year LRFS in the lowest and highest ranges of the estimated risks (F).

Considering the DRFS outcome and its modeling with a multivariable model (Figure 6A, Supplementary Table S11), NODAL<sup>MV</sup> confirmed its high weight for its association with such an outcome ( $p < 0.001$ , Figure 6B), furthermore LYMPHOID<sup>MV</sup> ( $p = 0.008$ , Figure 6C) and IT-CD8<sup>MV</sup> ( $p = 0.022$ , Figure 6D) were associated with DRFS following non-linear effects ( $p = 0.0037$ ,  $p = 0.0537$ , respectively). The lowest IT-CD8<sup>MV</sup> score, corresponding to low CD8 infiltration in all the tested areas of interest, were strictly related to a poor DRFS, also independently from the NODAL<sup>MV</sup> score, as shown in the contour plot in Figure 6E. By using the Likelihood ratio test, the removal of IT-CD8<sup>MV</sup> and LYMPHOID<sup>MV</sup> from the model significantly reduced its accuracy ( $p = 0.036$  and  $p = 0.013$ , respectively), further supporting the relevance of such variables for the DRFS outcome. By DCA, the model including MVs showed a benefit in terms of the prediction of the 5-year DSS, compared to the UICC-TNM pathological stage, shown in (Figure 6F).

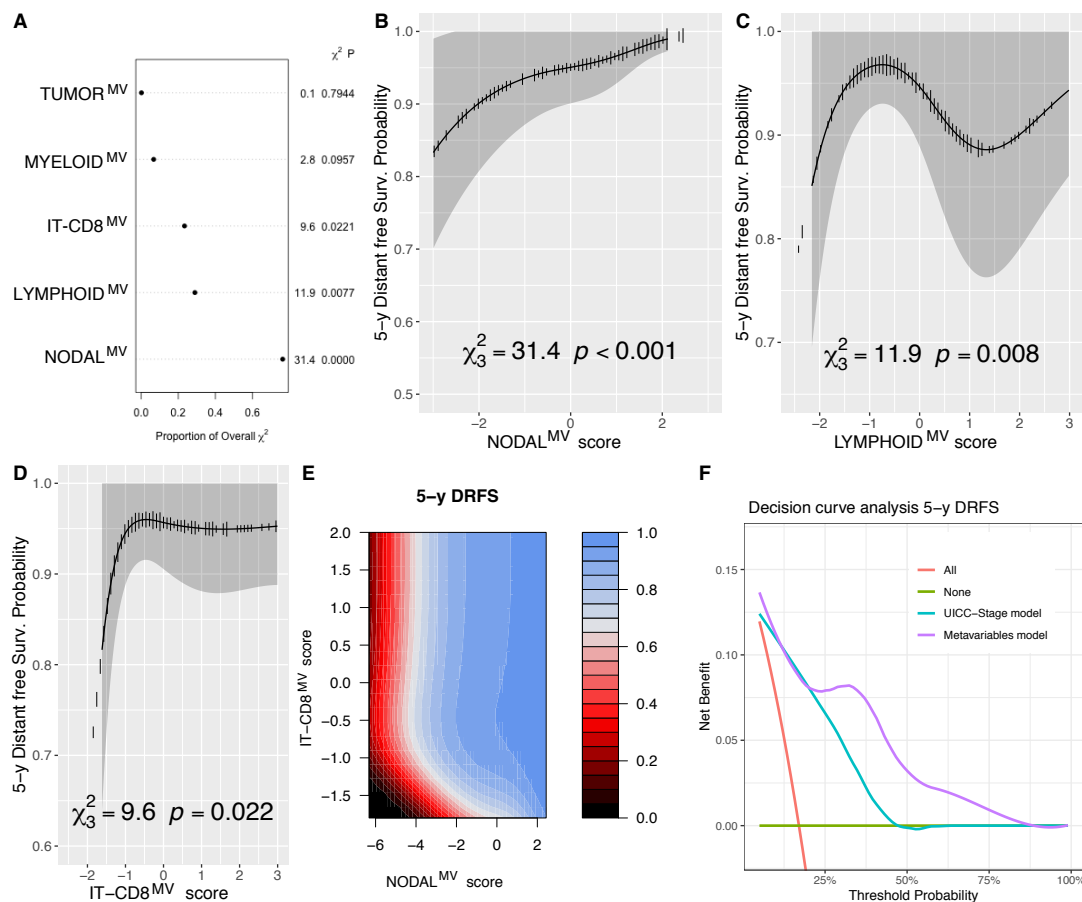


**Figure 6.** Chunk test results on the DRFS multivariable model reporting the proportion of the overall  $\chi^2$  of the model explained by each variable, the partial  $\chi^2$  and P value of the Wald test, testing the association between each variable and the outcome (A); adjusted marginal effect plots for the 5-year DRFS with CI<sub>95%</sub> (gray bands) of the NODAL<sup>MV</sup> (B); LYMPHOID<sup>MV</sup> (C) and IT-CD8<sup>MV</sup> (D) scores; contour plot showing isoprognostic DRFS bands according to the combined effect of the NODAL<sup>MV</sup> and IT-CD8<sup>MV</sup> scores for the 5-year DRFS estimate—the color scale represents the 5 y DRFS probability (E); and decision curve analysis (DCA) showing the better performance of the model including MVs compared to the one fitted with the UICC overall stage alone in predicting the 5-year DRFS (F).

#### 4. Discussion

In this study, we tested the clinical significance of peripheral blood and tumor-associated immune features in patients submitted to surgery-based treatments for OSCC.

Through a data reduction analysis, five metavariables (MV) were defined; the survival analysis showed their association with different types of oncological outcomes. Specifically, the NODAL<sup>MV</sup> was independently associated with all oncological outcomes tested, thus confirming the detrimental prognostic value of nodal involvement in OSCC. Information derived from peripheral blood biomarkers, and resumed in the MYELOID<sup>MV</sup> and LYMPHOID<sup>MV</sup>, significantly improved the accuracy of the models of DSS/LRFS and of OS/DRFS, respectively. Thus, these MV represent candidates for the development of predictors models. Interestingly, the IT-CD8<sup>MV</sup> was significantly associated with the DRFS, suggesting that the group of OSCC desert of CD8<sup>+</sup> T-cells should be deeply investigated to identify an innovative therapeutic strategy limiting distant spread. Furthermore, the proposed models including MVs outperform the UICC TNM stage in predicting most of the outcome analyzed.



It is well-known that several clinical variables (e.g., features describing the nodal involvement such as N category, number of positive nodes, LNR, presence of ENE, or high-risk features as PNI, LVI or grading and T category and bone involvement) are highly correlated and it is often difficult to select which variable has to be included in a prognostic regression model.

Building MV might represent an alternative strategy to keep all the available information for the survival modelling analysis. Applying the PCAmix as data reduction method, the explainability of each MV is well achieved, as each original variable can contribute just for one of the five identified MV. Finally, the clinical significance of higher and lower values of each score is easily understandable by inspecting the correlation/associations plots, as shown in Supplementary Figures S2–S6.

Our results confirm the prognostic relevance of nodal involvement, summarized in  $NODAL^{MV}$ , for all the outcomes analyzed. The highest squared loading for the  $NODAL^{MV}$  were observed for N category, the nodal ratio and number of positive nodes (Supplementary Table S10) underlining the relevant weight of these variables for the definition of the score and, therefore, their prognostic value. Such an observation is in keeping with the robust literature of recent decades [4,42], including the last update of the TNM classification system [43]. Features such as the nodal ratio [5] and the total number of positive nodes [44] are of main interest and were also tested for the proposal of a new staging systems in the OCSCC setting [45], which are easily available from any pathologic report.

One of the main findings obtained from this analysis suggests that tumor  $CD8^+$  T-cells depletion, derived by measuring  $CD8^+$  T-cell density in different tumoral compartments, and summarized within the  $IT-CD8^{MV}$ , is associated with a higher risk of distant failure, independently from the  $NODAL^{MV}$  score. Interestingly, the correlation with DRFS apparently displays a threshold effect, with a critical  $IT-CD8^{MV}$  score below which the risk of distant metastasis steadily increases (Figure 6D). Although limited to few studies, an association between high tumor  $CD8^+$  T-cell density and a better distant metastasis free-survival was already observed in solid tumors from different primary sites including breast [46], colon [47] or soft tissues [48]. Among head and neck malignancies, evidence derived from the analysis of nasopharyngeal carcinoma [49], hypopharyngeal carcinoma [50,51] or from carcinomas of mixed primary sites [52] further support this finding. For OSCC, the association of  $CD8^+$  T-cell infiltration and distant failure still needs to be better defined [53]; however, indirect but still limited findings [52], support their protective role.

The occurrence of metastatic disease is associated with systemic immune escape [54]. Cancer-cell intrinsic features as well as host response might represent relevant players in the T-cell exclusion (TCE) mechanism [55–57]. No data are available on the molecular basis sustaining TCE in OSCC. However, TCE can be bypassed by various immunotherapy strategies [58–63]. Currently, immune checkpoint inhibitors are investigated in the neoadjuvant setting in OCSCC, and this could allegedly enhance  $CD8^+$  T-cell activity and reverse tumor host interplay, thus reducing also the risk of tumor escape at distant sites [64–68].

Notably, as recently proposed, photodynamic therapy (PDT) combined with CTLA-4 blockade can enhance the cytotoxic  $CD8^+$  T-cell response to achieve durable tumor eradication and inducing an immunological memory [69]. This is worthwhile, since PDT is one of the treatment options for early or recurrent oral cavity squamous cell carcinoma [70,71] and its possible combination with immune checkpoint blockade drugs could pave the way for new trials design.

The main limits of our study are the retrospective design and the mono-institutional setting. Prospective and multi-institutional validation represents mandatory requirements to confirm our observations.

### 5. Conclusions

The results obtained from this study using data reduction methods confirm the key role of nodal involvement and intratumor  $CD8^+$  T-cell density on relevant survival endpoints.



Further investigations for the identification of TCE mechanisms will help to identify appropriate treatment strategies for the subgroup of CD8<sup>+</sup> T-cell in poor OSCC.

**Supplementary Materials:** The following are available online at <https://www.mdpi.com/article/10.3390/cells10092203/s1>, Supplementary Figure S1: Heatmap showing the missing data in the whole cohort (A); intersection plot of missing data (B). Supplementary Figure S2: Scatter plots showing the relationship between TI-CD8<sup>MV</sup> and the variables from which it is defined. P values are estimated by Spearman correlation test. Supplementary Figure S3: Box plots and scatter plots showing the relationship between the NODAL<sup>MV</sup> and the variables from which it is defined. P values are estimated by Kruskal–Wallis test, Wilcoxon sign-rank test or Spearman correlation test. Supplementary Figure S4: Scatter plots and box plots showing the relationship between the MYELOID<sup>MV</sup> and the variables from which it is defined. P values are estimated by the Spearman correlation test or Wilcoxon sign-rank test. Supplementary Figure S5: Scatter plots showing the relationship between the LYMPHOID<sup>MV</sup> and the variables from which it is defined. P values are estimated by the Spearman correlation test. Supplementary Figure S6: Box plots showing the relationship between the TUMOR<sup>MV</sup> and the variables from which it is defined. P values are estimated by Kruskal–Wallis test. Supplementary Table S1: R values of Spearman’s correlation analysis between continuous variables analyzed. Legend: \*\*\*\*,  $p < 0.0001$ ; \*\*\*,  $p < 0.001$ ; \*\*,  $p < 0.01$ ; \*,  $p < 0.05$ . Supplementary Table S2: Association analysis between peripheral or intratumoral biomarkers measures and sex. P values estimated by Wilcoxon test. Supplementary Table S3: Association analysis between peripheral or intratumoral biomarkers measures and pT category. P values estimated by Kruskal–Wallis test. Supplementary Table S4: Association analysis between peripheral or intratumoral biomarkers measures and pN category. P values estimated by Kruskal–Wallis test. Supplementary Table S5: Association analysis between peripheral or intratumoral biomarkers measures and extranodal extension (ENE). P values estimated by Wilcoxon test. Supplementary Table S6: Association analysis between peripheral or intratumoral biomarkers measures and grading. P values estimated by Kruskal–Wallis test. Supplementary Table S7: Association analysis between peripheral or intratumoral biomarkers measures and bone invasion. P values estimated by Kruskal–Wallis test. Supplementary Table S8: Association analysis between peripheral or intratumoral biomarkers measures and perineural invasion (PNI). P values estimated by Wilcoxon test. Supplementary Table S9: Association analysis between peripheral or intratumoral biomarkers measures and lymphovascular invasion (LVI). P values estimated by Wilcoxon test. Supplementary Table S10: Details of the loadings for each variable and level composing the 5 metavariables (<sup>MV</sup>). Supplementary Table S11: Extensive details of multivariable survival Cox proportional hazards models. Legend: d.f., degrees of freedom; Coefficient, regression coefficient; S.E., standard error.

**Author Contributions:** Conceptualization, F.M., S.C. and W.V.; methodology, F.M., M.B., W.V., D.M., S.L., A.M.B. and S.B.; formal analysis, F.M. and S.C.; investigation, F.M., M.B., D.M., D.L. and W.V.; resources, W.V., P.N. and C.P.; data curation, F.M. and D.M.; writing—original draft preparation, F.M. and W.V.; writing—review and editing, S.C., D.M., P.N., D.L., C.P. and W.V.; visualization, M.B., S.L., A.M.B. and S.B.; supervision, W.V., D.L., S.C. and P.N. All authors have read and agreed to the published version of the manuscript.

**Funding:** The research leading to these results has received funding from “Associazione Italiana per la Ricerca sul Cancro” (AIRC-IG-23179)—P.I. Vermi William.

**Institutional Review Board Statement:** The study was conducted according to the guidelines of the Declaration of Helsinki, and approved by the “Comitato Etico Provinciale della Provincia di Brescia” (protocol code NP 2066—WV-H&NCancer; date of approval 14-7-2015).

**Informed Consent Statement:** Informed consent was obtained from all subjects involved in the study.

**Data Availability Statement:** The full dataset will be available upon reasonable request to the corresponding author.

**Acknowledgments:** We thank the pathologists, technicians, clinicians, nurses and administrative employers that have provided support to the study and to the follow-up of OCs patients.

**Conflicts of Interest:** The authors declare no conflict of interest.

## References

1. Ferlay, J.; Soerjomataram, I.; Dikshit, R.; Eser, S.; Mathers, C.; Rebelo, M.; Parkin, D.M.; Forman, D.; Bray, F. Cancer incidence and mortality worldwide: Sources, methods and major patterns in GLOBOCAN 2012. *Int. J. Cancer* **2015**, *136*, e359–e386. [\[CrossRef\]](#)
2. Ghazawi, F.M.; Lu, J.; Savin, E.; Zubarev, A.; Chauvin, P.; Sasseville, D.; Zeitouni, A.; Litvinov, I.V. Epidemiology and Patient Distribution of Oral Cavity and Oropharyngeal SCC in Canada. *J. Cutan. Med. Surg.* **2020**, *24*, 340–349. [\[CrossRef\]](#)
3. Conway, D.I.; Purkayastha, M.; Chestnutt, I.G. The changing epidemiology of oral cancer: Definitions, trends, and risk factors. *Br. Dent. J.* **2018**, *225*, 867–873. [\[CrossRef\]](#)
4. Shah, J.P.; Cendon, R.A.; Farr, H.W.; Strong, E.W. Carcinoma of the oral cavity. Factors affecting treatment failure at the primary site and neck. *Am. J. Surg.* **1976**, *132*, 504–507. [\[CrossRef\]](#)
5. Gil, Z.; Carlson, D.L.; Boyle, J.O.; Kraus, D.H.; Shah, J.P.; Shaha, A.R.; Singh, B.; Wong, R.J.; Patel, S.G. Lymph node density is a significant predictor of outcome in patients with oral cancer. *Cancer* **2009**, *115*, 5700–5710. [\[CrossRef\]](#)
6. Patel, S.G.; Amit, M.; Yen, T.C.; Liao, C.T.; Chaturvedi, P.; Agarwal, J.P.; Kowalski, L.P.; Ebrahimi, A.; Clark, J.R.; Cernea, C.R.; et al. Lymph node density in oral cavity cancer: Results of the International Consortium for Outcomes Research. *Br. J. Cancer* **2013**, *109*, 2087–2095. [\[CrossRef\]](#) [\[PubMed\]](#)
7. Shiono, S.; Kawamura, M.; Sato, T.; Okumura, S.; Nakajima, J.; Yoshino, I.; Ikeda, N.; Horio, H.; Akiyama, H.; Kobayashi, K. Pulmonary metastasectomy for pulmonary metastases of head and neck squamous cell carcinomas. *Ann. Thorac. Surg.* **2009**, *88*, 856–860. [\[CrossRef\]](#) [\[PubMed\]](#)
8. D’Cruz, A.K.; Vaish, R.; Kapre, N.; Dandekar, M.; Gupta, S.; Hawaldar, R.; Agarwal, J.P.; Pantvaidya, G.; Chaukar, D.; Deshmukh, A.; et al. Elective versus Therapeutic Neck Dissection in Node-Negative Oral Cancer. *N. Engl. J. Med.* **2015**, *373*, 521–529. [\[CrossRef\]](#) [\[PubMed\]](#)
9. Garrel, R.; Poissonnet, G.; Moyà Plana, A.; Fakhry, N.; Dolivet, G.; Lallemand, B.; Sarini, J.; Vergez, S.; Guelfucci, B.; Choussy, O.; et al. Equivalence Randomized Trial to Compare Treatment on the Basis of Sentinel Node Biopsy Versus Neck Node Dissection in Operable T1-T2N0 Oral and Oropharyngeal Cancer. *J. Clin. Oncol. Off. J. Am. Soc. Clin. Oncol.* **2020**, *38*, 4010–4018. [\[CrossRef\]](#)
10. Ferris, R.L.; Blumenschein, G.J.; Fayette, J.; Guigay, J.; Colevas, A.D.; Licitra, L.; Harrington, K.; Kasper, S.; Vokes, E.E.; Even, C.; et al. Nivolumab for Recurrent Squamous-Cell Carcinoma of the Head and Neck. *N. Engl. J. Med.* **2016**, *375*, 1856–1867. [\[CrossRef\]](#)
11. Seiwert, T.Y.; Burtneiss, B.; Mehra, R.; Weiss, J.; Berger, R.; Eder, J.P.; Heath, K.; McClanahan, T.; Luceford, J.; Gause, C.; et al. Safety and clinical activity of pembrolizumab for treatment of recurrent or metastatic squamous cell carcinoma of the head and neck (KEYNOTE-012): An open-label, multicentre, phase 1b trial. *Lancet. Oncol.* **2016**, *17*, 956–965. [\[CrossRef\]](#)
12. Cohen, E.E.W.; Soulières, D.; Le Tourneau, C.; Dinis, J.; Licitra, L.; Ahn, M.-J.; Soria, A.; Machiels, J.-P.; Mach, N.; Mehra, R.; et al. Pembrolizumab versus methotrexate, docetaxel, or cetuximab for recurrent or metastatic head-and-neck squamous cell carcinoma (KEYNOTE-040): A randomised, open-label, phase 3 study. *Lancet* **2019**, *393*, 156–167. [\[CrossRef\]](#)
13. Bellmunt, J.; De Wit, R.; Vaughn, D.J.; Fradet, Y.; Lee, J.L.; Fong, L.; Vogelzang, N.J.; Climent, M.A.; Petrylak, D.P.; Choueiri, T.K.; et al. Pembrolizumab as second-line therapy for advanced urothelial carcinoma. *N. Engl. J. Med.* **2017**, *376*, 1015–1026. [\[CrossRef\]](#)
14. Brockstein, B.E.; Vokes, E.E. Treatment of metastatic and recurrent head and neck cancer. In *Treatment of Metastatic and Recurrent Head and Neck Cancer*; Post, T.W., Posner, M.R., Shah, S., Eds.; UpToDate: Waltham, MA, USA, 2021.
15. Brandwein-Gensler, M.; Teixeira, M.S.; Lewis, C.M.; Lee, B.; Rolnitzky, L.; Hille, J.J.; Genden, E.; Urken, M.L.; Wang, B.Y. Oral squamous cell carcinoma: Histologic risk assessment, but not margin status, is strongly predictive of local disease-free and overall survival. *Am. J. Surg. Pathol.* **2005**, *29*, 167–178. [\[CrossRef\]](#) [\[PubMed\]](#)
16. Brandwein-Gensler, M.; Smith, R.V.; Wang, B.; Penner, C.; Theilken, A.; Broughel, D.; Schiff, B.; Owen, R.P.; Smith, J.; Sarta, C.; et al. Validation of the histologic risk model in a new cohort of patients with head and neck squamous cell carcinoma. *Am. J. Surg. Pathol.* **2010**, *34*, 676–688. [\[CrossRef\]](#)
17. Troiano, G.; Rubini, C.; Togni, L.; Caponio, V.C.A.; Zhurakivska, K.; Santarelli, A.; Cirillo, N.; Lo Muzio, L.; Mascitti, M. The immune phenotype of tongue squamous cell carcinoma predicts early relapse and poor prognosis. *Cancer Med.* **2020**, *9*, 8333–8344. [\[CrossRef\]](#) [\[PubMed\]](#)
18. Borsetto, D.; Tomasoni, M.; Payne, K.; Polesel, J.; Deganello, A.; Bossi, P.; Tysome, J.R.; Masterson, L.; Tirelli, G.; Tofaneli, M.; et al. Prognostic Significance of CD4+ and CD8+ Tumor-Infiltrating Lymphocytes in Head and Neck Squamous Cell Carcinoma: A Meta-Analysis. *Cancers* **2021**, *13*, 781. [\[CrossRef\]](#) [\[PubMed\]](#)
19. Huang, Z.; Xie, N.; Liu, H.; Wan, Y.; Zhu, Y.; Zhang, M.; Tao, Y.; Zhou, H.; Liu, X.; Hou, J.; et al. The prognostic role of tumour-infiltrating lymphocytes in oral squamous cell carcinoma: A meta-analysis. *J. Oral Pathol. Med. Off. Publ. Int. Assoc. Oral Pathol. Am. Acad. Oral Pathol.* **2019**, *48*, 788–798. [\[CrossRef\]](#)
20. Cupp, M.A.; Cariolou, M.; Tzoulaki, I.; Aune, D.; Evangelou, E.; Berlanga-Taylor, A.J. Neutrophil to lymphocyte ratio and cancer prognosis: An umbrella review of systematic reviews and meta-analyses of observational studies. *BMC Med.* **2020**, *18*, 360. [\[CrossRef\]](#)
21. Bardash, Y.; Olson, C.; Herman, W.; Khaymovich, J.; Costantino, P.; Tham, T. Platelet-Lymphocyte Ratio as a Predictor of Prognosis in Head and Neck Cancer: A Systematic Review and Meta-Analysis. *Oncol. Res. Treat.* **2019**, *42*, 665–677. [\[CrossRef\]](#)

22. Yang, L.; Huang, Y.; Zhou, L.; Dai, Y.; Hu, G. High pretreatment neutrophil-to-lymphocyte ratio as a predictor of poor survival prognosis in head and neck squamous cell carcinoma: Systematic review and meta-analysis. *Head Neck* **2019**, *41*, 1525–1535. [[CrossRef](#)] [[PubMed](#)]
23. Cho, J.-K.; Kim, M.W.; Choi, I.S.; Moon, U.Y.; Kim, M.-J.; Sohn, I.; Kim, S.; Jeong, H.-S. Optimal cutoff of pretreatment neutrophil-to-lymphocyte ratio in head and neck cancer patients: A meta-analysis and validation study. *BMC Cancer* **2018**, *18*, 969. [[CrossRef](#)] [[PubMed](#)]
24. Royston, P.; Altman, D.G.; Sauerbrei, W. Dichotomizing continuous predictors in multiple regression: A bad idea. *Stat. Med.* **2006**, *25*, 127–141. [[CrossRef](#)]
25. Chan, J.Y.; Tan, G.F.; Yeong, J.; Ong, C.W.; Ng, D.Y.X.; Lee, E.; Koh, J.; Ng, C.C.-Y.; Lee, J.Y.; Liu, W.; et al. Clinical implications of systemic and local immune responses in human angiosarcoma. *NPJ Precis. Oncol.* **2021**, *5*, 11. [[CrossRef](#)]
26. Mattavelli, D.; Lombardi, D.; Missale, F.; Calza, S.; Battocchio, S.; Paderno, A.; Bozzola, A.; Bossi, P.; Vermi, W.; Piazza, C.; et al. Prognostic Nomograms in Oral Squamous Cell Carcinoma: The Negat Impact of Low Neutrophil to Lymph Ratio. *Front. Oncol.* **2019**, *9*, 1–13. [[CrossRef](#)]
27. Lonardi, S.; Missale, F.; Calza, S.; Bugatti, M.; Vescovi, R.; Debora, B.; Uppaluri, R.; Egloff, A.M.; Mattavelli, D.; Lombardi, D.; et al. Tumor-associated neutrophils (TANs) in human carcinoma-draining lymph nodes: A novel TAN compartment. *Clin. Transl. Immunol.* **2021**, *10*, e1252. [[CrossRef](#)]
28. Walsh, S.R.; Cook, E.J.; Goulder, F.; Justin, T.A.; Keeling, N.J. Neutrophil-lymphocyte ratio as a prognostic factor in colorectal cancer. *J. Surg Oncol.* **2005**, *91*, 181–184. [[CrossRef](#)]
29. Takenaka, Y.; Oya, R.; Kitamiura, T.; Ashida, N.; Shimizu, K.; Takemura, K.; Yamamoto, Y.; Uno, A. Platelet count and platelet-lymphocyte ratio as prognostic markers for head and neck squamous cell carcinoma: Meta-analysis. *Head Neck* **2018**, *40*, 2714–2723. [[CrossRef](#)]
30. Galon, J.; Pages, F.; Marincola, F.M.; Angell, H.K.; Thurin, M.; Lugli, A.; Zlobec, I.; Berger, A.; Bifulco, C.; Botti, G.; et al. Cancer classification using the Immunoscore: A worldwide task force. *J. Transl. Med.* **2012**, *10*, 205. [[CrossRef](#)] [[PubMed](#)]
31. Harrell, F.E. *Multivariable Modeling Strategies. Regression Modeling Strategies*, 2nd ed.; Springer: Cham, Switzerland, 2015; pp. 63–102.
32. Chavent, M.; Kuentz-Simonet, V.; Liquet, B.; Saracco, J. ClustOfVar: An R Package for the Clustering of Variables. *J. Stat. Softw.* **2011**, *50*, 1–16.
33. Vigneau, E.; Qannari, E.M. Clustering of Variables around Latent Components. *Commun. Stat.-Simul. Comput.* **2003**, *32*, 1131–1150. [[CrossRef](#)]
34. Van Buuren, S.; Groothuis-Oudshoorn, K. mice: Multivariate Imputation by Chained Equations in R. *J. Stat. Softw.* **2011**, *45*, 1–67. [[CrossRef](#)]
35. Durrleman, S.; Simon, R. Flexible regression models with cubic splines. *Stat. Med.* **1989**, *8*, 551–561. [[CrossRef](#)]
36. Harrell, F.E.J.; Lee, K.L.; Mark, D.B. Multivariable prognostic models: Issues in developing models, evaluating assumptions and adequacy, and measuring and reducing errors. *Stat. Med.* **1996**, *15*, 361–387. [[CrossRef](#)]
37. Pfeiffer, R.M.; Gail, M.H. Estimating the decision curve and its precision from three study designs. *Biom. J.* **2020**, *62*, 764–776. [[CrossRef](#)]
38. Vickers, A.J.; Cronin, A.M.; Elkin, E.B.; Gonen, M. Extensions to decision curve analysis, a novel method for evaluating diagnostic tests, prediction models and molecular markers. *BMC Med. Inform. Decis. Mak.* **2008**, *8*, 53. [[CrossRef](#)]
39. Vickers, A.J.; Elkin, E.B. Decision curve analysis: A novel method for evaluating prediction models. *Med. Decis. Mak. Int. J. Soc. Med. Decis. Mak.* **2006**, *26*, 565–574. [[CrossRef](#)]
40. Grambsch, P.M.; Therneau, T.M. Proportional hazards tests and diagnostics based on weighted residuals. *Biometrika.* **1994**, *81*, 515–526. [[CrossRef](#)]
41. Breheny, P.; Burchett, W. Package ‘visreg’: Visualization of Regression Models. *R J.* **2017**, *9*, 56–71. [[CrossRef](#)]
42. Cerezo, L.; Millán, I.; Torre, A.; Aragón, G.; Otero, J. Prognostic factors for survival and tumor control in cervical lymph node metastases from head and neck cancer. A multivariate study of 492 cases. *Cancer.* **1992**, *69*, 1224–1234. [[CrossRef](#)]
43. Amin, M.B.; Edge, S.; Greene, F.; Byrd, D.R.; Brookland, R.K.; Washington, M.K.; Gershenwald, J.E.; Compton, C.C.; Hess, K.R.; Sullivan, D.C.; et al. *AJCC Cancer Staging Manual*, 8th ed.; Springer: Cham, Switzerland, 2017.
44. Ho, A.S.; Kim, S.; Tighiouart, M.; Gudino, C.; Mita, A.; Scher, K.S.; Laury, A.; Prasad, R.; Shiao, S.L.; Van Eyk, J.E.; et al. Metastatic Lymph Node Burden and Survival in Oral Cavity Cancer. *J. Clin. Oncol. Off. J. Am. Soc. Clin. Oncol.* **2017**, *35*, 3601–3609. [[CrossRef](#)]
45. Mirian, C.; Gerds, T.A.; Pedersen, M.M.; de Ridder, M.; Balm, A.; Mattavelli, D.; Piazza, C.; Jensen, L.R.; Balasubramanian, D.; Subramaniam, N.; et al. Metrics of pN-staging in oral squamous cell carcinoma: An analysis of 1905 patients. *Eur. J. Cancer.* **2021**, *150*, 33–41. [[CrossRef](#)]
46. Papaioannou, E.; Sakellakis, M.; Melachrinou, M.; Tzoracoleftherakis, E.; Kalofonos, H.; Kourea, E. A Standardized Evaluation Method for FOXP3+ Tregs and CD8+ T-cells in Breast Carcinoma: Association with Breast Carcinoma Subtypes, Stage and Prognosis. *Anticancer Res.* **2019**, *39*, 1217–1232. [[CrossRef](#)] [[PubMed](#)]
47. Sperlich, A.; Balmert, A.; Doll, D.; Bauer, S.; Franke, F.; Keller, G.; Wilhelm, D.; Mur, A.; Respondek, M.; Friess, H.; et al. Genetic and immunological biomarkers predict metastatic disease recurrence in stage III colon cancer. *BMC Cancer* **2018**, *18*, 998. [[CrossRef](#)]

48. Fujii, H.; Arakawa, A.; Utsumi, D.; Sumiyoshi, S.; Yamamoto, Y.; Kitoh, A.; Ono, M.; Matsumura, Y.; Kato, M.; Konishi, K.; et al. CD8<sup>+</sup> tumor-infiltrating lymphocytes at primary sites as a possible prognostic factor of cutaneous angiosarcoma. *Int. J. Cancer* **2014**, *134*, 2393–2402. [[CrossRef](#)]
49. Wang, Y.Q.; Chen, L.; Mao, Y.P.; Li, Y.Q.; Jiang, W.; Xu, S.-Y.; Zhang, Y.; Chen, Y.P.; Li, X.-M.; He, Q.M.; et al. Prognostic value of immune score in nasopharyngeal carcinoma using digital pathology. *J. Immunother. Cancer* **2020**, *8*, e000334. [[CrossRef](#)] [[PubMed](#)]
50. Ono, T.; Azuma, K.; Kawahara, A.; Akiba, J.; Kakuma, T.; Chitose, S.; Umeno, H. Pre-treatment CD8(+) tumour-infiltrating lymphocyte density predicts distant metastasis after definitive treatment in patients with stage III/IV hypopharyngeal squamous cell carcinoma. *Clin. Otolaryngol. Off. J. ENT-UK Off. J. Neth. Soc. Oto-Rhino-Laryngol. Cerv.-Fac. Surg.* **2018**, *43*, 1312–1320. [[CrossRef](#)]
51. Wang, J.; Tian, S.; Sun, J.; Zhang, J.; Lin, L.; Hu, C. The presence of tumour-infiltrating lymphocytes (TILs) and the ratios between different subsets serve as prognostic factors in advanced hypopharyngeal squamous cell carcinoma. *BMC Cancer* **2020**, *20*, 731. [[CrossRef](#)]
52. Balermipas, P.; Michel, Y.; Wagenblast, J.; Seitz, O.; Weiss, C.; Rödel, F.; Rödel, C.; Fokas, E. Tumour-infiltrating lymphocytes predict response to definitive chemoradiotherapy in head and neck cancer. *Br. J. Cancer* **2014**, *110*, 501–509. [[CrossRef](#)]
53. Chen, W.Y.; Wu, C.T.; Wang, C.W.; Lan, K.H.; Liang, H.K.; Huang, B.S.; Chang, Y.L.; Kuo, S.H.; Cheng, A.L. Prognostic significance of tumor-infiltrating lymphocytes in patients with operable tongue cancer. *Radiat. Oncol.* **2018**, *13*, 1–8. [[CrossRef](#)] [[PubMed](#)]
54. Garner, H.; de Visser, K.E. Immune crosstalk in cancer progression and metastatic spread: A complex conversation. *Nat. Rev. Immunol.* **2020**, *20*, 483–497. [[CrossRef](#)]
55. Joyce, J.A.; Fearon, D.T. T cell exclusion, immune privilege, and the tumor microenvironment. *Science* **2015**, *348*, 74–80. [[CrossRef](#)]
56. Chen, D.S.; Mellman, I. Elements of cancer immunity and the cancer-immune set point. *Nature* **2017**, *541*, 321–330. [[CrossRef](#)]
57. Philip, M.; Schietinger, A. CD8(+) T cell differentiation and dysfunction in cancer. *Nat. Rev. Immunol.* **2021**. [[CrossRef](#)]
58. Devaud, C.; John, L.B.; Westwood, J.A.; Darcy, P.K.; Kershaw, M.H. Immune modulation of the tumor microenvironment for enhancing cancer immunotherapy. *Oncoimmunology* **2013**, *2*, e25961. [[CrossRef](#)]
59. Curran, M.A.; Montalvo, W.; Yagita, H.; Allison, J.P. PD-1 and CTLA-4 combination blockade expands infiltrating T cells and reduces regulatory T and myeloid cells within B16 melanoma tumors. *Proc. Natl. Acad. Sci. USA* **2010**, *107*, 4275–4280. [[CrossRef](#)]
60. Jin, D.; Fan, J.; Wang, L.; Thompson, L.F.; Liu, A.; Daniel, B.J.; Shin, T.; Curiel, T.J.; Zhang, B. CD73 on tumor cells impairs antitumor T-cell responses: A novel mechanism of tumor-induced immune suppression. *Cancer Res.* **2010**, *70*, 2245–2255. [[CrossRef](#)]
61. Li, J.; O'Malley, M.; Urban, J.; Sampath, P.; Guo, Z.S.; Kalinski, P.; Thorne, S.H.; Bartlett, D.L. Chemokine expression from oncolytic vaccinia virus enhances vaccine therapies of cancer. *Mol. Ther.* **2011**, *19*, 650–657. [[CrossRef](#)] [[PubMed](#)]
62. Park, J.; Wrzesinski, S.H.; Stern, E.; Look, M.; Criscione, J.; Ragheb, R.; Jay, S.M.; Demento, S.L.; Agawu, A.; Licona Limon, P.; et al. Combination delivery of TGF- $\beta$  inhibitor and IL-2 by nanoscale liposomal polymeric gels enhances tumour immunotherapy. *Nat. Mater.* **2012**, *11*, 895–905. [[CrossRef](#)]
63. John, L.B.; Howland, L.J.; Flynn, J.K.; West, A.C.; Devaud, C.; Duong, C.P.; Stewart, T.J.; Westwood, J.A.; Guo, Z.S.; Bartlett, D.L.; et al. Oncolytic virus and anti-4-1BB combination therapy elicits strong antitumor immunity against established cancer. *Cancer Res.* **2012**, *72*, 1651–1660. [[CrossRef](#)] [[PubMed](#)]
64. Schoenfeld, J.D.; Hanna, G.J.; Jo, V.Y.; Rawal, B.; Chen, Y.-H.; Catalano, P.S.; Lako, A.; Ciantra, Z.; Weirather, J.L.; Criscitiello, S.; et al. Neoadjuvant Nivolumab or Nivolumab Plus Ipilimumab in Untreated Oral Cavity Squamous Cell Carcinoma: A Phase 2 Open-Label Randomized Clinical Trial. *JAMA Oncol.* **2020**, *6*, 1563–1570. [[CrossRef](#)]
65. Uppaluri, R.; Zolkind, P.; Lin, T.; Nussenbaum, B.; Jackson, R.S.; Rich, J.; Pipkorn, P.; Paniello, R.; Thorstad, W.; Michel, L.; et al. Neoadjuvant pembrolizumab in surgically resectable, locally advanced HPV negative head and neck squamous cell carcinoma (HNSCC). *J. Clin. Oncol.* **2017**, *35*, 6012. [[CrossRef](#)]
66. Zuur, L.; Vos, J.L.; Elbers, J.B.; Krijgsman, O.; Qiao, X.; van der Leun, A.; Smit, L.; van den Brekel, M.W.; Tan, B.; Jasperse, B.; et al. LBA40 Neoadjuvant nivolumab and nivolumab plus ipilimumab induce (near-) complete responses in patients with head and neck squamous cell carcinoma: The IMCISION trial. *Ann. Oncol.* **2020**, *31*, S1169. [[CrossRef](#)]
67. Zuur, C.L.; Elbers, J.B.W.; Vos, J.L.; van der Leun, A.; Qiao, X.; Karakullukcu, B.; van den Brekel, M.W.M.; Tan, B.; Jasperse, B.; Vogel, W.V.; et al. Feasibility and toxicity of neoadjuvant nivolumab with or without ipilimumab prior to extensive (salvage) surgery in patients with advanced head and neck cancer (the IMCISION trial, NCT03003637). *J. Clin. Oncol.* **2019**, *37*, 2575. [[CrossRef](#)]
68. Horton, J.D.; Knochelmann, H.; Armeson, K.; Kaczmar, J.M.; Paulos, C.; Neskey, D. Neoadjuvant presurgical PD-1 inhibition in oral cavity squamous cell carcinoma. *J. Clin. Oncol.* **2019**, *37*, 2574. [[CrossRef](#)]
69. Kleinovink, J.W.; Fransen, M.F.; Löwik, C.W.; Ossendorp, F. Photodynamic-Immune Checkpoint Therapy Eradicates Local and Distant Tumors by CD8(+) T Cells. *Cancer Immunol. Res.* **2017**, *5*, 832–838. [[CrossRef](#)]
70. Civantos, F.J.; Karakullukcu, B.; Biel, M.; Silver, C.E.; Rinaldo, A.; Saba, N.F.; Takes, R.P.; Vander Poorten, V.; Ferlito, A. A Review of Photodynamic Therapy for Neoplasms of the Head and Neck. *Adv. Ther.* **2018**, *35*, 324–340. [[CrossRef](#)] [[PubMed](#)]
71. Meulemans, J.; Delaere, P.; Vander Poorten, V. Photodynamic therapy in head and neck cancer: Indications, outcomes, and future prospects. *Curr. Opin. Otolaryngol. Head Neck Surg.* **2019**, *27*, 136–141. [[CrossRef](#)]

## Immune-Contexture in Ovarian Cancer Subtypes

Ardighieri, L.#

**Missale, F.#**

Bugatti, M.

Gatta, L.B.

Pezzali, I.

Monti, M.

Gottardi, S.

Zanotti, L.

Bignotti, E.

Ravaggi, A.

Tognon, G.

Odicino, F.

Calza, S.

Missolo-Koussou, Y.

Ries, C.H.

Helft, J.

Vermi, W.

Frontiers in immunology  
2021;112, 690201. <https://doi.org/10.3389/fimmu.2021.690201>

#equally contributed as first authors



Supplementary material:





# Infiltration by CXCL10 Secreting Macrophages Is Associated With Antitumor Immunity and Response to Therapy in Ovarian Cancer Subtypes

Laura Ardighieri<sup>1†</sup>, Francesco Missale<sup>2,3†</sup>, Mattia Bugatti<sup>1,2†</sup>, Luisa Benerini Gatta<sup>2</sup>, Irene Pezzali<sup>2</sup>, Matilde Monti<sup>2</sup>, Stefano Gottardi<sup>4</sup>, Laura Zanotti<sup>5,6</sup>, Eliana Bignotti<sup>5,6</sup>, Antonella Ravaggi<sup>5,6,7</sup>, Germana Tognon<sup>6</sup>, Franco Odicino<sup>6,7</sup>, Stefano Calza<sup>8,9,10</sup>, Yoann Missolo-Koussou<sup>11</sup>, Carola Hermine Ries<sup>12</sup>, Julie Helft<sup>11</sup> and William Vermi<sup>1,2,13\*</sup>

## OPEN ACCESS

### Edited by:

Sizun Jiang,  
Beth Israel Deaconess Medical Center  
and Harvard Medical School,  
United States

### Reviewed by:

Majja Hollmén,  
University of Turku, Finland  
Mariolina Salio,  
University of Oxford, United Kingdom

### \*Correspondence:

William Vermi  
william.vermi@unibs.it

<sup>†</sup>These authors have contributed  
equally to the work

### Specialty section:

This article was submitted to  
Cancer Immunity  
and Immunotherapy,  
a section of the journal  
Frontiers in Immunology

**Received:** 02 April 2021

**Accepted:** 27 May 2021

**Published:** 18 June 2021

### Citation:

Ardighieri L, Missale F, Bugatti M,  
Gatta LB, Pezzali I, Monti M,  
Gottardi S, Zanotti L, Bignotti E,  
Ravaggi A, Tognon G, Odicino F,  
Calza S, Missolo-Koussou Y,  
Ries CH, Helft J and Vermi W (2021)  
Infiltration by CXCL10 Secreting  
Macrophages Is Associated With  
Antitumor Immunity and Response to  
Therapy in Ovarian Cancer Subtypes.  
*Front. Immunol.* 12:690201.  
doi: 10.3389/fimmu.2021.690201

<sup>1</sup> Unit of Pathology, ASST Spedali Civili di Brescia, Brescia, Italy, <sup>2</sup> Department of Molecular and Translational Medicine, University of Brescia, Brescia, Italy, <sup>3</sup> IRCCS Ospedale Policlinico San Martino, Genova, Italy, <sup>4</sup> Diatch Pharmacogenetics srl, Jesi, Italy, <sup>5</sup> 'Angelo Nocivelli' Institute of Molecular Medicine, ASST Spedali Civili of Brescia- University of Brescia, Brescia, Italy, <sup>6</sup> Division of Obstetrics and Gynecology, ASST Spedali Civili di Brescia, Brescia, Italy, <sup>7</sup> Department of Clinical and Experimental Science, University of Brescia, Brescia, Italy, <sup>8</sup> Unit of Biostatistics, Department of Molecular and Translational Medicine, University of Brescia, Brescia, Italy, <sup>9</sup> Department of Medical Epidemiology and Biostatistics, Karolinska Institutet, Stockholm, Sweden, <sup>10</sup> Big & Open Data Innovation Laboratory, University of Brescia, Brescia, Italy, <sup>11</sup> PSL University, Institut Curie Research Center, INSERM U932 & SiRIC, Center for Cancers Immunotherapy, Translational Immunotherapy Team, Paris, France, <sup>12</sup> Dr. Carola Ries Consulting, Penzberg, Germany, <sup>13</sup> Department of Pathology and Immunology, Washington University School of Medicine, St. Louis, MO, United States

Ovarian carcinomas (OCs) are poorly immunogenic and immune checkpoint inhibitors (ICIs) have offered a modest benefit. In this study, high CD3<sup>+</sup> T-cells and CD163<sup>+</sup> tumor-associated macrophages (TAMs) densities identify a subgroup of immune infiltrated high-grade serous carcinomas (HGSCs) with better outcomes and superior response to platinum-based therapies. On the contrary, in most clear cell carcinomas (CCCs) showing poor prognosis and refractory to platinum, a high TAM density is associated with low T cell frequency. Immune infiltrated HGSC are characterized by the 30-genes signature (OC-IS<sup>30</sup>) covering immune activation and IFN $\gamma$  polarization and predicting good prognosis (n = 312, TCGA). Immune infiltrated HGSC contain CXCL10 producing M1-type TAM (IRF1<sup>+</sup>pSTAT1Y701<sup>+</sup>) in close proximity to T-cells. A fraction of these M1-type TAM also co-expresses TREM2. M1-polarized TAM were barely detectable in T-cell poor CCC, but identifiable across various immunogenic human cancers. Single cell RNA sequencing data confirm the existence of a tumor-infiltrating CXCL10<sup>+</sup>IRF1<sup>+</sup>STAT1<sup>+</sup> M1-type TAM overexpressing antigen processing and presentation gene programs. Overall, this study highlights the clinical relevance of the CXCL10<sup>+</sup>IRF1<sup>+</sup>STAT1<sup>+</sup> macrophage subset as biomarker for intratumoral T-cell activation and therefore offers a new tool to select patients more likely to respond to T-cell or macrophage-targeted immunotherapies.

**Keywords:** ovarian cancer, macrophage, signature, CXCL10, polarization

## INTRODUCTION

Ovarian carcinomas (OCs) (1) represent a heterogeneous group with three main subtypes (high-grade serous carcinoma [HGSC], clear cell carcinoma [CCC] and endometrioid carcinoma [EC]) distinct by microscopic findings and molecular features. High-grade serous carcinoma (HGSC) represents the most common and lethal subtype. Patients with HGSC usually present with advanced disease involving the pelvic and peritoneal cavity associated with malignant ascites; in addition, transcoelomic metastases or distant spread can be observed at the diagnosis. Standard treatment consists of primary upfront debulking surgery followed by adjuvant cytotoxic platinum-taxane based therapy (1, 2). Most of the patients initially respond to this front-line approach; however, 70% relapses within three years. Therapy resistance mechanisms include genomic instability, epigenetic deregulation, and change in tumor microenvironment, leading to the cancer outgrowth (3, 4). A fraction of patients is refractory to platinum-based regimens and relapses early during treatment, displaying a rapid fatal course (1).

Few improvements in clinical outcomes have been obtained in OCs. Encouraging results have been achieved with the introduction of inhibitors targeting poly (ADP-ribose) polymerase (PARP), particularly effective in Homologous Recombination Deficiency (HRD) positive cases (5). HRD is detected in up to half of tumors due to inactivation of HRD genes by mutations or promoter hypermethylation (6). PARP inhibitors maintenance therapy improves progression-free survival (PFS) in platinum-sensitive newly diagnosed and recurrent OCs (7, 8). Immunotherapy based on immune checkpoint inhibitors (ICIs), has shown clinical efficacy in solid cancer (9). On the contrary, until now, the global response rate of HGSC to ICIs resulted modest, ranging from 10 to 25%, thus suggesting an urgent need for predictive biomarkers. It should be noted that OCs are characterized by low mutational burden and this could represent one of the possible explanations of lower response rate to ICIs in comparison to other cancer types (10). However, the recent combination of ICIs and PARP inhibitors in HRD<sup>+</sup> OCs has shown promising results (11), suggesting higher intrinsic immunogenicity associated with the HRD group.

The composition, density, and functional orientation of the immune contexture predict patient survival and response to various treatments in different cancers (12) including OCs, the latter being traditionally considered scarcely immunogenic. A set of studies challenged this view and demonstrated that a subgroup of OCs displays a higher CD3<sup>+</sup> TILs density associated with longer progression-free intervals and better survival in advanced-stage OCs (13). These observations were subsequently confirmed by others (14) and by a recent meta-analysis (15). In contrast to TILs, the clinical significance of tumor-associated macrophages (TAMs) is largely ignored with conflicting observations.

In the present study, we explored the tumor ecosystem of OCs on archival whole tumor sections. Data indicate that high density of CD3<sup>+</sup> T-cells and CD163<sup>+</sup> TAMs marks a consistent group of immune infiltrated HGSC, stratifies patients with different outcomes and correlates with a thirty-gene signature (OC-IS<sup>30</sup>) containing among others IFN $\gamma$ -regulated genes. On the contrary,

in most CCCs a high TAM density is not combined with a significant T-cell infiltration. By extending the analysis to The Cancer Genome Atlas, OC-IS<sup>30</sup> strongly predicts a favorable outcome in a large cohort of HGSC. By immunohistochemistry for pSTAT1 and IRF1 together with RNAscope-mediated detection of CXCL10, we could identify an M1-type macrophage (M $\phi$ ) population associated with immune infiltrated HGSC, but not CCC. We extended and confirmed these findings to other cancer types by immunohistochemistry and by an unbiased analysis of scRNAseq dataset.

## MATERIALS AND METHODS

### Collection of Patient Samples

Ninety-seven cases of ovarian carcinoma treated between 1999 and 2009 were identified from the archive files of the Department of Pathology, ASST Spedali Civili di Brescia (Brescia, Italy) and included in the study. Hematoxylin & Eosin (H&E) stained slides were reviewed by an expert (LA) for appropriate classification according to the WHO 4th Edition (2014). All patients were treated and followed at the Division of Obstetrics and Gynecology ASST Spedali Civili di Brescia, Brescia, Italy. Clinical and pathology data are summarized in **Table 1** and the full dataset in **Supplementary Table S1**. The study was approved by the local IRB (WW-IMMUNOCANCERhum, NP-906, NP-1284).

### Immunohistochemistry

Immunohistochemistry was performed on four-micron FFPE tissue sections with anti-CD3 (clone LN10, 1:100) anti-CD163 (clone 10D6, 1:50, Thermo Scientific) and anti-CD303/BDCA2 (clone 124B3.13, 1:75, Dendritics) antibodies, recognizing respectively T-cells, TAMs and plasmacytoid dendritic cells (PDCs). CD3 and CD163 stains were performed on Bond Max automatic immunostainer (Leica Biosystems). Immunostains for anti-CSF-1R (clone FER216, 1:1,500, Millipore), anti-IRF-1 (clone D5E4, 1:100, Cell Signaling), anti-phospho-STAT1 (clone Tyr701 rabbit, 1:500, Cell Signaling), TREM2 (anti-TREM2 antibody (clone D8I4C, 1:100, Cell Signaling Technology) and Granzyme-B (anti-GZMB antibody, clone GrB-7, 1:20, Dako) were performed manually upon microwave or thermostat bath oven epitope retrieval in ethylenediamine tetra-acetic acid (EDTA) buffer (pH 8.00). Immunoreaction was revealed by using Novolink Polymer (Leica Microsystem) followed diaminobenzidine as chromogen and with hematoxylin as nuclear counterstain. For double immunostain, after completing the first immune reaction, the second was visualized using Mach 4 MR-AP (Biocare Medical), followed by Ferangie Blue.

### RNAscope

To localize CXCL10 positive cells, tissues were analyzed with RNAscope assay (Advanced Cell Diagnostics, Newark, CA, USA) using RNAscope 2.5 HD Assay-RED kit and Hs-CXCL10-C2 probe (Cat No. 311851-C2) recognizing the nt 2 to 1,115 of the CXCL10 reference sequence NM\_001565. The sections from

**TABLE 1** | Clinicopathological features of the entire cohort of patients.

Patient characteristics		All	HGSC	CCC	EC
		n. (%)	n. (%)	n. (%)	n. (%)
<b>All</b>		97 (100)	59 (61)	18 (19)	20 (21)
<b>Age</b>	median (IQR)	58 (49–69)	61 (49–70)	56 (49–68.25)	53.5 (46–60)
<b>Menopause</b>	no	31 (32)	16 (27)	6 (33)	9 (45)
	yes	64 (66)	41 (69)	12 (67)	11 (55)
	NA	2 (2)	2 (3)	0 (0)	0 (0)
<b>FIGO Stage</b>	I–II	37 (38)	7 (12)	13 (72)	17 (85)
	III–IV	60 (62)	52 (88)	5 (28)	3 (15)
<b>Residual tumor</b>	No	52 (54)	18 (31)	15 (83)	20 (100)
	Yes	44 (45)	41 (69)	3 (17)	0 (0)
	NA	1 (1)	0 (0)	0 (0)	0 (0)
<b>Peritoneal cytology</b>	negative	38 (39)	12 (20)	11 (61)	15 (75)
	positive	55 (57)	47 (80)	6 (33)	3 (15)
	NA	4 (4)	0 (0)	1 (6)	2 (10)
<b>Chemotherapy response</b>	not response/partial	16 (16)	12 (20)	4 (22)	0 (0)
	complete	77 (79)	46 (78)	14 (78)	17 (85)
	NA	4 (4)	1 (2)	0 (0)	3 (15)
<b>Platinum sensitivity</b>	resistant	15 (15)	15 (25)	0 (0)	0 (0)
	partial sensitive	16 (16)	9 (15)	6 (33)	1 (5)
	sensitive	62 (64)	34 (58)	12 (67)	16 (80)
	NA	4 (4)	1 (2)	0 (0)	3 (15)
<b>Platinum re-eligibility</b>	no	19 (32)	19 (32)	–	–
	yes	39 (66)	39 (66)	–	–
	NA	1 (2)	1 (2)	–	–
<b>CD3 (cells/mm<sup>2</sup>)</b>	$\mu_g$	97	130	42	86
<b>CD163 (cells/mm<sup>2</sup>)</b>	$\mu_g$	365	446	285	253

HGSC, High-Grade Serous Carcinoma; CCC, Clear Cell Carcinoma; EC, Endometrioid Carcinoma; IQR, interquartile range; NA, not available;  $\mu_g$ , geometric mean.

fixed human tissue blocks were treated following the manufacturer's instructions. Briefly, freshly cut 3  $\mu$ m sections were deparaffinized in xylene and treated with the peroxidase block solution for 10 min at room temperature followed by the retrieval solution for 15 min at 98°C and by protease plus at 40°C for 30 min. Control probes included Hs-POLR2a-C2 (Cat No. 310451) and DapB-C2 (Cat No. 310043-C2). The hybridization was performed for 2 h at 40°C. The signal was revealed using RNAscope 2.5 HD Detection Reagent and FAST RED. Combined RNAscope and immunohistochemistry (for CD163, IRF1, Phospho-STAT1, CSFR1 and TREM2) were used to identify the cellular source of CXCL10. To this end, CXCL10 detection by RNAscope was followed by immunoreaction was visualized using Novolink Polymer (Leica Microsystems) followed by DAB or using Mach 4 MR-AP (Biocare Medical) followed by Ferangi Blue (Biocare Medical).

### Digital Image Analysis

Cell density of selected immune populations was analyzed using digital microscopy. The absolute cell count was quantified automatically using a custom-programmed script in Cognition

Network Language based on the Definiens Cognition Network Technology platform (Definiens AG, Munich, Germany). Briefly, CD3, CD163, and BDCA2 stained slides were digitalized using an Aperio ScanScope CS Slide Scanner (Aperio Technologies, Leica Biosystem, New Castle Ltd, UK) at 40 $\times$  magnification and analyzed using Tissue Studio 2.0 (Definiens AG). The quantitative scoring algorithm was customized using commercially available templates (**Supplementary Figure S1**). The image analysis pipeline comprised segmentation of nucleus objects and cell classification based on a pre-trained decision tree, according to staining intensity. Immune cell counts were expressed as the number of positive cells/mm<sup>2</sup> of ovarian cancer area.

### RNA Extraction and Gene Expression Analysis

A custom immune signature of 105 genes, selected on the basis of a PubMed literature search, was devised for the digital transcript counting, including targets for innate and adaptive immunity, co-stimulatory or immune effector molecules, and chemokines with their corresponding receptors (**Supplementary Table S2**).



A representative formalin-fixed and paraffin-embedded (FFPE) tumor block was retrieved from the biobank. Tissue was cut into 10/20  $\mu\text{m}$  sections and treated with Deparaffinization Solution (QIAGEN). RNA was extracted using Qiagen RNeasy FFPE kit (QIAGEN). Total RNA concentration and proteins contamination were determined by a Nanodrop spectrophotometer (Nanodrop Technologies, Ambion, Waltham, MA, USA). Quality of RNA was monitored using Agilent 2100 Bioanalyser System (AGILENT). Total RNA (100 ng) was assayed on a nCounter platform using NanoString technology (NanoString, Seattle, WA), testing the whole set of 105 endogenous genes, five housekeeping genes, six ERCC (External RNA Control Consortium) positive controls and eight ERCC negative controls (**Supplementary Table S2**). Raw mRNA counts were normalized applying a sample-specific correction factor to all the target probes per manufacturer's recommendations (technical normalization with Positive Controls Normalization spiked in every assay and biological normalization using housekeeping genes). The resulting normalized counts were used in downstream analyses. Pearson correlation analysis between log<sub>2</sub> IHC densities and log<sub>2</sub> mRNA Nanostring normalized counts were performed by Hommel correction for multiple comparisons deriving the OC-IS<sup>30</sup> Immune signature. A penalized linear ridge regression was applied to the Z-scores OC-IS<sup>30</sup> gene expression to weight the signature for its application in external datasets. For the Nanostring data heatmaps, the above values were turned into Z-scores. For Nanostring gene expression analysis, normalization and differential expression (DE) were performed with Nanostring nSolver™ 4.0 (Nanostring MAN-C0019-08), with Nanostring Advanced Analysis Module 2.0 plugin (Nanostring MAN-10,030-03) following the Nanostring Gene Expression Data Analysis Guidelines (Nanostring MAN-C0011-04).

### External Cohort Validation (TCGA)

For external cohort *in-silico* analysis, publicly available HGSC data from The Cancer Genome Atlas [TCGA-OV, N = 312 (6)] have been considered. Records of cases with full annotation on tumor stage, survival data, mutational status of BRCA1 and BRCA2 genes (both germline and somatic) and tumor mutational burden (TMB) were retrieved through the Computational Biology Center Portal (cBio): <http://www.cbioportal.org/> and downloaded on 15th Feb 2020. Data of mRNA expression profile (TCGA\_eset) were downloaded through the curated OvarianData v.1.24.0 R package (16)). The TCGA dataset was investigated computing the OC-IS<sup>30</sup> Immune signature and the whole immune fraction applying CIBERSORTx (17) using a signature matrix (18) able to compute the global immune transcriptome. Raw counts for primary solid tumor samples of further eight TCGA projects (TCGA-BLCA, TCGA-BRCA, TCGA-COAD, TCGA-HNSC, TCGA-LUAD, TCGA-LUSC, TCGA-SKCM, and TCGA-UCEC) were downloaded from GDC Legacy Archive (hg19) using TCGAbiolinks R/Bioconductor package. The FFPE samples were removed. Normalized expression levels, by upper quartile normalization measured in RSEM were obtained. Overall stage was included as

clinical variables and 4,496 cases, including the OV dataset, were available for the analysis.

### Generation of Human Monocyte-Derived M $\phi$

PBMCs were obtained from buffy coats of healthy volunteer blood donors (courtesy of the Centro Trasfusionale, ASST Spedali Civili, Brescia) by Ficoll-Paque (GE Healthcare, Milano, Italy) density gradient centrifugation at 360 $\times$ g for 30 min. Peripheral blood CD14<sup>+</sup> monocytes were magnetically sorted with human Pan Monocyte Isolation Kit (Cat. No. 130-096-537, Miltenyi Biotec, Bergisch Gladbach, Germany) following manufacturer's instructions. Isolated monocytes ( $7 \times 10^5$  cells/ml) were seeded in RPMI 1640 medium (Cat. No. 1-41-F01-I Bioconcept, Allschwil, Swiss) supplemented with 10% FBS (Biochrom GmbH, Berlin, Germany), GlutaMAX™-I (Cat. No. 35050-038, Life Technologies, Carlsbad, CA), 20 U/ml penicillin, 20  $\mu\text{g}/\text{ml}$  streptomycin (Cat. No. 15070-063, Life Technologies, Carlsbad, CA). After overnight culture, non-adherent cells were removed by washing with DPBS (Cat. No. 14190-094, Life Technologies, Carlsbad, CA) and adherent monocytes were cultured over 7 days in the presence of 100 ng/ml human M-CSF premium grade (Cat. No. 130-096-489, Miltenyi Biotec) to generate macrophages (M0). The medium was not replaced throughout the culture period. Macrophages polarization was obtained by replacing culture medium with fresh RPMI 1640 medium supplemented with 10% FBS and containing 50 ng/ml recombinant human IFN- $\gamma$  (Cat. No. 300-02, Peprotech, London, UK) or 20 ng/ml recombinant human IFN- $\gamma$  (Peprotech) + 100 ng/ml LPS from *Escherichia coli* O55:B5 (Cat. No. L6529 Sigma-Aldrich, St. Louis, MO) (for M1 polarization) or 20 ng/ml Recombinant human IL-4 premium-grade (Cat. No. 130-093-920, Miltenyi Biotec) or 20 ng/ml Recombinant human IL-10 research-grade (Cat. No. 130-093-948, Miltenyi Biotec) (for M2 polarization) for 4 or 18 h. M0 cultured with fresh medium without polarization cytokines was used as control.

### Cell-Block Preparation

Cell suspensions of macrophages were centrifuged for 10 min at 3,000 rpm. A solution of plasma (100  $\mu\text{l}$ , kindly provided by Centro Trasfusionale, ASST Spedali Civili, Brescia) and HemosIL8 RecombiPlasTin 2G (200  $\mu\text{l}$ , Instrumentation Laboratory, Bedford Ma, USA, Cat. No. 0020003050) (1:2) were added to cell pellets, mixed until the formation of a clot, then placed into a labeled cassette. The specimen was fixed in 10% formalin for 1 h followed by paraffin inclusion.

### qRT-PCR

IL-6, CXCL10 and COX2 mRNA targets were quantified by reverse transcription-polymerase chain reaction (qRT-PCR) assay using the Vii-A 7 Real-Time PCR System (Applied Biosystems, Thermo Fisher Scientific, Waltham, MA, USA). Total RNA was purified from M0, M1 and M2 macrophages using the RNeasy® Mini Kit (Cat. No. 74104, Qiagen). The cDNA was synthesized by iScript gDNA cDNA Synthesis kit (Cat. No. 1725035, Bio-Rad Laboratories Inc., Hercules, CA, U.S.A.) from 150 ng of total RNA, in a total volume of 20  $\mu\text{l}$ .

About 1  $\mu$ l of the cDNA synthesis reaction was used for the specific amplification of the target transcripts. The Ribosomal Protein S18 (RPS18) transcript was used as normalization control. The qPCR was performed in a total volume of 10  $\mu$ l with TaqMan<sup>®</sup> Universal Master Mix II (Cat. No. 4369016, Applied Biosystems, Thermo Fisher Scientific) and the Gene Expression Assay (**Supplementary Table S3**). The threshold cycle (Ct) was determined for each sample and quantification was performed using the comparative Ct method.  $\Delta$ Ct was derived as  $Ct_{\text{Target}} - Ct_{\text{Housekeeping}}$  and considered for statistical analysis.

### Western Blotting

The intracellular levels of targets and actin proteins were determined by western blotting. Cells were washed, re-suspended in RIPA lysis buffer (Cat. No. 89900, Pierce, Thermo Fischer Scientific) with a Protease Inhibitor Cocktail (Cat. No. 78440, Sigma-Aldrich) and sodium orthovanadate ( $\text{Na}_3\text{VO}_4$ ) (Cat. No. 450243, Sigma-Aldrich), and kept in ice for 10 min. After 20 min centrifugation at 12,000 $\times$ g at 4°C, the supernatant was collected and protein concentration determined by Bradford assay. A total of 20  $\mu$ g of proteins was loaded on 4–12% NuPAGE<sup>®</sup> Bis-Tris Mini Gels (Cat. No. NP0335, Invitrogen<sup>™</sup>, Thermo Fisher Scientific) under reducing condition and transferred onto a PVDF membrane (Cat. No. LC2007, Invitrogen<sup>™</sup>, Thermo Fisher Scientific). Membranes were incubated in the blocking solution 5% BSA (Cat. No. A3059, Sigma-Aldrich) in T-TBS (TBS, 0.05% Tween 20) (Cat. No. 28360, Invitrogen<sup>™</sup>, Thermo Fisher Scientific) for 1 h at room temperature; subsequently membranes were exposed to primary antibodies diluted in blocking solution, for 16 h at 4°C. Primary antibodies are listed in **Supplementary Table S4**. After washing in TBS-T, the blots were incubated with the appropriate secondary antibody (anti-Rabbit Cat. No. sc-2077 Santa Cruz Biotechnology, Inc., Dallas, TX, USA), conjugated with horseradish peroxidase for 1 h at room temperature. Immunoreactive proteins were detected by SuperSignal<sup>™</sup> West Pico Chemiluminescent Substrate (Cat. No. 34577, Thermo Fisher Scientific) and visualized by autoradiography.

### Statistical Analysis

For histological, clinical, and pathological analysis the qualitative variables were described as absolute and relative frequencies. We considered overall survival (OS) and progression-free survival (PFS). In the absence of any events, survivals were censored at last follow-up visit. Qualitative variables were compared between groups using Chi-square test, quantitative one by t-test, Mann-Whitney test or ANOVA, and post-hoc pairwise comparisons as appropriate. By evaluation of Q-Q plots and applying the Shapiro-Wilk Test immune cells densities' distribution followed a log-normal distribution; for statistical analysis  $\log_2$  values of densities were used. Median values of continuous variables' distributions were set as cut-offs for dichotomization. Univariable and multivariable analyses were performed with Cox proportional hazard models. For all analyses the proportional hazards assumption was tested and verified; estimates were reported as hazard ratio (H.R) with 95% Confidence Intervals (CI). In all analyses a two-tailed P value <0.05 was considered

significant. GraphPad Prism (San Diego, CA, USA), and R (version 3.6.2) were used for statistical analysis.

### scRNAseq Data Analysis

Processing of the Pan-Cancer Blueprint dataset. We downloaded the raw datasets and selected the myeloid cells dataset (using the article annotation with the mention "Myeloid" in the cell type metadata, 37,334 cells) of Qian et al. (19) from a web server (<http://blueprint.lambrechtslab.org>). Cells were merged using the Canonical Correlation Analysis (CCA) and the Mutual Nearest Neighbors (MNN) algorithms and we selected the 5,000 most variable genes (following the Seurat 3 pipeline). We next performed Louvain graph-based clustering. At the resolution 0.6 we obtained 27 clusters. Eleven clusters (c1, 2, 3, 4, 5, 9, 10, 12, 18, 19, 26) expressed high levels of CD68 and were labeled as macrophages.

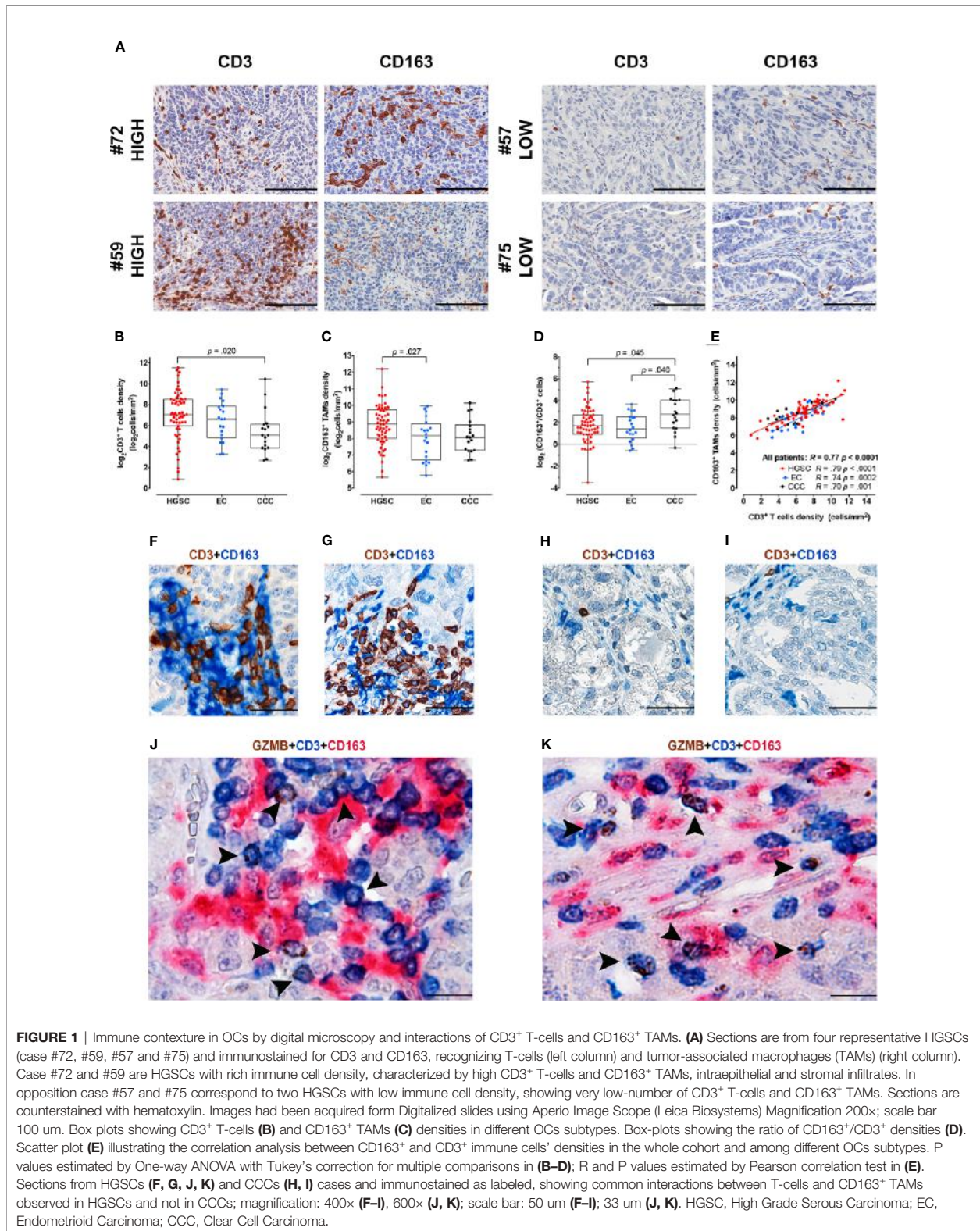
## RESULTS

### Heterogeneity of T-Cells and TAMs Immune Contexture in OC Subtypes

By digital image analysis on stained sections, we measured T-cells and M $\phi$  immune-contexture in a retrospective cohort of OC (n = 97) and explored associations (**Figures 1A–I**). To this end, serial sections from a representative tumor area of primary OC obtained from a single tissue block were stained for CD3 and CD163. The density of T-cells resulted extremely variable ranging from 2 to 2,967 cells/mm<sup>2</sup> (mean 283 cells/mm<sup>2</sup>, median 106 cells/mm<sup>2</sup>, IQR 34–311 cells/mm<sup>2</sup>); similarly, CD163<sup>+</sup> TAMs counts varied from 51 to 4,714 cells/mm<sup>2</sup> (mean 529 cells/mm<sup>2</sup>, median 372 cells/mm<sup>2</sup>, IQR 224–704 cells/mm<sup>2</sup>). The full dataset is reported in **Supplementary Table S1**. Both densities' distribution followed a log-normal distribution,  $\log_2$  values of densities were thus used for statistical analysis (**Supplementary Figure S2**). Subgroup analysis among OCs with different histology indicates that HGSCs are significantly more infiltrated by CD3 T-cells, compared to CCCs (p = .02, **Figure 1B**) and by CD163<sup>+</sup> TAMs, compared to ECs (p = .027, **Figure 1C**). Moreover, the TAMs/T-cells ratio resulted significantly higher in the CCC subtype compared to HGSC (p = .045) or to EC subtypes (p = .04, **Figure 1D**). Both immune populations resulted highly correlated (R = .77, p < .0001) also when considering the OC subgroups HGSC (R = .79, p < .0001), CCC (R = .74, p = .0002) and EC (R = .70, p = .001) respectively (**Figure 1E**). As indicated by double and triple stain for CD3, GZMB and CD163, T-cells/TAM interactions were commonly observed in HGSCs (**Figures 1F, G, J, K**) but not in CCCs (**Figures 1H, I**). This analysis highlights differences in immune contexture between OCs subtypes, with immune infiltrated HGSC and T-cell poor CCC positioned at the extreme of a functional spectrum.

### T-Cells and TAMs Immune-Contexture Predict Outcome in HGSC

We focused our clinical correlation analysis on HGSCs, the more represented OC subtype (**Table 1**). The mean  $\log_2$  CD3<sup>+</sup> T-cells





density was significantly higher in patients with low-risk features, such as Stages I–II ( $p = 0.03$ ) and negative peritoneal cytology ( $p = 0.016$ ). Moreover, a higher immune cells infiltrate was associated with a better response to first-line treatment. Specifically, a complete response to chemotherapy was associated with higher CD3<sup>+</sup> T-cells density ( $p = 0.04$ ). Moreover, platinum sensitivity and platinum re-eligibility were associated either with higher CD3<sup>+</sup> T-cell density ( $p = 0.008$ ,  $p = 0.009$ ) and CD163<sup>+</sup> TAM density ( $p = 0.028$ ,  $p = 0.031$ ). We further expanded this analysis by evaluating the relevance of the immune contexture in terms of clinical outcome. To this end, subgroups were defined using the median values of each immune cell densities' distributions as cut-offs (CD3<sup>Hi</sup> vs CD3<sup>Low</sup> and CD163<sup>Hi</sup> vs CD163<sup>Lo</sup>). The univariate survival analysis, reported in **Supplementary Table S5**, confirmed, both for OS and PFS respectively, the association with worse prognosis of well-known clinical variables as higher Stages III–IV (H.R. 10.56,  $p = .02$ ; H.R. 6.63,  $p = .009$ ), macroscopic residual tumor (H.R. 7.15,  $p < .001$ ; H.R. 2.89,  $p = .002$ ), and positive peritoneal cytology (H.R. 4.25,  $p < .007$ ; H.R. 4.41,  $p = .002$ ). The CD163<sup>Hi</sup> group experienced a better OS (H.R. 0.48,  $p = .019$ , **Figure 2A**) and better PFS (H.R. 0.56,  $p = .042$ , **Supplementary Figure S3A**); besides, the CD3<sup>Hi</sup> had a better OS (H.R. 0.35,  $p = .001$ , **Figure 2B** and **Supplementary Figure S3B**).

As both T-cells and TAMs were associated with favorable prognosis and were positively correlated, we further expanded our analysis by identifying three additional groups, namely the Immunoscore<sup>LoLo</sup> (CD3<sup>Lo</sup> and CD163<sup>Lo</sup>), the Immunoscore<sup>HiLo/LoHi</sup> (CD3<sup>Hi</sup> and CD163<sup>Lo</sup>, or CD3<sup>Lo</sup> and CD163<sup>Hi</sup>) and the Immunoscore<sup>HiHi</sup> (CD3<sup>Hi</sup> and CD163<sup>Hi</sup>) groups, as shown in the Treemap (**Figure 2C**). A higher Immunoscore was associated with both chemotherapy response ( $p = 0.04$ ) and platinum sensitivity ( $p = 0.03$ , **Figures 2C, D**). In addition, univariate survival analysis showed a better OS (Immunoscore<sup>HiLo/LoHi</sup>: H.R. 0.17,  $p < .001$ ; Immunoscore<sup>HiHi</sup>: H.R. 0.28,  $p < .001$ ; **Figure 2E**) and PFS (Immunoscore<sup>HiLo/LoHi</sup>: H.R. 0.23,  $p < .001$ ; Immunoscore<sup>HiHi</sup>: H.R. 0.41,  $p = 0.005$ ; **Supplementary Figure S3C** and **Supplementary Table S5**) for higher immunoscore compared to Immunoscore<sup>LoLo</sup> as reference group. In term of OS, the multivariable survival analysis (**Figure 2F**) confirmed a favorable prognosis for Immunoscore<sup>HiHi</sup> (H.R. 0.35,  $p = 0.008$ ) compared to Immunoscore<sup>LoLo</sup> OCs; moreover, a better PFS was observed for Immunoscore<sup>HiLo/LoHi</sup> (H.R. 0.40,  $p = 0.031$ ) and Immunoscore<sup>HiHi</sup> (H.R. 0.49,  $p = .037$ ) groups compared to Immunoscore<sup>LoLo</sup> OCs (**Supplementary Figure S3D**). The immunoscore variable was even more relevant than others clinical covariates as Stage or positive peritoneal cytology that lost the statistical significance in the multivariable model.

### OC-IS<sup>30</sup> Immune Signature Marks Immune Infiltrated OCs

We further expanded our findings by measuring the expression of a custom immune signature in the OC cohort using Nanostring technology. The custom immune signature included one-hundred and five targets covering genes relevant for innate and adaptive immunity, effector molecules, and

chemokine with their corresponding receptors (**Supplementary Table S2**). Eighty-one cases were deemed suitable for Nanostring-based gene expression analysis (GEA). A set of healthy ovarian tissue ( $n = 12$ ) was included as control group. Differential expression analysis revealed a significant up-regulation (adj.  $p$ -values  $< 0.05$ ) of a large set of targets in OCs compared to controls (**Supplementary Figure S4A**). A supervised analysis based on histology subgroups revealed lack of significant differences for most of the targets (**Supplementary Figure S4B**), with the exception of four targets including CSF1, the latter significantly higher in HGSC and correlating with a high density of CD163<sup>+</sup> TAMs (**Supplementary Table S6**). To extend the finding obtained by digital microscopy analysis, we correlated the GEA of OCs cases with the corresponding T-cell and TAMs density. Of technical relevance, among all 105 genes of the tested signature, none was inversely correlated with immune cells densities (**Figure 3A**). In addition, a set of thirty genes (from here referred as OC-IS<sup>30</sup>) (**Supplementary Table S6**) showed a significant direct positive correlation with CD3<sup>+</sup> T-cells or CD163<sup>+</sup> TAMs tissue densities (adj.  $p$ -value  $< 0.05$ ) (**Figures 3B–D**). This finding was confirmed and extended by applying CIBERSORTx (17) to the external OV-TCGA dataset using a signature matrix (18) able to compute T-cells and macrophages (**Figure 3E**). Of note, the OC-IS<sup>30</sup> gene set contained targets relevant to T-cell attracting chemokines (CXCL10, CXCL9, CXCL11, and CXCL16), immune effector function (GZMA, GNLY, PRF1, GZMB, GZMH), M $\phi$  biology (CSF1, CSF1R, CCL2, CCL4, and CD163), immune checkpoints (IDO1, CTLA4, CD274, PDCD1LG2, and PDCD1) and interferon signature (CXCL10, CXCL9, CXCL11, CXCL16, CD274, IDO1, STAT1, MX1, OAS1). The latter finding suggest an ongoing interferon response in immune infiltrated OCs; based on very low density of PDCs infiltration in primary OC (**Supplementary Figure S5**), our data are more consistent with an IFN $\gamma$  signature.

### OC-IS<sup>30</sup> Predicts Favorable Outcome in HGSC and Across Human Cancer Types

The clinical significance of OC-IS<sup>30</sup> was tested in the external OV-TCGA dataset (6) containing 312 HGSCs annotated in term of clinical and molecular finding (Stage, Overall Survival, mutational status of *BRCA1* and *BRCA2* genes, and tumor mutational burden (TMB)). OC-IS<sup>30</sup> expression was not significantly associated with tumor stage ( $p = 0.09$ ), *BRCA1-2* mutations ( $p = 0.098$ ) or TMB ( $p = 0.08$ ), as reported in **Supplementary Figures S6A–C**. For the distribution of OC-IS<sup>30</sup> score the median value was set as cut-off point for identification of rich (<sup>Hi</sup>) or poor (<sup>Lo</sup>) immune represented group. The <sup>Hi</sup>OC-IS<sup>30</sup> group was associated with a better OS at univariable analysis (H.R. 0.68, CI<sub>95%</sub> 0.50–0.91,  $p = 0.01$ , **Figure 4A**), as well as using a multivariable model including well known prognosticators (**Figure 4B**). Specifically, the multivariable analysis confirmed the favorable prognostic significance of OC-IS<sup>30-Hi</sup> (H.R. 0.72,  $p = 0.036$ ) independent from *BRCA1-2* mutations (H.R. 0.55,  $p = 0.004$ ) and TMB (H.R. 0.72,  $p = 0.01$ ); the positive combined effect of <sup>Hi</sup>OC-IS<sup>30</sup> and

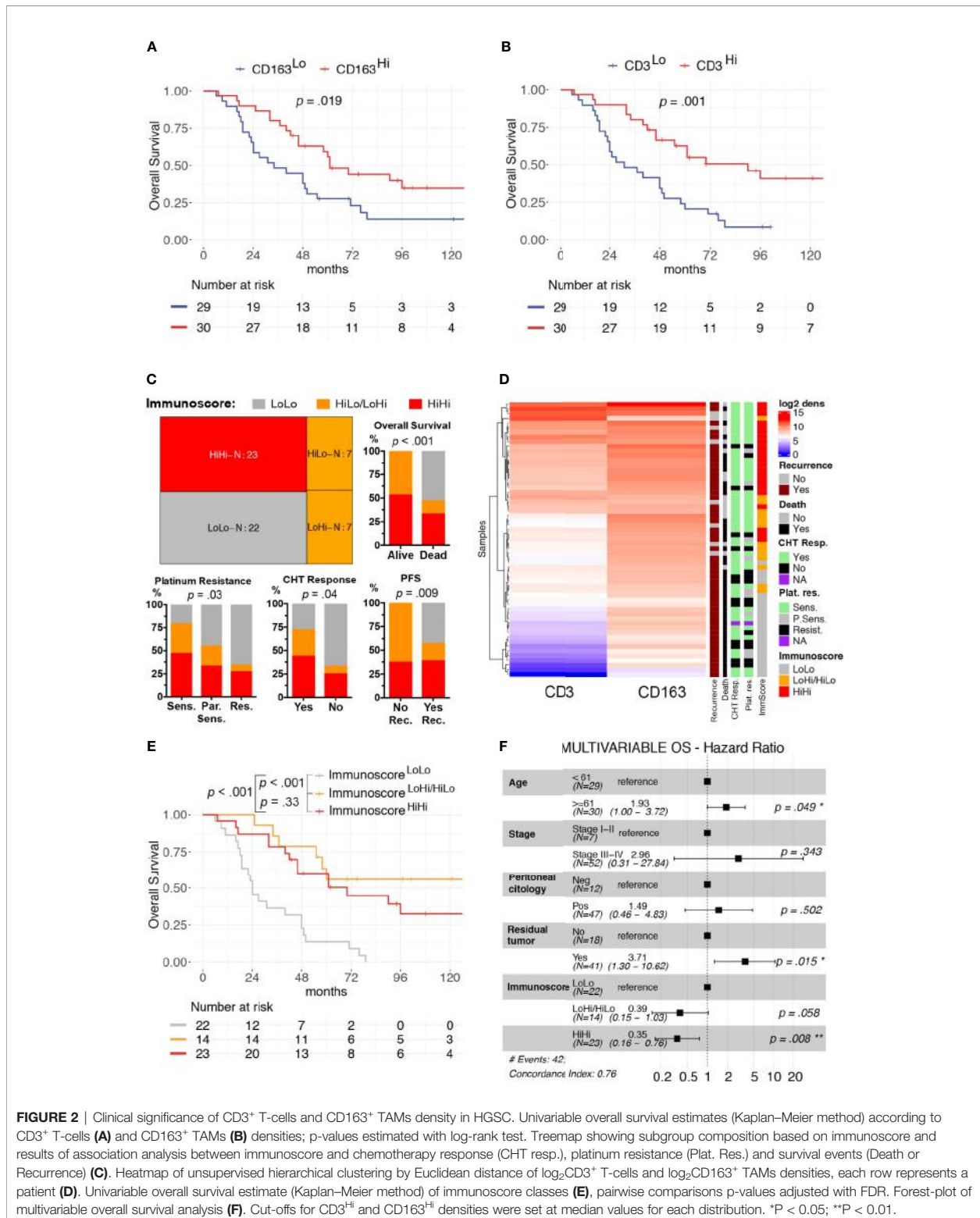


**FIGURE 2** | Clinical significance of CD3<sup>+</sup> T-cells and CD163<sup>+</sup> TAMs density in HGSC. Univariable overall survival estimates (Kaplan–Meier method) according to CD3<sup>+</sup> T-cells (A) and CD163<sup>+</sup> TAMs (B) densities; p-values estimated with log-rank test. Treemap showing subgroup composition based on immunoscore and results of association analysis between immunoscore and chemotherapy response (CHT resp.), platinum resistance (Plat. Res.) and survival events (Death or Recurrence) (C). Heatmap of unsupervised hierarchical clustering by Euclidean distance of log<sub>2</sub>CD3<sup>+</sup> T-cells and log<sub>2</sub>CD163<sup>+</sup> TAMs densities, each row represents a patient (D). Univariable overall survival estimate (Kaplan–Meier method) of immunoscore classes (E), pairwise comparisons p-values adjusted with FDR. Forest-plot of multivariable overall survival analysis (F). Cut-offs for CD3<sup>+</sup> and CD163<sup>+</sup> densities were set at median values for each distribution. \*P < 0.05; \*\*P < 0.01.

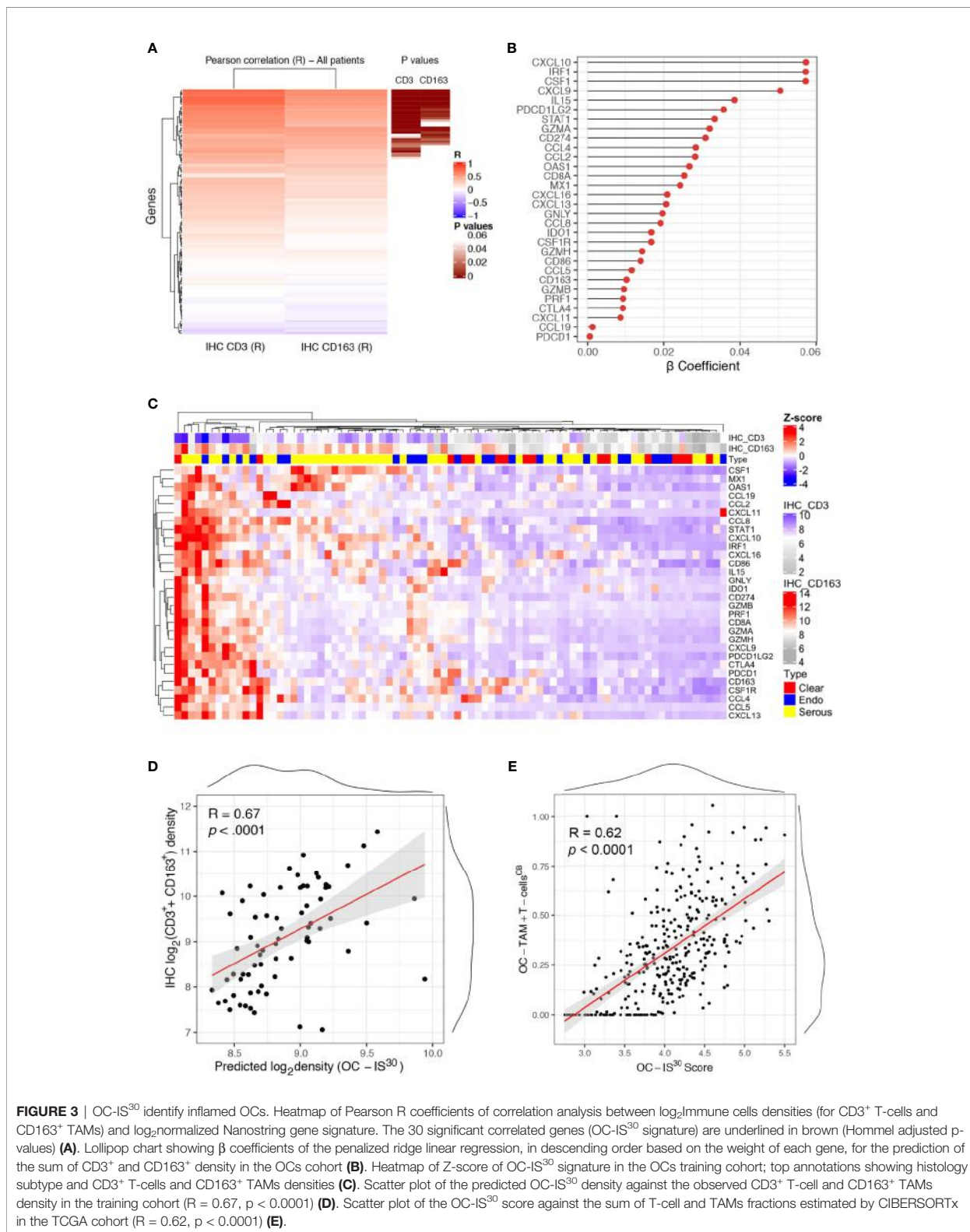


**FIGURE 3** | OC-IS<sup>30</sup> identify inflamed OCs. Heatmap of Pearson R coefficients of correlation analysis between log<sub>2</sub> Immune cells densities (for CD3<sup>+</sup> T-cells and CD163<sup>+</sup> TAMs) and log<sub>2</sub> normalized Nanostring gene signature. The 30 significant correlated genes (OC-IS<sup>30</sup> signature) are underlined in brown (Hommel adjusted p-values) (A). Lollipop chart showing  $\beta$  coefficients of the penalized ridge linear regression, in descending order based on the weight of each gene, for the prediction of the sum of CD3<sup>+</sup> and CD163<sup>+</sup> density in the OCs cohort (B). Heatmap of Z-score of OC-IS<sup>30</sup> signature in the OCs training cohort; top annotations showing histology subtype and CD3<sup>+</sup> T-cells and CD163<sup>+</sup> TAMs densities (C). Scatter plot of the predicted OC-IS<sup>30</sup> density against the observed CD3<sup>+</sup> T-cell and CD163<sup>+</sup> TAMs density in the training cohort ( $R = 0.67$ ,  $p < 0.0001$ ) (D). Scatter plot of the OC-IS<sup>30</sup> score against the sum of T-cell and TAMs fractions estimated by CIBERSORTx in the TCGA cohort ( $R = 0.62$ ,  $p < 0.0001$ ) (E).

BRCA1-2 mutations is reported by Kaplan–Meier curves in **Figure 4C**. By exploring the TCGA datasets, we expanded our analysis across different cancers and found that the OC- $IS^{30}$  predict favorable outcome independent from Overall Stage and cancer site (H.R. 0.85,  $CI_{95\%}$  0.79–0.91,  $p < 0.0001$ , **Figures 4D, E**).

### M1-Polarized TAMs Hallmark Immune-Infiltrated HGSC But Not T-Cell Poor CCC

Data from the literature (20) and from this study using OC- $IS^{30}$  indicate a clinical benefit of the IFN $\gamma$  response in OCs. The observed effect might derive from an IFN $\gamma$  response by tumor cells or host immune cells, particularly TAM. To answer this question at the single-cell level we tested the expression and cellular localization of a set of M1- and M2-type macrophages (M $\phi$ ) markers including IRF1, IRF4, CD163, and pSTAT1Y701 by immunohistochemistry. To validate these markers for formalin-fixed cells, we initially monitored their expression and cellular localization on cell-block sections of monocyte-derived macrophages. To this end, we generated monocyte-derived (M0) M $\phi$  and polarized them to M1-type (M1<sup>IFN $\gamma$</sup>  and M1<sup>IFN $\gamma$ +LPS</sup>) and M2-type (M2<sup>IL-4</sup> and M2<sup>IL-10</sup>) M $\phi$ , as also confirmed by the expression of IL6 and COX2 (**Supplementary Figure S7A, B**). We found that IRF1 and pSTAT1Y701 induction and nuclear localization were strictly coupled with M1 polarization, being limited (IRF1) or totally absent (pSTAT1Y701) in M2<sup>IL-4</sup> and M2<sup>IL-10</sup> M $\phi$  (**Supplementary Figures S7C, D**). On the contrary, IRF4 results strongly modulated in M1<sup>IFN $\gamma$ +LPS</sup> and M2<sup>IL-4</sup> M $\phi$  with a basal level of nuclear expression also in M1<sup>IFN $\gamma$</sup>  M $\phi$  (**Supplementary Figure S7E**). CD163 is induced in M $\phi$  generated by IL-10- and CSF1, as measured by flow cytometry (21), and for this reason it has been considered an M2-type M $\phi$  marker. We found that its cytoplasmic expression is, however, easily detectable by IHC in all polarization conditions (M0, M1, and M2) (**Supplementary Figure S7C**), suggesting that CD163 expression is promiscuous in M $\phi$  populations and cannot be used as M2-specific marker by IHC.

We subsequently analyze <sup>Hi</sup>OC- $IS^{30}$ CD163<sup>Hi</sup> ( $n = 15$ ) and <sup>Lo</sup>OC- $IS^{30}$ CD163<sup>Lo</sup> ( $n = 4$ ) from the HGSC group. In OCs tissues, nuclear pSTAT1Y701 and IRF1 were detected in tumor cells and cells of the microenvironment (**Figure 5A**). Based on a three-tiered IHC score, we found a significant positive correlation between protein biomarkers and the corresponding mRNA level, as detected by Nanostring (**Figure 5B**). Moreover, by double stain for CD163, we could confirm nuclear reactivity for pSTAT1Y701 and IRF1 in a fraction of CD163<sup>+</sup> TAMs (**Figures 5C, D**). As a relevant tissue pattern, we could detect tumor areas of “inducible” pSTAT1Y701 and IRF1 expression containing clusters of positive tumor cells and TAMs (**Figures 5A, C**). By quantitative analysis, <sup>Hi</sup>OC- $IS^{30}$ CD163<sup>Hi</sup> cases were significantly enriched of IRF1<sup>+</sup> tumor cells ( $p = .0086$ ) and pSTAT1Y701<sup>+</sup> TAMs ( $p = .007$ ) compared to <sup>Lo</sup>OC- $IS^{30}$ CD163<sup>Lo</sup> (**Figures 5E, F**). This observation suggests an M1-type polarization of CD163<sup>+</sup> TAMs in immune-infiltrated OCs. We extended these findings to CCC ( $n = 10$ ), a subtype displaying poor

T-cells infiltration in our cohort. By double immunohistochemistry for pSTAT1Y701 and CD163, CCC resulted largely devoid on pSTAT1Y701<sup>+</sup> TAMs (mean  $\pm$  SD =  $1.6 \pm 2.0\%$ , **Figure 5D**). These observations highlight heterogeneity in M1-type polarization in OC subtypes with diverse T-cell contexture.

### M1-Type TAMs Produce CXCL10 and Co-Localize With T-Cells

Among IFN $\gamma$  targets, the chemokine CXCL10 has been shown to control T-cell recruitment into the tumor environment (22). We tested mRNA expression by using qPCR and RNAscope-based *in situ* hybridization. Both approaches demonstrate that only M1<sup>IFN $\gamma$</sup>  and M1<sup>IFN $\gamma$ +LPS</sup> were associated with high induction of CXCL10 transcript, whereas M0, M2<sup>IL-4</sup> and M2<sup>IL-10</sup> M $\phi$  resulted largely negative (**Supplementary Figures S7F–G**). This data was confirmed by RNAscope-based *in situ* hybridization of formalin-fixed cell-block preparation (**Supplementary Figure S7F**). On biopsies, we could subsequently detect more abundant CXCL10 transcript in <sup>Hi</sup>OC- $IS^{30}$ CD163<sup>Hi</sup> ( $n = 3$ ) cases compared to <sup>Lo</sup>OC- $IS^{30}$ CD163<sup>Lo</sup> ( $n = 3$ ) (**Figure 5G**). Moreover, also most CCCs ( $n = 10$ ) were largely devoid of CXCL10 stain (**Figure 5H**). By combining RNAscope with IHC we could confirm a M1 M $\phi$  identity of a fraction of CXCL10<sup>+</sup> cells, in addition to CXCL10<sup>+</sup> cancer cells (**Figure 5I**). The analysis of double stained sections from immune infiltrated <sup>Hi</sup>OC- $IS^{30}$ CD163<sup>Hi</sup> ( $n = 3$ ) revealed that areas containing CXCL10<sup>+</sup> macrophages are enriched of T-cells (**Figure 5I**). These findings confirmed that immune infiltrated <sup>Hi</sup>OC- $IS^{30}$ CD163<sup>Hi</sup> are enriched of M1-type M $\phi$ , producing the T-cell attracting chemokine CXCL10 and surrounded by CD3<sup>+</sup> T-cells.

### A Fraction of M1-Type M $\phi$ in OCs Co-Expresses CSF1R and TREM2

As illustrated in **Supplementary Figure S4B**, CSF1 mRNA resulted significantly higher in HGSC compared to other OCs, and its level correlated with a high density of CD163<sup>+</sup> TAMs (**Supplementary Table S6**), as also supported by *in vitro* findings documenting CD163 regulation by CSF1 (21). Moreover, CSF1R expression by Nanostring strongly correlates with CSF1R protein expression in OCs (**Figure 5B**). Previous studies have suggested expression of CSF1R on cancer cells in OCs (23), however, our findings clearly indicate that the expression is largely restricted to TAMs (**Figure 6A**). CSF1R blockade on TAMs has obtained some meaningful level of clinical efficacy in human cancer with high level of CSF1 (21). TAMs modulation by CSF1R blockade encompasses a range of biological activities from depletion to their reprogramming, the latter further amplified by CD40 agonist (24). <sup>Hi</sup>OC- $IS^{30}$ CD163<sup>Hi</sup> cases were significantly enriched in pSTAT1Y701<sup>+</sup> TAMs ( $p = .007$ ) as indicated in **Figures 5E, F**. By using double immunohistochemistry, we could detect a fraction CSF1R<sup>+</sup> TAMs expressing pSTAT1Y701, IRF1 and CXCL10 (**Figure 6B**). Accordingly, also M1 type M $\phi$  generated from peripheral blood monocytes resulted CSF1R<sup>+</sup> by IHC (**Figure 6C**). We have recently reported that TREM2 is selectively expressed on TAMs in various human cancer (25).



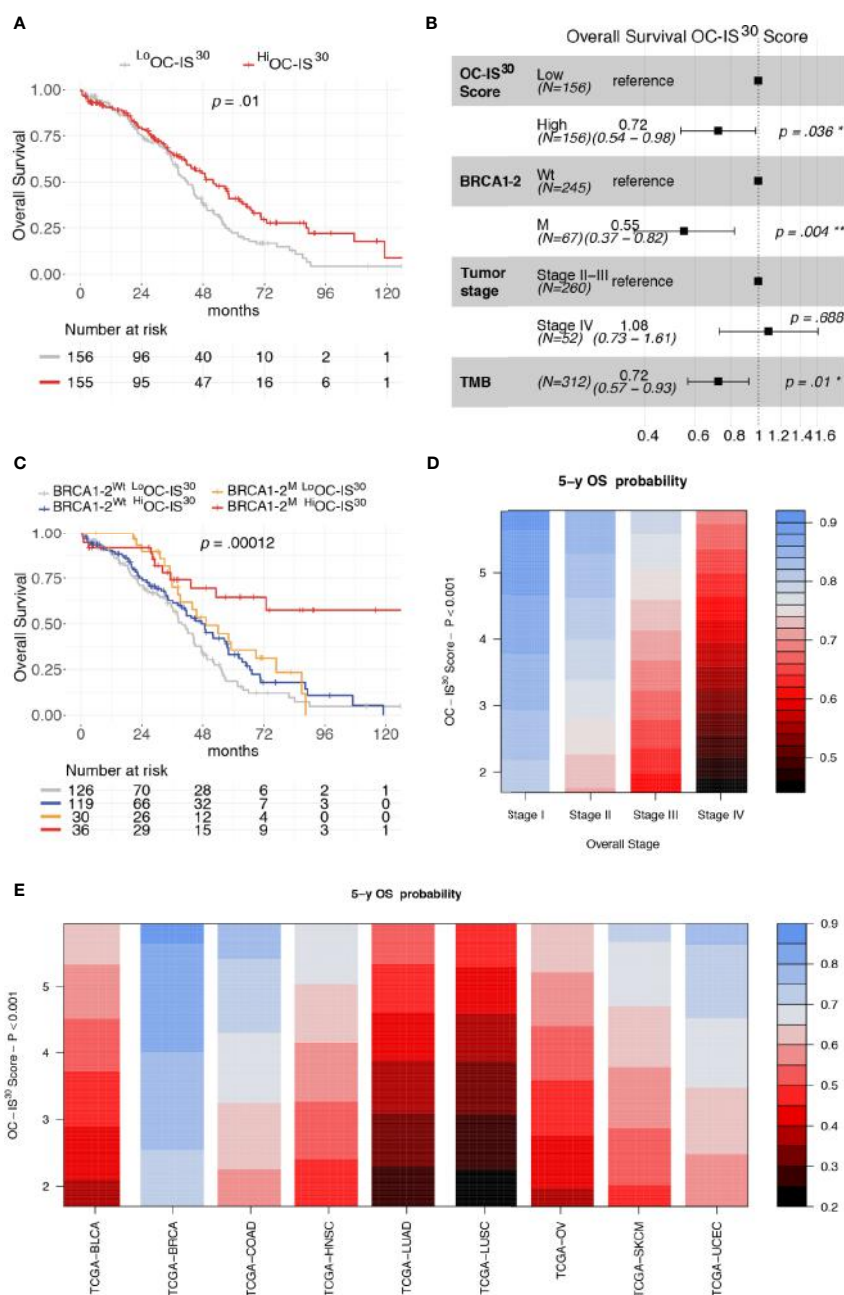


**FIGURE 4** | Prognostic significance of OC-IS<sup>30</sup> in the TCGA datasets. Prognostic significance of Hi OC-IS<sup>30</sup> group by univariable (A) and multivariable (B) overall survival analysis; Kaplan–Meier curves of the OC-IS<sup>30</sup> status combined with BRCA1 and BRCA2 mutational status (C). Contour plots from a multivariable Cox model analyzing samples from 9 TCGA datasets (N = 4,496) including the Overall Stage, the OC-IS<sup>30</sup> Score [weighted log(normalized gene expression+1) applying the coefficients defining the OC-IS<sup>30</sup> signature (Figure 3B)] and the tumor site showing the significant, independent and additive favorable prognostic significance (color gradient) of lower Stage (D) and higher OC-IS<sup>30</sup> score (E) across the different tumor sites. P values estimated by log-rank test in (C) and by Cox models in (A, B, D, E). BLCA, Bladder Urothelial Carcinoma; BRCA, Breast invasive carcinoma; COAD, Colon adenocarcinoma; HNSC, Head and Neck squamous cell carcinoma; LUAD, Lung adenocarcinoma; LUSC, Lung squamous cell carcinoma; OV, Ovarian serous high grade carcinoma; SKCM, Skin Cutaneous Melanoma; UCEC, Uterine Corpus Endometrial Carcinoma. \*P < 0.05; \*\*P < 0.01.

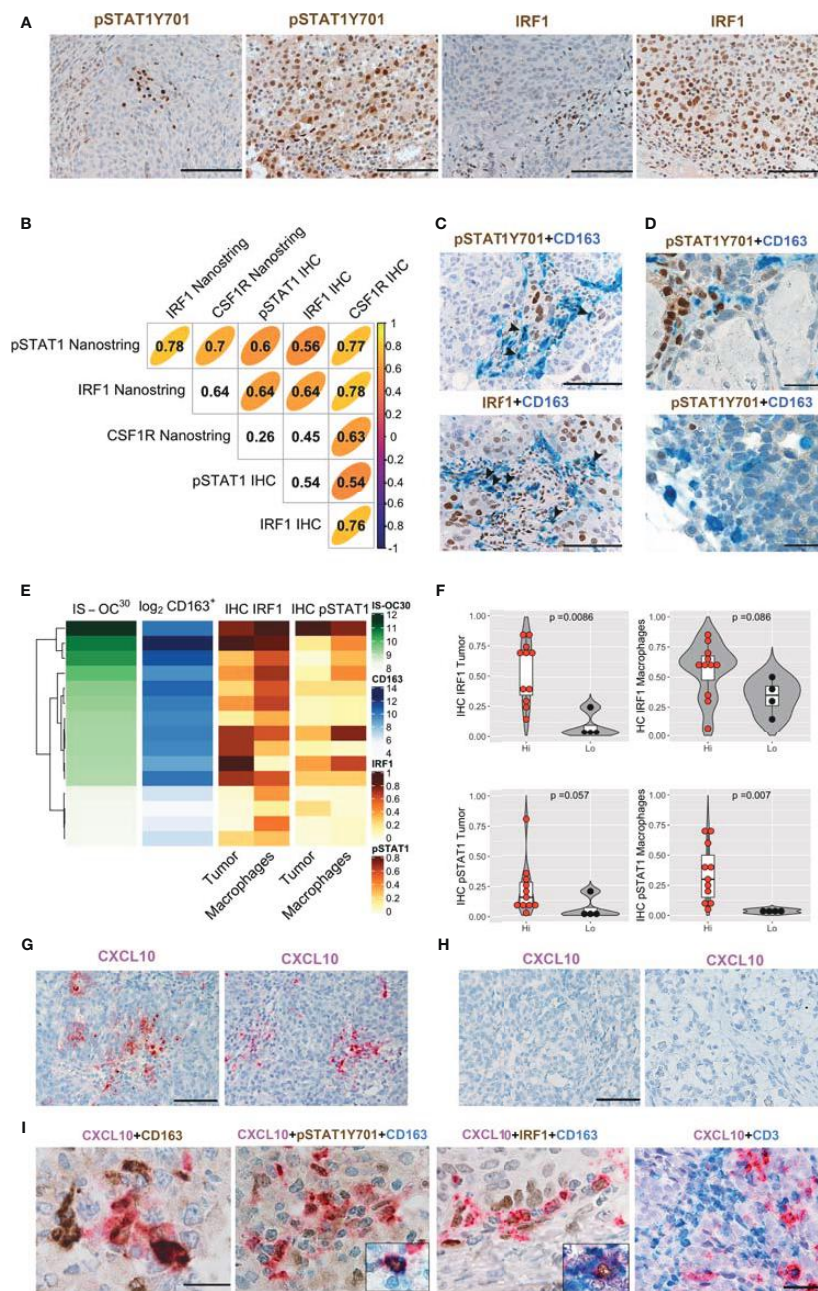


**FIGURE 5** | IFN $\gamma$  polarization on cancer cells and stromal M1 type macrophages (M $\phi$ ) in OCs. Sections from OCs cases and immunostained as labeled (**A**, **C**, **D**). Magnification 200 $\times$  (**A**, **C**; scale bar 100  $\mu$ m); magnification 400 $\times$  (**D**, scale bar 50  $\mu$ m). Different levels of pSTAT1Y701 and IRF1 expression in  $^{L}OC$ -IS $^{30}$ CD163 $^{-}$  and  $^{H}OC$ -IS $^{30}$ CD163 $^{H}$  HGSCs cases (**A**). Spearman correlogram of IRF1, pSTAT1Y701 and CSF1R in OCs by IHC and Nanostring (**B**). A fraction of HGSCs infiltrating CD163 $^{+}$  TAMs expresses pSTAT1Y701 and IRF1 (**C**). Sections of CCCs showing that this tumor histotype is largely devoid of pSTAT1Y701 $^{+}$  TAMs (**D**). Heatmap showing the IHC IRF1 and pSTAT1Y701 expression on different tissue compartments compared to the matched OC-IS $^{30}$  score and log $_{2}$ CD163 $^{+}$  density (**E**); Violin plots reporting the IHC IRF1 and pSTAT1Y701 expression in the  $^{H}OC$ -IS $^{30}$ CD163 $^{H}$  and  $^{L}OC$ -IS $^{30}$ CD163 $^{L}$  groups, p values estimated by Mann–Whitney test (**F**). (**G–I**) Sections from OCs immunostained or subjected to *in situ* hybridization as labeled; while CXCL10 is detected in  $^{H}OC$ -IS $^{30}$ CD163 $^{H}$  HGSCs (**G**) cases it is absent in a  $^{L}OC$ -IS $^{30}$ CD163 $^{L}$  CCCs cases (**H**). A fraction of CXCL10 $^{+}$  cells is confirmed to have a M1 M $\phi$  identity and areas containing CXCL10 $^{+}$  macrophages are enriched of T-cells (**I**). Magnification: (**G**, **H**) 200 $\times$  (scale bar 100  $\mu$ m) and (**I**) 600 $\times$  (scale bar 33  $\mu$ m, first three panels) and 400 $\times$  (scale bar 50  $\mu$ m, right panel). (**C**, **D**): arrowheads pointing double positive cells.

TREM2 is expressed on CSF1R<sup>+</sup> TAMs and is modulated by CSF1 and its blockade on TAMs results in delayed tumor growth, remodeling of the tumor immune contexture and increased ICI efficacy. We found that similarly to CD163 and CSF1R, TREM2 was also stably expressed by M1 type M $\phi$  generated from peripheral blood monocytes by IHC (Figure 6D). TREM2<sup>+</sup> TAMs infiltrate <sup>Hi</sup>OC-IS<sup>30</sup>CD163<sup>Hi</sup> (Figure 6E), however, only a minor fraction of them co-expressed pSTAT1Y701, IRF1 and CXCL10 (Figure 6F). All these findings indicate that appropriate characterization of M $\phi$  on OCs requires modified approaches and might help in patient selection to CSF1R- and TREM2-blockade alone in combination with existing ICI.

### M1-Type M $\phi$ Polarization Occurs Across M $\phi$ Subsets and Cancer Types

We found that the prognostic power of <sup>Hi</sup>OC-IS<sup>30</sup> extend to various cancer types (Figures 4D, E). By using double immunohistochemistry for CD163 and pSTAT1Y701, we screened a set of human cancers including melanomas (n = 4), head and neck squamous cell carcinomas (n = 8), MSI<sup>+</sup> colorectal carcinomas (n = 4), MSI<sup>+</sup> endometrial carcinomas (n = 4), breast carcinomas (n = 8) and lung carcinomas (n = 4). A significant fraction of these cancers contained CD163<sup>+</sup>pSTAT1Y701<sup>+</sup> M1-type M $\phi$  producing CXCL10 and surrounded by CD3 T-cell infiltration (Supplementary Figures S8A, B). These data extend our OCs findings across human cancer types.

Recent high dimensional studies of human tumor-associated myeloid cells have led to the identification of discrete TAM subsets based on their transcriptional profile. Specifically, emerging mononuclear phagocytes subsets in cancer are distinct on the basis of their ontogeny, differentiation state, functional orientation, proliferation potential and predictive power in response to ICI treatments (26, 27). To gain further insight on the transcriptional profile of M1-polarized TAMs in various cancer types we explored a pan-cancer scRNAseq dataset [n = 36; (19)] comprising ovarian HGSC, breast, lung and colorectal cancers. To this end, we merged 37,334 myeloid cells from all cancer types. Louvain Graph-based clustering at the resolution 0.6 identified 27 clusters of mononuclear phagocytes (Figure 7A). Among CD68<sup>+</sup>CD163<sup>+</sup> TAMs also expressing the recently identified TREM2 marker, we could identify a CXCL10<sup>+</sup>IRF1<sup>+</sup>STAT1<sup>+</sup> M1-type M $\phi$  population (Cluster 9) (Figures 7A, B) shared between all cancer types (Figure 7C). We next performed differential gene expression analysis between the CXCL10<sup>+</sup>IRF1<sup>+</sup> TAM cluster (cluster 9) and the rest of the myeloid cells. Gene pathway analysis showed that transcripts enriched in cluster 9 were involved in interferon signaling as well as in MHC-dependent antigen processing and in cross presentation (Figure 7D and Supplementary Table S7, Supplementary Figure S9). Altogether, these results show that M1-polarized TAMs form a functionally distinct subset of TAMs infiltrating various types of cancers. These M1-polarized TAMs are part of a T-cell infiltrated immune contexture positively correlating with better clinical outcome.

## DISCUSSION

This study reports the characterization of the immune contexture in OCs, by digital microscopy analysis of a retrospective institutional cohort. Heterogeneity in terms of CD3<sup>+</sup> T-cell and CD163<sup>+</sup> M $\phi$  infiltration emerged among OC subtypes, including immune-infiltrated HGSC and T-cell poor CCC. Immune-infiltrated HGSC display high density of CD3<sup>+</sup>T-cells and of CD163<sup>+</sup> TAMs associated with favorable clinical features and response to chemotherapy or platinum sensitivity. Gene expression analysis by using OC-IS<sup>30</sup> immune signature generated from our institutional cohort and extended to the OV-TCGA dataset (6), uncovers the existence of a clinically meaningful functional immune response, particularly in the BRCA mutated subgroup. Immune-infiltrated HGSC contain CXCL10-producing IFN $\gamma$ -polarized M1-type M $\phi$  surrounded by T-cells also expressing GZMB, indicating ongoing spontaneous T-cell response. All these findings were extended to and confirmed in other immunogenic human cancers types.

The clinical relevance of the endogenous immune response to ovarian carcinoma (OC), and specifically the favorable prognostic effect of CD3<sup>+</sup> T-cells and CD8<sup>+</sup> T-cells have been suggested by a set of observation from pre-clinical and clinical studies (13) and confirmed by a recent meta-analysis (15). Endogenous specific T-cell response has been documented in OCs. Neo-epitope specific CD8<sup>+</sup> T-cells and CD4<sup>+</sup> T-cells were identified both in peripheral blood and among TILs in immunotherapy-naïve OCs (28). Data on the role of M $\phi$  are less consistent. Early studies indicate that M $\phi$  purified from OCs ascites display functional heterogeneity (29), a finding consistent with distinct M $\phi$  polarizations associated to a bivalent behavior (30). In immune infiltrated OCs, the density of CD3<sup>+</sup> T-cells correlates with the density of CD163<sup>+</sup> TAMs and the two cell types resulted intermingled, suggesting their functional interaction. Of note, we found that a fraction of M1-type TAM in OCs produce abundant CXCL10, likely representing one of the relevant T-cell attracting chemokines in this neoplasm. To the other side of the spectrum, we identified a consistent subgroup of CCC containing macrophage deficient in M1-type polarization and lacking T-cell infiltration. CCC are distinct from HGSC in terms of molecular profile and response to systemic treatments; this study highlights distinct features also in terms of immune ecosystem likely accounting for their clinical behavior. Novel treatment options for CCC should consider these findings for a proficient bypass of the T-cell exclusion mechanisms.

The role of M $\phi$  in cancer immune surveillance is rapidly evolving (31, 32). In progressively growing cancer, TAMs modulate tumor progression by regulating various tumor-promoting functions including immunosuppression, angiogenesis, tumor cell proliferation, and stromal infiltration. However, recent findings indicate that similarly to other innate immune cells (33), human TAMs display a significant plasticity (34) as also confirmed by recent high dimensional analysis (26, 27). IFN $\gamma$ -dependent M1 polarization can be mediated by neighboring T-cells, as observed in this study, or by NK cells (35). M1 M $\phi$  initiates pro-inflammatory responses and promotes



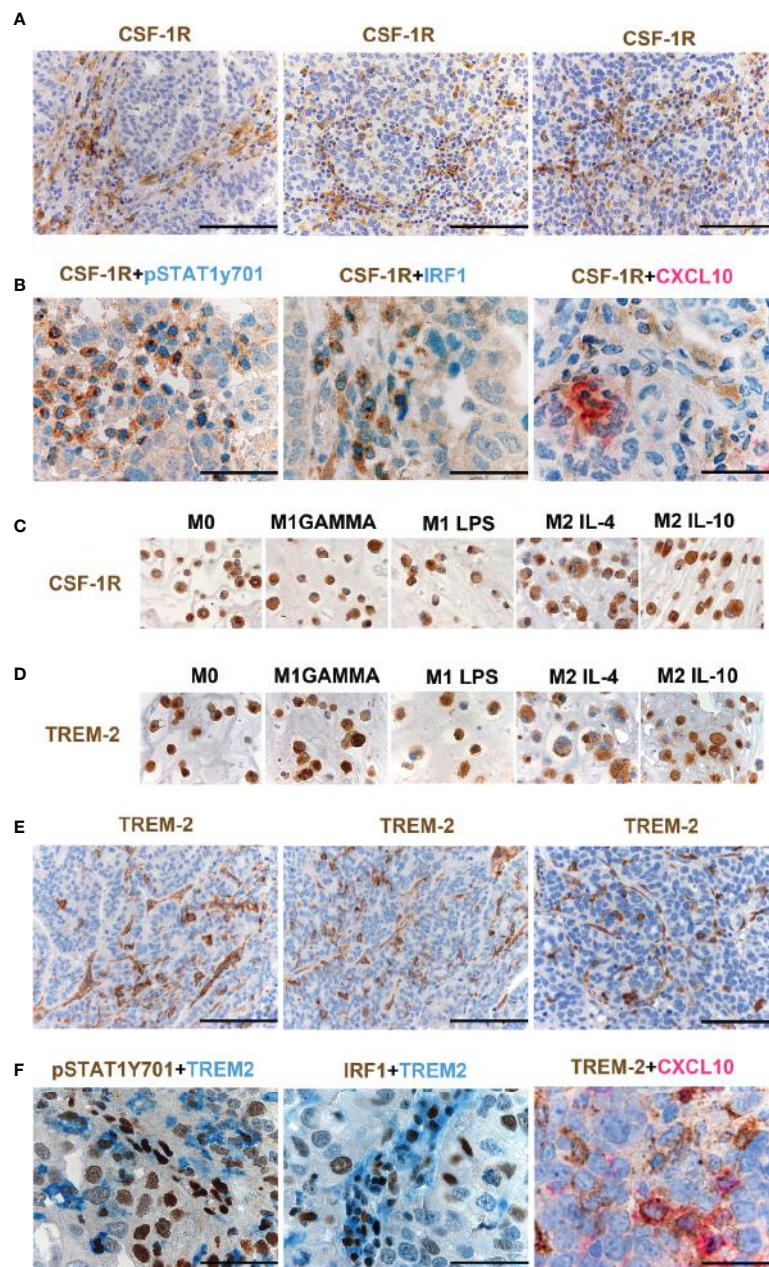


**FIGURE 6** | CSF1R and TREM-2 expression in OCs. Sections from HGSCs cases (**A, B, E, F**) and from cell-block preparations of polarized monocyte-derived M $\phi$  (**C, D**) immunostained as labeled. Magnification 200 $\times$  (**A, E**; scale bar 100  $\mu$ m) and 400 $\times$  (**B, F**; scale bar 50  $\mu$ m). CSF1R expression in OCs is largely restricted to TAMs (**A**). Double immunohistochemistry showing co-expression of pSTAT1Y701, IRF1 and CXCL10 in CSF1R $^{+}$  TAMs (**B**). M1 type and M2 type M $\phi$  generated from peripheral blood monocytes express CSF1R (**C**). M1 type M $\phi$  generated from peripheral blood monocytes express TREM2 (**D**). TREM2 is expressed on TAMs in HGSCs. TREM2 $^{+}$  TAMs detected in  $^{18}$ OC- $IS^{30}$ CD163 $^{hi}$  (**E**); a fraction of TREM2 $^{+}$  TAMs co-expressed pSTAT1Y701, IRF1 and CXCL10 (**F**).

direct or T-cell mediated antitumor effector functions (34, 36) particularly in highly immunogenic cancer (35). This plasticity accounts for a different prognostic relevance associated of TAMs. Based on this dichotomy, major approaches targeting these cells

are exploring novel paradigms such as TAMs reprogramming in addition to their depletion and recruitment blockade, as for CSF1R blockade (21, 24). Various biomarkers have been proposed for the identification of TAMs polarization on

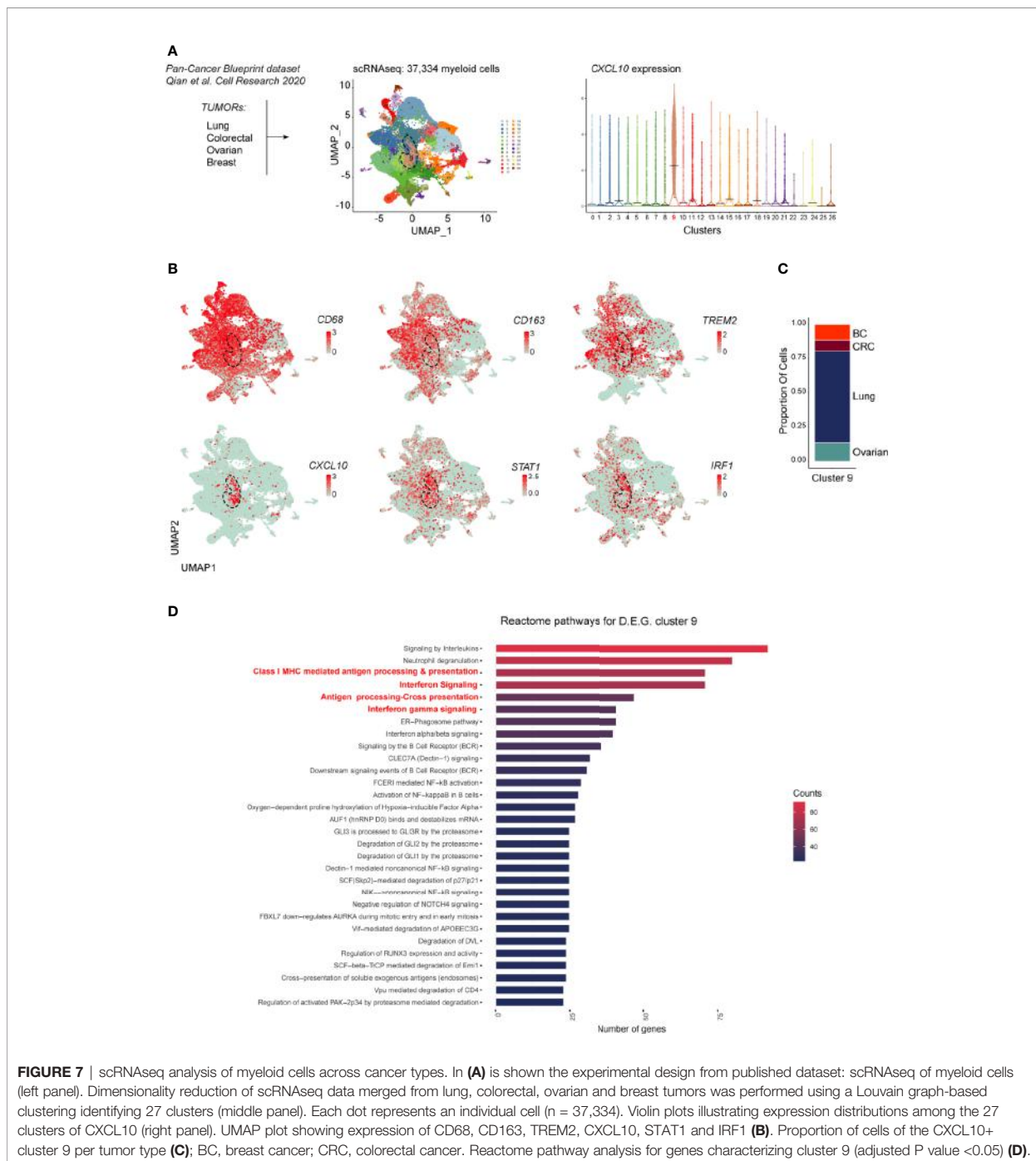


**FIGURE 7** | scRNAseq analysis of myeloid cells across cancer types. In **(A)** is shown the experimental design from published dataset: scRNAseq of myeloid cells (left panel). Dimensionality reduction of scRNAseq data merged from lung, colorectal, ovarian and breast tumors was performed using a Louvain graph-based clustering identifying 27 clusters (middle panel). Each dot represents an individual cell ( $n = 37,334$ ). Violin plots illustrating expression distributions among the 27 clusters of CXCL10 (right panel). UMAP plot showing expression of CD68, CD163, TREM2, CXCL10, STAT1 and IRF1 **(B)**. Proportion of cells of the CXCL10+ cluster 9 per tumor type **(C)**; BC, breast cancer; CRC, colorectal cancer. Reactome pathway analysis for genes characterizing cluster 9 (adjusted P value  $<0.05$ ) **(D)**.

archival tissue (37). By single-cell analysis of FFPE sections, this study identifies M1-type TAMs based on *in vitro* modeling of monocyte-derived  $M1^{IFN\gamma}$  and  $M1^{IFN\gamma+LPS}$ . OCs-associated M1-type TAMs resulted  $CXCL10^+IRF1^+STAT1p^+$ . Data analysis of scRNAseq pan-cancer dataset confirmed the existence of a  $CXCL10^+IRF1^+STAT1^+$  M1-type M $\phi$  across human cancers displaying activation of antigen presenting and cross presentation

gene programs. IRF1 represents a crucial transcriptional regulator of the  $IFN\gamma$ -response (38) and recent findings on human cancers identified IRF1 as a central hub in cancer immunity (39). In macrophages, IRF1 drives M1 polarization (39) by increasing the expression of pro-inflammatory cytokines and chemokines (40). In addition,  $IRF1^+$  M $\phi$  displays a tumoricidal activity (41) mediated by nitric oxide. The microRNA (miRNA)-processing

enzyme DICER is significantly down-modulated by IFN $\gamma$ . Of note, STAT1<sup>+</sup>IRF1<sup>+</sup> TAM have been observed in tumor-bearing mice with DICER conditional deletion (42) and resulted in tumor inhibition by recruitment of activated CTL.

Immune infiltrated HGSC are defined by CD3<sup>Hi</sup>CD163<sup>Hi</sup> immunoscore and display a better outcome, independently from other major prognosticators. Immune infiltrated HGSC are also enriched of OC-IS<sup>30</sup>. The immune cell component plays a relevant role in the clinical response to various HGSC treatments (43). The primary systemic treatments include chemotherapy with platinum-based regimens combined with taxanes. Of note, outcomes of platinum-based regimen are significantly dependent on the existing tumor immune microenvironment (44). In the last few years, Poly (ADP-ribose) polymerase (PARP) inhibitors have been included for HGSC showing HRD. Several trials demonstrated the efficacy of these compounds both as maintenance therapy after first-line chemotherapy (8, 45) or after the treatment of recurrent disease. The best performance for PARP inhibitors is observed in tumors with *BRCA1* or *BRCA2* mutation or with at least an HRD phenotype. A recent meta-analysis confirmed their efficacy with improvement of PFS in platinum-sensitive recurrent OC (7). The findings presented here indicate that a proficient immune microenvironment predicts a better outcome. *BRCA1* and *BRCA2* mutated tumors are also densely infiltrated by T-cells, however, we found that the prognostic effect of the OC-IS<sup>30</sup> signature, as tested in the TCGA cohort, is independent and additive from *BRCA* status and others prognosticator (Figure 4B).

The role of immunotherapy in OCs has been recently investigated by testing the efficacy of ICI (anti-PD1 or anti-PDL1) as single therapy. The results of the first trials with ICIs (46) showed a fair effectiveness. However, the recent combination of ICIs and PARPi provided better results (11, 47). The best results obtained applying ICIs in the subgroup of *BRCA1* or *BRCA2* mutated patients can be explained by recent studies showing that PD1 and PDL1 are highly expressed in *BRCA1* or *BRCA2* mutated patients. Moreover, PARPi administration to breast cancer cell lines further enhance PD-L1 by inactivating GSK3 $\beta$  (48), thus explaining the benefit obtained by the combination of PARPi and anti-PD-L1 therapy (11). It should be reminded that, particularly in HGSC, PD-L1 is primarily expressed by macrophages and that a high density of PD-L1<sup>+</sup> M $\phi$  correlates with CD8<sup>+</sup> T-cells and predicts favorable survival (49). The cellular source and the magnitude of expression of PD-L1 might variably dictate its immune escape potency (50). Based on our findings, it is highly likely that the major source of PD-L1 in OC is from innate immune resistance mechanisms with its dominant hub on M1-type TAMs, whose fine-tuned modulation might further enhance the clinical benefit. These findings identify the combined analysis of immune-contexture and immune signatures as a novel biomarker in OCs management, to be further investigated in the predictive setting.

In conclusion, the results of this study document a proficient immune contexture in a subgroup of primary OCs. Findings proposed here are in keeping with a relevant role of the innate TAMs compartment in OCs immune surveillance, likely

unleashing the endogenous adaptive T-cell response. However, T-cell exclusion occurs also in OCs, particularly in the CCC subtype, likely as a result of the lack of CXCL10<sup>+</sup>-producing M1-type M $\phi$ . Since CCC is already infiltrated by macrophages, their repolarization to a CXCL10<sup>+</sup>TAM might provide a clinical benefit. As an extension of this analysis, M1-type M $\phi$  sharing a common transcriptional activation state were also detected across various human immunogenic cancers. However, intratumor heterogeneity in TAM polarization emerged in this study, with also a fraction of CSF1R and TREM2 M1-type M $\phi$ . This indicates that using approaches targeting molecules of immunosuppressive myeloid cells such as CSF1R and TREM2 would partially affect the endogenous anti-tumor TAM component. Instead, implementation of reprogramming approaches that further bolster the already present macrophage component is needed.

## DATA AVAILABILITY STATEMENT

The original contributions presented in the study are included in the article/**Supplementary Material**. Further inquiries can be directed to the corresponding author.

## ETHICS STATEMENT

The study was approved by the local IRB, WW-IMMUNOCANCERhum, NP-906 and NP-1284. Written informed consent for participation was not required for this study in accordance with the national legislation and the institutional requirements.

## AUTHOR CONTRIBUTIONS

LA, FM, MB, LB, and WV contributed to conception and design of the study. LZ, EB, AR, GT, and FO organized the clinical database. MB, LB, IP, MM, SG, and YM-K performed experiments. FM and SC performed the statistical analysis. LA, FM, MB, LB, and WV wrote the first draft of the manuscript. CR and JH wrote sections of the manuscript. All authors contributed to the article and approved the submitted version.

## ACKNOWLEDGMENTS

We like to thank pathologists, technicians, clinicians, nurses and administrative employers that have provided support to the study and to the follow-up of OCs patients. WV is funded by "Associazione Italiana per la Ricerca sul Cancro" (AIRC-IG-23179).

## SUPPLEMENTARY MATERIAL

The Supplementary Material for this article can be found online at: <https://www.frontiersin.org/articles/10.3389/fimmu.2021.690201/full#supplementary-material>



## REFERENCES

- Colombo N, Sessa C, Du Bois A, Ledermann J, McCluggage WG, McNeish I, et al. ESMO-ESGO Consensus Conference Recommendations on Ovarian Cancer: Pathology and Molecular Biology, Early and Advanced Stages, Borderline Tumours and Recurrent Disease. *Ann Oncol* (2019) 30:672–705. doi: 10.1093/annonc/mdz062
- Matulonis UA, Sood AK, Fallowfield L, Howitt BE, Sehouli J, Karlan BY. Ovarian Cancer. *Nat Rev Dis Prim* (2016) 2:1–22. doi: 10.1038/nrdp.2016.61
- Patch AM, Christie EL, Etemadmoghadam D, Garsed DW, George J, Fereday S, et al. Whole-Genome Characterization of Chemoresistant Ovarian Cancer. *Nature* (2015) 521:489–94. doi: 10.1038/nature14410
- Junttila MR, De Sauvage FJ. Influence of Tumour Micro-Environment Heterogeneity on Therapeutic Response. *Nature* (2013) 501:346–54. doi: 10.1038/nature12626
- Gadducci A, Guarneri V, Peccatori FA, Ronzino G, Scandurra G, Zamagni C, et al. Current Strategies for the Targeted Treatment of High-Grade Serous Epithelial Ovarian Cancer and Relevance of BRCA Mutational Status. *J Ovarian Res* (2019) 12:1–8. doi: 10.1186/s13048-019-0484-6
- Cancer Genome Atlas Research Network. Integrated Genomic Analyses of Ovarian Carcinoma. *Nature* (2012) 474(7353):609–15. doi: 10.1038/nature10166
- Tomao F, Bardhi E, Di Pinto A, Sassu CM, Biagioli E, Petrella MC, et al. Parp Inhibitors as Maintenance Treatment in Platinum Sensitive Recurrent Ovarian Cancer: An Updated Meta-Analysis of Randomized Clinical Trials According to BRCA Mutational Status. *Cancer Treat Rev* (2019) 80:101909. doi: 10.1016/j.ctrv.2019.101909
- González-Martín A, Pothuri B, Vergote I, DePont Christensen R, Graybill W, Mirza MR, et al. Niraparib in Patients With Newly Diagnosed Advanced Ovarian Cancer. *N Engl J Med* (2019) 381:2391–402. doi: 10.1056/NEJMoa1910962
- Gravbrot N, Gilbert-Gard K, Mehta P, Ghotmi Y, Banerjee M, Mazis C, et al. Therapeutic Monoclonal Antibodies Targeting Immune Checkpoints for the Treatment of Solid Tumors. *Antibodies* (2019) 8:51. doi: 10.3390/antib8040051
- Cristescu R, Mogg R, Ayers M, Albright A, Murphy E, Yearley J, et al. Pan-Tumor Genomic Biomarkers for PD-1 Checkpoint Blockade-Based Immunotherapy. *Science* (80-) (2018) 362:363(6430). doi: 10.1126/science.aar3593. Erratum in: *Science*.
- Drew Y, de Jonge M, Hong SH, Park YH, Wolfer A, Brown J, et al. An Open-Label, Phase II Basket Study of Olaparib and Durvalumab (MEDIOLA): Results in Germline BRCA -Mutated (Gbrca M) Platinum-Sensitive Relapsed (PSR) Ovarian Cancer (OC). *Gynecol Oncol* (2018) 149:246–7. doi: 10.1016/j.ygyno.2018.04.555
- Galon J, Costes A, Sanchez-Cabo F, Kirilovsky A, Mlecnik B, Lagorce-Pages C, et al. Type, Density, and Location of Immune Cells Within Human Colorectal Tumors Predict Clinical Outcome. *Science* (80-) (2006) 313:1960–4. doi: 10.1126/science.1129139
- Zhang L, Conejo-Garcia JR, Katsaros D, Gimotty PA, Massobrio M, Regnani G, et al. Intratumoral T Cells, Recurrence, and Survival in Epithelial Ovarian Cancer. *N Engl J Med* (2003) 348:203–13. doi: 10.1056/NEJMoa020177
- Sato E, Olson SH, Ahn J, Bundy B, Nishikawa H, Qian F, et al. Intraepithelial CD8+ Tumor-Infiltrating Lymphocytes and a High CD8+/Regulatory T Cell Ratio Are Associated With Favorable Prognosis in Ovarian Cancer. *Proc Natl Acad Sci USA* (2005) 102:18538–43. doi: 10.1073/pnas.0509182102
- Hwang WT, Adams SF, Tahirovic E, Hagemann IS, Coukos G. Prognostic Significance of Tumor-Infiltrating T Cells in Ovarian Cancer: A Meta-Analysis. *Gynecol Oncol* (2012) 124:192–8. doi: 10.1016/j.ygyno.2011.09.039
- Ganzfried BF, Riestler M, Haibe-Kains B, Risch T, Tyekucheva S, Jazic I, et al. Curatedovariandata: Clinically Annotated Data for the Ovarian Cancer Transcriptome. *Database* (2013) 2013:bat013. doi: 10.1093/database/bat013
- Newman AM, Steen CB, Liu CL, Gentles AJ, Chaudhuri AA, Scherer F, et al. Determining Cell Type Abundance and Expression From Bulk Tissues With Digital Cytometry. *Nat Biotechnol* (2019) 37:773–82. doi: 10.1038/s41587-019-0114-2
- Essers PBM, van der Heijden M, Vossen D, de Roest RH, Leemans CR, Brakenhoff RH, et al. Ovarian Cancer Derived Copy Number Alterations Signatures Are Prognostic in Chemoradiotherapy Treated Head and Neck Squamous Cell Carcinoma. *Int J Cancer* (2020) 147:1732–9. doi: 10.1002/ijc.32962
- Qian J, Olbrecht S, Boeckx B, Vos H, Laoui D, Etiloglu E, et al. A Pan-Cancer Blueprint of the Heterogeneous Tumor Microenvironment Revealed by Single-Cell Profiling. *Cell Res* (2020) 30:745–62. doi: 10.1038/s41422-020-0355-0
- Cardenas H, Jiang G, Thomes Pepin J, Parker JB, Condello S, Nephew KP, et al. Interferon- $\gamma$  Signaling Is Associated With BRCA1 Loss-of-Function Mutations in High Grade Serous Ovarian Cancer. *NPJ Precis Oncol* (2019) 3:1–14. doi: 10.1038/s41698-019-0103-4
- Ries CH, Cannarile MA, Hoves S, Benz J, Wartha K, Runza V, et al. Targeting Tumor-Associated Macrophages With Anti-CSF-1R Antibody Reveals a Strategy for Cancer Therapy. *Cancer Cell* (2014) 25:846–59. doi: 10.1016/j.ccr.2014.05.016
- House IG, Savas P, Lai J, Chen AXY, Oliver AJ, Teo ZL, et al. Macrophage-Derived CXCL9 and CXCL10 are Required for Antitumor Immune Responses Following Immune Checkpoint Blockade. *Clin Cancer Res* (2020) 26(2):487–504. doi: 10.1158/1078-0432.CCR-19-1868
- Chambers SK, Kacinski BM, Ivins CM, Carcangiu ML. Overexpression of Epithelial Macrophage Colony-Stimulating Factor (CSF-1) and CSF-1 Receptor: A Poor Prognostic Factor in Epithelial Ovarian Cancer, Contrasted With a Protective Effect of Stromal CSF-1. *Clin Cancer Res* (1997) 3:999–1007.
- Hoves S, Ooi CH, Wolter C, Sade H, Bissinger S, Schmittnaegel M, et al. Rapid Activation of Tumor-Associated Macrophages Boosts Preexisting Tumor Immunity. *J Exp Med* (2018) 215:859–76. doi: 10.1084/jem.20171440
- Molgora M, Esaulova E, Vermi W, Hou J, Chen Y, Jingqin L, et al. TREM2 Modulation Remodels the Tumor Myeloid Landscape, Enhancing Anti-PD-1 Immunotherapy. *Cell* (2020) 182:P886–900.E17. doi: 10.1016/j.cell.2020.07.013
- Qu Y, Wen J, Thomas G, Yang W, Prior W, He W, et al. Baseline Frequency of Inflammatory Cxcl9-Expressing Tumor-Associated Macrophages Predicts Response to Avelumab Treatment. *Cell Rep* (2020) 32:108115. doi: 10.1016/j.celrep.2020.108115
- Bonavita E, Bromley CP, Jonsson G, Pelly VS, Sahoo S, Walwyn-Brown K, et al. Antagonistic Inflammatory Phenotypes Dictate Tumor Fate and Response to Immune Checkpoint Blockade. *Immunity* (2020) 53:1215–29. doi: 10.1016/j.immuni.2020.10.020
- Bobisse S, Genolet R, Roberti A, Tanyi JL, Racle J, Stevenson BJ, et al. Sensitive and Frequent Identification of High Avidity Neo-Epitope Specific CD8+ T Cells in Immunotherapy-Naive Ovarian Cancer. *Nat Commun* (2018) 9:1–10. doi: 10.1038/s41467-018-03301-0
- Mantovani A, Peri G, Polentarutti N, Bolis G, Mangioni C, Spreafico F. Effects on *In Vitro* Tumor Growth of Macrophages Isolated From Human Ascitic Ovarian Tumors. *Int J Cancer* (1979) 23:157–64. doi: 10.1002/ijc.2910230204
- Yuan X, Zhang J, Li D, Mao Y, Mo F, Du W, et al. Prognostic Significance of Tumor-Associated Macrophages in Ovarian Cancer: A Meta-Analysis. *Gynecol Oncol* (2017) 147:181–7. doi: 10.1016/j.ygyno.2017.07.007
- Lewis CE, Harney AS, Pollard JW. The Multifaceted Role of Perivascular Macrophages in Tumors. *Cancer Cell* (2016) 30:18–25. doi: 10.1016/j.ccell.2016.05.017
- Gordon S, Martinez FO. Alternative Activation of Macrophages: Mechanism and Functions. *Immunity* (2010) 32:593–604. doi: 10.1016/j.immuni.2010.05.007
- Fridlender ZG, Sun J, Kim S, Kapoor V, Cheng G, Ling L, et al. Polarization of Tumor-Associated Neutrophil Phenotype by TGF- $\beta$ : “N1” Versus “N2” Tan. *Cancer Cell* (2009) 16:183–94. doi: 10.1016/j.ccr.2009.06.017
- Bercovici N, Guérin MV, Trautmann A. The Remarkable Plasticity of Macrophages: A Chance to Fight Cancer. *Front Immunol* (2019) 10:1–9. doi: 10.3389/fimmu.2019.01563
- Sullivan TO, Saddawi-konefka R, Vermi W, Koebel CM, Arthur C, White JM, et al. Cancer Immunoediting by the Innate Immune System in the Absence of Adaptive Immunity. *J Exp Med* (2012) 209:1869–82. doi: 10.1084/jem.20112738
- Wanderley CW, Colón DF, Luiz JPM, Oliveira FF, Viacava PR, Leite CA, et al. Paclitaxel Reduces Tumor Growth by Reprogramming Tumor-Associated Macrophages to an M1 Profile in a TLR4-Dependent Manner. *Cancer Res* (2018) 78:5891–900. doi: 10.1158/0008-5472.CAN-17-3480
- Huang Y-K, Wang M, Sun Y, Di Costanzo N, Mitchell C, Achuthan A, et al. Macrophage Spatial Heterogeneity in Gastric Cancer Defined by Multiplex



- Immunohistochemistry. *Nat Commun* (2019) 10:3928. doi: 10.1038/s41467-019-11788-4
38. Martinez FO, Gordon S, Locati M, Mantovani A. Transcriptional Profiling of the Human Monocyte-to-Macrophage Differentiation and Polarization: New Molecules and Patterns of Gene Expression. *J Immunol* (2006) 177:7303–11. doi: 10.4049/jimmunol.177.10.7303
  39. Xie C, Liu C, Wu B, Lin Y, Ma T, Xiong H, et al. Effects of IRF1 and IFN- $\beta$  Interaction on the M1 Polarization of Macrophages and its Antitumor Function. *Int J Mol Med* (2016) 38:148–60. doi: 10.3892/ijmm.2016.2583
  40. Negishi H, Fujita Y, Yanai H, Sakaguchi S, Ouyang X, Shinohara M, et al. Evidence for Licensing of IFN-Gamma-Induced IFN Regulatory Factor 1 Transcription Factor by Myd88 in Toll-Like Receptor-Dependent Gene Induction Program. *Proc Natl Acad Sci USA* (2006) 103:15136–41. doi: 10.1073/pnas.0607181103
  41. Nascimento FRF, Gomes EA, Russo M, Lepique AP. Interferon Regulatory Factor (IRF)-1 Is a Master Regulator of the Cross Talk Between Macrophages and L929 Fibrosarcoma Cells for Nitric Oxide Dependent Tumoricidal Activity. *PLoS One* (2015) 10:e0117782. doi: 10.1371/journal.pone.0117782
  42. Baer C, Squadrito ML, Laoui D, Thompson D, Hansen SK, Kiialainen A, et al. Suppression of MicroRNA Activity Amplifies IFN- $\gamma$ -Induced Macrophage Activation and Promotes Anti-Tumour Immunity. *Nat Cell Biol* (2016) 18:790–802. doi: 10.1038/ncb3371
  43. Bösmüller H, Haïtchi-petnehazy S, Webersinke G, Marschon R. Intratumoral Lymphocyte Density in Serous Ovarian Carcinoma Is Superior to ERCC1 Expression for Predicting Response to Platinum-Based Therapy. (2011), 183–91. doi: 10.1007/s00428-011-1110-1
  44. Rottenberg S, Disler C, Perego P. The Rediscovery of Platinum-Based Cancer Therapy. *Nat Rev Cancer* (2020) 21:37–50. doi: 10.1038/s41568-020-00308-y
  45. Ray-Coquard I, Pautier P, Pignata S, Péro D, González-Martín A, Berger R, et al. Olaparib Plus Bevacizumab as First-Line Maintenance in Ovarian Cancer. *N Engl J Med* (2019) 381:2416–28. doi: 10.1056/NEJMoa1911361
  46. Hamanishi J, Mandai M, Ikeda T, Minami M, Kawaguchi A, Murayama T, et al. Safety and Antitumor Activity of Anti-PD-1 Antibody, Nivolumab, in Patients With Platinum-Resistant Ovarian Cancer. *J Clin Oncol* (2015) 33:4015–22. doi: 10.1200/JCO.2015.62.3397
  47. Konstantinopoulos PA, Waggoner S, Vidal GA, Mita M, Moroney JW, Holloway R, et al. Single-Arm Phases 1 and 2 Trial of Niraparib in Combination With Pembrolizumab in Patients With Recurrent Platinum-Resistant Ovarian Carcinoma. *JAMA Oncol* (2019) 5:1141–9. doi: 10.1001/jamaoncol.2019.1048
  48. Jiao S, Xia W, Yamaguchi H, Wei Y, Chen M, Hsu J, et al. PARP Inhibitor Upregulates PD-L1 Expression and Enhances Cancer-Associated Immunosuppression. *Clin Cancer Res* (2017) 23:711–20. doi: 10.1158/1078-0432.CCR-16-3215
  49. Webb JR, Milne K, Kroeger DR, Nelson BH. PD-L1 Expression is Associated With Tumor-Infiltrating T Cells and Favorable Prognosis in High-Grade Serous Ovarian Cancer. *Gynecol Oncol* (2016) 141:293–302. doi: 10.1016/j.ygyno.2016.03.008
  50. Noguchi T, Ward JP, Gubin MM, Arthur CD, Lee SH, Hundal J, et al. Temporally Distinct PD-L1 Expression by Tumor and Host Cells Contributes to Immune Escape. *Cancer Immunol Res* (2017) 5:106–17. doi: 10.1158/2326-6066.CIR-16-0391

**Conflict of Interest:** SG was employed by Diatech Pharmacogenetics srl and CR was employed by Dr Carola Ries Consulting.

The remaining authors declare that the research was conducted in the absence of any commercial or financial relationships that could be construed as a potential conflict of interest.

Copyright © 2021 Ardighieri, Missale, Bugatti, Gatta, Pezzali, Monti, Gottardi, Zanutti, Bignotti, Ravaggi, Tognon, Odicino, Calza, Missolo-Koussou, Ries, Helft and Vermi. This is an open-access article distributed under the terms of the Creative Commons Attribution License (CC BY). The use, distribution or reproduction in other forums is permitted, provided the original author(s) and the copyright owner(s) are credited and that the original publication in this journal is cited, in accordance with accepted academic practice. No use, distribution or reproduction is permitted which does not comply with these terms.



## TIM4+FOLR2+ Macrophages Localized in TLS Correlate to an Active Immune Infiltrate Across Several Cancer Types

Bugatti, M.#  
Bergamini, M.#  
**Missale, F.#**  
Monti, M.  
Ardighieri, L.  
Pezzali, I.  
Picinoli, S.  
Caronni, N.  
Missolo-Koussou, Y.  
Helft, J.  
Benvenuti, F.  
Vermi, W.

Cancer Immunol Res  
2022;10(11):1340-1353. doi: 10.1158/2326-6066.CIR-22-0271.

#equally contributed as first authors



Supplementary material:

# A Population of TIM4<sup>+</sup>FOLR2<sup>+</sup> Macrophages Localized in Tertiary Lymphoid Structures Correlates to an Active Immune Infiltrate Across Several Cancer Types



Mattia Bugatti<sup>1,2</sup>, Marco Bergamini<sup>1,3</sup>, Francesco Missale<sup>2,4</sup>, Matilde Monti<sup>2</sup>, Laura Ardighieri<sup>1</sup>, Irene Pezzali<sup>2</sup>, Sara Picinoli<sup>2</sup>, Nicoletta Caronni<sup>5</sup>, Yoann Missolo-Koussou<sup>6</sup>, Julie Helft<sup>7</sup>, Federica Benvenuti<sup>8</sup>, and William Vermi<sup>1,2,9</sup>

## ABSTRACT

TIM4 has previously been associated with antitumor immunity, yet the pattern of expression and the function of this receptor across human cancer tissues remain poorly explored. Here we combined extensive immunolabeling of human tissues with *in silico* analysis of pan-cancer transcriptomic data sets to explore the clinical significance of TIM4 expression. Our results unveil that TIM4 is expressed on a fraction of cavity macrophages (<sup>CA</sup>TIM4<sup>+</sup>MΦ) of carcinoma patients. Moreover, we uncover a high expression of TIM4 on macrophages of the T-cell zone of the carcinoma-associated tertiary lymphoid structures (<sup>TLS</sup>TIM4<sup>+</sup>MΦ). *In silico* analysis of a pan-cancer data set revealed a positive correlation between TIM4 expression and markers of B cells, effector CD8<sup>+</sup> T cells, and a 12-chemokine signature defining tertiary lymphoid structure. In addition, <sup>TLS</sup>TIM4<sup>+</sup>MΦ were enriched in cancers displaying microsatellite instability

and high CD8<sup>+</sup> T-cell infiltration, confirming their association with immune-reactive tumors. Both <sup>CA</sup>TIM4<sup>+</sup>MΦ and <sup>TLS</sup>TIM4<sup>+</sup>MΦ express FOLR2, a marker of tissue-resident MΦ. However, <sup>CA</sup>TIM4<sup>+</sup>MΦ had a higher expression of the immunosuppressive molecules TREM2, IL10, and TGFβ as compared with <sup>TLS</sup>TIM4<sup>+</sup>MΦ. By analyzing a scRNA sequence data set of tumor-associated myeloid cells, we identified two TIM4<sup>+</sup>FOLR2<sup>+</sup> clusters coherent with <sup>CA</sup>TIM4<sup>+</sup>MΦ and <sup>TLS</sup>TIM4<sup>+</sup>MΦ. We defined specific gene signatures for each subset and found that the <sup>CA</sup>TIM4<sup>+</sup>MΦ signature was associated with worse patient survival. In contrast, <sup>TLS</sup>TIM4<sup>+</sup>MΦ gene signature positively correlates with a better prognosis. Together, these data illustrate that TIM4 marks two distinct macrophage populations with distinct phenotypes and tissue localization and that may have opposing roles in tumor immunity.

## Introduction

Among T-cell immunoglobulin and mucin domain proteins, TIM4 was initially identified as a ligand for TIM1, the latter representing a potent costimulatory molecule for T cells (1). Subsequently, TIM4 was characterized as a phosphatidylserine (PtdSer) receptor expressed on mouse antigen-presenting cells (2). Its critical role in the engulfment of PtdSer-expressing apoptotic bodies by macrophages (MΦ) and dendritic cells was also confirmed in humans (3). Removal of PtdSer-exposing apoptotic bodies by MΦ is critical for the maintenance of tissue homeostasis and for the prevention of autoimmune responses

against intracellular antigens released from dying cells (4). Moreover, removal of PtdSer-expressing antigen-specific T cells in secondary lymphoid organs helps the contraction phase of the immune response, thus leading to peripheral tolerance (5).

TIM4 expression is restricted to antigen-presenting cells in primary and secondary lymphoid tissues (3, 5–7), and experimental mouse models have documented its essential role for the maintenance of the homeostatic state of peritoneal MΦ (8), dermal dendritic cells, and Langerhans cells (9). Other studies found that TIM4 marks long-lived tissue-resident MΦ with self-renewal properties in various tissues (10, 11). In human tissues, TIM4 is restricted to liver Kupffer cells, tangible-body MΦ (TBMΦ), and the splenic white pulp MΦ (3, 7), but data on its expression on human immune cells remain very scant.

The functions of TIM4 in cancer immunity in mouse and in human samples have been explored. TIM4 induces autophagy-mediated degradation of ingested tumor antigens by MΦ and dendritic cells, leading to reduced antigen presentation and antitumor immunity (12). We reported that TIM4 is highly expressed by pulmonary type 1 murine classic dendritic cells (cDC1) and was required for antigen uptake and priming of CD8<sup>+</sup> tumor-specific T cells. Accordingly, human *TIM4* transcripts increase the prognostic value of a cDC1 signature and predict responses to PD-1 treatment in lung adenocarcinomas (13). The mouse models of peritoneal carcinomatosis have proposed a protumoral role of TIM4<sup>+</sup> MΦ. Omental TIM4<sup>+</sup> tissue-resident MΦ support the acquisition of a cancer stem cell-like phenotype and the epithelial–mesenchymal transition of disseminated ovarian cancer cells promoting progression and metastatic spread (10). Moreover, TIM4<sup>+</sup> cavity MΦ in ovarian cancer display a high oxidative phosphorylation and mitochondrial function mediated by arginase-1 (14). Other work expanded

<sup>1</sup>ASST Spedali Civili di Brescia, Brescia, Italy. <sup>2</sup>Department of Molecular and Translational Medicine, University of Brescia, Brescia, Italy. <sup>3</sup>Department of Clinical and Experimental Science, University of Brescia, Brescia, Italy. <sup>4</sup>Department of Head and Neck Oncology and Surgery Otorhinolaryngology, Antoni Van Leeuwenhoek, Nederlands Kanker Instituut, Amsterdam, The Netherlands. <sup>5</sup>San Raffaele Telethon Institute for Gene Therapy (SR-TIGET), IRCCS San Raffaele Scientific Institute, Milan, Italy. <sup>6</sup>PSL University, Institut Curie Research Center, INSERM U932 and SIRIC, Center for Cancers Immunotherapy, Translational Immunotherapy Team, Paris, France. <sup>7</sup>Université Paris Cité, CNRS, INSERM, Institut Cochin, Phagocytes and Cancer Immunology Laboratory, Paris, France. <sup>8</sup>Cellular Immunology, International Centre for Genetic Engineering and Biotechnology (ICGEB), Trieste, Italy. <sup>9</sup>Department of Pathology and Immunology, Washington University School of Medicine, St. Louis, Missouri.

M. Bugatti, M. Bergamini, and F. Missale equally contributed to this article.

**Corresponding Author:** William Vermi, University of Brescia, 25123, Brescia, Italy. Phone: 3903-0399-8425; E-mail: william.vermi@unibs.it

Cancer Immunol Res 2022;XX:XX–XX

doi: 10.1158/2326-6066.CIR-22-0271

©2022 American Association for Cancer Research

# Chapter 7. TIM4+FOLR2+ Macrophages Localized in TLS Correlate to an Active Immune Infiltrate Across Several Cancer Types

Bugatti et al.

our understanding of the protumor role of TIM4<sup>+</sup> cavity-resident MΦ by showing their ability to sequester cytotoxic antitumor PtdSer<sup>+</sup>CD8<sup>+</sup> T cells (15). Together, these findings suggest context-specific, divergent roles of myeloid cells expressing TIM4. The characterization of TIM4 expression on immune cells associated with diverse human tumor types is ill-characterized and represents an important gap in understanding the role of this receptor in cancer.

Here we mapped TIM4 expression on human immune cells infiltrating various human tumors. We detected TIM4 expression in various MΦ populations capturing apoptotic cells and in a population of lymph node MΦ of the interfollicular area. In primary and metastatic cancer tissues, TIM4 expression is absent on conventional tumor-infiltrating MΦ. However, we identified two distinct TIM4<sup>+</sup>MΦ populations in the tumor microenvironment: those associated with tertiary lymphoid structures (TLS; <sup>TLS</sup>TIM4<sup>+</sup>MΦ) and those found in the pleural and peritoneal cavities of carcinoma patients (<sup>CA</sup>TIM4<sup>+</sup>MΦ). <sup>TLS</sup>TIM4<sup>+</sup>MΦ are mainly “non-phagocytic” and found in the T-cell zone of TLS, whose spatial organization resembles secondary lymphoid organs (16, 17) and are recurrent in immunogenic cancers. TLS represent ectopic secondary lymphoid structures found in cancer and inflamed peripheral tissues (16) and their density predicts good prognosis and response to immunotherapy (18, 19). Single-cell RNA analysis of tumor-infiltrating MΦ in breast tumors by members of our group previously identified a novel MΦ population expressing FOLR2 that localizes in the tumor stroma and within lymphoid aggregates (20). These cells efficiently prime and interact with effector CD8<sup>+</sup> T cells. We confirmed that <sup>TLS</sup>TIM4<sup>+</sup>MΦ and <sup>CA</sup>TIM4<sup>+</sup>MΦ coexpress FOLR2. Accordingly, by exploring a pan-cancer scRNA-seq data set of myeloid cells, we identified two TIM4<sup>+</sup>FOLR2<sup>+</sup> clusters. One cluster is enriched in *LYVE1*, *SLC40A1*, and *SEPP1* transcripts found in antitumor MΦ, whereas the other is reminiscent of immune-suppressive TREM2<sup>+</sup> MΦ. Immunostaining tumor sections revealed the immunosuppressive molecules TREM2 (21, 22), IL10 and TGFβ were highly expressed on <sup>CA</sup>TIM4<sup>+</sup>MΦ but not on <sup>TLS</sup>TIM4<sup>+</sup>MΦ. All these findings indicate that in addition to protumorigenic body cavity TIM4<sup>+</sup>TREM2<sup>+</sup>MΦ, a novel TIM4<sup>+</sup> population is observed in the T-cell area of cancer-associated TLS. Although the exact role of these cells is still undefined, their function within the TLS is likely to be associated with protective immunity.

## Materials and Methods

### Human tissues

IHC was performed on a set of tissue samples obtained from the archive of the Department of Pathology (ASST Spedali Civili di Brescia, Brescia, Italy). Analyzed tissues included nonlymphoid normal tissues ( $n = 42$ ) and reactive lymphoid normal tissues ( $n = 33$ ). Cancer tissues included samples from tissue microarray ( $n = 126$  primary carcinomas; Supplementary Table S1; ref. 23) and whole tissue blocks of primary ( $n = 135$ ) and metastatic ( $n = 30$ ) carcinomas, cell block from pleural effusion ( $n = 10$ ), peritoneal cytological specimen ( $n = 10$ ), pleural biopsies ( $n = 5$ ), and peritoneal biopsies ( $n = 10$ ) from lung and ovarian cancer specimens. The study was approved by the local IRB (WW-IMMUNOCANCERhum, NP-906, NP-1284) and conducted in accordance with the Declaration of Helsinki.

### Cell-block preparation

Cytologic specimens from pleural and peritoneal effusion were centrifuged for 10 minutes at 3,000 rpm. A solution of plasma

(100 μL, kindly provided by Centro Trasfusionale, ASST Spedali Civili di Brescia, Brescia, Italy) and HemosIL8 RecombiPlasTin 2G (200 μL, Instrumentation Laboratory; cat. no. 0020003050; 1:2) were added to cell pellets, mixed until the formation of a clot, and then placed into a labeled cassette. The specimen was fixed in 10% formalin (Bio-Optica; cat. no. 05-K01004) for 1 hour followed by paraffin inclusion.

### IHC and digital image analysis

Four micron-thick tissue sections were obtained from formalin-fixed, paraffin-embedded blocks. For IHC staining, endogenous peroxidase was blocked by incubation with methanol (Honeywell, cat. 603-001-00-X) and hydrogen peroxide (AppliChem; cat. no. 141076,1211) 0.03% for 20 minutes during rehydration. Immunostaining was performed using a set of primary antibodies (Supplementary Table S2) after pretreatment with microwave or waterbath in citrate buffer at pH 6.00 or EDTA buffer at pH 8.00, as indicated in Supplementary Table S2. The reaction was revealed using the Goat-on-rodent-HRP-System (Biocare Medical; cat. no. GHP516H) or Novolink Polymer (Leica Microsystems; cat. no. RE7280-CE) followed by diaminobenzidine (DAB, Dako; cat. no. K3467). Finally, the slides were counterstained with Meyer's Haematoxylin (Bio-Optica; cat. no. 05-M06002).

For double staining, after completing the first immune reaction, the second was visualized using Mach 4 MR-AP (Biocare Medical; cat. no. M4U536L) or Goat-on-rodent AP-System (Biocare Medical; cat. no. GAP514G), followed by Ferangi Blue (Biocare Medical, cat. no. FB813S). Localization of TIM4<sup>+</sup> cells within tertiary lymphoid structures was confirmed by double and triple staining combining TIM4 with CD20 and CD3. For triple IHC the third immune reaction was revealed using Mach 4 MR-AP (Biocare Medical), followed by ImmPACT Vector Red Substrate Kit, Alkaline Phosphatase (Vector Laboratories, cat. no. SK-4205).

For double sequential immunostains, the first reaction is deleted after first chromogen destain and stripping. Anti-TIM4 was used for the first immune reaction, revealed using Goat on rodent-HRP-Polymer (Biocare Medical) and developed in 3-amino-9-ethylcarbazole chromogen (AEC), counterstained with hematoxylin and cover-slipped using gelatin. Subsequently, the slides were digitally scanned, using Aperio Scanscope CS (Leica Microsystems). After coverslip removal, AEC was washed out and the slides were eluted using a 2-Mercaptoethanol (Fluka, cat. no. 63689)/SDS (Sigma-Aldrich, cat. no. L3771) solution (20 mL 10% w/v SDS with 12.5 mL 0.5 M Tris-HCl, pH6.8, 67.5 mL distilled water and 0.8 mL 2-ME). Slides were subsequently incubated in this solution in a waterbath preheated at 56°C for 30 minutes. Sections were washed for 1 hour in distilled water. After unmasking in microwave, anti-CD163 was revealed using Novolink Polymer (Leica) and AEC. The subsequent immunostains for anti-FOLR2 and anti-TREM2 was developed analogously, anti-FOLR2 was revealed using AEC and diaminobenzidine, respectively. CD3 was revealed using Mach 4 MR-AP and Ferangi blue as chromogen, and slides were counterstained with hematoxylin, cover-slipped, and digitally scanned. The digital slides were processed using ImageScope. Slides were synchronized and corresponding tissue regions were analyzed.

TLS count was performed in a cohort of 76 human lung adenocarcinomas (LUAD). Tumor-associated TLS were identified as ectopic dense mixed lymphoid aggregates composed of CD20<sup>+</sup> B cells and CD3<sup>+</sup> T cells located at the periphery of the neoplastic area (invasive margin) or in the surrounding noninvolved lung tissue. TLS count was performed on representative tumor sections containing enough non-involved tumor area, as evaluated on hematoxylin and eosin (H&E)

stained sections and was based on a three-tiered score (0 = absence of TLS; 1 = <5 TLS; 2 = ≥5 TLS). CD8<sup>+</sup> T-cell density was performed using Aperio Scanscope on digitalized sections. Stained slides were acquired using the Aperio CS2 digital scanner and ScanScope software (Leica biosystems). The whole tumor area was considered for the analysis, with the exclusion of necrotic areas. Data are expressed as absolute number of CD8<sup>+</sup> cells per mm<sup>2</sup>. Pearson correlation analysis and one-way ANOVA test with *post hoc* pairwise comparisons (Tukey correction for multiple comparisons) were performed between log<sub>2</sub>CD8<sup>+</sup> T-cell density and TLS score.

### Data processing of the TCGA data sets and statistical analysis

Raw counts for primary solid tumor samples of nine TCGA projects (TCGA-BLCA, TCGA-BRCA, TCGA-COAD, TCGA-HNSC, TCGA-LUAD, TCGA-LUSC, TCGA-OV, TCGA-SKCM, and TCGA-UCEC) were downloaded from GDC Legacy Archive (hg19) using the TCGA biolinks R/Bioconductor package ( $n = 3,850$  cases). Normalized expression was obtained by upper quartile normalization measured in RSEM. For downstream analysis, the log<sub>2</sub>-RSEM gene expression was considered. Gene expression of TIM4, TREM2, FOLR2, CD163, PAX5, CD247 (CD3) and of 12 chemokines (CCL2, CCL3, CCL4, CCL5, CCL8, CCL18, CCL19, CCL21, CXCL9, CXCL10, CXCL11, and CXCL13) was retrieved. The geometric mean of the 12 chemokines genes was defined as TLS signature (24, 25).

Qualitative variables were described as absolute and relative frequencies; standard descriptive statistics were used for continuous variables, expressing means, standard deviations, medians, and ranges. Correlations between quantitative variables were computed using the Pearson correlation coefficient, a Bonferroni's correction of significance was applied for multiple testing in each analysis.

The main outcome was considered the TIM4 gene expression, considered as dependent variable in the multivariable linear regression models. For achieving a qualitative description of coexpression of PAX5, CD3, and a 12-gene panel of chemokines defining the TLS signature, an exact Barnes–Hut t-distributed stochastic neighbor embedding (tSNE) was computed considering Z-scored immune cells infiltration, with Euclidean distance as similarity measure (26). Survival analysis was performed considering the overall survival (OS) and disease-free survival (DFS) as endpoints, and applying Cox proportional hazards models, stratified for tumor site and stage. Partial effects plots and graphs were rendered through “rms,” “ggplot2,” and “Rtsne” packages. In all analyses, a two-tailed  $P$  value < 0.05 was considered significant, and R (version 4.0.2) was used for statistical analysis and rendering graphs.

### RNAscope

To localize IL10- and TGFβ-positive cells, tissues were analyzed with RNAscope assay (Advanced Cell Diagnostics, Newark) using RNAscope 2.5 HD Assay-RED kit and Hs-IL10 probe (cat no. 602051) recognizing the nt 122–1,163 of the IL10 mRNA (reference sequence NM\_000572.2) and Hs-TGFB1 probe (cat. no. 400881) recognizing the nt 170–1,649 of the TGFB mRNA (reference sequence NM\_000660.4). The sections from fixed human tissue blocks were treated following the manufacturer's instructions. Briefly, freshly cut 3-μm sections were deparaffinized in xylene (Bio-Optica, cat. no. 06-1304F) and treated with the peroxidase block solution (ACD, cat. no. 322335) for 10 minutes at room temperature followed by the retrieval solution for 15 minutes at 98°C and by protease plus (ACD, cat. no. 322331) at 40°C for 30 minutes. Control probes included Hs-POLR2a-C2 (cat. no. 310451) and dapB-C2 (cat. no. 310043-C2). The hybridization was performed for 2 hours at 40°C. The signal was revealed

using RNAscope 2.5 HD Detection Reagent and FAST RED. Combined RNAscope and IHC for TIM4 were used to identify the cellular source of IL10 and TGFβ. To this end, IL10 and TGFβ detection by RNAscope was combined with immunoreaction visualized using Goat-on-Rodent AP-Polymer followed by Ferangi Blue (Biocare Medical).

### Processing of published data set

We downloaded the raw data sets and selected myeloid cells data set (using the article annotation with the mention “Myeloid” in the cell type metadata, 37,334 cells) of Qian and colleagues (36) from a web server (<http://blueprint.lambrechtslab.org>). Cells were merged using canonical correlation analysis and mutual nearest neighbors, and we selected the 5,000 most variable genes (following the Seurat 3 pipeline). We next performed Louvain graph-based clustering. At resolution 1.2, we obtained 37 clusters. Cluster 25 was expressing TIMD4. We did a subset of this cluster 25 to understand its heterogeneity. We discovered 4 subclusters using the pipeline previously describe. The differential analysis was performed using the Seurat function “FindMarkers” with logistic regression test, adding the tumor tissue type as a variable to correct. The parameter “min.pct” was set at 0.10, which means a gene has to be expressed in at least 10% of cells of a cluster to be considered in the differential analysis. For the visualization (violin and feature plots), we used adaptively thresholded low-rank approximation (ALRA) to improve the plot. ALRA is a pipeline to reduce dropout in a single-cell matrix. With ALRA our matrix went from 4.73% to 11.62% nonzero values. The k parameter calculated by the function “RunALRA” was 19.

To select macrophage-specific transcripts from C0 and C2 clusters, we downloaded the data set of Azizi and colleagues (GSE114725; ref. 27). We used the classic pipeline for single-cell analysis of Seurat V3 (without integration correction) from the raw count matrix (supplementary file GSE114725\_rna\_raw.csv.gz). We next perform Louvain graph-based clustering. At resolution 0.9, we obtained 39 clusters: 14 clusters of T cells, 6 clusters of B cells, 5 clusters of NK cells, 1 cluster of pDCs, DC1, DC2, CD16<sup>+</sup> monocytes, CD14<sup>+</sup> monocytes, neutrophils or mast cells, 3 clusters of macrophages, and 4 clusters of contaminating cells. We merged clusters of the same immune cell types.

### Data availability statement

The data generated in this study are available within the article and its supplementary data files. Expression profile data analyzed in this study were obtained from Gene-Expression Omnibus at GSE114725 and for data of TCGA, from GDC Legacy Archive (hg19) using TCGA biolinks R/Bioconductor package, considering the following projects: TCGA-BLCA, TCGA-BRCA, TCGA-COAD, TCGA-HNSC, TCGA-LUAD, TCGA-LUSC, TCGA-OV, TCGA-SKCM, and TCGA-UCEC. Single-cell expression profiles of myeloid cells of Qian and colleagues (36) were downloaded from a web server (<http://blueprint.lambrechtslab.org>).

## Results

### TIM4 expression identifies distinct populations of human MΦ

TIM4 expression has been reported in TBMΦ and in cells of the interfollicular area in human tonsils and spleen (3, 7). We extended the analysis of TIM4 expression on an institutional retrospective cohort including reactive lymphoid tissues and nonlymphoid normal tissues. In lymphoid tissues ( $n = 34$ ), TIM4 expression was confirmed on TBMΦ of reactive tonsils ( $n = 7$ ) and lymph nodes ( $n = 16$ ), in sinus



## Chapter 7. TIM4+FOLR2+ Macrophages Localized in TLS Correlate to an Active Immune Infiltrate Across Several Cancer Types

Bugatti et al.

MΦ and cells of the interfollicular area (Fig. 1A–C). In tonsils, we could also detect TIM4 reactivity in a minor fraction of 6-sulfo LacNAc<sup>+</sup> (slan<sup>+</sup>) cells, an MΦ population endowed with a high phagocytic capacity (Fig. 1D; ref. 23). As previously shown (3, 7), TIM4 reactivity was also detected in spleen MΦ (*n* = 6) that can be divided, based on their location and phenotype, into TIM4<sup>+</sup> marginal zone MΦ and TIM4<sup>+</sup>MΦ in the periarteriolar lymphoid sheaths (Fig. 1E and F). TIM4<sup>+</sup>MΦ were also detected in the thymus cortex (*n* = 2) and in the bone marrow (*n* = 3; Fig. 1G and H). Finally, TIM4 stains TBMΦ and a subset of cells localized in the T-cell area of intestinal Peyer's patches (Fig. 1I). Given that TIM4<sup>+</sup> cells in the nodal interfollicular areas (IF-TIM4<sup>+</sup>) had not been previously characterized, we set to define this population by double staining with MΦ markers. Indeed, TIM4<sup>+</sup> interfollicular cells coexpress a large set of MΦ

markers (Supplementary Fig. S1). We extended our analysis to dermatopathic lymphadenitis (ref. 28; *n* = 4) and found a population of TIM4<sup>+</sup>MΦ in T-cell nodules of the paracortex, intermingled with CD3<sup>+</sup> T cells (Supplementary Fig. S2). TIM4<sup>+</sup>TBMΦ, slan<sup>+</sup> cells, and thymic and bone marrow MΦ contained visible apoptotic bodies in their cytoplasm, as confirmed by costain for active caspase-3 (Supplementary Fig. S2), whereas TIM4<sup>+</sup>MΦ in the interfollicular area and in T-cell nodules of dermatopathic lymphadenitis were devoid of intracellular apoptotic bodies (Supplementary Fig. S2). In nonlymphoid tissues (*n* = 36), TIM4 expression was restricted to liver Kupffer cells (*n* = 4) and to a minor fraction of placental Hofbauer MΦ (*n* = 4; Supplementary Fig. S3). Unlike the mouse system (9), skin Langerhans cells (*n* = 4) were TIM4 negative (Supplementary Fig. S3).

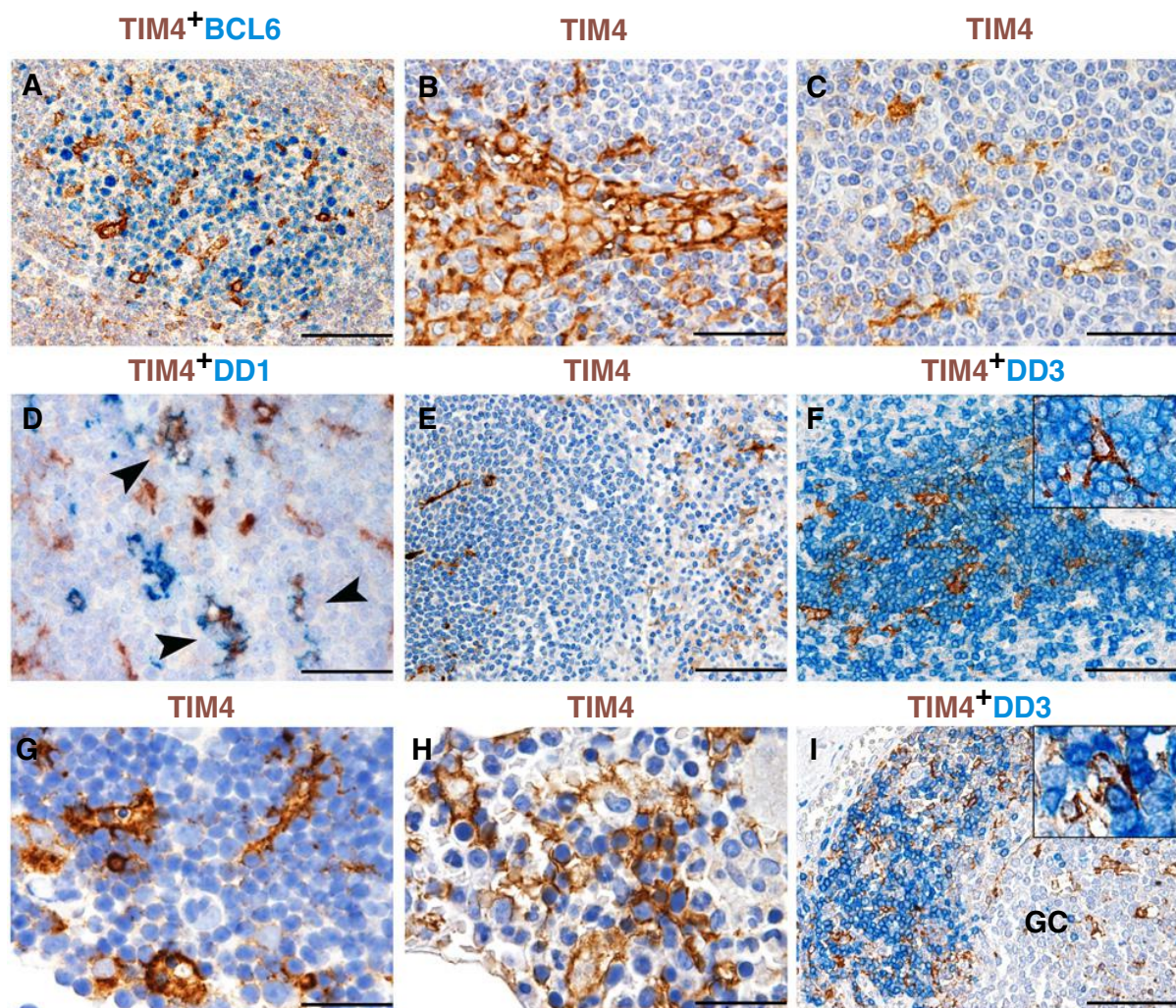


**Figure 1.**

TIM4 expression in human lymphoid tissues. Sections are from human reactive lymph nodes (A–C), tonsil (D), spleen (E and F), thymus (G) and bone marrow (H), and small intestine (I) and stained as labeled. In lymph nodes, TIM4 reactivity is detected in TBMs (A), sinus macrophages (B), and cells of the interfollicular area (C). In tonsils, TIM4 is expressed in a minor fraction of slan<sup>+</sup> cells (D). TIM4 reactivity is also detected in splenic marginal zone macrophages (E) and macrophages of the periarteriolar lymphoid sheaths (F). TIM4<sup>+</sup> macrophages are detected in the thymus cortex (G) and the bone marrow erythroid niches (H). In Peyer patches, TIM4 stains TBM and a subset of TIM4<sup>+</sup> macrophages localized in the T-cell area (I). Magnification: 100× (A, E, F, I), scale bar 200 μm; 400× (B, C, D, G, H), scale bar 50 μm.

Together, this analysis suggests that besides the already described class of highly phagocytic M $\Phi$ , TIM4 is expressed by a second group of nonphagocytic M $\Phi$  localized in the T-cell zone of various compartments.

#### TIM4 marks M $\Phi$ in the T-cell zone of carcinoma-associated tertiary lymphoid structures

Emerging findings indicate a complex phenotypic and genetic heterogeneity of tumor-associated M $\Phi$  (29–31); however, TIM4 expression on M $\Phi$  is poorly characterized in human cancers. Based on our findings on the role of mouse TIM4 in modulating the antitumor T-cell response in carcinomas (13), we further explored TIM4 expression in a set of primary carcinomas using tissue microarray ( $n = 126$ ; ref. 23). No reactivity could be detected in the tumor areas, thus excluding TIM4 expression on conventional tumor-infiltrating M $\Phi$  (Supplementary Fig. S4). However, TIM4 expression has been unequivocally detected in cancer tissues based on scRNA sequencing experiments (20). We thus extended our analysis on whole tumor sections, including the peritumoral area, of a cohort of human cancers ( $n = 135$ ) including non-small cell lung cancers ( $n = 37$ ), melanomas ( $n = 13$ ), cutaneous squamous cell carcinomas ( $n = 6$ ), cutaneous sebaceous carcinoma ( $n = 1$ ), colorectal carcinomas ( $n = 30$ ), endometrial carcinomas ( $n = 30$ ), luminal breast carcinomas ( $n = 5$ ), squamous cell carcinomas of the larynx ( $n = 8$ ), and gastric cancers ( $n = 5$ ). The analysis confirms the lack of TIM4 expression on conventional CD163<sup>+</sup>TREM2<sup>+</sup>M $\Phi$  infiltrating the tumor bed, as observed by immunostaining of sections from a pan-cancer tissue microarray (Fig. 2A–F). However, we could detect TIM4 expression in TLS surrounding the tumor area in primary and metastatic carcinomas (Fig. 2G and H; Supplementary Fig. S5). Immature TLS are composed of small aggregates of T cells, whereas fully mature TLS contain a B-cell area with germinal centers surrounded by a distinct T-cell zone. In addition to TBM $\Phi$ , TIM4 marks M $\Phi$  in immature TLS (Supplementary Fig. S5) and in the T-cell zone of mature TLS (from here referred to as <sup>TLS</sup>TIM4<sup>+</sup>; Fig. 2I and J). A large fraction (98.64%) of <sup>TLS</sup>TIM4<sup>+</sup> interacted with at least one surrounding T cell. Moreover, TLS-containing TIM4<sup>+</sup> cells frequently surrounded CD34<sup>+</sup> vessels (Supplementary Fig. S5). Based on double and sequential stains, we could confirm that <sup>TLS</sup>TIM4<sup>+</sup> cells in primary carcinomas express a large set of M $\Phi$  markers including MAFB, CD11c, C1q, APOE, CD163L1, CD14, CD163, CD16, CSF1R, PG-M1, and HLA-DR; heterogeneous expression was also found for MS4a4a (Fig. 3A–L), an M $\Phi$  marker essential for dectin-1-dependent activation of NK cell-mediated resistance to metastasis (32). Finally, based on double stains for active caspase-3, we observed that <sup>TLS</sup>TIM4<sup>+</sup> cells in primary carcinomas more rarely contain apoptotic cells/bodies compared with other TIM4<sup>+</sup>M $\Phi$  (Fig. 3M and N).

All these findings are in keeping with the existence of a specific TIM4<sup>+</sup>M $\Phi$  population (from here referred to as <sup>TLS</sup>TIM4<sup>+</sup>M $\Phi$ ) found in the T-zone of TLS, mostly interacting with T cells.

#### High TIM4 expression identifies immune-infiltrated immunogenic cancers enriched in TLS

Our microscopy findings suggest that <sup>TLS</sup>TIM4<sup>+</sup>M $\Phi$  are restricted to the group of TLS-containing carcinomas. This subgroup is particularly enriched in effector T cells and characterized by a better outcome (16). By analyzing transcriptional profiles of a large set ( $n = 3,850$ ) of human carcinomas from different primary sites (9 TCGA projects), we found that TIM4 expression strongly and positively correlates with the expression of a set of genes associated with infiltration of B cells (PAX5;  $R = 0.38$ ,  $P < 0.001$ ; Fig. 4A) and T cells

(CD3;  $R = 0.46$ ,  $P < 0.001$ ; Fig. 4B). Moreover, TIM4 expression correlates with a TLS signature composed of 12 TLS-related genes previously defined and validated (ref. 25;  $R = 0.46$ ,  $P < 0.001$ ; Fig. 4C). As visualized by tSNE, a group of cases across various cancer types (LUAD, LUSC, HNSC, and BRCA) resulted particularly enriched by TIM4, PAX5, CD3 transcripts, and the 12 TLS-related genes (Fig. 4D–J).

Immunogenic cancers are also defined by a high density of CD8<sup>+</sup> T cells (33, 34). We analyzed an institutional retrospective cohort of human LUAD and LUSC ( $n = 74$ ) and found that a significant fraction contained TLS ( $n = 53$ ; 71.6%). TLS regularly comprises <sup>TLS</sup>TIM4<sup>+</sup>M $\Phi$  and their density directly correlates with the density of CD8<sup>+</sup> T cells, as measured by digital microscopy (Supplementary Fig. S6A and S6B). This finding was also confirmed on the TCGA data sets both in LUSC ( $R = 0.55$ ,  $P < 0.001$ ) and LUAD ( $R = 0.34$ ,  $P < 0.001$ ), showing direct and positive correlation between TIM4 and CD8 transcripts.

To reinforce the notion that TIM4<sup>+</sup> cells may be enriched in immunoreactive tumors carrying abundant TLS we turned to analyze microsatellite unstable (MSI<sup>+</sup>) colorectal carcinomas (COAD), well-established examples of immune-infiltrated tumors (35). We directly correlated the occurrence of <sup>TLS</sup>TIM4<sup>+</sup>M $\Phi$  in COAD with associated DNA mismatch-repair defects (MLH-1 and PMS2) by IHC ( $n = 30$ ; Supplementary Fig. S6C). <sup>TLS</sup>TIM4<sup>+</sup>M $\Phi$  were detected in most of the COAD cases ( $n = 26/30$ ; 86%); however, its expression was restricted to TLS, resulting in largely negative conventional tumor-infiltrating M $\Phi$ . Molecular classifications have identified four consensus molecular subgroups of COAD according to their clinical, molecular, and immune features. Of note, CMS1 (containing MSI cases) and CMS4 are immune-infiltrated and highly enriched in TLS signature (Supplementary Fig. S6D), the latter being highly correlated with TIM4 expression (Supplementary Fig. S6E).

These findings indicate that <sup>TLS</sup>TIM4<sup>+</sup>M $\Phi$  are enriched in immune-infiltrated highly immunogenic cancers where they remain confined to the T-cell zone of TLS.

#### <sup>TLS</sup>TIM4<sup>+</sup>M $\Phi$ are transcriptionally distinct from tumor-infiltrating M $\Phi$

Tumor-infiltrating M $\Phi$  populations in human cancers show distinct phenotypes and localization, as revealed by the expression of TREM2 and FOLR2. FOLR2<sup>+</sup>M $\Phi$  are spatially segregated from TREM2<sup>+</sup>M $\Phi$  across human cancers (21), with a mutually exclusive expression (20). Specifically, TREM2<sup>+</sup>M $\Phi$  infiltrated the tumor nest, and its expression inversely correlated with patient survival in triple-negative breast cancer and colorectal cancer (21). By contrast, FOLR2<sup>+</sup>M $\Phi$  remain in the peritumoral stroma (20). Of note, FOLR2<sup>+</sup>M $\Phi$  could also be detected within TLS, and TIM4 transcript is part of the signature defining FOLR2<sup>+</sup>M $\Phi$  (20). To further extend this finding, we analyzed a set of primary carcinomas (TCGA;  $n = 3,850$ ; BLCA = bladder cancer; BRCA = breast cancer; COAD = colorectal cancer; HNSC = Head&Neck squamous cell carcinomas; LUAD = lung adenocarcinomas; LUSC = lung squamous cell carcinomas; OV = ovarian carcinomas; SKCM = skin cutaneous melanomas; UCEC = uterine corpus endometrial carcinoma). A multivariable linear regression model was fitted including covariates TIM4, TREM2, FOLR2, the tumor site, the stage, the TLS signature, PAX5, and CD3. The significantly direct correlation between PAX5, CD3, TLS, FOLR2 signature, and TIM4 expression was confirmed (Fig. 5A–D,  $P < 0.001$ ), whereas a lack of association was found with TREM2 expression (Fig. 5E). Accordingly, by dimensionality reduction, the cluster PAX5<sup>High</sup>CD3<sup>High</sup>TLS<sup>High</sup> was enriched of TIM4 and



## Chapter 7. TIM4+FOLR2+ Macrophages Localized in TLS Correlate to an Active Immune Infiltrate Across Several Cancer Types

Bugatti et al.

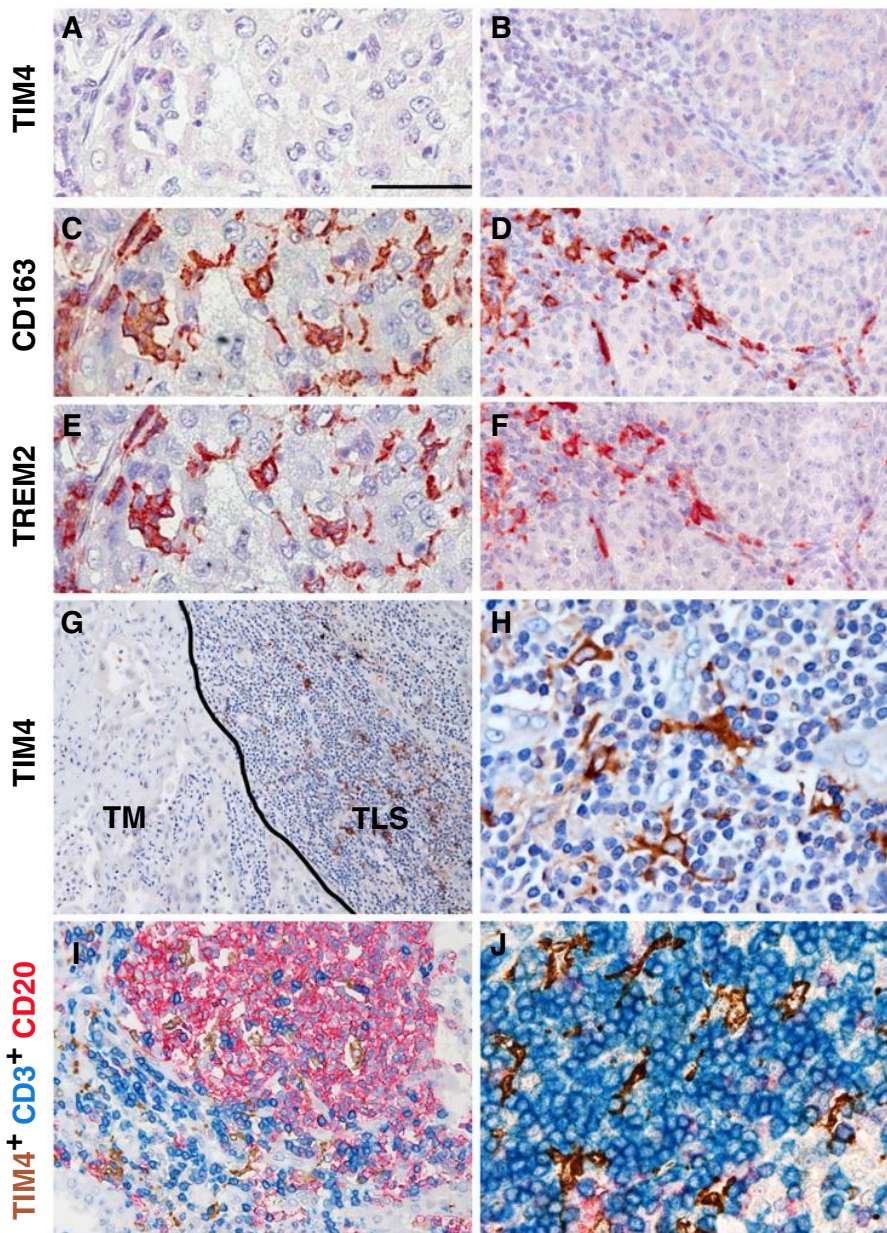


**Figure 2.** TIM4<sup>+</sup> macrophages in human cancers. Sections are from human high-grade serous ovarian carcinoma (A-F), lung adenocarcinoma (G, H), and squamous cell carcinoma of the larynx (I, J) and stained as labeled. TIM4 expression is absent on conventional CD163<sup>+</sup> TREM2<sup>+</sup> macrophages (A-F), as illustrated by sequential immunostain (performed on the same tissue section), but is detected in mature tertiary lymphoid structures surrounding the tumor area (G, low power view; H, high power view). Triple stain for CD20, CD3, and TIM4 highlights the localization of TIM4<sup>+</sup> cells in the B- and T-cell zone of the TLS (I) and their interaction with T cells (J, high power view). Magnification: 400× (A-F, H, J) scale bar 50 μm; 100× (G), scale bar 200 μm; 200× (I), scale bar 100 μm.

FOLR2 but not of TREM2 (Fig. 5F-I). These observations confirm a direct positive correlation in cancer tissues between FOLR2 and TIM4 expression with the local adaptive immune response and TLS formation.

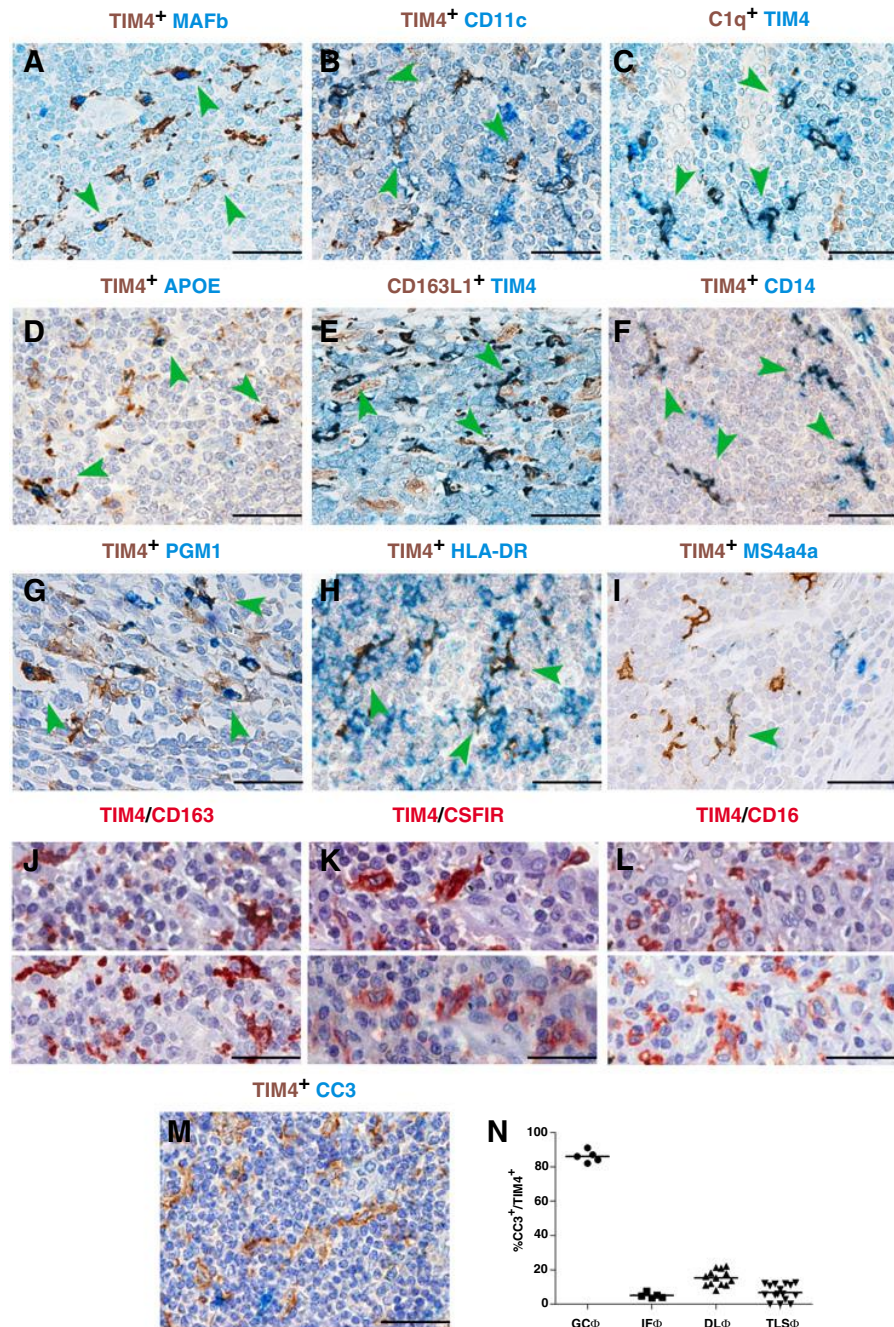
To gain further insight into the transcriptional profile of <sup>TLS</sup>TIM4<sup>+</sup>MF, we explored a pan-cancer scRNA-seq data set (36) comprising ovarian, breast, lung, and colorectal cancers. We merged 37,334 myeloid cells from all cancer types. Louvain graph-based clustering at the resolution 1.2 identified 37 clusters of mononuclear phagocytes (Fig. 6A). We identified a discrete cluster (C25) enriched in *TIM4* expression and macrophage transcripts (*CD163*, *CIQA*, *APOE*, *MAF*; ref. 37; Fig. 6B and C; Supplementary Table S3). We next investigated the heterogeneity of *TIM4*<sup>+</sup> C25. To this end, we

performed a new Louvain graph clustering of C25 and found 4 transcriptionally distinct subclusters (C0 to C4) at resolution 0.3 (Fig. 6D). The distinct subclusters expressed variable amounts of *FOLR2*, *TIM4*, and *TREM2* (Fig. 6E). C0 and C2 expressed *FOLR2* and *TIM4* more highly, as compared with C1 and C3 (Fig. 6E). This result suggests that C0 and C2 could represent <sup>TLS</sup>TIM4<sup>+</sup>MΦ and <sup>CA</sup>TIM4<sup>+</sup>MΦ. We found 50 differentially expressed genes between C0 and C2 (Supplementary Table S4). Among those genes, C2, with the highest expression of *FOLR2*, was enriched in *LYVE1*, *SLC40A1*, and *SEPP1* (Fig. 6E; Supplementary Table S5). We have previously shown that these transcripts are enriched in mammary gland-resident FOLR2<sup>+</sup> macrophages and predict good prognosis in a subgroup of breast cancer patients (20). C0 was enriched in genes reminiscent of



**Figure 3.**

Phenotype of  $^{TL5}TIM4^+$  macrophages in human cancer. Sections are from HNSCC (A-M) and stained as labeled. Double stain showing reactivity of  $^{TL5}TIM4^+$  macrophages to a large set of macrophage markers including MAFB (A), CD11c (B), C1q (C), APOE (D), CD163L1 (E), CD14 (F), PG-M1 (G), and HLA-DR (H); heterogeneous expression was found for MS4a4a (I). Sequential stains for TIM4 coupled with CD163 (J), CSF1R (K), and CD16 (L) showing coexpression of these markers in  $^{TL5}TIM4^+$  macrophages. By double stain for TIM4 and cleaved caspase-3 (CC3)  $^{TL5}TIM4^+$  macrophages are rarely engulfed by apoptotic cells/bodies (M, N). Magnification 400 $\times$  (A-M), scale bar 50 micron; GC = germinal center; IF = interfollicular area; DL = dermatopathic lymphadenitis; TLS = tertiary lymphoid structures.



$TREM2^+$  macrophages including *TREM2*, *FCN1*, and *PLAUR* (Fig. 6E; Supplementary Table S4; refs. 20, 21). We, therefore, concluded that  $TIMD4^+$ M $\Phi$  encompass two types of M $\Phi$  that might have a distinct function in the tumor microenvironment.  $TIMD4^+$  M $\Phi$  expressing *FOLR2* highly and *TREM2* lowly (C2) could be  $^{TL5}TIM4^+$ M $\Phi$  and could support antitumor responses as previously described for mammary gland-resident *FOLR2^+* macrophages (20).  $TIMD4^+$  M $\Phi$  expressing *TREM2* highly (C0) could be  $^{CA}TIM4^+$  M $\Phi$  with protumorigenic functions, as previously seen for  $TREM2^+$

macrophages (21, 38) or  $TIM4^+$  cavity and omentum resident macrophages (10, 15). We integrated the information derived from a previously defined expression matrix (ref. 20; Supplementary Fig. S7), by selecting among macrophage-restricted transcripts of the C0 and C2 clusters to be included in the definition of  $^{TL5}TIM4^+$ M $\Phi$  (average scaled expression of *TIMD4*, *FOLR2*, *SEPP1*, *SLC40A1*, *PMP22*, *MAMDC2*, and *NEURL2*) and  $^{CA}TIM4^+$  M $\Phi$  (average scaled expression of *TIMD4*, *TREM2*, *PLAUR*, *FN1*, *FCN1*, and *OLR1*) signatures. By exploring the TCGA data set with a pan-cancer analysis,

## Chapter 7. TIM4+FOLR2+ Macrophages Localized in TLS Correlate to an Active Immune Infiltrate Across Several Cancer Types

Bugatti et al.

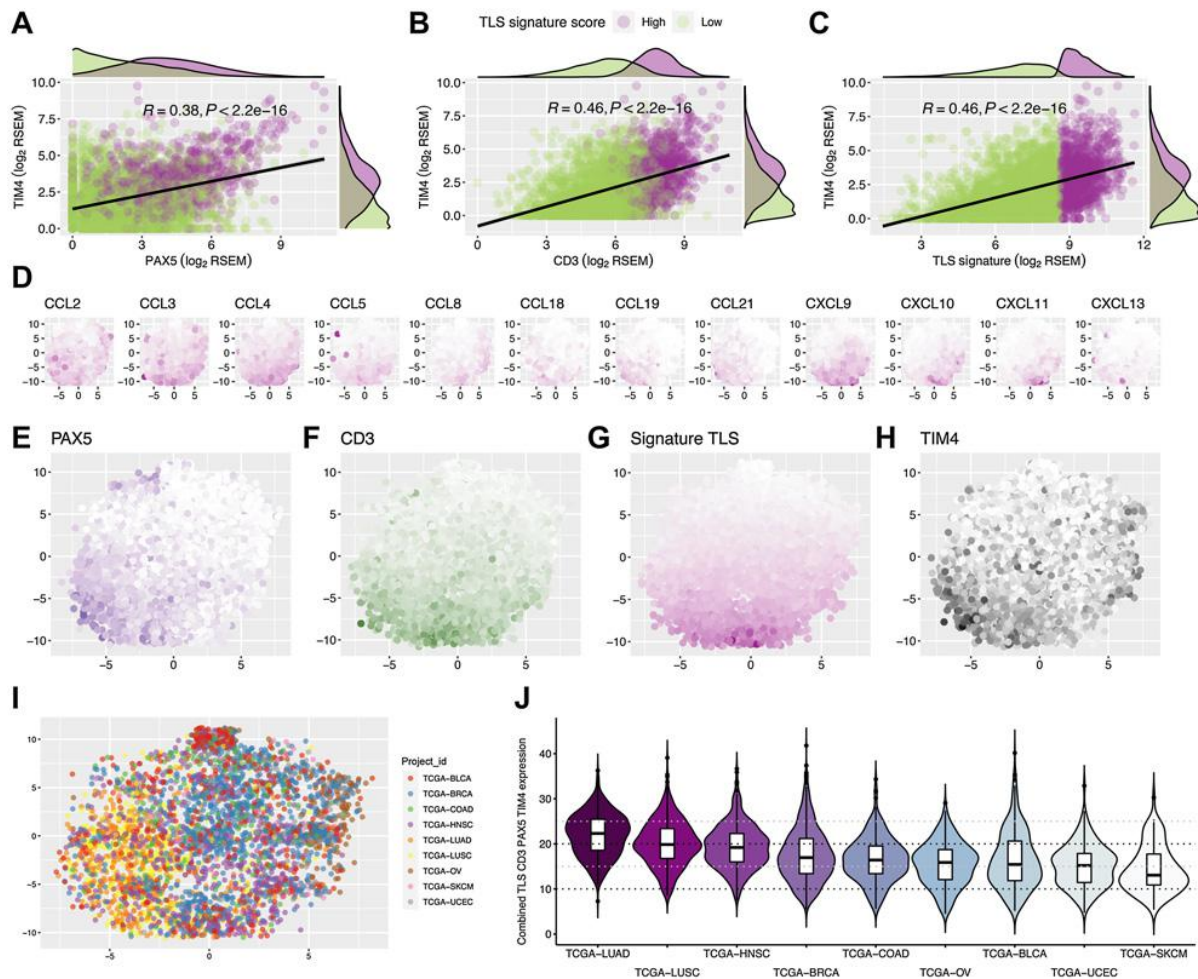


**Figure 4.**

TIM4 correlation with high lymphoid infiltration and TLS signature. Scatter plots showing the correlations between PAX5 (A), CD3 (B), TLS signature (C), and the TIM4 expression by Pearson test linear regression lines; colored marginal density plots highlight the TLS<sup>Low</sup> and TLS<sup>High</sup> groups applying as cutoff points the third quartile of TLS signature score distribution. tSNE plots devised by dimensionality reduction according to the expression of the 12 genes defining the TLS signature (D), PAX5 (E), and CD3 (F); the overall TLS signature score (G), the TIM4 expression (H), and tumor sites (I) are shown. Violin plots and box plots showing the sum of PAX5, CD3, TLS signature, and TIM4 among different tumor sites, in descending order according to the median values (J). Forest plots of two multivariable Cox models (both stratified for stage and TCGA project) of DFS and OS exploring in the selected data sets of the TCGA the clinical significance of the <sup>CA</sup>TIM4<sup>+</sup> MΦ signature (average scaled expression of TIMD4, TREM2, PLAUR, FNI, FCN1, and OLR1) and of the <sup>TL</sup>S-TIM4<sup>+</sup> MΦ one (average scaled expression of TIMD4, FOLR2, SEPP1, SLC40A1, PMP22, MAMDC2, and NEURL2); HR with 95% CI is shown. BLCA, bladder cancer; BRCA, breast cancer; COAD, colorectal cancer; HNSC, Head&Neck squamous cell carcinomas; LUAD, lung adenocarcinomas; LUSC, lung squamous cell carcinomas; OV, ovarian carcinomas; SKCM, skin cutaneous melanomas; UCEC, uterine corpus endometrial carcinoma.

we found that a higher expression of the <sup>CA</sup>TIM4<sup>+</sup> MΦ signature is associated with a significant worse DFS ( $P = 0.0093$ ) and OS ( $P = 0.005$ ), whereas a higher expression of the <sup>TL</sup>S-TIM4<sup>+</sup> MΦ signature predicts a significantly better DFS ( $P = 0.0096$ ; Fig. 6F and G).

### Cavitary TIM4<sup>+</sup> MΦ in pleural and peritoneal carcinoma localizations express immunosuppressive molecules

Studies on lung and ovarian cancer indicate that TIM4-expressing MΦ are found in pleural and peritoneal cavities as well as in the infiltrated omentum (10, 14, 15). Their occurrence has been associated with metastatic spread and worse outcome (10, 15), due to their capability to sequester neighboring T cells. By staining cell-

block sections, cavitary TIM4<sup>+</sup> MΦ were observed in fluid from noncancer patients ( $n = 5$ ) as a minor fraction of CD163<sup>+</sup> MΦ (Fig. 7A). In pleural ( $n = 10$ ) and peritoneal effusion ( $n = 10$ ) of patients with primary lung and ovarian carcinomas, we could confirm the existence of a cavity TIM4<sup>+</sup> MΦ subpopulation (from here referred as <sup>CA</sup>TIM4<sup>+</sup> MΦ) in all samples ( $n = 10/10$ ; Fig. 7A), showing a significantly increased percentage compared with non-neoplastic fluid ( $P = 0.0125$ ; Fig. 7A). We subsequently analyzed pleural and peritoneal biopsies from the same patient group and found that similar to other carcinoma sites, they also contained <sup>TL</sup>S-TIM4<sup>+</sup> MΦ (Fig. 7A). These microscopy findings identify two distinct TIM4<sup>+</sup> MΦ populations in patients with pleural and



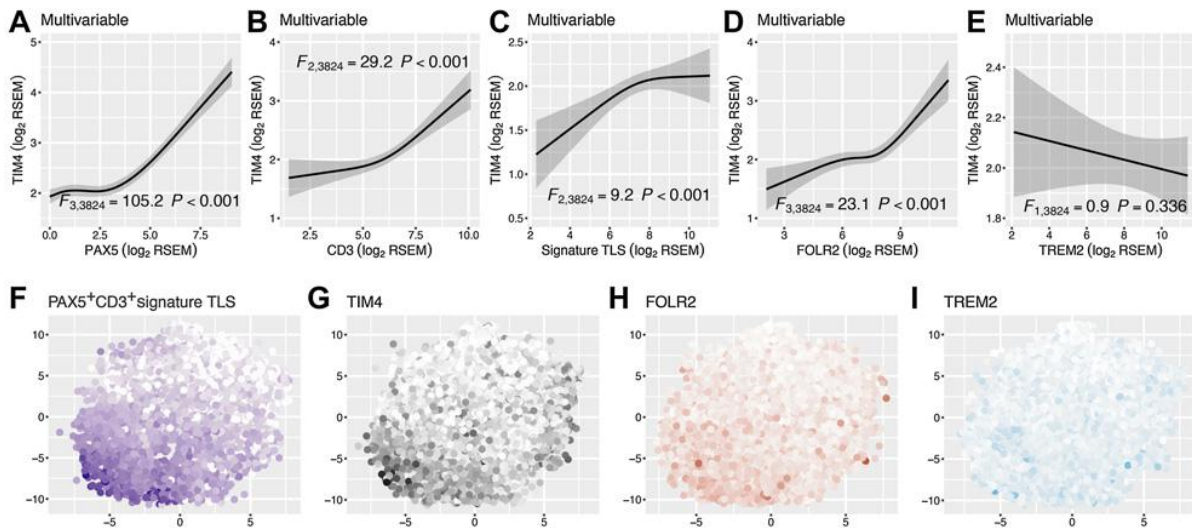


**Figure 5.** Coordinated expression of TIM4 and FOLR2 but not TREM2 in immune-infiltrated carcinomas. Partial effects plots derived from the multivariable linear regression model (multicancer TCGA data set;  $n = 3,850$ ) for the prediction of TIM4 expression, showing its association with PAX5, CD3, TLS signature score, and FOLR2, but not with TREM2 expression (A–E). tSNE plots highlighting the PAX5<sup>High</sup>CD3<sup>High</sup>TLS<sup>High</sup> cluster (F) enriched in TIM4 (G) and FOLR2 (H) but not associated with the TREM2 expression (I).

peritoneal effusions, including <sup>CA</sup>TIM4<sup>+</sup>MΦ and <sup>TLS</sup>TIM4<sup>+</sup>MΦ. We subsequently compared these two populations by phenotypes (Fig. 7B). By using multiple sequential stains, we found that <sup>CA</sup>TIM4<sup>+</sup>MΦ express regularly TREM2 (86.39%) and coexpress FOLR2, whereas <sup>TLS</sup>TIM4<sup>+</sup>MΦ expressed FOLR2 but lack TREM2 (Fig. 7B; Supplementary Fig. S8).

Moreover, a major fraction of <sup>TLS</sup>TIM4<sup>+</sup>FOLR2<sup>+</sup>TREM2<sup>-</sup>MΦ (98.64%) interacted with CD3<sup>+</sup> T cells (Fig. 7C). A similar phenotype (TIM4<sup>+</sup>FOLR2<sup>+</sup>TREM2<sup>-</sup>) was confirmed in MΦ of the interfollicular area in reactive lymphoid organs (Supplementary Fig. S8).

These findings indicate the existence of two TIM4<sup>+</sup>MΦ populations showing phenotypic diversity and distinct localization. TREM2 expression by <sup>CA</sup>TIM4<sup>+</sup>MΦ might likely account for their detrimental prognostic significance (10, 15). To further extend our analysis at the functional level, we tested the expression of IL10 and TGFβ by TIM4<sup>+</sup>MΦ in carcinoma-associated TLS ( $n = 7$ ) and in pleural/peritoneal effusions ( $n = 5$ ). Of relevance, only <sup>CA</sup>TIM4<sup>+</sup>MΦ showed a detectable and abundant IL10 and TGFβ mRNA signal, whereas <sup>TLS</sup>TIM4<sup>+</sup>MΦ resulted largely negative (Fig. 7D), as proved by combining TIM4 immunostaining and RNAscope *in situ* hybridization. Based on these findings, we quantified CD3<sup>+</sup>Foxp3<sup>+</sup> regulatory T cells (Treg) in cell blocks sections of pleural and peritoneal fluids and found an increased percentage of Treg in neoplastic cases compared with reactive conditions (Supplementary Fig. S9).

These findings confirm the existence of distinct TIM4<sup>+</sup> populations with diverse subsellular localization that may be associated with different functions.

## Discussion

TIM4 expression on human immune cells has been poorly investigated. By microscopic mapping, this study analyzed the cellular localization of TIM4 on human tissues. As previously reported (3, 7), we confirm that TIM4 is predominantly expressed

on MΦ in secondary lymphoid organs. TIM4<sup>+</sup>MΦ are also detected in the thymus and bone marrow. Among nonlymphoid organs, only liver Kupffer cells and a fraction of placenta Hofbauer cells were positive for TIM4. The most relevant and novel finding of this study was found in the analysis of cancer tissues. Specifically, TIM4 is lacking in conventional carcinoma-infiltrating MΦ but is expressed in specific MΦ of the T-cell zone in the tertiary lymphoid structures (referred to as <sup>TLS</sup>TIM4<sup>+</sup>MΦ) and in a fraction of cavity MΦ (referred to as <sup>CA</sup>TIM4<sup>+</sup>MΦ). The existence of <sup>TLS</sup>TIM4<sup>+</sup>MΦ was never reported, whereas <sup>CA</sup>TIM4<sup>+</sup>MΦ has been previously described (10). Based on *in silico* and IHC data, we envisage a protective role of <sup>TLS</sup>TIM4<sup>+</sup>MΦ by promoting adaptive T-cell immunity, whereas <sup>CA</sup>TIM4<sup>+</sup>MΦ might represent a protumor immune cell population based on their expression of TREM2.

As a novel finding on lymphoid tissues, this study uncovers TIM4 expression on cells of the interfollicular area. TIM4<sup>+</sup> interfollicular cells coexpress MΦ markers, thus corresponding to a fraction of nodal MΦ. TIM4 reactivity was also observed in dermatopathic lymphadenitis, particularly in MΦ intermingled with CD3<sup>+</sup> T cells in T-cell nodules of the paracortex. As has been shown (39), TIM4 plays a relevant role in the clearance of apoptotic B cells in germinal centers by TBMΦ (2). We could document colocalization of TIM4 and active caspase-3<sup>+</sup> apoptotic cells/bodies in TBMΦ. A similar finding was observed on thymic and bone marrow TIM4<sup>+</sup>MΦ as well as on tonsils slan<sup>+</sup> cells, an MΦ population with a high phagocytic capacity (23). Thymic TIM4<sup>+</sup>MΦ regulate T cell-positive selection (40, 41), whereas bone marrow TIM4<sup>+</sup>MΦ engulf PtdSer-exposing nuclei expelled from erythroid precursor cells during red blood cells maturation (42) and are thought to supply the erythroblasts with iron and growth factors (43). As documented in our previous study, slan<sup>+</sup> MΦ containing neoplastic B cells are detected in diffuse large B-cell lymphoma (44). At variance with TIM4<sup>+</sup>MΦ clearing of apoptotic cells, we found TIM4<sup>+</sup>MΦ from the interfollicular area, as well as <sup>TLS</sup>TIM4<sup>+</sup>MΦ, rarely contain apoptotic bodies. This finding suggests



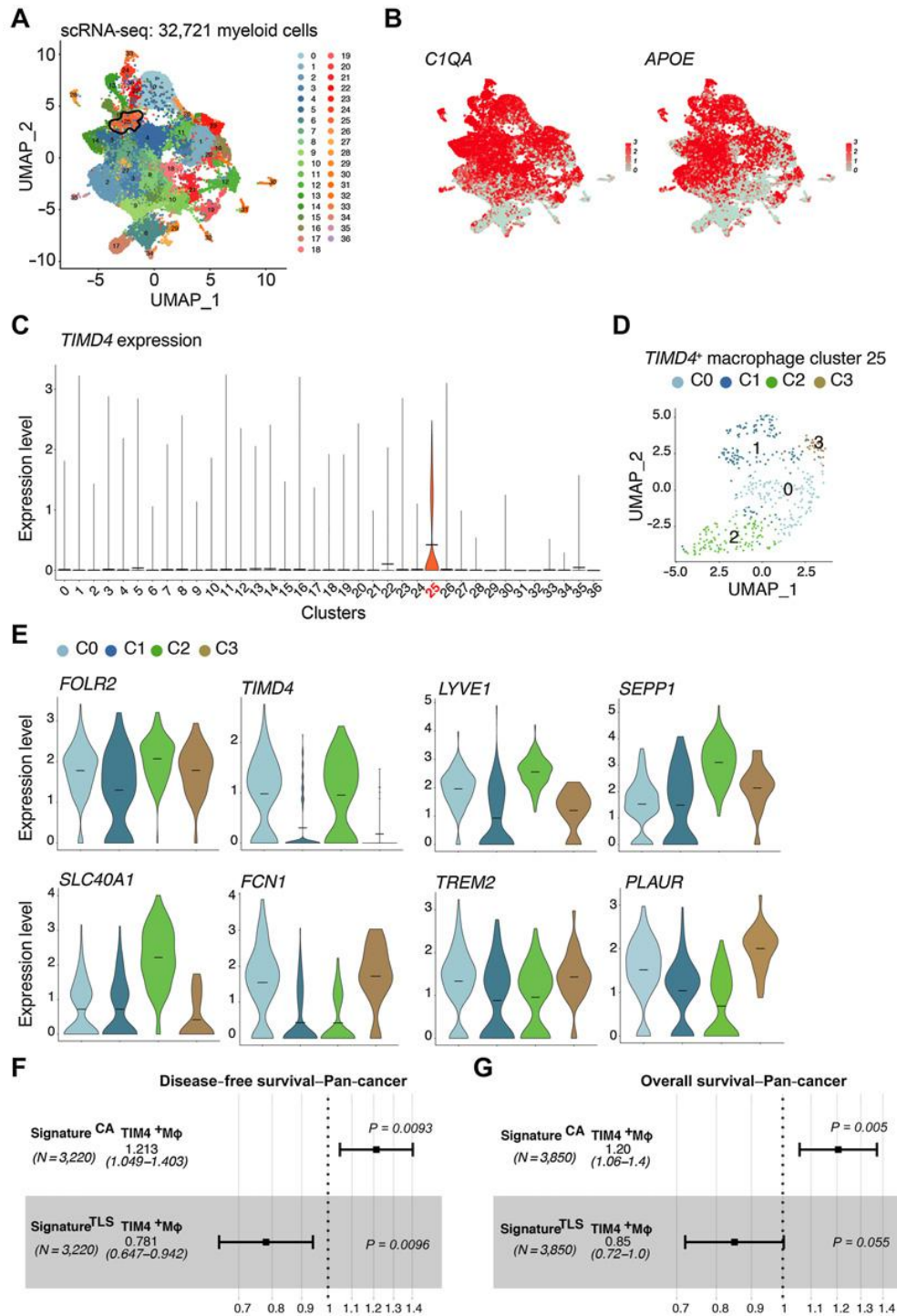


**Figure 6.**

scRNA-seq analysis of myeloid cells across cancer types. Dimensionality reduction of scRNA-seq data merged from lung, colorectal, ovarian, and breast tumors was performed using a Louvain graph-based clustering identifying 37 clusters (middle). Each dot represents an individual cell ( $n = 37,334$ ; **A**). Dimensionality reduction of scRNA-seq for *C1QA* and *APOE* (**B**). Violin plots illustrating expression distributions among the 37 clusters of *TIMD4* (right; **C**). UMAP visualization of *TIMD4*<sup>+</sup> macrophages (cluster 25) at a 0.3 resolution (**D**). Expression distributions of *FOLR2*, *TIMD4*, *LYVE1*, *SEPP1*, *SLC40A1*, *FCN1*, *TREM2*, and *PLAUR* across macrophage of C25 (**E**).

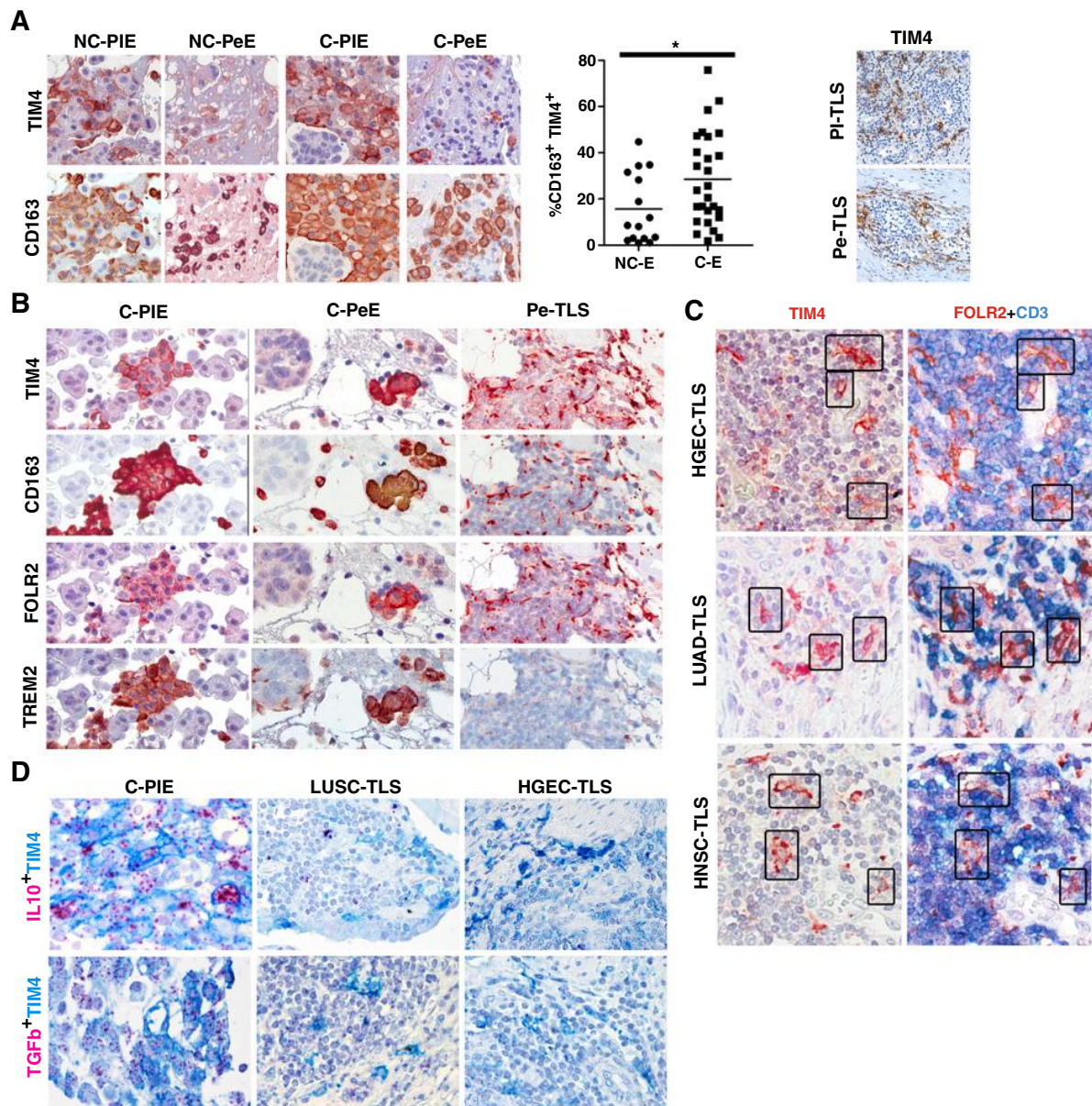


**Figure 7.**

Comparative phenotype of  $C^A$ TIM4<sup>+</sup> macrophages and  $T^L S$ TIM4<sup>+</sup> macrophages. Sections are from cell block obtained from human pleural (PIE) and peritoneal (PeE) effusion of noncancer (NC) and cancer (C) cases (A, B, D); pleural (PI-TLS) and peritoneal (Pe-TLS) biopsies containing TLS (A and B); a set of cancer containing TLS (C and D). TIM4<sup>+</sup> macrophages represent a fraction of CD163<sup>+</sup> macrophages in pleural and peritoneal effusion (A), with an increased percentage in cancer effusion compared with nonneoplastic fluid (graph in A);  $T^L S$ TIM4<sup>+</sup> macrophages are also identifiable in biopsies from pleural and peritoneal localization of carcinomas (A). Multiple sequential stains show  $C^A$ TIM4<sup>+</sup> macrophages strongly expressed FOLR2 and TREM2, whereas  $T^L S$ TIM4<sup>+</sup> macrophages lack TREM2 (B);  $T^L S$ TIM4<sup>+</sup>FOLR2<sup>+</sup>TREM2<sup>-</sup> macrophages interact with surrounding CD3<sup>+</sup> T cells (C), as highlighted by a black rectangle.  $C^A$ TIM4<sup>+</sup> macrophages show abundant IL10 and TGFβ mRNA signals, whereas  $T^L S$ TIM4<sup>+</sup> macrophages are absent (D). Original A–C images are obtained from digital slides using 400× magnification; scale bar, 66 μm [sections from human pleural (PIE) and peritoneal (PeE) effusion in A, B, C], scale bar, 200 μm [sections from pleural (PI-TLS) and peritoneal (Pe-TLS) biopsies containing TLS in A]. Magnification 400× (D); scale bar, 50 μm. HGEC, high-grade endometrial carcinomas; LUAD, lung adenocarcinoma; HNSC, head and neck squamous cell carcinoma.



# Chapter 7. TIM4+FOLR2+ Macrophages Localized in TLS Correlate to an Active Immune Infiltrate Across Several Cancer Types

Bugatti et al.

an alternative function of TIM4 in these cells. Based on their location and recurrent interaction with T cells (interfollicular and TLS T-cell zone), we propose their involvement in modulating T-cell responses.

The role of TIM4 in cancer immunity remains poorly explored. Based on this study, TIM4 is lacking in conventional tumor-infiltrating M $\Phi$ , whereas it marks cells in TLS, organized lymphoid structures found at the periphery of the tumor areas. TIM4<sup>+</sup> cells found in TLS express a set of M $\Phi$ -associated proteins, thus confirming their M $\Phi$  identity. Therefore, based on their localization, morphology, and phenotype, we propose that <sup>TLS</sup>TIM4<sup>+</sup>M $\Phi$  belong to a specific M $\Phi$  population distinct from classic tumor-infiltrating M $\Phi$ . <sup>TLS</sup>TIM4<sup>+</sup>M $\Phi$  in the T-cell compartment are poorly characterized. They might be involved in the regulation of antitumor effector responses developing in TLS. We observed that immunogenic cancers (including MSI<sup>+</sup> COAD, LUAD, and LUSC) are enriched in TIM4<sup>+</sup>M $\Phi$ -containing TLS, whose density directly correlates with the density of infiltrating CD8<sup>+</sup> T cells (this study and refs. 33 and 34). As previously reported (16), TLS represent privileged sites for local presentation of neighboring tumor antigens and subsequent activation of T- and B-cell responses. <sup>TLS</sup>TIM4<sup>+</sup>M $\Phi$  in the T-cell zone might thus instruct the antitumor adaptive immunity. TIM4<sup>+</sup>M $\Phi$  coexpress FOLR2, characterized by members of our group as a marker of tissue-resident M $\Phi$ , located in the peritumoral stroma and associated with antitumor T-cell response (20). By exploring a pan-cancer scRNA-seq data set, we identified a cluster of cells coexpressing TIM4<sup>+</sup>FOLR2<sup>+</sup> across human cancers. This cluster is enriched of M $\Phi$ -associated transcripts encoding for scavenger receptors, complement components, and M $\Phi$  chemokines. By subclustering of the same data set, we could identify two TIM4<sup>+</sup>FOLR2<sup>+</sup> clusters. One cluster is enriched in markers of perivascular M $\Phi$  like *LYVE1*, *SLC40A1*, and *SEPP1* transcripts, whereas the other is reminiscent of immune-suppressive TREM2<sup>+</sup> M $\Phi$  (21,22). The function of *LYVE1*, *SLC40A1*, and *SEPP1* in macrophage biology is diverse and highlights the role of perivascular macrophages in regulating homeostatic and inflammatory processes (45–47). Among other DEG enriched in <sup>TLS</sup>TIM4<sup>+</sup>M $\Phi$ , we also found genes associated with proinflammatory macrophages such as MT-CYB (48), MT-ATP6 (48), CTSB (49), and PLTP (50) or to some antitumor functions such as MAMDC2 (51). Finally, by survival analysis, a <sup>TLS</sup>TIM4<sup>+</sup>M $\Phi$  signature predicts a better OS and DFS.

By microscopic mapping of cell-block sections from pleural and peritoneal effusions of patients with carcinomas, we confirm the expression of TIM4 on cavitory M $\Phi$ . This <sup>CA</sup>TIM4<sup>+</sup>M $\Phi$  population is expanded in cancer patients (ovarian and lung carcinomas). Of note, <sup>CA</sup>TIM4<sup>+</sup>M $\Phi$  also express FOLR2; however, at variance with <sup>TLS</sup>TIM4<sup>+</sup>M $\Phi$ , <sup>CA</sup>TIM4<sup>+</sup>M $\Phi$  express the immunosuppressive molecule TREM2 (21, 22), supporting their protumor phenotype, as revealed by studies in ovarian cancer (10, 14, 15). Notably, by exploring a pan-cancer data set, we could confirm that <sup>CA</sup>TIM4<sup>+</sup>M $\Phi$  signature predicts worse OS and DFS. TREM2 is induced in human monocytes and mouse bone marrow cells upon exposure to GM-CSF and CSF-1 (52, 53). We envisage that coexpression of TREM2 in <sup>CA</sup>TIM4<sup>+</sup>M $\Phi$  may reflect the abundance of these cytokines in the cavity fluid of cancer patients, as previously observed (54–56); alternatively, phenotypic and molecular differences between <sup>TLS</sup>TIM4<sup>+</sup>M $\Phi$  and <sup>CA</sup>TIM4<sup>+</sup>M $\Phi$  might result from a different origin of the two populations (resident vs. monocyte-derived). At variance with <sup>TLS</sup>TIM4<sup>+</sup>M $\Phi$ , <sup>CA</sup>TIM4<sup>+</sup>M $\Phi$  expresses *IL10* and *TGF $\beta$*  mRNA, further supporting their immunosuppressive function. Accordingly, an increased frequency of Treg was observed in neoplastic cavitory fluids. These observations might suggest tailored intracavitary immunotherapy

approaches for the effusion component of advanced cancers (57), as those targeting the immunosuppressive molecule TREM2 (38).

TIM4 is selectively expressed in resident macrophages across several tissues (58) including cavities and omental macrophages in cancer patients (10, 15). TIM4 expression is highly regulated by tissue-derived signals; however, the signals inducing its expression are not unequivocally characterized. Retinoic acid regulates gut-resident macrophages via GATA6 (59), whereas in mouse peritoneal macrophages, TIM4 is under the control of the transcription factors KLF2 and KLF4 (60). Further, the TIM4 promoter contains binding sites for STAT6 that regulate its expression via p300 (61). Data from our study suggest that two classes of TIM4-expressing macrophages with divergent functions exist in cancer tissues. It remains to be established whether TIM4<sup>+</sup> macrophages commonly acquire the marker and then further diversify in subtissue localization or coacquire TIM4 and divergent programs directly in the final tissue location.

In conclusion, the identification and localization of TIM4 expression on tumor-associated cells in human cancer have been severely limited by the lack of appropriate reagents (14). This study identifies for the first time a specific population of human M $\Phi$ , topographically distinct from conventional tumor-infiltrating M $\Phi$ , that localize in the T-cell zone of tumor-associated TLS. The exact role and clinical relevance of these cells in the antitumoral immune response require further research. <sup>TLS</sup>TIM4<sup>+</sup>M $\Phi$  are also found in immature nascent TLS; whether these cells can also play a role in lymphoid tissue induction is an unresolved question. A more extended characterization of these cells in comparison with other tumor-associated macrophages (including TIM4<sup>+</sup> germinal center macrophages in TLS) based on spatial “omics” approaches will further extend our knowledge on the heterogeneity of tumor-associated M $\Phi$ .

## Authors' Disclosures

N. Caronni reports grants from AIRC during the conduct of the study. No disclosures were reported by the other authors.

## Authors' Contributions

**M. Bugatti:** Data curation, formal analysis, investigation, methodology, writing–review and editing. **M. Bergamini:** Data curation, formal analysis, investigation, writing–original draft. **F. Missale:** Software, formal analysis, investigation, writing–review and editing. **M. Monti:** Data curation, methodology. **L. Ardighieri:** Resources, investigation. **I. Pezzali:** Formal analysis. **S. Picinoli:** Formal analysis. **N. Caronni:** Data curation, methodology. **Y. Missolo-Koussou:** Data curation, software, methodology, writing–original draft. **J. Helft:** Investigation, writing–original draft. **F. Benvenuti:** Conceptualization, investigation, writing–original draft, writing–review and editing. **W. Vermi:** Conceptualization, resources, supervision, funding acquisition, writing–original draft, writing–review and editing.

## Acknowledgments

We would like to thank pathologists, technicians, clinicians, nurses, and administrative employers that have provided support to the study and to the follow-up of cancer patients. W. Vermi is funded by Associazione Italiana per la Ricerca sul Cancro (AIRC-IG-23179).

The publication costs of this article were defrayed in part by the payment of publication fees. Therefore, and solely to indicate this fact, this article is hereby marked “advertisement” in accordance with 18 USC section 1734.

## Note

Supplementary data for this article are available at Cancer Immunology Research Online (<http://cancerimmunolres.aacrjournals.org/>).

Received April 8, 2022; revised June 24, 2022; accepted September 12, 2022; published first September 19, 2022.

References

- Meyers JH, Chakravarti S, Schlesinger D, Illes Z, Waldner H, Umetsu SE, et al. TIM-4 is the ligand for TIM-1, and the TIM-1-TIM-4 interaction regulates T cell proliferation. *Nat Immunol* 2005;6:455–64.
- Miyaniishi M, Tada K, Koike M, Uchiyama Y, Kitamura T, Nagata S. Identification of Tim4 as a phosphatidylserine receptor. *Nature* 2007;450:435–9.
- Kobayashi N, Karisola P, Peña-Cruz V, Dorfman DM, Jinushi M, Umetsu SE, et al. TIM-1 and TIM-4 glycoproteins bind phosphatidylserine and mediate uptake of apoptotic cells. *Immunity* 2007;27:927–40.
- Rodriguez-Manzanet R, Sanjuan MA, Wu HY, Quintana FJ, Xiao S, Anderson AC, et al. T and B cell hyperactivity and autoimmunity associated with niche-specific defects in apoptotic body clearance in TIM-4-deficient mice. *Proc Natl Acad Sci U S A* 2010;107:8706–11.
- Albacker LA, Yu S, Bedoret D, Lee W-L, Umetsu SE, Monahan S, et al. TIM-4, expressed by medullary macrophages, regulates respiratory tolerance by mediating phagocytosis of antigen-specific T cells. *Mucosal Immunol* 2013;6:580–90.
- Shakhov AN, Rybtov S, Tumanov AV, Shulenin S, Dean M, Kuprash DV, et al. SMUCKLER/TIM4 is a distinct member of TIM family expressed by stromal cells of secondary lymphoid tissues and associated with lymphotoxin signaling. *Eur J Immunol* 2004;34:494–503.
- Dorfman DM, Hornick JL, Shahsafaei A, Freeman GJ. The phosphatidylserine receptors, T cell immunoglobulin mucin proteins 3 and 4, are markers of histiocytic sarcoma and other histiocytic and dendritic cell neoplasms. *Hum Pathol* 2010;41:1486–94.
- Wong K, Valdez PA, Tan C, Yeh S, Hongo J-A, Ouyang W. Phosphatidylserine receptor Tim-4 is essential for the maintenance of the homeostatic state of resident peritoneal macrophages. *Proc Natl Acad Sci U S A* 2010;107:8712–7.
- Zhang X, Liu Q, Wang J, Li G, Weiland M, Yu F-S, et al. TIM-4 is differentially expressed in the distinct subsets of dendritic cells in skin and skin-draining lymph nodes and controls skin Langerhans cell homeostasis. *Oncotarget* 2016;7:37498–512.
- Etzerodt A, Moulin M, Doktor TK, Delfini M, Mossadegh-Keller N, Bajenoff M, et al. Tissue-resident macrophages in omentum promote metastatic spread of ovarian cancer. *J Exp Med* 2020;217.
- Shaw TN, Houston SA, Wemyss K, Bridgeman HM, Barbera TA, Zangerle-Murray T, et al. Tissue-resident macrophages in the intestine are long lived and defined by Tim-4 and CD4 expression. *J Exp Med* 2018;215:1507–18.
- Baghdadi M, Yoneda A, Yamashina T, Nagao H, Komohara Y, Nagai S, et al. TIM-4 glycoprotein-mediated degradation of dying tumor cells by autophagy leads to reduced antigen presentation and increased immune tolerance. *Immunity* 2013;39:1070–81.
- Caronni N, Piperno GM, Simoncello F, Romano O, Vodret S, Yanagihashi Y, et al. TIM4 expression by dendritic cells mediates uptake of tumor-associated antigens and anti-tumor responses. *Nat Commun* 2021;12.
- Xia H, Li S, Li X, Wang W, Bian Y, Wei S, et al. Autophagic adaptation to oxidative stress alters peritoneal residential macrophage survival and ovarian cancer metastasis. *JCI insight* 2020;5:e141115.
- Chow A, Schad S, Green MD, Hellmann MD, Allaj V, Ceglia N, et al. Tim-4(+) cavity-resident macrophages impair anti-tumor CD8(+) T cell immunity. *Cancer Cell* 2021;39:973–88.e9.
- Sautés-Fridman C, Petitprez F, Calderaro J, Fridman WH. Tertiary lymphoid structures in the era of cancer immunotherapy. *Nat Rev Cancer* 2019;19:307–25.
- Nerviani A, Pitzalis C. Role of chemokines in ectopic lymphoid structures formation in autoimmunity and cancer. *J Leukoc Biol* 2018;104:333–41.
- Helmkink BA, Reddy SM, Gao J, Zhang S, Basar R, Thakur R, et al. B cells and tertiary lymphoid structures promote immunotherapy response. *Nature* 2020;577:549–55.
- Cabrita R, Lauss M, Sanna A, Donia M, Skaarup Larsen M, Mitra S, et al. Tertiary lymphoid structures improve immunotherapy and survival in melanoma. *Nature* 2020;577:561–5.
- Nalio Ramos R, Missolo-Koussou Y, Gerber-Ferder Y, Bromley CP, Bugatti M, Núñez NG, et al. Tissue-resident FOLR2(+) macrophages associate with CD8(+) T cell infiltration in human breast cancer. *Cell* 2022;185:1189–207.
- Molgora M, Esaulova E, Vermi W, Hou J, Chen Y, Luo J, et al. TREM2 modulation remodels the tumor myeloid landscape enhancing anti-PD-1 immunotherapy. *Cell* 2020;182:886–900.
- Katzenelenbogen Y, Sheban F, Yalin A, Yofe I, Svetlichnyy D, Jaitin DA, et al. Coupled scRNA-seq and intracellular protein activity reveal an immunosuppressive role of TREM2 in cancer. *Cell* 2020;182:872–85.
- Vermi W, Micheletti A, Lonardi S, Costantini C, Calzetti F, Nascimbene R, et al. slanDCs selectively accumulate in carcinoma-draining lymph nodes and marginate metastatic cells. *Nat Commun* 2014;5:3029.
- Coppola D, Nebozhyn M, Khalil F, Dai H, Yeatman T, Loboda A, et al. Unique ectopic lymph node-like structures present in human primary colorectal carcinoma are identified by immune gene array profiling. *Am J Pathol* 2011;179:37–45.
- Calderaro J, Petitprez F, Becht E, Laurent A, Hirsch TZ, Rousseau B, et al. Intra-tumoral tertiary lymphoid structures are associated with a low risk of early recurrence of hepatocellular carcinoma. *J Hepatol* 2019;70:58–65.
- Van der Maaten L, Hinton G. Visualizing data using t-SNE. *J Mach Learn Res* 2008;9.
- Azizi E, Carr AJ, Plitas G, Cornish AE, Konopacki C, Prabhakaran S, et al. Single-cell map of diverse immune phenotypes in the breast tumor microenvironment. *Cell* 2018;174:1293–308.
- Geissmann F, Dieu-Nosjean MC, Dezutter C, Valladeau J, Kaya S, Leborgne M, et al. Accumulation of immature Langerhans cells in human lymph nodes draining chronically inflamed skin. *J Exp Med* 2002;196:417–30.
- Mantovani A, Marchesi F, Jaillon S, Garlanda C, Allavena P. Tumor-associated myeloid cells: diversity and therapeutic targeting. *Cell Mol Immunol* 2021;18:566–78.
- Lopez-Yrigoyen M, Cassetta L, Pollard JW. Macrophage targeting in cancer. *Ann N Y Acad Sci* 2021;1499:18–41.
- Mulder K, Patel AA, Kong WT, Piot C, Halitzki E, Dunsmore G, et al. Cross-tissue single-cell landscape of human monocytes and macrophages in health and disease. *Immunity* 2021;54:1883–900.
- Mattiola I, Tomay F, De Pizzol M, Silva-Gomes R, Savino B, Gulic T, et al. The macrophage tetraspan MS4A4A enhances dectin-1-dependent NK cell-mediated resistance to metastasis. *Nat Immunol* 2019;20:1012–22.
- Loupakis F, Depetris I, Bason P, Intini R, Prete AA, Leone F, et al. Prediction of benefit from checkpoint inhibitors in mismatch repair deficient metastatic colorectal cancer: role of tumor infiltrating lymphocytes. *Oncologist* 2020;25:481–7.
- Lin A, Zhang J, Luo P. Crosstalk between the MSI status and tumor microenvironment in colorectal cancer. *Front Immunol* 2020;11:2039.
- De' Angelis GL, Bottarelli L, Azzoni C, De' Angelis N, Leandro G, Di Mario F, et al. Microsatellite instability in colorectal cancer. *Acta Biomed* 2018;89:97–101.
- Qian J, Olbrecht S, Boeckx B, Vos H, Laoui D, Etioglu E, et al. A pan-cancer blueprint of the heterogeneous tumor microenvironment revealed by single-cell profiling. *Cell Res* 2020;30:745–62.
- Ardighieri L, Missale F, Bugatti M, Gatta LB, Pezzali I, Monti M, et al. Infiltration by CXCL10 secreting macrophages is associated with antitumor immunity and response to therapy in ovarian cancer subtypes. *Front Immunol* 2021;12:690201.
- Binnewies M, Pollack JL, Rudolph J, Dash S, Abushawish M, Lee T, et al. Targeting TREM2 on tumor-associated macrophages enhances immunotherapy. *Cell Rep* 2021;37:109844.
- Gray EE, Cyster JG. Lymph node macrophages. *J Innate Immun* 2012;4:424–36.
- Wakimoto T, Tomisaka R, Nishikawa Y, Sato H, Yoshino T, Takahashi K. Identification and characterization of human thymic cortical dendritic macrophages that may act as professional scavengers of apoptotic thymocytes. *Immunobiology* 2008;213:837–47.
- Paessens LC, Fluitsma DM, van Kooyk Y. Haematopoietic antigen-presenting cells in the human thymic cortex: evidence for a role in selection and removal of apoptotic thymocytes. *J Pathol* 2008;214:96–103.
- Yeo JH, Lam YW, Fraser ST. Cellular dynamics of mammalian red blood cell production in the erythroblastic island niche. *Biophys Rev* 2019;11:873–94.
- Fraser ST, Midwinter RG, Coupland LA, Kong S, Berger BS, Yeo JH, et al. Heme oxygenase-1 deficiency alters erythroblastic island formation, steady-state erythropoiesis and red blood cell lifespan in mice. *Haematologica* 2015;100:601–10.
- Vermi W, Micheletti A, Finotti G, Tecchio C, Calzetti F, Costa S, et al. slan+ monocytes and macrophages mediate CD20-dependent b-cell lymphoma elimination via ADCC and ADCP. *Cancer Res* 2018;78:3544–59.
- Chakarov S, Lim HY, Tan L, Lim SY, See P, Lum J, et al. Two distinct interstitial macrophage populations coexist across tissues in specific subtissular niches. *Science* 2019;363:eaau0964.
- Knutson MD, Oukka M, Koss LM, Aydemir F, Wessling-Resnick M. Iron release from macrophages after erythrophagocytosis is up-regulated by ferroportin 1 overexpression and down-regulated by hepcidin. *Proc Natl Acad Sci U S A* 2005;102:1324–8.

## Chapter 7. TIM4+FOLR2+ Macrophages Localized in TLS Correlate to an Active Immune Infiltrate Across Several Cancer Types

Bugatti et al.

47. Kaushal N, Kudva AK, Patterson AD, Chiaro C, Kennett MJ, Desai D, et al. Crucial role of macrophage selenoproteins in experimental colitis. *J Immunol* 2014;193:3683–92.
48. Takiguchi H, Yang CX, Yang CWT, Sahin B, Whalen BA, Milne S, et al. Macrophages with reduced expressions of classical M1 and M2 surface markers in human bronchoalveolar lavage fluid exhibit pro-inflammatory gene signatures. *Sci Rep* 2021;11:8282.
49. Sendler M, Weiss F-U, Golchert J, Homuth G, van den Brandt C, Mahajan UM, et al. Cathepsin B-mediated activation of trypsinogen in endocytosing macrophages increases severity of pancreatitis in mice. *Gastroenterology* 2018;154:704–18.
50. Desrumaux C, Lemaire-Ewing S, Ogier N, Yessoufou A, Hammann A, Sequeira-Le Grand A, et al. Plasma phospholipid transfer protein (PLTP) modulates adaptive immune functions through alternation of T helper cell polarization. *Cell Mol Immunol* 2016;13:795–804.
51. Lee H, Park B-C, Soon Kang J, Cheon Y, Lee S, Jae Maeng P. MAM domain containing 2 is a potential breast cancer biomarker that exhibits tumour-suppressive activity. *Cell Prolif* 2020;53:e12883.
52. Bouchon A, Hernández-Munain C, Cella M, Colonna M. A DAP12-mediated pathway regulates expression of CC chemokine receptor 7 and maturation of human dendritic cells. *J Exp Med* 2001;194:1111–22.
53. Turnbull IR, Gilfillan S, Cella M, Aoshi T, Miller M, Piccio L, et al. Cutting edge: TREM-2 attenuates macrophage activation. *J Immunol* 2006;177:3520–4.
54. Blondy T, d'Almeida SM, Briolay T, Tabiasco J, Meiller C, Chéné A-L, et al. Involvement of the M-CSF/IL-34/CSF-1R pathway in malignant pleural mesothelioma. *J Immunother cancer* 2020;8:e000182.
55. Chechlinska M, Kaminska J, Markowska J, Kramar A, Steffen J. Peritoneal fluid cytokines and the differential diagnosis of benign and malignant ovarian tumors and residual/recurrent disease examination. *Int J Biol Markers* 2007;22:172–80.
56. Punnonen R, Teisala K, Kuoppala T, Bennett B, Punnonen J. Cytokine production profiles in the peritoneal fluids of patients with malignant or benign gynecologic tumors. *Cancer* 1998;83:788–96.
57. Donnenberg VS, Wagner PL, Luketich JD, Bartlett DL, Donnenberg AD. Localized intra-cavitary therapy to drive systemic anti-tumor immunity. *Front Immunol* 2022;13:846235.
58. Blériot C, Chakarov S, Ginhoux F. Determinants of resident tissue macrophage identity and function. *Immunity* 2020;52:957–70.
59. Okabe Y, Medzhitov R. Tissue-specific signals control reversible program of localization and functional polarization of macrophages. *Cell* 2014;157:832–44.
60. Roberts AW, Lee BL, Deguine J, John S, Shlomchik MJ, Barton GM. Tissue-resident macrophages are locally programmed for silent clearance of apoptotic cells. *Immunity* 2017;47:913–27.
61. Yang B, Li L-J, Xu L-Z, Liu J-Q, Zhang H-P, Geng X-R, et al. Histone acetyltransferase p300 modulates TIM4 expression in dendritic cells. *Sci Rep* 2016;6:21336.





## **Part II**

## **Part Two**



## Predictive nomograms for oral tongue SCC

Balasubramanian, D.

Subramaniam, N.

**Missale, F.**

Marchi, F.

Dokhe, Y.

Vijayan, S.

Nambiar, A.

Mattavelli, D.

Calza, S.

Bresciani, L.

Piazza, C.

Nicolai, P.

Peretti, G.



Thankappan, K,

Iyer, S.P.

Head Neck

2021;43(4):1043-1055. doi: 10.1002/hed.26554.

# Predictive nomograms for oral tongue squamous cell carcinoma applying the American Joint Committee on Cancer/Union Internationale Contre le Cancer 8th edition staging system

Deepak Balasubramanian MCh<sup>1</sup>  | Narayana Subramaniam MCh<sup>1</sup>  |  
 Francesco Missale MD<sup>2,3,4</sup> | Filippo Marchi MD<sup>2,5</sup> | Yogesh Dokhe MS<sup>1</sup> |  
 Smitha Vijayan MD<sup>6</sup> | Ajit Nambiar MD<sup>6</sup> | Davide Mattavelli MD<sup>7</sup> |  
 Stefano Calza PhD<sup>8,9,10</sup> | Lorenzo Bresciani MD<sup>11</sup> | Cesare Piazza MD<sup>11,12</sup> |  
 Piero Nicolai MD<sup>13</sup> | Giorgio Peretti MD<sup>2,3</sup> | Krishnakumar Thankappan MCh<sup>1</sup> |  
 Subramania Iyer MCh<sup>1</sup>

<sup>1</sup>Department of Head and Neck Oncology, Amrita Institute of Medical Sciences, Amrita Vishwa Vidyapeetham, Kochi, India

<sup>2</sup>IRCCS Ospedale Policlinico San Martino, Genoa, Italy

<sup>3</sup>Department of Otorhinolaryngology – Head and Neck Surgery, University of Genova, Genoa, Italy

<sup>4</sup>Department of Molecular and Translational Medicine, University of Brescia, Brescia, Italy

<sup>5</sup>Department of Plastic Surgery, Chang Gung Memorial Hospital, Chang Gung University and Medical College, Taoyuan, Taiwan

<sup>6</sup>Department of Pathology, Amrita Institute of Medical Sciences, Amrita Vishwa Vidyapeetham, Kochi, India

<sup>7</sup>Unit of Otorhinolaryngology – Head and Neck Surgery, Department of Medical and Surgical Specialties, Radiological Sciences and Public Health, University of Brescia, Brescia, Italy

<sup>8</sup>Unit of Biostatistics, Department of Molecular and Translational Medicine, University of Brescia, Brescia, Italy

<sup>9</sup>Department of Medical Epidemiology and Biostatistics, Karolinska Institute, Stockholm, Sweden

<sup>10</sup>Big & Open Data Innovation Laboratory, University of Brescia, Brescia, Italy

<sup>11</sup>Department of Otorhinolaryngology, Maxillofacial and Thyroid Surgery, Fondazione IRCCS, National Cancer Institute of Milan, Milan, Italy

<sup>12</sup>Department of Oncology and Oncohematology, University of Milan, Milan, Italy

<sup>13</sup>Section of Otorhinolaryngology – Head and Neck Surgery, Department of Neurosciences, University of Padua, Padua, Italy

## Correspondence

Deepak Balasubramanian, Department of Head and Neck Oncology, Amrita Institute of Medical Sciences, Amrita Vishwa Vidyapeetham, Kochi, India.  
 Email: deepabala@live.com

**Section Editor:** Claudio Cernea

## Abstract

**Background:** Nomograms applying the 8th edition of the TNM staging system aimed at predicting overall (OS), disease-specific (DSS), locoregional recurrence-free (LRRFS) and distant recurrence-free survivals (DRFS) for oral tongue squamous cell carcinoma (OTSCC) are still lacking.

**Methods:** A training cohort of 438 patients with OTSCC was retrospectively enrolled from a single institution. An external validation set of 287 patients was retrieved from two independent institutions.

**Results:** Internal validation of the multivariable models for OS, DSS, DRFS and LRRFS showed a good calibration and discrimination results with optimism-corrected c-indices of 0.74, 0.75, 0.77 and 0.70, respectively. The external validation confirmed the good performance of OS, DSS and DRFS

models (c-index 0.73 and 0.77, and 0.73, respectively) and a fair performance of the LRRFS model (c-index 0.58).

**Conclusions:** The nomograms herein presented can be implemented as useful tools for prediction of OS, DSS, DRFS and LRRFS in OTSCC.

#### KEYWORDS

nomogram, oral cancer, prognostication, squamous cell carcinoma, tongue cancer

## 1 | INTRODUCTION

Oral cavity squamous cell carcinoma is a significant contributor to the global cancer burden, with a high cancer-specific mortality.<sup>1</sup> Oral tongue is one of the most common subsites involved, accounting for up to half of all cases.<sup>2</sup> Typically, oral tongue squamous cell carcinomas (OTSCCs) have a propensity for early and extensive local invasion and regional lymphatic spread, leading to significant disease- and treatment-related morbidity. In spite of better expertise and multidisciplinary care, improvement in OTSCC oncologic outcomes over time has been modest.<sup>3</sup>

Although the Union for International Cancer Control (UICC)/American Joint Committee on Cancer (AJCC) 8th edition TNM staging systems for oral cancer<sup>4</sup> has shown improved performance when compared with previous systems, this classification, however, still remains largely insufficient. In early (stage I/II) cancers, up to a third of adequately treated patients can develop locoregional recurrences, which have been noted to have a strong correlation with adverse pathological features like perineural invasion (PNI), lymphovascular invasion (LVI) and degree of differentiation, which have so far not been incorporated into the staging system.<sup>5</sup> In advanced (stage III/IV) cancers prognostication based on tumor dimension with/without nodal spread alone also seems inadequate. This forms a highly heterogeneous group of patients in whom prediction of survival solely based on stage is unreliable. This lack of reliable substratification within the staging system has led highly variable outcomes among patients having the same TNM stage.

Nomograms have been considered to be user-friendly tools for prediction, and they have been proved to be more effective than the traditional staging system in several human cancers.<sup>6-10</sup> In literature, nomograms prognosticating OTSCC have been described.<sup>11-13</sup> Of these, some do not incorporate depth of invasion (DOI) and other valuable pathological information, while others do not measure all endpoints, and none of them are based on the 8th edition of the UICC/AJCC staging system. As a result, none of them can be reliably applied in a clinical context. The aim of this multicentric study was to derive

an updated set of nomograms for OTSCC based on the 8th edition of the UICC/AJCC staging system, which could be reliably applied to patients from different geographical regions.

## 2 | SUBJECTS AND METHODS

### 2.1 | Patients cohort

After institutional ethics committee clearance, medical records of previously untreated patients affected by OTSCC and undergoing surgery  $\pm$  adjuvant treatment with curative intent at Amrita Institute of Medical Sciences, Department of Head and Neck Surgery, Kerala, India, between January 1, 2006, and May 30, 2016 were retrospectively analyzed in the training cohort. Exclusion criteria were presence of distant metastases and/or synchronous head and neck squamous cell carcinoma, unavailable follow-up information, previous chemotherapy for any cancer and/or radiotherapy in the head and neck area, other synchronous or metachronous primary cancers, treatment with neoadjuvant therapy, or medical contraindications for surgery. In the training cohort, 450 patients were eligible; 438 patients were included in the analysis since in 12 patients the relevant data was missing (in 11 follow-up details were absent and in 1 nodal stage was incomplete).

Patients underwent standard preoperative workup, including a detailed medical history, complete physical examination, blood examination, CT or MRI scans of the head and neck to stage the primary tumor and PET-CT or chest CT to rule out metastatic spread. Patient and tumor characteristics were collected from the medical records: age, sex and stage of disease. Patients were defined as smokers if they had a history of smoking daily for at least 1 year. Although this is an unusual definition, this allowed us to group these patients with those having a history of smokeless chewed tobacco use, which is common in the Indian subcontinent. Quantification in pack years was not possible, as smokeless tobacco use cannot be accurately quantified because of wide variations in composition. Hence, for the purpose of analysis, both

smokers and tobacco chewers were considered “tobacco users”. Surgery was always performed upfront with curative intent. Resection was planned according to the site, extension and tumor depth. All patients underwent wide excision of tumor with a macroscopic margin of 1 to 1.5 cm, neck dissection and appropriate reconstruction. Bone involvement was managed by marginal or segmental mandibulectomy in case of cortical or medullary invasion, respectively.

Clinical data recorded included sex, age, tobacco use and treatment details. Pathological details recorded were surgical margin status, diameter, adverse pathological features, pN category and nodal metastases. All tumors were re-staged according to the 8th edition of UICC/AJCC staging system.<sup>4</sup>

Adjuvant treatment(s) was discussed case by case in the multidisciplinary tumor board. Adjuvant radiotherapy (RT) was administered for node positive tumors or advanced categories (T3 and T4). Adjuvant chemoradiotherapy (CRT) was administered for positive margins or extranodal extent (ENE).

Follow-up included clinical examination every month during the first year, every 2 months in the second year, every 3 months in the third year, every 4 months in the fourth year, and every 6 months during the fifth year. No routine radiological follow-up was performed unless patients had symptoms or suspicious clinical finding(s) of recurrence for which CT/PET was performed.

An external validation cohort of 287 patients, matching the same selection criteria, was enrolled from the Department of Otorhinolaryngology – Head and Neck Surgery, University of Brescia, Italy (2000-2016) and the Department of Otorhinolaryngology, Maxillofacial and Thyroid Surgery of the National Cancer Institute of Milan, University of Milan, Italy (2009-2016). Patients with missing data were excluded.

## 2.2 | Data analysis and statistical methods

As survival endpoints, we analyzed the locoregional recurrence-free survival (LRRFS), the distant recurrence-free survival (DRFS), overall survival (OS) and disease-specific survival (DSS) defined as the time between surgery and the date of the corresponding event (locoregional recurrence, distant recurrence, death for any cause and cancer-related death) or last follow-up visit. Clinical and pathological variables available for the analysis were as following: sex, age, tobacco use, treatment, status of the surgical margins, distance of the tumor from the surgical margin (mm), DOI (mm),

diameter of the tumor (mm), grading, PNI, LVI, bone invasion, pT category, pN category, maximum dimension of metastatic nodes and evidence of ENE.

Multivariable model building was carried out by a penalized variables selection (adaptive-elastic net method) estimating the best  $\alpha$  and  $\lambda$  parameters by lambda.min rule and cross-validation with 200 resamples.<sup>14,15</sup> Semiparametric proportional-hazard Cox models were then fitted managing categorical variables as factors. Each model was internally validated using bootstrap with 200 resamples. The accuracy of predictions was evaluated by estimating the model's calibration at 2 and 5 years and discrimination was measured by the concordance index (c-index). The c-index is the probability that for two randomly selected patients, the patient who experienced the event first has a higher predicted probability of having the event. Therefore, a c-index of 0.5 represents an agreement by chance alone, while a c-index of 1 means perfect discrimination.<sup>16</sup> c-index are reported as naive model estimates, their bootstrap estimates (average of individual bootstrap estimates) as well as optimism-corrected estimates.

Calibration curves at 2 and 5 years were drawn with the “hare” smooth approach; calibration results were shown also grouping patients into quartiles with considering their nomogram-predicted probabilities and plotting the mean of predicted probabilities for each group with the mean observed Kaplan-Meier estimate. External validation of the models was performed assessing the calibration accuracy at 2 and 5 years and estimating the c-index as discrimination measure.

For graphical estimation of 1-, 2- and 5-year survival probabilities, nomograms for OS, DSS, LRRFS and DRFS were plotted. Interactive shinyapps for each model were built by DynNom package. For all tests, a 2-tailed *P*-value <.05 was considered significant. R (version 3.5.2) and R Studio (version 1.1.463) with the packages “hdnom,”<sup>17</sup> “survival,” “survminer,” “rms” and “DynNom” and GraphPad Prism 6.0 (San Diego, California) were used for statistical analysis.

## 3 | RESULTS

### 3.1 | Patient clinical-pathological data

Among the 438 patients, 312 (71.2%) were men, and 126 (28.8%) women. In the entire cohort, 207 (47.3%) were tobacco users. The mean age was 54 years, ranging from 23 to 85 years. The most common TNM stage was IV in 154 patients (35.2%), followed by III in 108 (26.7%). Positive margins were detected in 3.2% of surgical specimens. In case of negative margins, the mean distance



**TABLE 1** Clinical-pathological characteristics of the training and validation patients' cohorts

	Training cohort (N = 438)	Validation cohort (N = 287)	Overall (N = 725)
<b>Sex</b>			
Men	312 (71.2%)	177 (61.7%)	489 (67.4%)
Women	126 (28.8%)	110 (38.3%)	236 (32.6%)
<b>Tobacco use</b>			
No	231 (52.7%)	80 (27.9%)	311 (42.9%)
Yes	207 (47.3%)	165 (57.5%)	372 (51.3%)
Missing	0 (0%)	42 (14.6%)	42 (5.8%)
<b>Treatment</b>			
Surgery	218 (49.8%)	146 (50.9%)	364 (50.2%)
Surgery + RT	63 (14.4%)	71 (24.7%)	134 (18.5%)
Surgery + CRT	157 (35.8%)	70 (24.4%)	227 (31.3%)
<b>Margins</b>			
Negative	424 (96.8%)	201 (70.0%)	625 (86.2%)
Positive or close	14 (3.2%)	86 (30.0%)	100 (13.8%)
<b>Differentiation</b>			
G1	220 (50.2%)	45 (15.7%)	265 (36.6%)
G2	197 (45.0%)	152 (53.0%)	349 (48.1%)
G3	21 (4.8%)	90 (31.4%)	111 (15.3%)
<b>PNI</b>			
No	286 (65.3%)	153 (53.3%)	439 (60.6%)
Yes	152 (34.7%)	134 (46.7%)	286 (39.4%)
<b>LVI</b>			
No	314 (71.7%)	198 (69.0%)	512 (70.6%)
Yes	124 (28.3%)	89 (31.0%)	213 (29.4%)
<b>Bone invasion</b>			
No	420 (95.9%)	271 (94.4%)	691 (95.3%)
Yes	18 (4.1%)	16 (5.6%)	34 (4.7%)
<b>pT category (8th)</b>			
T1	97 (22.1%)	68 (23.7%)	165 (22.8%)
T2	142 (32.4%)	75 (26.1%)	217 (29.9%)
T3	181 (41.3%)	128 (44.6%)	309 (42.6%)
T4	18 (4.1%)	16 (5.6%)	34 (4.7%)
<b>pN category (8th)</b>			
N0	247 (56.4%)	165 (57.5%)	412 (56.8%)
N1	41 (9.4%)	33 (11.5%)	74 (10.2%)
N2	55 (12.6%)	30 (10.5%)	85 (11.7%)
N3	95 (21.7%)	59 (20.6%)	154 (21.2%)
<b>DOC or DOD</b>			
No	336 (76.7%)	186 (64.8%)	522 (72.0%)
Yes	102 (23.3%)	101 (35.2%)	203 (28.0%)
<b>DOD</b>			
No	349 (79.7%)	219 (76.3%)	568 (78.3%)
Yes	89 (20.3%)	68 (23.7%)	157 (21.7%)

**TABLE 1** (Continued)

	Training cohort (N = 438)	Validation cohort (N = 287)	Overall (N = 725)
Locoregional recurrence			
No	309 (70.5%)	203 (70.7%)	512 (70.6%)
Yes	129 (29.5%)	84 (29.3%)	213 (29.4%)
Distant recurrence			
No	391 (89.3%)	250 (87.1%)	641 (88.4%)
Yes	47 (10.7%)	37 (12.9%)	84 (11.6%)

Abbreviations: CRT, chemoradiotherapy; DOC, died of causes other than cancer; DOD, died of cancer; LVI, lymphovascular invasion; PNI, perineural invasion; RT, radiotherapy.

**TABLE 2** Summary statistics for continuous variables in the training cohort

	Min	25th percentile	Median	Mean	75th percentile	Max
Age	23	43	55	54	64	85
Margins (mm)	1	5	7	7.8	10	20
DOI (mm)	1	5	10	12.1	18	50
Diameter (mm)	5	15	22	25.1	33	100
Maximum node size	0	0	0	5.9	10	70

Abbreviation: DOI, depth of invasion.

from tumor was 10.2 mm (range, 5-20 mm). Adjuvant treatment(s) was administered in 50.2% of patients. Mean DOI was 12.1 mm. PNI was detected in 152 patients (34.7%), and LVI in 124 (28.3%). In 18 patients (4.1%) the resected bone was involved by the tumor. All clinical characteristics are reported in Tables 1 and 2.

### 3.2 | Oncological outcomes

Among survivors the mean follow-up was 42 months (range, 1-186). For all outcomes approximately 60% of censored patients were observed for at least 2 years after surgical treatment, with more than 70% of events recorded within 24 months. The calibration analysis in the training cohort showing predicted probabilities of survival against observed rates is shown in Table 3. Cumulative and relative frequency distribution of censoring times and of times to events is shown in Figures 1 and 2. One hundred and fifty (34.2%) patients experienced recurrence; 103 (23.5%) had locoregional recurrence alone, 21 (4.8%) had distant recurrence alone and 26 (5.9%) had both of them. One hundred and two (23.3%) patients died during follow-up: 89 of such deaths (87.3%) were cancer-related, while 13 (12.7%) were not cancer-related. Two- and five-year estimates for OS were 78.7% (CI95% [74.5%-83.1%]) and 68.5% (CI95% [63.2%-

74.3%]); for DSS 80.5% (CI95% [76.4%-84.8%]) and 71.9% (CI95% [66.7%-77.4%]); for LRRFS 75.7% (CI95% [71.5%-80.2%]) and 63.2% (CI95% [57.9%-69.1%]) and for DRFS 88.9% (CI95% [85.6%-92.3%]) and 86.3% (CI95% [82.4%-90.3%]), respectively.

#### 3.2.1 | Overall survival

In the final Cox model for OS nomogram building, five variables were included: grading, PNI, LVI, pT category and pN category (Figure 1A). The c-index of the OS model is 0.76 (CI95% [0.72-0.81]), by the internal validation analysis its bootstrap estimation is 0.76 (CI95% [0.73-0.82]) and the optimism corrected c-index 0.73 (CI95% [0.70-0.79]). The 2- and 5-year calibration curves were satisfactory with a mean absolute calibration error of 0.016 and 0.020, respectively, with a 0.9 quantile of calibration error of 0.023 and 0.009, respectively (Figure 1B, C). The external validation analysis confirmed the accuracy of the OS model with a c-index of 0.73 with a good calibration at 2 and 5 years with a mean absolute calibration error of 0.045 and 0.028, respectively, with a 0.9 quantile of calibration error of 0.123 and 0.067 (Figure 1D,E). An interactive shinyapp of the OS model, built by DynNom package, is available at: [https://missalefrancesco.shinyapps.io/Tongue\\_SCC\\_OS\\_Nomogram/](https://missalefrancesco.shinyapps.io/Tongue_SCC_OS_Nomogram/).

2-year OS		5-year OS	
Predicted	Observed (CI95%)	Predicted	Observed (CI95%)
0.49	0.45 (0.32-0.57)	0.31	0.34 (0.16-0.51)
0.77	0.8 (0.75-0.86)	0.64	0.64 (0.54-0.73)
0.86	0.91 (0.87-0.95)	0.78	0.86 (0.81-0.92)
0.94	0.94 (0.92-0.96)	0.90	0.87 (0.83-0.91)
2-year DSS		5-year DSS	
Predicted	Observed (CI95%)	Predicted	Observed (CI95%)
0.50	0.47 (0.35-0.6)	0.33	0.4 (0.24-0.56)
0.78	0.78 (0.73-0.84)	0.68	0.63 (0.53-0.72)
0.86	0.92 (0.88-0.96)	0.79	0.87 (0.81-0.92)
0.94	0.94 (0.92-0.96)	0.91	0.89 (0.85-0.92)
2-year DRFS		5-year DRFS	
Predicted	Observed (CI95%)	Predicted	Observed (CI95%)
0.66	0.69 (0.61-0.77)	0.58	0.63 (0.52-0.73)
0.88	0.86 (0.81-0.91)	0.85	0.77 (0.7-0.85)
0.94	0.97 (0.96-0.99)	0.91	0.97 (0.96-0.99)
0.97	0.96 (0.94-0.98)	0.96	0.96 (0.94-0.98)
2-year LRRFS		5-year LRRFS	
Predicted	Observed (CI95%)	Predicted	Observed (CI95%)
0.52	0.51 (0.4-0.62)	0.33	0.4 (0.22-0.58)
0.73	0.75 (0.69-0.81)	0.58	0.57 (0.46-0.67)
0.80	0.78 (0.73-0.83)	0.68	0.68 (0.61-0.76)
0.92	0.96 (0.94-0.98)	0.86	0.83 (0.77-0.89)

Abbreviations: CI95%, 95% confidence interval; DRFS, distant recurrence-free survival; DSS, disease-specific survival; LRRFS, locoregional recurrence-free survival; OS, overall survival.

**TABLE 3** Calibration analysis in the training cohort showing predicted probabilities against observed Kaplan-Meier ones (CI95%)

### 3.2.2 | Disease-specific survival

Analyzing the DSS, the most relevant variables affecting the outcome and used to draw the nomogram were grading, pT category and pN category (Figure 2A). The c-index of the DSS model is 0.76 (CI95% [0.72-0.81]), by the internal validation analysis its bootstrap estimation is 0.77 (CI95% [0.74-0.82]) and the optimism corrected c-index 0.75 (CI95% [0.70-0.80]). The 2- and 5-year calibration curves were satisfactory with a mean absolute calibration error of 0.023 and 0.025, respectively, with a 0.9 quantile of calibration error of 0.007 and 0.011, respectively (Figure 2B,C). The external validation analysis confirmed the accuracy of the DSS model with a c-index of 0.77 with a good calibration at 2 and 5 years with a mean absolute calibration error of 0.071 and 0.081, respectively with a 0.9 quantile of calibration error of 0.075 and 0.093 (Figure 2D,E). An interactive shinyapp of the DSS model, built by DynNom package,

is available at: [https://missalefrancesco.shinyapps.io/Tongue\\_SCC\\_DSS\\_Nomogram/](https://missalefrancesco.shinyapps.io/Tongue_SCC_DSS_Nomogram/).

### 3.2.3 | Distant recurrence-free survival

The variables selected for the DRFS model were pT category, grading and LVI (Figure 3A). The c-index of the DSS model is 0.79 (CI95% [0.73-0.86]), by the internal validation analysis its bootstrap estimation is 0.80 (CI95% [0.74-0.87]) and the optimism-corrected c-index 0.77 (CI95% [0.70-0.84]). The 2- and 5-year calibration curves were satisfactory with a mean absolute calibration error of 0.009 and 0.013, respectively, with a 0.9 quantile of calibration error of 0.010 and 0.018, respectively (Figure 3B,C).

The external validation analysis showed a c-index of 0.73 with a fair calibration at 2 and 5 years with a mean absolute calibration error of 0.076 and 0.061, but poorer

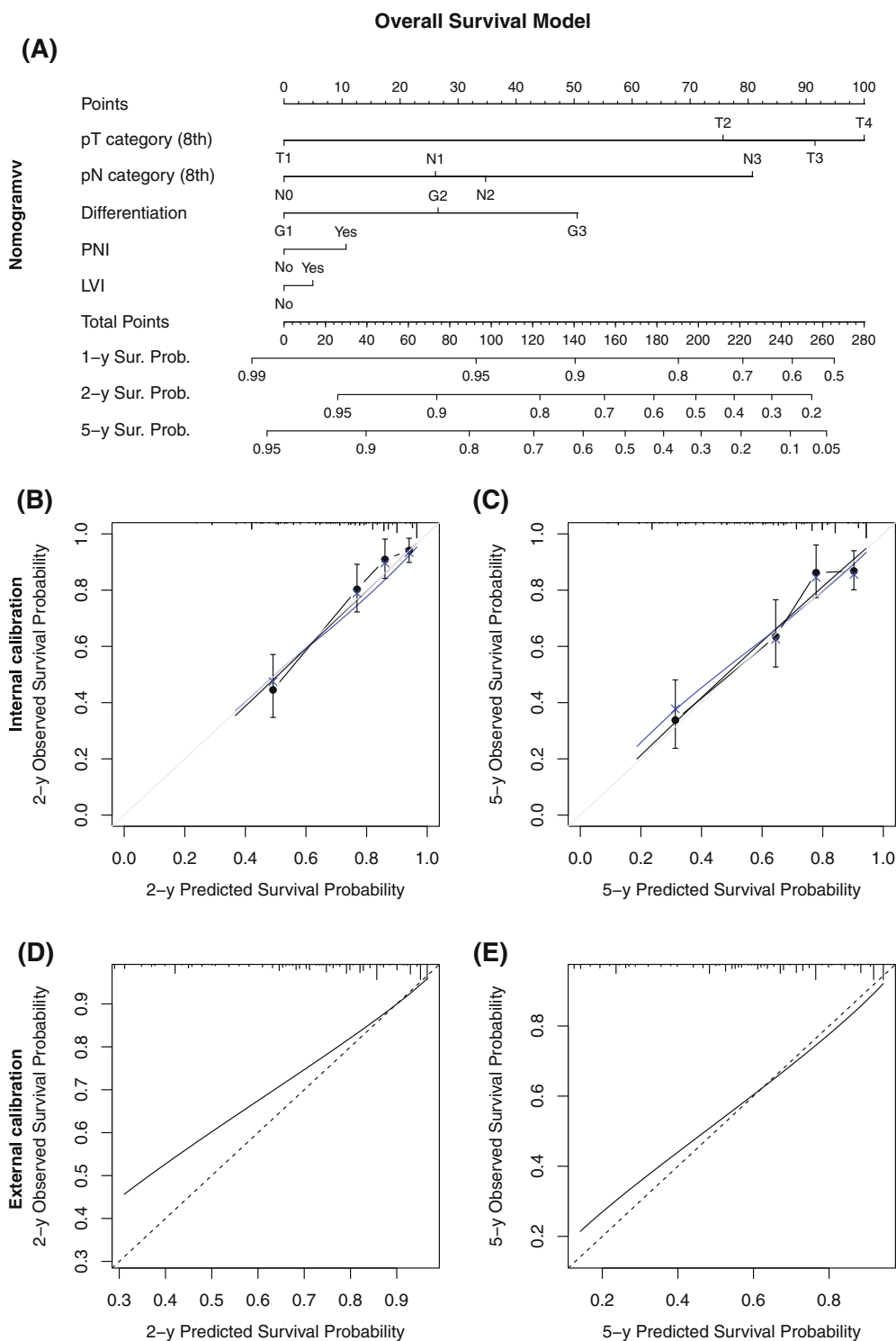


**FIGURE 1** A, Nomogram for overall survival (OS). Bootstrap internal validation of calibration curve at 2 years, B, and 5 years, C; dots showing apparent calibration accuracy;  $\times$  are bootstrap estimates corrected for overfitting, based on binning predicted survival probabilities and computing Kaplan-Meier estimates. Black and blue curve are the estimated observed relationship using “hare” and the overfitting-corrected one, respectively. The gray line represents the ideal relationship. External calibration curves at 2 years, D, and 5 years, E; dotted line represents the ideal relationship [Color figure can be viewed at [wileyonlinelibrary.com](http://wileyonlinelibrary.com)]

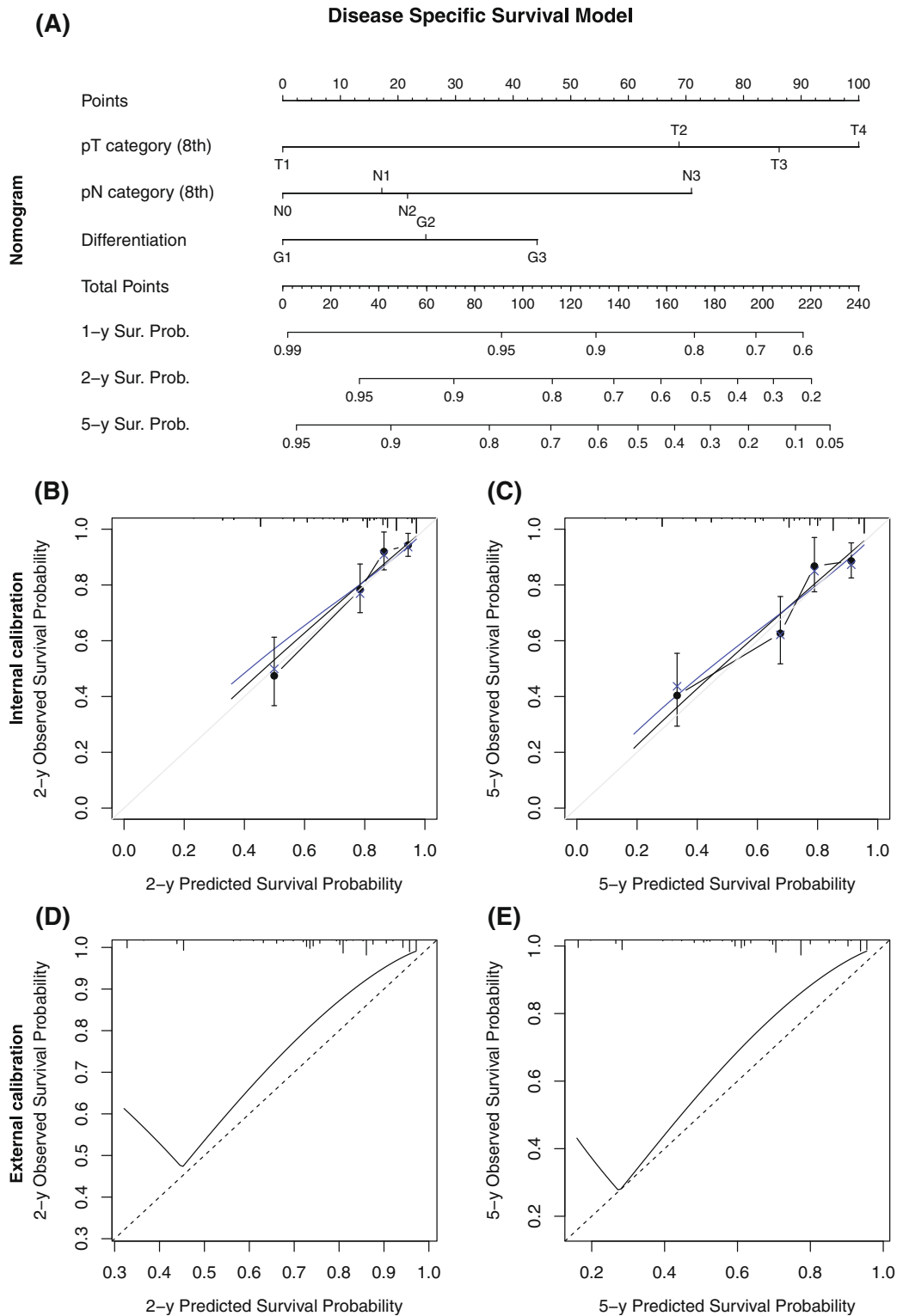


**FIGURE 2** A, Nomogram for disease-specific survival (DSS). Bootstrap internal validation of calibration curve at 2 years, B, and 5 years, C; dots showing apparent calibration accuracy; × are bootstrap estimates corrected for overfitting, based on binning predicted survival probabilities and computing Kaplan-Meier estimates. Black and blue curve are the estimated observed relationship using “bare” and the overfitting-corrected one, respectively. The gray line represents the ideal relationship. External calibration curves at 2 years, D, and 5 years, E; dotted line represents the ideal relationship [Color figure can be viewed at [wileyonlinelibrary.com](http://wileyonlinelibrary.com)]

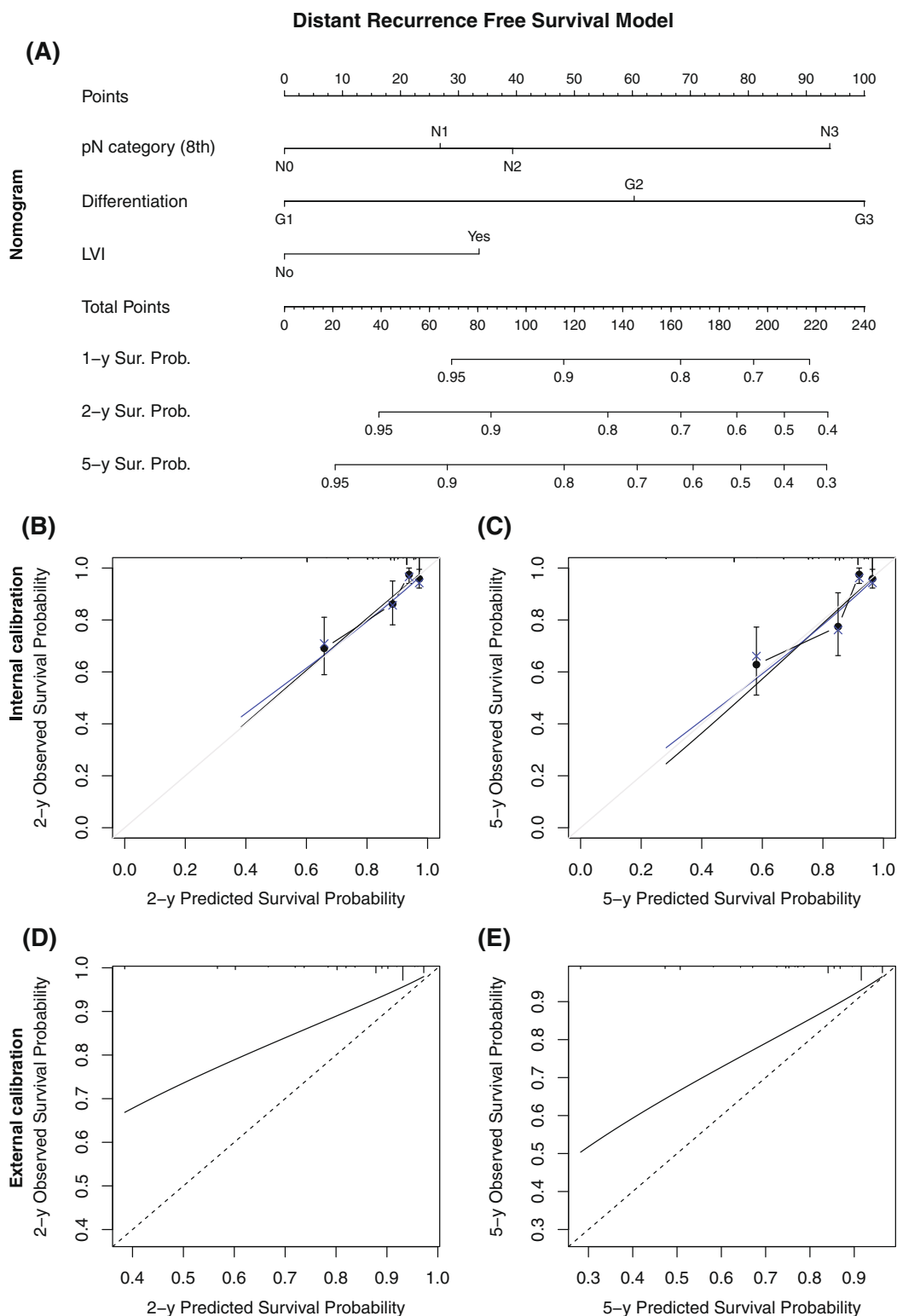


**FIGURE 3** A, Nomogram for distant recurrence-free survival (DRFS). Bootstrap internal validation of calibration curve at 2 years, B, and 5 years, C; dots showing apparent calibration accuracy; × are bootstrap estimates corrected for overfitting, based on binning predicted survival probabilities and computing Kaplan-Meier estimates. Black and blue curve are the estimated observed relationship using “hare” and the overfitting-corrected one, respectively. The gray line represents the ideal relationship. External calibration curves at 2 years, D, and 5 years, E; dotted line represents the ideal relationship [Color figure can be viewed at [wileyonlinelibrary.com](http://wileyonlinelibrary.com)]



0.9 quantile of calibration error of 0.191 and 0.161 (Figure 2D,E). An interactive shinyapp of the DRFS model, built by DynNom package, is available at: [https://missalefrancesco.shinyapps.io/Tongue\\_SCC\\_DRFS\\_Nomogram/](https://missalefrancesco.shinyapps.io/Tongue_SCC_DRFS_Nomogram/).

### 3.2.4 | Locoregional recurrence-free survival

By the penalized adaptive elastic net algorithm selection, seven candidate predictors were selected: pT category, pN category, grading, PNI, LVI, tobacco use and distance of the tumor from the surgical margins. A tentative external validation of such defined model failed with a c-index of 0.51 and, at 2 and 5 years, a mean absolute calibration error of 0.224 and 0.321, and 0.9 quantile of calibration error of 0.461 and 0.582, respectively. Furthermore, missing data regarding tobacco use ( $n = 42$ , 14.6%) and of the distance of the tumor from the surgical margins ( $n = 192$ , 66.9%) in the validation cohort limited the testing of such model. A further simplification of the LRRFS model was performed, to reduce overfitting biases and improve its external application, including as covariate pT category, pN category, grading, PNI and LVI ( $P = .076$  by likelihood ratio test comparing these models on the training cohort, ensuring their comparable performance).

The nomogram derived from the simplified LRRFS model is presented in Figure 4A; and the c-index of such model is 0.70 (CI95% [0.67-0.76]). The internal validation showed a bootstrap estimated c-index of 0.71 (CI95% [0.69-0.77]) and the optimism corrected one was 0.67 (CI95% [0.63-0.73]). The 2- and 5-year calibration curves were good at 2 years and just fair at 5 years, with a mean absolute calibration error of 0.029 and 0.22, respectively, with a 0.9 quantile of calibration error of 0.034 and 0.029, respectively (Figure 4B,C). The external validation analysis improved obtaining a c-index of 0.58 with a fair calibration at 2 and at 5 years with a mean absolute calibration error of 0.099 and 0.153, and 0.9 quantile of calibration error of 0.233 and 0.337 (Figure 4D,E). An interactive shinyapp of the LRRFS model, built by DynNom package, is available at: [https://missalefrancesco.shinyapps.io/Tongue\\_SCC\\_LRRFS\\_Nomogram/](https://missalefrancesco.shinyapps.io/Tongue_SCC_LRRFS_Nomogram/).

## 4 | DISCUSSION

The UICC/AJCC 8th edition for oral cavity cancer has been already externally validated in several studies.<sup>18-20</sup> However, it does not account for several well-established prognostic determinants. These are unlikely to be

incorporated in any future editions as well, to avoid further complexity and heterogeneity in the staging system that can adversely impact ease of use and application. In order to accurately predict survival with standard treatment, nomograms are the best solution.

Although several nomograms have been described for oral SCC,<sup>21-26</sup> attempts at devising a nomogram for OTSCC alone have been limited. Li and colleagues used data from the SEER database on 12 674 patients to design such a nomogram including the variables age, race, marital status, TNM stage and tumor grading.<sup>11</sup> Pathological features like DOI, ENE, LVI and PNI were not included, probably because these details were unavailable in the SEER data set. Nonetheless, this nomogram accurately predicted survival in OTSCC. For T4 OTSCC, Sun and colleagues reviewed again the SEER database and identified 1550 patients.<sup>12</sup> Age, race, marital status, tumor site, UICC/AJCC TNM status and RT were recognized as independent prognostic factors associated with OS as well as cancer-specific survival. Chang and colleagues incorporated DOI in their nomogram for OTSCC.<sup>13</sup> DOI and neck dissection were independent predictors for survival in their model. Compared to our cohort, they had fewer patients included in their study and their nomogram only predicted for OS and not for the other survival endpoints.

In our study the model buildings and nomograms validation have been performed following the UICC/AJCC criteria for risk models for individualized prognosis,<sup>27</sup> complying with all criteria and based on the most updated staging system for cancer. Additionally we considered four distinct endpoints: OS, DSS, LRRFS and DRFS. The reasons for this were to determine accurate survival estimates for each of these endpoints, and also to understand which were patterns and predictors of failure which could potentially identify candidates for future clinical trials.

For OS, grading, pN category, pT category, PNI and LVI were included in the predictive model; analyzing the DSS, the most relevant variables affecting the outcome and used to draw the nomogram were grading, pT category and pN category. Analyzing patterns of recurrence, the model for the DRFS prediction included grading, pN category and LVI as relevant predictors, whereas the one for LRRFS prediction included grading, PNI, LVI, pT category and pN category. The nomograms showed good performance and had the ability to stratify well groups with different prognosis, especially regarding OS and DSS. From a preliminary analysis on the training cohort alone, smoking status and distance of the tumor from the surgical margins were selected for being further relevant predictors of LRRFS, and these should be further tested in external cohorts.

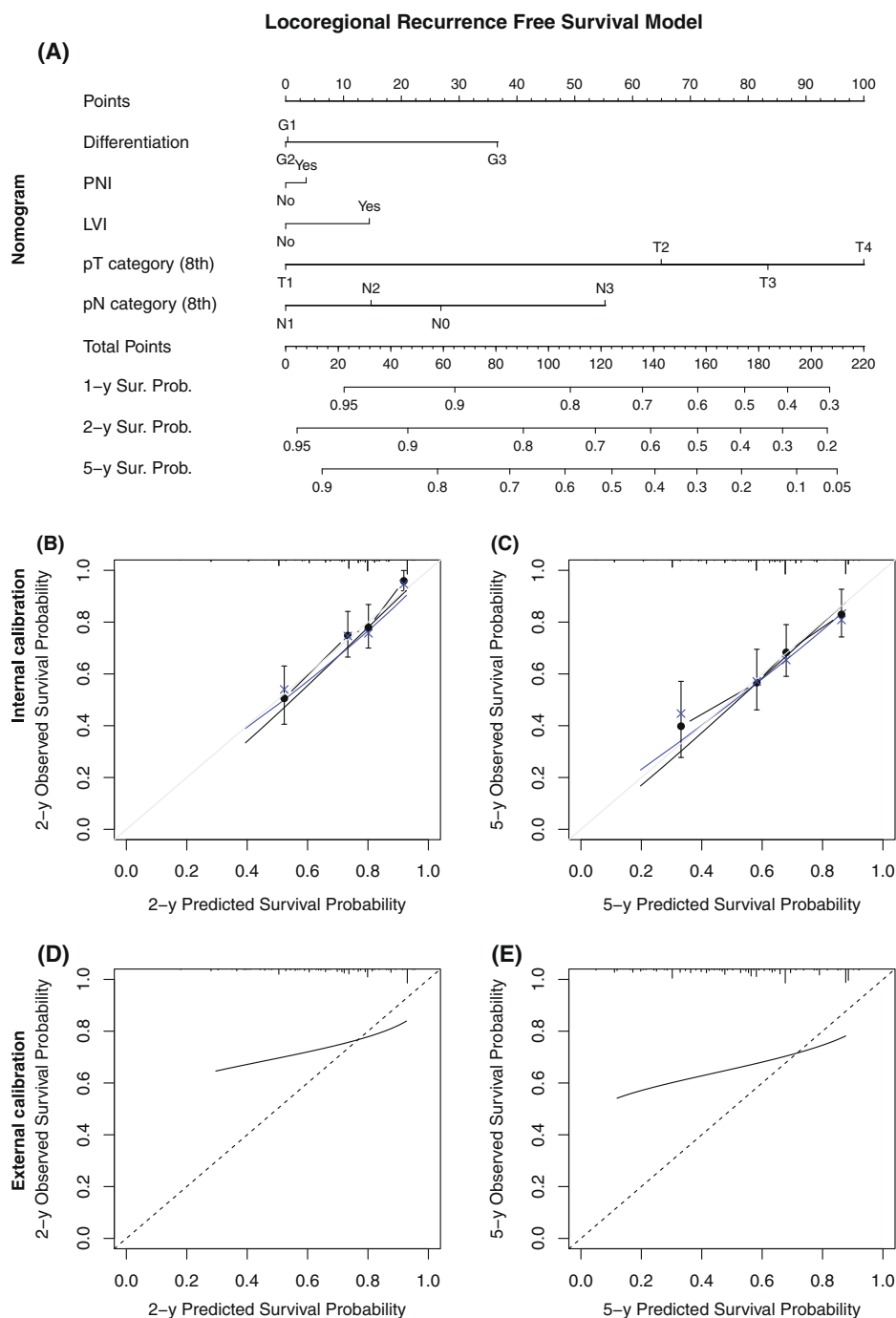


**FIGURE 4** A, Nomogram for locoregional recurrence-free survival (LRRFS). Bootstrap internal validation of calibration curve at 2 years, B, and 5 years, C; dots showing apparent calibration accuracy; × are bootstrap estimates corrected for overfitting, based on binning predicted survival probabilities and computing Kaplan-Meier estimates. Black and blue curve are the estimated observed relationship using “bare” and the overfitting-corrected one, respectively. The gray line represents the ideal relationship. External calibration curves at 2 years, D, and 5 years, E; dotted line represents the ideal relationship [Color figure can be viewed at [wileyonlinelibrary.com](http://wileyonlinelibrary.com)]

Adverse pathological features were seen to affect survival differently. pT category impacted OS, DSS and LRRFS, while pN category and differentiation impacted

OS, DSS, LRRFS and DRFS. LVI impacted OS, LRRFS and DRFS. As these patients were treated as per National Comprehensive Cancer Network (NCCN) guidelines,

most patients with high nomogram scores were already given adjuvant therapy; hence, these nomograms cannot be used to determine treatment escalation and should be used only to provide survival estimates.

The OS, DSS and DRFS nomograms performance was satisfactory, with optimism corrected c-indexes of 0.73, 0.75 and 0.77 in the training cohort and c-indexes of 0.73, 0.77 and 0.73 in the external validation cohort, respectively. This confirmed that they were robust and could be reliably applied in western countries as well. The satisfactory performance of LRRFS models in the training cohort with optimism corrected c-index of 0.70, but poorer performance in the external validation cohort with a c-index of 0.58 limits its application in western countries cohorts and suggests further research regarding geographical or ethnic differences in patterns of recurrence and their determinants (demographic or risk factors) and tumor-related factors (genomic or tumor immune microenvironment) is warranted.

Although based on retrospective data, the strength of our nomograms is that the training data was from a single institution with uniform treatment guidelines as mentioned by the NCCN. The validation with an external independent testing cohort coming from two large referral Italian head and neck cancer centers also showed good concordance in particular for OS, DSS and DRFS. Moreover, the different origins of the populations in the training and validation cohorts (India and Italy, respectively) further support the generalizability of our nomograms. Moreover, the availability of four shinyapps, derived from each model, can further improve the use of such prediction tools after a radical oncologic treatment. These could be useful to design new prospective studies to improve the follow-up in these patients.

## 5 | CONCLUSION

The OTSCC nomograms being proposed in this paper embrace several fundamental variables, have good accuracy, consider the latest edition of the UICC/AJCC staging system and can be used to individually predict the most relevant oncologic outcomes. The variables used are routinely available making it easy to adopt and include in everyday clinical practice.

### CONFLICT OF INTEREST

The authors declare no potential conflict of interest.

### DATA AVAILABILITY STATEMENT

Data available on request subject to ethical clearance

### ORCID

Deepak Balasubramanian  <https://orcid.org/0000-0001-7404-1452>

Narayana Subramaniam  <https://orcid.org/0000-0002-5153-3136>

### REFERENCES

1. Marur S, Forastiere AA. Head and neck squamous cell carcinoma: update on epidemiology, diagnosis, and treatment. *Mayo Clin Proc.* 2016;91(3):386-396.
2. Moore SR, Johnson NW, Pierce AM, Wilson DF. The epidemiology of tongue cancer: a review of global incidence. *Oral Dis.* 2000;6(2):75-84.
3. Riemann M, Knipfer C, Rohde M, et al. Oral squamous cell carcinoma of the tongue: prospective and objective speech evaluation of patients undergoing surgical therapy. *Head Neck.* 2016;38(7):993-1001.
4. Brierley JD, Gospodarowicz MK, Wittekind C. *TNM classification of malignant tumours – 8th edition.* Geneva, Switzerland: Union for International Cancer Control; 2016.
5. Subramaniam N, Balasubramanian D, Murthy S, et al. Predictors of locoregional control in stage I/II oral squamous cell carcinoma classified by AJCC 8th edition. *Eur J Surg Oncol.* 2019;45(11):2126-2130.
6. Hirabayashi S, Kosugi SI, Isobe Y, et al. Development and external validation of a nomogram for overall survival after curative resection in serosa-negative, locally advanced gastric cancer. *Ann Oncol.* 2014;25(6):1179-1184.
7. Liang W, Zhang L, Jiang G, et al. Development and validation of a nomogram for predicting survival in patients with resected non-small-cell lung cancer. *J Clin Oncol.* 2015;33(8):861-869.
8. Kim JH, Kim HS, Seo WY, et al. External validation of nomogram for the prediction of recurrence after curative resection in early gastric cancer. *Ann Oncol.* 2012;23(2):361-367.
9. Kawai K, Ishihara S, Yamaguchi H, et al. Nomogram prediction of metachronous colorectal neoplasms in patients with colorectal cancer. *Ann Surg.* 2015;261(5):926-932.
10. Paris PL, Weinberg V, Albo G, et al. A group of genome-based biomarkers that add to a kattan nomogram for predicting progression in men with high-risk prostate cancer. *Clin Cancer Res.* 2010;16(1):195-202.
11. Li Y, Zhao Z, Liu X, et al. Nomograms to estimate long-term overall survival and tongue cancer-specific survival of patients with tongue squamous cell carcinoma. *Cancer Med.* 2017;6(5):1002-1013.
12. Sun W, Cheng M, Zhuang S, Chen H, Yang S, Qiu Z. Nomograms to predict survival of stage IV tongue squamous cell carcinoma after surgery. *Medicine (Baltimore).* 2019;98(26):e16206.
13. Chang B, He W, Ouyang H, et al. A prognostic nomogram incorporating depth of tumor invasion to predict long-term overall survival for tongue squamous cell carcinoma with R0 resection. *J Cancer.* 2018;9(12):2107-2115.
14. Xiao N, Xu QS. Multi-step adaptive elastic-net: reducing false positives in high-dimensional variable selection. *J Stat Comput Simul.* 2015;85(18):3755-3765.
15. Xiao N hdnom: building nomograms for penalized Cox models with high-dimensional survival data. 2016; bioRxiv (065524):1-21.

16. Harrell FE, Califf RM, Pryor DB, Lee KL, Rosati RA. Evaluating the yield of medical tests. *J Am Med Assoc.* 1982;247(18): 2543-2546.
17. Jalali A, Alvarez-Iglesias A, Roshan D, Newell J. Visualising statistical models using dynamic nomograms. *PloS One.* 2019; 14(11):e0225253.
18. Murthy S, Low TH (Hubert), Subramaniam N, et al. Validation of the eighth edition AJCC staging system in early T1 to T2 oral squamous cell carcinoma. *J Surg Oncol* 2019;119(4):449–454.
19. Pollaers K, Hinton-Bayre A, Friedland PL, Farah CS. AJCC 8th edition oral cavity squamous cell carcinoma staging – Is it an improvement on the AJCC 7th edition? *Oral Oncol.* 2018;82:23-28.
20. Koyfman S, Joshi NP, Lamarre E, et al. Validating the AJCC 8th edition of the oral cavity cancer staging system: a multi-institutional collaborative study. *Int J Radiat Oncol.* 2018;102 (3):S22.
21. Gross ND, Patel SG, Carvalho AL, et al. Nomogram for deciding adjuvant treatment after surgery for oral cavity squamous cell carcinoma. *Head Neck.* 2008;30(10):1352-1360.
22. Chen F, Lin L, Liu F, et al. Three prognostic indexes as predictors of response to adjuvant chemoradiotherapy in patients with oral squamous cell carcinoma after radical surgery: a large-scale prospective study. *Head Neck.* 2019;41(2): 301-308.
23. Bobdey S, Balasubramaniam G, Mishra P. Nomogram prediction for survival of patients with oral cavity squamous cell carcinoma. *Head Neck.* 2016;38(12):1826-1831.
24. Montero PH, Yu C, Palmer FL, et al. Nomograms for preoperative prediction of prognosis in patients with oral cavity squamous cell carcinoma. *Cancer.* 2014;120(2): 214-221.
25. Ju J, Wang J, Ma C, et al. Nomograms predicting long-term overall survival and cancer-specific survival in head and neck squamous cell carcinoma patients. *Oncotarget.* 2016;7(32): 51059-51068.
26. Wang SJ, Patel SG, Shah JP, et al. An oral cavity carcinoma nomogram to predict benefit of adjuvant radiotherapy. *JAMA Otolaryngol Head Neck Surg.* 2013;139(6):554-559.
27. Kattan MW, Hess KR, Amin MB, et al. American Joint Committee on Cancer acceptance criteria for inclusion of risk models for individualized prognosis in the practice of precision medicine. *CA Cancer J Clin.* 2016;66(5):370-374.

**How to cite this article:** Balasubramanian D, Subramaniam N, Missale F, et al. Predictive nomograms for oral tongue squamous cell carcinoma applying the American Joint Committee on Cancer/Union Internationale Contre le Cancer 8th edition staging system. *Head & Neck.* 2021;43: 1043–1055. <https://doi.org/10.1002/hed.26554>

## Compartmental surgery vs WLE in oral tongue and FOM cancer

**Missale, F.**  
Marchi, F.  
Iandelli, A.  
Subramaniam, N.  
Dokhe, Y.  
Sampieri, C.  
Mattavelli, D.  
Bresciani, L.  
Carobbio, A.L.C.  
Grammatica, A.  
Thankappan, K.  
Iyer, S.P.  
Fontanella, W.  
Giannini, L.  
Peretti, G.  
Parrinello, G.  
Balasubramanian, D.  
Piazza, C.

Oral Oncology  
2022;135:106210. doi: 10.1016/j.oraloncology.2022.106210.

Supplementary material:





Contents lists available at ScienceDirect

## Oral Oncology

journal homepage: [www.elsevier.com/locate/oraloncology](http://www.elsevier.com/locate/oraloncology)

## Oncological outcomes of compartmental surgery and wide local excision in oral tongue and floor of the mouth cancer

Francesco Missale<sup>a,b,c,1</sup>, Filippo Marchi<sup>b,d,1</sup>, Andrea Iandelli<sup>b,\*</sup>, Narayana Subramaniam<sup>e</sup>, Yogesh Dokhe<sup>e</sup>, Claudio Sampieri<sup>b</sup>, Davide Mattavelli<sup>f</sup>, Lorenzo Bresciani<sup>g</sup>, Andrea Luigi Camillo Carobbio<sup>h</sup>, Alberto Grammatica<sup>f</sup>, Krishnakumar Thankappan<sup>e</sup>, Subramania Iyer<sup>e</sup>, Walter Fontanella<sup>i</sup>, Lorenzo Giannini<sup>i</sup>, Giorgio Peretti<sup>b,d</sup>, Giampiero Parrinello<sup>b</sup>, Deepak Balasubramanian<sup>e,2,\*</sup>, Cesare Piazza<sup>f,2</sup>

<sup>a</sup> Department of Molecular and Translational Medicine, University of Brescia, 25125 Brescia, Italy

<sup>b</sup> Department of Otorhinolaryngology - Head and Neck Surgery, IRCCS Ospedale Policlinico San Martino, 16132 Genoa, Italy

<sup>c</sup> Department of Surgery Otorhinolaryngology, Antoni Van Leeuwenhoek, Nederlands Kanker Instituut, 1066 Amsterdam, the Netherlands

<sup>d</sup> Department of Surgical Sciences and Integrated Diagnostics (DISC), University of Genoa, Genoa, Italy

<sup>e</sup> Department of Head and Neck Surgery, Amrita Institute of Medical Sciences, Amrita Vishwa Vidyapeetham, Kochi, Kerala, India

<sup>f</sup> Unit of Otorhinolaryngology - Head and Neck Surgery, Department of Medical and Surgical Specialties, Radiological Sciences and Public Health, University of Brescia, Brescia, Italy

<sup>g</sup> Unit of Pediatric Otorhinolaryngology and Maxillofacial Surgery, ASST Spedali Civili of Brescia, Italy

<sup>h</sup> Section of Otorhinolaryngology - Head and Neck Surgery, Department of Neurosciences, University of Padua, Padua, Italy

<sup>i</sup> Unit of Otorhinolaryngology, Maxillofacial, and Thyroid Surgery, Fondazione IRCCS, National Cancer Institute of Milan, University of Milan, Italy

## ARTICLE INFO

## Keywords:

Oral cancer  
Tongue cancer  
Propensity score matching  
Squamous cell carcinoma  
Compartmental surgery

## ABSTRACT

**Objectives:** Oral tongue carcinomas represent more than half of the tumors arising in the oral cavity, a site with a high cancer specific mortality and impact on quality of life. Current guidelines are lacking for a standardized surgical approach of these tumors. The aim of this study is to compare two currently adopted surgical strategies, compartmental surgery (CTS) and wide local excision (WLE), with loco-regional control as the main oncological endpoint.

**Materials and methods:** An observational retrospective multicentric study was carried out enrolling a cohort of patients affected by oral tongue or floor of the mouth squamous cell carcinoma and surgically treated in 4 international tertiary referral centers. Survival analysis was performed by propensity-score matching approach and multivariable Cox regression analysis.

**Results:** A cohort of 933 patients was enrolled. CTS was applied in 113 patients (12.1%) and WLE in 820 (87.9%). Analyzing a propensity-score matched cohort (98 CTS vs. 172 WLE) and applying a survival multivariable modeling strategy on the whole cohort, both confirmed that CTS and WLE are comparable and oncologically safe. Parameters such as number of positive lymph nodes, depth of invasion, and lymphovascular invasion still represent the key prognosticators.

**Abbreviations:** SCC, squamous cell carcinoma; OTSCC, oral tongue SCC; DOI, depth of invasion; PNI, perineural invasion; LVI, lympho-vascular invasion; OS, overall survival; DSS, disease-specific survival; CTS, compartmental surgery; WLE, wide local excision; T-N tract, tumor-lymph node tract; MDT, multidisciplinary team; US, Ultrasound; MR, magnetic resonance; CT, computed tomography; PET, positron emission tomography; NCCN, National Comprehensive Cancer Network (NCCN); RT, radiotherapy; CRT, chemoradiotherapy; ENE, extranodal extension; LRRFS, locoregional recurrence free survival; DRFS, distant recurrence free survival; HR, hazard ratio; CI, confidence interval.

\* Corresponding authors at: Department of Otorhinolaryngology - Head and Neck Surgery, IRCCS Ospedale Policlinico San Martino, 16132 Genoa, Italy (A. Iandelli). Department of Head and Neck Surgery, Amrita Institute of Medical Sciences, Amrita Vishwa Vidyapeetham, Kochi, Kerala, India (D. Balasubramanian).

**E-mail addresses:** [Missale.francesco@gmail.com](mailto:Missale.francesco@gmail.com) (F. Missale), [filippomarchi@hotmail.it](mailto:filippomarchi@hotmail.it) (F. Marchi), [Davide\\_mattavelli85@yahoo.it](mailto:Davide_mattavelli85@yahoo.it) (D. Mattavelli), [Lorenzo\\_bresciani@unimi.it](mailto:Lorenzo_bresciani@unimi.it) (L. Bresciani), [A.carobbio@studenti.unibs.it](mailto:A.carobbio@studenti.unibs.it) (A.L.C. Carobbio), [albertogrammatica@libero.it](mailto:albertogrammatica@libero.it) (A. Grammatica), [Krishnakumart@aims.amrita.edu](mailto:Krishnakumart@aims.amrita.edu) (S. Iyer), [Walter.fontanella@istitutotumori.mi.it](mailto:Walter.fontanella@istitutotumori.mi.it) (W. Fontanella), [Lorenzo.giannini@istitutotumori.mi.it](mailto:Lorenzo.giannini@istitutotumori.mi.it) (L. Giannini), [iandelliandrea@gmail.com](mailto:iandelliandrea@gmail.com), [Claudio\\_sampieri@outlook.com](mailto:Claudio_sampieri@outlook.com) (G. Parrinello), [deepakbala@live.com](mailto:deepakbala@live.com) (D. Balasubramanian), [ceceplaza@libero.it](mailto:ceceplaza@libero.it) (C. Piazza).

<sup>1</sup> These authors share the first authorship since equally contributed to this manuscript.

<sup>2</sup> These authors share the last authorship since equally contributed to this manuscript.

<https://doi.org/10.1016/j.oraloncology.2022.106210>

Received 15 July 2022; Received in revised form 6 October 2022; Accepted 7 October 2022

Available online 25 October 2022

1368-8375/© 2022 Elsevier Ltd. All rights reserved.



**Conclusion:** The main goals for surgical resection of oral cancer remain its three-dimensional circumferential clearance with adequate margins and en-bloc removal of the tumor-lymph node tract, independently of the technique adopted (CTS or WLE). Further prospective studies including quality of life evaluation are needed to better understand if one of these approaches can provide superior functional outcomes.

### Introduction

Oral cavity squamous cell carcinoma (SCC) is a significant contributor to global cancer burden, with high cancer-specific mortality [1]. The oral tongue is one of the most common subsites involved, accounting for up to half of all cases [2]. Typically, oral tongue SCC (OTSCC) has a propensity for extensive local invasion and regional lymphatic spread, leading to significant disease- and treatment-related morbidities. Despite better expertise and multidisciplinary care, improvement in oncologic outcomes of OTSCC has been modest over time. From 2013 through 2017, death rates among males decreased for most cancers, while increasing for the oral cavity [3]. Moreover, the incidence of OTSCC in developed nations is also rising in young females [4,5], the causes of which remain to be fully understood.

The inclusion of depth of invasion (DOI) in the 8th Edition of the TNM staging systems for oral cancer [6] improved its prognostic performance [7,8]. However, one-third of OTSCC with a DOI < 10 mm can develop loco-regional recurrences [9], which has been noted to have a strong correlation with adverse pathological features such as perineural (PNI), lympho-vascular invasion (LVI), degree of differentiation, and pattern of invasion [10,11]. A recently validated nomogram for OTSCC confirmed the prognostic impact of these parameters on overall (OS) and disease-specific survivals (DSS) [12]. However, nodal and margins status still represent the most relevant prognosticators [13]. Since the latter is the only one under the surgeon's control, tumor size and DOI are critical parameters in choosing the surgical approach to ensure adequate tumor-free resection margins. In this regard, it should be kept in mind that 10 mm represents the average distance between the tongue mucosal surface and the extrinsic muscles [14] (this layer named "cover" according to Takemoto) [15]. Thus, a tumor transgressing that distance increases the risk of loco-regional recurrence by 4 times [16]. However, it is difficult to preoperatively determine whether or not the major bulk of extrinsic muscles (referred to as "core") [15] are involved because their depth changes according to which part of the organ is taken into account [14,17].

Based on these considerations and following the principles for treatment of soft tissue sarcomas [18], Calabrese [19] described a novel surgical strategy for OTSCC, called compartmental surgery (CTS), which de-emphasizes the role of wide local excision (WLE), generally defined as a tumor resection within 1 cm of healthy tissue in every direction. CTS is based on the following considerations: 1) the tongue is a symmetrically paired organ consisting of two halves, or compartments, the boundaries of which are represented by the mandibular/hyoid periosteum and the midline lingual raphe; 2) an adjunctive territory at risk of metastasis (the so-called tumor-lymph node [T-N] tract), is composed by the parenchymal structures between the primary and the cervical lymphatic chain, including the muscular (mylohyoid), neuro-vascular (lingual and hypoglossal nerves, lingual vessels), lymphatic (vessels and sublingual nodes), and glandular (sublingual) tissues. This hypothesis was first demonstrated by analyzing OTSCC specimens where tumor cells migration occurred longitudinally along and between the intrinsic and extrinsic muscle fibers; in contrast, the median lingual raphe was supposed to represent a barrier against tumor invasion. Therefore, CTS aims to extirpate the entire compartment affected by OTSCC in case of extrinsic muscle invasion, i.e. the entire hemitongue, the parenchymal structures within the floor of mouth (T-N tract) in continuity with the neck dissection specimen. A few years later, Calabrese reported significant oncological improvements using CTS compared to the traditional WLE following adequate tumor margins:

16.8% in 5-year local control, 24.4% in loco-regional control, and 27.3% in OS [20].

There is no universally accepted consensus on the amount of tissue that can be considered as a "safe margin" for OTSCC resection [21]. Considering that disease removal must be the main goal, clarifying which surgical approach can guarantee adequate tumor control without unnecessary functional impairment is of paramount interest. For these reasons, the current study compared the oncological outcomes of the largest multi-institutional cohort of OTSCC treated by CTS vs. WLE to date.

### Materials and methods

#### Study design

An observational retrospective multicentric study was carried out enrolling a cohort of patients affected by OTSCC and surgically treated in 4 tertiary referral centers: University of Genoa (Italy), National Cancer Institute of Milan (Italy), University of Brescia (Italy), and Amrita Hospital of Cochin (India). The study was conducted in accordance with the Declaration of Helsinki and approved by the respective local Ethics Committees (CER Liguria 133/2021). All patients had been submitted to surgery after multidisciplinary team (MDT) discussion and comprehensive preoperative work-up, including computed tomography (CT) or magnetic resonance (MR) of the head and neck, and PET-CT or chest CT. Exclusion criteria were: diagnosis of distant metastases and/or synchronous head and neck SCC, unavailable follow-up information, previous treatment(s) for head and neck cancer, other synchronous or metachronous primary tumors, or treatment with neoadjuvant therapy.

Upfront surgery was performed with curative intent. Resection was planned according to the tumor site, extension, and DOI. All patients underwent tumor excision, neck dissection, and appropriate reconstruction. Selective or modified radical neck dissections were performed in adherence with the National Comprehensive Cancer Network (NCCN) guidelines [22]. WLE was defined as the resection of OTSCC aiming for at least 1 cm gross circumferential margins, both mucosal and deep, without necessarily following the compartmental boundaries. For superficial early cancers the defects corresponded to a partial glossectomy, while for more advanced cancers it corresponded to hemiglossectomy with possible marginal mandibulectomy, excluding both subtotal and total glossectomies.

Adjuvant treatment was discussed by the MDT in adherence with NCCN guidelines [22]. Adjuvant radiotherapy (RT) was administered for node-positive tumors or advanced tumor stages. In addition, adjuvant chemoradiotherapy (CRT) was administered for close/positive margins, more than 2 positive nodes, or extranodal extension (ENE).

Follow-up included clinical examination every month in the first year, every two months in the second year, every three months in the third year, every four months in the fourth year, and every six months in the fifth year. PET-CT or MR were performed in patients reporting symptoms or in case of suspicious clinical findings.

Clinical and pathological variables were retrieved from patients' clinical records, including demographic features, current or former smoking habits, type of surgical approach (WLE or CTS) to the primary, details of pathologic results including margins status, grading, PNI, LVI, DOI, and pathological staging according to the current 8th edition of the AJCC-TNM staging system (second revision of June 2018) [6].

**Table 1**Patient characteristics in the original and matched cohorts. P-value estimated by Chi-square test<sup>#</sup> or Mann-Whitney test<sup>§</sup>.

	Original cohort			P-value	Matched cohort		
	Total (N = 933)	WLE (N = 820)	Compartmental (N = 113)		WLE (N = 172)	Compartmental (N = 98)	P value
<b>Age</b>							
Mean (SD)	57.3 (14.2)	56.0 (13.3)	66.9 (16.6)	<0.001§	63.7 (11.6)	65.2 (16.3)	0.428§
Median [Min, Max]	58.0 [18.0, 98.0]	57.0 [18.0, 93.0]	69.0 [26.0, 98.0]		64.0 [32.0, 93.0]	63.0 [26.0, 94.0]	
<b>Sex</b>							
Female	256 (27.4%)	221 (27.0%)	35 (31.0%)	0.37#	51 (29.7%)	28 (28.6%)	0.89#
Male	677 (72.6%)	599 (73.0%)	78 (69.0%)		121 (70.3%)	70 (71.4%)	
<b>Subsite</b>							
FOM	105 (11.3%)	95 (11.6%)	10 (8.8%)	0.524#	31 (18.0%)	9 (9.2%)	0.0519#
Tongue	828 (88.7%)	725 (88.4%)	103 (91.2%)		141 (82.0%)	89 (90.8%)	
<b>pT category (8th Ed.)</b>							
pT1	182 (19.5%)	179 (21.8%)	3 (2.7%)	<0.001#			
pT2	303 (32.5%)	273 (33.3%)	30 (26.5%)		61 (35.5%)	28 (28.6%)	0.505#
pT3	307 (32.9%)	247 (30.1%)	60 (53.1%)		79 (45.9%)	50 (51.0%)	
pT4	141 (15.1%)	121 (14.8%)	20 (17.7%)		32 (18.6%)	20 (20.4%)	
<b>pN category (8th Ed.)</b>							
pN0	496 (53.2%)	446 (54.4%)	50 (44.2%)	0.0165#	79 (45.9%)	41 (41.8%)	0.898
pN1	111 (11.9%)	94 (11.5%)	17 (15.0%)		25 (14.5%)	17 (17.3%)	
pN2a	13 (1.4%)	13 (1.6%)	0 (0%)		0 (0%)	0 (0%)	
pN2b	70 (7.5%)	52 (6.3%)	18 (15.9%)		24 (14.0%)	12 (12.2%)	
pN2c	43 (4.6%)	39 (4.8%)	4 (3.5%)		8 (4.7%)	4 (4.1%)	
pN3a	5 (0.5%)	5 (0.6%)	0 (0%)		0 (0%)	0 (0%)	
pN3b	195 (20.9%)	171 (20.9%)	24 (21.2%)		36 (20.9%)	24 (24.5%)	
<b>DOI (mm)</b>							
Mean (SD)	11.9 (8.60)	11.7 (8.80)	13.3 (6.88)	0.0302§	13.0 (6.55)	13.4 (6.96)	0.627§
Median	10.0 [0.500, 60.0]	10.0 [0.500, 60.0]	12.0 [1.00, 50.0]		12.0 [1.00, 40.0]	12.0 [1.00, 50.0]	
[Min, Max]							
<b>Max Diameter (mm)</b>							
Mean (SD)	26.3 (14.0)	25.6 (14.2)	31.9 (11.5)	<0.001§	31.7 (13.0)	32.3 (11.8)	0.681§
Median [Min, Max]	24.0 [3.00, 100]	22.0 [3.00, 100]	30.0 [7.00, 60.0]		30.0 [10.0, 80.0]	30.0 [7.00, 60.0]	
<b>Grading</b>							
G1	312 (33.4%)	303 (37.0%)	9 (8.0%)	<0.001#	22 (12.8%)	9 (9.2%)	0.658#
G2	476 (51.0%)	405 (49.4%)	71 (62.8%)		101 (58.7%)	61 (62.2%)	
G3	145 (15.5%)	112 (13.7%)	33 (29.2%)		49 (28.5%)	28 (28.6%)	
<b>PNI</b>							
No	537 (57.6%)	510 (62.2%)	27 (23.9%)	<0.001#	49 (28.5%)	25 (25.5%)	0.671#
Yes	396 (42.4%)	310 (37.8%)	86 (76.1%)		123 (71.5%)	73 (74.5%)	
<b>LVI</b>							
No	655 (70.2%)	597 (72.8%)	58 (51.3%)	<0.001#	96 (55.8%)	49 (50.0%)	0.376#
Yes	278 (29.8%)	223 (27.2%)	55 (48.7%)		76 (44.2%)	49 (50.0%)	
<b>Treatment</b>							
Surgery	420 (45.0%)	390 (47.6%)	30 (26.5%)	<0.001#	50 (29.1%)	27 (27.6%)	0.971#
Surgery and RT	234 (25.1%)	187 (22.8%)	47 (41.6%)		65 (37.8%)	38 (38.8%)	
Surgery and CRT	279 (29.9%)	243 (29.6%)	36 (31.9%)		57 (33.1%)	33 (33.7%)	
<b>Margins</b>							
Negative	761 (81.6%)	697 (85.0%)	64 (56.6%)	<0.001#	125 (72.7%)	55 (56.1%)	<0.001#
Close	133 (14.3%)	89 (10.9%)	44 (38.9%)		29 (16.9%)	39 (39.8%)	
Positive	39 (4.2%)	34 (4.1%)	5 (4.4%)		18 (10.5%)	4 (4.1%)	

### Statistical analysis

Standard descriptive statistics were used to summarize data. Fisher's exact test was applied for comparisons with qualitative variables, and Wilcoxon test for quantitative ones.

The primary survival endpoint was locoregional recurrence free survival (LRRFS); additional survival outcomes considered were OS, DSS, and distant recurrence free survival (DRFS). LRRFS was defined as the time between the date of surgery and that of local or nodal recurrence/last visit, OS as the time between the date of surgery and the date of death/last consultation, DSS as the time between the date of surgery and that of cancer-related death/last visit, and DRFS as the time between the date of surgery and distant recurrence/last visit.

Survival analysis was performed by estimating the survival curves with the Kaplan-Meier method or fitting Cox proportional-hazards models, estimating p values by log-rank test or Wald statistic, respectively. Survival estimates were reported as hazard ratio (HR) with 95% confidence interval (95 %CI), and estimating the 2- and 5-year survival

probability with 95 %CI for variables of clinical interest. The combined effect of different continuous variables, describing tumor features, on the 5-year survival estimates is also shown with contour plots [23]. In all analyses, two-tail tests with a significance level of 5% were applied. R (version 3.5.1) was used for statistical analysis.

### Propensity-score matching

A propensity-score matching algorithm was applied to obtain an unbiased estimate of treatment effect to compare patients whose primary tumor was treated with WLE or CTS. Based on literature-derived knowledge and clinical expertise, pre-treatment features including demographics (age), subsite (tongue or floor of the mouth), pT, pN categories, DOI, tumor maximum diameter, grading, and presence of PNI or LVI were taken into account for estimation of the propensity-score. The propensity-score, representing the estimated probability of receiving WLE or CTS for each patient, was calculated using a logistic regression model based on the observed baseline covariates. A greedy nearest

neighbor matching was applied to match patients treated with WLE 2:1 to similar ones treated with CTS using the “MatchIt” package [24,25]. The calipers were set with a width equal to 0.2 of the standard deviation of the logit of the propensity-score [25,26]. Evaluation of matching was done by estimating the standardized mean differences of baseline characteristics and inspecting plots of histogram of distance values and plots of the mean of each covariate against the estimated propensity-score in each arm of treatment. Quantile-quantile plots were used to evaluate the success of the matching procedure.

Sample size estimation

Planning a propensity-score matched groups comparison with a 2:1 ratio between control and experimental subjects as arms of treatment, the previous results obtained by Calabrese et al. [20] showed a HR for the LRRFS risk of control subjects relative to experimental subjects of 2.77. With an accrual interval of 120 months and an additional follow-up of 36 months, we needed to study at least 53 experimental subjects and 106 controls to be able to reject the null hypothesis that their survival curves are equal with a power of 0.95 and a type I error probability associated with this test of this null hypothesis of 0.05 (alpha).

Results

Cohort of patients

A cohort of 933 patients treated between 2000 and 2021 was enrolled. The mean age ± standard deviation was 57.3 ± 14.2 years; 677 patients were males (72.6%) and the epicenter of the lesion was the oral tongue in 828 cases (88.7%). Kochi contributed with 20,680 person-months (57.92%), University of Brescia with 8963 person-months (25.10%), National Cancer Institute of Milan with 4928 person-months (13.80%), and University of Genoa with 1133 person-months (3.17%). The median follow-up time was 29 months (IQR, 12–55; range, 0–191). In the available dataset, 0.4% of values were missing and were imputed with a MICE algorithm; comprehensive information on missingness is summarized in Supplementary Figure 1, and summary statistics of the entire cohort are described in Table 1, and Supplementary Tables S1. In the entire cohort, 820 patients (87.9%) underwent WLE, whereas in 113 cases (12.1%) the CTS approach was chosen (applied at the Universities of Brescia, Genoa and, after June 2017, at the National Cancer Institute of Milan).

The choice of performing a CTS approach was associated both with tumor features such as pT category (p < 0.001), higher DOI (p = 0.0302), and higher maximum diameter (p < 0.001) (Table 1), as well as with center-related preferences (p < 0.001, Supplementary Table S1).

Propensity-score matching

Since T1 lesions (n = 182) were rarely treated by CTS (n = 3, 1.7%), these were excluded from the analysis; therefore, only 641 patients treated by WLE and 110 with CTS were available for matching extraction. Using the variables age, subsite of tumor, pT, pN categories, DOI, maximum diameter, grading, PNI, and LVI, we were able to match with a 2:1 ratio 172 patients treated with WLE to 98 treated with CTS and having similar propensity-scores (Table 1). The unbalanced composition of these groups among the variables chosen for the paired matching (p < 0.05) was well adjusted when examining the matched cohort (p > 0.05), as shown in Table 1, Supplementary Figure S2, and Supplementary Figure S3. Supplementary Figure S2 shows the distributions of propensity scores in the unmatched groups and in the matched ones. As result of an effective matching such distributions in the matched groups were similar. Interestingly, although treatment was not chosen as a matching variable, the pre-matching association (p < 0.001) between treatment group and the entire treatment plan (Surgery, Surgery + RT, or Surgery + CRT) was lost in the matched cohort (p = 0.97). This

Table 2

Univariable LRRFS analysis on the matched cohort. Legend: HR, Hazard Ratio; M, male; F, female; FOM, floor of the mouth; WLE, wide local excision; DOI, depth of invasion; PNI, perineural invasion; LVI, lymphovascular invasion.

Variable		N° (%)	LRRFS - univariable HR (CI95%, P value)
Center	Kochi	96 (35.6%)	reference
	Brescia	111 (41.1%)	0.73 (0.42–1.28, p = 0.274)
	Genoa	21 (7.8%)	0.83 (0.32–2.18, p = 0.710)
	Milan INT	42 (15.6%)	0.95 (0.49–1.84, p = 0.881)
Age	Mean (SD)	64.2 (13.5)	1.02 (1.00–1.04, p = 0.072)
	Sex	F	79 (29.3%)
Sex	M	191 (70.7%)	0.66 (0.41–1.07, p = 0.094)
	Subsite	FOM	40 (14.8%)
Tongue		230 (85.2%)	0.90 (0.48–1.67, p = 0.731)
Compartmental surgery	WLE	172 (63.7%)	reference
	Compartmental	98 (36.3%)	0.90 (0.54–1.49, p = 0.679)
Treatment	Surgery	77 (28.5%)	reference
	Surgery and RT	103 (38.1%)	0.93 (0.53–1.63, p = 0.809)
	Surgery and CRT	90 (33.3%)	0.71 (0.39–1.29, p = 0.256)
	Margin	Negative	180 (66.7%)
Margin	Close	68 (25.2%)	0.77 (0.42–1.39, p = 0.381)
	Positive	22 (8.1%)	1.08 (0.49–2.39, p = 0.855)
pT category (8th Ed.)	pT2	89 (33.0%)	reference
	pT3	129 (47.8%)	1.07 (0.63–1.82, p = 0.811)
	pT4a	52 (19.3%)	1.26 (0.65–2.46, p = 0.490)
pN category (8th Ed.)	pN0	120 (44.4%)	reference
	pN1	42 (15.6%)	2.11 (1.10–4.05, p = 0.025)
	pN2a	0 (0%)	–
	pN2b	36 (13.3%)	1.88 (0.97–3.67, p = 0.062)
	pN2c	12 (4.4%)	3.18 (1.10–9.22, p = 0.033)
	pN3a	0 (0%)	–
	pN3b	60 (22.2%)	1.24 (0.64–2.41, p = 0.528)
	N° positive nodes	Mean (SD)	1.58 (2.50)
ENE	No	195 (72.2%)	reference
	Yes	75 (27.8%)	1.02 (0.60–1.75, p = 0.940)
DOI (mm)	Mean (SD)	13.1 (6.70)	1.00 (0.97–1.04, p = 0.923)
Maximum diameter (mm)	Mean (SD)	31.9 (12.6)	0.99 (0.97–1.01, p = 0.287)
Grading	G1	31 (11.5%)	reference
	G2	162 (60.0%)	2.73 (0.98–7.60, p = 0.055)
	G3	77 (28.5%)	2.51 (0.87–7.30, p = 0.090)
PNI	No	74 (27.4%)	reference
	Yes		

(continued on next page)

Table 2 (continued)

Variable		N° (%)	LRRFS - univariable HR (CI95%, P value)
LVI	No	196 (72.6%)	1.55 (0.87–2.74, p = 0.135) reference
	Yes	125 (46.3%)	1.72 (1.07–2.75, p = 0.024)

confirms the similarity between centers in terms of overall treatment plan. In contrast, in both the pre-matching and matched cohort, a significantly higher rate of at least one close margin was observed in the group treated by CTS ( $p < 0.001$  and  $p < 0.001$ , respectively). Thus,

propensity-score matching allowed an unbiased comparison of survival rates between patients treated with WLE vs. CTS.

Survival analysis: propensity-score matching

The main survival outcome considered was loco-regional control and, in the matched cohort, the HR for LRRFS in the CTS group compared to WLE was 0.90 (CI95% 0.54–1.49,  $p = 0.679$ ), as shown in Table 2 and Fig. 1A. The lack of association between treatment arm and survival was also observed by analyzing OS [HR 1.08 (CI95% 0.71–1.63,  $p = 0.721$ ), Fig. 1B], DSS [HR 0.73 (CI95% 0.42–1.26,  $p = 0.263$ ), Figure 1C], and DFS [HR 0.85 (CI95% 0.55–1.433,  $p = 0.478$ ), Figure 1D]. The 5-year survival rates of CTS vs. WLE were 75% vs. 64% for LRRFS, 58% vs. 55% for OS, 76% vs. 63% for DSS, and 66% vs. 55% for

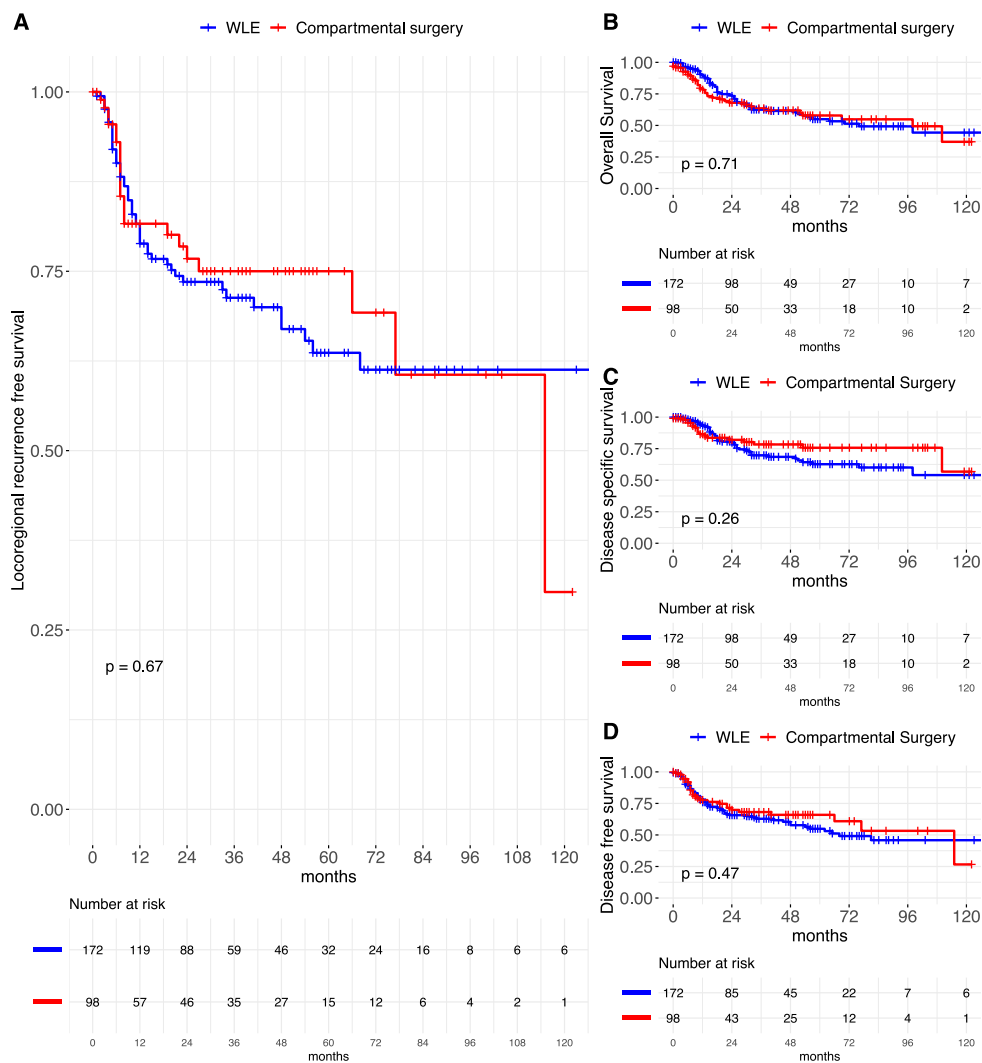


Fig. 1. Kaplan Meier curves in the matched cohort analyzing the arm of surgical treatment in relation with the LRRFS (A), OS (B), DSS (C), and DFS (D).

**Table 3**  
Survival estimated with 95% CI for each survival outcome at 12, 24, 36, 60 and 120 months for the entire matched cohort and in both treatment arms.

Time	Entire matched cohort (N = 270) Estimate (CI95%)	WLE (N = 172) Estimate (CI95%)	CTS (N = 98) Estimate (CI95%)
<b>Overall survival (OS)</b>			
12 months	85 (81–90)	89 (84–94)	78 (70–87)
24 months	71 (66–78)	73 (66–81)	68 (59–79)
36 months	63 (57–70)	63 (55–71)	63 (54–75)
60 months	56 (49–64)	55 (46–65)	58 (47–71)
120 months	42 (32–56)	44 (33–59)	37 (19–70)
<b>Disease specific survival (DSS)</b>			
12 months	91 (87–95)	93 (89–97)	86 (79–94)
24 months	80 (75–86)	80 (73–87)	82 (74–91)
36 months	73 (66–79)	70 (62–78)	78 (69–89)
60 months	67 (60–75)	63 (54–73)	76 (66–87)
120 months	57 (45–72)	54 (41–71)	57 (32–100)
<b>Disease free survival (DFS)</b>			
12 months	76 (71–82)	76 (69–83)	78 (69–87)
24 months	67 (61–74)	66 (58–74)	70 (60–81)
36 months	65 (58–71)	63 (55–71)	68 (58–80)
60 months	58 (52–66)	55 (46–65)	66 (56–78)
120 months	42 (30–59)	46 (36–59)	27 (6.4–100)
<b>Loco-regional recurrence-free survival (LRRFS)</b>			
12 months	80 (75–85)	79 (73–86)	82 (74–94)
24 months	75 (69–80)	74 (67–81)	77 (68–87)
36 months	72 (67–79)	71 (64–79)	75 (66–86)
60 months	67 (61–75)	64 (55–74)	75 (66–86)
120 months	54 (40–73)	61 (52–72)	30 (7.3–100)

for DFS (Table 3).

Although pT and pN categories were significantly associated with OS, achieving its good stratification (Fig. 2A–B), no association was found with LRRFS (Fig. 2C–D). Conversely, other covariates related with the disease biological behavior, namely LVI (HR 1.72, CI95% 1.07–2.75;  $p = 0.024$ ) and number of metastatic nodes (HR 1.11, CI95% 1.00–1.23;  $p = 0.051$ ), were the most significant covariates associated with different LRRFS (Table 2). Most tumoral biological features (LVI, number of positive nodes, ENE) were also significantly associated with other relevant survival outcomes such as OS, DSS, and DFS; in contrast, margin status was not associated with any survival outcome (Supplementary Table S2 3).

#### Survival analysis: multivariable modeling

A further multivariable model analysis, considering LRRFS and OS as outcomes, was applied to the entire cohort. This was aimed at confirming the results obtained applying the propensity-score matching and investigating possible center-specific differences. This also allowed an extensive study of continuous variables of interest such as the number of positive nodes, DOI, and maximum tumor diameter.

Multivariable models were built (Fig. 3 and Supplementary Figure S4), including the variables: center, surgical approach, DOI, number of positive nodes, margin status, LVI, and treatment. By restricted cubic spline functions, a possible non-linear relationship between continuous variables (DOI, maximum diameter, number of positive nodes) and LRRFS was ruled out, whereas for OS modeling a non-linear relationship was observed for maximum diameter and DOI (Supplementary Figures S5–S6). Thus, these variables were modelled with restricted cubic spline functions with 4 and 3 knots, respectively (Supplementary Figures S5–S6). First-term interactions were also included between DOI, number of positive nodes, surgical approach, and adjuvant treatment.

Considering both LRRFS and OS, the surgical approach was

confirmed to not be a prognostic covariate ( $p = 0.633$ ,  $p = 0.835$ ), while the number of positive lymph nodes ( $p < 0.001$ ,  $p < 0.001$ ), LVI ( $p = 0.003$ ,  $p = 0.001$ ), and DOI ( $p = 0.001$ ,  $p = 0.024$ ) were confirmed. No significant difference was observed among treating centers regarding LRRFS and OS ( $p = 0.576$ ,  $p = 0.428$ ), as shown in Supplementary Figure S4.

A significant interaction was observed between treatment and number of positive nodes considering OS as outcome ( $p = 0.0006$ ), meaning a different benefit on the survival prediction applying adjuvant treatments, depending on the number of positive lymph nodes. In Fig. 3A can be seen that, increasing the number of nodes involved, the treatment associated with the best OS is adjuvant CRT, and the benefit seems to be clinically relevant for  $\geq 2$  positive nodes. Similar plots can also be seen for LRRFS (Fig. 3B), although no significant interaction was observed ( $p = 0.302$ ). Considering DOI, a significant interaction with treatment and LRRFS was shown ( $p = 0.0166$ ); considering the plots in Fig. 3C–3D, worse prognosis was seen for patients not undergoing adjuvant treatment with the increment of DOI, as expected. Lastly, no interactions were observed between type of surgical approach and number of positive nodes or DOI (Fig. 3E–3H). Contour plots were also built (Fig. 4A–H) to better understand the combined effect of different continuous variables describing tumor features (DOI, maximum diameter and number of positive nodes) on the 5-year OS and LRRFS predictions. It could be observed that in both groups the effect of the maximum diameter is limited, whereas with an increasing of number of positive nodes or DOI the survival predictions change dramatically. Scatter plots including two-dimensional density maps representing quartiles of the distribution of values clarify the area of contour plots where most data are present, and thus where the plotted survival estimated probability is more reliable (Fig. 4I–4L).

#### Discussion

The anatomical complexity of the tongue, wherein vessels, muscles, and nerves are intermingled in a three-dimensional framework, and its unique function and volume modification as a muscular hydrostat [15] leads to significant challenges for the surgeon facing OTSCC. The main goal in such a field is to define an oncologically safe procedure easily reproducible, teachable, and not overly disabling. When first described by Calabrese [19], CTS appeared as an extremely attractive concept, being technically wise, well standardized and easily reproducible by a well-trained head and neck surgeon with good oncological outcomes, that were apparently superior to those previously reported with WLE. The main limit of this latter procedure, in fact, has traditionally been considered the fact of being more related to personal experience and intraoperative judgement of the surgeon. While in WLE the resection must be maintained at least within 1 cm of free surgical margins, and this can be not so intuitive especially in the depth of the surgical field, the philosophy behind the CTS approach leads to an anatomy-driven ablation following well-recognizable structures. This allows surgeons, even in non-high-volume centers, to perform safe, standardized, and effective resections. Moreover, since the resulting defect is roughly constant, it is possible to establish the reconstructive requirements in a preoperative setting, thereby avoiding time-consuming refinements during flap inset. In this respect, Grammatica et al. demonstrated that the CTS technique, along with free flaps reconstruction, provides consistent functional results in terms of speech and swallowing [27]. After the seminal study by Calabrese [19], a subsequent publication [20] showed significant oncological benefit from this approach compared to traditional WLE.

However, a recent paper has drawn attention to the fact that patients undergoing CTS may have received more adjuvant therapy, which could have skewed survival data [28]. Another concern is that although the tongue may be divided into compartments, a standardized approach can result in either too little or too extended resections. Consequently, the reported improvement in survival from adopting CTS might be biased.

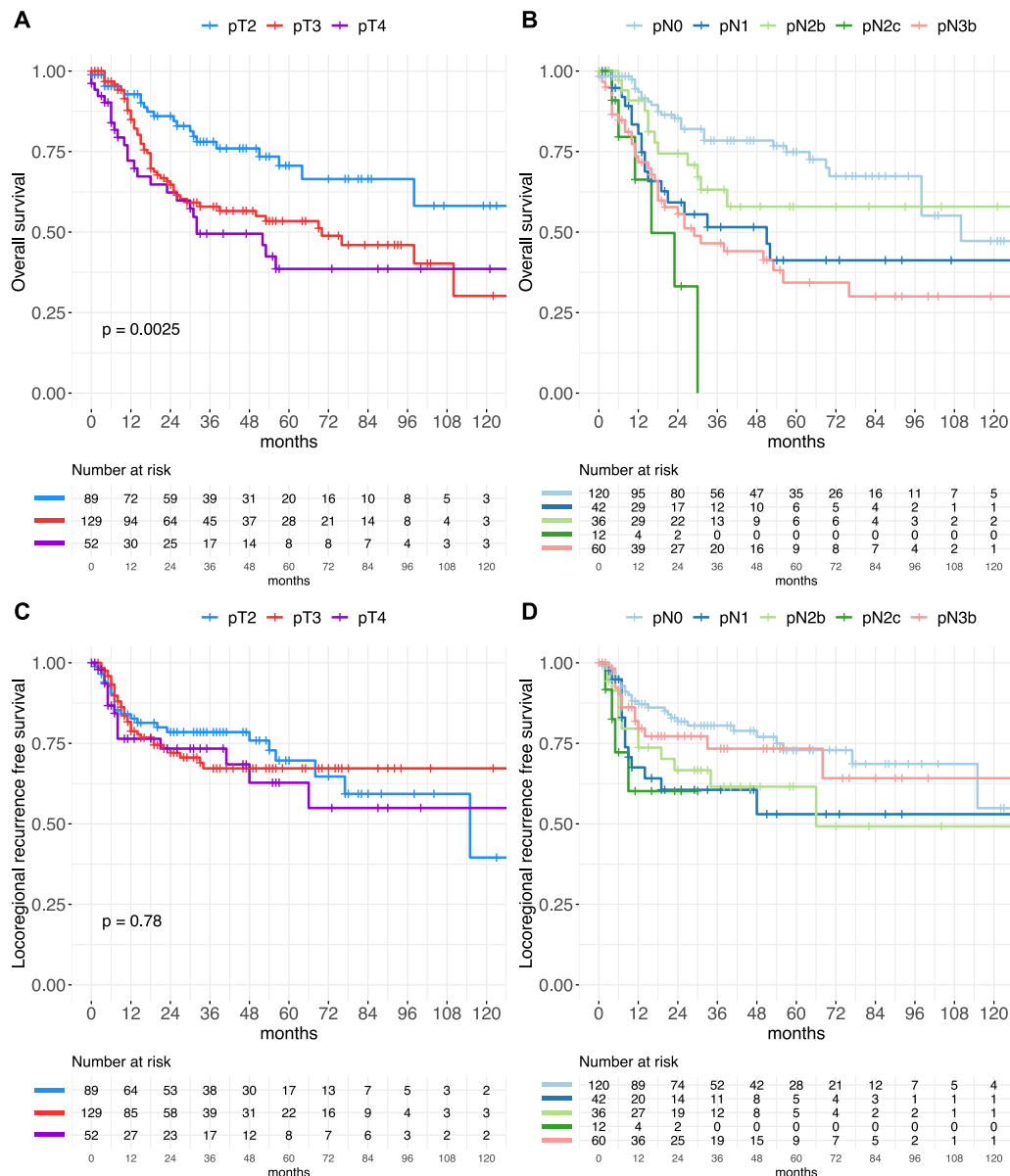


Fig. 2. Kaplan Meier curves of OS (A, B) and LRRFS (C, D) in the matched cohort by pT and pN categories.

Therefore, while a reproducible technique is of value for training residents and young surgeons and also helps to standardize reconstruction, questions still remain as to what should be considered the ideal approach from an oncological point of view. In this study, our intention was therefore to revisit this concept and determine if CTS and WLE are equally valid in a large, geographically diverse cohort of patients.

After propensity-score matching, our data yielded two interesting findings: 1) tumors with larger superficial diameter and DOI were more often chosen for CTS, irrespective of their T and N categories; 2) patients treated with CTS had a higher incidence of close or positive margins,

especially along the midline lingual raphe, which is considered an anatomically resistant barrier. This latter element, however, might especially represent, from another point of view, a potential drawback of a procedure that traditionally aims for wide macroscopic free margins. Furthermore, even though some authors [29] have emphasized that OTSCC can invade the surrounding tissues traveling throughout the muscular fascia, recent studies [30,31] have demonstrated that tumors with particularly aggressive behavior are characterized by the presence of tumor budding and scattered satellitosis which might escape more easily from the muscular compartment itself.



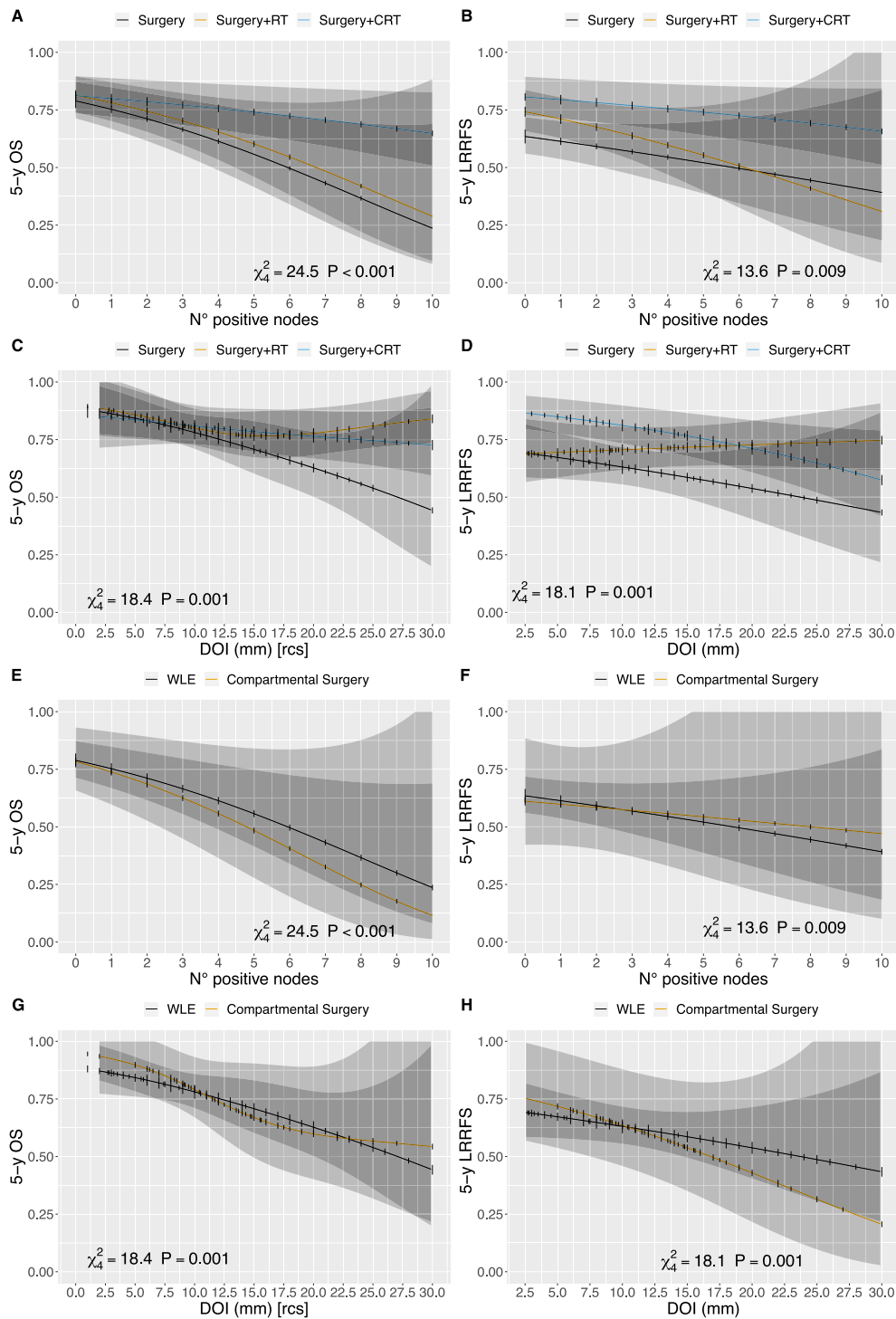


**Fig. 3.** Plots representing the estimated 5-year LRRFS and OS probability derived from the fitted multivariable models. Partial effects plots of number of positive nodes and DOI combined with treatment and surgical approach are presented. In A and G the relationship between the continuous variables of DOI and survival outcome in the Cox regression model is modelled with a restricted cubic spline function with 4 knots. P value, referred to each continuous variable, estimated by Wald test.

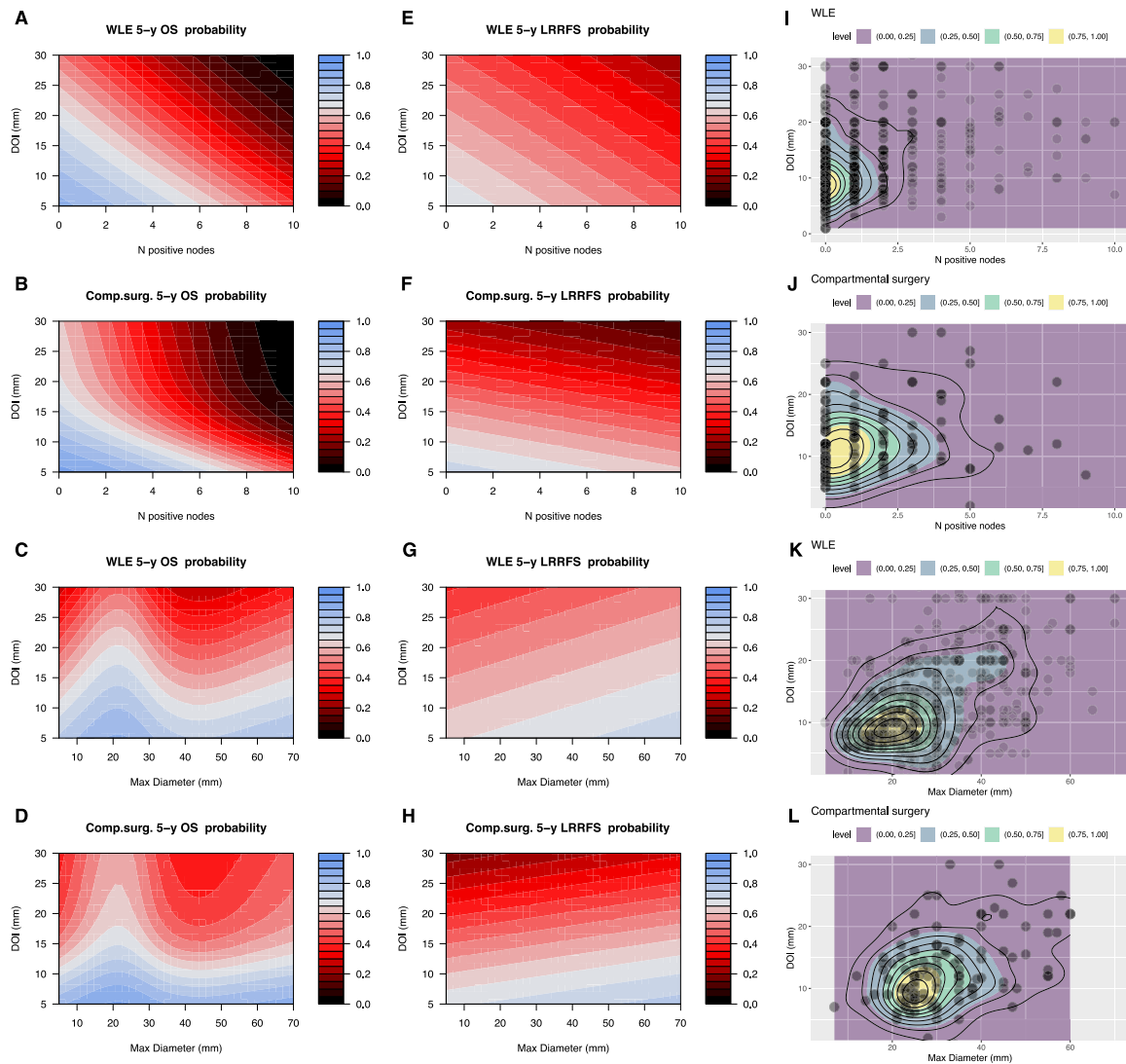


**Fig. 4.** Contour plots derived from multivariable OS (A-D) and LRRFS (E-H) models fitted on the entire cohort of pT2-T4a tumors and showing partial effects plots of the DOI and number of positive nodes in the WLE or Compartmental surgery groups and the combined effect of DOI and maximum diameter in such groups of treatments, with the color scale representing 5-year probability of OS or LRRFS, and showing on x and y axes the marginal effect of each variable values. These plots help to interpret the combined effect of different continuous variables describing tumor features (DOI, maximum diameter and number of positive nodes) on the survival prediction. Notably, it could be observed that in both groups the effect of the maximum diameter is limited (minimal color change increasing the x value in C-H), whereas increasing the number of positive nodes or DOI value, the survival predictions change dramatically. In I-L are represented scatter plots of the distribution of each couple of variables in each treatment arm, showing with 2D density maps in which area of the xy plane is located each quartile of the distribution (color scale) and each decile (black levels line); these plots help the interpretation of each contour plot on the left side, showing the area where most of tumors are located, and thus where survival predictions are supported by data.

Our survival analysis showed no statistically significant difference between WLE and CTS regarding local recurrence, DFS, and OS (even though a positive trend in favor of CTS should be noticed). The fact that the difference in margins status did not impact survival can be explained by two arguments: 1) the median lingual septum acts as a real anatomical barrier to prevent further tumor spread and, therefore, close margins at the level of the midline can be considered of secondary importance; 2) the similar oncological outcomes reflect appropriate use of adjuvant treatments. In fact, before propensity-score matching, the

WLE cohort was treated by surgery alone in 47.6% of cases, compared to only 26.5% for CTS. These findings downplay the basic tenet that radical local clearance only is needed to improve survival. In contrast, other factors were found to significantly impact local recurrence and survival, namely ENE, number of metastatic nodes, and DOI. This demonstrates our more recent understanding that variables reflecting tumor biology (e.g., PNI, LVI, nodal burden, and worst pattern of invasion) can often play a more critical role in treatment outcomes than margin status alone [12]. Interestingly, the number of positive nodes, although not included

as staging criteria [32], nor a risk factor for adjuvant treatment delivery [33], was demonstrated to be an emerging prognosticator in our cohort as well in several other studies [34–36].

Although CTS is a theoretically and functionally sound concept, the improved survival attributed to this technique is likely to be an unintended bias in the original analysis [20], which failed to account for the increased adjuvant therapy following CTS and patients selection. Although tumors treated by CTS were likely to have a higher T category, modifications to the 8TNM make it challenging to know what percentage of patients would be down-staged due to extrinsic muscles involvement (in the 7TNM equaling pT4) being removed from the staging considerations. This is why propensity-matching for heterogeneous groups like these is crucial to avoid erroneous conclusions when comparing dissimilar patient cohorts. WLE was shown in our study to have a higher chance of achieving clear margins, arguably with less resection of superficial uninvolved tissue, at least towards the tip and base of the tongue, but less so at the midline level. These are crucial considerations in OTSCC patients who, after surgical resection/reconstruction and adjuvant therapy, may experience a reduced quality of life [37]. Moreover, it has to be noted that WLE strictly refers to the procedure herein described, where the aim is to obtain a three-dimensional gross margin of at least 1 cm around the entire tumor, i.e. a radical procedure for complete oncological clearance, the only difference with CTS being that uninvolved structures beyond 1 cm from the tumor are not resected.

Additionally, it is important to note that for larger tumors there may be an overlap in the extent and type of surgical defects after WLE and CTS. It is our belief that these findings are more relevant for mid-sized tumors (pT2-3), which is also arguably the group of patients in whom even moderate increases in the extent of resection can have significant impact on tongue functionality and quality of life. These data support the fact that in patients with larger tumors and aggressive biology, adjuvant therapy is more likely to improve survival than the extent of resection itself, as long as margins are adequate. Therefore, although WLE might require more complex resections and more experience on the surgeon's side, it appears to be the technique that best guarantees clear microscopic margins. Nevertheless, CTS may still be indicated based on tumor location, especially considering its advantages in reproducibility and ease of reconstruction. Of note, these approaches have comparable outcomes only if performed with appropriate surgical technique, as described in the Materials and Methods section. Nonetheless, the choice of the most adequate approach needs to be patient-specific and revolves around three-dimensional circumferential tumor clearance. Further meaningful head-to-head evaluations of CTS and WLE will require prospective randomized studies also assessing function and quality of life, with the success following CTS and WLE reconstruction being another attractive field to explore.

The retrospective nature of our study represents its main limitation. On the other hand, enrolling 4 international tertiary referral centers allowed us to collect a large series with detailed data. Propensity-score matching ensured that possible biases derived from heterogeneity of groups comparison were minimized. Lastly, the different origins of the populations in the matched cohorts further support the generalizability of our results.

#### Declaration of Competing Interest

The authors declare that they have no known competing financial interests or personal relationships that could have appeared to influence the work reported in this paper.

#### Acknowledgements

None.

#### Appendix A. Supplementary material

Supplementary data to this article can be found online at <https://doi.org/10.1016/j.oraloncology.2022.106210>.

#### References

- [1] Ferlay J, Colombet M, Soerjomataram I, Mathers C, Parkin DM, Piñeros M, et al. GLOBOCAN sources and methods. *Int J Can* 2019;144(8):1941–53.
- [2] Marur S, Forastiere AA. Head and neck squamous cell carcinoma: update on epidemiology, diagnosis, and treatment. *Mayo Clin Proc* 2016;91:386–96. <https://doi.org/10.1016/j.mayocp.2015.12.017>.
- [3] Henley SJ, Ward EM, Scott S, Anderson RN, Firth AU, Thomas CC, et al. Annual report to the nation on the status of cancer. Part I: Natl Can Statist 2020:1–25. <https://doi.org/10.1002/cncr.32802>.
- [4] Satgunaseelan L, Allanson BM, Asher R, Reddy R, Low HTH, Veness M, et al. The incidence of squamous cell carcinoma of the oral tongue is rising in young non-smoking women: an international multi-institutional analysis. *Oral Oncol* 2020; 110:104875. <https://doi.org/10.1016/j.oraloncology.2020.104875>.
- [5] Paderno A, Morello R, Piazza C. Tongue carcinoma in young adults: a review of the literature. *Acta Otorinolaryngol Ital Organo Uff Della Soc Ital Di Otorinolaryngol e Chir Cerv-Facc* 2018;38(3):175–80.
- [6] Cancer AJC on. *AJCC Cancer Staging Manual*. 8th ed. 2017.
- [7] Lydiatt WM, Patel SG, O'Sullivan B, Brandwein MS, Ridge JA, Migliacci JC, et al. Head and neck cancers—major changes in the American Joint Committee on cancer eighth edition cancer staging manual: Head and Neck Cancers—Major 8th Edition Changes. *CA Can J Clin* 2017;67(2):122–37.
- [8] Mattavelli D, Ferrari M, Taboni S, Morello R, Paderno A, Rampinelli V, et al. The 8th TNM classification for oral squamous cell carcinoma: what is gained, what is lost, and what is missing. *Oral Oncol* 2020;111:104937.
- [9] Subramaniam N, Balasubramanian D, Murthy S, Kumar N, Vidhyadharan S, Vijayan SN, et al. Predictors of locoregional control in stage I/II oral squamous cell carcinoma classified by AJCC 8th edition. *Eur J Surg Oncol* 2019;45(11):2126–30.
- [10] Chatterjee D, Bansal V, Malik V, Bhagat R, Punia RS, Handa U. Tumor Budding and Worse Pattern of Invasion Can Predict Nodal Metastasis in Oral Cancers and Associated With Poor Survival in Early-Stage Tumors 2019:1–8. doi:10.1177/0145561319848669.
- [11] Li Y, Bai S, Carroll W, Dayan D, Dort JC, Heller K, et al. Validation of the risk model: high-risk classification and tumor pattern of invasion predict outcome for patients with low-stage oral cavity squamous cell carcinoma. *Head Neck Pathol* 2013;7(3):211–23.
- [12] Balasubramanian D, Subramaniam N, Missale F, Marchi F, Dokhe Y, Vijayan S, et al. Predictive nomograms for oral tongue squamous cell carcinoma applying the American Joint Committee on Cancer/Union Internationale Contre le Cancer 8th edition staging system. *Head Neck* 2021;43(4):1043–55.
- [13] Zanoni D, Montero P, Migliacci J, Shah J, Ganly I, Patel SG. Survival outcomes after treatment of cancer of the oral cavity (1985–2015). *Oral Oncol* 2020;115–21. <https://doi.org/10.1016/j.oraloncology.2019.02.001>. SURVIVAL.
- [14] Sanders I, Mu L. A 3-dimensional atlas of human tongue muscles. *Anat Rec* 2014; 296:1102–14. <https://doi.org/10.1002/ar.22711>.
- [15] Takemoto H. Morphological analyses of the human tongue musculature for three-dimensional modeling. *J Speech Lang Hear Res* 2001;44:95–107. [https://doi.org/10.1044/1092-4388\(2001\)0099](https://doi.org/10.1044/1092-4388(2001)0099).
- [16] Faisal M, Bakar MA, Sarwar A, Adeel M, Batool F, Malik KI, et al. Depth of invasion (DOI) as a predictor of cervical nodal metastasis and local recurrence in early stage squamous cell carcinoma of oral tongue (ESSCOT) 2018:1–10.
- [17] Piazza C, Montalto N, Paderno A, Taglietti V, Nicolai P. Is it time to incorporate “depth of infiltration” in the T staging of oral tongue and floor of mouth cancer? *Curr Opin Otolaryngol Head Neck Surg* 2014;22:81–9. <https://doi.org/10.1097/MOO.0000000000000038>.
- [18] Enneking WF, Malawer MM. The effect of the anatomic setting on the results of surgical procedures for soft parts sarcoma of the thigh. *Cancer* 1980;47:1005–22.
- [19] Calabrese L, Giugliano G, Bruschini R, Ansarin M, Navach V, Grosso E, et al. Compartmental surgery in tongue tumours: description of a new surgical technique. *Acta Otorinolaryngol Ital Organo Uff Della Soc Ital Di Otorinolaryngol e Chir Cerv-Facc* 2009;29:259–64.
- [20] Calabrese L, Bruschini R, Giugliano G, Ostuni A, Maffini F, Massaro MA, et al. Compartmental tongue surgery: long term oncologic results in the treatment of tongue cancer. *Oral Oncol* 2011;47(3):174–9.
- [21] Zanoni DK, Service N, Sloan M, Cancer K, Migliacci JC, Service N, et al. A Proposal to Redefine Close Surgical Margins in Squamous Cell Carcinoma of the Oral Tongue. *JAMA Otolaryngol Head Neck Surg* 2017;143:555–60. doi:10.1001/jamaoto.2016.4238.A.
- [22] Bruce JY, Darlow S, et al. *NCCN Clinical Practice Guidelines in Oncology (NCCN Guidelines®)*. Head and Neck Cancers 2020.
- [23] Breheny P, Burchett W. Visualization of regression models using visreg. *R J* 2017;9: 56.
- [24] Ho D, Imai K, King G, Matchitt SEA. Nonparametric preprocessing for parametric causal inference. *J Stat Software* 2011;1(8):pp.
- [25] Austin PC. A comparison of 12 algorithms for matching on the propensity score. *Stat Med* 2014;33:1057–69. <https://doi.org/10.1002/sim.6004>.

- [26] Austin PC. Optimal caliper widths for propensity-score matching when estimating differences in means and differences in proportions in observational studies. *Pharm Stat* 2011;10:150–61. <https://doi.org/10.1002/pst.433>.
- [27] Grammatica A, Piazza C, Montalto N, Del Bon F, Frittoli B, Mazza M, et al. Compartmental surgery for oral tongue cancer: objective and subjective functional evaluation. *Laryngoscope* 2021;131(1). <https://doi.org/10.1002/lary.28627>.
- [28] Piazza C, Grammatica A, Montalto N, Paderno A, Del Bon F, Nicolai P. Compartmental surgery for oral tongue and floor of the mouth cancer: oncologic outcomes. *Head Neck* 2018;41:110–5. <https://doi.org/10.1002/hed.25480>.
- [29] Rana M, Iqbal A, Warraich R, Ruecker M, Eckardt AM, Gellrich N-C. Modern surgical management of tongue carcinoma – a clinical retrospective research over a 12 years period. *Head Neck Oncol* 2011;3:43. <https://doi.org/10.1186/1758-3284-3-43>.
- [30] Xu B, Salama AM, Valero C, Yuan A, Khimraj A, Saliba M, et al. The prognostic role of histologic grade, worst pattern of invasion, and tumor budding in early oral tongue squamous cell carcinoma: a comparative study. *Virchows Arch* 2021;479(3):597–606.
- [31] Hori Y, Kubota A, Yokose T, Furukawa M, Matsushita T, Oridate N. Association between pathological invasion patterns and late lymph node metastases in patients with surgically treated clinical No early oral tongue carcinoma. *Head Neck* 2020;42:238–43. <https://doi.org/10.1002/hed.25994>.
- [32] Amin MB, Greene FL, Edge SB, Compton CC, Gershenwald JE, Brookland RK, et al. The Eighth Edition AJCC Cancer Staging Manual: Continuing to build a bridge from a population-based to a more “personalized” approach to cancer staging: The Eighth Edition AJCC Cancer Staging Manual. *CA Cancer J Clin* 2017;67(2):93–9.
- [33] Golevas AD, Yom SS, Pfister DG, Spencer S, Adelstein D, Adkins D, et al. NCCN guidelines @ insights head and neck cancers featured updates to the NCCN guidelines. *J Natl Compr Canc Netw* 2018;16:479–90. <https://doi.org/10.6004/jncn.2018.0026>.
- [34] Subramaniam N, Balasubramanian D, Kumar N, Murthy S, Vijayan SN, Nambiar A, et al. Lymph node staging systems in oral squamous cell carcinoma: a comparative analysis. *Oral Oncol* 2019;97:92–8.
- [35] Tsai T-Y, Iandelli A, Marchi F, Huang Y, Tai S-F, Hung S-Y, et al. The prognostic value of lymph node burden in oral cavity cancer: systematic review and meta-analysis. *Laryngoscope* 2022;132(1):88–95.
- [36] Liao C-T, Lee L-Y, Hsueh C, Lin C-Y, Fan K-H, Wang H-M, et al. Pathological risk factors stratification in pN3b oral cavity squamous cell carcinoma: Focus on the number of positive nodes and extranodal extension. *Oral Oncol* 2018;86:188–94.
- [37] Dobbins M, Gunson J, Bale S, Neary M, Ingrams D, Brown M. Improving patient care and quality of life after laryngectomy/glossectomy. *Br J Nurs* 2005;14:634–40. <https://doi.org/10.12968/bjon.2005.14.12.18283>.

## Laryngeal Compartmentalization Does Not Affect the Prognosis of LSCC Treated by Total Laryngectomy

Marchi, F. #  
**Missale, F. #**  
Sampieri, C.  
Filauro, M.  
Iandelli, A.  
Parrinello, G.  
Incandela, I.  
Smeele, L.E.  
van den Brekel, M.W.M.  
Del Bon, F.  
Nicolai, P.  
Piazza, C.  
Peretti, G.

Cancers  
2020;12, 2241. doi: <https://doi.org/10.3390/cancers12082241>

#equally contributed as first authors



Supplementary material:



Article

## Laryngeal Compartmentalization Does Not Affect the Prognosis of T3-T4 Laryngeal Cancer Treated by Upfront Total Laryngectomy

Filippo Marchi <sup>1,2,3,†</sup> , Francesco Missale <sup>1,4,†</sup> , Claudio Sampieri <sup>1,2,\*</sup> , Marta Filauro <sup>1,2,5</sup> , Andrea Iandelli <sup>1,2,6</sup>, Giampiero Parrinello <sup>1</sup>, Fabiola Incandela <sup>7</sup>, Ludwig E. Smeele <sup>8</sup>, Michiel W. M. van den Brekel <sup>8</sup> , Francesca Del Bon <sup>9</sup>, Piero Nicolai <sup>10</sup>, Cesare Piazza <sup>7,11</sup> and Giorgio Peretti <sup>1,2</sup>

- <sup>1</sup> IRCCS Ospedale Policlinico San Martino, 16132 Genoa, Italy; filippomarchi@hotmail.it (F.M.); missale.francesco@gmail.com (F.M.); mfilauro@yahoo.com (M.E.); iandelliandrea@gmail.com (A.I.); giampiero.parrinello@gmail.com (G.P.); giorgioperetti18@gmail.com (G.P.)
  - <sup>2</sup> Department of Surgical Sciences and Integrated Diagnostics (DISC), University of Genoa, 16132 Genoa, Italy
  - <sup>3</sup> Department of Plastic and Reconstructive Surgery, Chang Gung Memorial Hospital, Taipei 33305, Taiwan
  - <sup>4</sup> Department of Molecular and Translational Medicine, University of Brescia, 25100 Brescia, Italy
  - <sup>5</sup> Department of Experimental Medicine (DIMES), University of Genoa, 16132 Genoa, Italy
  - <sup>6</sup> Department of Head and Neck Surgery, Chang Gung Memorial Hospital, Chang Gung University and Medical College, Taoyuan 33305, Taiwan
  - <sup>7</sup> Department of Otorhinolaryngology, Maxillofacial and Thyroid Surgery, Fondazione IRCCS, National Cancer Institute of Milan, 20133 Milan, Italy; Fabiola.Incandela@istitutotumori.mi.it (F.I.); ceceplaza@libero.it (C.P.)
  - <sup>8</sup> Department of Head & Neck Oncology & Surgery Otorhinolaryngology, Antoni Van Leeuwenhoek, Nederlands Kanker Instituut, 1066 Amsterdam, The Netherlands; l.smeele@nki.nl (L.E.S.); m.vd.brekel@nki.nl (M.W.M.v.d.B.)
  - <sup>9</sup> Department of Otorhinolaryngology—Head and Neck Surgery, University of Brescia, 25123 Brescia, Italy; delbonfrancesca@gmail.com
  - <sup>10</sup> Section of Otorhinolaryngology—Head and Neck Surgery, Department of Neurosciences, University of Padua, Via Giustiniani, 2-35128 Padua, Italy; pieronicolai@icloud.com
  - <sup>11</sup> Department of Oncology and Oncohematology, University of Milan, 20122 Milan, Italy
- \* Correspondence: claudio.sampieri@outlook.com  
† These authors equally contributed to the work.

Received: 7 July 2020; Accepted: 7 August 2020; Published: 11 August 2020



**Abstract:** A picture is emerging in which advanced laryngeal cancers (LCs) are potentially not homogeneous and may be characterized by subpopulations which, if identified, could allow selection of patients amenable to organ preservation treatments in contrast to those to be treated with total laryngectomy (TL). This work aims to analyze a multicentric cohort of T3-T4a LCs treated by upfront TL, investigating the clinical and pathological features that can best predict oncologic outcomes. A total of 149 previously untreated patients who underwent TL for T3-T4a LC at four institutions were analyzed. Survival and disease-control were considered as the main outcomes. A secondary end-point was the identification of covariates associated with nodal status, investigating also the tumor thickness. T and N categories were significantly associated with both overall and disease-specific survival. The number of positive nodes and tracheal involvement were associated with loco-regional failure; post-cricoid area invasion and extra-nodal extension with distant failure. Posterior laryngeal compartment involvement was not a significant prognostic feature, by either univariable and multivariable analyses. These results support the conclusion that laryngeal compartmentalization has no impact on survival in patients treated by upfront TL and the current TNM staging system remains a robust prognosticator in advanced LC.



**Keywords:** laryngeal neoplasms; total laryngectomy; paraglottic space; tumor thickness; prognosis; multicentric study

---

### 1. Introduction

Laryngeal cancer (LC), based on the Surveillance, Epidemiology, and End Results (SEER) database for the period 2009–2015, accounts for 0.7% of all new malignant tumors diagnosed in the United States each year. The estimated 5-year overall survival (OS) rate, considering all stages, is 60.3% and has not changed appreciably over the past several decades [1–3]. Moreover, a majority of patients are still diagnosed with locally advanced (T3–T4) disease and evidence of regional nodal metastases, with survival rates generally inferior to 50% [4]. During recent decades, two milestone studies have demonstrated that organ preservation (OP) was achievable even for advanced LC using non-surgical strategies [5,6]. Consequently, chemoradiation (CRT) has become increasingly popular, causing a therapeutic paradigm shift from upfront total laryngectomy (TL) to concurrent/induction CRT. Nevertheless, several epidemiologic studies have reported a decline in survival for patients with LC, possibly attributable to the indiscriminate use of OP protocols [2]. In response to this, the latest American Society of Clinical Oncology (ASCO) position paper, recommendation 2.2, points out that “for selected patients with extensive T3 or large T4a lesions and/or poor pre-treatment laryngeal function, better survival rates and quality of life may be achieved with TL rather than with OP approaches and may be the preferred treatment” [4].

Indeed, the standard of care for intermediate-advanced LC is still a matter of international debate. To further complicate this issue, the 8th Edition of the AJCC UICC TNM staging system includes a wide gamut of different lesions under the generic label of locally advanced LC, ranging from T3 with minimal vs. massive paraglottic space (PGS) involvement (with normal or impaired/fixed vocal cord and arytenoid mobility), T3 with pre-epiglottic space (PES) infiltration, T3 with inner cortex thyroid cartilage erosion, T4 with full-thickness infiltration of the laryngeal framework, and/or T4 with extra-laryngeal extension [7]. In fact, contemporary endoscopic [8] and radiologic [9,10] work-up have dramatically reduced the diagnostic uncertainty during pre-treatment evaluation, leading to better profiling of advanced LC subcategories, and allowing a more tailored treatment choice for each in terms of oncological and functional outcomes.

For example, regarding open partial horizontal laryngectomies (OPHLs) applied to T3–T4 LCs, some authors have recently shown that tumor extension (distinguished in anterior vs. posterior PGS involvement, based on a virtual coronal plane passing through the arytenoid vocal process and perpendicular to the ipsilateral thyroid lamina) is a major prognosticator [11,12]. They therefore concluded that anterior cT3 tumors, without arytenoid fixation, can be successfully managed by OPHLs, and this approach could also be proposed for treatment of anterior cT4aN0, whereas it should be considered less safe in posterior cT3 tumors with crico-arytenoid joint fixation, since these lesions have clinical and biological behaviors that are quite similar to cT4a tumors. As a consequence, a picture is gradually emerging in which advanced LCs appear to be not non-homogeneous, but rather consist of different subpopulations which, if identified, could allow selection of patients who respond better to OP treatments, in contrast to those who should be immediately selected for upfront TL.

With this work we tried to verify if laryngeal compartmentalization may be the result of a different biological behavior of LC or, if instead, it is only a treatment-related prognosticator. Accordingly, we investigated if this feature still impacts on prognosis when applying a more aggressive surgical treatment as TL. Moreover, we evaluated the survival impact of each clinical, radiological, and pathological feature that defines LC as “advanced”, including different tumor extensions to the visceral PGS and PES, pathways of spread, infiltration of the laryngeal framework, involvement of extra-laryngeal soft tissues, and TNM stage. In addition, we investigated the role of promising prognosticators such as tumor thickness (TT) and number of positive nodes. We believe that these findings may allow physicians to

better target some of the most relevant prognostic determinants in the advanced LC scenario, thus helping in the difficult aim of maximizing both OP and oncologic cure rates.

## 2. Materials and Methods

Between January 2010 and September 2018, a total of 169 patients affected by advanced LC who underwent upfront TL were enrolled at four different centers. These included the Unit of Otorhinolaryngology—Head and Neck Surgery of the Ospedale Policlinico San Martino, Genoa, Italy (N = 40), ASST Spedali Civili, Brescia, Italy (N = 78), National Cancer Institute, Milan, Italy (N = 31), and the Netherlands Kanker Instituut, Amsterdam, The Netherlands (N = 20). The study was conducted in accordance with the Declaration of Helsinki, and the study was approved by the local Ethics Committee (CER Liguria: 230/2019). All patients had been submitted to surgery after multidisciplinary team (MDT) discussion and preoperative counseling between head and neck surgeons, and radiation and medical oncologists. Patients were selected for upfront TL if not amenable to OP strategies, either surgical (transoral laser microsurgery (TLM), or OPHL) and non-surgical CRT protocols [13]. Other selection criteria for inclusion in this retrospective analysis were: (1) no history of previous LC; (2) no history of previous laryngeal treatments; (3) availability of imaging and endoscopies performed no more than 4 weeks before surgery; (4) final histopathologic report confirming squamous cell carcinoma (SCC); (5) and final pathologic staging of pT3-pT4a LC.

All data concerning comorbidities, preoperative staging, surgical outcomes, histopathology, adjuvant therapies, and follow-up were collected in a single dedicated database. Preoperative work-up was standardized for all patients and consisted of endoscopic and imaging evaluation. The endoscopic work-up included preoperative transnasal videolaryngoscopy to assess vocal fold/arytenoid mobility, and intraoperative rigid endoscopy by 0°, 30°, and 70° telescopes with white light (WL) and narrow band imaging (NBI, Olympus Medical System Corporation, Tokyo, Japan) to better define the superficial extension of the lesion [8]. Either computed tomography (CT) or magnetic resonance (MR) were used for preoperative imaging. Neck ultrasound (US) with or without fine-needle aspiration cytology was routinely performed. The radiologic work-up allowed to meticulously assess 3D tumor extension, the entity of PGS and/or PES involvement, the presence of cartilaginous framework transgression, and invasion of extra-laryngeal soft tissues [14]. Tumors were classified according to the 8th Edition of the AJCC UICC TNM staging system [7].

PGS involvement was retrospectively re-assessed according to previously published criteria, considering a frontal plane passing through the arytenoid vocal process and perpendicular to the ipsilateral thyroid lamina as the boundary between anterior vs. posterior PGS [10–12]. Laryngeal motility and involvement of the medial wall of the piriform sinus were also considered as ancillary signs for the definition of anterior vs. posterior topography of each tumor (T-topography). Therefore, tumors were considered to involve the posterior laryngeal compartment when posterior PGS was radiologically invaded and/or the arytenoid was fixed and/or medial wall of the piriform sinus was entirely involved.

The main histopathological features considered in the present analysis were: status of surgical margins (close margins defined as <1 mm), perineural invasion (PNI), lympho-vascular invasion (LVI), number of lymph nodes involved, and extra-nodal extension (ENE). Further features regarding the pathways of diffusion of each tumor were also considered; these encompassed: laryngeal framework infiltration or extension to the tracheal rings, soft tissues of the neck, thyroid gland, and base of tongue or retro-cricoid area. Moreover, in 68% of patients in our cohort, TT, derived from microscopic measurements within the histopathologic specimen, was also available and studied in relation to nodal status.

### 2.1. Treatments and Follow-Up

All patients underwent TL or TL combined with partial pharyngectomy (PPH). Selective (SND) or modified radical neck dissections (MRNDs) were performed in adherence with National Comprehensive Cancer Network (NCCN) guidelines for cT3 and cT4 LC [15].

Postoperative radiotherapy (PORT) was discussed by the MDT board and proposed based on pathological findings of pT4a category, close or positive resection margins, nodal category  $\geq$ pN2a, and

presence of PNI and/or LVI in the final histopathologic report, according to NCCN guidelines [15]. PORT dose ranged from 54 to 66 Gy. Platinum-based chemotherapy (CHT) was offered in combination with RT to all patients with positive resection margins or ENE, taking into account the patients' age and comorbidities.

Follow-up was performed by clinical examination of the remaining upper aero-digestive tract and neck and, according to European Laryngological Society (ELS) guidelines, included CT/MR and/or PET-CT if indicated by clinical doubts after endoscopic evaluation [16]. The mean follow-up time in the present cohort was 36 months (range, 6–180).

### 2.2. Statistical Analysis

Standard descriptive statistics was used for data summarizing. For group comparisons in qualitative variables, the Chi-square test was applied. Survival analysis, considering as outcomes overall (OS), disease-specific (DSS), loco-regional recurrence-free (LRRFS), and distant recurrence-free survivals (DRFS), was performed with uni- and multivariable Cox proportional-hazards models. OS was defined as the time between the date of surgery and date of death/last visit, DSS as the time between the date of surgery and date of cancer-related death/last visit, LRRFS as the time between the date of surgery and date of local or nodal recurrence/last visit, and DRFS as the time between the date of surgery and date of distant recurrence/last visit.

Cut-offs in continuous predictors were estimated using maximally selected log-rank statistics [17]. Uni- and multivariable logistic regressions were built considering the presence of positive lymph nodes as the dependent variable. Multivariable Cox models were built by stepwise covariates selection keeping T-topography as an investigative variable inside all multivariable models. Survival estimates were reported as hazard ratio (HR) with 95% confidence interval (95% CI) and estimating the 2- and 5-year survival probability with 95% CI for variables of main clinical interest. Univariable survival curves were plotted by the Kaplan–Meier method and compared with the Log-rank test. In all analyses, two-tail tests with a significance level of 5% were applied. Stata (version 13.0, College Station, TX, USA) and R (version 3.5.1, R Foundation for Statistical Computing, Vienna, Austria) were used for statistical analysis.

## 3. Results

### 3.1. Demographics

A total of 169 patients met the inclusion criteria for retrospective analysis. Due to missing data, only 149 were available for statistical analysis. Mean age was 67 years (range, 41–92), while there were 126 males (84.6%) and 23 females (15.4%). A total of 142 (95.3%) patients were or had been smokers, and 75 (50.3%) were routine alcohol consumers.

### 3.2. Treatments and Tumor Features

In total, 60 (40.3%) patients underwent TL or TL with PPH alone, while 72 (48.3%) received PORT and 17 (11.4%) adjuvant CRT. A total of 112 (75.2%) received a bilateral neck dissection, 34 (22.8%) a unilateral one, and three (2%) received none due to major medical comorbidities.

A total of 138 tumors were located in multiple laryngeal sites (92.6%), whereas six (4%) were confined to the supraglottis, four (2.7%) involved the glottis alone, and one (0.7%) was a purely subglottic tumor.

At the final histopathologic report, 69 (46.3%) tumors were classified as pT3, and 80 (53.7%) as pT4a. In total, eight (5.4%), 89 (59.7%), and 52 (34.9%) tumors were described as well-, moderately-, and poorly-differentiated SCCs, respectively. Furthermore, 75 (43.6%) patients had nodal metastases (11 pN1, 10 pN2a, 14 pN2b, 3 pN2c, and 28 pN3b). In particular, pathologic ENE was found in 38 (25.5%) patients, PNI in 80 (53.7%), and LVI in 74 (49.7%). Positive margins were reported in 11 (7.4%) patients, while close margins were present in 19 (12.8%). Thyroid cartilage was partially invaded in 30 (20.1%) cases, and involved with full-thickness in 35 (23.5%). Cricoid cartilage was infiltrated in 36 (24.2%) and tumors reached the tracheal rings in eight (5.4%). Soft-tissue extra-laryngeal extension was confirmed in 50 (33.6%) specimens. Pathologic TT was reported in 102 (68.4%) patients, with a mean value of 14.6 mm (range, 1.1–31).

Regarding T-topography, tumors were considered posteriorly compartmentalized when the posterior PSG was radiologically invaded, and/or the arytenoid was fixed, and/or the medial wall of the piriform sinus was entirely involved. As a result of this categorization, they were divided in 19 (12.7%) anterior pT3 tumors, 50 (33.6%) posterior pT3, 21 (14.1%) anterior pT4a, and 59 (39.6%) posterior pT4a. Full clinical and pathological data are reported in Table 1.

**Table 1.** Clinical and pathologic characteristics of the cohort.

Variables	Category	No.	%
Gender	Female	23	15.4
Smoking habit	Yes	142	95.3
Alcohol habit	Yes	75	50.3
Arytenoid fixation	Yes	90	60.4
Medial piriform sinus wall involvement	Yes	40	26.8
Radiologic posterior PGS involvement	Yes	70	47
T-topography	Posterior	109	73.2
Supraglottic involvement	Yes	122	81.9
Subglottic involvement	Yes	84	56.4
Base of tongue involvement	Yes	11	7.4
Retro-cricoid area involvement	Yes	8	5.4
Thyroid cartilage involvement	Inner cortex	30	20.1
	Full thickness	35	23.5
Cricoid cartilage involvement	Yes	36	24.2
Tracheal involvement	Yes	8	5.4
Cervical soft tissues involvement	Yes	50	33.6
Thyroid gland involvement	Yes	8	5.4
pT category	pT3	69	46.3
	Anterior pT3	19	12.7
	Posterior pT3	50	33.6
	pT4a	80	53.7
	Anterior pT4a	21	14.1
	Posterior pT4a	59	39.6
pN category	pN1	11	7.4
	pN2a	10	6.7
	pN2b	14	9.4
	pN2c	3	2
	pN3b	28	18.8
ENE	Yes	38	25.5
Surgical margins	Close	19	12.8
	Positive	11	7.4
Grading	G1	8	5.4
	G3	52	34.9
PNI	Yes	80	53.7
LVI	Yes	74	49.7
Treatments	S+PORT	72	48.3
	S+POCRT	17	11.4

Legend: ENE, extranodal extension; PNI, perineural invasion; LVI, lympho-vascular invasion; S, surgery; PORT, postoperative radiotherapy; POCRT, postoperative chemoradiotherapy.

### 3.3. Survival Estimates

Median OS was 82 months, with a mean follow-up time of 36 months (range, 6–180). At the last follow-up (November 2019), 45 (30.2%) patients had died: 28 (18.8%) for disease progression, and 17 (11.4%) for other causes. The remaining 104 (69.8%) were alive with no evidence of disease. A total of 47 recurrences were recorded, 26 of which were diagnosed at distant sites and 21 loco-regional. Seven patients experienced both loco-regional and distant recurrences. In total, 10 of the recurrences were treated surgically with curative intent, while 7 were managed by palliative RT, 15 with palliative CHT, and 15 by best supportive care.

The 2- and 5-year OS rates for the entire cohort were 77% and 63%, respectively, while 2- and 5-year DSS rates were 84% and 75%. Further details of 2- and 5-year survival estimates are summarized in Table S1.

### 3.4. Univariable Survival Analysis

End-points considered for uni- and multivariable survival analyses with Cox-proportional hazards models were OS, DSS, LRRFS, and DRFS. For all outcomes analyzed, pT category (pT4a vs. pT3), pN category, histopathologic evidence of ENE, number of positive nodes, and involvement of the retro-cricoid area were significant predictors at univariable analysis, as reported in Table 2; Table 3. Regarding OS and DSS, the full-thickness involvement of thyroid cartilage ( $p = 0.008$  and  $p = 0.006$ , respectively), presence of extra-laryngeal extension ( $p = 0.018$  and  $p = 0.16$ , respectively), and need for adjuvant therapy ( $p < 0.05$  for both) were also adverse prognostic features at univariable analysis (Table 2).

Conversely, tracheal ( $p = 0.001$ ) and retro-cricoid area involvement ( $p = 0.040$ ) were associated with worse LRRFS, while close margins ( $p = 0.006$ ), need for adjuvant CRT ( $p = 0.011$ ), tracheal involvement ( $p = 0.036$ ), and LVI ( $p = 0.032$ ) were associated with worse DRFS at univariable analysis (Table 3). Of note, the anterior vs. posterior laryngeal compartmentalization was not associated with different oncologic outcomes (Tables S2 and S3). Further details of univariable survival analysis are reported in Tables S1 and S3 and Figure S1.

**Table 2.** Univariable overall (OS) and disease specific survival (DSS) analysis (significant variables for at least one outcome are reported, while additional variables analyzed are reported in Table S2).

Variables	Category	OS			DSS		
		HR	CI95	<i>p</i>	HR	95% CI	<i>p</i>
T-topography	Posterior	1.51	(0.75–3.06)	0.252	1.28	(0.54–3.04)	0.571
pT category	pT4a	4.26	(2.03–8.96)	<b>&lt;0.001 *</b>	5.98	(2.05–17.43)	<b>0.001 *</b>
pN category	pN1	1.64	(0.47–5.77)	0.440	2.90	(0.56–14.95)	0.204
	pN2a	3.71	(1.40–9.79)	<b>0.008 *</b>	8.88	(2.70–29.15)	<b>&lt;0.001 *</b>
	pN2b	3.45	(1.30–9.14)	<b>0.013 *</b>	7.36	(2.12–25.54)	<b>0.002 *</b>
	pN2c	2.30	(0.30–17.66)	0.424	5.68	(0.66–48.79)	0.113
	pN3b	4.72	(2.22–10.03)	<b>&lt;0.001 *</b>	6.14	(1.99–18.93)	<b>0.002 *</b>
ENE	Yes	3.23	(1.77–5.90)	<b>&lt;0.001 *</b>	3.57	(1.67–7.63)	<b>0.001 *</b>
No. of positive nodes		1.16	(1.07–1.27)	<b>0.001 *</b>	1.17	(1.05–1.30)	<b>0.004 *</b>
Thyroid cartilage	Inner Cortex	1.09	(0.48–2.48)	0.845	1.27	(0.43–3.72)	0.661
	Full thickness	2.44	(1.27–4.71)	<b>0.008 *</b>	3.26	(1.41–7.57)	<b>0.006 *</b>
Soft tissues involvement	Yes	2.05	(1.13–3.73)	<b>0.018 *</b>	2.56	(1.19–5.50)	<b>0.016 *</b>
Retro-cricoid areainvolvement	Yes	2.88	(1.01–8.17)	<b>0.047 *</b>	4.80	(1.62–14.17)	<b>0.005 *</b>
Treatment	S+PORT	2.06	(1.01–4.19)	<b>0.047 *</b>	2.82	(1.03–7.67)	<b>0.043 *</b>
	S+POCRT	3.26	(1.25–8.56)	<b>0.016 *</b>	4.74	(1.35–16.60)	<b>0.015 *</b>

**Legend:** OS, overall survival; DSS, disease-specific survival; HR, hazard ratio; CI95, 95% confidence interval; ENE, extranodal extension; S, surgery; PORT, postoperative radiotherapy; POCRT, postoperative chemoradiotherapy; \*Bold-italic, statistically significant results.



## Chapter 10. Laryngeal Compartmentalization Does Not Affect the Prognosis of LSCC Treated by Total Laryngectomy

Cancers 2020, 12, 2241

8 of 18

**Table 3.** Univariable loco-regional recurrence-free survival (LRRFS) and distant recurrence-free survival (DRFS) analysis (significant variables for at least one outcome are reported, while additional variables analyzed are reported in Table S3).

Variables	Category	LRRFS			DRFS		
		HR	95% CI	<i>p</i>	HR	95% CI	<i>p</i>
T-topography	Posterior	1.23	(0.45–3.39)	0.689	1.83	(0.68–4.88)	0.230
pT category	pT4a	5.47	(1.60–18.69)	<b>0.007 *</b>	3.49	(1.39–8.76)	<b>0.008 *</b>
pN category	pN1	3.99	(0.73–21.79)	0.110	1.07	(0.13–8.71)	0.949
	pN2a	6.47	(1.45–28.93)	<b>0.015 *</b>	6.64	(2.10–20.99)	<b>0.001 *</b>
	pN2b	5.03	(1.12–22.52)	<b>0.035 *</b>	2.30	(0.47–11.13)	0.301
	pN2c	7.10	(0.79–63.67)	0.080	-	-	-
	pN3b	6.13	(1.79–20.97)	<b>0.004 *</b>	5.99	(2.26–15.88)	<b>&lt;0.001 *</b>
ENE	Yes	3.26	(1.36–7.85)	<b>0.008 *</b>	5.61	(2.51–12.52)	<b>&lt;0.001 *</b>
No. of positive nodes		1.20	(1.07–1.36)	<b>0.002 *</b>	1.26	(1.13–1.41)	<b>&lt;0.001 *</b>
Surgical margins	Close	1.77	(0.58–5.38)	0.314	3.58	(1.44–8.91)	<b>0.006 *</b>
	Positive	1.76	(0.40–7.75)	0.457	3.05	(0.88–10.65)	0.080
LVI	Yes	1.55	(0.63–3.79)	0.340	2.52	(1.09–5.86)	<b>0.032 *</b>
Treatment	S+PORT	2.13	(0.76–5.91)	0.148	2.63	(0.95–7.28)	0.063
	S+POCRT	0.75	(0.09–6.42)	0.792	5.04	(1.45–17.55)	<b>0.011 *</b>
Tracheal involvement	Yes	6.65	(2.18–20.27)	<b>0.001 *</b>	3.70	(1.09–12.51)	<b>0.036 *</b>
Retro-cricoid area involvement	Yes	3.64	(1.06–12.47)	<b>0.040 *</b>	8.39	(2.96–23.81)	<b>&lt;0.001 *</b>

**Legend:** LRRFS, loco-regional recurrence-free survival; DRFS, distant recurrence-free survival; HR, hazard ratio; 95% CI, 95% confidence interval; ENE, extranodal extension; LVI, lympho-vascular invasion; S, surgery; PORT, postoperative radiotherapy; POCRT, postoperative chemoradiotherapy; \*Bold-italic, statistically significant results.

3.5. Multivariable Survival Analysis

By a stepwise covariate selection, keeping T-topography as an investigative variable inside all multivariable models, a Cox proportional hazards model for each oncologic outcome was built.

Both multivariable OS (Figure 1) and DSS models (Figure 2) included pT and pN categories as significant and independent covariates, confirming their value as prognostic factors in the setting of TL for advanced LC. Interestingly, histopathologic evidence of ENE (HR 4.93,  $p < 0.001$ ) and involvement of the retro-cricoid area (HR 5.42,  $p = 0.005$ ) were strongly significant and independent worse prognostic factors for DRFS (Figure 3).

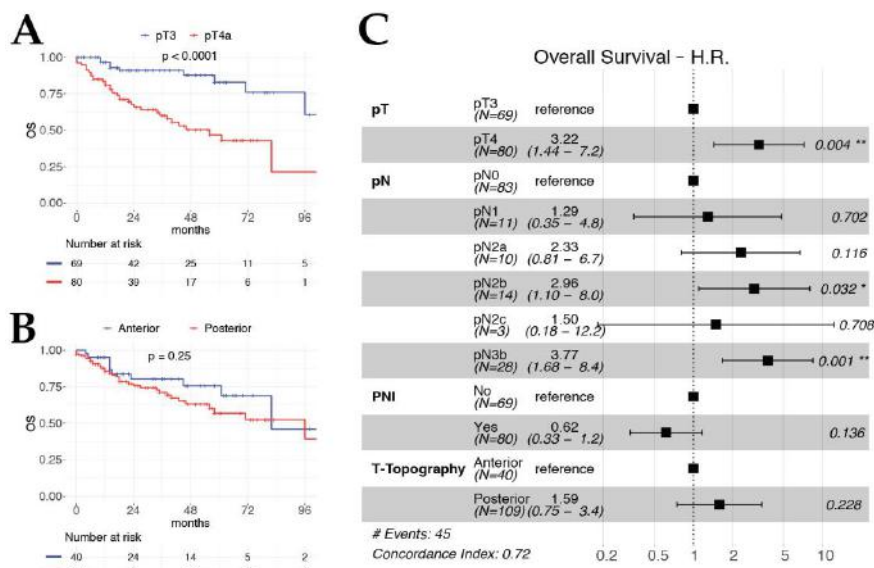


Figure 1. Kaplan–Meier curves for OS according to pT category (A) and T-topography (B). (C) Forest plot of OS multivariable model.

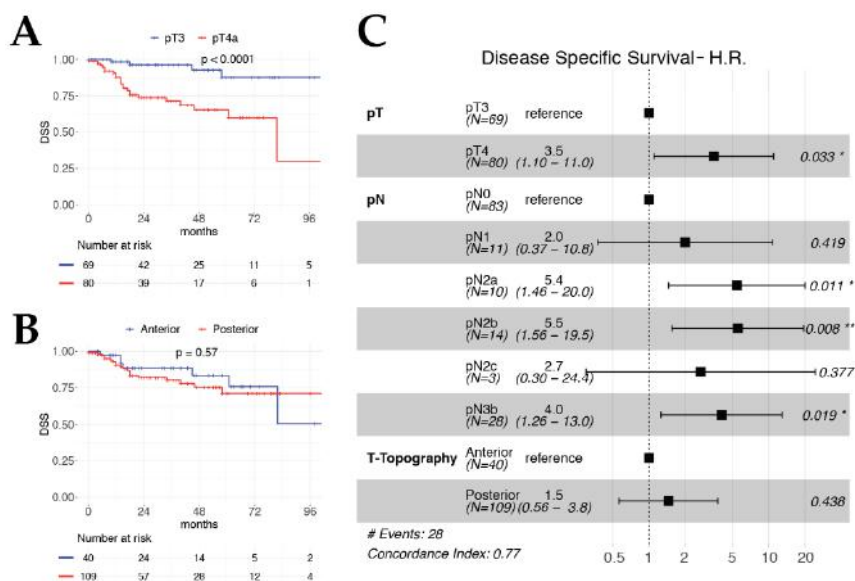
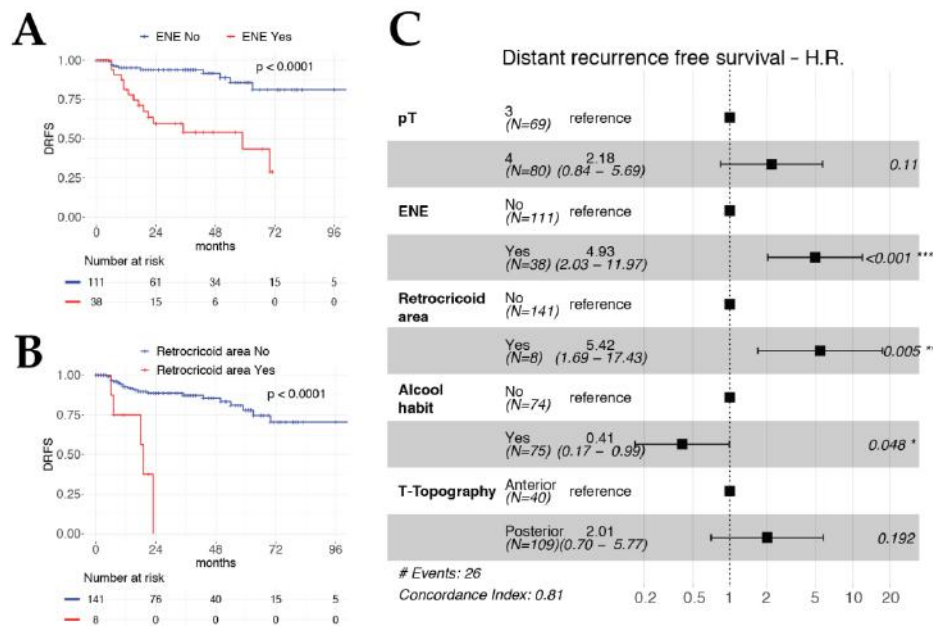
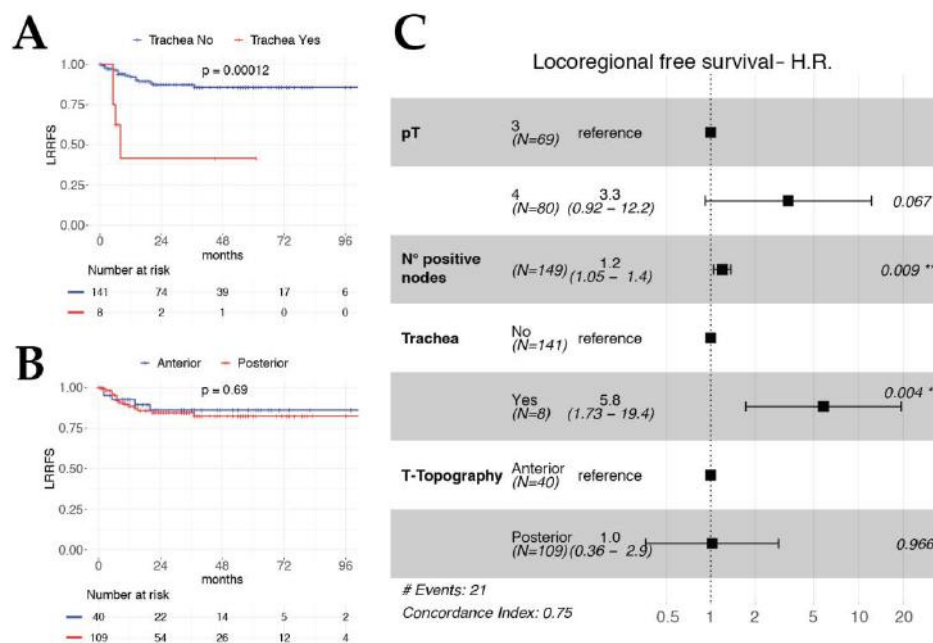


Figure 2. Kaplan–Meier curves for DSS according to pT category (A) and T-topography (B). Forest plot of DSS multivariable model (C).



**Figure 3.** Kaplan–Meier curves for DRFS according to ENE status (A) and retro-cricoid area involvement (B). Forest plot of DRFS multivariable model (C).

Considering the LRRFS multivariable model, the absolute number of positive lymph nodes, an emerging feature in the head and neck oncology field, was found to be an independent significant predictor (HR 1.2,  $p = 0.009$ ). The same held true for tracheal rings involvement (HR 5.8,  $p = 0.004$ ) (Figure 4). No significant interactions nor multicollinearity was observed in any model.



**Figure 4.** Kaplan–Meier curves for LRRFS according to the tracheal involvement (A) and T-topography (B). Forest plot of LRRFS multivariable model (C).

3.6. Search for the Best Cut-Off for Total Number of Positive Lymph Nodes for LRRFS Prognostic Factor

The prognostic clinical relevance of the number of positive lymph nodes for LRRFS was consistent and stable considering it alone in a univariable model (Figure 5A), and after adjusting its effect (estimated by the HR) with the covariates included in the LRRFS multivariable model (Figure 5B). Identification of the total number of positive lymph nodes as one of the main prognostic features associated with loco-regional failure raised the question of if an optimal cut-off for this variable could be identified to better predict the ensuing outcomes in a dichotomic fashion. Applying the maximally selected log-rank statistics, a robust method that takes into account the multiplicity of tests, the best cut-off was zero positive nodes ( $p = 0.001$ , Figure 5C), splitting up pN0 vs. pN+ patients and confirming the relevance of this biologic and easy to measure feature (Figure 5D).

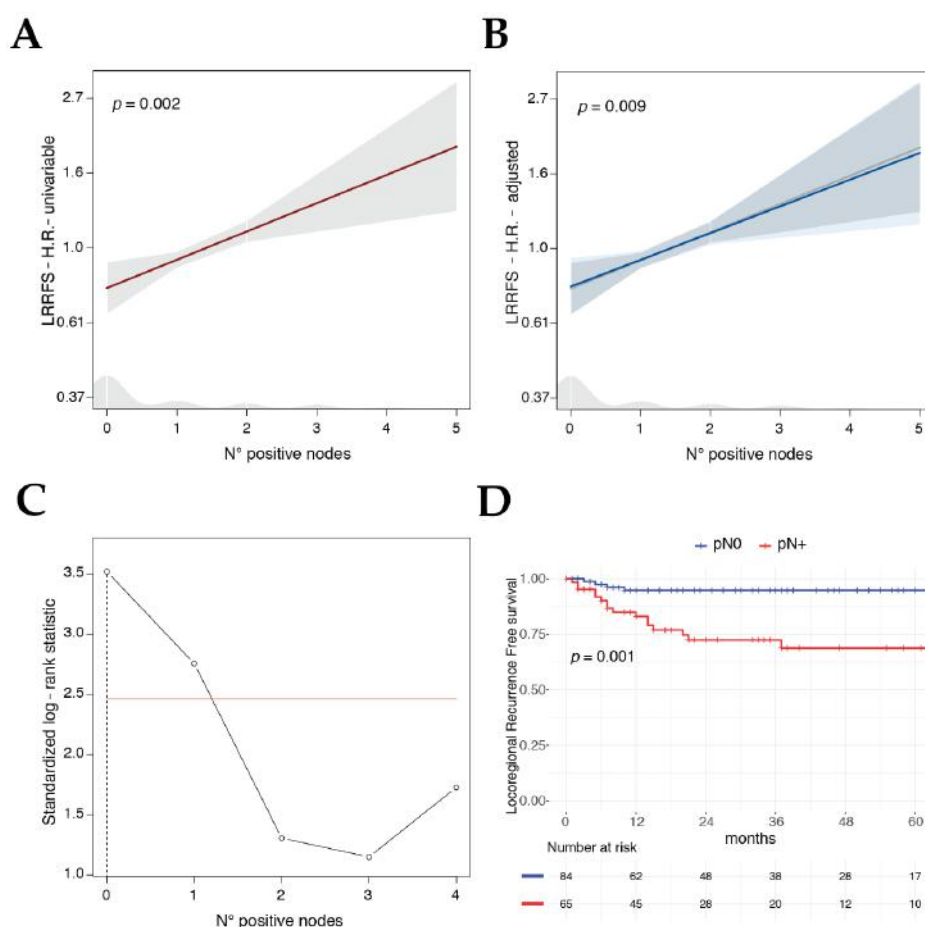


**Figure 5.** Plots showing the HR estimates and 95%CI (shadow area) of the number of histopathologic positive nodes derived from the univariable LRRFS Cox model (A) and from the multivariable one (B), adjusting the effect for pT category, tracheal involvement, and T-topography (gray line on the background refers to the univariable estimate). Plot of the standardized log-rank statistic, identifying 0 positive nodes as best cut-off for number of positive nodes for the prediction of LRRFS (C), red line indicating the adjusted significance level, vertical dotted line showing the best cut-off point. Kaplan–Meier curve of N status (N0 vs. N+) for LRRFS, p value adjusted for multiple tests showed (D).

3.7. Clinical Significance of Histopathologic Tumor Thickness

As the presence of metastatic lymph nodes was one of the main factors associated with loco-regional failure, histopathologic TT, available for 102 (68%) patients of the cohort, was investigated by logistic

regression models for the prediction of the binary outcome pN0 vs. pN+. The univariable logistic model including just TT showed a significant association of this covariate with the presence of metastatic lymph nodes (OR 3.94,  $p = 0.001$ ; Figure 6A,B). All available potential predictors, the covariates included in the survival analysis, were investigated in a multivariable logistic regression; the best model was built by a stepwise variable selection, keeping the TT inside the model as investigative variable (Figure 6A). Tumor category T4a (OR 8.44,  $p = 0.002$ ), poor differentiation (OR 4.51,  $p = 0.011$ ), presence of LVI (OR 6.15,  $p = 0.001$ ), and involvement of the medial wall of the piriform sinus (OR 3.63,  $p = 0.041$ ) were significantly and independently associated with the presence of lymph node metastases (Figure 6A,C,D), whereas TT in the multivariable model lost its association with the binary outcome N0 vs. N+ ( $p = 0.316$ ) (Figure 6A,C).

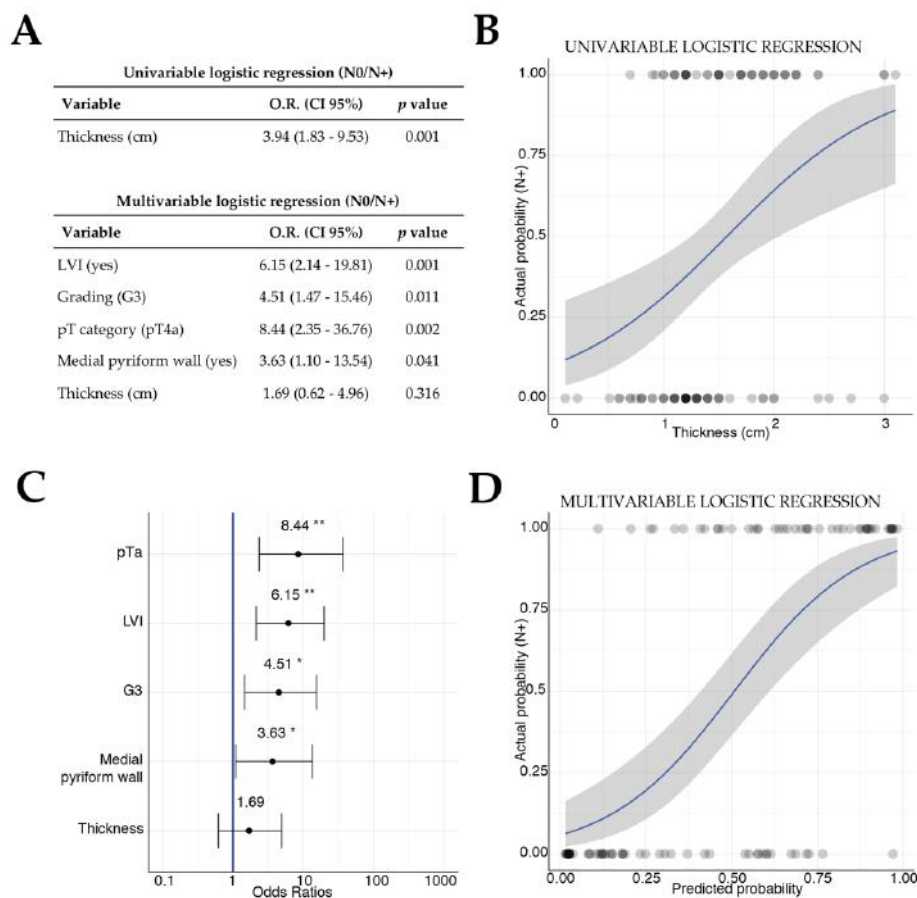


**Figure 6.** (A) Univariable logistic model including tumor thickness for the prediction of the N0 vs. N+ status and the multivariable one by stepwise variables selection. (B) Logistic function of the univariable logistic model including tumor thickness as covariate. (C) Forest plot of odds ratios and 95% CI of the multivariable logistic model for N status prediction. (D) Logistic function of the predicted probability in the multivariable logistic model against the actual probability of being N0 vs. N+. For logistic functions, 95% CI is showed with gray filling.

#### 4. Discussion

The potential for long-term survival in patients with advanced LC is nowadays significant and, consequently, the choice of the most adequate treatment option is of paramount value for optimizing cancer control, functional outcomes, and residual quality of life. Contemporary advances in endoscopic and radiologic diagnostic tools have allowed the scientific community to clearly understand that

laryngeal CRT protocols should be reserved to highly selected patients with low-volume cancers, preserved airway patency and proper swallowing function, without the need for pre-treatment tracheostomy or feeding tube, limited cartilage destruction, and who can tolerate the toxicity of CHT associated with RT [4]. Following these recommendations, the population that ideally should undergo CRT protocols would result in a small fraction of T3-T4 LC patients. On the other hand, even OPHLs should be preferably reserved for patients <70 years of age who are neurologically intact and able to complete successful postoperative swallowing rehabilitation (a forecast so far left to the good, but largely fallible, clinical judgement of physicians), with good cardio-pulmonary function, and tumors not extending too far posteriorly and/or massively involving and ankylosing one crico-arytenoid unit [18]. Considering all these caveats and selection criteria, it is clear that TL still maintains a fundamental role in management of advanced LC. In this respect, the updated guidelines of ASCO rightly recommended TL for patients with large-volume T4 and/or poor pre-treatment laryngeal functions, since such a mutilating surgical procedure has nonetheless shown to be associated with better survival and, surprisingly, even superior quality of life compared to CRT or RT alone [4]. Facing this highly heterogeneous population of advanced LCs, and the even more differentiated gamma of therapeutic options available, each with its pros and cons, the relative paucity of information about which subgroup of patients might preferably benefit from primary OP protocols vs. upfront TL is definitively worrisome [19].

As a contribution to this topic, two recent studies have been published claiming that T-topography (distinguished in anterior vs. posterior involvement of the PGS) could represent a significant prognosticator in patients to be treated by OPHLs for T3-T4 LCs [11,12]. By contrast, in the present retrospective study focused on patients treated by upfront TL, we did not find a similar significant difference in survival outcomes comparing tumors with anterior vs. posterior laryngeal compartmentalization. The 5-year OS and DSS for anterior vs. posterior tumors, in fact, did not significantly differ at either univariable ( $p = 0.252$  and  $p = 0.571$ , respectively) or multivariable analysis ( $p = 0.228$  and  $p = 0.438$ , respectively). This should not represent a major source of disappointment if one considers that TL is able to radically remove the entirety of either an anterior or posterior advanced LC, possibly flattening the discrepancies in biological behavior and pathways of spread observed for more conservative surgical options such as TLM and OPHLs. Therefore, the concept of anterior vs. posterior laryngeal compartmentalization, while useful in deciding which lesions can be successfully managed by OP approaches, loses its appeal when considering survival after TL. On the other hand, pT category as currently defined by the 8th Edition of the TNM staging system maintains its role as a significant prognosticator for both 5-year OS and DSS estimates, as confirmed at multivariable analysis ( $p = 0.004$  and  $p = 0.033$ , respectively), with values of 83% and 88% for pT3, and 47% and 65% for pT4a, respectively (Table S1).

Apart from the T issue, it is well established that, in advanced LCs, even N category plays a crucial role in treatment selection. In line with this, our data clearly show the survival impact of different nodal diseases (at OS and DSS univariable analysis, HR ranged respectively from 1.64 and 2.90 for pN1 to 4.72 and 6.14 for pN3 compared to the pN0 category). Moreover, as confirmation of the recent emphasis given to the ENE by the 8th Edition of the TNM staging system, its role as a negative prognosticator was confirmed at OS and DSS univariable analysis, with an HR of 3.23 and 3.57 compared to lymph nodes without ENE. Therefore, considering the last edition of the TNM staging system, it seems to efficiently stratify survival according to neck status, as also confirmed by a large study from the MD Anderson Cancer Center where node positive disease at presentation was associated with increased overall mortality ( $p < 0.0001$ ) [20]. It is clear that patients with higher nodal category perform poorly regardless of treatment modality, and this poses a challenging problem particularly for advanced LC. In this scenario, while CRT is associated with worse OS compared to TL in some patients with T4 disease, no difference is seen among patients with T3 LC with minimal cartilage erosion, regardless of N status [21]. Dissecting these specific patients accurately, Choi et al. underlined that the survival improvement offered by primary surgery in T4 disease was significant only in N0-N1 patients, and not



in those with higher neck categories [22]. In this cohort of patients, in fact, the survival benefit of TL was lost, whereas the performance of CRT remained stable between the T4N0-1 and T4N2-3 scenarios. This topic was further addressed by Patel et al. in a recent national database analysis, underlining that there are no differences in survival between surgical (TL and OPHL) and non-surgical approaches (CRT) for non-T4 lesions with low nodal burden, while non-T4 tumors with high nodal burden benefit more from CRT. Nevertheless, it was pointed out that TL remains advantageous in patients with T4 LC [19]. According to these findings, adequate local control is more critical in patients with limited nodal involvement, as they have a relatively lower risk of distant metastasis, while patients with higher N categories are more exposed to distant failure. In this setting, patients with advanced nodal involvement might benefit more, starting at the beginning, from systemic therapeutic regimens that aim to control distant metastases [22].

In this regard, our investigation introduces another valuable piece of information: analyzing LRRFS, in fact, the impact of the number of tumor deposits in neck nodes was a detrimental prognostic factor at univariable analysis with an HR of 1.2 ( $p = 0.002$ ), meaning an increase in risk of 20% for each positive node detected. This result was also confirmed at multivariable analysis, as both the number of positive nodes (HR 1.2,  $p = 0.009$ ) and tracheal involvement (HR 5.8,  $p = 0.004$ ) were significant covariates associated with loco-regional failure, independently of the T category. In this respect, Choi et al. proposed a new classification system for laryngeal and hypopharyngeal tumors treated with surgery, including the number of positive nodes and showing better performance for OS and DSS prediction compared to both the 7th and 8th Editions of the TNM staging system [23]. Of note, the relationship between the number of positive nodes and LRRFS highlighted in our study, has not been previously reported. Nonetheless, these findings are in accordance with those reported in the literature for other head and neck tumors [24], even though this topic was mainly investigated in the context of oral cavity squamous cell carcinoma [25–27].

One of the novel findings of our study is the preliminary investigation of the effects of TT in LC. To the best of our knowledge, the literature has rarely addressed this aspect, and most of the attempts to date present several drawbacks. Hirano, almost 30 years ago, tried to investigate the depth of vocal muscle invasion to better understand the pathophysiological mechanism of vocal fold hypomobility, although he did not relate it with LC prognosis [28]. A recent study partly addressed this issue, demonstrating worse outcomes resulting from the histopathological finding of deep infiltration into vocal muscle in early LC, though not correlating the ensuing prognosis with a continuous linear measurement [29]. On the other hand, Yilmaz et al. analyzed the role of deep neoplastic invasion in 74 laryngeal specimens, finding a direct correlation between this parameter and survival: in their work, the authors evaluated the correlation between depth of invasion (DOI) and nodal disease, showing that the mean DOI for N0, N1, N2, and N3 categories were 6.33, 8.72, 9.54, and 5.53 mm, respectively [30]. In addition, Kiliç et al. analyzed 85 patients treated by partial laryngectomies, aiming to correlate the occurrence of nodal metastasis with DOI [31]. In their study it was reported the presence of positive nodes starting from a DOI of 4 mm and this correlation proved to be significant only from a DOI of 20 mm by applying the Chi-square test. Ye et al. retrospectively analyzed a cohort of 127 patients affected by hypopharyngeal (93 patients) and supraglottic LC (34 patients), finding that DOI correlated with the probability of nodal metastasis both at univariable and multivariable analysis and proposing 4.5 mm as cut-off value for elective neck dissection; anyway glottic LC was not addressed in their study [32].

When investigating DOI in LC, the anatomical complexity of the larynx, which has a peculiar microanatomical structure that varies consistently, should be considered [33]. Advanced tumors can easily subvert the already compacted microstructures inside the laryngeal box: these pathological changes together with the complex microanatomy of this organ may complicate the evaluation of DOI in LC, as no study so far reported a standardized method to measure laryngeal DOI. Our investigation consequently addressed the TT, easily available retrospectively from pathological reports, to study its correlation with the risk of nodal disease. Interestingly, even if univariate analysis showed an

association between TT and the presence of nodal metastasis, the multivariable logistic model revealed that other pathologic features such as T category, grading, LVI, and involvement of the medial wall of piriform sinus were significant and independent predictors for the presence of nodal metastases, overcoming the relevance of TT (Figure 6). This result might not seem of great interest in primary T4a LC, since most patients receive simultaneous elective neck dissection anyway. However, if this topic would be further investigated taking into account a standardized DOI (as extensively demonstrated for oral cavity squamous cell carcinoma), the implications could be of paramount importance even for LC. In those patients where, according to the NCCN guidelines, indications for neck dissection are not clear or debatable [15], as in selected T3 glottic cancers treated by TLM, T1-small T2 supraglottic cancers treated by transoral approaches, and recurrent/persistent LC failed after CRT and previously staged as cN0 [34], this information might be of great help in choosing to electively treat in one-stage or not both the T and N sites. In fact, as previously demonstrated, very few T3 glottic cancers fail regionally [13,35], while the role of neck dissection after CRT failure in cN0 neck is still controversial, some authors supporting an aggressive policy [36] and others maintaining a more cautious attitude [37].

Lastly, we analyzed the impact of LC extension to different subsites and found that involvement of the retro-cricoid area is a strong predictor for distant failure, especially at multivariable analysis (HR 5.42,  $p = 0.005$ ). The best way to look at this finding is probably to compare it with what has been described for primary retro-cricoid hypopharyngeal carcinoma, frequently presenting with positive nodal disease and usually reported to have a poor prognosis with a 5-year OS ranging from 20% to 52% [38,39]. This type of localization, together with the piriform sinus, as pointed out in a large retrospective series [40], is prone to distant metastasis with a 17.2% rate. LC involving the post-cricoid area probably acquire a behavior similar to that of hypopharyngeal cancers, characterized by richer lymphatic drainage and a higher rate of nodal metastasis. As demonstrated by the authors, the incidence of distant disease is also directly related to positive lymph nodes, increasing the risk 3-fold [40]. Finally, at multivariable analysis, LC tracheal extension was shown to heavily affect LRRFS (HR 5.8,  $p = 0.004$ ). In fact, achieving negative margins at this level is more challenging if the surgeon wants to preserve enough tracheal rings to tailor a good stoma and place the tracheo-esophageal speech prosthesis without risking locating it into the thoracic esophagus. Moreover, lymphatic drainage of the subglottis and trachea is prominent and may explain the rapid tumor spread observed when these locations are involved [41].

The retrospective nature of this study represents its main limit. More specifically, the addition of PORT and chemotherapy was discussed for every specific case at the MDT and cannot be fully standardized as it would be in a prospective randomized study. However, in pN1 LSCC, based on our results and some emerging evidence, even if it is not strictly indicated by the NCCN Guideline, the use of PORT might be considered. To the best of our knowledge, despite no survival differences were seen in T3 N0 or T3 N+ comparing TL+ PORT and CRT, the role of PORT is controversial in the subgroup of surgically treated T3N1, even retrieving the data from the largest and most comprehensive population-based studies [21,42]. We hope that further study will clarify if this very specific subset of patients might benefit or not of adjuvant treatment, or even curative RT/CRT. In such setting, more interesting pathological factors could be studied as the lymph-node size, the micro vs. macro ENE and the laryngeal DOI, to advocate the need for adjuvant treatment.

## 5. Conclusions

The data presented in this retrospective analysis support the hypothesis that laryngeal compartmentalization has no impact on survival in patients treated by upfront TL, but, most likely, it is a useful tool to identify ideal and unfavorable candidates for OP strategies. On the other hand, our findings demonstrate that the 8th Edition of the AJCC UICC TNM staging system is a robust prognosticator for advanced LC in terms of both T and N categories. Combining this information with previous reports, we might be able to better refine the decision-making process between CRT and upfront TL for advanced LC.

The retrospective nature of our study has inherent limitations that should be ideally overcome by a large scale, prospective study of surgically treated LC, in order to thoroughly investigate the value of TT and DOI for all disease categories, trying to find a correlation of histopathologic data with those obtainable in the pre-treatment setting by radiologic imaging. Lastly, a valuable topic to be investigated further is the impact of T-topography and laryngeal compartmentalization in patients to be managed by CRT as an alternative to OP surgery and TL.

**Supplementary Materials:** The following are available online at <http://www.mdpi.com/2072-6694/12/8/2241/s1>. Table S1: Survival estimates at 2 years (2-y) and 5 years (5-y) for main clinical interest covariates. Table S2: Univariable OS and DSS analysis, additional variables. Table S3: Univariable LRRFS and DRFS analysis, additional variables. Figure S1: Kaplan–Meier curves of univariable overall survival (OS) and disease-specific survival (DSS) considering radiologic posterior PGS involvement and arytenoid motility.

**Author Contributions:** Conceptualization, F.M. (Filippo Marchi), C.P., G.P. (Giorgio Peretti); data curation, F.M. (Francesco Missale), C.S., M.F., A.I., G.P. (Giampiero Parrinello), F.I., F.D.B.; formal analysis, F.M. (Francesco Missale); investigation, F.M. (Francesco Missale), C.S., M.F., A.I., G.P. (Giampiero Parrinello), F.I., F.D.B.; methodology, F.M. (Filippo Marchi), F.M. (Francesco Missale); supervision, C.P. and G.P. (Giorgio Peretti); writing—original draft, F.M. (Filippo Marchi), F.M. (Francesco Missale), C.S.; writing—review and editing, L.E.S., M.W.M.v.d.B., P.N., C.P., G.P. (Giorgio Peretti). All the authors have made a significant contribution to this manuscript, have seen and approved the final manuscript, and have agreed to its submission to Cancers. All authors have read and agreed to the published version of the manuscript.

**Funding:** This research received no external funding.

**Conflicts of Interest:** The authors declare no conflict of interest.

### References

1. Surveillance, Epidemiology, and End Results (SEER) Program. Available online: <https://seer.cancer.gov> (accessed on 15 March 2020).
2. Hoffman, H.T.; Porter, K.; Karnell, L.H.; Cooper, J.S.; Weber, R.S.; Langer, C.J.; Ang, K.; Gay, G.; Stewart, A.; Robinson, R.A. Laryngeal Cancer in the United States: Changes in Demographics, Patterns of Care, and Survival. *Laryngoscope* **2006**, *116*, 1–13. [[CrossRef](#)] [[PubMed](#)]
3. Chen, A.Y.; Halpern, M. Factors Predictive of Survival in Advanced Laryngeal Cancer. *Arch. Otolaryngol. Head Neck Surg.* **2007**, *133*, 1270–1276. [[CrossRef](#)] [[PubMed](#)]
4. Forastiere, A.; Lewin, J.S.; Nathan, C.A.; Adelstein, D.J.; Eisbruch, A.; Fass, G.; Fisher, S.G.; Laurie, S.A.; Le, Q.; Malley, B.O.; et al. Use of Larynx-Preservation Strategies in the Treatment of Laryngeal Cancer: American Society of Clinical Oncology Clinical Practice Guideline Update. *J. Clin. Oncol.* **2018**, *36*, 1143–1169. [[CrossRef](#)]
5. Department of Veterans Affairs Laryngeal Cancer Study Group. Induction chemotherapy plus radiation compared with surgery plus radiation in patients with advanced laryngeal cancer. *N. Engl. J. Med.* **1991**, *324*, 1685–1690. [[CrossRef](#)]
6. Forastiere, A.A.; Goepfert, H.; Maor, M.; Pajak, T.F.; Weber, R.; Morrison, W.H.; Glisson, B.; Trotti, A.; Ridge, J.A.; Chao, C.; et al. Concurrent Chemotherapy and Radiotherapy for Organ Preservation in Advanced Laryngeal Cancer. *N. Engl. J. Med.* **2003**, *349*, 2091–2098. [[CrossRef](#)]
7. Caancer, A.J.C. *AJCC Cancer Staging Manual*, 8th ed.; Springer: Berlin/Heidelberg, Germany, 2017; ISBN 9783319406176.
8. Piazza, C.; Cocco, D.; Del Bon, F.; Mangili, S.; Nicolai, P.; Peretti, G. Narrow band imaging and high definition television in the endoscopic evaluation of upper aero-digestive tract cancer. *Acta Otorhinolaryngol. Ital.* **2011**, *31*, 70–75.
9. Maroldi, R.; Ravanelli, M.; Farina, D. Magnetic resonance for laryngeal cancer. *Curr. Opin. Otolaryngol. Head Neck Surg.* **2014**, *22*, 131–139. [[CrossRef](#)]
10. Ravanelli, M.; Paderno, A.; Del Bon, F.; Montalto, N.; Pessina, C.; Battocchio, S.; Farina, D.; Nicolai, P.; Maroldi, R.; Piazza, C. Prediction of Posterior Paraglottic Space and Cricopharyngeal Unit Involvement in Endoscopically T3 Glottic Cancer with Arytenoid Fixation by Magnetic Resonance with Surface Coils. *Cancers* **2019**, *11*, 67. [[CrossRef](#)]

11. Succo, G.; Crosetti, E.; Bertolin, A.; Piazza, C.; Molteni, G.; Cirillo, S.; Petracchini, M.; Tascone, M.; Sprio, A.E.; Berta, G.N.; et al. Treatment for T3 to T4a laryngeal cancer by open partial horizontal laryngectomies: Prognostic impact of different pathologic tumor subcategories. *Head Neck* **2018**, *40*, 1897–1908. [[CrossRef](#)] [[PubMed](#)]
12. Del Bon, F.; Piazza, C.; Lancini, D.; Paderno, A.; Bosio, P.; Taboni, S.; Morello, R.; Montalto, N.; Missale, F.; Incandela, F.; et al. Open Partial Horizontal Laryngectomies for T3–T4 Laryngeal Cancer: Prognostic Impact of Anterior vs. Posterior Laryngeal Compartmentalization. *Cancers* **2019**, *11*, 289. [[CrossRef](#)] [[PubMed](#)]
13. Marchi, F.; Filauro, M.; Missale, F.; Parrinello, G. A Multidisciplinary Team Guided Approach to the Management of cT3 Laryngeal Cancer: Retrospective Analysis of 104 Cases. *Cancers* **2019**, *11*, 717. [[CrossRef](#)] [[PubMed](#)]
14. Becker, M.; Casselman, J.W.; Kohler, R.; Dulguerov, P.; Becker, C.D. Neoplastic Invasion of Laryngeal Cartilage: Reassessment of Criteria for Diagnosis at MR Imaging 1 Methods; Results; Conclusion. *Radiology* **2008**, *249*, 551–559. [[CrossRef](#)] [[PubMed](#)]
15. Colevas, A.D.; Yom, S.S.; Pfister, D.G.; Spencer, S.; Adelstein, D.; Adkins, D.; Brizel, D.M.; Burtness, B.; Busse, P.M.; Caudell, J.J.; et al. NCCN Guidelines @Insights Head and Neck Cancers Featured Updates to the NCCN Guidelines. *J. Natl. Compr. Cancer Netw.* **2018**, *16*, 479–490. [[CrossRef](#)] [[PubMed](#)]
16. Simo, R.; Bradley, P.; Chevalier, D.; Dikkers, F.; Eckel, H.; Matar, N.; Peretti, G.; Piazza, C.; Remacle, M.; Quer, M. European Laryngological Society: ELS recommendations for the follow-up of patients treated for laryngeal cancer. *Eur. Arch. Otorhinolaryngol.* **2014**, *271*, 2469–2479. [[CrossRef](#)] [[PubMed](#)]
17. Hothorn, T.; Lausen, B. On the Exact Distribution of Maximally Selected Rank Statistics. *Comput. Stat. Data Anal.* **2003**, *43*, 121–137. [[CrossRef](#)]
18. Succo, G.; Crosetti, E. Limitations and Opportunities in Open Laryngeal Organ Preservation Surgery: Current Role of OPHLs. *Front. Oncol.* **2019**, *9*, 1–8. [[CrossRef](#)]
19. Patel, S.A.; Qureshi, M.M.; Dyer, M.A.; Jalisi, S.; Grillone, G.; Truong, M.T. Comparing Surgical and Nonsurgical Larynx-Preserving Treatments With Total Laryngectomy for Locally Advanced Laryngeal Cancer. *Cancer* **2019**, *125*, 3367–3377. [[CrossRef](#)]
20. Fuller, C.; Mohamed, A.S.R.; Garden, A.S.G.; Gunn, B.; Mulcahy, C.F.; Zafereo, M.; Phan, J.; Lai, S.Y.; Lewin, J.S.; Hutcheson, K.A.; et al. Long-Term Outcomes Following Multi-Disciplinary Management of T3 Larynx Squamous Cell Carcinomas: Modern Therapeutic Approaches Improve Functional Outcomes and Survival. *Head Neck* **2016**, *38*, 1739–1751. [[CrossRef](#)]
21. Bates, J.E.; Amdur, R.J.; Morris, C.M.; Hitchcock, K.E.; Dziegielewski, P.T.; Boyce, B.J.; Silver, N.L.; Shaw, C.; Mendenhall, W.M. Curative-dose Chemoradiotherapy Versus Total Laryngectomy For Stage T3-T4 Squamous Cell Carcinoma of the Larynx An “Apples-to-Apples”. *Anal. Natl. Cancer Database* **2019**, *42*, 527–533.
22. Choi, Y.S.; Park, S.G.; Song, E.; Cho, S.; Park, M.; Park, K.U.; Lee, K. Comparison of the therapeutic effects of total laryngectomy and a larynx-preservation approach in patients with T4a laryngeal cancer and thyroid cartilage invasion: A multicenter retrospective review. *Head Neck* **2016**, *38*, 1271–1277. [[CrossRef](#)]
23. Choi, Y.; Bin-Manie, M.; Roh, J.L.; Cho, K.J.; Lee, Y.S.; Choi, S.H.; Nam, S.Y.; Kim, S.Y. Metastatic lymph node burden predictive of survival in patients undergoing primary surgery for laryngeal and hypopharyngeal cancer. *J. Cancer Res. Clin. Oncol.* **2019**, *145*, 2565–2572. [[CrossRef](#)] [[PubMed](#)]
24. Roberts, T.J.; Colevas, A.D.; Hara, W.; Holsinger, F.C. Number of Positive Nodes Is Superior to the Lymph Node Ratio and American Joint Committee on Cancer N Staging for the Prognosis of Surgically Treated Head and Neck Squamous Cell Carcinomas. *Cancer* **2016**, *122*, 1388–1397. [[CrossRef](#)] [[PubMed](#)]
25. Subramaniam, N.; Balasubramanian, D.; Kumar, N.; Murthy, S.; Vijayan, S.N.; Nambiar, A.; Vidhyadharan, S.; Thankappan, K.; Iyer, S. Lymph node staging systems in oral squamous cell carcinoma: A comparative analysis. *Oral Oncol.* **2019**, *97*, 92–98. [[CrossRef](#)]
26. Lee, H.; Roh, J.L.; Cho, K.J.; Choi, S.H.; Nam, S.Y.; Kim, S.Y. Number of positive lymph nodes better predicts survival for oral cavity cancer. *J. Surg. Oncol.* **2019**, *119*, 675–682. [[CrossRef](#)] [[PubMed](#)]
27. Rajappa, S.K.; Maheshwari, U.; Jaipuria, J.; Singh, A.K.; Goyal, S.; Batra, U.; Kumar, R.; Dewan, A.K. Number of positive nodes—Current relevance in determining prognosis of oral cavity cancer after the recent AJCC staging update. *Oral Oncol.* **2019**, *90*, 1–5. [[CrossRef](#)] [[PubMed](#)]
28. Hirano, M.; Kurita, S.; Matsuoka, H.; Tateishi, M. Vocal fold fixation in laryngeal carcinomas. *Acta Otolaryngol.* **1991**, *111*, 449–454. [[CrossRef](#)]

29. Lionello, M.; Bertolin, A.; Nardello, E.; Giacomelli, L.; Fabio, B.D.; Giuseppe, C.; Lucioni, M.; Marioni, G. Could the infiltration of the thyroarytenoid muscle define the pT2 glottic carcinoma? *Head Neck* **2019**, *41*, 3639–3646. [[CrossRef](#)] [[PubMed](#)]
30. Yilmaz, T.; Hogal, A.S.; Gedikoglu, G.; Turan, E.; Ayas, K. Prognostic Significance of Depth of Invasion in Cancer of the Larynx. *Laryngoscope* **1998**, *108*, 764–768. [[CrossRef](#)]
31. Kiliç, C.; Tunçel, Ü.; Kaya, M.; Cömert, E.; Özlügedik, S. Long-Term Results of Partial Laryngectomized Patients. *J. Craniofac. Surg.* **2016**, *27*, 698–701. [[CrossRef](#)]
32. Ye, L.L.; Rao, J.; Fan, X.W.; Kong, F.F.; Hu, C.S.; Ying, H.M. The prognostic value of tumor depth for cervical lymph node metastasis in hypopharyngeal and supraglottic carcinomas. *Head Neck* **2019**, *41*, 2116–2122. [[CrossRef](#)]
33. Sato, K. *Functional Histoanatomy of the Human Larynx*; Springer: Singapore, 2018.
34. Lin, C.; Puram, S.V.; Bulbul, M.G.; Sethi, R.K.; Rocco, J.W.; Old, M.O.; Kang, S.Y. Elective neck dissection for salvage laryngectomy: A systematic review and. *Oral Oncol.* **2019**, *96*, 97–104. [[CrossRef](#)] [[PubMed](#)]
35. Piazza, C.; Filauro, M.; Paderno, A.; Marchi, F.; Perotti, P.; Morello, R.; Taboni, S.; Parrinello, G.; Incandela, F.; Iandelli, A.; et al. Three-Dimensional Map of Isoprognostic Zones in Glottic Cancer Treated by Transoral Laser Microsurgery as a Unimodal Treatment Strategy. *Front. Oncol.* **2018**, *8*, 175. [[CrossRef](#)] [[PubMed](#)]
36. Gross, J.H.; Vila, P.M.; Simon, L.; Rizvi, Z.H.; Zenga, J.; Jackson, R.S.; Pipkorn, P. Elective neck dissection during salvage laryngectomy: A systematic review and meta-analysis. *Laryngoscope* **2020**, *130*, 899–906. [[CrossRef](#)] [[PubMed](#)]
37. Farrag, T.Y.; Lin, F.R.; Cummings, C.W.; Koch, W.M.; Flint, P.W.; Califano, J.A.; Broussard, J.; Bajaj, G.; Tufano, R.P. Neck Management in Patients Undergoing Postradiotherapy Salvage Laryngeal Surgery for Recurrent/Persistent Laryngeal Cancer. *Laryngoscope* **2006**, *116*, 1864–1866. [[CrossRef](#)]
38. Asakage, T.; Nakao, K.; Ebihara, Y.; Fujishiro, Y.; Watanabe, K. A clinical study of post-cricoid carcinoma. *Acta Oto-Laryngol.* **2007**, *127*, 118–122. [[CrossRef](#)]
39. Din, H.A.; Zhan, K.Y.; Bolin, C.; Nguyen, S.; Lentsch, E.J. Predictors of Survival in Posterior Cricoid Squamous Cell Carcinoma: A Study of 248 Cases. *Laryngoscope* **2016**, *127*, 1093–1096. [[CrossRef](#)]
40. Spector, J.G.; Sessions, D.G.; Haughey, B.H.; Chao, K.S.C.; Simpson, J.; El Mofty, S.; Perez, C.A. Delayed Regional Metastases, Distant Metastases, and Second Primary Malignancies in Squamous Cell Carcinomas of the Larynx and Hypopharynx. *Laryngoscope* **2001**, *111*, 1079–1087. [[CrossRef](#)]
41. Liu, Y.-H.; Xu, S.-C.; Tu, L.-L.; Zhang, K.-L.; Lu, D.-H.; Zhang, M. A rich lymphatic network exists in the inferior surface of the vocal cord. *Surg. Radiol. Anat.* **2006**, *28*, 125–128. [[CrossRef](#)]
42. Dziegielewski, P.T.; O'Connell, D.A.O.; Klein, M.; Fung, C.; Singh, P.; Mlynarek, A.; Fung, D.; Harris, J.R.; Seikaly, H. Primary Total Laryngectomy versus Organ Preservation for T3/T4a Laryngeal Cancer: A Population-Based Analysis of Survival Primary. *J. Otolaryngol. Neck Surg.* **2012**, *41*, S56–S64.



© 2020 by the authors. Licensee MDPI, Basel, Switzerland. This article is an open access article distributed under the terms and conditions of the Creative Commons Attribution (CC BY) license (<http://creativecommons.org/licenses/by/4.0/>).





**Validation of the ELS classification of glottic vascular changes  
as seen by NBI**

**Missale, F.**  
Taboni, S.  
Carobbio, A.  
Mazzola, F.  
Berretti, G.  
Iandelli, A.  
Fragale, M.  
Mora, F.  
Paderno, A.  
Del Bon, F.  
Parrinello, G.  
Deganello, A.  
Piazza, C.

Peretti, G. *European archives of Oto-Rhino-Laryngology*

2021;278(7)2397-2409. <https://doi.org/10.1007/s00405-021-06723-7>



## Validation of the European Laryngological Society classification of glottic vascular changes as seen by narrow band imaging in the optical biopsy setting

Francesco Missale<sup>1,2</sup> · Stefano Taboni<sup>3,4</sup> · Andrea Luigi Camillo Carobbio<sup>1,5</sup> · Francesco Mazzola<sup>6</sup> · Giulia Berretti<sup>7</sup> · Andrea Iandelli<sup>1,5</sup> · Marco Fragale<sup>1,5</sup> · Francesco Mora<sup>1,5</sup> · Alberto Paderno<sup>7</sup> · Francesca Del Bon<sup>7</sup> · Giampiero Parrinello<sup>1</sup> · Alberto Deganello<sup>7</sup> · Cesare Piazza<sup>7</sup> · Giorgio Peretti<sup>1,5</sup>

Received: 7 December 2020 / Accepted: 23 February 2021 / Published online: 12 March 2021  
© The Author(s) 2021

### Abstract

**Purpose** In 2016, the European Laryngological Society (ELS) proposed a classification for vascular changes occurring in glottic lesions as visible by narrow band imaging (NBI), based on the dichotomic distinction between longitudinal vessels (not suspicious) and perpendicular ones (suspicious). The aim of our study was to validate this classification assessing the interobserver agreement and diagnostic test performance in detecting the final histopathology.

**Methods** A retrospective study was carried out by reviewing clinical charts, preoperative videos, and final pathologic diagnosis of patients submitted to transoral microsurgery for laryngeal lesions in two Italian referral centers. In each institution, two physicians, independently re-assessed each case applying the ELS classification.

**Results** The cohort was composed of 707 patients. The pathologic report showed benign lesions in 208 (29.5%) cases, papillomatosis in 34 (4.8%), squamous intraepithelial neoplasia (SIN) up to carcinoma in situ in 200 (28.2%), and squamous cell carcinoma (SCC) in 265 (37.5%). The interobserver agreement was extremely high in both institutions ( $k = 0.954$ ,  $p < 0.001$  and  $k = 0.880$ ,  $p < 0.001$ ). Considering the diagnostic performance for identification of at least SIN or SCC, the sensitivity was 0.804 and 0.902, the specificity 0.793 and 0.581, the positive predictive value 0.882 and 0.564, and the negative predictive value 0.678 and 0.908, respectively.

**Conclusion** The ELS classification for NBI vascular changes of glottic lesions is a highly reliable tool whose systematic use allows a better diagnostic evaluation of suspicious laryngeal lesions, reliably distinguishing benign ones from those with a diagnosis of papillomatosis, SIN or SCC, thus paving the way towards confirmation of the optical biopsy concept.

**Keywords** Narrow band imaging · European Laryngological Society classification · Optical biopsy · Laryngeal cancer · Vascular changes · Endoscopy

Francesco Missale and Stefano Taboni have equally contributed to the manuscript.

Cesare Piazza and Giorgio Peretti have equally contributed as senior authors.

✉ Andrea Luigi Camillo Carobbio  
a.carobbio@studenti.unibs.it

<sup>1</sup> IRCCS Ospedale Policlinico San Martino, Genoa, Italy

<sup>2</sup> Department of Molecular and Translational Medicine, University of Brescia, Brescia, Italy

<sup>3</sup> Section of Otorhinolaryngology, Head and Neck Surgery, Azienda Ospedaliera di Padova, University of Padua, Padua, Italy

<sup>4</sup> Department of Clinical and Experimental Sciences, University of Brescia, Brescia, Italy

<sup>5</sup> Department of Surgical Sciences and Integrated Diagnostics (DISC), University of Genoa, Genoa, Italy

<sup>6</sup> Department of Otolaryngology, Head and Neck Surgery, IRCCS Regina Elena National Cancer Institute, Rome, Italy

<sup>7</sup> Unit of Otorhinolaryngology, Head and Neck Surgery, ASST Spedali Civili di Brescia, University of Brescia, Brescia, Italy

## Introduction

Early detection and diagnosis of laryngeal squamous cell carcinoma (SCC) are crucially involved not only in reducing mortality, but also to optimize therapeutic approaches aimed at achieving the best organ and functional preservation [1, 2]. Fortunately, glottic SCC, the most common laryngeal tumor localization, is more frequently detected at an earlier stage than tumors originating in other subsites of the head and neck due to its early (albeit highly non-specific) symptoms [3]. Laryngeal SCC examination is usually performed by flexible (video)endoscopy under white light (WL) and relies on the analysis of superficial characteristics (size, color, location, single or multifocal appearance) and visible morphological features (smoothness, irregularity, keratinization, ulceration, submucosal growth), per se non-pathognomonic and possibly overlapping each other in malignant and benign pathologies, especially when diagnosed at early stages. This implies the frequent need to obtain an incisional biopsy before deciding on the therapeutic approach, with an increase in costs, anesthetic risks, and potential undue damage to the vocal cords.

Computed tomography and magnetic resonance imaging definitively play a major role in diagnosis of more advanced diseases, providing information about the involvement of laryngeal structures and lateral neck lymph nodes, while, on the other hand, they fall shortly in identifying and characterizing superficial mucosal lesions. By contrast, the judicious use of high definition and better contrasted videoendoscopic images now offer staggering details in evaluation of epithelial and superficial vascular patterns. Moreover, clinicians can increasingly benefit from novel optical diagnostic methods, providing information even closer to those obtained by formal histopathological examination, thus differentiating between normal mucosa and discrete lesions and, among the latter, between those with benign versus malignant behaviors [4]. In this context, narrow band imaging (NBI) is a well-established bioendoscopic technique using filtered wavelengths to enhance microvascular alterations associated with preneoplastic and neoplastic transformation of the upper aerodigestive tract (UADT) mucosa [5–8]. Since its first introduction in the late 1990s, the use of NBI has considerably upgraded physicians' ability for non-invasive detection and delineation of suspicious mucosal lesions, and is thus beneficial in the diagnosis of a variety of benign and malignant lesions [9]. However, the need for a common language to be shared among clinicians to describe NBI-enhanced vascular patterns led to the proposal of different classifications during the last decades [10–12]. In 2016, the Working Committee on Endoscopic Laryngeal Imaging of the European Laryngological Society (ELS) published a new proposal for a simplified (dichotomic) description

of vocal fold vascular changes as seen under NBI [12]. In this system, the authors distinguished between normal and pathologic vascular patterns of the vocal folds. The latter, in turn, were divided into longitudinal and perpendicular vascular changes. Longitudinal vessels characterize benign lesions, while perpendicular ones (i.e. dot-like intrapapillary capillary loops [IPCL], enlarged and worm-like vessels) are considered signs of benign neoplasms (such as papillomatosis), squamous intraepithelial neoplasia (SIN), or frankly malignant lesions.

The present study aims to assess the performance of the ELS classification of vascular changes in a broad multicenter cohort, testing its interobserver agreement as primary endpoint, and analyzing its accuracy in predicting the final pathological results in an optical biopsy setting, i.e. by evaluating the diagnostic accuracy of NBI by comparing it with the final histopathologic diagnosis obtained after complete removal of the glottic lesion.

## Methods

### Study population

A retrospective study was carried out enrolling patients treated at the Departments of Otorhinolaryngology—Head and Neck Surgery of the Universities of Genoa (Center A; from January 2012 to December 2016) and Brescia (Center B; from January 2015 to December 2018), Italy.

All patients enrolled were affected by laryngeal lesions; a pre-treatment videoendoscopic evaluation with both WL and NBI was performed in the office as well as in the operatory theater, and the records were saved in his/her medical chart; the laryngeal lesion was treated by a transoral microsurgical approach by either cold instrumentation and carbon dioxide (CO<sub>2</sub>) laser; postoperative histopathologic assessment was obtained to classify the resected tissue as benign, dysplastic or malignant. Histopathological diagnosis was performed according to the WHO classification system [13].

### Clinical diagnostic work-up

All patients were preoperatively evaluated by high-definition television (HDTV)-WL and HDTV-NBI through a videorhinolaryngoscope ENF-VQ or ENF-VH coupled to an Evis Exera II HDTV camera connected to an Evis Exera II CLV-180B light source (Olympus Medical System Corp., Tokyo, Japan). Just before surgery, in the operating room, with patient under general anesthesia, intraoperative HDTV-WL and HDTV-NBI rigid endoscopy with 0° and 70° telescopes (Karl Storz, Tuttlingen, Germany) was also systematically performed. On the basis of this diagnostic work-up, laryngeal lesions were subsequently removed by either a

phonosurgical approach (in case of benign lesions) or excisional biopsy (in case of papillomatosis, SIN, carcinoma in situ [CIS] or invasive SCC) by type I–III cordectomies according to the ELS classification of cordectomies [14].

### Clinical evaluation applying the ELS classification

Clinical records of the study population, including demographic features and information on previous treatments in terms of laryngeal surgery, head and neck radiotherapy,

or other treatments before the index transoral microsurgical procedure were retrieved from the hospital databases. Two independent physicians from each institution with at least a 3-year-experience in the use of NBI, blinded to the final histopathologic result, retrospectively and independently reviewed the intraoperative videoendoscopic recordings. Applying the ELS classification for laryngeal vascular changes [15], each case was categorized as suspicious for malignancy (presence of perpendicular vascular abnormalities as shown in Fig. 1) or non-suspicious

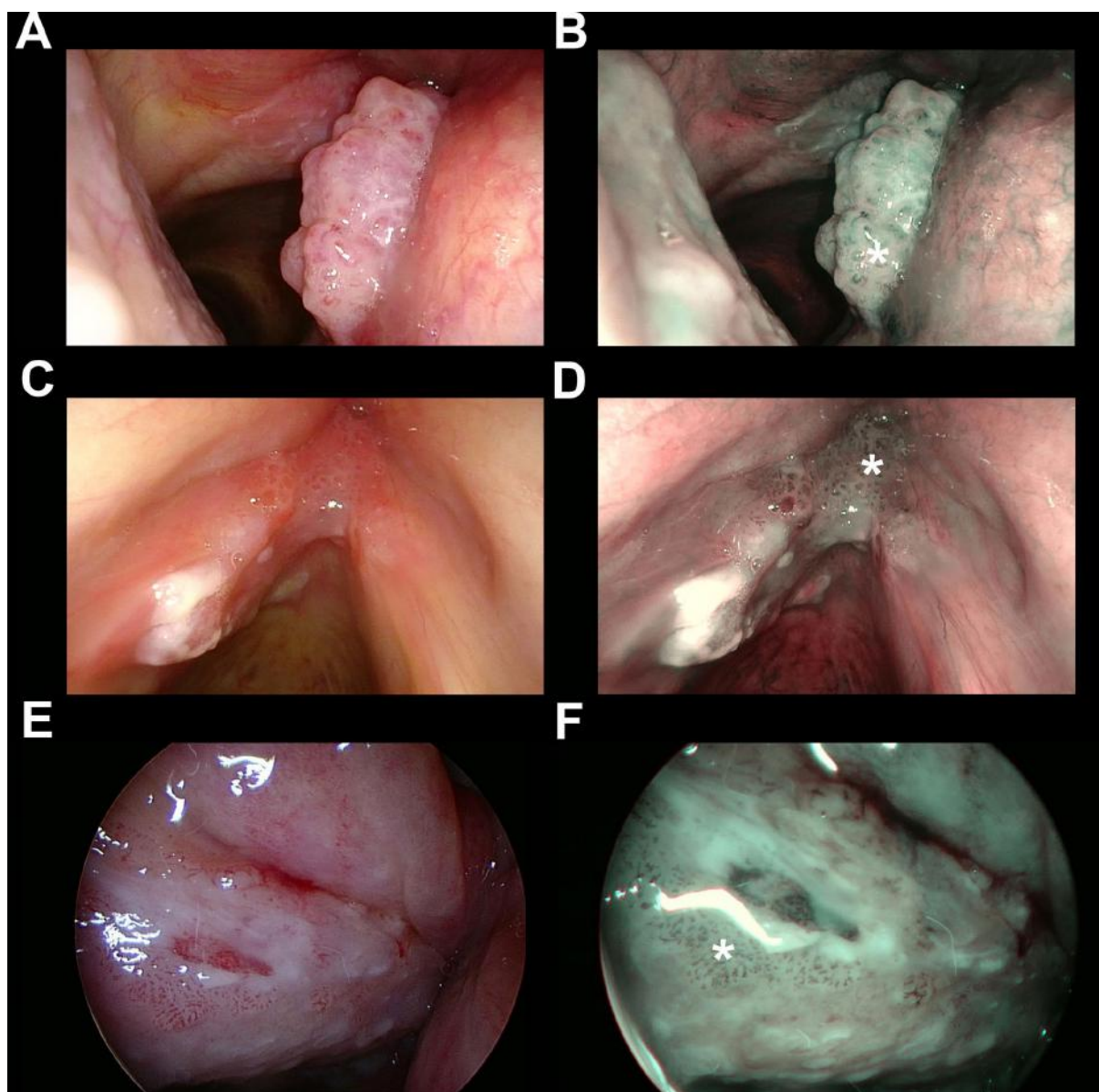


**Fig. 1** Endoscopic picture of three representative cases of SCC (a–d) or CIS (e, f) correctly identified as suspicious by the presence of perpendicular vascular abnormalities (\* in all panels) evaluating the NBI endoscopic appearance (b, d, f) and applying the ELS classification



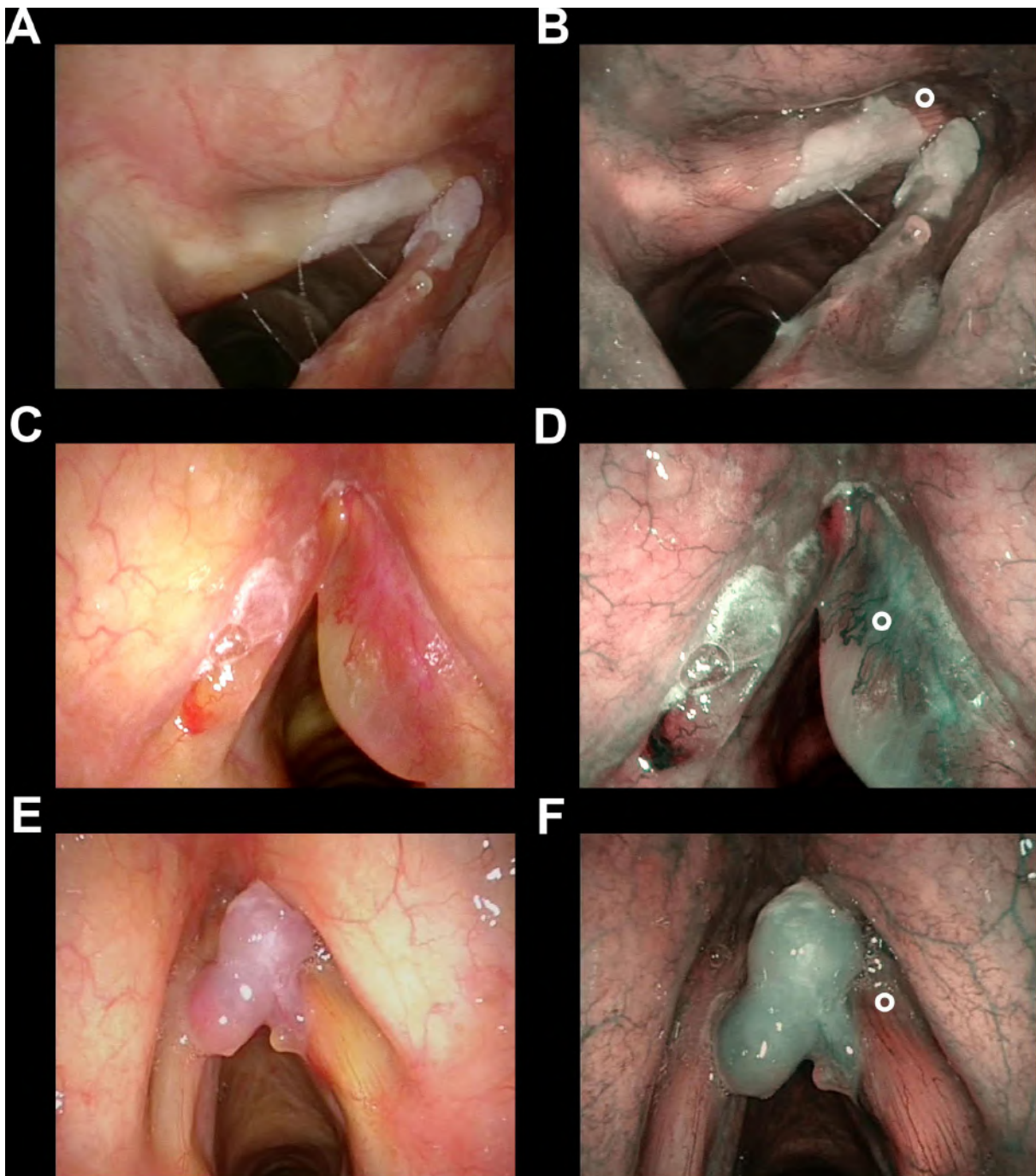


**Fig. 2** Endoscopic picture of three representative cases of benign glottic lesions: keratosis without atypia (**a, b**), Reinke's edema (**c, d**) and polyp (**e, f**) correctly identified as benign lesions without identifying any perpendicular vascular abnormalities evaluating the NBI

endoscopic appearance (**b, d, f**) and applying the ELS classification. The ° in all panels points to non-suspicious longitudinal vascular abnormalities that can be observed inside the lesion (**d**) of at its boundary (**b, f**)

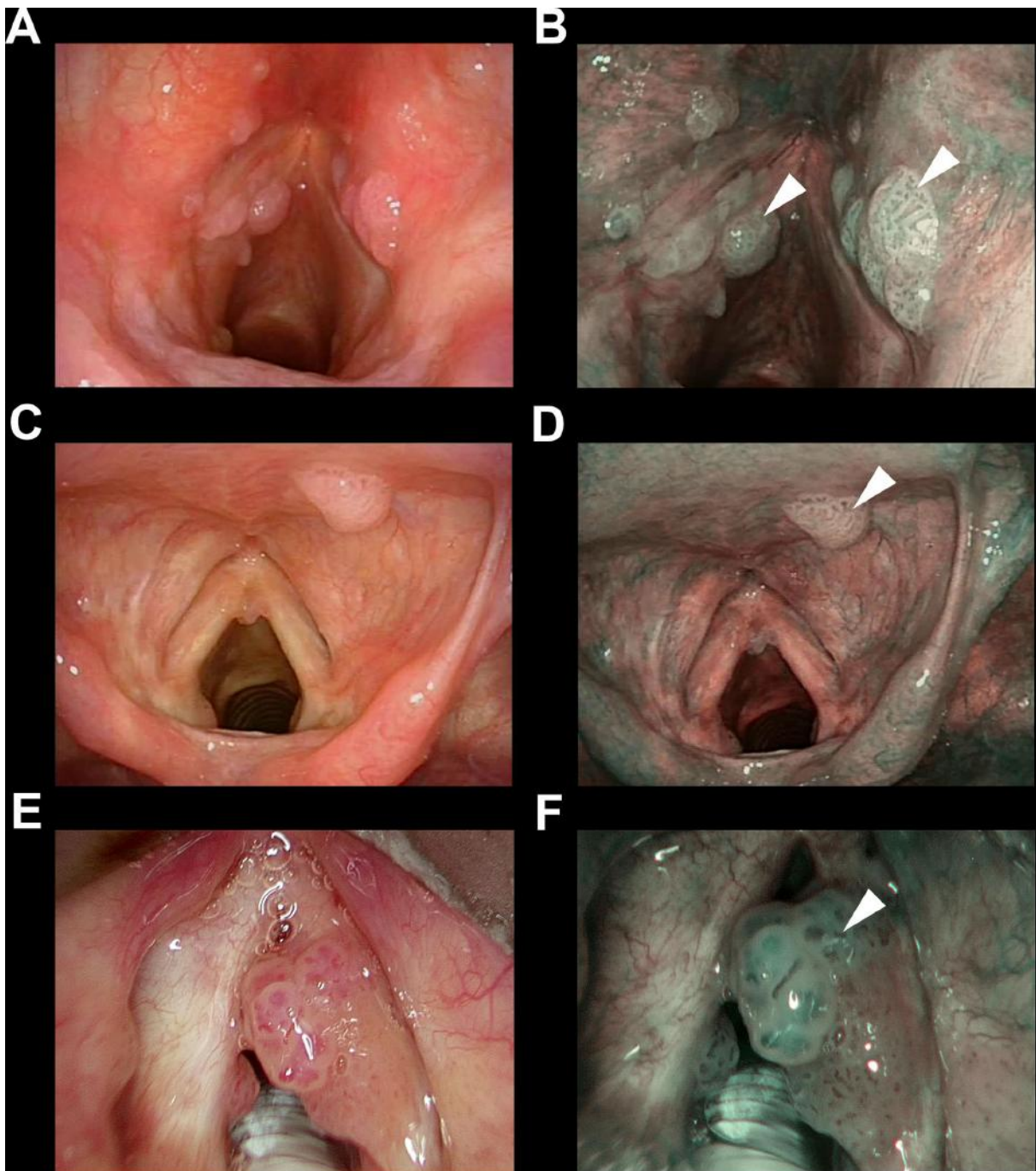


**Fig. 3** Endoscopic pictures of three representative cases (**a, b; c, d; and e, f**) of recurrent laryngeal papillomatosis correctly identified detecting wide angle IPCLs (arrowheads in all panels) evaluating the NBI endoscopic appearance (**b, d, f**)

(undetectable perpendicular vascular changes or longitudinal ones as shown in Fig. 2). In case of interobserver disagreement, consensus was reached by direct comparison between the examiners. The identification of features of respiratory

papillomatosis (i.e., wide angle IPCL) was also considered as a secondary endpoint (Fig. 3).



**Table 1** Definition of interrater agreement qualitative scores according to Altman et al. [15, 16] and Clinical Utility indexes grading according to Mitchell [18]

Agreement classification		Clinical Utility Index classification	
$\kappa$	Strength of agreement	CU+Ve or CU–Ve	Grading
<0.21	Poor	<0.49	Poor utility
0.21–0.40	Fair	0.49–0.63	Satisfactory utility
0.41–0.60	Moderate	0.64–0.80	Good utility
0.61–0.80	Good	0.81–1.00	Excellent utility
0.81–1.00	Very good		

CU + Ve positive clinical utility index, CU–Ve negative clinical utility index

**Statistical analysis**

Clinical data were reported as absolute and relative frequencies. The reliability of the ELS classification was assessed for each independent cohort measuring the Cohen’s k statistic and the strength of agreement graded according to Altman et al. [16, 17], as reported in Table 1. Considering the final consensus of the evaluation, we assessed the performance of the diagnostic test for prediction of the final pathologic result (at least SIN1, up to SCC) in an optical biopsy setting. For better understanding of the clinical utility of applying the classification and

detecting papillomatosis-like features, the Clinical Utility (CU) indexes were also derived, taking into account the measures of occurrence (sensitivity or specificity) together with the possibility of discrimination (positive [PPV] or negative predictive values [NPV]), and their qualitative grading were judged accordingly [18, 19] (Table 1). The Positive Clinical Utility Index (CU + Ve) is defined as sensitivity\*PPV, and a high CU + Ve results should characterize “case finding” tests. By contrast, good Negative Clinical Utility Index (CU–Ve), defined as specificity\*NPV, should be ideal for “screening” tests [18, 19].

In all analyses, a two-tailed *p* value < 0.05 was considered significant. GraphPad Prism (San Diego, CA, USA), Stata (version 13.0, College Station, Texas, USA) and R (version 3.6.2) were used for statistical analysis and rendering graphs.

**Results**

**Clinical data**

A total of 707 patients met enrolment criteria: 434 (61.3%) had been evaluated and treated at the center A, and 273 (38.7%) at the center B. Five-hundred and fifty six (78.6%) were males and 151 (21.4%) females, with a mean age of 61.8 years (range 18–91). Four-hundred and seventy-eight

**Table 2** Clinical features of the cohort

Variables	All		Longitudinal vessels		Perpendicular vessels	
	<i>n</i>	%	<i>n</i>	%	<i>n</i>	%
All	707	100.0	283	40.0	424	60.0
Gender						
Male	556	78.6	184	26.0	372	52.6
Female	151	21.4	99	14.0	52	7.4
Previous treatments <sup>o</sup>						
No	478	67.6	221	31.3	257	36.4
Previous surgery	174	24.6	45	6.4	129	18.2
Previous RT	17	2.4	4	0.6	13	1.8
Previous biopsy	54	7.6	8	1.1	46	6.5
Histology						
Benign	208	29.4	184	26.0	24	3.4
Papillomatosis without atypia	34	4.8	0	0.0	34	4.8
SIN1	46	6.5	24	3.4	22	3.1
SIN2	61	8.6	26	3.7	35	5.0
SIN3/CIS	93	13.2	15	2.1	78	11.0
SCC	265	37.5	26	3.7	239	33.8

The sum of rows is 723 since 16 patients had two different previous treatments

RT radiotherapy, SIN squamous intraepithelial neoplasia, CIS in situ carcinoma, SCC squamous cell carcinoma

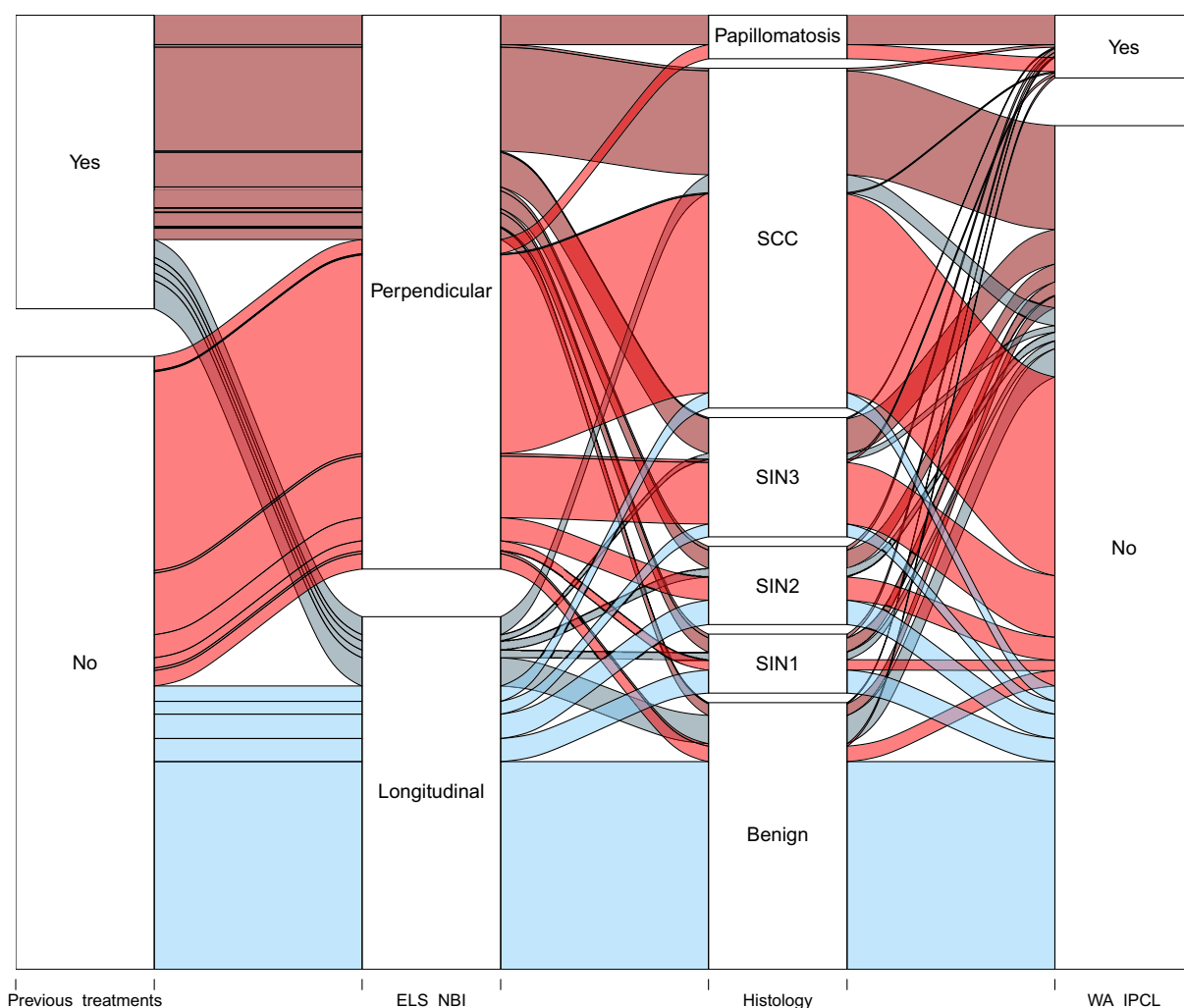


**Fig. 4** Alluvial chart showing frequency distribution of previous treatment, ELS classification results, histology, and presence of wide angle IPCL features (WA IPCL). Color code according to different matching of previous treatments and ELS classification results

(67.6%) patients were submitted to endoscopic evaluation and surgical procedures without previous treatments, whereas 174 (24.6%) had been already surgically treated,

17 (2.4%) received head and neck radiotherapy, and 54 (7.6%) had been previously biopsied elsewhere. The final pathologic report was consistent with a benign lesion in 208

**Table 3** Agreement analysis by Cohen’s *k* test

Institution	Type of lesion	<i>N</i>	%	Agreement (%)	$\kappa$	95% CI ( $\kappa$ )	<i>p</i>
University of Genoa (Center A)	All	434	100	97.7	0.954	0.86–1.0	<0.0001
	Untreated	284	65.4	97.5	0.949	0.833–1.0	<0.0001
	Previous biopsy/surgery/RT	150	34.6	98.0	0.945	0.785–1.0	<0.0001
University of Brescia (Center B)	All	273	100	94.9	0.872	0.754–0.991	<0.0001
	Untreated	194	71.1	94.3	0.864	0.723–1.0	<0.0001
	Previous biopsy/surgery/RT	79	28.9	96.2	0.894	0.674–1.0	<0.0001

(29.5%) cases, papillomatosis without atypia in 34 (4.8%), mild SIN (SIN1) in 46 (6.5%), moderate SIN (SIN2) in 61 (8.6%), severe SIN (SIN3) or CIS in 93 (13.1%), and SCC in 265 (37.5%). Full details are summarized in Table 2, Fig. 4.

### ELS classification interobserver reliability

Cohen's  $\kappa$  statistic was used to assess the agreement between judgment of each lesion by two independent raters in each institution applying the ELS classification. According to the criteria by Altman et al. [16, 17], reported in Table 1, for the entire cohort the result was satisfactory and showed a very good agreement between observers at both the center A ( $\kappa=0.954$ ; 95% confidence interval [CI] 0.86–1.0,  $p < 0.0001$ ) and the center B ( $\kappa=0.872$ ; 95% CI 0.754–0.991,  $p < 0.0001$ ) (Table 3). The agreement was consistent and significant ( $p < 0.0001$ ) for both Institutions, as well as for untreated ( $\kappa=0.949$ ; 95% CI 0.833–1.0 and  $\kappa=0.864$ ; 95% CI 0.723–1.0, respectively) and previously treated patients ( $\kappa=0.945$ ; 95% CI 0.785–1.0 and  $\kappa=0.894$ ; 95% CI 0.674–1.0, respectively) (Table 3).

### Diagnostic performance

Considering the final score in the entire cohort (24 cases with initial disagreement were resolved between the examiners), performance of the diagnostic test was assessed investigating the detection of at least SIN1-SCC (Table 4). The best sensitivity and NPV were obtained for detection of SCC (0.90 and 0.91, respectively) and, accordingly, the best specificity and PPV for diagnosis of at least SIN1 (0.79

and 0.88, respectively). Considering previous treatments as a potential source of bias, for untreated patients the ELS classification reached the best performance with sensitivity and NPV for detection of SCC of 0.93 and 0.95, respectively, and specificity and PPV for diagnosis of at least SIN1 of 0.88 and 0.91, respectively. In previously treated patients, the performance of endoscopic evaluation was still satisfactory in terms of sensitivity (from 0.82 to 0.86), while it was poorer in terms of specificity (from 0.34 to 0.49), NPV (from 0.46 to 0.76), and PPV (from 0.45 to 0.84) (Table 4, Fig. 5).

The measurement of the CU indexes confirmed this observation with a good CU + Ve and CU – Ve for all outcomes except one in untreated patients, whereas no more than satisfactory or even poorer results were obtained for most outcomes in previously treated or biopsied patients, as shown in Table 5.

### Diagnostic performance in respiratory papillomatosis

Among perpendicular vascular changes, the ELS classification well defines the vascular pattern of recurrent respiratory papillomatosis lesions, characterized by vessel loops with wide angle turning point, embedded in a three-dimensional warty structure [15]. We tested the identification of these features by NBI in our cohort, confirming their value for correct identification of this disease with a sensitivity of 1.0 (95% CI 0.90–1.0), specificity of 0.98 (95% CI 0.96–0.99), PPV of 0.69 (95% CI 0.55–0.82), and NPV of 1.0 (95% CI 0.99–1.0), as shown in Table 4. Moreover, the measure of CU indexes confirmed the excellent performance of NBI

**Table 4** Diagnostic test results

	Sensitivity (95% CI)	Specificity (95% CI)	PPV (95% CI)	NPV (95% CI)
All				
At least SIN1	0.80 (0.77–0.84)	0.79 (0.74–0.84)	0.88 (0.85–0.91)	0.68 (0.62–0.73)
At least SIN2	0.84 (0.80–0.87)	0.75 (0.70–0.80)	0.83 (0.79–0.87)	0.76 (0.71–0.81)
At least SIN3	0.89 (0.85–0.92)	0.69 (0.64–0.74)	0.75 (0.70–0.79)	0.86 (0.81–0.89)
SCC	0.90 (0.86–0.94)	0.58 (0.53–0.63)	0.56 (0.52–0.61)	0.91 (0.87–0.94)
Untreated				
At least SIN1	0.80 (0.75–0.84)	0.88 (0.83–0.93)	0.91 (0.87–0.95)	0.74 (0.67–0.79)
At least SIN2	0.85 (0.80–0.89)	0.86 (0.81–0.90)	0.88 (0.84–0.92)	0.82 (0.76–0.87)
At least SIN3	0.90 (0.86–0.94)	0.81 (0.75–0.86)	0.81 (0.76–0.86)	0.90 (0.86–0.94)
SCC	0.93 (0.88–0.96)	0.68 (0.63–0.74)	0.61 (0.55–0.67)	0.95 (0.91–0.97)
Previous biopsy/surgery/RT				
At least SIN1	0.82 (0.75–0.87)	0.49 (0.35–0.63)	0.84 (0.77–0.89)	0.46 (0.33–0.59)
At least SIN2	0.83 (0.76–0.89)	0.44 (0.33–0.56)	0.75 (0.68–0.82)	0.56 (0.42–0.69)
At least SIN3	0.85 (0.78–0.91)	0.40 (0.31–0.51)	0.65 (0.58–0.72)	0.68 (0.54–0.79)
SCC	0.86 (0.77–0.92)	0.34 (0.26–0.43)	0.45 (0.41–0.57)	0.76 (0.63–0.86)
Papillomatosis detection	1.00 (0.90–1.00)	0.98 (0.96–0.99)	0.69 (0.55–0.82)	1.00 (0.99–1.00)

PPV positive predictive value, NPV negative predictive value, CI confidence interval, SIN squamous intraepithelial neoplasia, SCC squamous cell carcinoma

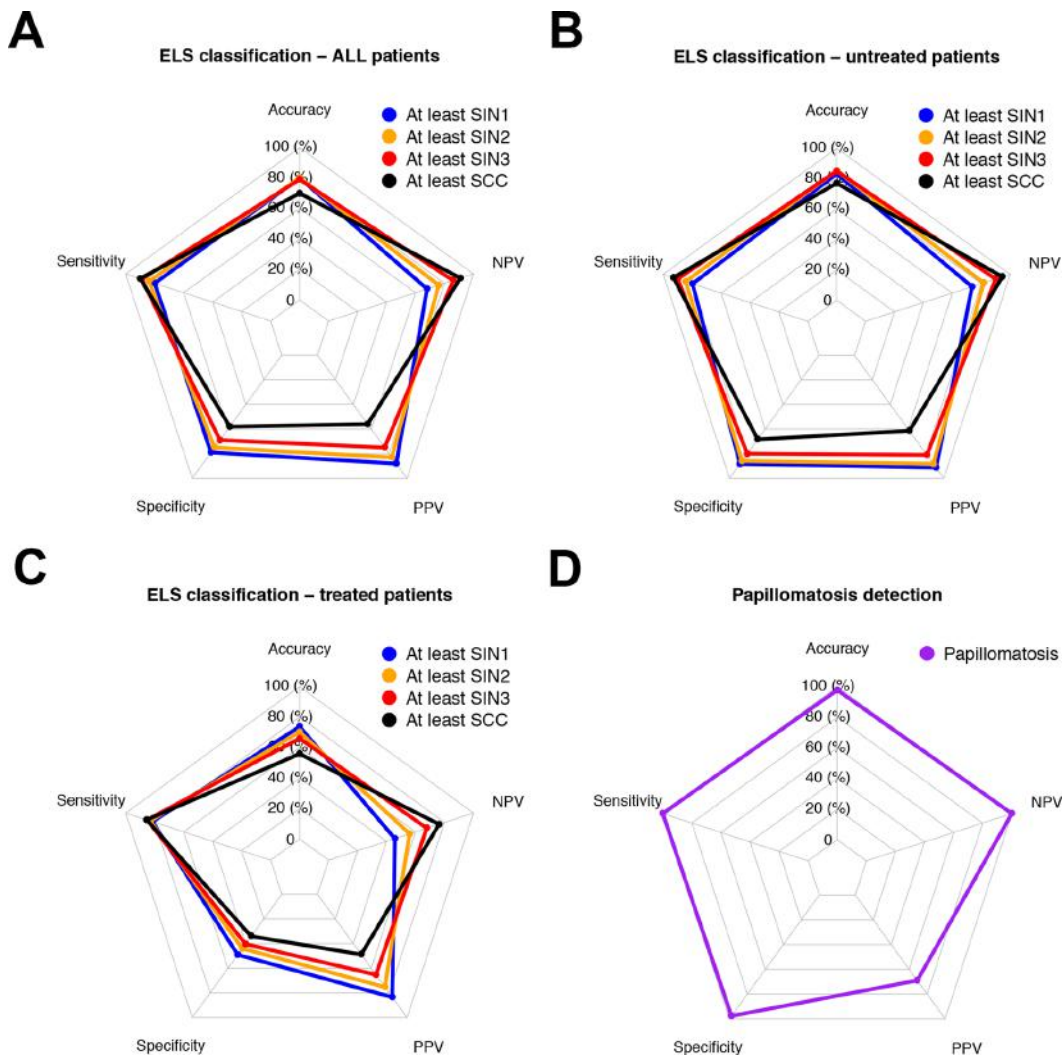


**Fig. 5** Radar charts showing the diagnostic test applying the ELS classification for the detection of different histologic targets in the whole cohort (a), in the untreated group (b), and in the previously

surgical or RT treated group (c). Diagnostic test results referred to the detection of wide angle IPCLs for the diagnosis of laryngeal papillomatosis (d)

with a CU–Ve of 0.98 (95% CI 0.97–0.99) and good performance in terms of CU + Ve of 0.69 (95% CI 0.56–0.83), as reported in Table 5.

**Discussion**

Among the several bioendoscopic techniques now available for routine evaluation of the UADT, NBI appears to be the most effective in evaluation of the larynx, hypopharynx, oral and oropharyngeal cavities [1, 20, 21]. The easy use of NBI and other bioendoscopic tools based on similar principles, which aims to enhance the vascular features of tissues (e.g. SPIES [22] or iSCAN [20]), is mainly due to

full integration of high-definition videoendoscopes, easily activated by pressing a button during in-office endoscopic examination or during pre- and intraoperative assessment. Interestingly, the superior in-depth evaluation of the bioendoscopic features of a given lesion may pave the way to the proof of concept of the optical biopsy, i.e. the capability to understand the nature of a given vocal fold mucosal lesion before its removal, thus modulating its excisional biopsy and optimizing hospitalization time, costs, and undue damage to surrounding healthy structures [23].

The need for a common language to categorize and share the findings from NBI evaluation led to a number of different classification systems. The first to have widespread diffusion in the head and neck scientific community was proposed

**Table 5** Clinical Utility indexes and utility grading results according to Mitchell [18]

	CU+Ve (95% CI)	CU+Ve Judgment	CU–Ve (95% CI)	CU–Ve Judgment
All				
At least SIN1	0.71 (0.67–0.75)	Good	0.54 (0.49–0.58)	Satisfactory
At least SIN2	0.70 (0.65–0.74)	Good	0.57 (0.53–0.62)	Satisfactory
At least SIN3	0.66 (0.61–0.71)	Good	0.59 (0.55–0.63)	Satisfactory
SCC	0.51 (0.45–0.57)	Satisfactory	0.53 (0.49–0.57)	Satisfactory
Untreated				
At least SIN1	0.73 (0.68–0.78)	Good	0.65 (0.60–0.70)	Good
At least SIN2	0.75 (0.69–0.80)	Good	0.70 (0.66–0.74)	Good
At least SIN3	0.73 (0.68–0.79)	Good	0.73 (0.69–0.77)	Good
SCC	0.57 (0.50–0.64)	Satisfactory	0.65 (0.61–0.69)	Good
Previous biopsy/surgery/RT				
At least SIN1	0.68 (0.61–0.75)	Good	0.23 (0.11–0.34)	Poor
At least SIN2	0.63 (0.55–0.70)	Satisfactory	0.25 (0.14–0.35)	Poor
At least SIN3	0.56 (0.47–0.64)	Satisfactory	0.27 (0.17–0.38)	Poor
SCC	0.42 (0.32–0.52)	Poor	0.26 (0.16–0.36)	Poor
Papillomatosis detection	0.69 (0.56–0.83)	Good	0.98 (0.97–0.99)	Excellent

CU + Ve positive clinical utility index, CU–Ve negative clinical utility index, CI confidence interval, SIN squamous intraepithelial neoplasia, SCC squamous cell carcinoma

by Ni et al. [11]. These authors divided the different IPCL changes in five types (I–V), judging them as benign (from types I–IV), suspected malignant, and frankly malignant (type V). However, apart from its intrinsic complexity, this classification clearly showed a lack of a clear-cut threshold between benign and malignant diseases. In fact, different authors proposed different cut-offs for the worst endoscopic feature of each lesion to be considered suspicious, ranging from type III [24], to type IV [25–27], and type V [9, 11, 28].

Therefore, in 2016 the ELS proposed a new classification system for the interpretation of glottic vascular abnormalities detected during NBI-guided endoscopies [15]. This classification considers vascular abnormalities as IPCL perpendicular to the epithelium surface as suspicious, whereas longitudinal vascular changes (e.g. dilated or tortuous vessels, increased vessels numbers) are considered as not suspicious to harbor respiratory papillomatosis, pre-malignant, or cancerous lesions. The first attempt to apply this dichotomic classification was in the study by Šifrer et al. [29] who analyzed 80 vocal cords lesions in which the identification of a perpendicular vascular pattern was diagnostic for CIS-SCC with a sensitivity of 100%, specificity of 95%, PPV of 88%, and NPV of 100%. Further analysis evaluating a larger cohort of 288 vocal cords gave similar results (sensitivity 98%, specificity 95%, PPV 88%, and NPV 99%) [30].

Our results, obtained in two of the European pioneer centers applying NBI for evaluation of the UADT since 2007, herein confirm the intrinsic value of the ELS classification for laryngeal vascular changes in the identification of lesions

harboring pre-cancerous or frankly neoplastic alterations. In particular, we applied this diagnostic tool to demonstrate its possible role in performing a so-called optical biopsy. In fact, our policy has always been, for early glottic lesions, a one-stage modulated excisional biopsy based on a number of pre- and intraoperative diagnostic tests in which WL and NBI rigid endoscopy under general anesthesia has always played a paramount role [23]. Moreover, as asserted by many authors, NBI is capable of enhancing small lesions that are undetectable by WL alone, thus ameliorating the treatment of laryngeal SCC, as well as assessing the potential multifocality of the disease and correct evaluation of intraoperative margins [31], as well as early identification of small recurrences during follow-up that may still allow application of minimally invasive treatments such as laser office-based procedures or second-look microlaryngoscopic operations [32–35]. Of note, the present study demonstrated a lower diagnostic accuracy of NBI in the previously treated patients compared to the untreated ones, thus confirming the potential confounding factor played by invasive sampling procedures when not directed to the full removal (excisional biopsy) of the entire visible lesion within safe margins.

The excellent interobserver reliability of the ELS classification with a  $k > 0.81$  in all scenarios tested and reproducible in two independent centers confirms the reproducibility of the operators' findings in applying this classification tool. The high interobserver reliability of the ELS classification can be explained by its intrinsic simple application and dichotomic arrangement, providing better performance compared to other proposed classification systems such as that by Ni, which is complicated by a 5-tier structure and



associated with moderate/substantial interrater concordance, with a  $k$  ranging from 0.55 to 0.69 [36, 37].

On the other hand, it has to be noted that all the observers involved in this study had a minimum experience of 3 years in the use of NBI technology. Even though application of the ELS Classification on vocal fold vascular changes as observed by NBI is no more subjective than any other diagnostic performance, evaluation of certain subtle and sometimes ambiguous neoangiogenic patterns still may require a higher level of expertise, for which a learning curve is inevitably necessary. However, data derived from the gastrointestinal field show that less than a year of training evaluating 200 cases is enough to guarantee an accurate evaluation of NBI frames and that the motivation of the trainer itself can significantly improve the overall performance [38].

Investigating the diagnostic test, having as a target all the possible grades of pre-malignant or malignant transformation, allowed us to depict the capability of the ELS classification in helping to correctly identify pre-malignant cases with the highest PPV and specificity for at least SIN1 diagnosis. The lower performance of such parameters observed for the final diagnosis of glottic SCC can be explained by the presence, and progressively increase, of perpendicular vascular changes at early stages of pre-malignant transformation (SIN1-SIN2). By contrast, for diagnosis of laryngeal SCC, the ELS classification had good performance in terms of sensitivity and NPV, with a low rate of false negative cases and good confidence in a negative result (absence of perpendicular vascular changes).

Furthermore, several authors have underlined the utility of NBI for detection of recurrent respiratory papillomatosis and its ability to increase the detection rate of small lesions that invisible by WL alone [29, 33, 39–42]. The excellent performance in terms of CU + Ve and CU–Ve searching for wide angle IPCLs in the identification of respiratory papillomatosis mandates, as previously suggested by the recent literature [33, 39–44], the use of biologic endoscopy tools like NBI, and should be considered the endoscopic gold standard for optical biopsy and follow-up of patients affected by laryngeal papillomas.

The main limits of our study are represented by its retrospective design, balanced by analyzing a broad bicentric cohort. Nevertheless, among the estimator analyzed, the suboptimal performance in terms of specificity, negative predictive value, and CU–Ve could have been underestimated having chosen among the inclusive criteria the need for a histopathological diagnosis: several patients without any suspicious lesion at the first evaluation and along time could be considered as true negatives too, thus improving the values of such estimators.

Further developments in this field might include the analysis of a prospective cohort of patients, implementing the enrollment of true negative cases and developing a real-time

software applicable in the head and neck, based on artificial intelligence algorithms already tested on retrospective studies [45, 46], thus improving the objectivity and detection rate of these diagnostic tools, as already devised for gastrointestinal tract tumors [47, 48].

## Conclusion

The ELS classification for NBI vascular changes of laryngeal lesions, herein validated in a large multicenter cohort, is a highly reliable tool with good diagnostic performance in the optical biopsy setting, confirming its overall value. The systematic use of this classification seems to allow better (and purely endoscopic) diagnostic capability of suspicious glottic lesions, reliably distinguishing benign ones from those with a diagnosis of papillomatosis, SIN, or invasive SCC. The excellent performance of NBI for correct identification of respiratory papillomatosis also confirms its usefulness in this clinical setting.

**Funding** Open access funding provided by Università degli Studi di Genova within the CRUI-CARE Agreement.

**Availability of data and materials** Full dataset will be available at: “ELS\_NBI\_Classification\_Validation\_Dataset”, Mendeley Data, V1, <https://doi.org/10.17632/txzzw9n7xs.1> <https://doi.org/10.17632/txzzw9n7xs.1> (Embargo date: 6th December 2021).

## Declarations

**Conflict of interest** The authors certify that they have no affiliation with or involvement in any organization or entity with any financial interest.

**Ethical approval** The research did not involve any animal models; the research involved human participants in accordance with the ethical standards of the institutional and/or national research committees and with the 1964 Helsinki Declaration and its later amendments or comparable ethical standards.

**Informed consent** Informed consent for disclosure of privacy in managing personal data for scientific purposes was obtained from all participants included in the study.

**Open Access** This article is licensed under a Creative Commons Attribution 4.0 International License, which permits use, sharing, adaptation, distribution and reproduction in any medium or format, as long as you give appropriate credit to the original author(s) and the source, provide a link to the Creative Commons licence, and indicate if changes were made. The images or other third party material in this article are included in the article's Creative Commons licence, unless indicated otherwise in a credit line to the material. If material is not included in the article's Creative Commons licence and your intended use is not permitted by statutory regulation or exceeds the permitted use, you will



need to obtain permission directly from the copyright holder. To view a copy of this licence, visit <http://creativecommons.org/licenses/by/4.0/>.

## References

- Sun C, Han X, Li X et al (2017) Diagnostic performance of narrow band imaging for laryngeal cancer: a systematic review and meta-analysis. *Otolaryngol Head Neck Surg* 156:589–597. <https://doi.org/10.1177/0194599816685701>
- Watanabe A, Taniguchi M, Tsujie H et al (2009) The value of narrow band imaging for early detection of laryngeal cancer. *Eur Arch Otorhinolaryngol*. <https://doi.org/10.1007/s00405-008-0835-1>
- Chu EA, Kim YJ (2008) Laryngeal cancer: diagnosis and preoperative work-up. *Otolaryngol Clin North Am* 41:673–695
- Green B, Cobb ARM, Brennan PA, Hopper C (2014) Optical diagnostic techniques for use in lesions of the head and neck: review of the latest developments. *Br J Oral Maxillofac Surg* 52:675–680. <https://doi.org/10.1016/j.bjoms.2014.06.010>
- Muto M, Nakane M, Katada C et al (2004) Squamous cell carcinoma in situ at oropharyngeal and hypopharyngeal mucosal sites. *Cancer* 101:1375–1381. <https://doi.org/10.1002/cncr.20482>
- Piazza C, Dessouky O, Peretti G et al (2008) Narrow-band imaging: a new tool for evaluation of head and neck squamous cell carcinomas. Review of the literature. *Acta Otorhinolaryngol Italorgano Uff della Soc Ital di Otorinolaringol e Chir Cerv-facc* 28:49–54
- Piazza C, Del Bon F, Peretti G, Nicolai P (2012) Narrow band imaging in endoscopic evaluation of the larynx. *Curr Opin Otolaryngol Head Neck Surg* 20:472–476
- Cohen J (2008) Comprehensive atlas of high resolution endoscopy and narrowband imaging (1st edn)
- Kraft M, Fostiropoulos K, Gurtler N et al (2016) Value of narrow band imaging in the early diagnosis of laryngeal cancer. *Head Neck* 38:15–20. <https://doi.org/10.1002/hed.23838>
- Lin YC, Wang WH, Lee KF et al (2012) Value of narrow band imaging endoscopy in early mucosal head and neck cancer. *Head Neck* 34:1574–1579
- Ni X-G, He S, Xu Z-G et al (2011) Endoscopic diagnosis of laryngeal cancer and precancerous lesions by narrow band imaging. *J Laryngol Otol*. <https://doi.org/10.1017/S0022215110002033>
- Takano JH, Yakushiji T, Kamiyama I et al (2010) Detecting early oral cancer: narrowband imaging system observation of the oral mucosa microvasculature. *Int J Oral Maxillofac Surg* 39:208–213. <https://doi.org/10.1016/j.ijom.2010.01.007>
- Barnes L, Eveson JW, Reichart P, Sidransky D (2005) World Health Organization Classification of Head and Neck Tumours. WHO Classif Tumour
- Remacle M, Eckel HE, Antonelli A et al (2000) Endoscopic cordectomy. A proposal for a classification by the working committee, European Laryngological Society. *Eur Arch Otorhinolaryngol* 257:227–231. <https://doi.org/10.1007/s004050050228>
- Arens C, Piazza C, Andrea M et al (2016) Proposal for a descriptive guideline of vascular changes in lesions of the vocal folds by the committee on endoscopic laryngeal imaging of the European Laryngological Society. *Eur Arch Otorhinolaryngol* 273:1207–1214. <https://doi.org/10.1007/s00405-015-3851-y>
- Altman DG (1991) Practical statistics for medical research. Chapman and Hall. *Stat Med*. <https://doi.org/10.1002/sim.4780101015>
- Landis JR, Koch GG (1977) The measurement of observer agreement for categorical data. *Biometrics*. <https://doi.org/10.2307/2529310>
- Mitchell AJ (2008) The clinical significance of subjective memory complaints in the diagnosis of mild cognitive impairment and dementia: a meta-analysis. *Int J Geriatr Psychiatry* 23:1191–1202. <https://doi.org/10.1002/gps.2053>
- Mitchell AJ (2011) Sensitivity x PPV is a recognized test called the clinical utility index (CUI+). *Eur J Epidemiol* 26:251–252. <https://doi.org/10.1007/s10654-011-9561-x>
- Hawkshaw MJ, Sataloff JB, Sataloff RT (2013) New concepts in vocal fold imaging: a review. *J Voice* 27:738–743. <https://doi.org/10.1016/j.jvoice.2013.05.011>
- Deganello A, Paderno A, Morello R et al (2020) Diagnostic accuracy of narrow band imaging in patients with oral lichen planus: a prospective study. *Laryngoscope*. <https://doi.org/10.1002/lary.29035>
- Staničková L, Walderová R, Jančátová D et al (2018) Comparison of narrow band imaging and the Storz Professional Image Enhancement System for detection of laryngeal and hypopharyngeal pathologies. *Eur Arch Otorhinolaryngol* 275:1819–1825. <https://doi.org/10.1007/s00405-018-4987-3>
- Mora F, Carta F, Missale F et al (2020) Laryngeal mid-cord erythroleukoplakias: how to modulate the transoral CO<sub>2</sub> laser excisional biopsy. *Cancers (Basel)*. <https://doi.org/10.3390/cancers12082165>
- Rzepakowska A, Sielska-Badurek E, Cruz R et al (2018) Narrow band imaging versus laryngovideoscopy in precancerous and malignant vocal fold lesions. *Head Neck* 40:927–936. <https://doi.org/10.1002/hed.25047>
- Ni XG, Zhu JQ, Zhang QQ et al (2019) Diagnosis of vocal cord leukoplakia: the role of a novel narrow band imaging endoscopic classification. *Laryngoscope* 129:429–434. <https://doi.org/10.1002/lary.27346>
- Vilaseca I, Valls-Mateus M, Nogués A et al (2017) Usefulness of office examination with narrow band imaging for the diagnosis of head and neck squamous cell carcinoma and follow-up of premalignant lesions. *Head Neck* 39:1854–1863. <https://doi.org/10.1002/hed.24849>
- De Vito A, Meccariello G, Vicini C (2017) Narrow band imaging as screening test for early detection of laryngeal cancer: a prospective study. *Clin Otolaryngol* 42:347–353. <https://doi.org/10.1111/coa.12728>
- Rzepakowska A, Sielska-Badurek E, Żurek M et al (2018) Narrow band imaging for risk stratification of glottic cancer within leukoplakia. *Head Neck* 40:2149–2154. <https://doi.org/10.1002/hed.25201>
- Šifrer R, Rijken JA, Leemans CR et al (2018) Evaluation of vascular features of vocal cords proposed by the European Laryngological Society. *Eur Arch Otorhinolaryngol* 275:147–151. <https://doi.org/10.1007/s00405-017-4791-5>
- Šifrer R, Šereg-Bahar M, Gale N, Hočevnar-Boltežar I (2020) The diagnostic value of perpendicular vascular patterns of vocal cords defined by narrow-band imaging. *Eur Arch Otorhinolaryngol*. <https://doi.org/10.1007/s00405-020-05864-5>
- Fiz I, Mazzola F, Fiz F et al (2017) Impact of close and positive margins in transoral laser microsurgery for Tis-T2 glottic cancer. *Front Oncol* 7:245. <https://doi.org/10.3389/fonc.2017.00245>
- Ivancic R, Iqbal H, deSilva B et al (2018) Current and future management of recurrent respiratory papillomatosis. *Laryngoscope Investig Otolaryngol* 3:22–34. <https://doi.org/10.1002/lio2.132>
- Ochsner MC, Klein AM (2015) The utility of narrow band imaging in the treatment of laryngeal papillomatosis in awake patients. *J Voice* 29:349–351. <https://doi.org/10.1016/j.jvoice.2014.08.002>
- Zeitels SM, Burns JA, Franco RA et al (2004) Office-based treatment of glottal dysplasia and papillomatosis with the 585-nm pulsed dye laser and local anesthesia. *Ann Otol Rhinol Laryngol* 113:265–276. <https://doi.org/10.1177/000348940411300403>

35. Motz KM, Hillel AT (2016) Office-based management of recurrent respiratory papilloma. *Curr Otorhinolaryngol Rep* 4:90–98. <https://doi.org/10.1007/s40136-016-0118-0>
36. Nogués-Sabaté A, Aviles-Jurado FX, Ruiz-Sevilla L et al (2018) Intra and interobserver agreement of narrow band imaging for the detection of head and neck tumors. *Eur Arch Otorhinolaryngol* 275:2349–2354. <https://doi.org/10.1007/s00405-018-5063-8>
37. Zwakenberg MA, Dikkers FG, Wedman J et al (2016) Narrow band imaging improves observer reliability in evaluation of upper aerodigestive tract lesions. *Laryngoscope* 126:2276–2281. <https://doi.org/10.1002/lary.26008>
38. Dias-Silva D, Pimentel-Nunes P, Magalhães J et al (2014) The learning curve for narrow-band imaging in the diagnosis of precancerous gastric lesions by using Web-based video. *GastrointestEndosc* 79:910–920. <https://doi.org/10.1016/j.gie.2013.10.020> (quiz 983-e1, 983.e4)
39. TjonPianGi REA, Halmos GB, Van Hemel BM et al (2012) Narrow band imaging is a new technique in visualization of recurrent respiratory papillomatosis. *Laryngoscope* 122:1826–1830. <https://doi.org/10.1002/lary.23344>
40. Lukes P, Zabrodsky M, Lukesova E et al (2014) The role of NBI HDTV magnifying endoscopy in the prehistologic diagnosis of laryngeal papillomatosis and spinocellular cancer. *Biomed Res Int*. <https://doi.org/10.1155/2014/285486>
41. Dippold S, Becker C, Nusseck M et al (2015) Narrow band imaging: a tool for endoscopic examination of patients with laryngeal papillomatosis. *Ann OtolRhinolLaryngol* 124:886–892. <https://doi.org/10.1177/0003489415590656>
42. Jackowska J, Klimza H, Winiarski P et al (2018) The usefulness of narrow band imaging in the assessment of laryngeal papillomatosis. *PLoS ONE* 13:1–9. <https://doi.org/10.1371/journal.pone.0205554>
43. Imaizumi M, Okano W, Tada Y, Omori K (2012) Surgical treatment of laryngeal papillomatosis using narrow band imaging. *Otolaryngol Head Neck Surg (United States)* 147:522–524. <https://doi.org/10.1177/0194599812448162>
44. Adachi K, Umezaki T, Kiyohara H, Komune S (2015) New technique for laryngomicrosurgery: narrow band imaging-assisted video-laryngomicrosurgery for laryngeal papillomatosis. *J LaryngolOtol* 129:S74–S76. <https://doi.org/10.1017/S0022215114002436>
45. Moccia S, De Momi E, Guarnaschelli M et al (2017) Confident texture-based laryngeal tissue classification for early stage diagnosis support. *J Med Imaging (Bellingham, Wash)* 4:34502. <https://doi.org/10.1117/1.JMI.4.3.034502>
46. Moccia S, Vanone GO, De ME et al (2018) Learning-based classification of informative laryngoscopic frames. *Comput Methods Programs Biomed* 158:21–30. <https://doi.org/10.1016/j.cmpb.2018.01.030>
47. Mori Y, Kudo S-E, Misawa M et al (2018) Real-time use of artificial intelligence in identification of diminutive polyps during colonoscopy: a prospective study. *Ann Intern Med* 169:357–366. <https://doi.org/10.7326/M18-0249>
48. Guo L, Xiao X, Wu C et al (2020) Real-time automated diagnosis of precancerous lesions and early esophageal squamous cell carcinoma using a deep learning model (with videos). *GastrointestEndosc* 91:41–51. <https://doi.org/10.1016/j.gie.2019.08.018>

**Publisher's Note** Springer Nature remains neutral with regard to jurisdictional claims in published maps and institutional affiliations.

## Immunonutrition in head and neck surgery: analysis of peri-operative outcomes

Ascoli, A.#  
**Missale, F.#**  
Giordano, G.G.  
Vallin, A.  
Gradaschi, R.  
Guiddo, E.  
Schenone, G.  
Sukkar, S.G.  
Copello, F.  
Parrinello, G.  
Iandelli, A.  
Peretti, G.  
Marchi, F.







Head Neck  
2023 Feb;45(2):449-463. doi: 10.1002/hed.27270. Epub 2022 Dec 9.

#equally contributed as first authors



Supplementary material:

# Immunonutrition in major oncologic head and neck surgery: Analysis of complications, plasmatic equilibrium, and costs

Alessandro Ascoli MD<sup>1,2</sup>  | Francesco Missale MD<sup>1,3,4</sup>  |  
 Giorgio-Gregory Giordano MD<sup>1,2</sup>  | Alberto Vallin MD<sup>1,2</sup>  |  
 Raffaella Gradaschi, dietician<sup>1,5</sup> | Erica Guidido, dietician<sup>1,5</sup> |  
 Guido Schenone MD<sup>1</sup> | Samir Giuseppe Sukkar MD<sup>1,5</sup> |  
 Francesco Copello, administration<sup>1,6</sup> | Giampiero Parrinello MD<sup>1</sup> |  
 Andrea Iandelli MD<sup>1</sup>  | Giorgio Peretti MD<sup>1,2</sup> | Filippo Marchi MD<sup>1,2</sup> 

<sup>1</sup>IRCCS Ospedale Policlinico San Martino, Genoa, Italy

<sup>2</sup>Department of Surgical Sciences and Integrated Diagnostics (DISC), University of Genova, Genoa, Italy

<sup>3</sup>Department of Molecular and Translational Medicine, University of Brescia, Brescia, Italy

<sup>4</sup>Department of Head & Neck Oncology & Surgery Otorhinolaryngology, Antoni Van Leeuwenhoek, Nederlands Kanker Instituut, Amsterdam, The Netherlands

<sup>5</sup>Dietetics and Clinical Nutrition Unit, University of Genova, Genoa, Italy

<sup>6</sup>Occupational Medicine Unit, IRCCS Ospedale Policlinico San Martino, Genoa, Italy

## Correspondence

Giorgio-Gregory Giordano and Alberto Vallin, IRCCS Ospedale Policlinico San Martino, Unit of Otorhinolaryngology-Head and Neck Surgery, Largo Rosanna Benzi 10, 16132 Genoa, Italy.  
 Email: [giojordan92@outlook.it](mailto:giojordan92@outlook.it) and [a.vallin07@gmail.com](mailto:a.vallin07@gmail.com)

## Abstract

**Background:** Malnutrition, in patients with solid tumors, is associated with a worse clinical outcome and about 40% of patients affected by head and neck cancers (HNC) are malnourished at the time of cancer diagnosis. We investigated the potential benefit of a standardized immunonutritional protocol (INP) to patients with HNC receiving major ablative surgery.

**Methods:** An observational study was conducted enrolling 199 patients: 50 treated with the INP and 149 with standard enteral nutrition. Complication rates, need for medications, and costs were considered as outcomes.

**Results:** INP played a protective role in development of major surgical complications (OR 0.23,  $p = 0.023$ ), albumin administration (RR 0.38,  $p = 0.018$ ), and antibiotic duration ( $p < 0.001$ ) and is cost-effective in patients with moderate or severe malnutrition (−6083€ and −11 988€,  $p < 0.05$ ).

**Conclusions:** Our study supports the utility of INP, and accurate nutritional screening can help to identify malnourished patients who would receive the most benefits from this protocol.

## KEYWORDS

albumin, complications, cost analysis, head and neck cancer, immunonutrition, surgery

## 1 | INTRODUCTION

Head and neck cancers (HNC) represent the seventh cause of cancer-related death globally and 4% of solid

cancers.<sup>1,2</sup> The most common subsite is the oral cavity (41%), followed by the larynx (24%) and pharynx (22%).<sup>2</sup> Moreover, advanced head and neck cancers are associated with chewing and swallowing impairment and worsening nutrition status, thus causing malnutrition. Previous studies have shown that about 40% of patients with HNC are malnourished at the time of cancer diagnosis<sup>3</sup> and 25%–

Alessandro Ascoli and Francesco Missale contributed equally to this study and are first authors.

50% had involuntary weight loss.<sup>4</sup> According to the World Health Organization, malnutrition refers to deficiencies, excesses, or imbalances in a person's intake of energy and nutrients (<https://www.who.int/news-room/questions-and-answers/item/malnutrition>).

There are three main reasons for weight loss. First, tumors arising in the oral cavity, oropharynx, hypopharynx, and larynx can lead to dysphagia due to organ dysfunction.<sup>3-5</sup> Second, the cancer secretes cytokines, such as TNF-alpha and interleukins, which increase the catabolic processes and contribute to the loss of muscle mass; lastly, pre-existing chronic malnutrition, associated with alcohol and tobacco consumption, can worsen an already critical malnutrition status.<sup>6</sup> Third, treatment intensity, including surgery, radiotherapy, chemotherapy, or a combination of these, can further aggravate<sup>7</sup> the malnutrition already present at diagnosis of HNC.<sup>3,4,8,9</sup> It is also well established that nutritional status can significantly influence the clinical and therapeutic course of different diseases, especially for patients affected by cancer.<sup>10-16</sup>

Malnutrition is associated with a worse clinical course due to a higher risk of complications, significant toxicity, reduced treatment compliance, and a worse quality of life.<sup>7</sup>

Adequate nutritional support is crucial in reducing the risk of complications during hospitalization.<sup>8,17-20</sup>

Malnutrition compromises the immune system of patients, thus altering the response to pathogens and increasing rates of infection.<sup>21-23</sup> The insufficient caloric intake and specific macronutrients and/or micronutrients alters the function of nonspecific defenses and acquired immunity such as the antibody-mediated response.<sup>24,25</sup>

Moreover, the recent literature has suggested that peri-operative nutritional supplements with immunonutritional additives can positively modulate the immune and inflammatory response, both *in vitro* and *in vivo*.<sup>26-28</sup>

Since April 2019, in our center a specific intervention protocol was implemented to improve the nutritional status of patients undergoing major head and neck surgery requiring postoperative enteral feeding. This retrospective case-control study aimed to investigate the potential benefit of applying the immunonutritional protocol (INP), compared to a historical cohort, investigating as endpoints complications and support needed during hospitalization, such as need for blood units and/or albumin. A cost analysis was also carried out.

## 2 | MATERIALS AND METHODS

### 2.1 | Study design

An observational retrospective study was conducted enrolling patients treated from 2012 to 2021 in a single

Institution, the Unit of Otorhinolaryngology-Head and Neck Surgery of Ospedale Policlinico San Martino, Genoa, Italy. It was approved by the Ethics Committee under the identification number "2021-133 ImmunoHNC," in accordance with the Declaration of Helsinki.

Patients with neoplasms of the upper aerodigestive tract who underwent major ablative surgery were enrolled. Exclusion criteria were distant metastatic disease, pregnancy, final histopathologic report confirming nonmalignant neoplasia, and age younger than 18 years. Of the 292 patients initially selected, 199 met the inclusion criteria and were included. All patients had been submitted to surgery after multidisciplinary team (MDT) discussion and preoperative counseling between head and neck surgeons, nutritionists, dietologists, geriatrics, radiation, and medical oncologists. The follow-up time in the present cohort was 30 days, exclusively to evaluate hospital re-admission.

The entire cohort was divided into two groups: the "study group" included patients treated since April 2019 when a specific immunonutritional protocol (INP) was implemented in clinical practice of the Unit; the "control group" (CG) received standard postoperative nutrition, including a historical cohort of patients, from 2012 to March 2019. The control group did not receive any nutritional examination or additional nutritional support preoperatively. The postoperative administration rate, volume, and type of product used, for both enteral nutrition (NET) and parenteral nutrition (NPT), was managed subjectively by the Otolaryngologist or dietician on duty. All products used in both groups are shown in Table S2, Supporting Information.

### 2.2 | Diagnostic workup

Preoperative workup was standardized for all patients and consisted of endoscopic, imaging, and nutritional status evaluation. The endoscopic workup included transnasal panendoscopy in white light (WL) and narrow-band imaging (NBI, Olympus Medical System Corporation, Tokyo, Japan) to better define the superficial extension of the lesion.<sup>29,30</sup> Computed tomography (CT) or magnetic resonance (MR) and positron emission tomography (PET) were used for tumor staging. Neck ultrasound (US) was routinely performed with or without fine-needle aspiration cytology. The radiologic workup allowed the meticulous assessment of tumor extension.<sup>31</sup> Tumors were classified according to the 8th Edition of the AJCC UICC TNM staging system.<sup>32</sup> The anesthesiologist assessed patients before surgery. The ASA scores (The American Society of Anesthesiologists classification

of physical condition) were transcribed and included in the statistical analysis.<sup>33</sup>

## 2.3 | Study group protocol

### 2.3.1 | Specific dietological evaluation

All patients were initially evaluated using the Nutritional Risk Screening 2002 (NRS-2002) recommended by ESPEN (European Society for Clinical Nutrition and Metabolism).<sup>34</sup> The nutritional screening consisted of evaluation of the baseline status by measuring morphometric parameters such as weight, height, BMI (according to World Health Organization Expert Consultation), and waist and arms circumferences; a recent occurrence of weight loss and including administration of the Nutritional Risk Screening 2002 (NRS-2002) aimed at predicting worsening of nutritional status.

A detailed nutritional intervention was planned if the NRS final score was  $\geq 3$ . A personalized schedule was then established with the correct food consistency characteristics according to “the IDDSI framework document” (International Dysphagia Diet Standardization Initiative)<sup>35</sup> to cover the patient’s calorie/protein requirements. This dietary plan considered: the neoplasm (location, stage); nutritional status of the patient, comorbidities, symptoms that may limit nutrition, eating habits (preferences, aversions), and psychological and social factors of the patient.

The dietary pattern was tailored to the patient’s needs. Specifically, it takes into account the frequency, distribution, and consistency of meals, the quality of the food introduced, giving preference to the most caloric foods, and the amount of specific macronutrients and micronutrients (total calories, grams of protein, lipids, carbohydrates, simple sugars and their percentages of total calories, grams of fiber, plus the calculation of other disease-specific micronutrients).

Specific oral supplements such as whole proteins, BCCA amino acids, and maltodextrins were prescribed when the patient was affected by comorbidities such as diabetes, kidney failure, or liver disease.

If the oral intake was not sufficient, the surgeon and nutritionist advocate placing a nasogastric tube or a percutaneous gastrostomy. Lastly, based on the former evaluation, the dietologist estimated the risk of nutrition worsening considering the chosen treatment and stage of the disease. In addition, the following information were collected: dietary history quantifying the intake of foods, nutrients, and physical activity in a typical day; dietary food impairment detecting the abuse of medications, alcohol, caffeine, and supplements; lastly, the socio-sanitary condition.

The patient was entrusted to the nutritionist and immediately supported by oral diet or enteral diet supplements until the week before the surgery; then, the specific INP with oral impact was administered. Nonmalnourished patients were supported the week before surgery with the INP.

### 2.3.2 | Immunonutritional protocol

The INP started 1 week before surgery. It consists of two or three flasks of Oral IMPACT<sup>®</sup> (Nestle Health Science, Vevey, Switzerland) every day at home (depending on nutritional status and volume of preserved oral diet). IMPACT<sup>®</sup> is an oral nutraceutical that provides 1.0 kcal/ml when reconstituted with water (74 g powder plus 250 ml water; content 16.7 g protein; 8.3 g fat; 40.2 g carbohydrates; and total energy 302.8 kcal). This product is enriched with x-3 fatty acids, arginine, ribonucleotides, and soluble fiber (3.74 g arginine; 1.0 g x-3 fatty acids; 0.39 g ribonucleotides; and 3 g soluble guar fibers). All patients took the dose of Impact prescribed. In addition, nondiabetic patients received the following the evening before and 3 h before surgery: 100 and 50 g of maltodextrins in 500 ml of water to reduce insulin resistance in the immediate postoperative course.<sup>36–39</sup>

### 2.3.3 | Nutritional support during hospitalization

After surgery, we applied the enhanced recovery after surgery (ERAS) protocol guidelines.<sup>40</sup> The specific nutrition started 12 h after surgery. We have adopted a combined enteral (Impact enteral and Nutrison Energy, ©Nestlé, Vevey, Suisse) and parenteral diet (Olimel N9E, ©Baxter, Rome, Italy) in the first 2 days to overcome the caloric and protein deficit and allow the NET to gradually avoid episodes of reflux or vomiting that could compromise the operation and be better tolerated by the patient. The dietary support ensures sufficient caloric and protein intake in the immediate postoperative period.<sup>41</sup> The infusion speed was 30 ml/h and progressively increased by 20–30 ml/h every 24 h until the daily nutritional goal (31.0 total kcal/kg; 25.0 nonprotein kcal/kg; 1.5 g protein/kg) was reached.

Parenteral nutrition was stopped, and exclusive enteral nutrition at full speed with three enteral Impacts on Day 3, two enteral Impacts and a Nutrison energy on Day 4, and finally one enteral Impact and 2 Nutrison energy on Day 5 continued until the patient resumed oral feeding at 12–14 days after surgery (Table S1).

The dietitians checked patients’ nutritional status twice a week until discharge, adjusting the distribution of



calories or proteins according to the patient's needs. Patients were followed in the dietician's office throughout adjuvant treatment or until an autonomous and sufficient diet was achieved.

## 2.4 | Endpoints and protocol effectiveness

Blood parameters of the entire cohort were collected to assess preoperative and postoperative hemoglobin (Hb), mean corpuscular volume, mean corpuscular Hb, mean corpuscular Hb concentration, red blood cell distribution width, erythrocytes, glucose, serum albumin (ALB), leukocytes, neutrophils, lymphocytes, platelets, transferrin, ferritin, TSH reflex, INR, fibrinogen, prothrombin, and D-dimer.<sup>41,42</sup>

Blood samples were drawn before surgery, the first postoperative day, and every 48 h until the patient resumed feeding on a creamy diet by natural means.

We evaluated the incidence of surgical major (requiring surgical reintervention) and minor complications (manageable with medications), number of blood units transfused, number of ALB vials, duration of antibiotic therapy, re-admission within 30 days from discharge, and length of hospital stay (LOS) defined as total nights spent in the hospital.

Blood parameters were compared in both groups to assess the effectiveness of treatment and identify any factor that could influence the perioperative course. A cost analysis was also performed.

## 2.5 | Cost estimation

The cost analysis was conducted according to the financial budget data of 2019 before the Covid-19 pandemic.

Data were calculated on direct costs (human resources, material, and diagnostics for inpatient days). The average cost/hour of the operating room is €350.51, which includes surgeons, anesthesiologists, nurses, and the rest of the staff, as well as general consumables.

The daily cost of admission to the ward is €453.31 and all parameters taken into account for cost analysis, including nutritional products, are reported in Table S2.

## 2.6 | Statistical analysis

Standard descriptive statistic was used to summarize data. For group comparisons in qualitative variables, Fisher's exact test was applied, while for quantitative ones the Wilcoxon test was used. Associations between

covariates and binary outcomes were investigated by univariable and multivariable logistic regression models; association with outcomes with Poisson's regression models. Cost analysis was performed with univariable and multivariable linear models with the entire cost imputable to each perioperative treatment as a dependent variable.

Estimates were reported as odds ratios (OR) or rate ratios (RR) with 95% confidence interval (95% CI). Two-tailed tests with a significance level of 5% were applied in all analyses. R (version 4.0.2) was used for statistical analysis including the use of the following packages: rms, Hmisc, MASS, ggplot2, mice, visdat, finalfit, ggpubr, car, and fitdistrplus.

## 3 | RESULTS

### 3.1 | Demographics and clinical features

During the recruitment time from 2012 to December 2020, following the inclusion and exclusion criteria, 199 patients were identified for the current study: 149 in the CG and 50 in the INP.

In the entire cohort, the mean age was 64.6 years (range 27–89), 153 were males (76.9%) and 46 females (23.1%); the mean body mass index (BMI) was 24.6 kg/m<sup>2</sup> (range 14.3–41.1).

The preoperative nutritional status was judged as compromised in 89 patients (44.7%), and in 59 (29.6%) was mild, moderate in 22 (11.1%), and severe in 8 (4.0%); 77 patients (38.7%) also reported dysphagia evaluated with IDDSI. The ASA score was >II in 90.5% of cases, III in 55 patients (27.6%), and IV in 7 patients (3.5%). In addition, 23 patients (11.5%) had diabetes, of whom 16 (8% insulin-dependent). Detailed clinical features are reported in Table 1.

### 3.2 | Treatments and tumor features

The primary tumor was located in the larynx in 118 cases (59.3%), oral cavity in 50 (25%), hypopharynx in 24 (12.1%), and oropharynx or nasal cavity in 7 (3.5%). Surgical procedures included total laryngectomy in 92 cases (46.2%), open partial laryngectomy in 26 (18.1%), partial glossectomy in 23 (11.6%), transoral laser microsurgery 14 (7.0%), mandibulectomy in 14 (7.0%), maxillectomy in 8 (4.0%), or other composite resections in 12 (6.0%). A total of 179 patients (89.9%) received unilateral or bilateral neck dissection, 55 patients underwent free flap reconstruction (55 patients, 27.6%), and 46 pedicle flap reconstruction (23.1%). Of note, 34 patients

TABLE 1 Clinical features of the entire cohort and the control and study groups

	All (N = 199)	CG (N = 149)	INP (N = 50)	p-value
<b>Age</b>				
Mean (SD)	64.6 (10.5)	64.6 (10.5)	64.4 (10.6)	0.882
Median (min, max)	65.0 (27.0, 89.0)	65.0 (27.0, 89.0)	64.5 (42.0, 88.0)	
<b>Sex</b>				
F	46 (23.1%)	35 (23.5%)	11 (22.0%)	1
M	153 (76.9%)	114 (76.5%)	39 (78.0%)	
<b>Preoperative RT</b>				
No	165 (82.9%)	125 (83.9%)	40 (80.0%)	0.521
Yes	34 (17.1%)	24 (16.1%)	10 (20.0%)	
<b>Site primary tumor</b>				
Larynx	118 (59.3%)	100 (67.1%)	18 (36.0%)	<0.001
Hypopharynx	24 (12.1%)	16 (10.7%)	8 (16.0%)	
Oral cavity	50 (25.1%)	32 (21.5%)	18 (36.0%)	
Oropharynx-nose	7 (3.5%)	1 (0.7%)	6 (12.0%)	
<b>Neck dissection</b>				
No	20 (10.1%)	17 (11.4%)	3 (6.0%)	0.415
Yes	179 (89.9%)	132 (88.6%)	47 (94.0%)	
<b>Reconstruction</b>				
No	98 (49.2%)	81 (54.4%)	17 (34.0%)	<0.001
Yes, free flap	55 (27.6%)	30 (20.1%)	25 (50.0%)	
Yes, pedicled flap	46 (23.1%)	38 (25.5%)	8 (16.0%)	
<b>pT category</b>				
pTis-T1	12 (6.0%)	10 (6.7%)	2 (4.0%)	0.783
pT2	30 (15.1%)	22 (14.8%)	8 (16.0%)	
pT3	62 (31.2%)	44 (29.5%)	18 (36.0%)	
pT4	95 (47.7%)	73 (49.0%)	22 (44.0%)	
<b>pN category</b>				
N0	114 (57.3%)	86 (57.7%)	28 (56.0%)	0.0075
pN1	23 (11.6%)	16 (10.7%)	7 (14.0%)	
pN2	49 (24.6%)	42 (28.2%)	7 (14.0%)	
pN3	13 (6.5%)	5 (3.4%)	8 (16.0%)	
<b>BMI</b>				
Mean (SD)	24.6 (4.26)	24.6 (4.11)	24.6 (4.74)	0.999
Median (min, max)	24.2 (14.3, 41.1)	24.3 (16.3, 41.1)	23.8 (14.3, 37.8)	
<b>Preoperative dysphagia</b>				
0	122 (61.3%)	94 (63.1%)	28 (56.0%)	0.167
1	71 (35.7%)	49 (32.9%)	22 (44.0%)	
2	6 (3.0%)	6 (4.0%)	0 (0%)	
<b>Nutritional status</b>				
Normal	110 (55.3%)	85 (57.0%)	25 (50.0%)	0.81
Mild malnutrition	59 (29.6%)	42 (28.2%)	17 (34.0%)	
Moderate malnutrition	22 (11.1%)	16 (10.7%)	6 (12.0%)	
Severe malnutrition	8 (4.0%)	6 (4.0%)	2 (4.0%)	

(Continues)

TABLE 1 (Continued)

	All (N = 199)	CG (N = 149)	INP (N = 50)	p-value
Diabetes				
No	176 (88.4%)	132 (88.6%)	44 (88.0%)	0.52
Yes, insulin dependent	16 (8.0%)	13 (8.7%)	3 (6.0%)	
Yes, oral hypoglycemic therapy	7 (3.5%)	4 (2.7%)	3 (6.0%)	
ASA				
1	19 (9.5%)	11 (7.4%)	8 (16.0%)	0.0245
2	118 (59.3%)	84 (56.4%)	34 (68.0%)	
3	55 (27.6%)	47 (31.5%)	8 (16.0%)	
4	7 (3.5%)	7 (4.7%)	0 (0%)	

TABLE 2 Outcomes in the entire cohort and the control and study groups

	Whole cohort (N = 199)	CG (N = 149)	IN (N = 50)	p-value
Medical complications				
No	131 (65.8%)	99 (66.4%)	32 (64.0%)	0.863
Yes	68 (34.2%)	50 (33.6%)	18 (36.0%)	
Surgical complications				
No	131 (65.8%)	98 (65.8%)	33 (66.0%)	1
Yes	68 (34.2%)	51 (34.2%)	17 (34.0%)	
Major surgical complications				
No	166 (83.4%)	119 (79.9%)	47 (94.0%)	0.0262
Yes	33 (16.6%)	30 (20.1%)	3 (6.0%)	
Minor surgical complications				
No	158 (79.4%)	123 (82.6%)	35 (70.0%)	0.0696
Yes	41 (20.6%)	26 (17.4%)	15 (30.0%)	
Antibiotics duration (days)				
Mean (SD)	16.3 (10.4)	18.1 (11.1)	10.8 (5.05)	<0.001
Median (min, max)	14.0 (0, 114)	16.0 (6.00, 114)	9.00 (0, 26.0)	
Blood transfusion				
No	171 (85.9%)	132 (88.6%)	39 (78.0%)	0.0971
At least one	28 (14.1%)	17 (11.4%)	11 (22.0%)	
Albumin reintegration				
No	142 (71.4%)	103 (69.1%)	39 (78.0%)	0.28
At least one time	57 (28.6%)	46 (30.9%)	11 (22.0%)	
Duration of hospitalization (days)				
Mean (SD)	22.6 (12.7)	22.0 (12.7)	24.2 (12.7)	0.296
Median (min, max)	19.0 (6.00, 114)	19.0 (6.00, 114)	19.5 (6.00, 55.0)	
New re-admission				
No	183 (92.0%)	136 (91.3%)	47 (94.0%)	0.765
Yes	16 (8.0%)	13 (8.7%)	3 (6.0%)	

(17.1%) had previously received head and neck radiation. Full details of the clinical and pathological characteristics are reported in Table 1. Among INP and CG, there were

differences in terms of primary tumor site ( $p < 0.001$ ), choice of reconstruction ( $p < 0.001$ ), and ASA score ( $p = 0.0245$ ), whereas the distribution of age, sex,

previous RT, need for neck dissection, BMI, preoperative dysphagia, nutritional status, and prevalence of diabetes were similar ( $p > 0.05$ ), as reported in Table 1.

### 3.3 | Outcomes of interest and comparisons between study and control groups

The main outcomes considered and univariable comparisons between groups are shown in Table 2. Medical complications (including cardiovascular disorders, infectious complications, broncho-pulmonary disorders, organ failure, neuropsychiatric disorders, and others) were observed in 68 patients (34.2%) with no significant differences between INP and CG (36.0% and 33.6%, respectively,  $p = 0.863$ ), similar to surgical complications (34.0% and 34.2% respectively,  $p = 1$ ). In all, 33 patients (16.6%) experienced major surgical complications in the entire cohort. In INP, we observed a significant reduction of major surgical complications (6.0% vs. 20.1%,  $p = 0.026$ ). The median duration of antibiotics was 14.0 days (range 0–114 days), which was significantly lower in the study group (median 9 days vs. 16 days,  $p < 0.001$ ).

At least one blood transfusion was needed in 28 patients (14.1%) with no significant differences between groups (22.0% vs. 11.4%,  $p = 0.097$ ). ALB reintegration was required in 57 patients (28.6%) without significant differences (22.0% vs. 30.9%,  $p = 0.28$ ). However, the variable defined as the number of ALB vials used has an asymmetric negative binomial distribution (Figure S1), and was thus studied with negative binomial regression models.

The median LOS was 19 days (range 6–114) and no significant differences were observed between groups (19.5 vs. 19.0 days,  $p = 0.296$ ) similar to re-admission to hospital within 30 days from the discharge date (6.0% vs. 8.7%,  $p = 0.765$ ).

### 3.4 | Higher ASA score (The American Society of Anesthesiologists classification of physical condition) and malnutrition status are associated with medical complications

Although no significant differences were observed between groups, baseline clinicopathological features were studied to investigate associations with postoperative medical complications. The univariate logistic regression analysis showed that the presence of preoperative dysphagia (OR 2.01, 95% CI 1.09–3.72,  $p = 0.026$ ), severe

malnutritional status (OR 7.65, 95% CI 1.66–54.14,  $p = 0.016$ ), and ASA score  $\geq 2$  ( $p < 0.05$ ) were associated with a higher risk of medical complications.

### 3.5 | Immunonutritional protocol is a protective factor for development of major surgical complications

The univariable logistic regression analysis, considering as outcome the occurrence of major surgical complications, confirmed that the INP was associated with a lower risk (OR 0.25, 95% CI 0.06–0.76,  $p = 0.029$ ), and no other variables were linked to this outcome in univariable analysis. A multivariable logistic model adjusting for the effect of relevant clinical covariates, as the need for a reconstruction, tumor site, ASA score, and group of intervention, confirmed the independent association between INP and a lower risk of major surgical complications (OR 0.20, 95% CI 0.05–0.74,  $p = 0.015$ ) (Figure 1A).

### 3.6 | Immunonutritional protocol is associated with less need for postoperative albumin reintegration

The association between clinical baseline covariates and number of vials of ALB used in the postoperative period, as the latter were distributed as a negative binomial distribution, was studied with negative binomial regression models. The univariable analysis showed that a higher preoperative ALB (RR 0.59, 95% CI 0.37–0.92,  $p = 0.29$ ), Hb value (RR 0.75, 95% CI 0.61–0.90,  $p = 0.001$ ), lymphocytes count (RR 0.74, 95% CI 0.55–0.96,  $p = 0.033$ ), and the intervention group submitted to INP (RR 0.54, 95% CI 0.28–1.09,  $p = 0.081$ ) were associated with a lower number of ALB vials used. The need for a free flap (RR 2.38, 95% CI 1.15–5.04,  $p = 0.022$ ) or pedicled (RR 3.93, 95% CI 1.89–8.50,  $p < 0.001$ ) reconstruction ( $p < 0.05$ ) was also associated with a higher number of ALB vials infused (Table S3). The multivariable analysis, adjusted for tumor site and reconstruction, confirmed the protective effect of the INP (RR 0.37,  $p = 0.021$ ) and the risk effects of the need for a flap ( $p < 0.05$ ), as shown in Figure 1B,C.

### 3.7 | Plasmatic homeostasis of albumin and hemoglobin

ALB and Hb were studied over time to understand if their levels were associated with different patient

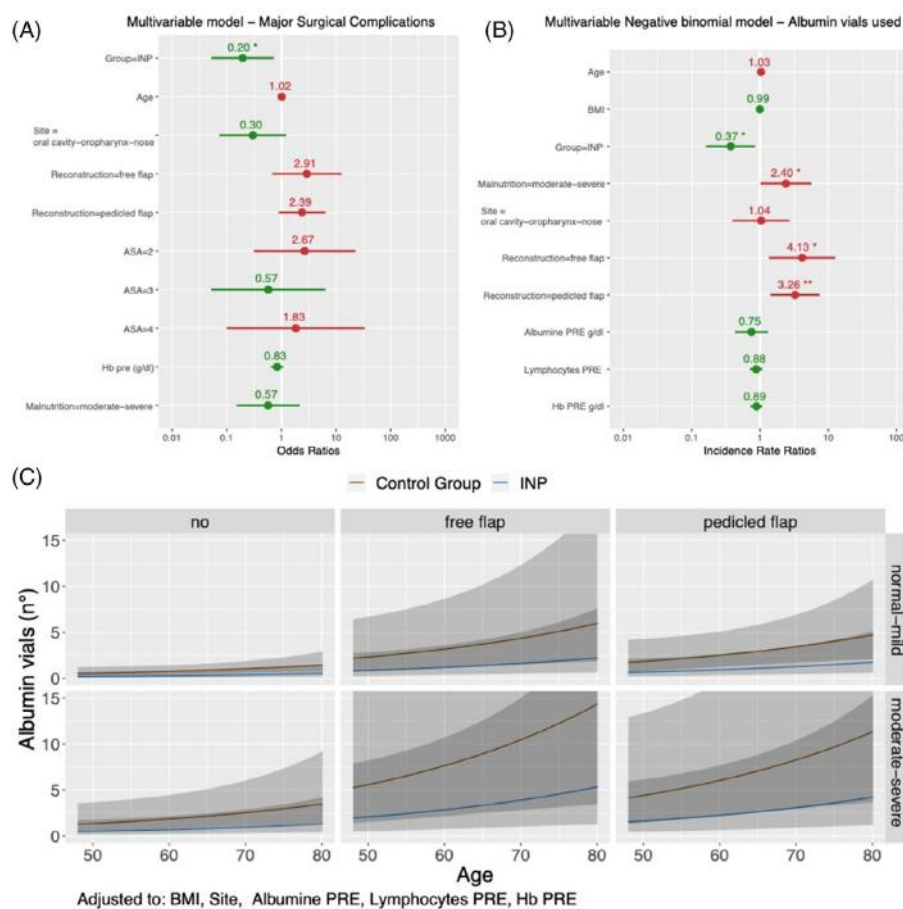


FIGURE 1 Forrest plots showing the partial effect, in terms of odds ratios and 95% CI of each covariate on the multivariable logistic model including as independent variable the occurrence of major surgical complications (A) or the negative binomial model predicting the number of vials of albumin used (B). Partial effect plots derived from the multivariable negative binomial model for the prediction of vials of albumin used showing the combined effect with 95% CI (gray bands) of reconstruction choice and malnutrition status (C) [Color figure can be viewed at [wileyonlinelibrary.com](http://wileyonlinelibrary.com)]

features and treatment policy. We observed in both groups a significant decrease of ALB in the first postoperative day compared to the preoperative value. Adjusting for malnutrition, tumor site, and reconstruction choice, on Day +5 a significant increase was seen (compared to Day +1), and, only in INP, a further improvement with stabilization on Day +7 (Figure 2A–C). Furthermore, preoperative ALB values were associated with an increased ALB level along the postoperative course (Figure 2D). We observed a significant Hb decrease postoperatively. Interestingly, a higher preoperative value was protective. Multivariate analysis demonstrated that belonging to the INP, in moderately and severely malnourished patients, conferred a significant increase in Hb values (Figure 3).

### 3.8 | Immunonutritional protocol is associated with lower costs in patients with malnutrition

The estimated median cost for each patient in the entire cohort was 12455€ (IQR 10258–16071€; min-max 3831–57845). The most relevant expenses contributing to the entire amount were LOS (72.44%), OR (23.63%), antibiotics (1.16%), ALB use (0.80%), IMPACT use (0.79%), and parenteral feeding (0.68%).

By univariable linear regression, for the estimation of the entire cost, a significant association was found with tumor site, with hypopharynx (+3881€,  $p = 0.008$ ), need for neck dissection (+3776€,  $p = 0.015$ ), severe malnutritional status (+8142€,  $p = 0.001$ ), occurrence of major

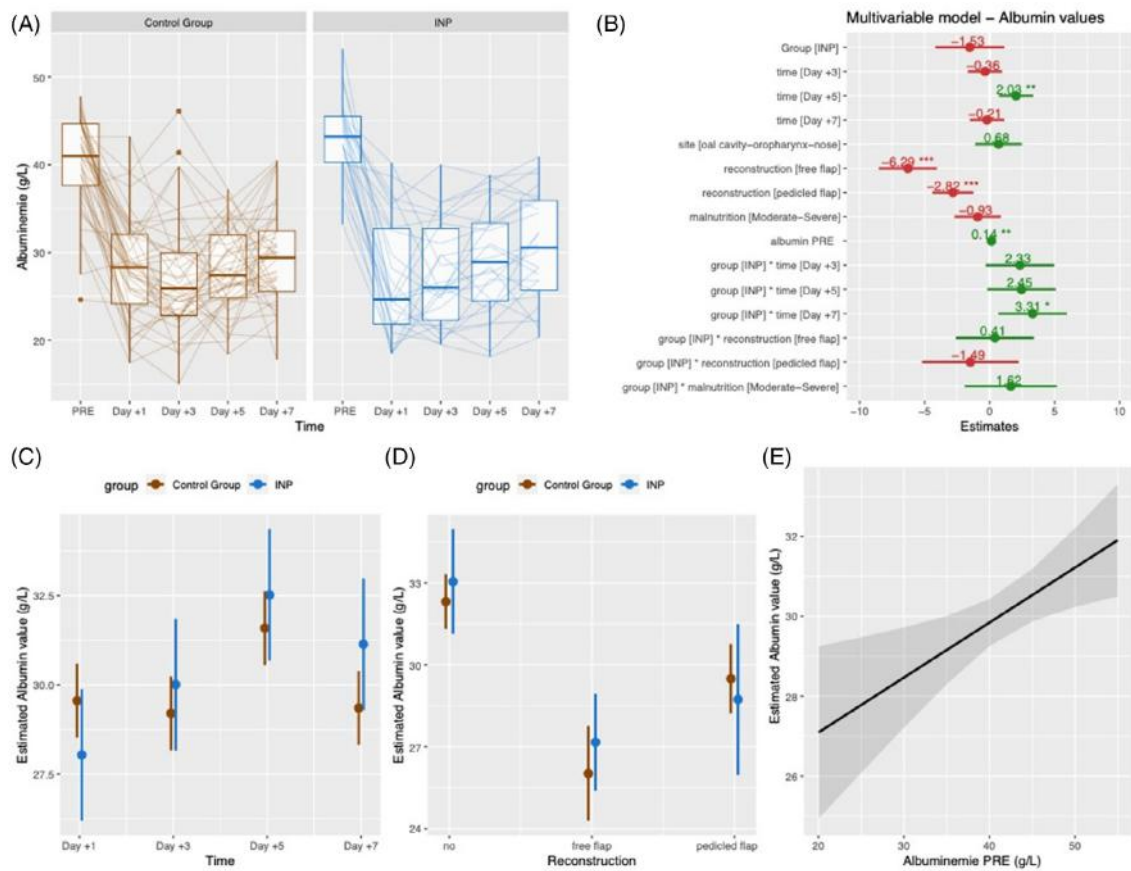


FIGURE 2 Box plots showing the distribution of preoperative blood albumin values and during hospitalization; lines connect the values for individual patients (A). Forrest plots showing the partial effect, in terms of odds ratios and 95% CI of each covariate on the multivariable linear model including blood albumin values as the independent variable (B). Partial effect plots, derived from the multivariable linear model for the prediction of blood albumin values, showing the partial effect of time and treatment (C) and preoperative blood albuminemia (D) [Color figure can be viewed at [wileyonlinelibrary.com](http://wileyonlinelibrary.com)]

(+5504€,  $p < 0.001$ ) or minor (+303€,  $p = 0.001$ ) surgical or medical (+3902€,  $p < 0.001$ ) complications, and the execution of a tracheotomy (+2670€,  $p = 0.042$ ) were all significant risk factors. In multivariable analysis, belonging to the INP was associated with higher costs only in patients without malnutrition (+2627€,  $p < 0.05$ ) but was cost-effective in patients with severe malnutrition (−11988€,  $p < 0.05$ ) (Figure 4).

#### 4 | DISCUSSION

It is known that 35%–60% of patients affected by HNSCC suffer from malnutrition. Several studies have found significant associations between malnutrition indicators, such as weight loss, cachexia, and a worse perioperative

and survival outcomes.<sup>3,43–45</sup> Moreover, malnutritional status is related to impaired immune system function, as cell-mediated immunity and occurrence of immunosuppression, thus justifying the poorer oncological outcomes observed for malnourished patients.<sup>46–48</sup> This observation supports the rationale of active nutritional interventions in patients affected by HNSCC and the investigation of alternative medical interventions, such as immune-enhancing nutrients, whose effectiveness in this specific oncological setting is not yet demonstrated.<sup>9,43</sup>

Oral Impact (Nestle Health Science, Vevey, Switzerland) is an oral nutraceutical enriched with x-3 fatty acids, arginine, ribonucleotides, and soluble fiber. Arginine is a semi-essential amino acid that positively affects immune function and reparative collagen synthesis. It plays an essential role in T- and B-cell immunity



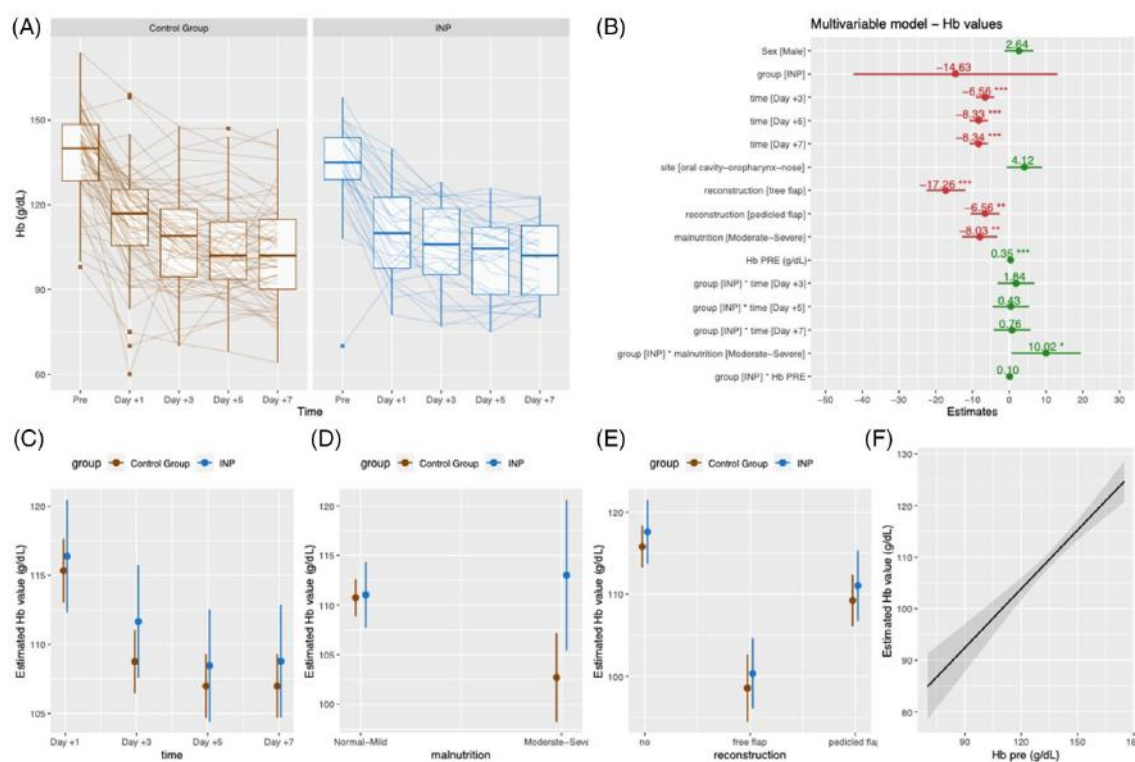


FIGURE 3 Box plots showing the distribution of preoperative blood hemoglobin values and during hospitalization; lines connect the values for individual patients (A). Forrest plots showing the partial effect, in terms of odds ratios and 95% CI of each covariate on the multivariable linear model including blood hemoglobin as an independent variable (B). Partial effect plots, derived from the multivariable linear model for the prediction of blood hemoglobin values, showing the partial effect of time and treatment group (C), malnutrition status and treatment group (D), or preoperative blood hemoglobin value (E) [Color figure can be viewed at [wileyonlinelibrary.com](http://wileyonlinelibrary.com)]

and nitric oxide production. The nucleotides are derived from RNA and provide the necessary substrates for DNA and RNA formation. The omega-3 fatty acids have an anti-inflammatory function.<sup>39,49–51</sup>

Trying to understand if optimizing perioperative nutritional status in HNSCC could be beneficial, we studied a cohort of 199 patients affected by HNSCC and submitted to major surgery. A historical cohort of 149 patients was compared to a group of 50 patients treated after establishing a dedicated nutritional protocol with an active role of the nutritionist and the use of immunonutrition products, including IMPACT®, for enteral feeding. Univariable and multivariable analysis showed that the INP experienced a significantly lower rate of major complications and lower need for ALB reintegration. Moreover, in case of moderate or severe malnutritional status, the protocol was cost-effective.

Giannotti et al. conducted one of the first prospective randomized clinical trials, testing the potential benefits of perioperative immunonutrition in the context of oncological gastrointestinal surgery<sup>27</sup>; enrolling 305 patients with

preoperative weight loss <10%, the authors show that supplemented diet significantly improved perioperative outcomes as infection rates and length of hospital stay.<sup>27</sup> These results were the cornerstone for many other studies. Evidence from a systematic review and meta-analysis support the benefits of immunonutrition in oncologic gastrointestinal surgery to prevent complications and reduce length of hospital stay.<sup>52,53</sup> Thus, the current guidelines of the American Society of Parenteral Nutrition recommend immunonutrition for patients undergoing major abdominal surgery.<sup>54</sup>

To the best of our knowledge, the study by Riso et al.<sup>41</sup> was the first attempt to demonstrate the benefits of postoperative immunonutrition in patients undergoing surgery for HNSCC. Analyzing a cohort of 44 patients, this study concluded that an arginine-rich diet immediately after surgery can improve immunological status in terms of CD3 and CD4 T cells counts and, in malnourished patients, can reduce the rate of complications and the length of hospital stay.<sup>41</sup>

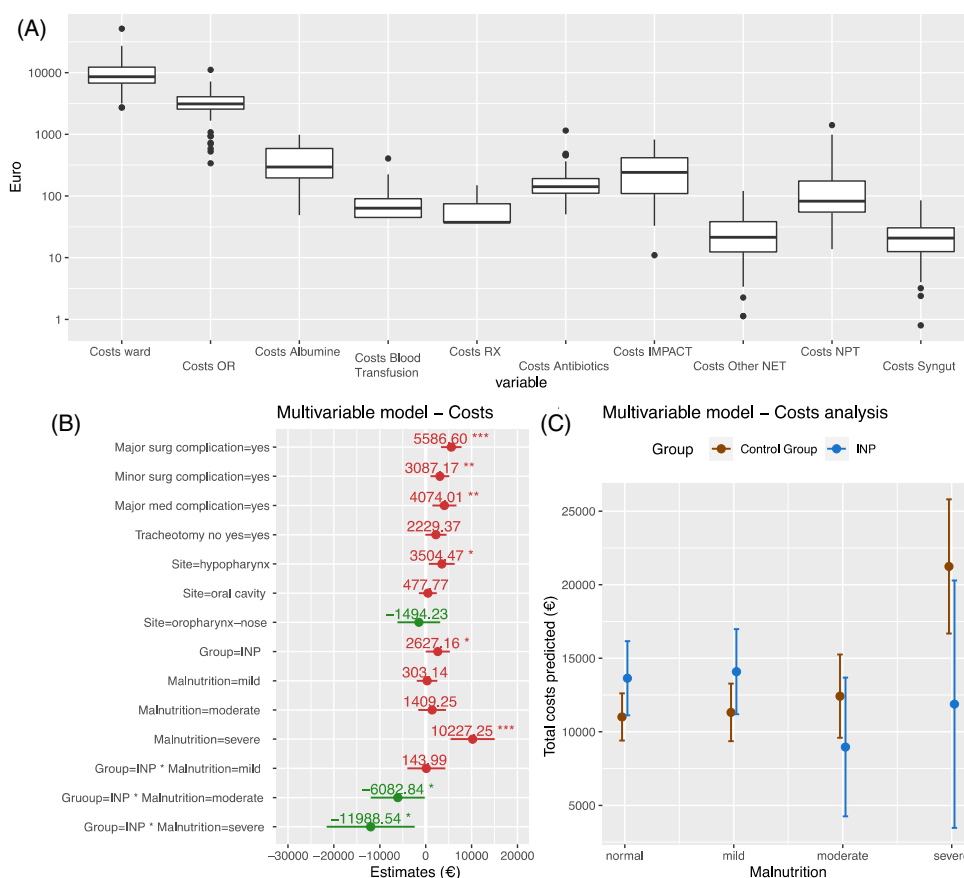


**FIGURE 4** Box plots showing the distribution of individual costs ascribable to each parameter shown on log<sub>10</sub> scale (A). Forrest plot of the multivariable linear model for the entire cost estimation, showing the estimated cost with 95% CI compared to reference levels and adjusted for the other covariates (B). Partial effect plot derived from the multivariable linear model showing the combined effect of treatment group and malnutrition status and the effect of the significant interaction between these two variables, with a cost-effectiveness of INP for moderate to severely malnourished patients (C) [Color figure can be viewed at [wileyonlinelibrary.com](http://wileyonlinelibrary.com)]

Several clinical trials have investigated different nutritional supplements and dosing schedules in patients with HNSCC in the last 10 years, but methodological differences hamper comparisons and robust conclusions. In addition, the diversity of interventions, small number of patients, and type of surgery did not permit a precise evaluation of the efficacy of the intervention.<sup>55</sup> However, the critical role of arginine, omega-3 fatty acids, and ribonucleotides as immunonutrition supplements was shown to boost the immune response.<sup>9,56</sup>

#### 4.1 | Surgical complications

The investigated protocol, including perioperative immunonutrition, succeeded in lowering the risk of surgical

complications, defined as complications at the surgical site requiring further surgical intervention. (see Table S4 for the details on the types of complications). This was confirmed by multivariate logistic analysis, adjusted for relevant clinical features, including tumor site and reconstruction, as covariates in all models, showing the independent protective effect of INP for major surgical complications (OR 0.20,  $p = 0.015$ ). Although surgical complications might differ in terms of occurrence and management according the head and neck subsite, we overcame this confounding variable with multivariate regression.

Of note, no association with overall surgical complications was observed; therefore, the improved immunonutritional status could have prevented the need for re-exploration, limiting the severity of local complications

and preventing morbidity and costs of new surgical procedures.

The results of the study of Rowan et al.<sup>57</sup> and of a systematic review and meta-analysis<sup>58</sup> agree with our observation, showing that for patients undergoing INP there was a significant reduction of pharyngeal leak (fistula), surgical site infections, and LOS. Furthermore, the reduced rate of pharyngeal leak was also shown by De Luis et al.<sup>59</sup> in a randomized clinical trial setting and by Aeberhard et al. who reported a reduction of fistula in 411 patients.<sup>51</sup> However, the author reported missing “dynamic and laboratory parameters, and postoperative diet for each patient available.”<sup>56</sup> Interestingly, applying patients, Riso et al.<sup>41</sup> identified a significant reduction of major complications and LOS selectively in the malnourished subgroup.

#### 4.2 | Medical complications

Univariate logistic regression analysis showed that postoperative medical complications were correlated with preoperative dysphagia (OR 2.01, 95% CI 91.09–3.72,  $p = 0.026$ ), severe malnutritional status (OR 7.65, 95% CI 1.66–54.14,  $p = 0.016$ ), and ASA score  $\geq 2$  ( $p < 0.05$ ). Our data did not demonstrate any effect of INP on the rate of medical complications (including systemic infections), in agreement with the prospective randomized control study by Falwee et al.<sup>22</sup> that failed to demonstrate any association between patients and medical complications or surgical site infections, as shown in other clinical studies.<sup>21,57–60</sup> By contrast, Mueller et al.<sup>56</sup> reported the positive effects of preoperative patients on local or systemic complications in previously irradiated patients with HNSCC.

#### 4.3 | Length of hospital stay

The length of hospital stay (LOS) is a meaningful endpoint to be studied in this clinical setting, as it is well known that prolonged hospitalization can lead to higher risk of complications such as hospital infection, and is directly related with higher costs. While our analysis did not show any associations between groups, the available literature reports conflicting results in both head and neck surgery and abdominal surgery. Some authors have obtained a reduction of the LOS for the patients receiving both support.<sup>22,51–53,55,61</sup> Other authors have not observed any positive effects on LOS.<sup>21,22,51–53,55,56,59,60,62</sup> It is worthy to underline that this is a surrogate endpoint, since it depends on the occurrence of complications and could be strictly related to the patient's age, fragility, and

rehabilitation needed. Patients submitted to major head and neck surgical procedures involving the upper aerodigestive tract are likely to require postoperative rehabilitation. Despite the absence of any adverse event, the rehabilitation path could be the reason for prolonged hospitalization. Moreover, the need for rehabilitation increases the chance of developing aspiration pneumonia, as shown in patients undergoing partial laryngectomy, a further reason for prolonged hospitalization.<sup>63</sup>

#### 4.4 | Necessity of reintegration with human-derived components, albumin, or full blood

ALB is a plasmatic protein involved in many different functions such as oncotic pressure, capacity to bind substances (steroid, antibiotics, folate, and vitamin D), acid–base function (decrease in serum ALB leads to metabolic alkalosis), antioxidant function, and anticoagulant effects (heparin-like activity through enhancement of neutralization of factor Xa by antithrombin III).<sup>63</sup>

Postoperative hypoalbuminemia has been identified as a risk factor for developing medical and surgical complications.<sup>64–66</sup> Consequently, ALB correction to the target level leads to a better concentration of the antibiotic in the blood and hemodynamic and perfusion stability of the reconstruction.

In our multivariable analysis, we showed that INP reduced the need ALB supplementation ( $p = 0.018$ ). This is the mirror of a more stable plasmatic homeostasis attributable to INP. By multivariate analysis, hypopharyngeal and oral cavity cancers, ASA score higher than 1, reconstruction, and a moderate or severe malnutrition all increased the chance of pharmacological correction, despite the nutritional protocol adopted. As expected, higher preoperative ALB and Hb values were associated with a lower number of ALB vials used.

The analysis blood parameters, during the course of hospitalization, confirmed a possible benefit of INP in maintaining more stable values of ALB and Hb, particularly in malnourished patients.

#### 4.5 | Cost effectiveness

To the best of our knowledge, our study is one the first in the HNSCC field that carried out an accurate cost analysis using institutional budget data. Multivariate regression showed that the implemented nutritional support was cost-effective in malnourished patients. Specifically, in INP, in case of moderate malnutrition, we saved €6082.84 per patient, while in case of severe malnutrition,

the average gain increased to €11988.54. Two studies have previously explored the economic impact of immunonutrition in patients with cancer. In 2005, Braga et al. showed that preoperative supplementation in gastrointestinal surgery was a cost-effective strategy.<sup>67</sup> The authors gathered data from a randomized clinical trial on 305 patients with gastrointestinal cancer where the costs of complications were based on resources used for treatment and on LOS. In patients with HNSCC, Rowan et al. tried to estimate the clinical and economical benefits of both, but did not conduct an accurate cost-effective analysis.<sup>57</sup> They calculated the total cost of preoperative and postoperative nutrition for each patient (\$112.44) and compared this with the hypothetical cost of an additional 2.8 days of hospital stay, concluding that the cost of the specific nutrition is negligible compared to the cost of 2.8 days of hospital stay.

#### 4.6 | Conclusions

Our specific INP decreased major surgical complications, obtaining a significant reduction of revision surgery. The effectiveness of the protocol was also confirmed by the stabilization of serum ALB values and reduction of human derived ALB reintegration. Furthermore, in patients with moderate and severe malnutrition our intervention was cost-effective and decreased the need for blood transfusion. A limitation of our study is that the difference between various types of dysphagia (i.e., laryngeal vs. oropharyngeal cancers) was not detailed. Even if the pathophysiology may be different, the common consequence is insufficient oral intake leading to malnutrition and eventually cachexia. The nutritional protocol is guided by nutritional status and positioning of a feeding tube is chosen if dysphagia affects adequate oral intake, regardless of the cause. Our study supports the utility of accurate nutritional screening and patient selection. Standard nutritional support remains a good choice for nonmalnourished patients.

#### AUTHOR CONTRIBUTIONS

**Alessandro Ascoli:** Conceptualization; methodology; investigation; data curation; writing – original draft. **Francesco Missale:** Conceptualization; methodology; formal analysis; investigation; data curation; writing – review & editing; supervision. **Giorgio-Gregory Giordano:** Investigation; data curation; writing – original draft. **Alberto Vallin:** Investigation; data curation; writing – original draft. **Raffaella Gradaschi:** Investigation; data curation. **Erica Guido:** Investigation; data curation. **Guido Schenone:** Investigation; resources. **Samir Giuseppe Sukkar:** Methodology; resources. **Francesco**

**Copello:** Methodology; resources. **Giampiero Parrinello:** Investigation; resources. **Andrea Iandelli:** Validation; data curation; writing – review & editing. **Giorgio Peretti:** Conceptualization; resources; writing – review & editing; supervision. **Filippo Marchi:** Validation; investigation; writing – review & editing; supervision.


#### CONFLICT OF INTEREST

The authors declare that there is no conflict of interest that could be perceived as prejudicing the impartiality of the research reported.

#### DATA AVAILABILITY STATEMENT

Data are available on request from the authors.

#### ORCID

**Alessandro Ascoli**  <https://orcid.org/0000-0002-7375-5581>

**Francesco Missale**  <https://orcid.org/0000-0002-5357-5348>

**Giorgio-Gregory Giordano**  <https://orcid.org/0000-0002-7853-2889>

**Alberto Vallin**  <https://orcid.org/0000-0003-0471-2286>

**Andrea Iandelli**  <https://orcid.org/0000-0003-1187-3045>

**Filippo Marchi**  <https://orcid.org/0000-0002-7997-964X>

#### REFERENCES

1. Ferlay J, Shin HR, Bray F, Forman D, Mathers C, Parkin DM. Estimates of worldwide burden of cancer in 2008: GLOBOCAN 2008. *Int J Cancer*. 2010;127(12):2893-2917.
2. Simard EP, Torre LA, Jemal A. International trends in head and neck cancer incidence rates: differences by country, sex and anatomic site. *Oral Oncol*. 2014;50(5):387-403.
3. Hammerlid E, Wirblad B, Sandin C, et al. Malnutrition and food intake in relation to quality of life in head and neck cancer patients. *Head Neck*. 1998;20(6):540-548.
4. van Wayenburg CAM, Rasmussen-Conrad EL, van den Berg MGA, et al. Weight loss in head and neck cancer patients little noticed in general practice. *J Prim Health Care*. 2010;2(1):16-21.
5. Ackerman D, Laszlo M, Provisor A, Yu A. Nutrition management for the head and neck cancer patient. *Cancer Treat Res*. 2018;174:187-208.
6. de van der Schuer B, van Leeuwen PA, Kuik DJ, et al. The impact of nutritional status on the prognoses of patients with advanced head and neck cancer. *Cancer*. 1999;86(3):519-527.
7. Yanni A, Dequanter D, Lechien JR, et al. Malnutrition in head and neck cancer patients: impacts and indications of a prophylactic percutaneous endoscopic gastrostomy. *Eur Ann Otorhinolaryngol Head Neck Dis*. 2019;136(3):S27-S33.
8. Geeganage C, Beavan J, Ellender S, Bath PMW. Interventions for dysphagia and nutritional support in acute and subacute stroke. *Cochrane Database Syst Rev*. 2012;10:CD000323.
9. Bianchini C, Ciorba A, Stomeo F, Pelucchi S, Pastore A. Immunonutrition in head and neck cancer: Have a look before surgery! *Eur Arch Otorhinolaryngol*. 2012;269(1):5-8.

10. Correia MITD, Waitzberg DL. The impact of malnutrition on morbidity, mortality, length of hospital stay and costs evaluated through a multivariate model analysis. *Clin Nutr.* 2003;22(3): 235-239.
11. Spiro A, Baldwin C, Patterson A, Thomas J, Andreyev HJN. The views and practice of oncologists towards nutritional support in patients receiving chemotherapy. *Br J Cancer.* 2006; 95(4):431-434.
12. Sorensen J, Kondrup J, Prokopowicz J, et al. EuroOOPS: an international, multicentre study to implement nutritional risk screening and evaluate clinical outcome. *Clin Nutr.* 2008;27(3): 340-349.
13. Senesse P, Assenat E, Schneider S, et al. Nutritional support during oncologic treatment of patients with gastrointestinal cancer: who could benefit? *Cancer Treat Rev.* 2008;34(6): 568-575.
14. Dewys WD, Begg C, Lavin PT, et al. Prognostic effect of weight loss prior to chemotherapy in cancer patients. Eastern Cooperative Oncology Group. *Am J Med.* 1980;69(4):491-497.
15. Pan H, Cai S, Ji J, et al. The impact of nutritional status, nutritional risk, and nutritional treatment on clinical outcome of 2248 hospitalized cancer patients: a multi-center, prospective cohort study in chinese teaching hospitals. *Nutr Cancer.* 2013; 65(1):62-70.
16. Wie G-A, Cho Y-A, Kim S-Y, Kim S-M, Bae J-M, Joung H. Prevalence and risk factors of malnutrition among cancer patients according to tumor location and stage in the National Cancer Center in Korea. *Nutrition.* 2010;26(3):263-268.
17. Iwamoto M, Higashibeppu N, Arioka Y, Nakaya Y. Swallowing rehabilitation with nutrition therapy improves clinical outcome in patients with dysphagia at an acute care hospital. *J Med Invest.* 2014;61(3-4):353-360.
18. Ordoñez AM, Madalozzo Schieferdecker ME, Cestonaro T, Cardoso Neto J, Ligocki Campos AC. Nutritional status influences the length of stay and clinical outcomes in patients hospitalized in internal medicine wards. *Nutr Hosp.* 2013;28(4): 1313-1320.
19. Pearce CB, Duncan HD. Enteral feeding. Nasogastric, nasojejunal, percutaneous endoscopic gastrostomy, or jejunostomy: its indications and limitations. *Postgrad Med J.* 2002;78(918):198-204.
20. Valente da Silva HG, Santos SO, Silva NO, Ribeiro FD, Josua LL, Moreira ASB. Nutritional assessment associated with length of inpatients' hospital stay. *Nutr Hosp.* 2012;27(2): 542-547.
21. Howes N, Atkinson C, Thomas S, Lewis SJ. Immunonutrition for patients undergoing surgery for head and neck cancer. *Cochrane Database Syst Rev.* 2018;8(8):CD010954.
22. Falewee MN, Schilf A, Boufflers E, et al. Reduced infections with perioperative immunonutrition in head and neck cancer: exploratory results of a multicenter, prospective, randomized, double-blind study. *Clin Nutr.* 2014;33(5):776-784.
23. de Luis DA, Culebras JM, Aller R, Eiros-Bouza JM. Surgical infection and malnutrition. *Nutr Hosp.* 2014;30(3):509-513.
24. Chandra RK. Nutrition and the immune system: an introduction. *Am J Clin Nutr.* 1997;66(2):460-463.
25. Gombart AF, Pierre A, Maggini S. A review of micronutrients and the immune system-working in harmony to reduce the risk of infection. *Nutrients.* 2020;12(1):236.
26. Di Carlo V, Gianotti L, Balzano G, Zerbi A, Braga M. Complications of pancreatic surgery and the role of perioperative nutrition. *Dig Surg.* 1999;16(4):320-326.
27. Gianotti L, Braga M, Nespoli L, Radaelli G, Beneduce A, Di Carlo V. A randomized controlled trial of preoperative oral supplementation with a specialized diet in patients with gastrointestinal cancer. *Gastroenterology.* 2002;122(7): 1763-1770.
28. Wu GH, Zhang YW, Wu ZH. Modulation of postoperative immune and inflammatory response by immune-enhancing enteral diet in gastrointestinal cancer patients. *World J Gastroenterol.* 2001;7(3):357-362.
29. Piazza C, Del Bon F, Peretti G, Nicolai P. Narrow band imaging in endoscopic evaluation of the larynx. *Curr Opin Otolaryngol Head Neck Surg.* 2012;20(6):472-476.
30. Piazza C, Del Bon F, Paderno A, et al. The diagnostic value of narrow band imaging in different oral and oropharyngeal sub-sites. *Eur Arch Otorhinolaryngol.* 2016;273(10):3347-3353.
31. Seeburg DP, Baer AH, Aygun N. Imaging of patients with head and neck cancer: from staging to surveillance. *Oral Maxillofac Surg Clin North Am.* 2018;30(4):421-433.
32. Amin MB, Edge SB. *AJCC Cancer Staging Manual.* Vol 17. Springer; 2017:1032.
33. Dripps RD. New classification of physical status. *Anesthesiology.* 1963;24:111.
34. Kondrup J, Rasmussen HH, Hamberg O, Stanga Z. Nutritional risk screening (NRS 2002): a new method based on an analysis of controlled clinical trials. *Clin Nutr.* 2003;22(3):321-336.
35. Lam P, Stanschus S, Zaman R, Cichero JA. The International Dysphagia Diet Standardisation Initiative (IDDSI) framework: the Kempen pilot. *Br J Neurosci Nurs.* 2017;13(Suppl. 2): S18-S26.
36. Müller-Richter U, Betz C, Hartmann S, Brands RC. Nutrition management for head and neck cancer patients improves clinical outcome and survival. *Nutr Res.* 2017;48:1-8.
37. Barazzoni R, Deutz NEP, Biolo G, et al. Carbohydrates and insulin resistance in clinical nutrition: recommendations from the ESPEN expert group. *Clin Nutr.* 2017;36(2):355-363.
38. Duncan AE. Hyperglycemia and perioperative glucose management. *Curr Pharm des.* 2012;18(38):6195-6203.
39. Kirk SJ, Barbul A. Role of arginine in trauma, sepsis, and immunity. *JPEN J Parenter Enteral Nutr.* 1990;14(Suppl. 5): 226-229.
40. Ljungqvist O. ERAS-enhanced recovery after surgery: moving evidence-based perioperative care to practice. *JPEN J Parenter Enteral Nutr.* 2014;38(5):559-566.
41. Riso S, Aluffi P, Brugnani M, Farinetti F, Pia F, D'Andrea F. Postoperative enteral immunonutrition in head and neck cancer patients. *Clin Nutr.* 2000;19(6):407-412.
42. Forget P, Echeverria G, Giglioli S, Bertrand B, et al. Biomarkers in immunonutrition programme, is there still a need for new ones? A brief review. *Ecancermedicalscience.* 2015;9:546.
43. Alshadwi A, Nadershah M, Carlson ER, Young LS, Burke PA, Daley BJ. Nutritional considerations for head and neck cancer patients: a review of the literature. *J Oral Maxillofac Surg.* 2013;71(11):1853-1860.
44. van Bokhorst-de van der Schueren MA, van Leeuwen PA, Sauerwein HP, Kuik DJ, Snow GB, Quak JJ. Assessment of malnutrition parameters in head and neck cancer and their



- relation to postoperative complications. *Head Neck*. 1997;19(5):419-425.
45. Friedlander AH, Tajima T, Kawakami KT, Wang MB, Tomlinson J. The relationship between measures of nutritional status and masticatory function in untreated patients with head and neck cancer. *J Oral Maxillofac Surg*. 2008;66(1):85-92.
  46. Penn I. Immunosuppression and cancer. Importance in head and neck surgery. *Arch Otolaryngol*. 1975;101(11):667-670.
  47. Duray A, Demoulin S, Hubert P, Delvenne P, Saussez S. Immune suppression in head and neck cancers: a review. *Clin Dev Immunol*. 2010;2010:1-15.
  48. Tong CCL, Kao J, Sikora AG. Recognizing and reversing the immunosuppressive tumor microenvironment of head and neck cancer. *Immunol Res*. 2012;54(1-3):266-274.
  49. Fanslow WC, Kulkarni AD, Van Buren CT, Rudolph FB. Effect of nucleotide restriction and supplementation on resistance to experimental murine candidiasis. *JPEN J Parenter Enteral Nutr*. 1988;12(1):49-52.
  50. Surette ME. The science behind dietary omega-3 fatty acids. *C Can Med Assoc J*. 2008;178(2):177-180.
  51. Aeberhard C, Mayer C, Meyer S, et al. Effect of preoperative immunonutrition on postoperative short-term outcomes of patients with head and neck squamous cell carcinoma. *Head Neck*. 2018;40(5):1057-1067.
  52. Marimuthu K, Varadhan KK, Ljungqvist O, Lobo DN. A meta-analysis of the effect of combinations of immune modulating nutrients on outcome in patients undergoing major open gastrointestinal surgery. *Ann Surg*. 2012;255(6):1060-1068.
  53. Zhang Y, Gu Y, Guo T, Li Y, Cai H. Perioperative immunonutrition for gastrointestinal cancer: a systematic review of randomized controlled trials. *Surg Oncol*. 2012;21(2):e87-e95.
  54. Weimann A, Braga M, Carli F, et al. ESPEN guideline: Clinical nutrition in surgery. *Clin Nutr*. 2017;36(3):623-650.
  55. Stableforth WD, Thomas S, Lewis SJ. A systematic review of the role of immunonutrition in patients undergoing surgery for head and neck cancer. *Int J Oral Maxillofac Surg*. 2009;38(2):103-110.
  56. Mueller SA, Mayer C, Bojaxhiu B, et al. Effect of preoperative immunonutrition on complications after salvage surgery in head and neck cancer. *J Otolaryngol Head Neck Surg*. 2019;48(1):1-9.
  57. Rowan NR, Johnson JT, Fratangelo CE, Smith BK, Kemerer PA, Ferris RL. Utility of a perioperative nutritional intervention on postoperative outcomes in high-risk head & neck cancer patients. *Oral Oncol*. 2016;54:42-46.
  58. Vidal-Casariago A, Calleja-Fernández A, Villar-Taibo R, Kyriakos G, Ballesteros-Pomar MD. Efficacy of arginine-enriched enteral formulas in the reduction of surgical complications in head and neck cancer: a systematic review and meta-analysis. *Clin Nutr*. 2014;33(6):951-957.
  59. de Luis DA, Izaola O, Cuellar L, Terroba MC, Martin T, Aller R. Clinical and biochemical outcomes after a randomized trial with a high dose of enteral arginine formula in postsurgical head and neck cancer patients. *Eur J Clin Nutr*. 2007;61(2):200-204.
  60. van Bokhorst-de van der Schueren MA, Quak JJ, von Blomberg-van der Flier BM, et al. Effect of perioperative nutrition, with and without arginine supplementation, on nutritional status, immune function, postoperative morbidity, and survival in severely malnourished head and neck cancer patients. *Am J Clin Nutr*. 2001;73(2):323-332.
  61. Mueller SA, Mayer C, Bojaxhiu B, et al. Effect of preoperative immunonutrition on complications after salvage surgery in head and neck cancer. *J Otolaryngol Head Neck Surg*. 2019;48(1):25.
  62. de Luis DA, Aller R, Izaola O, Cuellar L, Terroba MC. Postsurgical enteral nutrition in head and neck cancer patients. *Eur J Clin Nutr*. 2002;56(11):1126-1129.
  63. Nicholson JP, Wolmarans MR, Park GR. The role of albumin in critical illness. *Br J Anaesth*. 2000;85(4):599-610.
  64. Huang W, Tang Y, Nong L, Sun Y. Risk factors for postoperative intra-abdominal septic complications after surgery in Crohn's disease: a meta-analysis of observational studies. *J Crohns Colitis*. 2015;9(3):293-301.
  65. Galata C, Busse L, Birgin E, et al. Role of albumin as a nutritional and prognostic marker in elective intestinal surgery. *Can J Gastroenterol Hepatol*. 2020;2020:7028216-7028218.
  66. Truong A, Hanna MH, Moghadamyeghaneh Z, Stamos MJ. Implications of preoperative hypoalbuminemia in colorectal surgery. *World J Gastrointest Surg*. 2016;8(5):353-362.
  67. Braga M, Gianotti L, Vignali A, Schmid A, Nespoli L, Di Carlo V. Hospital resources consumed for surgical morbidity: effects of preoperative arginine and omega-3 fatty acid supplementation on costs. *Nutrition*. 2005;21(11-12):1078-1086.

## SUPPORTING INFORMATION

Additional supporting information can be found online in the Supporting Information section at the end of this article.

**How to cite this article:** Ascoli A, Missale F, Giordano G-G, et al. Immunonutrition in major oncologic head and neck surgery: Analysis of complications, plasmatic equilibrium, and costs. *Head & Neck*. 2022;1-15. doi:[10.1002/hed.27270](https://doi.org/10.1002/hed.27270)



## Conclusion and future perspectives

The management of patients affected by HNSCC is often a challenging scenario. Despite it is well known that the immune system plays a crucial and detrimental role for the biological development and clinical progression of solid tumors, this is not yet taken into account for the current clinical management of patients affected by HSNCC. Furthermore, such management should take into account not alone the healing from the disease but also the consequences of the possible treatments in terms of change of the quality of life. The identification of new immune and molecular prognostic factors, as it is already done for oropharyngeal carcinoma (HPV-related tumor with a significant better prognosis), is of relevance to detect, for example, low-risk patients that could benefit of de-intensification strategies, avoiding side-effects related to the treatments. Studying the relationship between the immune system and cancer has also a secondary and very ambitious goal: the detection of mechanisms targetable by new drugs or known drugs already used for other indications. The results of my research suggest that three immune populations could have a role in the clinical behavior of HNSCC, specifically the tumor associated neutrophils (TAN), a population of intratumoral B-cells with pro-tumoral phenotype and the CD8+ T-reg subset. It was possible also to test methods to summarize multiple immunological features into metavariables to be used in new classifiers with satisfactory results, compared to the current TNM staging system. Furthermore, carrying on the clinical studies, reported in the second part of the thesis, it has been possible to contribute for the knowledge that could help in a precision-oncology approach. In a broad way, this can be also seen as the accurate estimation of survival predictions (helping in the clinical practice for the patient counseling), the comparison of different treatment techniques, the validation of new classifiers, the identification of clinical protocols as the immunonutrition, and the clinical settings for which its application is most suitable. Nowadays, the most powerful revolution regarding the treatment of solid tumors is the advent of immunotherapy, by the use of checkpoint blockade antibodies. In the field of HNSCC it is already approved for the palliative setting, but in the curative setting its use is still confined to clinical trials. The experience gained in the Netherlands Cancer Institute during my abroad staying permitted to get exposure to this novel and experimental treatment approach in the neoadjuvant setting (before the standard of care) for patients affected by HNSCC or cutaneous SCC. The already published results of the Phase I-II

IMCISION (NCT03003637) trial are satisfactory, confirming that the use of immunotherapy before surgical treatments for HNSCC is safe, and that achieving a major pathological response in the primary tumor is also a good biomarker for long-term oncological success. Besides that, two observed scenarios are of main interest: (1) the occurrence of a mixed pathological response in different tumor sites (primary tumor and lymph-nodes) in the same patient; (2) the occurrence of a complete clinical response (before the planned standard of care treatment) after the use of neoadjuvant immunotherapy. My current future research goal is the understanding of the biological reasons for a mixed response in different tumor sites within the same patient for patients enrolled in the IMCISION (NCT03003637) and MATISSE (NCT04620200) trials at the Netherlands Cancer Institute. In the controlled setting on a single patient where the mixed response is observed, it will be possible to understand if different tumor clones determine resistance to the therapy or if that role should be given to a different immune contexture.

**List of publications 11/2019 - 11/2022**

1. Ascoli, A., **Missale F.**, Giordano, G. G., Vallin, A., Gradaschi, R., Guido, E., ... & Marchi, F. (2022). Immunonutrition in major oncologic head and neck surgery: Analysis of complications, plasmatic equilibrium, and costs. *Head & Neck*.
2. **Missale F.**, Marchi, F., Iandelli, A., Subramaniam, N., Dokhe, Y., Sampieri, C., ... & Piazza, C. (2022). Oncological outcomes of compartmental surgery and wide local excision in oral tongue and floor of the mouth cancer. *Oral Oncology*, 135, 106210.
3. Bugatti, M.#, Bergamini, M.#, **Missale F.#.**, Monti, M., Laura, A., Pezzali, I., ... & Vermi, W. (2022). A population of TIM4+ FOLR2+ macrophages localized in tertiary lymphoid structures correlates to an active immune infiltrate across several cancer types. *Cancer Immunology Research*. #equally contributed as first authors
4. Filauro, M., **Missale F.**, Vallin, A., Mora, F., Marrosu, V., Carta, F., ... & Peretti, G. (2022). Functional outcomes after transoral CO2 laser treatment for posterior glottic stenosis: a bicentric case series. *European Archives of Oto-Rhino-Laryngology*, 1-9.
5. Fragale, M., Sampieri, C., Santori, G., Tripodi, C., **Missale F.**, Roustan, V., ... & Barbieri, M. (2022). Treatment of primary epiglottis collapse in OSA in adults with glossoepiglottopexy: a 5-year experience. *ACTA Otorhinolaryngologica Italica*, 1-8.
6. **Missale F.**, Ioppi, A., Ascoli, A., Camerino, P. L., Carobbio, A. L. C., Larghi, M., ... & Canevari, F. R. M. (2022). Cerebrospinal fluid leak repair: utility of intrathecal fluorescein for correct topographic identification of the skull base defects. *World neurosurgery*.

7. Monti M, Celli J, **Missale F**, Cersosimo F, Russo M, Belloni E, Di Matteo A, Lonardi S, Vermi W, Ghigna C, & Giurisato E. Clinical Significance and Regulation of ERK5 Expression and Function in Cancer. *Cancers*. 2022; 14(2):348. <https://doi.org/10.3390/cancers14020348>
  
8. Iandelli, A. #, **Missale F#\***, Laborai, A., Filauro, M., Marchi, F., Del Bon, F., Perotti, P., Parrinello, G., Piazza, C., & Peretti, G. (2021). Surgical management and oncological outcome of non-squamous cell carcinoma of the larynx: a bicentric study. *European archives of oto-rhino-laryngology*, <https://doi.org/10.1007/s00405-021-07076-x> #equally contributed, \* corresponding author
  
9. **Missale F\***, Bugatti, M., Mattavelli, D., Lonardi, S., Lombardi, D., Nicolai, P., Piazza, C., Battocchio, S., Bozzola, A. M., Calza, S., & Vermi, W. (2021). Metavariables Resuming Host Immune Features and Nodal Involvement Are Associated with Oncological Outcomes in Oral Cavity Squamous Cell Carcinoma. *Cells*, 10(9), 2203. <https://doi.org/10.3390/cells10092203> corresponding author
  
10. Filauro, M., Vallin, A., Marcenaro, E., **Missale F\***, Fragale, M., Mora, F., Marrosu, V., Sampieri, C., Carta, F., Puxeddu, R., & Peretti, G. (2021). Quality of life after transoral CO2 laser posterior cordotomy with or without partial arytenoidectomy for bilateral adductor vocal cord paralysis. *European archives of oto-rhino-laryngology*, 10.1007/s00405-021-06971-7. Advance online publication. <https://doi.org/10.1007/s00405-021-06971-7> corresponding author
  
11. **Missale F**, Taboni, S., Carobbio, A., Mazzola, F., Berretti, G., Iandelli, A., Fragale, M., Mora, F., Paderno, A., Del Bon, F., Parrinello, G., Deganello, A., Piazza, C., & Peretti, G. (2021). Validation of the European Laryngological Society classification of glottic vascular changes as seen by narrow band imaging in the optical biopsy setting. *European archives of oto-rhino-laryngology*, 278(7), 2397-2409. <https://doi.org/10.1007/s00405-021-06723-7>
  
12. Ardighieri, L.#, **Missale F#**, Bugatti, M., Gatta, L. B., Pezzali, I., Monti, M., Gottardi, S., Zanotti, L., Bignotti, E., Ravaggi, A., Tognon, G., Odicino, F., Calza, S., Missolo-Koussou, Y., Ries, C. H., Helft, J., & Vermi, W. (2021). Infiltration by CXCL10 Secreting Macrophages Is Associated With Antitumor Immunity and Response to Therapy in Ovarian Cancer Subtypes. *Frontiers in immunology*, 12, 690201. <https://doi.org/10.3389/fimmu.2021.690201> #equally contributed

13. Battaglini, D., **Missale F.**, Schiavetti, I., Filauro, M., Iannuzzi, F., Ascoli, A., Bertazzoli, A., Pascucci, F., Grasso, S., Murgolo, F., Binda, S., Maraggia, D., Montrucchio, G., Sales, G., Pascarella, G., Agró, F. E., Faccio, G., Ferraris, S., Spadaro, S., Faló, G., ... & Pelosi, P. (2021). Tracheostomy Timing and Outcome in Severe COVID-19: The WeanTrach Multicenter Study. *Journal of clinical medicine*, 10(12), 2651. <https://doi.org/10.3390/jcm10122651>
14. Fenoglio D, Belgioia L, Parodi A, **Missale F**, Bacigalupo A, Tarke A, Incandela F, Negrini S, Vecchio S, Altosole T, Vlah S, Astone G, Costabile F, Ascoli A, Ferrera F, Schenone G, De Palma R, Signori A, Peretti G, Corvó R, Filaci G. Development of Exhaustion and Acquisition of Regulatory Function by Infiltrating CD8+CD28- T Lymphocytes Dictate Clinical Outcome in Head and Neck Cancer. *Cancers*. 2021; 13(9):2234. <https://doi.org/10.3390/cancers13092234>
15. Lonardi, S.#, **Missale F#**. Calza, S., Bugatti, M., Vescovi, R., Debora, B., Uppaluri, R., Egloff, A. M., Mattavelli, D., Lombardi, D., Benerini Gatta, L., Marini, O., Tamassia, N., Gardiman, E., Cassatella, M. A., Scapini, P., Nicolai, P., & Vermi, W. (2021). Tumor-associated neutrophils (TANs) in human carcinoma-draining lymph nodes: a novel TAN compartment. *Clinical & translational immunology*, 10(2), e1252. <https://doi.org/10.1002/cti2.1252>. #equally contributed
16. Balasubramanian D, Subramaniam N, **Missale F**, Marchi F, Dokhe Y, Vijayan S, Nambiar A, Mattavelli D, Calza S, Bresciani L, Piazza C, Nicolai P, Peretti G, Thankappan K, Iyer S. Predictive nomograms for oral tongue squamous cell carcinoma applying the American Joint Committee on Cancer/Union Internationale Contre le Cancer 8th edition staging system. *Head Neck*. 2021 Feb 2. doi: 10.1002/hed.26554. Epub ahead of print. PMID: 33529403.
17. Carobbio ALC, Vallin A, Ioppi A, **Missale F**, Ascoli A, Mocellin D, Bagnasco D, Mora R, Peretti G, Canevari FRM. Application of bioendoscopy filters in endoscopic assessment of sinonasal Schneiderian papillomas. *Int Forum Allergy Rhinol*. 2021 Jan 12. doi: 10.1002/alr.22760. Epub ahead of print. PMID: 33438339.
18. Picchiotti N, Salvioli M, Zanardini E, **Missale F#**. COVID-19 pandemic: a mobility-dependent SEIR model with undetected cases in Italy, Europe, and US. *Epidemiol Prev*. 2020 Sep-Dec;44(5-6 Suppl 2):136-143. English. doi: 10.19191/EP20.5-6.S2.112. PMID: 33412804. #equally contributed

19. Carobbio ALC, **Missale F\***, Fragale M, Mora F, Guastini L, Parrinello G, Canevari FRM, Peretti G, Mattos LS. Transoral laser microsurgery: feasibility of a new exoscopic HD-3D system coupled with free beam or fiber laser. *Lasers Med Sci.* 2021 Jan 3. doi: 10.1007/s10103-020-03221-w. Epub ahead of print. PMID: 33389311. \*corresponding author
20. Lombardi D, Tomasoni M, Paderno A, Mattavelli D, Ferrari M, Battocchio S, **Missale F**, Mazzola F, Peretti G, Mocellin D, Borsetto D, Fussey JM, Nankivell P, Skalidi N, Bussi M, Giordano L, Galli A, Arrigoni G, Raffetti E, Pracy P, Vander Poorten V, Nicolai P. The impact of nodal status in major salivary gland carcinoma: A multicenter experience and proposal of a novel N-classification. *Oral Oncol.* 2020 Oct 30;112:105076. doi: 10.1016/j.oraloncology.2020.105076. Epub ahead of print. PMID: 33137587.
21. Filauro M, **Missale F**, Marchi F, Iandelli A, Carobbio ALC, Mazzola F, Parrinello G, Barabino E, Cittadini G, Farina D, Piazza C, Peretti G. Intraoral ultrasonography in the assessment of DOI in oral cavity squamous cell carcinoma: a comparison with magnetic resonance and histopathology. *Eur Arch Otorhinolaryngol.* 2020 Oct 21. doi: 10.1007/s00405-020-06421-w. Epub ahead of print. PMID: 33084951.
22. Marchi, F.#; **Missale Francesco#**; Sampieri, C.; Filauro, M.; Iandelli, A.; Parrinello, G.; Incandela, F.; Smeele, L.E.; van den Brekel, M.W.M.; Del Bon, F.; Nicolai, P.; Piazza, C.; Peretti, G. Laryngeal Compartmentalization Does Not Affect the Prognosis of T3-T4 Laryngeal Cancer Treated by Upfront Total Laryngectomy. *Cancers* 2020, 12, 2241. doi: <https://doi.org/10.3390/cancers12082241> #equally contributed
23. Mora, F.; Carta, F.; **Missale Francesco\***; Laborai, A.; Parrinello, G.; Piazza, C.; Puxeddu, R.; Peretti, G. Laryngeal Mid-Cord Erythroleukoplakias: How to Modulate the Transoral CO2 Laser Excisional Biopsy. *Cancers* 2020, 12, 2165. doi: <https://doi.org/10.3390/cancers12082165> \*corresponding author
24. Incandela F#, **Missale Francesco\*#**, Mora F, Marchi F, Fiz I, Piazza C, et al. Transoral management of adult benign laryngeal stenosis. *Eur Arch Oto-Rhino-Laryngology.* 2020; doi: <https://doi.org/10.1007/s00405-020-06210-5>. \*corresponding author; #equally contributed
25. Carobbio ALC, Filauro M, Parrinello G, **Missale Francesco\***, Peretti G. Microsurgical procedures during COVID-19 pandemic: the VITOM 3D-HD exoscopic system as alternative to



- the operating microscope to properly use personal protective equipment (PPE). *Eur Arch Oto-Rhino-Laryngology*. 2020; doi: <https://doi.org/10.1007/s00405-020-06239-6> \*corresponding author
26. Parrinello G, **Missale Francesco\***, Sampieri C, Carobbio ALC, Peretti G. Safe management of laryngectomized patients during the COVID-19 pandemic. *Oral Oncol*. 2020;107:104742. doi: <https://doi.org/10.1016/j.oraloncology.2020.104742> \*corresponding author
27. Giulio Eugenio Mandelli#, **Missale Francesco#**, Debora Bresciani, Luisa Benerini Gatta, Patrizia Scapini, Elena Cavegion, Elisa Roca, Mattia Bugatti, Matilde Monti, Luca Cristinelli, Sandra Belotti, Claudio Simeone, Stefano Calza, Laura Melocchi and William Vermi. Tumor Infiltrating Neutrophils Are Enriched in Basal-Type Urothelial Bladder Cancer. *Cells* 9.2 (2020): 291. #equally contributed
28. Narayana Subramanian, Filippo Marchi, Andrea Luigi Camillo **Missale Francesco**, Deepak Balasubramanian, Krishnakumar Thankappan, Subramania Iyer. Induction Chemotherapy in Sinonasal Malignancies: A Review of Literature. *Journal of Head & Neck Physicians and Surgeons*, 2019, 7.2: 52.
29. Filauro M, Mazzola F, **Missale F\***, Canevari FR, Peretti G. Endoscopic preoperative assessment, classification of stenosis, decision-making. *Journal: Frontiers in pediatrics*. 2020, 7: 532. \*corresponding author